**Université de Mons**
Faculté Polytechnique

**Université catholique de Louvain**
Ecole Polytechnique

**von Karman Institute for Fluid Dynamics**

# Numerical and experimental investigations of the meandering phenomenon in wind turbine wakes

Nicolas COUDOU

Thesis presented in partial fulfillment of the requirements for the degree of Doctor in Engineering Sciences and Technology

February 2021

**Jury**

Prof. Laurent Bricteux (UMONS), supervisor
Prof. Philippe Chatelain (UCLouvain), supervisor
Prof. Jeroen van Beeck (VKI), supervisor
Prof. Pierre Manneback (UMONS), chairperson
Prof. Grégoire Winckelmans (UCLouvain), secretary
Prof. Sandrine Aubrun (ECN)
Prof. Grégory Coussement (UMONS)
Dr. Matthieu Duponcheel (UCLouvain)
Prof. Véronique Feldheim (UMONS)
Prof. Thomas Pardoen (UCLouvain)

©2021
Nicolas Coudou
All Rights Reserved

# Abstract

The low-frequency oscillatory motion of wind turbine wakes, also known as wake meandering, is crucial in wind farms as it causes the wake to "periodically" and partially impact downstream machines, thus leading to aggravated unsteady fatigue loads. The wake meandering is therefore a central and fundamental challenge for the development of reliable and affordable wind energy. This research aims at the investigation of the horizontal axis wind turbine wake meandering physics through the combination of numerical and experimental tools.

The first step to study this phenomenon is to track the wake centerline. Several methods are assessed on Large-Eddy Simulations (LES) results of the NREL 5-MW wind turbine subjected to a synthetic turbulent inflow. The most robust technique is then applied to LES performed with several inflow turbulence levels. These simulations reveal that the wake meandering amplitude increases with the downstream distance from the rotor and with the inflow turbulence level, and that the wake meandering starts closer to the rotor when the inflow turbulence level increases. Furthermore, the wake meandering amplitude appears weaker in the vertical than in the horizontal plane due to the inflow anisotropy. From fairly constant wavelengths mainly ranging between $2.75D$ and $4.0D$ (with $D$ the wind turbine rotor diameter), Strouhal numbers between 0.2 and 0.3 are obtained using Taylor's frozen turbulence hypothesis. The strong correlations between the inflow centroid, the machine loads and the wake centroids in the near wake, and the fact that the wake meandering amplitude decreases when the inflow integral length scales are smaller, highlight the significant influence of the inflow turbulent scales on the wake meandering. In addition, it is shown that a modeling approach affordable at wind farm scale, i.e. a fourth-order finite difference code combined with an advanced actuator disk, provides equivalent results in terms of wake meandering compared to a method with a higher fidelity level, i.e. a Vortex Particle-Mesh method combined with immersed lifting lines, especially in the near wake or for the lowest inflow turbulence intensities.

Within the framework of this thesis, a complete experimental setup, including a control/acquisition board and a torque sensor system, is developed for a three-row three-column wind farm. This setup enables among others to measure the electrical and aerodynamic power produced by each machine. Time-resolved Particle Image Velocimetry (TR-PIV) measurements are performed in the horizontal plane at hub height for several configurations including an isolated wind turbine, a row of three wind turbines, a three-row three-column wind farm, and porous disks with various solidities. Each configuration is subjected to two Atmospheric Boundary Layers (ABLs). The incoming ABLs appear to largely influence the wake meandering characteristics obtained from the wake centerlines tracked in the horizontal plane. Investigating the various configurations shows that the wake meandering amplitude increases within the row of wind turbines, and that the lateral rows of the wind farm have no influence on the wake meandering characteristics of the central row. For the porous disks, the wake meandering amplitude decreases when the solidity decreases for only one of the two ABLs, which highlights the significant influence of the inflow. For the various configurations tested, wavelengths ranging between $2.50D$ and $3.75D$ were obtained, what results in Strouhal numbers ranging between 0.19 and 0.29 using Taylor's frozen turbulence hypothesis.

A modal analysis, referred to as multi-scale Proper Orthogonal Decomposition (mPOD), applied to the TR-PIV data enables to investigate the wake meandering dynamics and its dependency from the inflow.

Finally, numerical results obtained at wind tunnel scale show a good agreement with the experimental results in terms of wake meandering characteristics.

# Acknowledgments

I would like to thank in particular my supervisors Prof. Laurent Bricteux (UMONS), Prof. Philippe Chatelain (UCLouvain) and Prof. Jeroen van Beeck (VKI) for following me during this thesis. Thank you for always being available to discuss, for the time you dedicated to me, and for the numerous advice you provided to me all over the past few years. Three promotors is a lot but you were really complementary, which allowed me to have three different points of view on my research. That was really enriching for me!

I would like to thank the steering committee members of my thesis, i.e. Prof. Véronique Feldheim (UMONS), Prof. Pierre Manneback (UMONS), and Prof. Grégoire Winckelmans (UCLouvain) for their advice and guidance throughout this work. I would also like to thank all the members of my jury, i.e. in addition to the steering committee members, Prof. Sandrine Aubrun (ECN), Prof. Grégory Coussement (UMONS), Ir. Matthieu Duponcheel (UCLouvain), and Prof. Thomas Pardoen (UCLouvain) for accepting reviewing this work. All your comments and our discussions during the private defense enabled me to improve the quality of this manuscript.

I would like to acknowledge the VKI industrial engineers: Mathieu Delsipée for his help concerning the conception of several components of the wind turbine, Gertjan Glabeke for his technical advice concerning the facilities and the experimental setup, and Jimmy Freitas Monteiro for his help with Labview. I would also like to thank the drawing office members for the conception of several components of the wind turbine and the workshop for the manufacturing of the parts. I would like to thank Pierre Cuvelier and Remy Vostes from the electronic lab for the development of the acquisition/control board of the scale-model wind farm, as well as Terence Boyens and Oswald Divers for their meticulous assembly of the components of the models, especially concerning the torque sensor system. My thanks also go to the EA-VKI technical team Didier, Laurent, Michel, Momo, and Yves for their help in the preparation and instrumentation of the facilities involved in this study. My thanks go again to Prof. Grégory Coussement (UMONS) who made it possible to lend me the time-resolved PIV system of UMONS, and also to Alban Bourgeois for helping me with the installation of this system. The access to this state-of-the-art PIV system was a real plus for conducting my experimental research. My special thanks go to Miguel Alfonso Mendez for introducing me to modal analysis and for sharing with me his knowledge about it.

I would also like to acknowledge all the Short Training Program, Master, and Research Master students who contributed in one way or another to this thesis: Ahmad Zohreh Nejad, Romain Cums, Alexandre Gouttière, Louis Helbert, Salvatore Asaro, and Tobias Oswald.

I would like to thank my office mates Giulia, Maria Teresa, and Adriana. It was a pleasure to share the office with you, you are for sure much more than office mates. Thanks also to my other VKI colleagues and friends Arnaud, Ivan, Ludo, Mathieu, Sara, and Tânia. Thanks to my VKI Green Office mates, especially to Tânia! I am convinced that any step that could make the world greener is important, no matter how small it is. Thanks to my colleagues of UMONS and UCLouvain. I will remember the good work and sports atmosphere that reigns at TFL! Particular thanks to Thomas and DG for helping me with the VPM simulations and to Maud for her help with BigFlow simulations. Thanks also to all for all these good moments during conferences.

I would also like to thank my college friends Alessio, Laura, Luca, and Pierre for their support since the first baccalaureate, as well as my Research Master buddy, JB.

Finally, I would like to thank my family. Thanks mom for cheering me up when I was trying to solve bugs in the code and when I had problems with the experimental setup. Thanks Tom for your interest in my work and for our discussions about wind energy. Thanks grandma for always encouraging me. Thanks also to Margaux's parents for their encouragement. Last but not least, thank you Margaux for supporting me all the way, thank you for your understanding, in particular during the intensive testing campaigns and during the writing of this manuscript!

I would like to thank the *Fonds pour la Formation à la Recherche dans l'Industrie et dans l'Agriculture (FRIA)* which funded most of this thesis (September 2016 - September 2020) and the von Karman Institute for Fluid Dynamics for the additional funding (October 2020 - December 2020). Computational resources have been provided by the *Consortium des Équipements de Calcul Intensif (CÉCI)*, funded by the *Fonds de la Recherche Scientifique de Belgique (F.R.S.-FNRS)* under Grant No. 2.5020.11 and by the Walloon Region. The present research also benefited from computational resources made available on the Tier-1 supercomputer of the *Fédération Wallonie-Bruxelles*, infrastructure funded by the Walloon Region under the grant agreement No. 1117545.

# Contents


**1 Introduction** **1**
- 1.1 Context and motivations . . . 1
- 1.2 The wind turbine wake meandering phenomenon . . . 1
  - 1.2.1 Wind turbine wake . . . 1
  - 1.2.2 Wind turbine wake meandering . . . 3
- 1.3 Objectives and outline of the thesis . . . 6

**2 Numerical, experimental and analytical tools** **9**
- 2.1 Numerical tools . . . 9
  - 2.1.1 The Vortex Particle-Mesh (VPM) code . . . 9
  - 2.1.2 The fourth-order finite difference (FD4) code . . . 11
- 2.2 Experimental tools . . . 13
  - 2.2.1 VKI facilities . . . 13
  - 2.2.2 Measurements techniques . . . 15
- 2.3 Multi-scale Proper Orthogonal Decomposition (mPOD) . . . 21

**3 Wind turbine wake tracking algorithms** **27**
- 3.1 Numerical setup . . . 27
  - 3.1.1 VPM simulations . . . 27
  - 3.1.2 FD4 simulations . . . 28
- 3.2 Wake centroid detection in a cross-flow plane . . . 28
  - 3.2.1 Wake centroid computation through first order moment . . . 28
  - 3.2.2 Wake centerline detection through convolution . . . 32
- 3.3 Wake centroid detection in a horizontal plane . . . 41
- 3.4 Conclusions . . . 44

**4 Numerical study of wind turbine wake meandering characteristics at full scale** **45**
- 4.1 Numerical setup . . . 45
  - 4.1.1 VPM simulations . . . 45
  - 4.1.2 FD4 simulations . . . 45
  - 4.1.3 Turbulent inflow . . . 46
- 4.2 Results . . . 46
  - 4.2.1 Effects of the inflow turbulence intensity on the wake meandering characteristics 46
  - 4.2.2 Effects of the inflow integral length scales on the wake meandering characteristics 59
  - 4.2.3 Correlation between inflow, machine loads and wake centroid . . . 61
- 4.3 Conclusions . . . 67

**5 Wind turbine scale model and ABL modeling in low speed L-1B wind tunnel** **69**
- 5.1 Three-bladed wind turbine scale model . . . 69
  - 5.1.1 Model description . . . 69
  - 5.1.2 Performance curves . . . 70
  - 5.1.3 Airfoil aerodynamic coefficients . . . 80
- 5.2 Porous disks . . . 82
- 5.3 ABL modeling in low speed L-1B wind tunnel . . . 84

5.3.1 Atmospheric Boundary Layer (ABL) . . . 84
5.3.2 Stability of the atmosphere . . . 84
5.3.3 ABL modeling and characterization . . . 85
5.4 Conclusions . . . 97

**6 Wind turbine wake characteristics at wind tunnel scale 99**
6.1 Experimental setup . . . 99
6.1.1 Time-resolved PIV setup . . . 99
6.1.2 Wind turbine configurations and design of experiments . . . 101
6.1.3 Quality assessment of the TR-PIV measurements . . . 103
6.2 Inflow . . . 106
6.3 Isolated wind turbine . . . 108
6.3.1 Influence of the incoming ABL . . . 108
6.3.2 Influence of Reynolds number . . . 108
6.3.3 Influence of the wind turbine operating conditions . . . 112
6.4 Row of three wind turbines . . . 115
6.4.1 Isolated wind turbine vs. first and second wind turbines . . . 115
6.4.2 Isolated wind turbine vs. third wind turbine . . . 118
6.5 Wind farm . . . 121
6.5.1 Row vs. wind farm: first and second wind turbines . . . 121
6.5.2 Row vs. wind farm: third wind turbine . . . 123
6.6 Porous disks . . . 126
6.7 Conclusions . . . 130

**7 Wind turbine wake meandering characteristics at wind tunnel scale 133**
7.1 Experimental results . . . 133
7.1.1 Isolated wind turbine . . . 134
7.1.2 Row of three wind turbines . . . 145
7.1.3 Wind farm . . . 154
7.1.4 Porous disks . . . 162
7.2 Numerical results . . . 168
7.2.1 Numerical setup . . . 168
7.2.2 Comparison between numerical and experimental results . . . 171
7.3 Conclusions . . . 177

**8 Modal analysis of wind turbine wakes 179**
8.1 Inflow . . . 180
8.2 Isolated wind turbine . . . 185
8.2.1 mPOD analysis . . . 185
8.2.2 Wake tracking from mPOD field . . . 197
8.3 Wind turbine row . . . 201
8.3.1 Isolated wind turbine vs. first and second wind turbines . . . 201
8.3.2 Isolated wind turbine vs. third wind turbine . . . 211
8.4 Wind farm . . . 221
8.5 Porous disks . . . 221
8.5.1 Porous disk vs. three-bladed wind turbine model . . . 221
8.5.2 Influence of the porous disk solidity . . . 231
8.6 Conclusions . . . 239

**9 Conclusions & Perspectives 241**
9.1 Summary of investigations and major contributions . . . 241
9.2 Major findings . . . 244
9.3 Perspectives . . . 246

**A Computational aspects 255**
A.1 Tier-1 facilities . . . 255
A.2 Computational costs . . . 255

**B Probability distribution of the wake meandering amplitudes and wavelengths obtained from numerical simulations** **257**

**C Wind turbine blade characteristics** **263**

**D Uncertainty analysis** **265**
D.1 Uncertainty on wind speed from Pitot-static . . . 265
D.2 Uncertainty on electrical power . . . 267
D.3 Uncertainty on mechanical power . . . 268
D.4 Uncertainty on mechanical power measured from current . . . 270
D.5 Uncertainty on the thrust coefficient . . . 271
D.6 Uncertainty on airfoil lift/drag coefficients . . . 272
D.7 Uncertainty analysis for PIV . . . 274
D.7.1 Systematic error or bias error . . . 274
D.7.2 Random error . . . 277
D.7.3 Uncertainty on the measurements . . . 277
D.8 Uncertainty analysis for 3C-HWA . . . 278
D.8.1 Systematic error or bias error . . . 278
D.8.2 Random error . . . 279
D.8.3 Uncertainty on the measurements . . . 279

**E Faulhaber generator** **281**
E.1 Evolution of electrical and mechanical quantities . . . 281
E.2 Calibration of the balance for the thrust measurements . . . 282
E.3 Uncertainty on the thrust . . . 282

**F Wind turbine characteristics with 118516 Maxon generator** **283**

**G Aerodynamic coefficients of wind turbine airfoil** **289**
G.1 Drawings . . . 289
G.2 Calibrations . . . 292
G.2.1 Balance . . . 292
G.2.2 Pitot static . . . 292
G.3 Results . . . 293

**H Wind farm power production** **297**

**I Probability distribution of the wake meandering amplitudes and wavelengths** **301**
I.1 Isolated wind turbine . . . 302
I.1.1 Influence of Reynolds number . . . 302
I.1.2 Influence of wind turbine operating conditions . . . 304
I.2 Row of wind turbines . . . 306
I.2.1 Isolated wind turbine vs. first and second wind turbines . . . 306
I.2.2 Isolated wind turbine vs. third wind turbine . . . 308
I.3 Wind farm . . . 310
I.3.1 Row vs. wind farm: first and second wind turbines . . . 310
I.3.2 Row vs. wind farm: third wind turbine . . . 312
I.3.3 Porous disks . . . 314

**J mPOD results for wind farm configuration** **315**
J.1 Row vs. wind farm: first and second wind turbines . . . 315
J.2 Row vs. wind farm: third wind turbine . . . 324

# List of Symbols

## Acronyms

| | |
|---|---|
| ABL | Atmospheric Boundary Layer |
| AD | Actuator Disk |
| BEM | Blade Element Momentum |
| CAPEX | Capital expenditures |
| CFD | Computational Fluid Dynamics |
| CFL | Courant-Friedrichs-Lewy |
| DFT | Discrete Fourier Transform |
| DC | Direct Current |
| DMD | Dynamic Mode Decomposition |
| DWM | Dynamic Wake Meandering |
| FD | Finite Difference |
| FFT | Fast Fourier Transform |
| HAWT | Horizontal Axis Wind Turbine |
| HWA | Hot-Wire Anemometry |
| 3C-HWA | Three Components Hot-Wire Anemometry |
| LCOE | Levelized Cost of Energy |
| LDA | Laser Doppler Anenometry |
| LES | Large Eddy Simulation |
| mPOD | multi-scale Proper Orthogonal Decomposition |
| MRA | Multi-resolution Analysis |
| NREL | National Renewable Energy Laboratory |
| PIV | Particle Image Velocimetry |
| POD | Proper Orthogonal Decomposition |
| TR-PIV | Time-Resolved Particle Image Velocimetry |
| RVM | Regularized Variational Multiscale |
| S/N | Signal-to-Noise ratio |
| SVD | Singular Value Decomposition |
| TKE | Turbulent Kinetic Energy |

| | |
|---|---|
| TSR | Tip-speed ratio |
| VKI | von Karman Institute |
| VPM | Vortex Particle-Mesh |

## Roman symbols

| | | |
|---|---|---|
| $A$ | wake meandering amplitude | m |
| | surface in cross-flow plane | $m^2$ |
| $BF$ | Blockage factor | - |
| $c$ | chord length | m |
| $C_D$ | drag coefficient | - |
| $C_L$ | lift coefficient | - |
| $C_p$ | wind turbine power coefficient | - |
| $C_T$ | thrust coefficient | - |
| $D$ | wind turbine rotor diameter | m |
| | data matrix | m/s |
| $\Delta t$ | time step | s |
| $(\mathbf{e}_x, \mathbf{e}_y, \mathbf{e}_z)$ | orthonormal vectors | - |
| $f$ | frequency | Hz |
| $g$ | gravitational force | $N$ |
| $I$ | turbulence intensity | - |
| | current | A |
| $i_x$ | linear impulse | m/s |
| $K$ | temporal correlation matrix | $m^2/s^2$ |
| $L$ | turbulent integral length scale | m |
| $l_x$ | angular impulse | $m^2/s$ |
| $n$ | reduced frequency | - |
| $R$ | electrical resistance | $\Omega$ |
| | wind turbine rotor radius | m |
| $rk$ | rank | - |
| $p$ | pressure | Pa |
| | power density | $W/m^2$ |
| $Q$ | torque | Nm |
| $Re$ | Reynolds number | - |
| $St$ | Strouhal number | - |
| $s_1$ | velocity deficit | m/s |
| $s_2$ | momentum deficit | $m^2/s^2$ |

| | | |
|---|---|---|
| $U_\infty$ | free-stream velocity | m/s |
| $u_*$ | friction velocity | m/s |
| $T$ | temperature | K |
| | integral time scale | s |
| | thrust | N |
| $TSR$ | tip-speed ratio | - |
| $t_c$ | convective time | s |
| $t^*$ | normalized time | - |
| $V$ | Voltage | V |
| $y_c$ | wake centroid in the horizontal plane | m |
| $z_c$ | wake centroid in the vertical plane | m |
| $z_0$ | aerodynamic roughness length | m |

## Greek symbols

| | | |
|---|---|---|
| $\alpha$ | power law coefficient | - |
| | angle of attack | $^\circ$ |
| $\kappa$ | von Karman constant | - |
| $\lambda$ | wake meandering wavelength | m |
| $\nu$ | kinematic viscosity | $m^2/s$ |
| $\omega$ | vorticity | 1/s |
| | rotational speed | rad/s |
| $\rho$ | density | $kg/m^3$ |
| | auto-correlation coefficient | - |
| $\sigma$ | standard deviation | - |
| | porous disk solidity | - |
| $\tau$ | time lag | s |
| $\phi$ | spatial structure | - |
| $\psi$ | temporal structure | - |
| $\Phi$ | spatial structures | - |
| $\Psi$ | temporal structures | - |

## Sub- and Superscripts

| | |
|---|---|
| $FT$ | flow-through |
| $\bullet^{aero}$ | aerodynamic |
| $\bullet_c$ | convective |

| | |
|---|---|
| $\bullet^{elec}$ | electrical |
| $\bullet'$ | fluctuation |
| $\bullet_{\mathcal{F}}$ | related to Fourier transform |
| $\bullet_{fs}$ | full scale |
| $\bullet_{hub}$ | hub height |
| $\bullet_{\mathcal{M}}$ | related to mPOD |
| $\bullet_{\mathcal{P}}$ | related to POD |
| $\bullet_{rnd}$ | random |
| $\bullet_{ref}$ | reference |
| $\langle\bullet\rangle$ | space average |
| $\overline{\bullet}$ | time average |
| $\bullet_{WF}$ | wind farm |
| $\bullet_{WT}$ | wind turbine |

Chapter 1

# Introduction

## 1.1 Context and motivations

Between the years 2000 and 2019, the cumulative wind-power installations in the European Union increased from 12.9 GW to 205 GW [1, 2]. Based on the European Wind Energy Association's central scenario [3], wind-energy installations could amount to over 320 GW in 2030. This important rise in the use of wind energy over the years results in more and larger clustered wind farms. However, the development of wind energy as a primary and mainstream energy source still faces several challenges. Some of them lie in the very integration of such an uncertain and intermittent source into our energy grids but some quite fundamental challenges can be identified in the causes of these uncertainties.

Indeed, the wind flow conditions inside wind farms are quite uncertain; this is due to the wind resource and weather effects but also to the wakes of the wind turbines themselves. These regions of lower wind and increased turbulence are inherent to the energy extraction and impact turbines which are located downstream in the farm. This so-called wake phenomenon is one of the pivotal issues in wind farms and it is made worse by the trend to ever larger machines and wind farm sizes. These wakes dramatically affect the production, the reliability and the lifetime of wind farms, and therefore also impact the financial aspects (CAPEX), and the resulting levelized costs of energy (LCOE). This thesis investigates more closely one aspect of the wake dynamics, which is still poorly understood, the so-called wake meandering: the large-scale sweeping oscillatory motion of the wake.

This motion causes the wake to "periodically" and partially impact downstream machines, thus leading to aggravated unsteady fatigue loads, for the rotor blades, the drivetrain, and the nacelle yaw actuation system. Wake meandering is therefore a central and fundamental challenge for the development of reliable and affordable wind energy. This thesis aims at the investigation of wake meandering physics through the combination of numerical simulations and experimental studies.

## 1.2 The wind turbine wake meandering phenomenon

### 1.2.1 Wind turbine wake

The wake of a wind turbine (Fig. 1.1) is generally divided into near and a far wake regions [4]. The former is the region where the shape of the flow field is determined by the turbine geometry (blade

profile, hub and nacelle geometry), and extends from the turbine to approximately two to five rotor diameters downstream. As widely demonstrated in the literature, the most striking features of a turbine near-wake is perhaps the tip and root vortices shedding from the rotor blades [5]. In the near-wake region, the axial pressure gradient is important for the development of the wake deficit. The shed vortices undergo instabilities, merging, and reconnections to result eventually in a turbulent shear layer over the extend of the near wake. This shear layer thickens when moving downstream. When it becomes so thick that it reaches the wake axis, the end of the near-wake has been reached. The far wake is the region in which the actual detailed features of the wind turbine have less influence. Instead, global wind turbine parameters, such as the thrust and power coefficient, and incoming flow conditions, are sufficient to predict the mean flow distribution in this region [5]. In this part of the wake, the pressure gradients are negligible and the velocity deficit gradually decays, depending strongly on the turbulence level.

The grouping of wind turbines in a wind farm leads to substantial power losses, due to the reduced wind speed in the wakes, as well as to increased fatigue loads and associated maintenance costs, due to the increased turbulence levels [5]. Lissaman [6] showed that the wind farm layout and the ambient turbulence intensity are the two most important factors influencing array efficiency (i.e. the generated power of the total wind farm divided by the total power that could be generated by the same number of wind turbines if standing isolated). The influence of the wind farm layout is clear. Regarding the ambient turbulence intensity, a higher ambient turbulence level improves the momentum transfer into the wake. That reduces the velocity deficit and consequently the distance over which the wake recovers. Other factors that influence the array efficiency are the terrain configuration, the wind-frequency distribution (wind rose) and the operating settings of the turbines (e.g. thrust coefficient) [4]. Apart from the ambient turbulence, the additional turbulence created by the turbine is also important. In general, a higher turbulence level in the wake leads to larger loads for downstream turbines. However, due to the increased turbulence levels generated by the upstream turbine (compared with ambient turbulence levels), the turbulent mixing in the wake of a downstream turbine is more significant than in the wake of the upstream turbine. The wake of the downstream turbine recovers therefore more quickly than that of the upstream one. Consequently, while the second turbine experiences a significant decrease in power, the loss for the third turbine (and other successive machines) is much smaller [4].

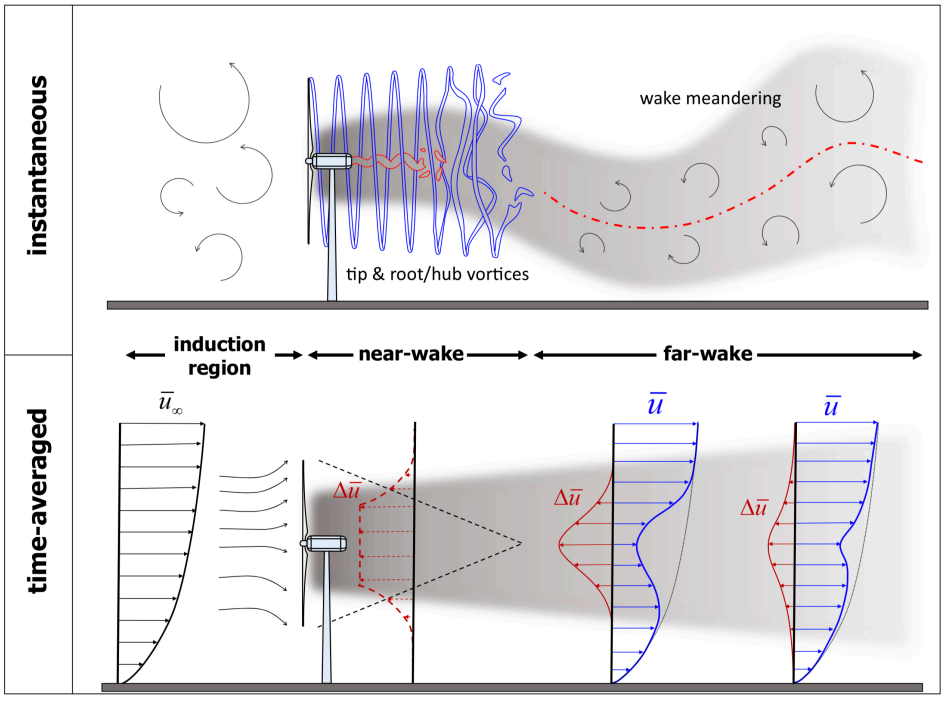



***Figure 1.1:*** *Wind turbine wake [5]*

### 1.2.2 Wind turbine wake meandering

Although the wind turbine wake meandering phenomenon (Figs. 1.1 and 1.2) is not yet well known, two main possible reasons for its formation have been suggested over the past few years. First, the intrinsic instabilities of the wake that could be associated with a periodic vortex shedding within the wake [7], the rotor swept disk of the wind turbine acting as a porous bluff body with decreasing permeability as the tip-speed ratio increases. Secondly, the effects of the large-scale turbulent eddies contained in the atmospheric boundary layer (ABL) as it is observed for plume-dispersion analysis [7].

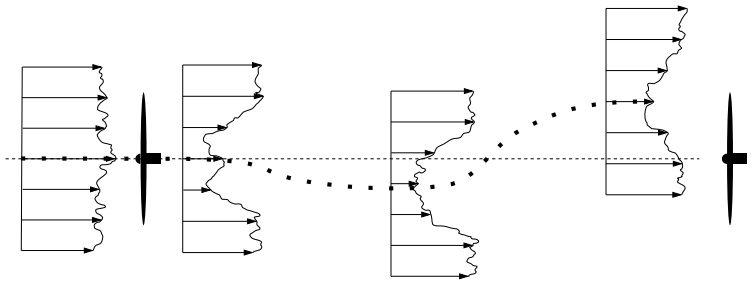


***Figure 1.2:*** *Wind turbine wake meandering, adapted from [8]*

The study performed by Medici and Alfredsson [9, 10] using a two-bladed wind turbine scale model submitted to a uniform free-stream revealed a low-frequency shedding of vortical structures from the turbine. They argued that the 3D low-frequency vortex shedding might be responsible for the wake-meandering motion. This shedding was observed both with and without free-stream turbulence and seems to be similar to the vortex shedding occurring for solid disks. The frequency of this shedding, expressed as a Strouhal number, was shown to be independent of the free-stream velocity or turbulence level, but the low-frequency fluctuation was only observed when the tip-speed ratio, or the thrust coefficient, were high ($TSR \geqslant 3$ or $C_T \geqslant 0.7$) [10]. Their measurements were supported by a theoretical study performed by Okulov and Sorensen [11]. However, as mentioned in the article of Larsen et al. [12], the vortex-shedding reported in Medici and Alfredsson [10] is believed to be associated with unrealistic loading conditions compared to the conditions present for a full-scale wind turbine located in the atmospheric boundary layer. Medici and Alfredsson [13] further complemented earlier studies of wind turbine wake meandering by studying the influence of the number of blades, the blade pitch angle and the tip-speed ratio on the meandering frequency. While all these parameters influence the thrust of the turbine, they showed that it is not only the thrust that influences the meandering frequency. They only observed meandering for the two- and three-bladed turbines when the rotational speed was high enough. Their measurements showed that the related Strouhal number may vary between 0.1 and 0.3 depending on the rotor configuration and on the wind turbine operating conditions.

Larsen et al. [12] consider wake meandering primary to be the result of large-scale air movements, in which the turbulent diffusion is of secondary importance. The fundamental assumption behind the theory developed by Larsen et al. [12] is that the wake meandering process can therefore be described as a series of consecutive wake "releases", each advected downstream with the mean wind field and displaced, in the plane perpendicular to the mean wind direction, by the large-scale turbulent structures. In relation to the large-scale turbulent structures, the individual wake "releases" are thus presumed to behave like passive tracers [12]. Based on this assumption, a dynamic wake meandering (DWM) model was developed by Larsen et al. [12, 14].

España et al. provided experimental evidence of the role of the large eddies on the wake meandering phenomenon behind a wind turbine modeled with a static porous disk [7, 15, 16]. Experiments were performed in neutral ABL conditions, and in homogeneous and isotropic turbulence (HIT) conditions. The results showed that the meandering process is only generated when the turbulent length scales are larger than the disk diameter, and that the meandering phenomenon, characterized by random oscillations of the wake, cannot be attributed to the periodic vortex shedding. It was also

observed that, in ABL conditions, horizontal displacements are higher than the vertical ones with a proportion in agreement with the ratio between the transverse and vertical turbulence intensities which was of two-thirds. Bastankhah and Porte-Agel [17] hypothesized yet that this difference is due to the lateral meandering tendency of very-large-scale motions (VLSMs) present in the incoming boundary layer. VLSMs or superstructures are very long low- and high-momentum structures observed both in the atmospheric surface layer and in the logarithmic region of a laboratory-scale boundary layer [18, 19].

From large-eddy simulations (LES) of an infinitely long row of turbines modeled using the actuator line technique, Andersen et al. [20] concluded that the large-scale motions of the wakes are mainly governed by the turbine spacing and to a lesser degree by the equivalent bluff body shedding ($St \simeq 0.19$). Therefore, they argue that low-frequency dynamics are not only related to the large scales of the atmospheric turbulence as implicitly assumed in DWM models but that the large-scale motions are an integrated and inseparable part of the entire wake dynamics.

Chamorro et al. [21] provided evidence of wake meandering for a hydrokinetic turbine located in a turbulent boundary layer. From Acoustic Doppler Velocimetry (ADV) measurements they reported that, at distances greater than three rotor diameters, the wake shows a strong lateral periodic motion of low frequency corresponding to a Strouhal number $St = 0.28$ at $x/D = 4$. They argued that this phenomenon could be related to the stability of the tip vortices as observed by Felli et al. [22] for a propeller wake.

Kang et al. [23] carried out a LES of the experimental flow of Chamorro et al. [21] to investigate the structure of turbulence in the wake of the turbine and to elucidate the mechanism that gives rise to wake meandering. They argue that the spiral instability (precession) of the hub vortex plays a major role in triggering and/or augmenting the intensity of far-field wake meandering. Indeed, they observed that the meandering of the wake is initiated close to the location where the hub vortex intercepts the outer shear layer.

From Laser Doppler Anemometry (LDA) measurements performed in the wake of a three-bladed wind turbine rotor mounted on a long arm and located in a water flume, Okulov et al. [24] found that the far wake oscillates periodically with a constant Strouhal number of approximately 0.23, independently of the operating conditions ($TSR$ and $U_\infty$). Based on particle image velocimetry (PIV) measurements, they argued that the oscillations of the far wake are associated with the precession of a helical vortex as observed in the far wake behind a sphere.

The works performed by Muller et al. [25] using static porous disks located in a neutral ABL showed that the instantaneous horizontal wake position correlates well with the transverse velocity measured one diameter upstream of the porous disk for wavelengths larger than three times the disk diameter, whereas it is not at all the case for wavelengths smaller than twice the disk diameter. This provides additional evidence of the role of the large turbulent structures on the wake meandering phenomenon. It was also argued that the lateral force is a better candidate than the upstream transverse velocity to predict in real time the meandering process since the coherent frequency range between the position of the wake and the lateral force is wider than the coherence with the upstream transverse velocity [25, 26]. Finally, using two porous disks located $5D$ apart from each other allowed to observe an amplification of the wake meandering for the downstream turbine because of the upstream wake. The experimental results presented in [25] were used to validate LES of a wind turbine modeled by an actuator disk and subjected to an atmospheric boundary layer. The numerical results show that the wake meandering is reproduced qualitatively and tend to demonstrate that the inflow low frequency content (large-scale turbulent structures) is an important parameter when simulating wake meandering and plays a significant role [27].

The DWM model originally introduced by Larsen et al. [12, 14] was validated with field data from the Egmond aan Zee offshore wind plant (OWEZ) [28], and was also compared to LES of the OWEZ in a study performed by Churchfield et al. [29] . This comparison showed that the overall wake effects on performance seen in the field data are reproduced by the DWM model, at much less cost than LES. However, DWM model fails to capture some aspects of wake meandering that occur deeper into a wind plant, and needs to be enhanced to account for multiple wake merging behavior.

From Particle Image Velocimetry (PIV) measurements performed in the wake of two three-bladed scale models placed in a neutral ABL, Howard et al. [30] reported that the velocity deficit in the wake, resulting from specific turbine operating conditions, appears to be a key governing parameter for meandering. Indeed, they noticed that a larger velocity deficit compresses the wake meanders in both horizontal directions. Moreover, they observed large-scale oscillations corresponding to $St \simeq 0.3$ for a wind turbine scale model operating at optimal tip-speed ratio.

Foti et al. [31] supplemented this study by conducting a LES of Howard's experimental setup. Their main conclusion is that the wake meandering emerges in the far wake when the precessing hub vortex begins to interact with the tip shear layer; the wake meandering frequency ranging in $0.15 < St < 0.3$.

The wake of a three-bladed wind turbine scale model in onshore (*moderately rough*) and offshore (*slightly rough*) neutral ABL conditions was investigated by Barlas et al. [32]. For offshore conditions, i.e. low turbulence level ($I = 7.5\%$ at hub height), a wake meandering mechanism was detected through a low-frequency peak in the turbulent energy spectrum. It was found that the Strouhal number related to this meandering was always $\simeq 0.25$, which is a typical value for bluff body vortex shedding [33]. Additional investigations were performed in offshore and onshore conditions downstream of a three-row three-column wind farm but, as for the isolated wind turbine in onshore conditions ($I = 17.5\%$ at hub height), the incoming turbulence level was too high for the meandering to survive [34]. A complementary study [35] performed for a three-row three-column wind farm shows that the meandering phenomenon persists in the scaled wind farm for a slightly higher turbulence intensity in the incoming boundary layer ($I = 10.5\%$ at hub height). A spatial analysis of the meandering structures existing in the large velocity fields obtained through PIV measurements and a temporal analysis of hot-wire anemometry measurements performed in the wake of the wind turbines lead both to a Strouhal number $St = fD/U_{hub} \simeq 0.20 - 0.22$.

Bastankhah and Porté-Agel [36] performed PIV measurements in the wake of an isolated wind turbine scale model ($D = 0.15$ m) subjected to an atmospheric boundary layer corresponding to a smooth terrain. They observed that the magnitude of the wake meandering is almost identical for different operating conditions, i.e. different tip-speed ratios and yaw angles, which in turn supports the hypothesis that the magnitude of wake meandering mainly depends on incoming boundary layer characteristics rather than turbine operating conditions.

Foti et al. [37] also investigated the similarity of wake meandering for different wind turbine designs for different scales. In their work, they observed similar wake meandering characteristics regardless of the wind turbine size and design, in particular a low frequency of $St = 0.25 - 0.3$ occurring only in the far wake. They also propose several quantities to scale properly the various parameters characterizing wake meandering. Furthermore, they observed that the tip-speed ratio and incoming turbulence intensity have a secondary effect on wake meandering dynamics compared to turbine thrust.

Mao and Sørensen [38] developed a 3D nonlinear solver to compute the optimal inflow eddies for the flow around a wind turbine, modeled as an actuator disk, to clarify the mechanisms behind wake meandering at low Reynolds number ($Re \leqslant 8000$). Their observations indicate that the wake meandering phenomenon is induced by large-scale (the same order as the turbine rotor) and low frequency free-stream eddies. They also observed a dominant Strouhal number $St = 0.16$ at $Re = 3000$ and that the meandering frequency becomes independent on the Reynolds number for $Re \geqslant 3000$. They conclude that wake meandering can be decomposed into two steps: firstly the large-scale inflow perturbations are amplified by the shear in the wake, and then the large coherent vortex structures in the wake are tilted and distorted by the amplified perturbations to induce meandering.

Foti et al. studied with LES the influence of the nacelle and of the operating conditions on the wake meandering for a scale model wind turbine [39]. They concluded that neither a nacelle nor an unstable hub vortex is a necessary requirement for the existence of wake meandering but that the unstable hub vortex - present when the nacelle is modeled - energizes the wake meandering. Indeed, they observed that the amplitude of wake meandering is less for the simulations without a nacelle (involving a stable and columnar hub vortex). Furthermore, they observed that the amplitude of

wake meandering varies with the operating conditions while the wavelength of wake meandering is similar regardless of nacelle modeling or turbine operating conditions. Finally, the spectral analysis they conducted reveals a wake meandering frequency most prevalent at $St = 0.3$.

As a conclusion, the different factors causing or influencing the wind turbine wake meandering, that were highlighted in the present literature review, are:

- a periodic vortex shedding within the wake, the rotor swept disk of the wind turbine acting as a porous bluff body with decreasing permeability as the tip-speed ratio increases [9, 10];
- the effects of the large-scale turbulent eddies contained in the ABL as observed for plume-dispersion analysis [7, 12, 15, 16, 36];
- the instability of the tip vortices [21] as observed for a propeller wake [22];
- the spiral instability (precessing motion) of the hub vortex, the meandering of the wake being initiated close to the location where the hub vortex intercepts the outer shear layer [23, 24, 31];
- the amplification of large-scale inflow perturbations by the shear in the wake, and then the inclination and distortion of the large coherent vortex structures in the wake by the amplified perturbations to induce meandering [38].

We stress that it is very likely that several of these factors causing or influencing the wind turbine wake meandering are present at once.

## 1.3 Objectives and outline of the thesis

The aim of this work is to investigate the wake meandering physics through the combination of cutting-edge numerical and experimental tools.

More specifically, the main objectives are:

- to develop algorithms to track the wake centerline of horizontal axis wind turbines;
- to develop reliable experimental systems (control/acquisition board, torque sensor) for a three-row three-column scale-model wind farm;
- to determine the wake meandering characteristics in terms of amplitude, wavelength and characteristic frequency for specific configurations: an isolated full-scale wind turbine, an isolated wind turbine scale model, a row of three wind turbine scale models, a three-row three-column scale-model wind farm, and isolated porous disks;
- to study the influence of the inflow turbulence intensity and inflow integral length scales on the wake meandering characteristics;
- to study the effects of the fidelity level of numerical simulations on the wake meandering characteristics;
- to analyze the wake meandering dynamics through modal analysis;
- to compare wake meandering characteristics obtained at wind tunnel scale and at full scale.

Chapter 2 describes the numerical and experimental tools. First, the Vortex Particle-Mesh (VPM) and the fourth-order finite difference (FD4) codes, used to perform the numerical simulations, are presented. Then, come the facilities and the measurements techniques used during this work. Finally, a particular modal analysis, developed by Mendez [40] (VKI) and referred to as multi-scale Proper Orthogonal decomposition (mPOD), is described at the end of the chapter.

Several wake tracking algorithms for horizontal axis wind turbines are proposed in Chapter 3. These algorithms are assessed on the numerical data obtained with the VPM and FD4 codes for an isolated wind turbine subjected to a turbulent inflow.

In Chapter 4, the most efficient algorithm of Chapter 3 is applied to study the wake meandering phenomenon, particularly in terms of amplitude, wavelength and characteristic frequency. The influence of the inflow turbulence, of the inflow integral length scales, as well as the influence of the fidelity level of the numerical simulations is assessed in this chapter. Finally, the correlation between the inflow, the machine loads and the wake centroid is investigated.

Chapter 5 describes the wind turbine scale models used in the experiments in terms of geometry, control/acquisition system, and electrical and aerodynamic performances. Finally, the ABL modeling in the VKI wind engineering wind tunnel is described at the end of the chapter.

Chapter 6 presents time-resolved PIV measurements performed for an isolated wind turbine, a row of three wind turbines, a three-row three-column wind farm, and isolated porous disks with several solidities, all subjected to two incoming ABLs. The mean streamwise velocity, the turbulence intensity and the power production are compared for the various configurations.

The wake meandering characteristics (amplitude, wavelength, and frequency) obtained at wind tunnel scale from the time-resolved PIV measurements are presented in Chapter 7. These results are then compared with numerical simulations performed at wind tunnel scale with the FD4 code.

In Chapter 8, the multi-scale Proper Orthogonal Decomposition (mPOD), is applied to the time-resolved PIV data presented in Chapter 7.

The conclusions and perspectives of this work are finally brought out in Chapter 9.

Chapter 2

# Numerical, experimental and analytical tools

This chapter describes the numerical and experimental tools, as well as the theory behind the multi-scale Proper Orthogonal Decomposition (mPOD). First, the Vortex Particle-Mesh (VPM) and the fourth-order finite difference (FD4) codes are presented. Then, come the facilities and the measurements techniques used during this work. Finally, the mPOD developed by Mendez [40] is described at the end of the chapter.

## 2.1 Numerical tools

### 2.1.1 The Vortex Particle-Mesh (VPM) code

#### 2.1.1.1 Flow solver

The Vortex Particle-Mesh code used in this work was jointly developed at ETH Zurich and UCLouvain. It combines the advantages of a particle method and of a mesh-based approach. This Vortex Particle-Mesh code [41, 42, 43] relies on the discretization of the velocity ($\mathbf{u}$)-vorticity ($\boldsymbol{\omega} = \nabla \times \mathbf{u}$) formulation of the Navier-Stokes equations in a Lagrangian form. For an incompressible flow, it gives

$$\frac{D\boldsymbol{\omega}}{Dt} = (\boldsymbol{\omega} \cdot \nabla)\,\mathbf{u} + \nu \nabla^2 \boldsymbol{\omega}, \tag{2.1}$$

$$\nabla \cdot \mathbf{u} = 0, \tag{2.2}$$

where $\frac{D}{Dt} = \frac{\partial}{\partial t} + \mathbf{u} \cdot \nabla$ denotes the Lagrangian derivative and $\nu$ is the kinematic viscosity.

Vortex particle methods [41, 42, 43, 44] discretize the vorticity field with particles, characterized by a position $\mathbf{x}_p$, a volume $V_p$ and a strength $\alpha_p = \int_{V_p} \boldsymbol{\omega} d\mathbf{x} \approx \boldsymbol{\omega}_p V_p$. Particles are advected by the flow field and their strength is modified to account for vortex stretching and diffusion [41]

$$\frac{d\mathbf{x}_p}{dt} = \mathbf{u}\left(\mathbf{x}_p\right), \tag{2.3}$$

$$\frac{d\boldsymbol{\alpha}_p}{dt} = \int_{V_p} \left((\boldsymbol{\omega} \cdot \nabla)\,\mathbf{u} + \nu \nabla^2 \boldsymbol{\omega}\right) d\mathbf{x} \tag{2.4}$$

$$\simeq \left((\boldsymbol{\omega} \cdot \nabla)\,\mathbf{u} + \nu \nabla^2 \boldsymbol{\omega}\right)_p V_p. \tag{2.5}$$

Since particles are used solely for the advection treatment, they enable to avoid dispersion errors and waive classical time stability constraints (CFL number). They also exploit the compactness of vorticity support. The velocity field $\mathbf{u}$, which is needed for the above particles evolution equations, can be recovered from the vorticity through a Helmholtz decomposition $\mathbf{u} = \mathbf{U}_\infty + \mathbf{u}_\omega$ and the Poisson equation

$$\nabla^2 \mathbf{u}_\omega = -\nabla \times \boldsymbol{\omega}. \tag{2.6}$$

The use of a mesh along with the particles in the VPM method offers several advantages. The mesh enables the treatment of the Lagrangian distortion through the periodic regularization onto the grid of the particles set (remeshing) [44]. In addition, the mesh handles the computationally intensive tasks: the evaluation of differential operators and the use of a Fourier-based fast Poisson solver for the computation of velocity, which allows the combination of unbounded directions and inlet/outlet boundaries. The solving of the Poisson equation in the unbounded domain using FFTs is based on the algorithm proposed by Hockney and Eastwood [45, 46]. The use of an unbounded computational domain proves to be very convenient for wind energy applications to avoid blockage effects while keeping a limited computational domain size. Both discretizations communicate through high-order interpolation.

Since the flow passing a wind turbine is a complex turbulent flow at high Reynolds number, it quite naturally imposes the use of a large-eddy simulation (LES) approach. The LES vorticity-velocity equations become then

$$\frac{D\boldsymbol{\omega}}{Dt} = (\boldsymbol{\omega} \cdot \nabla)\,\mathbf{u} + \nu \nabla^2 \boldsymbol{\omega} + \nabla \cdot \mathbf{T}^M \tag{2.7}$$

where $\boldsymbol{\omega}$ and $\mathbf{u}$ are the LES truncated vorticity and velocity fields, respectively, and $\mathbf{T}^M$ is the subgrid-scale stress model. In this work, the Regularized Variational Multiscale (RVM) model [47] is used. It is designed as an eddy viscosity model acting only on the small scales

$$\mathbf{T}^M = \nu_{SGS} \left( \nabla \boldsymbol{\omega}^s - \nabla^T \boldsymbol{\omega}^s \right) \tag{2.8}$$

where $\boldsymbol{\omega}^s$ represents the small-scales part of the vorticity field. The subgrid-scale eddy viscosity $\nu_{SGS} = C_r^{(n)} \Delta^2 \left(2S : S\right)^{1/2}$ is evaluated using the complete velocity field, i.e. the strain rate tensor is given by $S = \frac{1}{2}(\nabla \mathbf{u} + \nabla^T \mathbf{u})$. The LES cutoff $\Delta$ is taken equal to the mesh size $h$ [48]. The small scale vorticity field is computed by removing a low pass filtered vorticity field $\bar{\boldsymbol{\omega}}^{(n)}$

$$\boldsymbol{\omega}^s = \boldsymbol{\omega} - \bar{\boldsymbol{\omega}}^{(n)} \tag{2.9}$$

itself obtained by the iterated application of a discrete filter in physical space (n = 1 in the present work). A more detailed exposition of the subgrid-scale model can be found in [49].

Concerning the spatial and temporal discretization, a fourth-order finite difference scheme is used to carry out the differential operators and a third-order low-storage Runge-Kutta scheme is used for the time integration.

The numerical simulations were performed on the Tier-1 supercomputer *Zenobe*, whose main characteristics are presented in Appendix A.1.

#### 2.1.1.2 Blade modeling through immersed lifting lines

The generation of vorticity along the rotor blades is accounted for through immersed lifting lines. Under the assumption of slender blades, a blade can be approximated as a concentrated bound vortex going through the quarter-chord line, and the flow around the airfoil can be treated as essentially two-dimensional. For a steady flow, the lift per unit span $\mathbf{L}$ and the bound circulation $\boldsymbol{\Gamma}(r,t)$ are then related by the Kutta-Joukowski theorem

$$\mathbf{L} = \rho \mathbf{V}_{rel} \times \boldsymbol{\Gamma} \tag{2.10}$$

where $\rho$ is the air density and $\mathbf{V}_{rel} = \mathbf{u} - \mathbf{u}_{blade}$ is the velocity relative to the blade. The application of such a relationship in unsteady flow conditions means that the approach makes a quasi-steady assumption about the generation of lift and circulation around the airfoil. Since the lift can also be

obtained from the relative velocity and the airfoil lift coefficient $C_l$, the bound circulation $\mathbf{\Gamma}(r,t)$ can be computed as well as the shed vortex sheet from the solenoidal property of $\boldsymbol{\omega}$ (Fig. 2.1). The particle discretization of this bound vortex and the particle-mesh toolset then enable the interpolation of the velocity field onto these particles and the geometric construction of the shed vorticity with Lagrangian tracers à la vortex lattice method, accounting for time and space variations of the circulation $\mathbf{\Gamma}(r,t)$ (Fig. 2.1). This treatment is fully Lagrangian and allows large time steps unconstrained by the blade tip speed, unlike an actuator line technique [42].

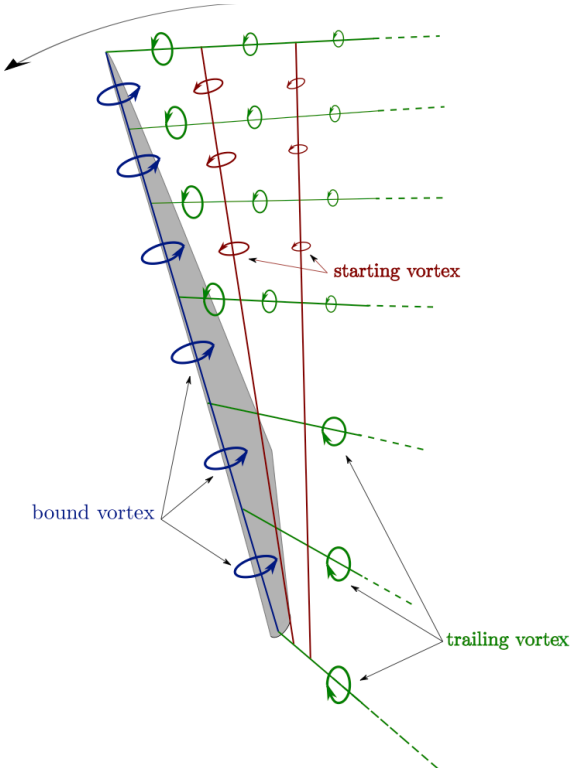



***Figure 2.1:*** *Immersed lifting line: blade vorticity sources modeled through a lifting line approach [42]*

#### 2.1.1.3 Turbulent inflow

The turbulent inflow velocity field $\mathbf{u}'$ can be either computed in a preliminary LES of homogeneous isotropic turbulence or synthesized through Mann's algorithm [50]. The second approach was followed in this work. In order to carry the turbulence into the domain through the inflow plane, this turbulent velocity field is translated into a set of vorticity particles, more adequate for the Lagrangian method used. Note that because of the unbounded conditions in the $y-$ and $z-$directions, this initially periodic velocity field is made compact through a smooth clipping along its edges. More detailed information about the inflow can be found in [42, 43].

### 2.1.2 The fourth-order finite difference (FD4) code

The VPM approach is well suited for high-fidelity and high-resolution simulations of an isolated wind turbine. However, it becomes unaffordable for simulations at wind farm scale for which another approach is required: LES on coarse meshes, performed using a fourth-order finite difference (FD4) code [51, 52, 53, 54, 55].

#### 2.1.2.1 Flow solver

The fourth-order finite difference code [51, 52, 53, 54, 55] used in this work was developed at UCLouvain and enables to perform LES of incompressible flows. It is formulated in primitive

variables, i.e. velocity and pressure, and used a staggered mesh arrangement. The evolution equations for the LES truncated velocity field are formulated as

$$\nabla \cdot \mathbf{u} = 0, \tag{2.11}$$

$$\frac{\partial \mathbf{u}}{\partial t} + (\mathbf{u} \cdot \nabla)\mathbf{u} = -\nabla P + \nu \nabla^2 \mathbf{u} + \nabla \cdot \boldsymbol{\tau}^M + \mathbf{f}, \tag{2.12}$$

where $P = \frac{1}{\rho} p$ is the reduced pressure field, $\rho$ is the fluid density, $\nu$ is the kinematic viscosity, $\boldsymbol{\tau}^M$ is the modeled SGS stress tensor which is a classical Smagorinsky model in this work, and $\mathbf{f}$ is the external body force introduced to model the effect of the wind turbine rotor onto the flow (see Section 2.1.2.2).

The system of equations (2.11) and (2.12) is solved using a fractional-step method with the "delta" form for the pressure [56]. The equations are discretized in space using a fourth-order finite difference scheme and an explicit second-order Adams-Bashforth scheme is used for the time integration. The Poisson equation for the pressure is solved using a multigrid solver with a Gauss-Seidel smoother [56].

For the simulations at wind tunnel scale with an ABL, a wall stress model for a rough wall is used [57].

The numerical simulations were performed on the Tier-1 supercomputer *Zenobe*, whose main characteristics are presented in Appendix A.1.

#### 2.1.2.2 Blade modeling through an actuator disk with tip-loss correction

The wind turbine rotor is modeled using an advanced AD for which the loads are estimated from local disk velocities [56]. With this AD modeling, information has to be exchanged between the rotor mesh, which is polar, and the LES Cartesian mesh (Fig. 2.2(a)). The radial and azimuthal resolutions of the polar mesh are fixed so that the larger polar cells are roughly the size of a cartesian cell [56]. The exchange of information is performed using high-order interpolation kernels as in the particle-mesh method. Once the velocities have been interpolated from the LES Cartesian grid to the polar grid, the axial and azimuthal velocity components, respectively $u_n$ and $u_\theta$, can be determined on each surface element $\Delta S = \Delta\theta \Delta r$ of the polar grid (Fig. 2.2(a)).

From $u_n$ and $u_\theta$, the rotor specifications (chord, twist and pitch angles) and the airfoil aerodynamic properties at the radius $r$, the aerodynamic loads can be computed for each $\Delta S$. For a blade element of length $\Delta r$, the lift $L$ and the drag $D$ forces (Fig. 2.2(b)) can be evaluated as

$$(L, D) = \frac{1}{2} \rho V_{\text{rel}}^2 \, c \Delta r \, (C_l, C_d) \tag{2.13}$$

where $V_{\text{rel}}$ is the relative velocity defined as

$$V_{\text{rel}} = \sqrt{u_n^2 + (\Omega r + u_\theta)^2} \tag{2.14}$$

with the rotor speed $\Omega$, the chord length $c$, and the lift and drag coefficients $C_l$ and $C_d$, respectively. These are obtained from the effective angle of attack $\alpha$ and tabulated 2D airfoil data; $\alpha$ being computed from the difference between the flow angle, $\phi = \arctan\left(\frac{u_n}{\Omega r + u_\theta}\right)$, and the sum of the twist $\beta$ and pitch $\gamma$ angles [56].

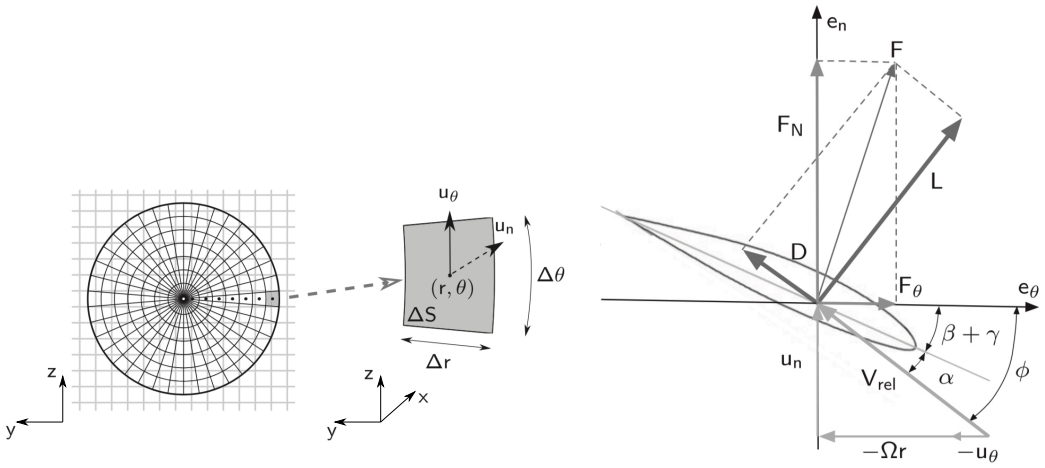
The forces in the normal and tangential directions to the disk plane can then be computed from the lift $L$ and drag $D$ forces, and the flow angle $\phi$ (Fig. 2.2(b))

$$F_N = L \cos\phi + D \sin\phi \quad \text{and} \quad F_\theta = L \sin\phi - D \cos\phi. \tag{2.15}$$

The loads on $\Delta S$ can then be obtained by multiplying $F_N$ and $F_\theta$ by the number of blades $N_b$ and by a weight that corresponds to the ratio between the surface element and the total annular surface at the given radius $r$ [56]

$$\begin{aligned} F_{N,AD} &= F_N N_b \tfrac{\Delta S}{2\pi r \Delta r}, \\ F_{\theta,AD} &= F_\theta N_b \tfrac{\Delta S}{2\pi r \Delta r}. \end{aligned} \tag{2.16}$$

These forces are finally translated into external body forces $\mathbf{f}$ (Eq. (2.12)) using a second-order mollifier that ensures a non-oscillatory projection of these forces onto the mesh [56].




(a) (b)

***Figure 2.2:*** *Schematics of the Cartesian and polar meshes (a), and of the airfoil element (b), adapted from [56]*

The actuator disk approach presented above is based on an azimuthal averaging of the loading due to $N_b$ blades. This means that all fluid particles passing through the disk at the same radius $r$ will experience the same change of momentum. For an actual rotor, however, the change of momentum is larger close to the blades than between the blades. This is why, if one wants to perform an airfoil performance lookup, it is necessary to account for this induction to obtain the correct velocity and angle of attack at the blade. Additionally, the discrete nature of the shed tip vortices strongly modifies the induced velocities in the vicinity of the blade tips; these are the so-called tip-loss effects. Tip-loss corrections exist but have to be applied on the induction factors, which requires the definition of an upstream velocity. To recover the actual induction at a blade location, the present AD model has therefore been supplemented with a tip-loss correction based on a local estimation of the effective upstream velocity at every point of the AD [56, 57].

#### 2.1.2.3 Turbulent inflow

As for the VPM approach, the turbulent inflow velocity fields $\mathbf{u}'$ are synthesized through Mann's algorithm [50]. For the simulations at wind tunnel scale with an ABL, a logarithmic law is superimposed on the velocity field obtained with the Mann's algorithm.

## 2.2 Experimental tools

### 2.2.1 VKI facilities

#### 2.2.1.1 Low speed L-2B wind tunnel

The L-2B facility (Fig. 2.3) is a low speed, Eiffel-type (open circuit) wind tunnel. It incorporates several interchangeable test sections of 0.35 meter height, 0.35 meter width and various lengths from 0.9 meter to 2 meters. A test section which opens into a larger chamber of 0.50 meter height and 0.65 meter width, designed to reproduce an open jet facility and thus reduce the blockage effect, is also available. This test section was used in the context of this thesis. The axial fan at the end of a circular diffuser is driven, through a belt, by a 4.4 kW variable-speed DC motor, providing a maximum velocity of 35 m/s [58]. In order to generate a uniform velocity profile with low turbulence intensity in the test section, an air inlet fitted with honeycomb and meshes, as well

as a two-dimensional contraction nozzle are used [58, 59]. Based on [60], the turbulence intensity is approximately 1%.

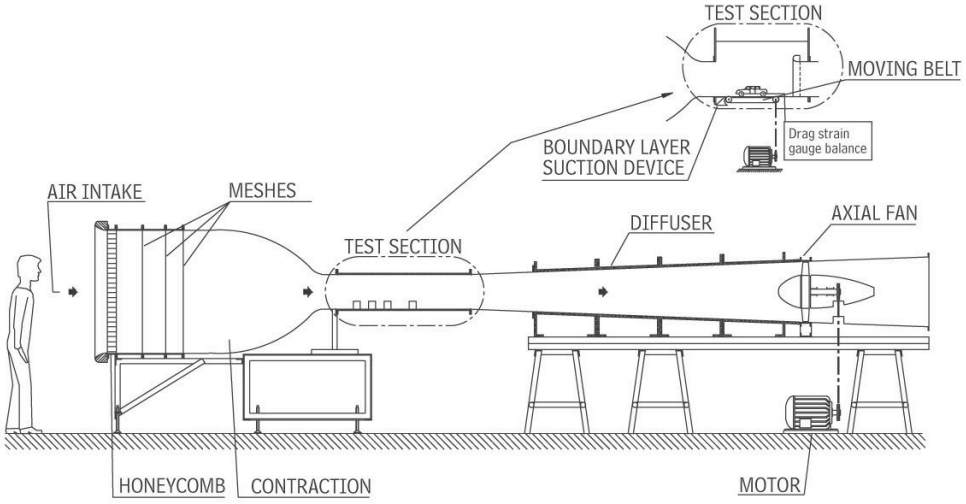



***Figure 2.3:*** *Schematic of the low speed L-2B wind tunnel [61]*

#### 2.2.1.2 Low speed L-1B wind tunnel

The L-1B wind engineering facility is a low-speed, closed-loop wind tunnel. Two contra-rotating fans driven by a 580 kW DC motor allow to vary the flow velocity between 2 m/s and 50 m/s making it one of the most powerful facilities of this type. The rectangular test section of the L-1B wind tunnel is 2 m high, 3 m wide, and 20 m long. Different floors with variable roughness elements enable the growth and the control of a turbulent boundary layer similar in nature to the lower part of the atmospheric neutral boundary layer. At the end of the section, a 2.6 m diameter turntable is provided for investigation of building aerodynamics as a function of wind direction in order to evaluate pedestrian wind comfort, and for studying wind resource for turbine siting and the wake effect in and outside wind farms [62, 63].

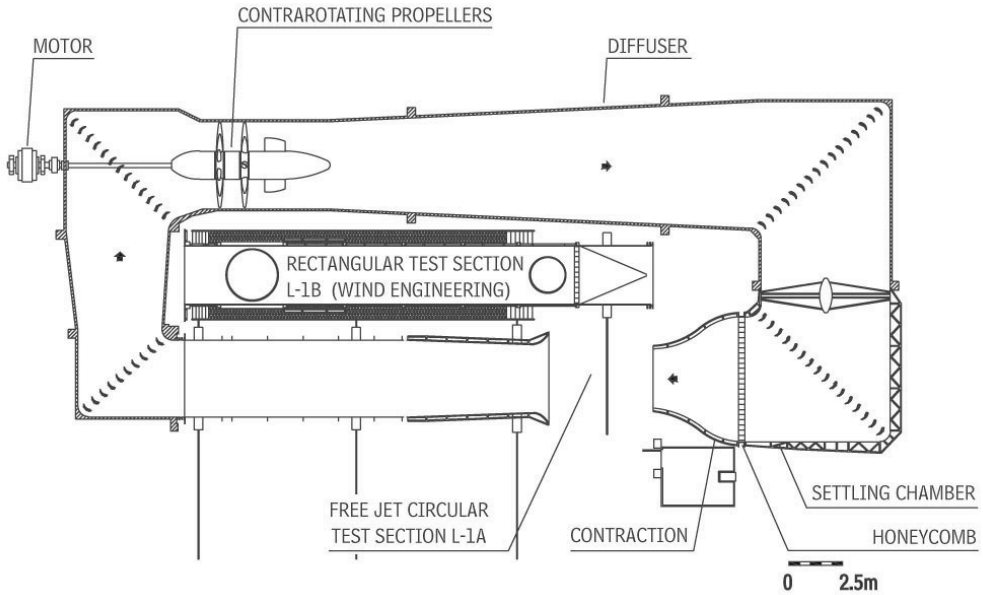



***Figure 2.4:*** *Schematic of the low speed L-1B wind tunnel [62]*

## 2.2.2 Measurements techniques

### 2.2.2.1 Particle image velocimetry

Particle Image Velocimetry (PIV) is a non-intrusive technique (except for the presence of seeding particles in the flow) whose basic principle is the following: the instantaneous velocity of a fluid is measured through the determination of the displacements, during a time interval $\Delta t$, of tracer particles illuminated by a laser light sheet [64] (Fig. 2.5). This technique consists consequently in two main steps: the first one is the recording of pairs of images, the images composing a pair being separated by a time interval $\Delta t$, and the second one is the processing of the images using cross-correlation to determine the tracer displacements.

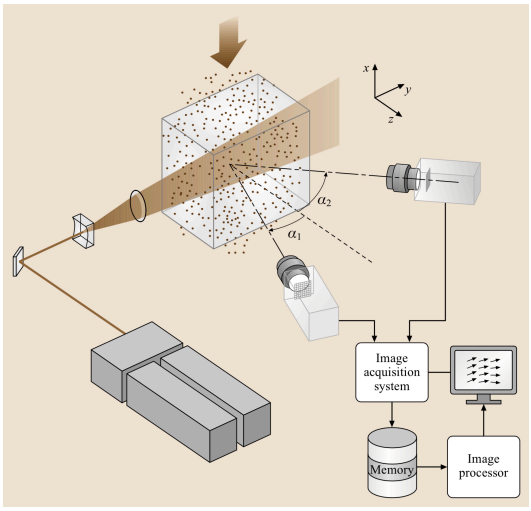



***Figure 2.5:*** *Schematic of a typical PIV measurement system [65]*

#### Seeding of the flow

The PIV technique measures the velocity of tracers added to the flow. These tracers have to be small enough to genuinely follow the flow while having a sufficient size to produce enough scattering for images to be recorded [64]. Moreover, particles concentration is one of the most important parameter that determines the quality of the measurement. In practice, in order to be able to measure velocity at every location of the 2D plane, tracers concentration has to be adjusted to the highest possible value staying in the PIV mode, i.e. that particle images are still distinguishable from each other.

#### Sheet illumination

Two pulsed lasers are used to provide a very short and bright light flash to "freeze" the tracer particles in the measurement plane. The optics after the laser are settled to produce a thin laser light sheet. The alignment of this laser light sheet with the flow direction is of utmost importance. Indeed, if the laser light sheet is not correctly aligned with the mean flow direction, a loss of particles occurs between the two images as the particles illuminated by the light sheet during the first laser pulse are no longer in the light sheet during the second pulse.

#### Camera(s)

For two-dimensions two-components PIV (2D2C-PIV), the camera(s) has/have to be placed perpendicularly to the laser light sheet to obtain a well-focused image of the illuminated tracer particles. As the tracer particles have to be small enough to follow the flow, they only scatter a small amount of light. Since this light is collected at 90° from the incoming laser light, a large aperture has to be use in order to collect the largest possible amount of light [64]. Using a large

aperture requires then to adjust the focusing of the camera with great care as the depth of field is consequently very small.

**Processing**

The successive images constituting a pair, separated by a time interval $\Delta t$, are processed to find the instantaneous velocity field. The first step of the processing consists in splitting the images pair in several cells called interrogation windows. The cross-correlation between each couple of corresponding windows is then computed to determine the statistical mean displacement $d$ [px] given by the position of the correlation peak. To ensure a good quality of the correlation between two corresponding interrogation windows, i.e. a sufficiently high signal-to-noise ratio (defined as the ratio between the highest peak and the second highest peak of the cross-correlation map), most of the particles present in the interrogation window of the first image of a pair should remain in the corresponding interrogation window of the second image. In order to ensure this, it is commonly accepted that the maximum expected displacement of the tracer particles should not to exceed one quarter of the initial window size. This rule is known as the *one-quarter rule*. This rule is quite restrictive for the resolution. A way to overcome it is to apply so-called refinement steps: 1) the windows size is fixed by the *one-quarter rule* and a cross-correlation is applied to determine the average velocity of the windows; 2) the windows are refined and a second cross-correlation is performed after removing the mean displacement calculated in the first step. The remaining displacements being very small, the windows can be refined several times, improving a lot the resolution. However, since the cross-correlation is a statistical operation, a minimum number of particles has to be present in each window. It is commonly accepted that at least 10 particles should be present to apply the cross-correlation function. To overcome this limitation on the final windows size and therefore to increase the spatial resolution, an overlapping procedure can be applied to the last refinement step (the windows can overlap each other in each direction instead of being positioned side-to-side).

Since the correlation map is obtained on a discrete mesh after image processing, the precision of the measurement of the displacement is $\pm 0.5$ pixels. In order to increase the precision in the displacement determination, an interpolating function can be used to fit the cross-correlation peak [64]. This technique is known as the sub-pixel interpolation. The most commonly used method for the sub-pixel estimation of the displacement is the three-point Gaussian peak fit [65]. The application of the sub-pixel interpolation can nevertheless introduce a systematic error known as peak locking. The effect originates from the fact that the displacement-correlation peak increasingly deviates from its assumed Gaussian shape for decreasing size of the image of the tracer particles, what enhances biasing towards integer pixel displacements [65]. Peak locking can for instance be overcome using particle images whose size is larger than two pixels and by avoiding pixel displacement of $k + 0.5$, $k$ being an integer [65].

From the magnification factor $M$ [mm/px] determined through calibration, the flow velocity $u$ [mm/s] can be computed from the displacement of the particle images $d$ [px] and the time interval $\Delta t$ [s] between successive images constituting a pair as

$$u = M \frac{d}{\Delta t} + \Delta u \tag{2.17}$$

where $\Delta u$ is a parameter which takes into account that the information of the images differ from the flow field due to the velocity lag of the tracer particle from acceleration and projection procedure from 3-D physical space to 2-D image plane [66]. Usually, this last term is neglected ($\Delta u$ assumed zero).

The interested reader can find additional information in [64] and [65].

#### 2.2.2.2 Three components hot-wire anemometry

**Basic principles**

The hot-wire anemometer, composed of a probe and electronics, is a basic research tool, essential in turbulent flow measurements. The working principle of a constant temperature anemometer

(CTA) is the following. The electronics provide a controlled amount of electrical current to heat, at a constant temperature, the very thin wire held between two prongs. When the wind blows, it cools down the wire and a higher tension is needed to maintain the wire at its chosen temperature. Therefore, after a careful calibration to link the flow velocity to the tension supplied by the electronics to the wire to maintain its temperature, the wind velocity can be computed from the tension acquired. The main advantage of this technique is its very short response time; the frequency response can typically reach 15 kHz. Its main drawbacks are that it depends on the air temperature, it is fragile due to the dimensions of the wire, and it is a point-wise and intrusive technique [60].

### Frames and rotation matrix

The incoming wind profiles modeled in the wind tunnel were characterized using a Dantec 55P91 triple hot-wires probe (Fig. 2.6). This triple hot-wires probe is composed of three hot-wires laid out to be orthogonal to each other in order to measure the three velocity components ($U$, $V$, and $W$). Each wire, which is in tungsten and has a diameter of 9 $\mu$m, is connected with its own Wheatstone bridge to obtain the best frequency response.



(a) (b)

***Figure 2.6:*** *Picture (a) and schematic (b) [67] of the Dantec 55P91 triple hot-wires probe*

The three orthogonal wires of the probe are forming the wire frame $(X_1, X_2, X_3)$. This frame is rotated in two directions compared to the probe frame $(X, Y, Z)$ which is also the wind tunnel frame, i.e. that the velocity components $(U, V, W)$ are aligned with the streamwise, transverse and vertical directions $(X, Y, Z)$, respectively (Fig. 2.7) [60]. From the two angles $\theta$ and $\varphi$, around $X_3$ and $Y$ respectively, a rotation matrix $R$ can be defined to go from one frame to the other. Considering the velocity components, it gives

$$\begin{pmatrix} U \\ V \\ W \end{pmatrix} = R \cdot \begin{pmatrix} U_1 \\ U_2 \\ U_3 \end{pmatrix} \tag{2.18}$$

with

$$R = \begin{pmatrix} \cos\varphi \cdot \cos\theta & \cos\varphi \cdot \sin\theta & \sin\varphi \\ -\sin\theta & \cos\theta & 0 \\ -\sin\varphi \cdot \cos\theta & -\sin\varphi \cdot \sin\theta & \cos\varphi \end{pmatrix} = \begin{pmatrix} 1/\sqrt{3} & 1/\sqrt{3} & 1/\sqrt{3} \\ -1/\sqrt{2} & 1/\sqrt{2} & 0 \\ -1/\sqrt{6} & -1/\sqrt{6} & 2/\sqrt{6} \end{pmatrix} \tag{2.19}$$

where $\theta = 45°$ around $X_3$ and $\varphi = 35.3°$ around $Y$.

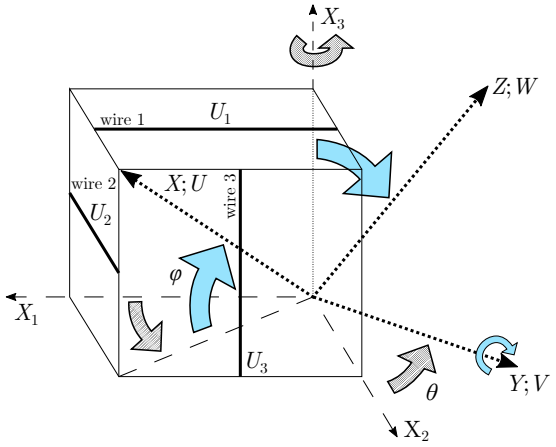



***Figure 2.7:*** *Wire frame* $(X_1, X_2, X_3)$ *and probe frame* $(X, Y, Z)$ *of the Dantec 55P91 triple hot-wires probe, adapted from [60]*

### Effective cooling velocity

The effective cooling velocity $U_{eff}$ of a wire is linked to the three components of the velocity in the frame of the wire by the Jørgensen law [68]

$$U_{eff}^2 = U_N^2 + U_B^2 \cdot h^2 + U_T^2 \cdot k^2 \tag{2.20}$$

with the velocity component normal to the wire $U_N$, the velocity component bi-normal to the wire $U_B$, the velocity component tangential to the wire $U_T$, and the sensitivity coefficients $h$ and $k$ for the pitch and the yaw angle, respectively.

The Jørgensen law applied to each wire gives three equations. In this particular case of three orthogonal wires, the normal direction of the first wire is also the tangential direction of the second wire and the bi-normal direction of the third wire; this relationship between wires being maintained in a cyclic order [60]. The Jørgensen law written for each wire reduces therefore to a system of three equations with three unknowns and without additional rotation

$$\begin{pmatrix} U_{eff_1}^2 \\ U_{eff_2}^2 \\ U_{eff_3}^2 \end{pmatrix} = J_{\text{ø}} \cdot \begin{pmatrix} U_1^2 \\ U_2^2 \\ U_3^2 \end{pmatrix} \tag{2.21}$$

with the effective cooling velocity of the wire $i$ $U_{eff_i}$, the velocity in the frame linked to the wires $U_i$, and the Jørgensen matrix $J_{\text{ø}}$ defined with the pitching and yawing coefficients as

$$J_{\text{ø}} = \begin{pmatrix} k_1^2 & 1 & h_1^2 \\ h_2^2 & k_2^2 & 1 \\ 1 & h_3^2 & k_3^2 \end{pmatrix}, \tag{2.22}$$

$h_i$ and $k_i$ being determined by a directional calibration of the probe.

### Directional calibration

The directional calibration is an aerodynamic calibration linked to the shape of the probe and therefore has normally to be performed only once. It consists in determining the pitching and yawing coefficients $h$ and $k$ from the Jørgensen matrix (Eq. (2.22)). The probe, submitted to a known calibration velocity, is tested for different angles. In order to determine the Jørgensen matrix, the procedure should be performed wire by wire but it is commonly accepted that $k$ and $h$ are independents from the wire, i.e. $h_i = h$ and $k_i = k$ [60, 69]. For these experiments, the values of $h^2 = 1.02$ and $k^2 = 0.15$ were used [69].

**Velocity calibration**

For the calibration, the hot wire anemometer is placed in the core of a low-turbulent and uniform jet created by a nozzle (Fig. 2.8). The velocity of the jet is determined by applying the Bernoulli's equation with the pressure difference between the ambient pressure and the pressure in the settling chamber measured with a water manometer. First, the dynamic response of the hot-wire is set in the conditions of the test and for the maximum wind speed. It is usually around 7 kHz. Then, the static velocity calibration can be performed (Fig. 2.9, left part). It consists in applying a range of known velocities to the probe, these velocities being usually in the $X$-direction, i.e. $U = U, V = 0, W = 0$. The velocities imposed can then be decomposed in the wire frame using the inverse of the rotation matrix (Eqs. (2.18) and (2.19)), what gives $(U_1, U_2, U_3)$. The effective cooling velocities are then determined thanks to the Jørgensen law (Eqs. (2.21) and (2.22)). For each calibration velocity, the voltage output of every wire is recorded. The effective cooling velocity $U_{eff}$ of a wire is then related to the output voltage $E$ by a $4^{\text{th}}$ order polynomial (P) fitting (Fig. 2.10)

$$U_{eff} = P_0 + P_1.E + P_2.E^2 + P_3.E^3 + P_4.E^4. \tag{2.23}$$

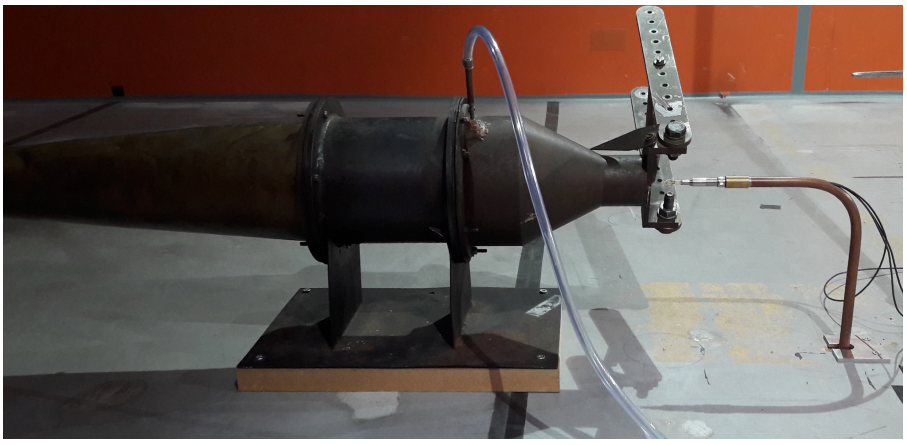


***Figure 2.8:*** *Calibration of the Dantec 55P91 triple hot-wire probe*

For the experiments presented in this work, the calibration velocity $U$ was ranging from 0.25 m/s to 18 m/s. The calibration was repeated at the beginning and at the end of each campaign to verify that no drift, due in particular to temperature variations, was present.

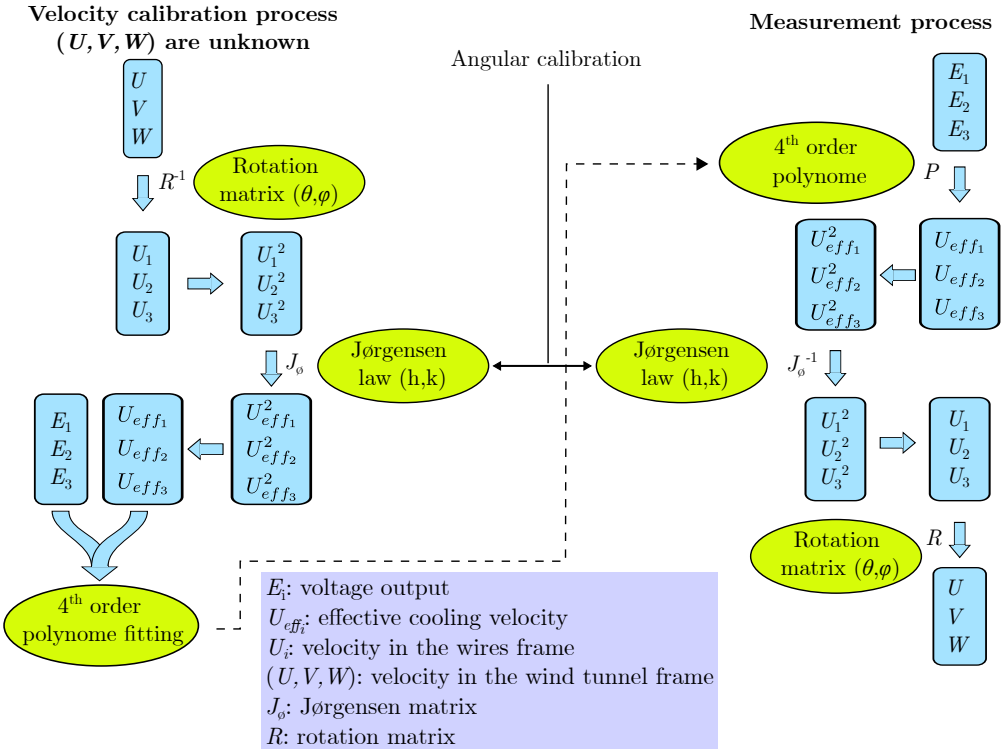



***Figure 2.9:*** *Summary of the calibration and measurement procedure for the three components HWA, adapted from [60]*

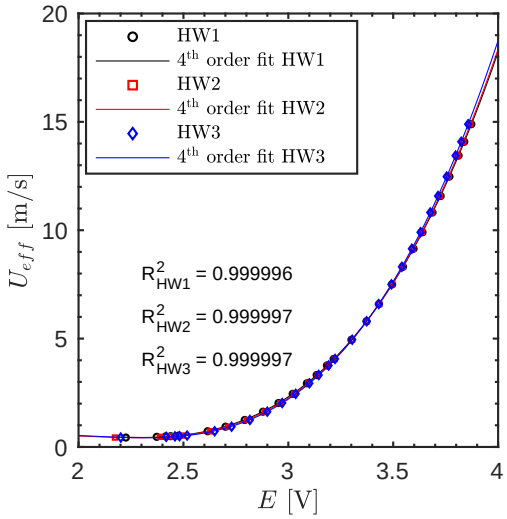


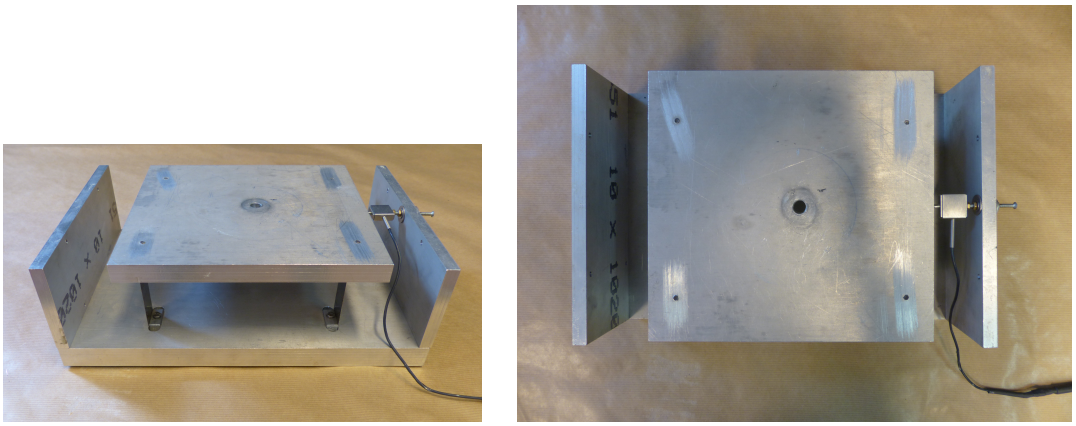

***Figure 2.10:*** *Example of a $4^{th}$ order polynomial fitting on the calibration data*

**Determination of the velocity**

In order to obtain the velocity in the wind tunnel frame from the output voltage of each wire, the process described on the right of Fig. 2.9 is followed. First, the polynomial fitting ($P$) is applied to the recorded voltage to get the effective cooling velocity. Then, the system (Eq. (2.21)) is solved to get the velocity components $(U_1, U_2, U_3)$ in the frame of the wires $(X_1, X_2, X_3)$. Finally, the rotation matrix $R$ (Eq. (2.19)) is applied to get the velocity components $(U, V, W)$ in the frame of the wind tunnel $(X, Y, Z)$. For the uniqueness of the solution, the velocity measured has to stay in a 35.3° cone.

#### 2.2.2.3 Aerodynamic balance

The single-component aerodynamic balance used in this work was designed and produced in 2013 at the von Karman Institute as part of a Master Thesis [70]. It consists in a plate mounted on four slats restricting its motion to a single direction in which a load cell is installed (Fig. 5.17). It enables therefore to measure a force acting along one direction in the horizontal plane through a Futek LSB200 load cell which tolerates a maximum force of 4.5 N.



(a) (b)

***Figure 2.11:*** *Photographs of the aerodynamic balance equipped with a Futek LSB200 load cell*

## 2.3 Multi-scale Proper Orthogonal Decomposition (mPOD)

This section is based on [40] where a very detailed description of the multi-scale Proper Orthogonal Decomposition (mPOD) can be found.

Data-driven decompositions represent the data as a linear combination of basis elements, referred to as modes, having spatial and temporal structures with a certain energy contribution [40]. There are two major classes of these decompositions, namely energy-based and frequency-based. The fundamental data-driven and energy-based decomposition is the Proper Orthogonal Decomposition (POD), whose optimality guarantees the identification of the most energetic contributions within a few modes. However, different phenomena can have very similar energy content despite the fact that they occur at largely different frequencies. In such a case, the POD cannot distinguish between the various contributions, which consequently share the same POD structures, resulting in spectral mixing. Conversely, a single frequency is assigned to each mode in frequency-based methods. Such methods are data-driven adaptations of the Discrete Fourier Transform (DFT) and infer the frequency of each mode from the data rather than defining it a priori, like in the DFT, from the time discretization. The fundamental data-driven and frequency-based method is the Dynamic Mode Decomposition (DMD).

In this work, a novel hybrid decomposition developed by Mendez [40] and, referred to as multi-scale Proper Orthogonal Decomposition (mPOD), is used. This approach combines the optimality

constraints of the POD and the frequency constraint of frequency-based methods. The proposed mPOD borrows several ideas from the Wavelet literature [40]. The main steps of this novel hybrid decomposition are described hereafter.

Each time realization of the data, i.e. snapshot with the temporal index $k$, is reshaped into a column vector $d_k[\mathbf{i}]$ with $\mathbf{i} \in [1, \ldots, n_s]$ the spatial linear index depending on the Cartesian grid $\mathbf{x}_i$ of size $n_x \times n_y$ and on the number of components $n_C$ of the data in case of vector quantities, i.e. $n_s = n_C\, n_x\, n_y$. For the PIV data that will be presented in this work, $n_C = 2$ since only two components of the velocity field were measured (2D2C TR-PIV). For $n_t$ snapshots ($k \in [1, \ldots, n_t]$), the data matrix is defined as

$$D[\mathbf{i}, k] = \begin{bmatrix} d_1[1] & \ldots & d_k[1] & \ldots & d_{n_t}[1] \\ \vdots & \vdots & \vdots & \vdots & \vdots \\ d_1[n_s] & \ldots & d_k[n_s] & \ldots & d_{n_t}[n_s] \end{bmatrix}. \tag{2.24}$$

The ordering of the elements of each column vector is irrelevant, provided that the same criterion is used when reshaping back the results of the decomposition. The main idea behind the decomposition is to describe $D$ as

$$D = \sum_{r=1}^{rk(D)} \sigma_r \phi_r \psi_r^T = \Phi \Sigma \Psi^T \tag{2.25}$$

where $rk(D)$ is the rank of the data matrix; $rk(D) = n_t$ corresponds to a full rank representation of the matrix $D$ while truncating the summation at $r_c < rk(D)$ leads to an approximation $\tilde{D}$ of rank $r_c$. $\Phi = \left[\phi_1[\mathbf{i}], \ldots, \phi_{rk(D)}[\mathbf{i}]\right]$ is a $n_s \times rk(D)$ matrix where each column represents a spatial structure, $\Psi = \left[\psi_1[k], \ldots, \psi_{rk(D)}[k]\right]$ is a $n_t \times rk(D)$ matrix where each column represents a temporal structure, and the superscript $^T$ denotes the matrix transpose. $\Phi$ and $\Psi$ are such that each column vector has a unitary energy (according to the 2-norm or Euclidean norm), i.e.

$$\|\phi_r\|_2^2 = \frac{1}{n_s} \phi_r^\dagger \phi_r = 1 \quad ; \quad \|\psi_r\|_2^2 = \frac{1}{n_t} \psi_r^\dagger \psi_r = 1 \tag{2.26}$$

where $\dagger$ represents the Hermitian transpose. $\Sigma = \mathrm{diag}\left[\sigma_1, \sigma_2, \ldots, \sigma_{rk(D)}\right]$ is the diagonal matrix of size $rk(D) \times rk(D)$ containing the whole energy contribution of each mode.

It is worth noticing that since $\Sigma$ is diagonal and $\Phi$ and $\Psi$ have normalized columns, the factorization in Eq. (2.25) is entirely defined by either $\Phi$ or $\Psi$ [40]. As in [40], we focus on the projections in the time (row) domain of the dataset, i.e. that Eq. (2.25) is defined by the temporal structures $\Psi$. From Eq. (2.25), the spatial structures can be obtained through a matrix inversion

$$\Phi\Sigma = D\left(\Psi^T\right)^{-1} = C \tag{2.27}$$

$$\Phi = C\Sigma^{-1} \tag{2.28}$$

and the amplitudes can be computed through a column-wise normalization

$$\sigma_r = ||C_r||_2, \tag{2.29}$$

$C_r$ being the $r^{th}$ column of the matrix $C$.

In the particular case of the POD, the temporal structures $\Psi_\mathcal{P}$ are defined so that the energy content $\sigma_k$ of each mode decays as quickly as possible when $k$ increases. These POD temporal structures $\Psi_\mathcal{P}$ are the eigenvectors of the temporal correlation matrix

$$K = D^\dagger D = \Psi_\mathcal{P} \Sigma_\mathcal{P}^2 \Psi_\mathcal{P}^T. \tag{2.30}$$

If $D$ is real, as it is the case in this work, $\Psi_\mathcal{P}$ are orthonormal and real vectors. For the choice of a temporal basis in Eq. (2.30), Eq. (2.25) yields the well-known singular Value Decomposition (SVD), here denoted as $D = \Phi_\mathcal{P} \Sigma_\mathcal{P} \Psi_\mathcal{P}^T$ [40].

The temporal basis $\Psi_\mathcal{M}$ for the multi-scale Proper Orthogonal Decomposition (mPOD) is computed by setting frequency constraints to the classical POD. The algorithm consists of three major steps [40].

- The temporal correlation matrix $K = D^\dagger D$ is split into the contributions of different scales via multi-resolution analysis (MRA). This is performed using an appropriate filter bank that preserves the symmetry of the correlation matrix.
- Each of these contributions is diagonalized to obtain the orthonormal basis corresponding to each scale, as in the classical POD.
- The bases of each scale are merged into the final temporal basis $\Psi_{\mathcal{M}}$, and the decomposition is completed via the projection (Eqs. (2.27) and (2.28)) and the normalization (Eq. (2.29)).

Since the multi-resolution analysis (MRA) used in the first major step is applied in the frequency domain, it is interesting to introduce the Discrete Fourier Transform (DFT) of the correlation matrix $K$. Indeed, since the DFT of a column vector is obtained via left multiplication by $\bar{\Psi}_{\mathcal{F}}$, while the DFT of a row vector is obtained via a right multiplication by $\bar{\Psi}_{\mathcal{F}}$, the 2D Fourier transform of the correlation matrix $K$ is given by

$$\widehat{K} = \bar{\Psi}_{\mathcal{F}} K \bar{\Psi}_{\mathcal{F}} \tag{2.31}$$

with the DFT the temporal structures $\Psi_{\mathcal{F}}$ defined a priori, regardless of the dataset at hand, as columns of the well known Fourier Matrix

$$\Psi_{\mathcal{F}} = \frac{1}{\sqrt{n_t}} \begin{bmatrix} 1 & 1 & 1 & \dots & 1 \\ 1 & w & w^2 & \dots & w^{n_t-1} \\ \vdots & \vdots & \ddots & \vdots & \\ 1 & w^{n_t-1} & w^{2(n_t-1)} & \dots & w^{(n_t-1)^2} \end{bmatrix} \tag{2.32}$$

where $w = \exp\left(2\pi \mathrm{j}/n_t\right)$, with $\mathrm{j} = \sqrt{-1}$.

As in [40] and for the sake of clarity, the temporal filtering of the dataset will be illustrated for the 1D Fourier transform $\widehat{d}_p = d_p \bar{\Psi}_{\mathcal{F}}$ of the temporal evolution (row-wise) of the data for a given point of spatial location $\mathbf{i}_p$, i.e. $d_p[k] = D\left[\mathbf{i}_p, k\right]$. The objective is to split the spectra $\widehat{d}_p$ into $M$ scales, each retaining a portion of $\widehat{d}_p$ with negligible overlapping as depicted in Fig. 2.12. The frequency bandwidths of these scales $\Delta f_m = f^c_{m+1} - f^c_m$, with $m \in [1, \dots, M-1]$, are defined by a frequency splitting vector $F_V = \left[f^c_1, f^c_2, \dots, f^c_{M-1}\right]$. This vector is bounded by the minimum and the maximum possible frequencies, i.e. $f^c_0 = 0$ and $f^c_M = f_s/2$ ($f_s$ being the sampling frequency) respectively.

From the frequency splitting vector $F_V$, a filter bank consisting of a low-pass filter with a cut-off frequency $f^c_1$, a high-pass filter with cut-off frequency $f^c_{M-1}$, and $M-2$ band-pass filters between these, can be defined. Following the lossless formulation from multiresolution analysis (MRA), these filters are constructed from a set of $m$ low-pass filters with transfer function $\mathcal{H}_{\mathcal{L}_m}$. Of these low-pass filters, only the first one ($\mathcal{H}_{\mathcal{L}_1}$) is retained, while the others (shown in Fig. 2.12 with dashed line) are only used to build the bandpass filters as complementary differences $H_{\mathcal{H}m} = H_{\mathcal{L}_{m+1}} - H_{\mathcal{L}_m}$, and to build the high-pass filter as $H_{\mathcal{H}_{M-1}} = \underline{1} - \mathcal{H}_{\mathcal{L}_{M-1}}$. The resulting set of transfer functions (with modulus sketched in Fig. 2.12 with continuous line) is, by construction, such that $H_{\mathcal{L}_1} + H_{\mathcal{H}_1} + \ldots + H_{\mathcal{H}_{M-1}} = \underline{1}$, and therefore the entire spectra of the dataset is retained [40]. Considering the filtering in the frequency domain, this operation is performed via simple multiplication.

The choice of the frequency splitting vector $F_V$ is a fundamental step which will set the spectral constraints to the mPOD modes. Furthermore, it is interesting to note that this choice also allows the mPOD to move from the energy optimality of the POD to the spectral purity of the DFT [40]. Indeed, a single scale mPOD ($F_V = [\varnothing]$) corresponds to a standard POD since all the eigenvectors $\psi$ are allowed to span the entire set of discrete frequencies available. At the opposite, for $F_V = [f_s/\left(\Delta t n_t\right), \dots, r f_s/\left(\Delta t n_t\right), \dots, (n_t-1) f_s/\left(\Delta t n_t\right)]$, every scale is constrained to a single frequency and the mPOD reduces to the DFT, inheriting its finest spectral resolution but also its limits [40].

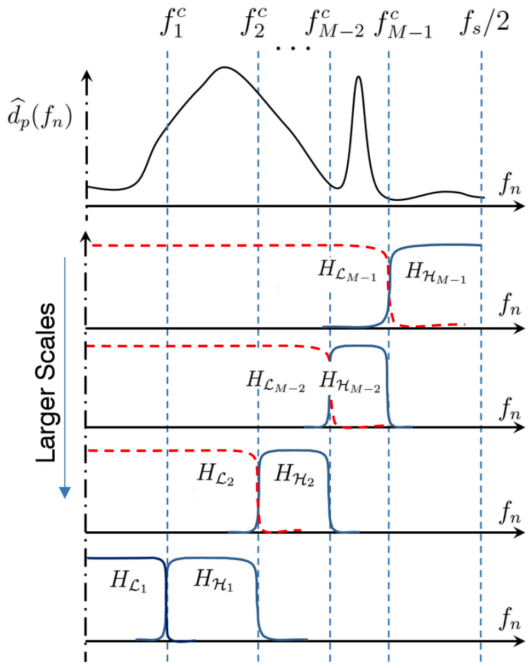



***Figure 2.12:*** *Multi-Resolution Analysis (MRA) of a signal $d_p[k]$ along its spectrum $\widehat{d}_p[n]$. Using a filter bank with a frequency splitting vector $F_V = \left[f_1^c, f_2^c, \ldots, f_{M-1}^c\right]$, the MRA splits the spectra into a set of M scales. This set is composed of a large scale (transfer function $H_{\mathcal{L}_1}$), a fine scale (transfer function $H_{\mathcal{H}_{M-1}}$) and $M-2$ intermediate scales (transfer functions from $H_{\mathcal{H}_1}$ to $H_{\mathcal{H}_{M-2}}$). Only the positive portion of the spectra is shown, the negative one being mirrored along the ordinates [40]*

The correlation matrix $K$ can then be split into M contributions. Disregarding the mixed terms ($D_{\mathcal{L}_m}^{\dagger} D_{\mathcal{H}_m}$ and $D_{\mathcal{H}_m}^{\dagger} D_{\mathcal{L}_m}$) in each scale, and reconstructing only the 'pure' terms ($D_{\mathcal{L}_m}^{\dagger} D_{\mathcal{L}_m}$ and $D_{\mathcal{H}_m}^{\dagger} D_{\mathcal{H}_m}$), the correlation matrix is approximated as

$$K \approx \Psi_{\mathcal{F}} \left[\widehat{K} \odot \mathcal{H}_{\mathcal{L}_1}\right] \Psi_{\mathcal{F}} + \sum_{m=1}^{M} \Psi_{\mathcal{F}} \left[\widehat{K} \odot \mathcal{H}_{\mathcal{H}_m}\right] \Psi_{\mathcal{F}} \approx K_{\mathcal{L}_1} + \sum_{m=1}^{M-1} K_{\mathcal{H}_m} \tag{2.33}$$

with the Hadamard product $\odot$ corresponding to a simple element-wise multiplication in matrix notation. Each 'pure' term is then diagonalized as

$$K \approx \Psi_{\mathcal{L}_1} \Sigma_{\mathcal{L}_1}^2 \Psi_{\mathcal{L}_1}^T + \sum_{m=1}^{M-1} \Psi_{\mathcal{H}m} \Sigma_{\mathcal{H}_m}^2 \Psi_{\mathcal{H}_m}^T. \tag{2.34}$$

The full set of eigenvalues $[diag(\Sigma_{\mathcal{L}_1}), diag(\Sigma_{\mathcal{H}_1}), \ldots, diag(\Sigma_{\mathcal{H}_{M-1}})]$ is then sorted in decreasing order and the required permutation matrix $P_\Sigma$ is stored. This matrix is then used to re-arrange the eigenvector matrices $[\Psi_{\mathcal{L}_1}, \ldots, \Psi_{\mathcal{H}_{M-1}}]$ into one single matrix (temporal basis) regardless of their scale of origin

$$\Psi_{\mathcal{M}}^0 = \left[\Psi_{\mathcal{L}_1}, \Psi_{\mathcal{H}_1}, \Psi_{\mathcal{H}_2} \ldots \Psi_{\mathcal{H}_{M-1}}\right] P_\Sigma. \tag{2.35}$$

The temporal matrix (Eq. (2.35)) is orthonormal if a perfect spectral separation is achieved. Due to the finite size of the transition band of the filters, this is generally not the case in practice, and a minor loss of orthogonality usually occurs [40]. This imperfection is treated by polishing the temporal structure via a reduced $QR$ factorization $\Psi_{\mathcal{M}}^0 = \Psi_{\mathcal{M}} R$ so that $\Psi_{\mathcal{M}} = \Psi_{\mathcal{M}}^0 R^{-1}$. As stated in [40], this compensates for the losses of orthogonality and the upper triangular matrix $R$ offers an indication of the quality of the filtering process, being close to the identity when the spectral overlapping is negligible.

Finally the decomposition is completed via the projection (Eqs. (2.27) and (2.28)) and the normalization (Eq. (2.29)), as for any orthogonal decomposition.

The steps of the mPOD algorithm proposed by [40] and described above are listed in Algorithm 1.

**Algorithm 1** : Multi-scale Proper Orthogonal Decomposition of a dataset $D$ of size $n_s \times n_t$ [40]

**Input:** Set of $n_t$ snapshots of a dataset $D(\mathbf{x_i}, t_k)$ on a Cartesian grid $\mathbf{x}_i$ of size $n_x \times n_y$

1: Reshape snapshots into column vectors $d_k[\mathbf{i}]$ of size $n_s \times 1$ and assemble $D[\mathbf{i}, k]$ in Eq. (2.24)

2: Compute time correlation matrix $K = D^\dagger D$ and $\widehat{K} = \bar{\Psi}_\mathcal{F} K \bar{\Psi}_\mathcal{F}$ in Eq. (2.31)

3: Prepare the filter bank $\mathcal{H}_{\mathcal{L}_1}, \ldots, \mathcal{H}_{\mathcal{H}_M}$, and split $K$ into M contributions via Eq. (2.33)

4: Diagonalize each 'pure' term $K_m = \Psi_m \Sigma_m^2 \Psi_m^T$ as in Eq. (2.34)

5: Sort the contribution of all the scales into $\Psi^0_\mathcal{M}$ as in Eq. (2.35)

6: Enforce orthogonality via QR factorization, $\Psi^0_\mathcal{M} = \Psi_\mathcal{M} R \rightarrow \Psi_\mathcal{M} = \Psi^0_\mathcal{M} R^{-1}$

7: Compute the spatial basis $\Phi_\mathcal{M} = D\left(\Psi^T_\mathcal{M}\right)^{-1} \Sigma^{-1}_\mathcal{M}$ from Eq. (2.27) and sort the results in descending order of energy contribution

**Output:** Spatial $\Phi_\mathcal{M}$ and temporal $\Psi_\mathcal{M}$ structures with corresponding amplitudes $\Sigma_\mathcal{M}$ of the $n_t$ mPOD modes

In order to improve the quality of the mPOD analysis, this algorithm was applied on the zero-mean shifted dataset. This implied that all the temporal structures have zero mean, since an orthogonal decomposition is considered [40]. Note that this mean removal can only be applied if the data are statistically stationary.

Chapter 3

# Wind turbine wake tracking algorithms

This chapter concerns the development of algorithms to track the centerline of horizontal axis wind turbine (HAWT) wakes. Several methods are used in the literature [71, 72, 73, 74], usually to detect the position of the wake for turbines in yaw. In these methods, the wake center position as a function of the streamwise location is determined by fitting a Gaussian function to each velocity deficit profile [71, 72, 73], by using the "center of mass" method [74] or by locating the center of a disk of minimum available power in the wake [73].

In this chapter it is proposed to assess the performance and robustness of several algorithms developed to track the wake meandering in large-eddy simulation of the NREL offshore 5-MW baseline wind turbine subjected to a turbulent inflow. All the wake centerline diagnostics presented hereafter were first validated for a laminar inflow before applying them to the turbulent inflow case. For the sake of conciseness, only the results for an inflow with a turbulence intensity of 8.4% are presented in this chapter.

## 3.1 Numerical setup

### 3.1.1 VPM simulations

The simulations are performed for an isolated NREL offshore 5-MW baseline wind turbine ($D = 126$ m) [75] operating at its optimum tip-speed ratio ($TSR = \omega R/U_\infty$) of 7.55. Only the blades of the machine are modeled using immersed lifting lines. The spatial resolution is such that 32 points are used to model each blade. The computational domain (Fig. 3.1) initially extends over $14D \times 4D \times 4D$; the domain is unbounded in $y-$ and $z-$directions. Based on the spatial resolution of the blades, it leads to an initial grid with approximately 58.7 million nodes. The wind turbine rotor is located $3D$ after the inlet and is subjected to a uniform (no shear) turbulent inflow synthesized through Mann's algorithm [50] in a $26D \times 4D \times 4D$ box. The inflow velocity is $U_\infty = 9$ m/s in the $x-$direction and the inflow turbulence intensity is $I = \sqrt{\frac{1}{3}(\sigma_u^2 + \sigma_v^2 + \sigma_w^2)}/U_\infty = 8.4\%$. The time step ($\Delta t$) is set such that $\Delta t \cdot \frac{U_\infty}{D} = 10 \cdot 10^{-3}$. The flow was allowed to establish itself during two flow through times $t_{FT} = 14D/U_\infty$.

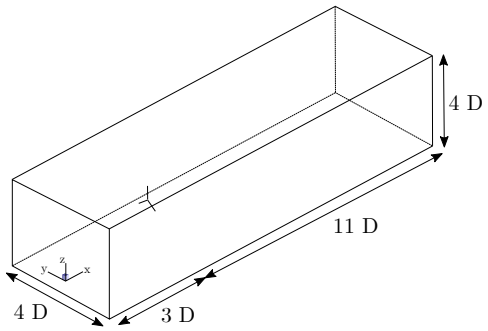



***Figure 3.1:*** *Computational domain used in VPM*

### 3.1.2 FD4 simulations

Again, we consider the NREL 5-MW machine at the same operating conditions. Only the blades of the machine are modeled using an advanced actuator disk (AD). The domain size is $14D \times 9D \times 9D$ in order to be as close as possible to the unbounded conditions used in the VPM code. In order to evaluate whether the FD4 code could be a suitable tool to study wake meandering at wind farm scale, the resolution is kept to a typical resolution used for a wind farm: 16 points per rotor diameter, which leads to a grid with approximately 4.6 million nodes. The AD is located at $3D$ from the inlet and the inflow conditions are the same as those used for the VPM code. The time step ($\Delta t$) is set such that $CFL = U_\infty \Delta t / \Delta x = 0.11$. As for the VPM code, the flow was allowed to establish itself during two flow through times $t_{FT} = 14D/U_\infty$.

## 3.2 Wake centroid detection in a cross-flow plane

The proposed diagnostics take advantage of the specific signatures of a wind turbine wake, namely its vortical structures, the deficits of mass flow, momentum, and available power in the flow.

From the vorticity in a cross-flow plane, the densities of linear $i_x$ and angular $l_x$ impulse, along and about $\mathbf{e}_x$, can be defined as

$$i_x = \frac{1}{2}\left(\mathbf{x} \times \boldsymbol{\omega}\right) \cdot \mathbf{e}_x \,,\; l_x = \frac{1}{3}\left(\mathbf{x} \times \left(\mathbf{x} \times \boldsymbol{\omega}\right)\right) \cdot \mathbf{e}_x. \tag{3.1}$$

One can also use the analogy with the displacement and momentum thicknesses of a boundary layer [76] and exploit the densities of velocity/momentum deficits in a cross-flow plane in the wake

$$s_1 = U_\infty - u \,,\; s_2 = \left(U_\infty - u\right) u. \tag{3.2}$$

Finally, the available power density in a cross-flow plane in the wake can be defined as

$$p = \frac{1}{2} u |\mathbf{u}|^2. \tag{3.3}$$

From these densities, two main approaches were tested to determine the wake centroid in a plane normal to the streamwise direction.

### 3.2.1 Wake centroid computation through first order moment

The first approach to determine the wake centroid $(y_c, z_c)$ in a cross-flow plane consists in computing the first order moment of the density $q = i_x, l_x, s_1,$ or $s_2$ to obtain the "center of mass" [74]

$$y_c = \frac{\int y\, q\, dS}{\int q\, dS} \;,\; z_c = \frac{\int z\, q\, dS}{\int q\, dS}. \tag{3.4}$$

By repeating this approach in each cross-flow plane (their number depending on the mesh resolution) in the wake of a machine, the complete wake centerline can be obtained.

The methods exploiting the vorticity in the wake of the wind turbine lead to noisy wake centerlines that follow roughly the wake for a laminar inflow and that are too sensitive to turbulent fluctuations to be exploited for a turbulent inflow. Therefore, the results obtained with these methods are not presented in this chapter for the sake of conciseness. Nonetheless, the methods exploiting the velocity/momentum deficit in the wake are less sensitive to the turbulent fluctuations and enable to track the wake centerline (Fig. 3.2). Figures 3.2(a) and 3.2(c) show the instantaneous velocity and momentum deficits in a cross-flow plane at $x/D = 5$ for $t^* = t/(D/U_\infty) = 54.2$, on which the wake centroid is superimposed. As it can be observed on the instantaneous streamwise velocity field (Fig. 3.2(b) and 3.2(d)), the algorithm seems to capture properly the wake centerline except in the near wake. This poorer performance in the near wake is due to the presence of a jet since only the blades, without the nacelle, are modeled in the simulations.

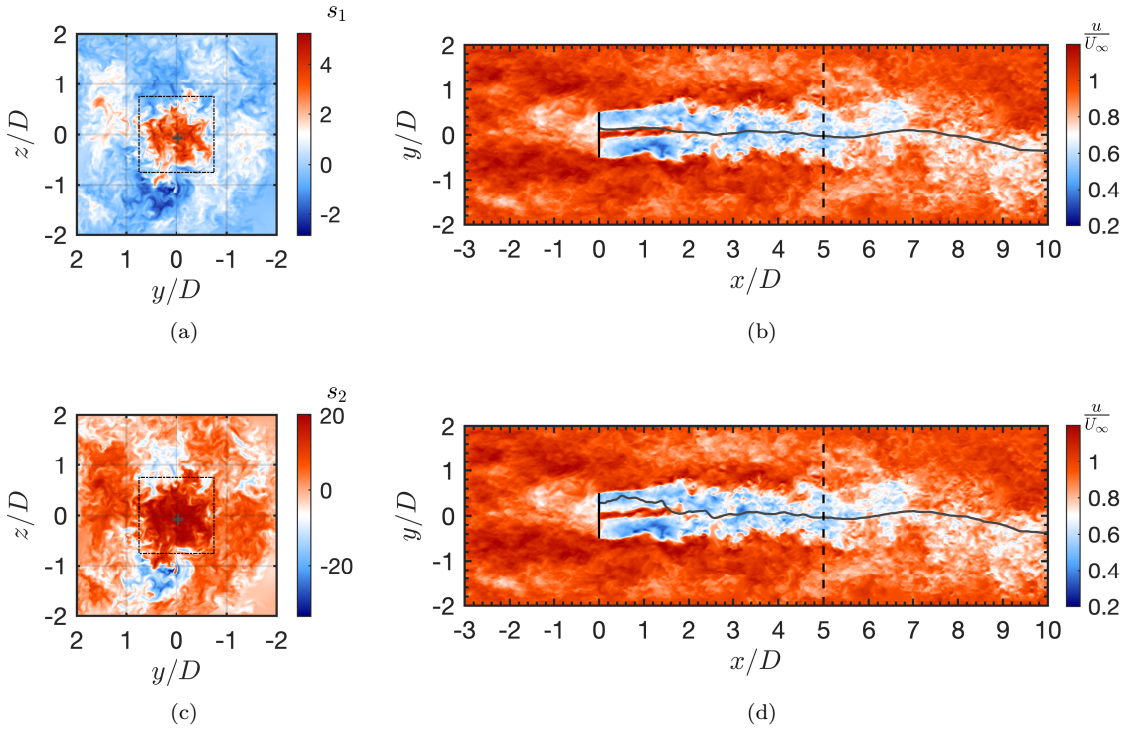



***Figure 3.2:*** *Wake centroid at $x/D = 5$ and wake centerline obtained by computing the first order moment of the velocity (a)-(b) / momentum (c)-(d) deficit for $t^* = t/(D/U_\infty) = 54.2$*

The wake centroid position obtained through the computation of the first order moment depends nevertheless on the size of the integration surface used in the computation (Eq. (3.4)), as illustrated in Fig. 3.3. This influence was studied for the computation of the first order moment of the velocity (Fig. 3.3 (a)-(b)-(c)) / momentum (Fig. 3.3 (d)-(e)-(f)) deficit by setting the integration surface width to $1.5D$, $2D$, and $3D$. As it can be observed, the integration surface size has an impact on the wake centroid position and, bigger is the integration surface, bigger is the distance between the wake centroid and the origin of the rotor (0,0) for the specific instant considered.

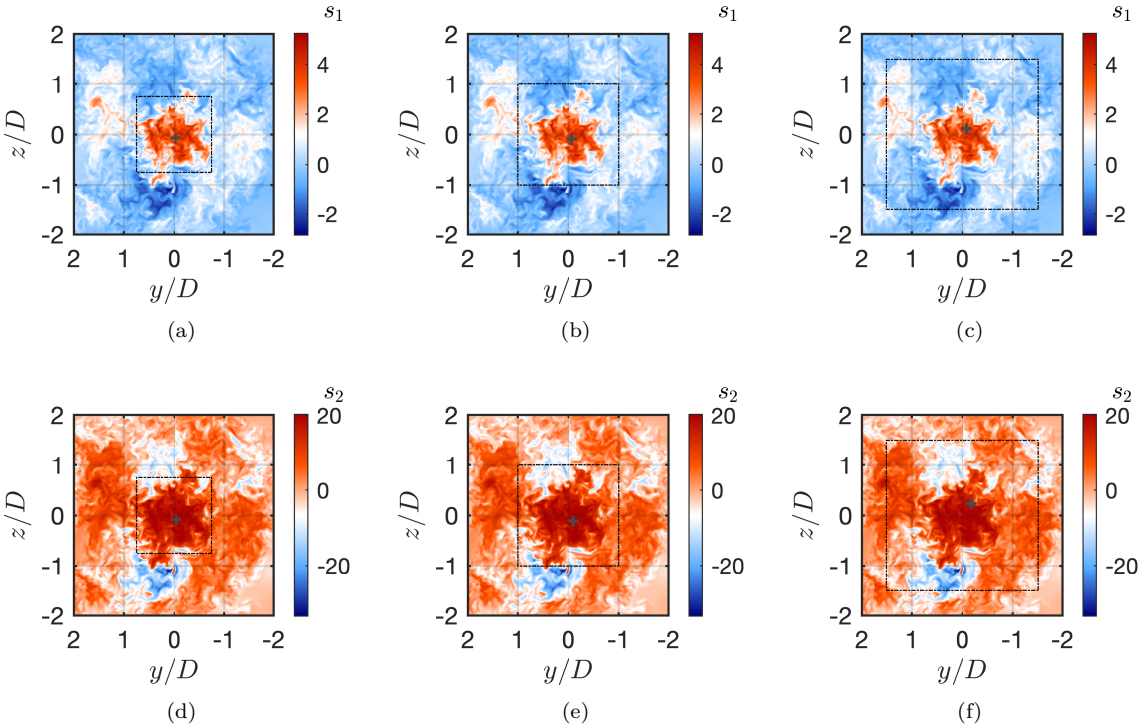



***Figure 3.3:*** *Wake centroid at $x/D = 5$ obtained by computing the first order moment of the velocity (a)-(b)-(c) / momentum (d)-(e)-(f) deficit with various integration surfaces of $(1.5D)^2$ (a)-(d), $(2D)^2$ (b)-(e), and $(3D)^2$ (c)-(f) for $t^* = 54.2$*

Furthermore, the reference velocity used to compute the velocity/momentum deficit has an impact on the wake centroid location. This can be observed by making the comparison between Fig. 3.3 and Fig. 3.4 where the inflow velocity $U_\infty$ used to compute the wake centroid was replaced by the mean streamwise velocity $\langle U \rangle$ in the cross-flow plane

$$\langle U \rangle = \frac{\int u \, dydz}{\int dydz}. \tag{3.5}$$

One can observe that the influence of the reference velocity is more significant for a larger integration surface, the wake centroid being even out of the field of view for Fig. 3.4(f). Finally, Fig. 3.5 shows that, at some specific instant, the methods based on the first order moment computation do not capture properly the position of the wake centroid. The method presented in the next section enables to eliminate these shortcomings.

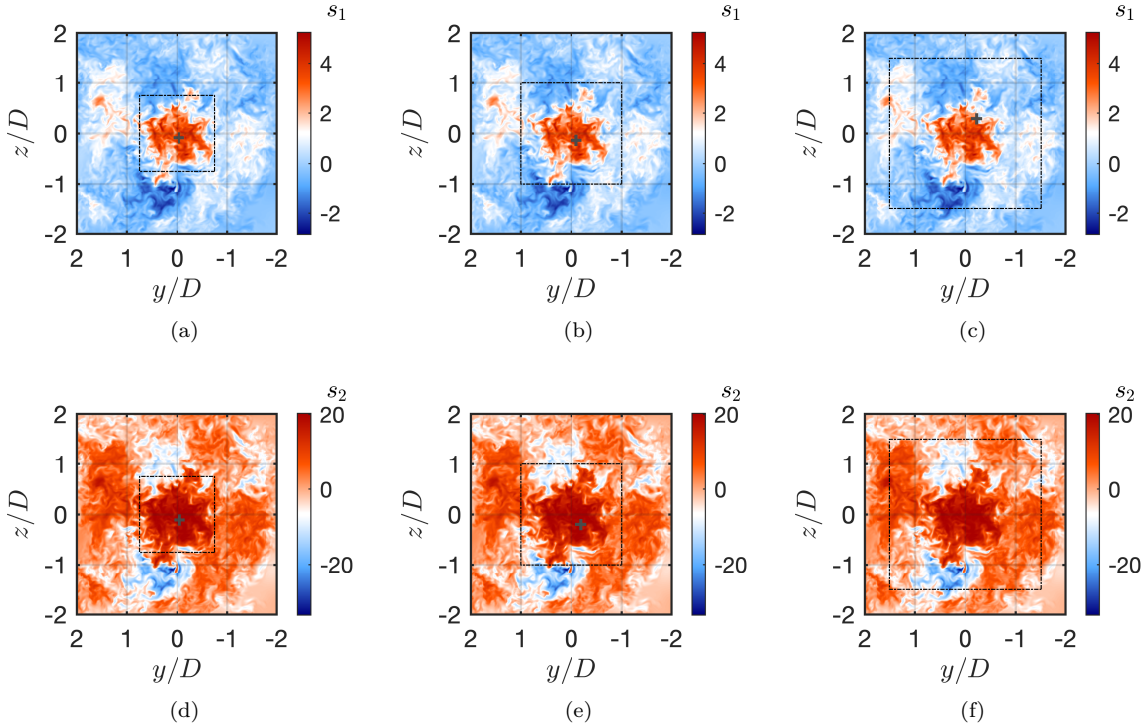



***Figure 3.4:*** *Wake centroid at $x/D = 5$ obtained by computing the first order moment of the velocity (a)-(b)-(c) / momentum (d)-(e)-(f) deficit with various integration surfaces of $(1.5D)^2$ (a)-(d), $(2D)^2$ (b)-(e), and $(3D)^2$ (c)-(f) using the mean streamwise velocity $\langle U \rangle$ in the cross-flow plane as reference velocity for $t^* = 54.2$*

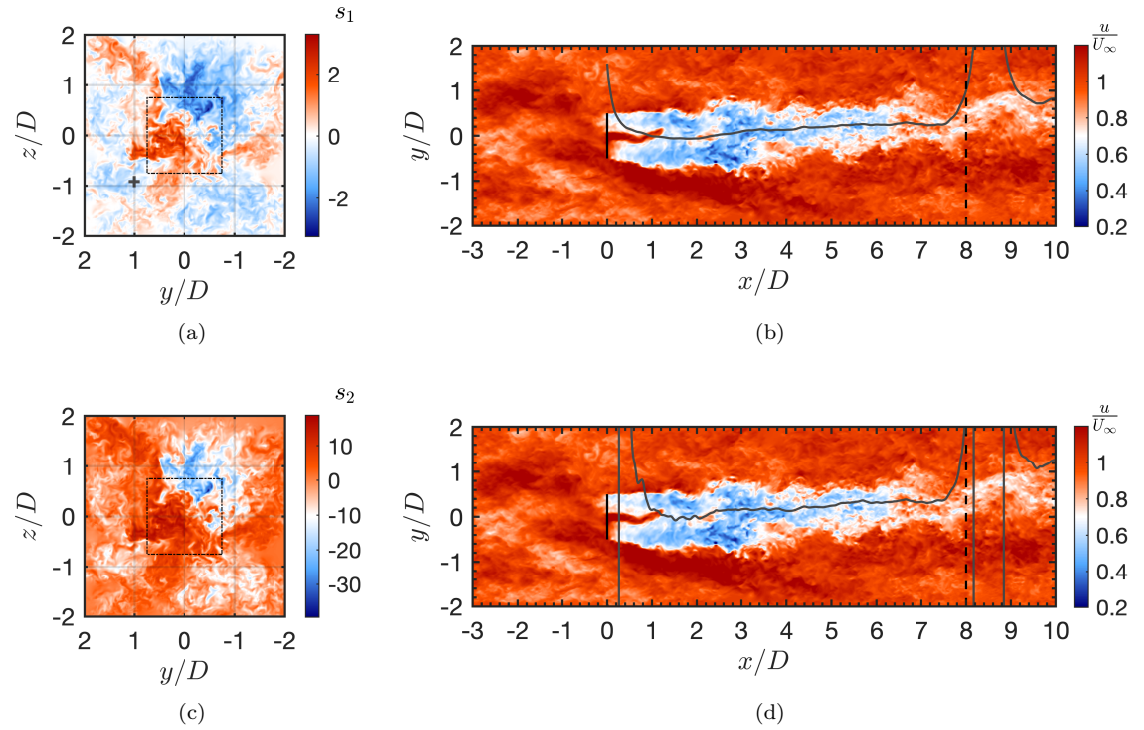



***Figure 3.5:*** *Wake centroid at $x/D = 8$ and wake centerline obtained by computing the first order moment of the velocity (a)-(b) / momentum (c)-(d) deficit; evidence of robustness issue for $t^* = 37.3$*

### 3.2.2 Wake centerline detection through convolution

#### 3.2.2.1 2D convolution computation

The second approach consists in locating the maximum of the convolution between the density $q = s_1, s_2,$ or $p$ and a masking function $f$

$$(y_c, z_c) = \text{argmax}\,(q * f)\,, \tag{3.6}$$

where $(*)$ is the convolution operator.

First, a simple masking function set to minus unity inside the rotor disk and to zero outside of it was used

$$f_s(y,z) = \begin{cases} -1 \text{ for } y^2 + z^2 < \left(\frac{D}{2}\right)^2, \\ 0 \text{ otherwise.} \end{cases} \tag{3.7}$$

Considering the power density field for physical interpretation, it corresponds to compute the available power inside a disk of diameter equal to the rotor diameter $D$ and located in the cross-flow plane. This disk center position can be shifted in the $y-$ and $z-$directions; the wake center then corresponds to the disk position for which the available power is minimum [73]. Furthermore, the influence of the masking function was investigated by replacing the discontinuous function by a Gaussian function

$$f_G(y,z) = A\,\exp\left(-\left(\frac{y^2}{2\sigma_y^2} + \frac{z^2}{2\sigma_z^2}\right)\right) \tag{3.8}$$

with $A = -1$, and $\sigma_{y,z} = D/4$.

Finally, the influence of the mask size was studied for the Gaussian function. Instead of testing several $\sigma_{y,z}$, a method to perform an automatic adaptation of $\sigma_{y,z}$ according to space and time was developed. It exploits the property that the Laplacian at the extrema of the convolution between two Gaussian functions is minimum when $\sigma_{y,z_{|1}} = \sigma_{y,z_{|2}}$. Therefore, if we assume a Gaussian shape for the quantity of interest $q$, the closer the shape of the Gaussian masking function from the shape of $q$, the lower the Laplacian at the extrema of the convolution between these two quantities. For each streamwise position and at each time step, two additional convolutions are thus computed for mask widths corresponding to $\sigma_{y,z} = \sigma_{y,z} \pm \Delta\sigma_{y,z}$, with $\Delta\sigma_{y,z} = 0.01D$. The convolution with the narrower extremum (lower Laplacian) is then selected by comparing the Laplacians computed at the position of the extrema, and the wake centroid is determined from the position of the narrower extremum. The updated $\sigma_{y,z}$, i.e. $\sigma_{y,z} + \Delta\sigma_{y,z}$ or $\sigma_{y,z} - \Delta\sigma_{y,z}$, are then used as reference for the next time step, what results in an automatic adaptation of the mask size according to space and time. The only drawback of this method is that it requires $\sigma_y = \sigma_z$.

It is interesting to note that, while there is no constraint on the wake centroid position obtained through the first order moment, the wake centroid position obtained by the convolution depends on the mesh resolution.

The methods presented hereafter are based on the computation of the convolution between a field density and a masking function (Eq. (3.6)). First, the wake centroid (Fig. 3.6(a)) was determined by computing the convolution between the available power in the flow (Eq. (3.3)) and a disk of diameter $D$ (Eq. (3.7)) set to minus unity. In order to obtain the complete wake centerline (Fig. 3.6(b)), the technique was applied in each cross-flow plane in the wake of the machine. Compared to the algorithms based on the first order moment computation (Fig. 3.2), the convolution method enables to perform a finer tracking of the wind turbine wake.

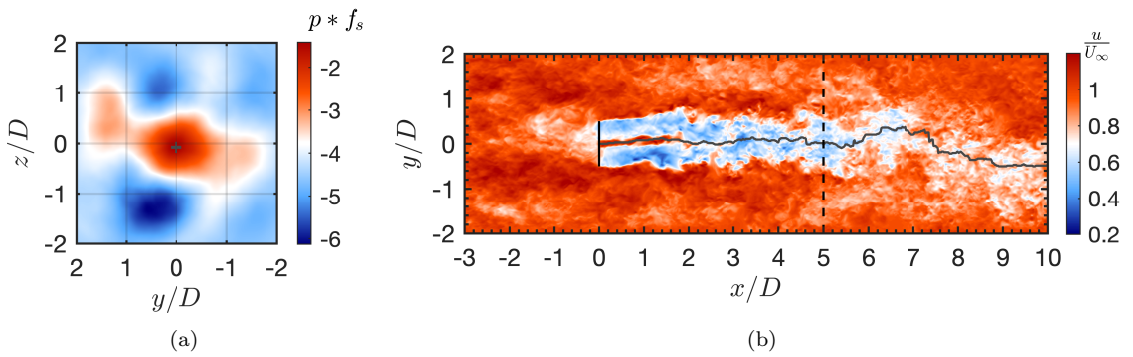



***Figure 3.6:*** *Wake centroid at $x/D = 5$ and wake centerline obtained through the convolution between a disk and the available power in the flow for $t^* = 54.2$*

The influence of the field density (Fig. 3.7) was investigated by substituting the power density field by the velocity/momentum deficits used to determine the wake centroid through the computation of the first order moment. As it can be observed in Fig. 3.8, the field density used in the convolution does not have any influence on the wake centroid location. Furthermore, this method shows more reliable detection capabilities (Fig. 3.9) than the method based on the first order moment computation (see Fig. 3.5).

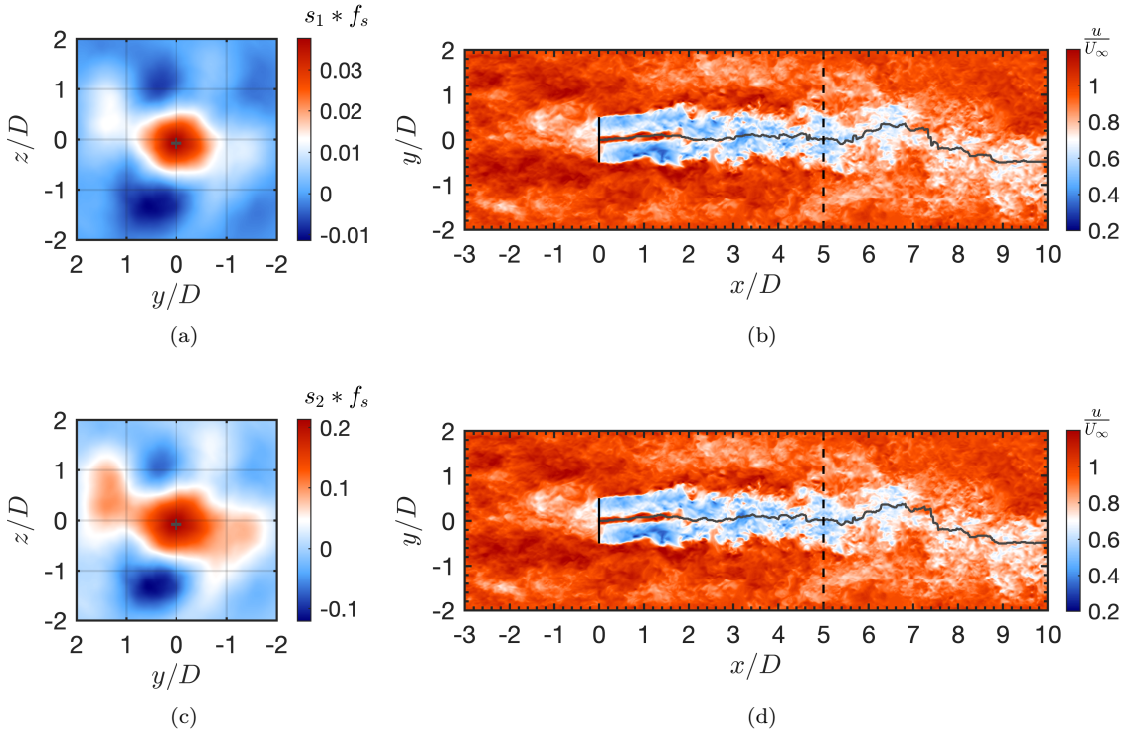



***Figure 3.7:*** *Wake centroid at $x/D = 5$ and wake centerline obtained through the convolution between a disk and the velocity (a)-(b) / momentum (c)-(d) deficit in the wake for $t^* = 54.2$*

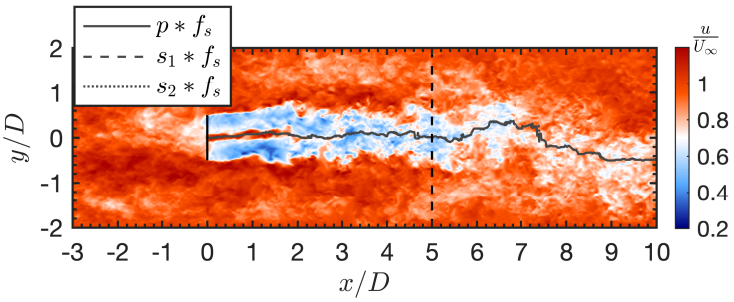



***Figure 3.8:*** *Wake centerline obtained through the convolution between a disk and the available power, the velocity deficit and the momentum deficit in the wake for* $t^* = 54.2$

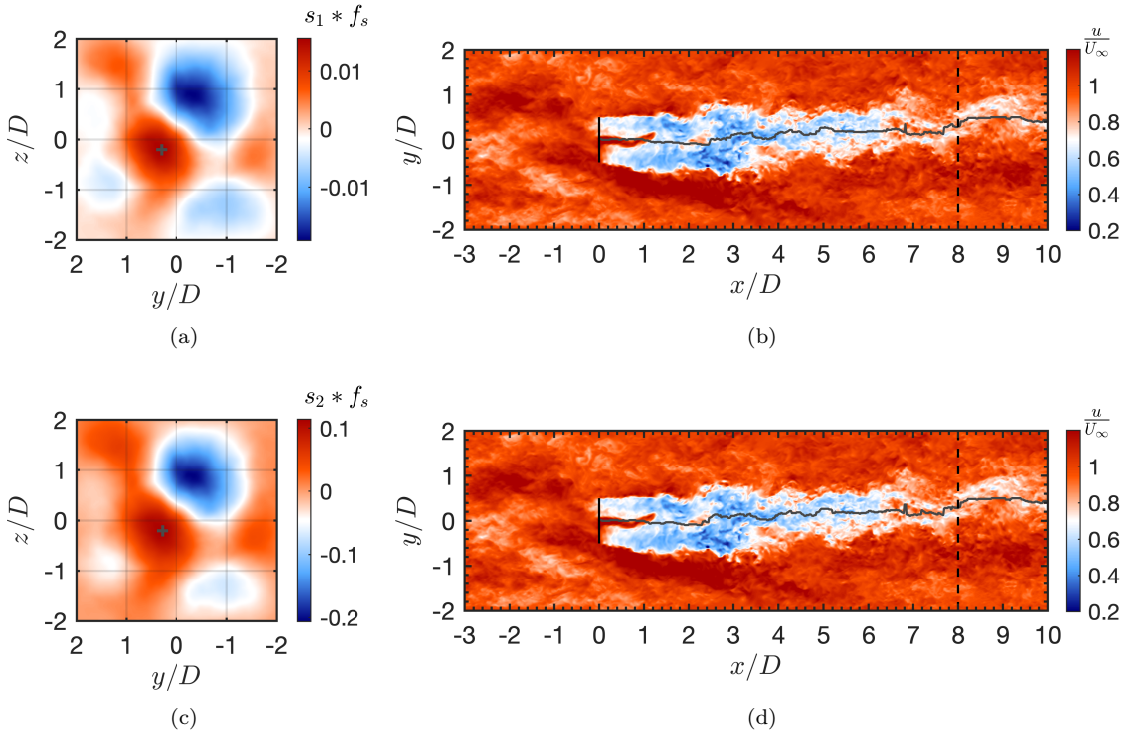



***Figure 3.9:*** *Wake centroid at* $x/D = 8$ *and and wake centerline obtained by computing the convolution between a disk and the velocity (a)-(b) / momentum (c)-(d) deficit in the wake; evidence of robustness for* $t^* = 37.3$

The influence of the mask shape was then investigated by substituting the disk by a Gaussian masking function (Eq. (3.8)). As it can be observed in Fig. 3.10, the Gaussian mask does not have a major influence on the wake centerline location but leads to smoother results.

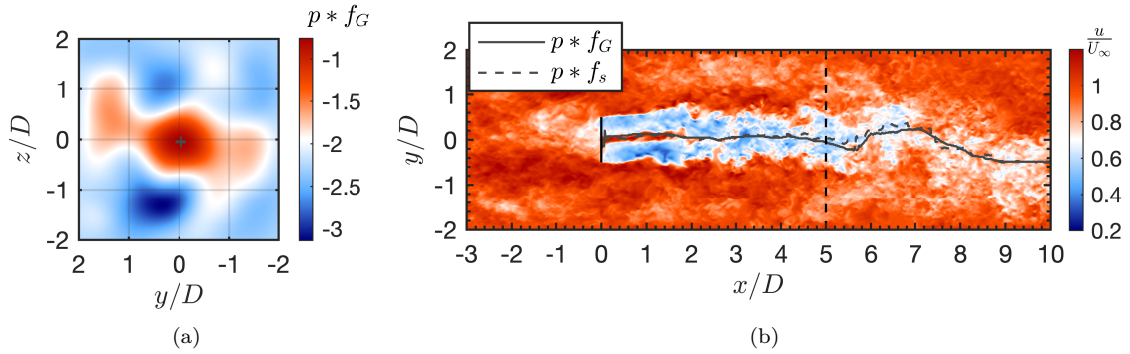



***Figure 3.10:*** *Wake centroid at $x/D = 5$ and wake centerline obtained through the convolution between a disk/Gaussian mask and the available power in the flow for $t^* = 54.2$*

With the same idea as in Section 3.2.1, the influence of the mask size was investigated. Nonetheless, instead of running several simulations with various mask sizes, an automatic adaptation of the mask size was implemented inside the simulation tool. This automatic adaptation is based on the computation of Laplacians as explained previously. Figure 3.11 shows the evolution of the mask size in space for $t^* = 54.2$. As it can be observed, the mask size is around $0.4D$ up to $4D$ downstream of the rotor and then starts to increase to reach $\sim 0.5D$. This mask adaptation does not, however, have any influence on the wake centroid location (Fig 3.12). Nevertheless, an interest of the mask size adaptation is that it enables to locate the wake borders and could be used to determine the wake expansion. The wake borders shown in Fig. 3.13 are set to $\pm 1.35\sigma_{y,z}$ from the wake centerline position obtained with the available power in the flow.

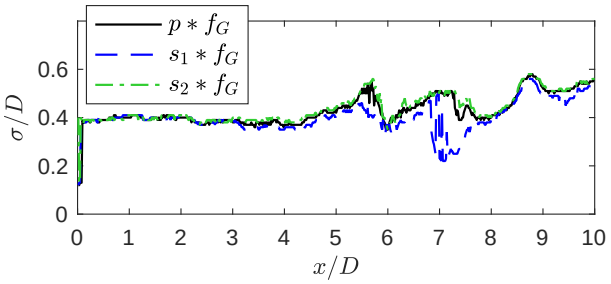



***Figure 3.11:*** *Mask size evolution in space for the computation of the convolution between a Gaussian mask adapted in space and time, and the available power, the velocity, and the momentum deficit in the wake for $t^* = 54.2$*

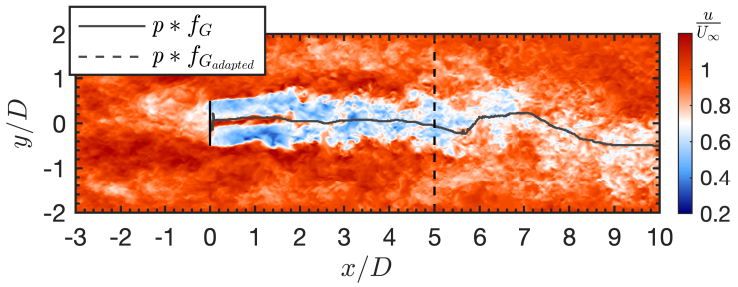



***Figure 3.12:*** *Wake centerline obtained through the convolution between a Gaussian mask adapted in space and time and the available power in the flow for* $t^* = 54.2$

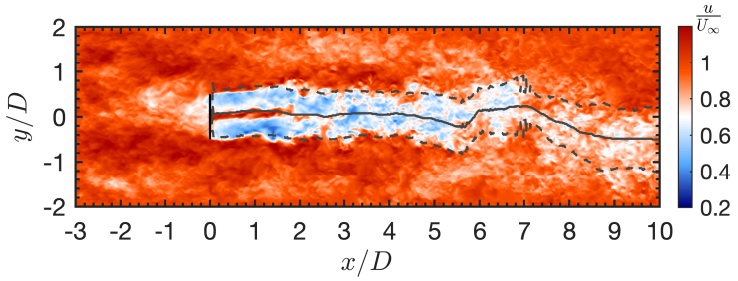



***Figure 3.13:*** *Wake centerline and wake borders obtained through the convolution between a Gaussian mask adapted in space and time and the available power in the flow for* $t^* = 54.2$

The 2D convolution method proves to be the most robust of the techniques investigated. Since it was observed that the quantity used in the 2D convolution does not influence the tracking (Fig. 3.8) and since the Gaussian mask enables to obtain a smooth wake centerline (Fig. 3.10), the technique that seems ideal to perform wake tracking is the convolution between the available power in the flow and a Gaussian masking function. However, it shows some limitations in terms of wake centroid detection for some specific times for which discontinuities appear in the wake centerline, as illustrated in Fig. 3.14. Therefore, to improve the robustness of the method, the 2D convolution was combined with a predictor of the wake centroid position, as presented in the next section.

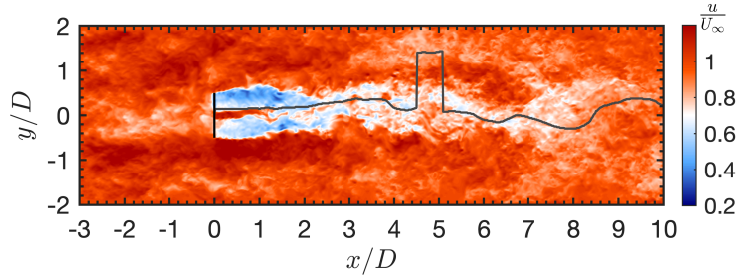



***Figure 3.14:*** *Evidence of the presence of discontinuities in the wake centerline determined through the convolution between a Gaussian mask and the available power in the flow field obtained at* $t^* = 30.5$

#### 3.2.2.2 2D convolution computation with a wake centroid predictor

The method is based on the 2D convolution described above to which a constraint has been added: the maximum in the convolution field should be located in the vicinity of a predicted wake centroid position $(y_{c_{pred}}, z_{c_{pred}})$. Equation (3.6) becomes therefore

$$(y_c, z_c) = \text{argmax}\,(p * f_G) \text{ with } \begin{cases} y_c \in \left[y_{c_{pred}} \pm 0.3D\right] \\ z_c \in \left[z_{c_{pred}} \pm 0.3D\right] \end{cases} . \tag{3.9}$$

The search limits of $\pm 0.3D$ used to locate the maximum of the convolution turn out to be a good compromise to avoid the detection of erroneous extreme wake centroid positions without limiting yet the detection of the larger wake deflections actually taking place. Indeed, from time $t_s$ to $t_s + \Delta t_s$, the wake centroid is not expected to present a large displacement. The subscript $s$ is used to differentiate the sampling time interval of the data ($\Delta t_s$) from the time step ($\Delta t$) used for the simulation. The first can be larger than the second in order to limit non-volatile memory required to store the data when the tracking is performed as a post-processing step.

For the first time step, the classical 2D convolution presented in the previous section is applied, while Eq. (3.9) is used for all the following time steps. The wake centroid position predictor at the position of index $i$ and at the current time step $(y^n_{c_{pred_i}}, z^n_{c_{pred_i}})$ is obtained by averaging, for the previous time step $(n-1)$, the eight wake centroid positions distributed upstream of the point of index $i$ over a distance of one rotor diameter. Mathematically, it gives

$$y^n_{c_{pred_i}} = \begin{cases} \frac{1}{i+1} \sum_{j=0}^{i/M} y^{n-1}_{c_{i-Mj}} \text{ for } i < Mj \\ \frac{1}{N+1} \sum_{j=0}^{N} y^{n-1}_{c_{i-Mj}} \text{ for } \ i \geqslant Mj \end{cases} , \tag{3.10}$$

where $N$ is the number of points located upstream of the point of index $i$. $N$ is fixed to 8 and $M$ depends on the resolution: $M = 8$ for the VPM approach and $M = 2$ for the FD4 code in order to distribute the eight points over a length of one rotor diameter. $z^n_{c_{pred_i}}$ is computed similarly.

Figure 3.15 shows that the use of a predictor enables to correct for the erroneous wake centroid positions obtained with the "simple" 2D convolution method, without modifying the rest of the wake centerline.

The method was then validated on the lower resolution flow obtained with the FD4 code. Figure 3.16(a) shows that the use of a predictor enables also to correct for the erroneous wake centroid positions obtained with the "simple" 2D convolution. Furthermore, as it can be observed in Fig. 3.16(b), the use of search limits of $\pm 0.3D$ does not limit the detection of steeper transition in the wake centerline (around $x/D = 9$).

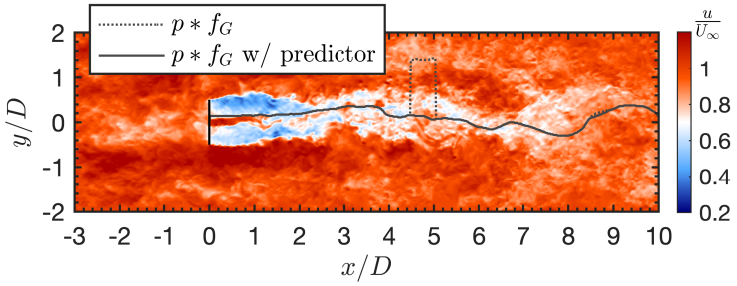
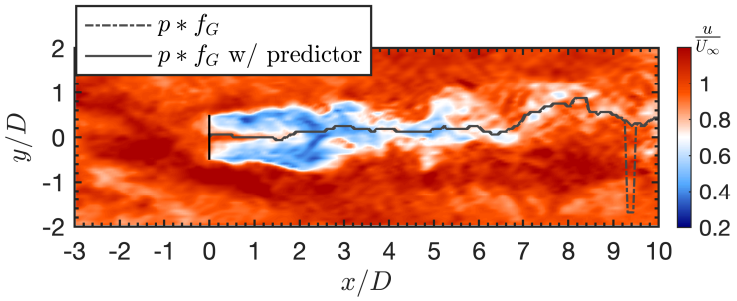
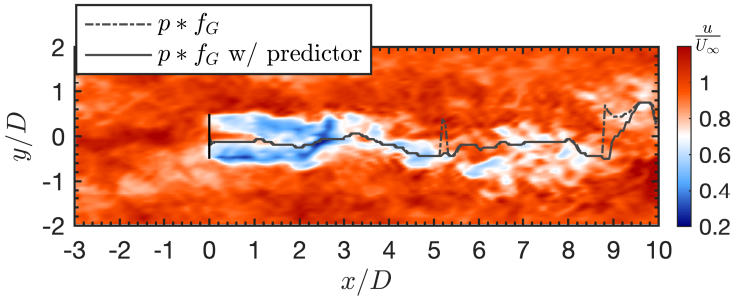



***Figure 3.15:*** *Evidence of the interest of using the predictor step for the wake centerline determination through the convolution between a Gaussian mask and the available power in the flow field obtained at* $t^* = 30.5$




(a)




(b)

***Figure 3.16:*** *Evidence of the interest of using the predictor step for the wake centerline determination through the convolution between a Gaussian mask and the available power in the flow field obtained with the FD4 code for* $t^* = 36.1$ *(a) and* $t^* = 44.1$ *(b)*

#### 3.2.2.3 3D convolution computation

An alternative to the 2D convolution approach supplemented with a wake centroid predictor (see Section 3.2.2.2) is the use of the 3D convolution. Instead of applying the 2D convolution in cross-flow planes, this method consists in convoluting 3D quantities and locating the wake centroid $(y_c, z_c)$ by searching for the maximum of the convolution field in each cross-flow plane

$$(y_c, z_c) = \text{argmax}\left(p_{3D} * f_{G_{3D}}\right), \tag{3.11}$$

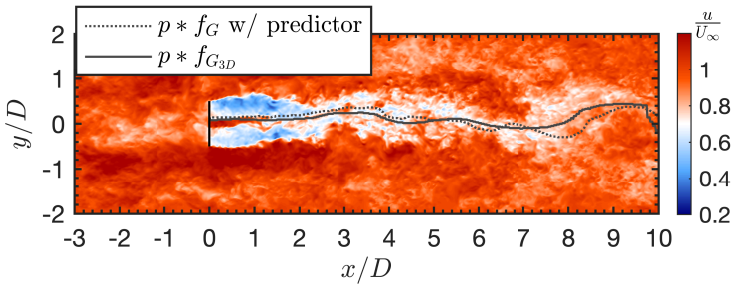
where the 3D Gaussian function is defined as

$$f_{G_{3D}}(x, y, z) = A \exp\left(-\left(\frac{x^2}{2\sigma_x^2} + \frac{y^2}{2\sigma_y^2} + \frac{z^2}{2\sigma_z^2}\right)\right) \tag{3.12}$$

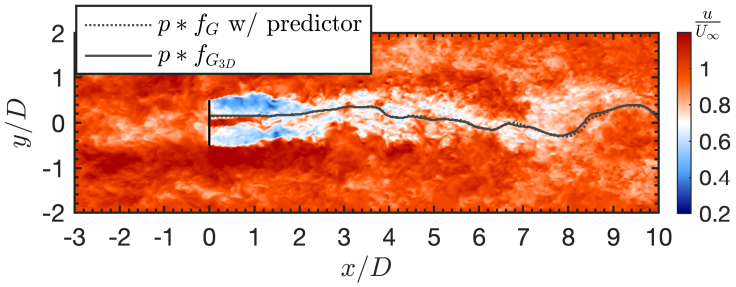
with $A = -1$, $\sigma_x = D/4$, and $\sigma_{y,z} = D/4$. The thickness $\sigma_x$ of the blob defined by Eq. (3.12) enables to obtain a smoother wake centerline without discontinuities compared to the 2D convolution.

As it can be observed in Fig. 3.17(a), the 3D convolution provides a filtered version of the wake centerline obtained using the predictor step, so the wake centerline does not present any spurious discontinuities. Reducing the size of the blob in the streamwise direction from $\sigma_x = D/4$ to $\sigma_x = D/16$ enables to obtain a wake centerline very similar to that obtained using the predictor step (Fig. 3.17(b)). The 3D convolution method was also validated on the lower resolution flow obtained with the FD4 code. As it can be observed in Fig. 3.18, the 3D convolution enables to track properly the wake centerline even in complex situations, as illustrated by Fig. 3.18(b) and 3.18(c).

The interest of the 3D convolution, over the 2D convolution with a wake centroid predictor, is that it paves the way for wake tracking of wind turbines subjected to an inflow with varying direction; the main axis of the blob can be easily aligned with the inflow direction. For the next chapters, it was nevertheless decided to stick to the simplest effective method that can be easily implemented and that is more modular, i.e. the 2D convolution with a predictor of the wake centroid.

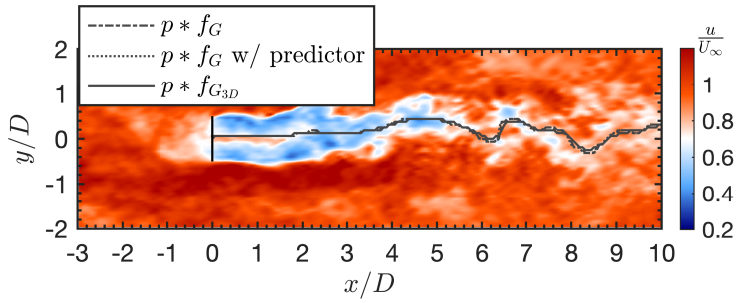



(a)

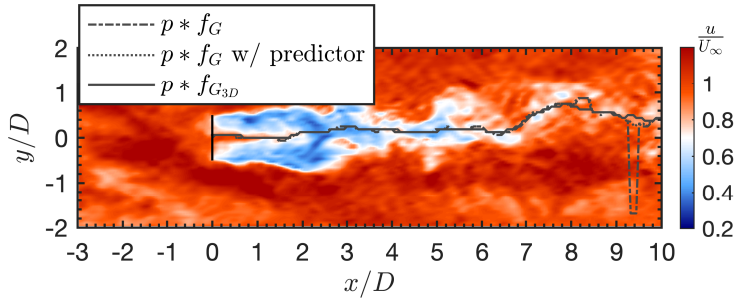



(b)

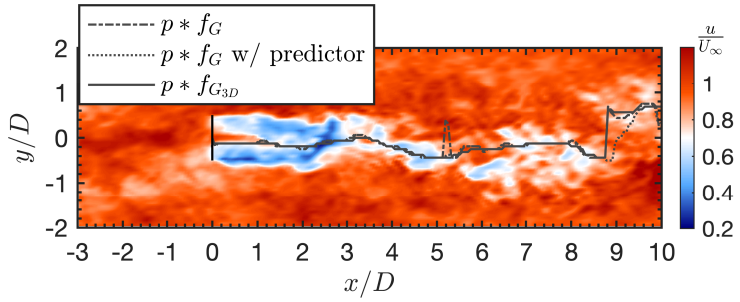
***Figure 3.17:*** *Comparison of the wake centerlines obtained with the 2D and 3D convolution between a Gaussian mask and the available power in the flow for* $t^* = 30.5$*;* $\sigma_x = D/4$ *(a) and* $\sigma_x = D/16$ *(b)*




(a)




(b)




(c)

***Figure 3.18:*** *Comparison of the wake centerlines obtained with the 2D, 2D with predictor and 3D convolution between a Gaussian mask and the available power in the flow field obtained with the FD4 code for* $t^* = 32.2$ *(a),* $t^* = 36.1$ *(b), and* $t^* = 44.1$ *(c)*

## 3.3 Wake centroid detection in a horizontal plane

While numerical simulations provide the flow quantities along the three dimensions of the computational domain, experimental techniques still generally provide the instantaneous flow quantities inside 2D planes (nowadays tomographic PIV enables to perform measurements in a complete 3D measurement volume but of limited size). The wake tracking algorithms presented above can directly be applied to experimental data obtained in cross-flow planes. In order to extend the application of the tracking to a wider range of experimental data, the convolution technique was adapted so as to be applicable in 2D horizontal planes.

The simplest adaptation of the convolution method presented above consists in performing, for each cross-flow line, the 1D convolution between the available power in the flow along this line $p_{1D}$ and a 1D Gaussian function

$$f_{G_{1D}}(y) = A \exp\left(-\frac{y^2}{2\sigma_y^2}\right) \tag{3.13}$$

with $A = -1$, and $\sigma_y = D/4$. The wake centroid being obtained by locating the maximum of the convolution performed for each cross-flow line

$$y_c = \text{argmax}\left(p_{1D} * f_{G_{1D}}\right). \tag{3.14}$$

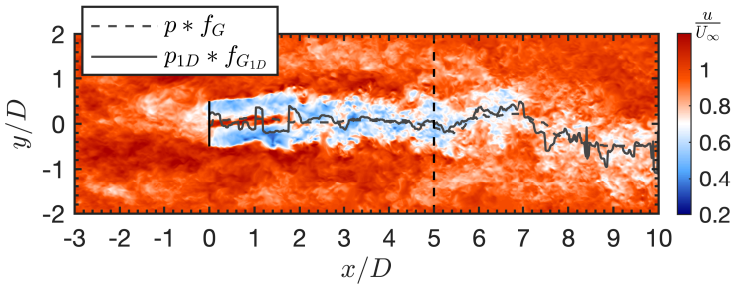
As it could be expected, the wake centerline is more prone to present oscillations when the tracking is performed along a single dimension instead of two (Fig. 3.19(a)). In order to obtain a cleaner wake centerline, the idea behind the 3D convolution was exploited for the tracking in 2D horizontal planes. That is to perform the convolution between the power available in a 2D horizontal plane $p_{2D_{hp}}$ and a 2D Gaussian function defined, this time, in the horizontal plane

$$f_{G_{2D_{hp}}}(x, y) = A \exp\left(-\left(\frac{x^2}{2\sigma_x^2} + \frac{y^2}{2\sigma_y^2}\right)\right) \tag{3.15}$$

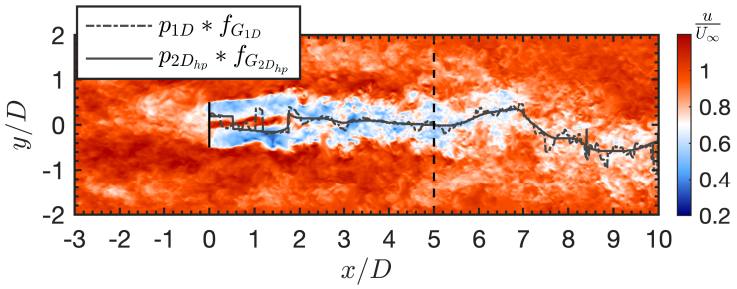
with $A = -1$, $\sigma_x = D/4$, and $\sigma_y = D/4$. The wake centroid $y_c$ is then located by searching for the maximum of the convolution field for each cross-flow line

$$y_c = \text{argmax}\left(p_{2D_{hp}} * f_{G_{2D_{hp}}}\right). \tag{3.16}$$

As it can be observed in Fig. 3.19(b), this technique enables to obtain a smoother wake centerline. This technique was then validated on velocity fields obtained with the FD4 code (Fig. 3.20). It enables to track properly the wake centerline (Fig. 3.20(a)) while avoiding the detection of erroneous extreme wake centroid positions (Fig. 3.20(b)) without limiting yet the detection of the large wake deflections actually taking place (Fig. 3.20(c)).

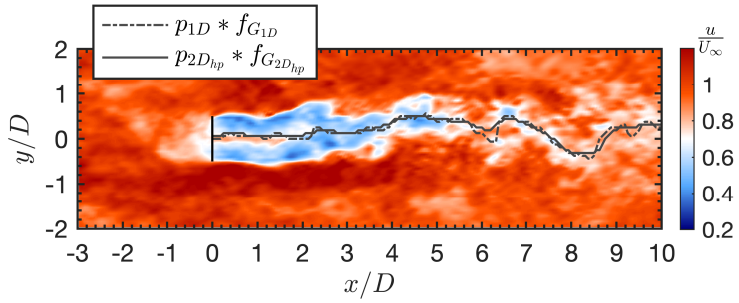



(a)

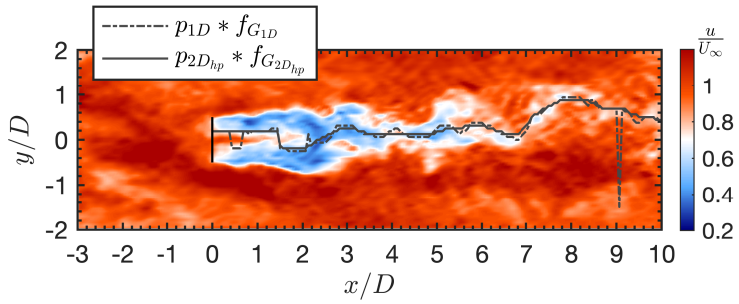



(b)

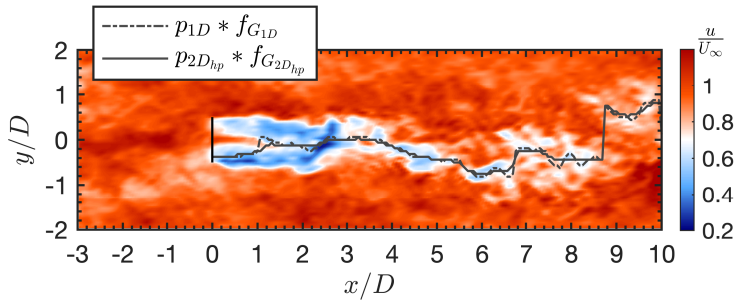
***Figure 3.19:*** *Comparison between the wake centerlines obtained with the 1D convolution in the horizontal plane and the 2D convolution in cross-flow planes (a) and between the wake centerlines obtained with the 2D convolution in the horizontal plane and the 1D convolution in the horizontal plane (b) with the VPM code for* $t^* = 54.2$




(a)




(b)




(c)

***Figure 3.20:*** *Comparison between the wake centerlines obtained with the 2D convolution in the horizontal plane and the 1D convolution in the horizontal plane between a Gaussian mask and the available power in the flow field obtained with the FD4 code for* $t^* = 32.2$ *(a) ,* $t^* = 36.1$ *(b), and* $t^* = 44.1$ *(c)*

## 3.4 Conclusions

In this chapter, several diagnostics were proposed to track the wake centerline of a horizontal axis wind turbine. These methods were first assessed on LES results of the NREL 5-MW wind turbine subjected to a laminar inflow ($I = 0\%$) and then with a turbulent inflow ($I = 8.4\%$). The tracking algorithms were first applied to cross-flow planes. The results indicate a better robustness of the technique based on the convolution compared to technique based on the computation of the first order moment. Additional investigations for the convolution method highlight that the density field used in the convolution does not impact the wake tracking and that replacing the square mask by a Gaussian mask enables to obtain a smoother wake centerline. The influence of the Gaussian mask size $\sigma_{y,z}$ was then investigated. Instead of testing several $\sigma_{y,z}$, a method to adapt $\sigma_{y,z}$ according to space and time was developed. Even if the adaptation of $\sigma_{y,z}$ has no major influence on the wake centerline localization, the results show that this method allows to track the wake borders and to capture the wake expansion.

While the convolution between the available power in the flow and a Gaussian masking function has proved to be the most robust technique for wake tracking, it shows some limitations in terms of wake centroid detection for some specific times for which discontinuities appear in the wake centerline because of erroneous wake centroid detections. To alleviate this problem, the 2D convolution had to be supplemented with a wake centroid predictor or to be replaced by a 3D convolution. The interest of the 3D convolution, over the 2D convolution with a wake centroid predictor, is that it paves the way for wake tracking of wind turbines subjected to an inflow with varying direction. For the next chapters, it was decided to stick to the simplest effective method that can be easily implemented and that is more modular, i.e. the 2D convolution supplemented with a predictor of the wake centroid.

In order to extend the application of the tracking to a wider range of data, and in particular to the TR-PIV measurements performed in a horizontal plane, the convolution technique was adapted so as to be applicable in 2D horizontal planes. From the idea behind the 3D convolution, a clean wake centerline could be obtained in a 2D horizontal plane by performing the convolution between the available power in this plane and a 2D Gaussian function defined, this time, in the horizontal plane.

Note that the various algorithms presented in this Chapter were implemented within the VPM code, what enables to perform run-time tracking of the wake centerline. In addition to avoiding the need to store a large amount of data necessary for the tracking as a post-processing step, the run-time tracking opens a door towards real-time alleviation control of the wake meandering.

Chapter 4

# Numerical study of wind turbine wake meandering characteristics at full scale

The aim of this chapter is to characterize the wind turbine wake meandering phenomenon, especially in terms of amplitude, wavelength and frequency. The influence of the turbulence intensity and of the integral length scales on the wake meandering characteristics is investigated for an isolated NREL 5-MW wind turbine subjected to several synthetic turbulent inflows. On top of that, it is verified that the modeling approach, affordable at wind farm scale, in this case the FD4 code combined with advanced actuator disks, provides equivalent results in terms of wake centerline position compared to a higher level of fidelity tool, i.e. the VPM code combined with immersed lifting lines. Finally, the correlation between the inflow, the machine loads and the wake centroid is investigated.

## 4.1 Numerical setup

### 4.1.1 VPM simulations

The numerical setup is similar to which of Section 3.1. For the sake of conciseness, only the parameters that vary are presented. The wind turbine rotor is subjected to several uniform (no shear) turbulent inflows synthesized through Mann's algorithm [50] in a $32D \times 4D \times 4D$ box. The turbulence intensities tested are $I = \sqrt{\frac{1}{3}(\sigma_u^2 + \sigma_v^2 + \sigma_w^2)}/U_\infty = 0\%, 4.8\%, 8.4\%$ and $12.0\%$. The time step ($\Delta t$) is set such that $\Delta t \cdot \frac{U_\infty}{D} = 8.9 \cdot 10^{-3}$. The computational costs of the VPM simulations can be found in Appendix A.2.

### 4.1.2 FD4 simulations

Again, the numerical setup is similar to which of Section 3.1. For the sake of conciseness, only the parameters that vary are presented. The wind turbine rotor is subjected to several uniform (no shear) turbulent inflows synthesized through Mann's algorithm [50] in a $32D \times 4D \times 4D$ box. The turbulence intensities tested are $I = 0\%, 4.8\%, 8.4\%$ and $12.0\%$. The computational costs of the FD4 simulations can be found in Appendix A.2.

### 4.1.3 Turbulent inflow

Uniform (no shear) turbulent velocity fields $\mathbf{u}'$ corresponding to turbulence intensities of 4.8%, 8.4%, and 12.0% were synthesized through Mann's algorithm [50]. As the same seed (for the random number generator) was used within the Mann's algorithm to generate the inflows, the averaged integral length scales, computed from the generated inflow, are the same for the three turbulence intensities (Table 4.1); ${}^{x}L_u$ denotes the integral length scale of the longitudinal component in the longitudinal direction, and ${}^{x}L_v$ and ${}^{x}L_w$ denote the integral length scales of the lateral and vertical component in the longitudinal direction. An additional inflow with smaller integral length scales was then generated to study the influence of the integral length scales on the wake meandering phenomenon (Table 4.2). For the generation of this inflow, it was not possible to enforce rigorously identical turbulence intensity components when varying the size of the integral length scales. The turbulence intensity components remain however close to each other. Note that the labels $I = 8.4\%$ and ${}^{x}L_u/D = 1.5$ refer to the same inflow.

| | ${}^{x}L_u/D$ | ${}^{x}L_v/D$ | ${}^{x}L_w/D$ | $I_u$ | $I_v$ | $I_w$ |
|---|---|---|---|---|---|---|
| $I = 4.8\%$ | 1.47 | 0.49 | 0.23 | 0.061 | 0.047 | 0.033 |
| $I = 8.4\%$ | 1.47 | 0.49 | 0.23 | 0.106 | 0.082 | 0.057 |
| $I = 12.0\%$ | 1.47 | 0.49 | 0.23 | 0.152 | 0.116 | 0.081 |

***Table 4.1:*** *Averaged integral length scales and turbulence intensity components of the inflows referred to as $I = 4.8\%$, $I = 8.4\%$, and $I = 12.0\%$; ${}^{x}L_u$ denotes the integral length scale of the longitudinal component in the longitudinal direction, and ${}^{x}L_v$ and ${}^{x}L_w$ denote the integral length scales of the lateral and vertical component in the longitudinal direction*

| | ${}^{x}L_u/D$ | ${}^{x}L_v/D$ | ${}^{x}L_w/D$ | $I_u$ | $I_v$ | $I_w$ |
|---|---|---|---|---|---|---|
| ${}^{x}L_u/D = 1.5$ | 1.47 | 0.49 | 0.23 | 0.106 | 0.082 | 0.057 |
| ${}^{x}L_u/D = 0.75$ | 0.75 | 0.18 | 0.10 | 0.106 | 0.077 | 0.053 |

***Table 4.2:*** *Averaged integral length scales and turbulence intensity components of the inflows referred to as ${}^{x}L_u/D = 1.5$ and ${}^{x}L_u/D = 0.75$*

## 4.2 Results

Among the algorithms assessed in Chapter 3, the most robust technique to perform the tracking of the wake centroid in a cross-flow plane located downwind of a machine subjected to a turbulent inflow is based on the 2D convolution between the available power density in the flow and a Gaussian masking function. In this chapter, the version of the algorithm supplemented by a predictor of the wake centroid is used, which makes the tracking more robust.

### 4.2.1 Effects of the inflow turbulence intensity on the wake meandering characteristics

Figures 4.1 and 4.2 show the wake centerlines, superimposed on snapshots of the streamwise velocity, obtained with the VPM (solid line) and with the FD4 (dash-dot line) codes in the horizontal plane at hub height (Fig. 4.1) and in the vertical plane passing through the hub (Fig. 4.2) for inflow turbulence intensities of 0%, 4.8%, 8.4%, and 12.0%. As expected, the wake does not meander for $I = 0\%$. Even if the wake obtained with the VPM code for $I = 0\%$ presents some oscillations in the very far wake, these oscillations however appear to be of a different nature of meandering and seem to be caused by an internal dynamics of the wake structures. These oscillations are not present for the wake obtained with the FD4 code because of the lower resolution of the method. For the higher

turbulence intensities, the wake meandering is clearly present. As it can be observed, the wake centerlines obtained at the higher turbulence intensities properly follow the wake displacements. The wake tracking is nevertheless easier at lower turbulence intensities and closer from the machine. Indeed, because of the wake recovery, the wakes are less well defined when the distance from the machine increases, especially for a high inflow turbulence level. Qualitatively, there is a good agreement between the wake centerlines obtained with the two approaches at least up to four rotor diameters downstream of the machine for the most complex situation, i.e. the highest inflow turbulence level. Beyond this distance, the obtained wake centerlines start to differ from each other, especially as the inflow turbulence level increases. This is due to differences in the wakes obtained with the two approaches, the differences being more pronounced when the distance from the rotor increases, especially for a higher inflow turbulence level because of the faster wake recovery.

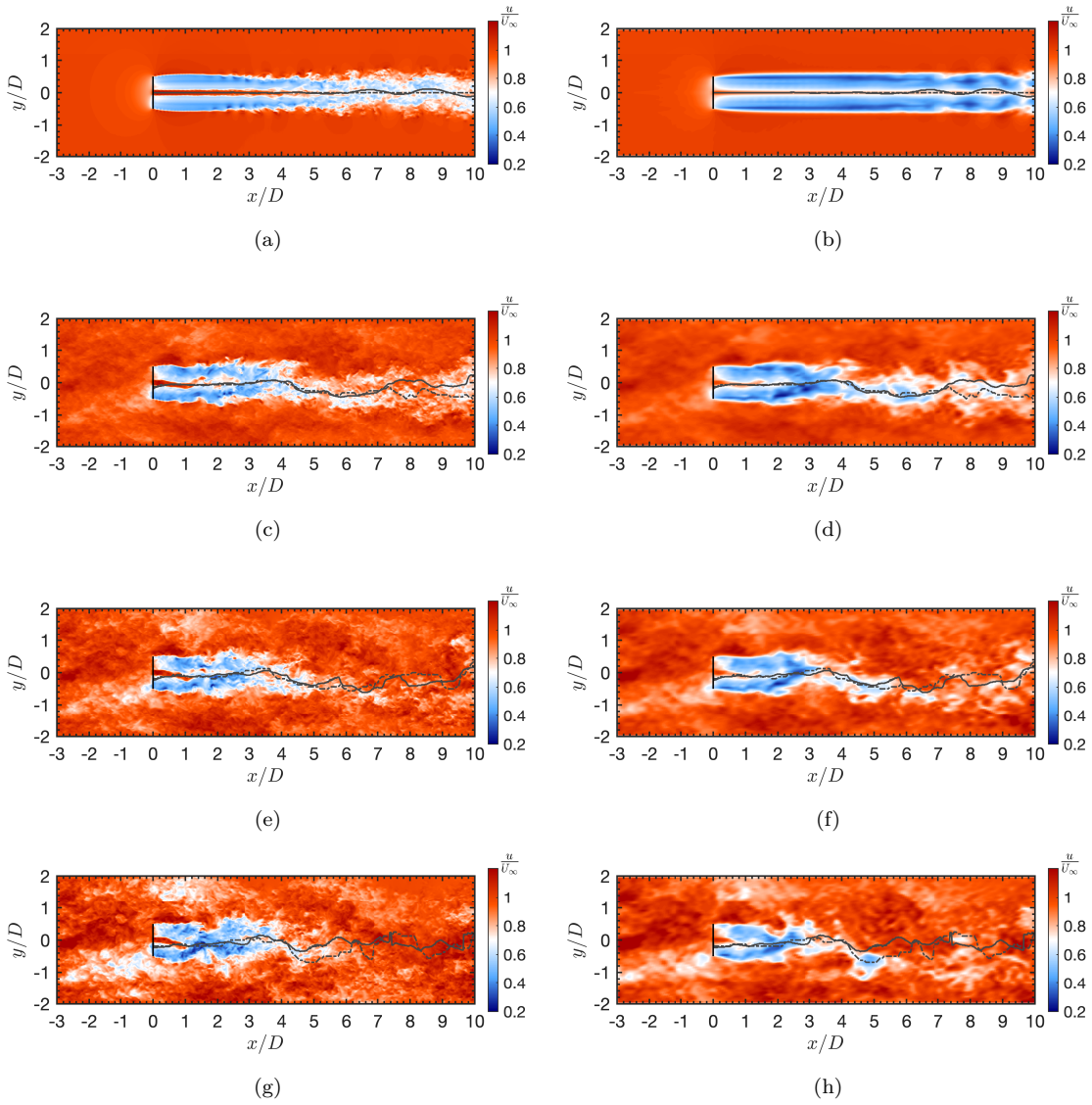



***Figure 4.1:*** *Snapshots in the horizontal plane at hub height of the streamwise velocity obtained with the VPM (a)-(c)-(e)-(g) and FD4 (b)-(d)-(f)-(h) codes on which the wake centerlines obtained with VPM (solid line) and with FD4 (dash-dot line) codes are superimposed for several inflow turbulence intensities:* $I = 0\%$ *(a)-(b),* $I = 4.8\%$ *(c)-(d),* $I = 8.4\%$ *(e)-(f), and* $I = 12.0\%$ *(g)-(h)*

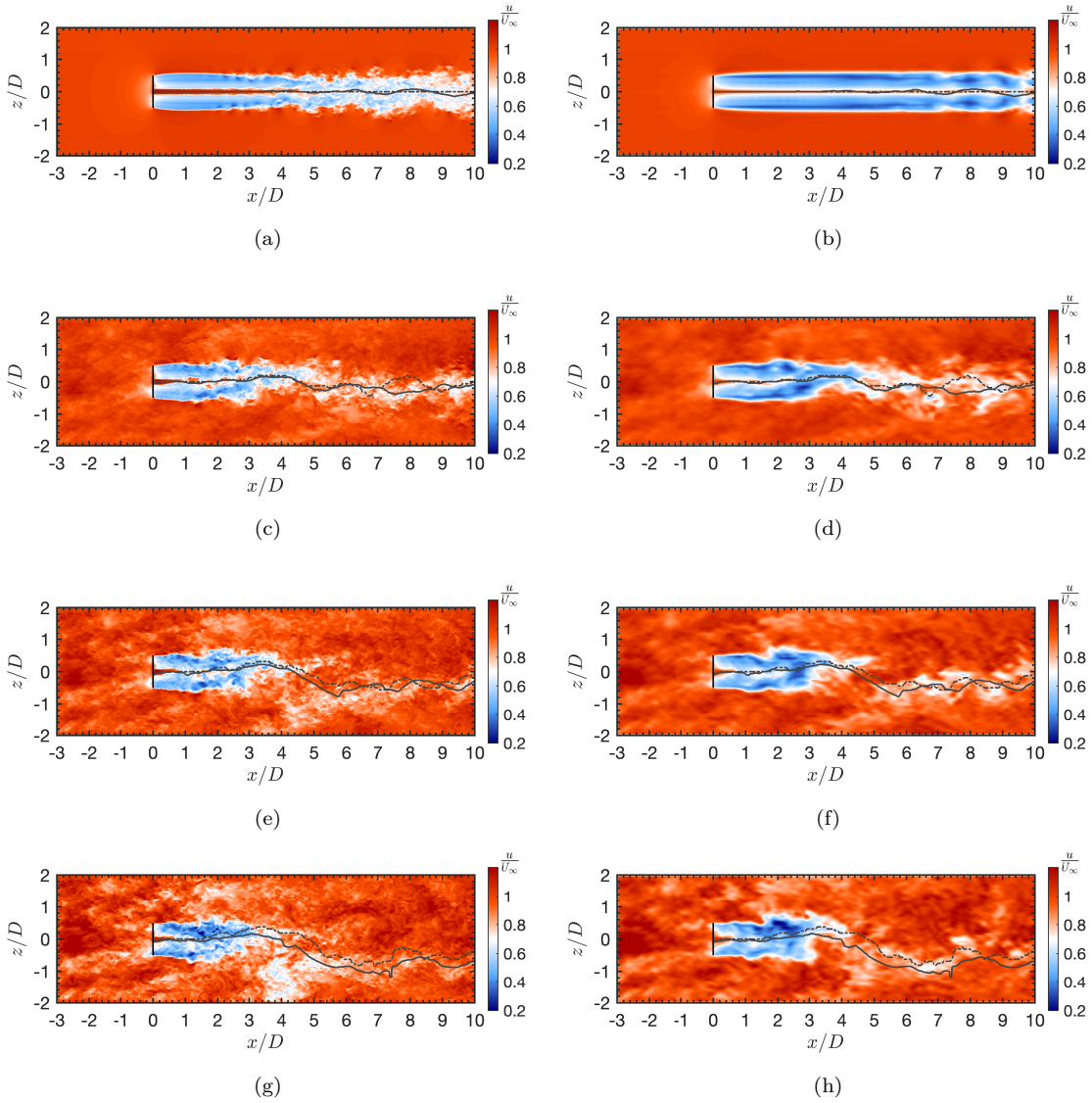



***Figure 4.2:*** *Snapshots in the vertical plane passing through the hub of the streamwise velocity obtained with VPM (a)-(c)-(e)-(g) and FD4 (b)-(d)-(f)-(h) codes on which the wake centerlines obtained with VPM (solid line) and with FD4 (dash-dot line) codes are superimposed for several inflow turbulence intensities: $I = 0\%$ (a)-(b), $I = 4.8\%$ (c)-(d), $I = 8.4\%$ (e)-(f), and $I = 12.0\%$ (g)-(h)*

In the next paragraphs, the wake centerlines obtained with the two approaches are compared quantitatively. The statistics are computed from the data of the last 77 rotor revolutions, i.e. approx. 32 convective times ($t_c = D/U_\infty$). The wake centroid positions as a function of dimensionless space ($x/D$) and time ($t^* = t \cdot U_\infty/D$) are represented in Figs. 4.3 and 4.4 for the four inflow turbulence intensities tested. In order to obtain the wake centerline (i.e. wake centroid evolution as a function of space) in the horizontal or vertical plane at a specific time, one can simply extract the data along a horizontal line from Fig. 4.3 and 4.4, respectively. This is illustrated in Figs. 4.3 and 4.4 by the dashed lines corresponding to the time at which the wake centerlines presented in Figs. 4.1 and 4.2 were extracted. At the opposite, the data along a vertical line represent the evolution of the wake centroid as a function of time at a specific position behind the rotor. As it can be observed, the wake centroid displacements obtained with the two approaches are similar in shape but vary in magnitude. These differences in magnitude are due to differences in the wakes themselves as it can be observed in Figs. 4.1 and 4.2. Focusing on the vertical motion of the wake centroids (Fig. 4.4), one can observe that the patterns obtained with both approaches are very

similar but that there is a shift towards negative values for the wake centroids obtained with the VPM code. This is due to a general vertical deflection of the wakes obtained with the VPM code. Furthermore, comparing Figs. 4.3 and 4.4 highlights that the wake deflections are less pronounced in the vertical plane. Since no ground is modeled in the simulations, the differences in wake deflections between the horizontal and the vertical planes are entirely due to the velocity fluctuations that are larger in the horizontal plane than in the vertical plane. Indeed, $\sigma_v = 0.77\,\sigma_u$ and $\sigma_w = 0.54\,\sigma_u$ in the turbulent inflows (regardless of the turbulence intensity) that were generated by the Mann's algorithm. These ratio are in good agreement with what was reported by Counihan [77] and what can be found in the VDI guidelines [78]: $\sigma_v = 0.75\,\sigma_u$ and $\sigma_w = 0.5\,\sigma_u$. This influence of the ratio of the turbulence intensity components on the wake deflections is in agreement with what was observed in [16] and is further discussed later.

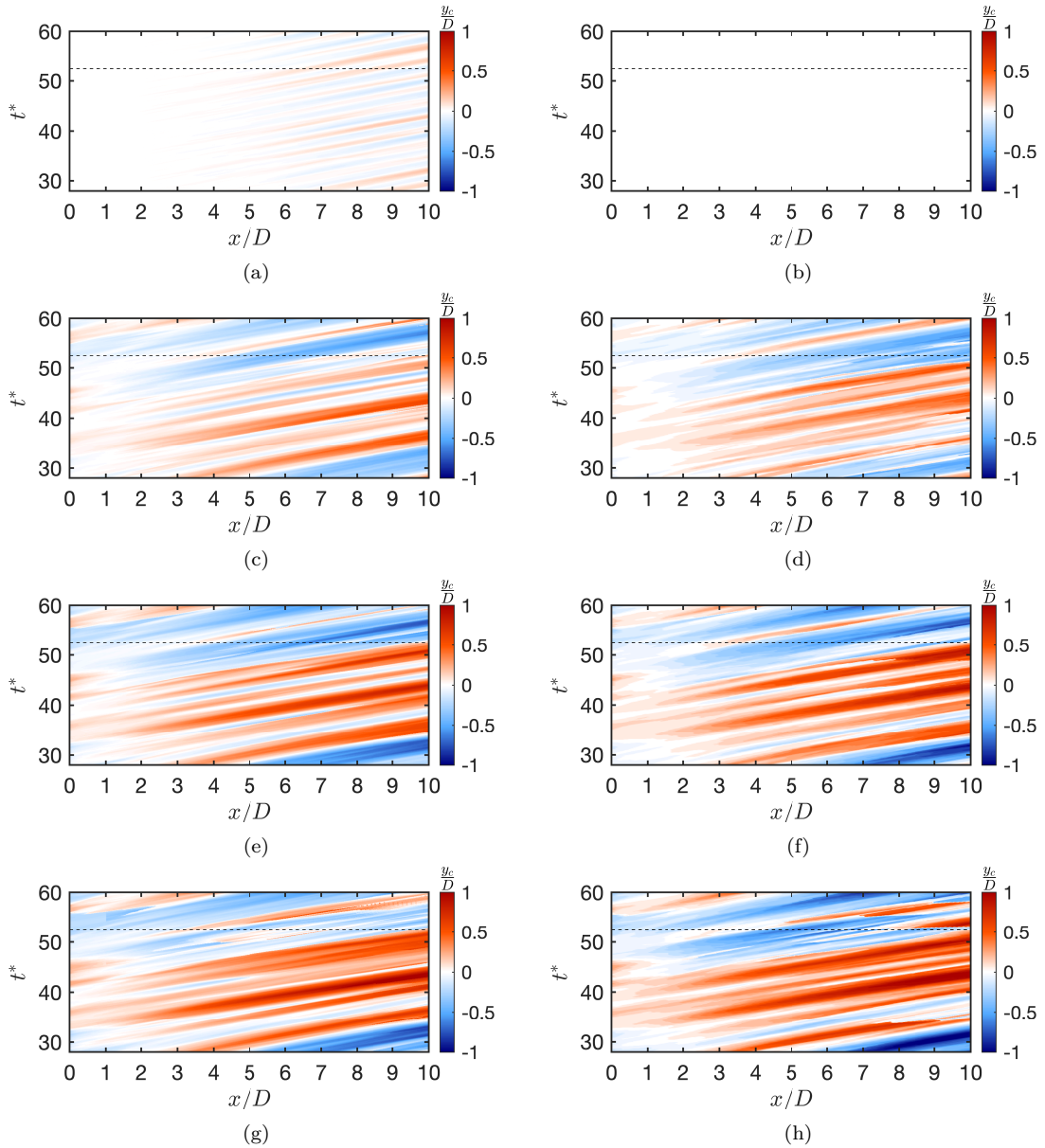



***Figure 4.3:*** *Dimensionless horizontal motion of the wake centerline as a function of space and time obtained with the VPM (a)-(c)-(e)-(g) and FD4 (b)-(d)-(f)-(h) codes for several inflow turbulence intensities: $I = 0\%$ (a)-(b), $I = 4.8\%$ (c)-(d), $I = 8.4\%$ (e)-(f), and $I = 12.0\%$ (g)-(h)*

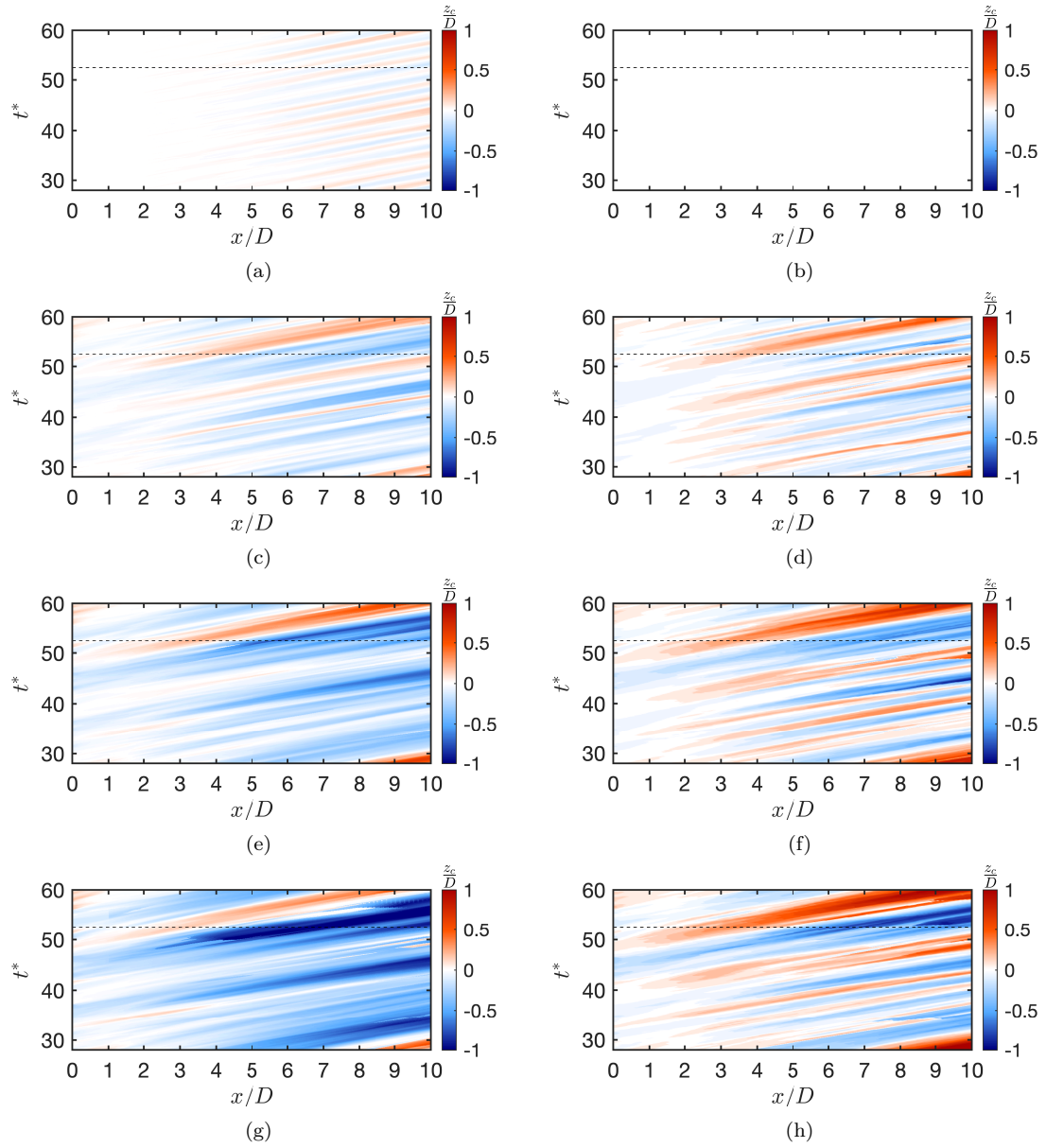



***Figure 4.4:*** *Dimensionless vertical motion of the wake centerline as a function of space and time obtained with the VPM (a)-(c)-(e)-(g) and FD4 (b)-(d)-(f)-(h) codes for several inflow turbulence intensities: $I = 0\%$ (a)-(b), $I = 4.8\%$ (c)-(d), $I = 8.4\%$ (e)-(f), and $I = 12.0\%$ (g)-(h)*

Figures 4.5 and 4.6 show the probability distribution of the wake centroid position as a function of the streamwise position. These figures reveal that the wake centroid distribution becomes larger with the downstream distance from the rotor and with the inflow turbulence level. Furthermore, one can observe that the wake meandering starts closer from the rotor when the inflow turbulence level increases and that the distributions of the wake centroid are wider in the horizontal plane than in the vertical one (Figs. 4.5 and 4.6).

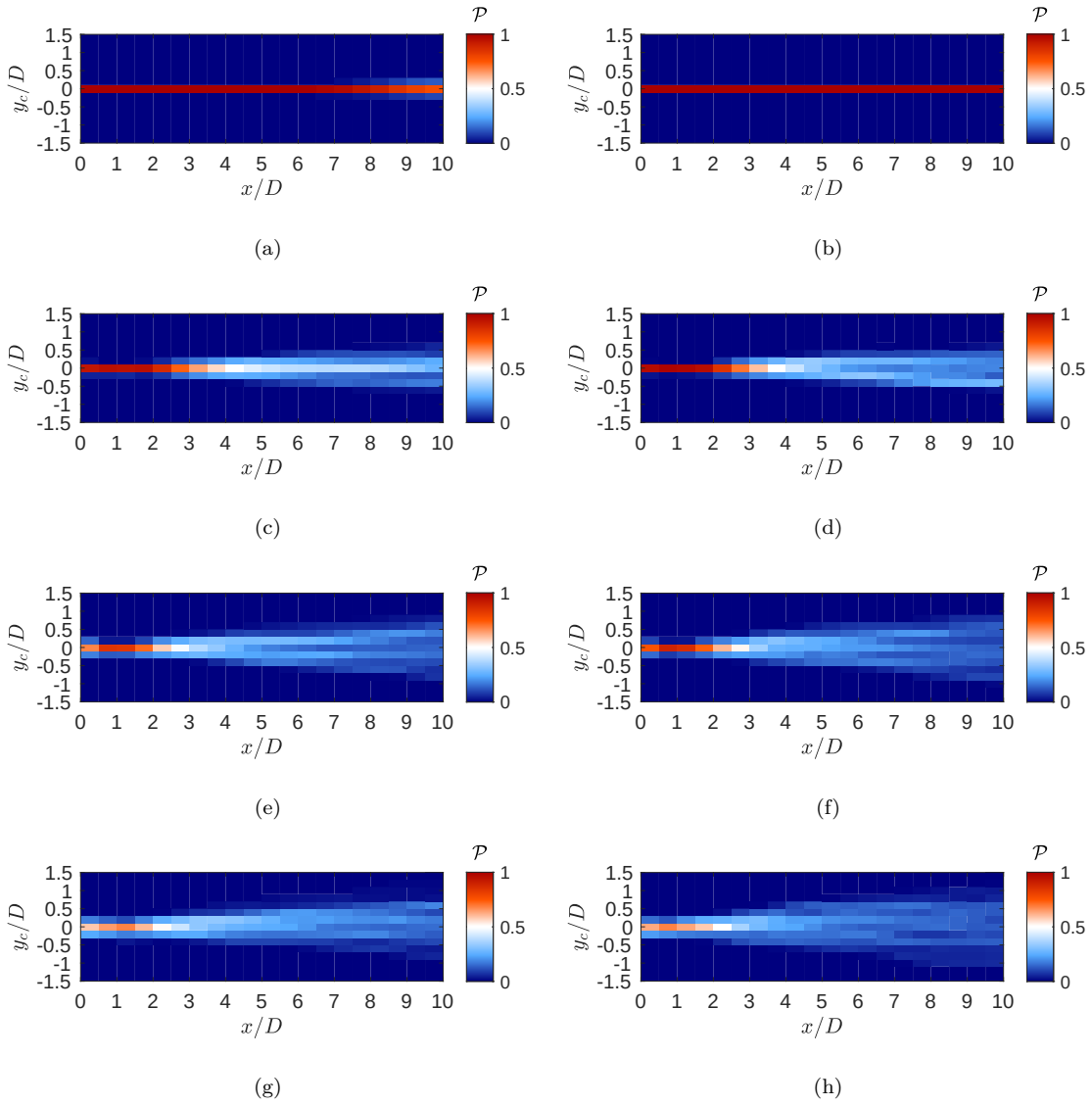



***Figure 4.5:*** *Probability of finding a wake centroid at a certain location in the horizontal plane at hub height, obtained with the VPM (a)-(c)-(e)-(g) and FD4 (b)-(d)-(f)-(h) codes for several inflow turbulence intensities: $I = 0\%$ (a)-(b), $I = 4.8\%$ (c)-(d), $I = 8.4\%$ (e)-(f), and $I = 12.0\%$ (g)-(h), the bins width is $D/5$*

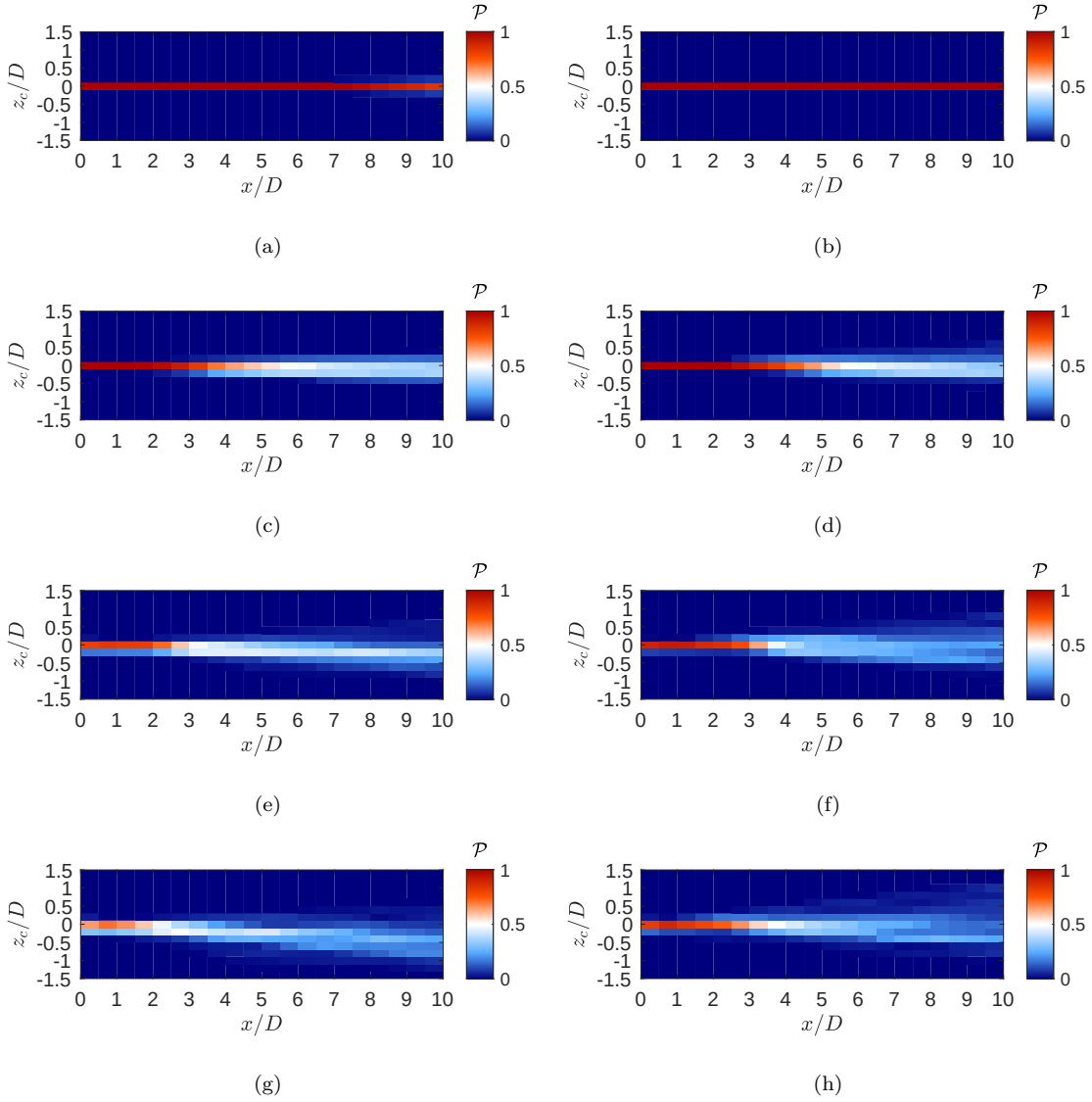



***Figure 4.6:*** *Probability of finding a wake centroid at a certain location in the vertical plane passing through the hub, obtained with the VPM (a)-(c)-(e)-(g) and FD4 (b)-(d)-(f)-(h) codes for several inflow turbulence intensities: $I = 4.8\%$ (a)-(b), $I = 4.8\%$ (c)-(d), $I = 8.4\%$ (e)-(f), and $I = 12.0\%$ (g)-(h), the bins width is $D/5$*

The wake centerline envelopes (Fig. 4.7) were obtained by considering the maximum deflection of the wake centroid for each position behind the rotor. This can be illustrated in Figs. 4.3 and 4.4 for the horizontal and vertical plane, respectively. Indeed, the maximum deflection of the wake centroid at a specific location corresponds to the maximum and minimum values along a vertical line located at the relevant position in Figs. 4.3 and 4.4. The wake centerline envelopes (Fig. 4.7) show that the maximum deflections of the wake centerlines increase with the downstream distance from the rotor and with the inflow turbulence intensity. As it can be observed, there is a good agreement between the envelopes obtained with the VPM code and from the flow computed with the FD4 code, especially in the horizontal plane. As expected, the discrepancies between the envelopes increase with the downstream distance from the rotor and with the inflow turbulence level, except for $I = 0\%$ for which oscillations are present in the far wake obtained with the VPM code but not with the FD4 code.

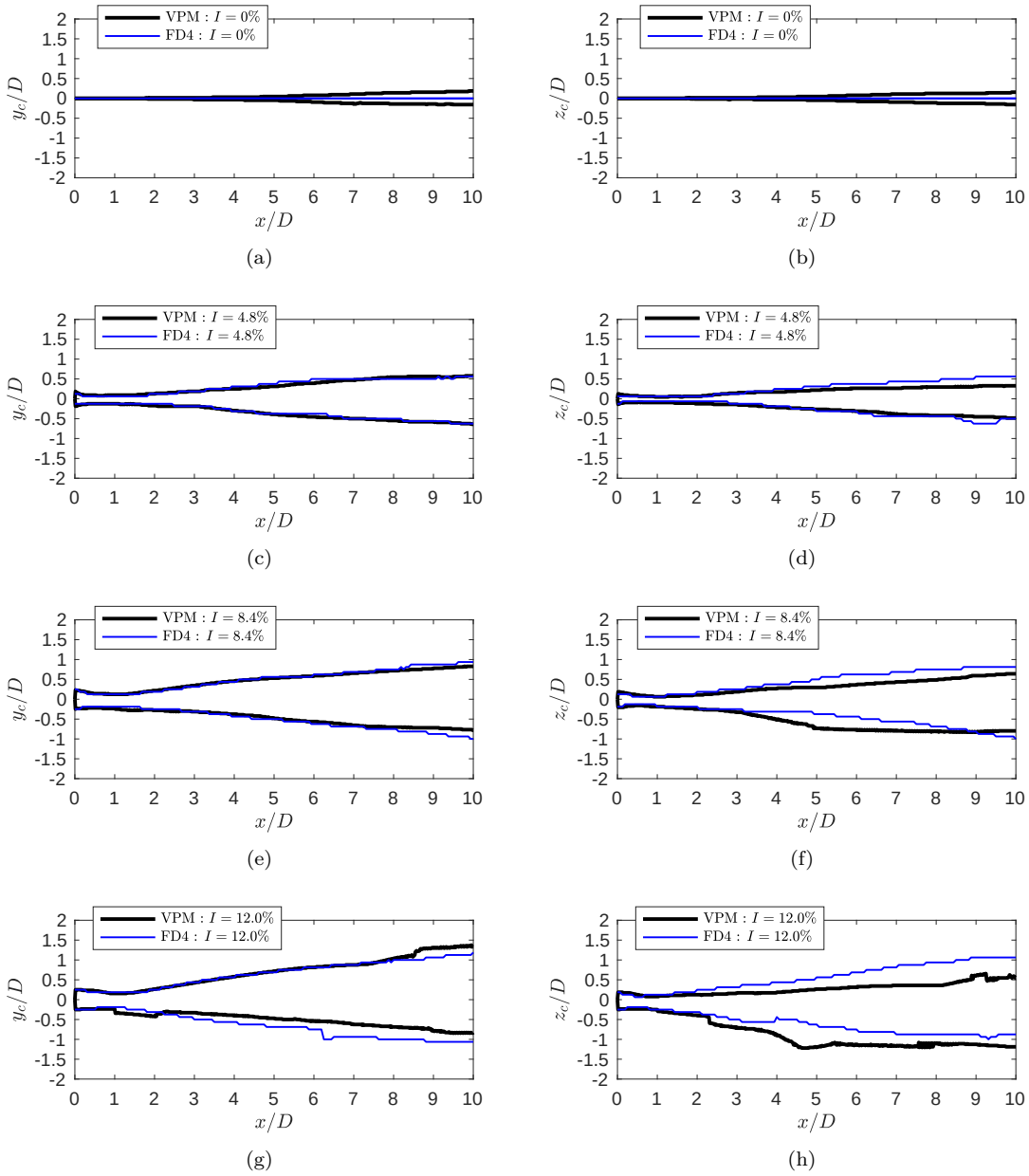



***Figure 4.7:*** *Dimensionless wake centerline envelopes obtained with the VPM and FD4 codes in the horizontal plane at hub height (a)-(c)-(e)-(g) and in the vertical plane passing through the hub (b)-(d)-(f)-(h) for several inflow turbulence intensities: $I = 0\%$ (a)-(b), $I = 4.8\%$ (c)-(d), $I = 8.4\%$ (e)-(f), and $I = 12.0\%$ (g)-(h)*

In addition, a quantitative analysis of the wake centerline characteristics was performed on the basis of the work of Foti et al. [37]. First, each wake centerline is low-pass filtered spatially with a cut-off length $L_{cut-off} = 1D$. The amplitude of wake meandering is then computed as half the cross-wind distance between consecutive maximum-minimum of the filtered wake centerline while the wavelength is computed as the streamwise distance between two consecutive maxima or minima (Fig. 4.8). The downstream position of these quantities was set to the intermediate position of the two points involved in the computation. The quantities were then binned, with respect to the downwind distance from the rotor, into half-diameter bins and the mean values were computed. The wake oscillations are captured in the horizontal plane at hub height and in the vertical plane passing through the hub. Note that, for the sake of transparency, downwind distances ranging from

$0D$ to $10D$ are presented in Figs. 4.9 and 4.13, even if the exploitable part of the graphs is for $3 \lesssim x/D \lesssim 7$ due to the method used to determine the amplitude and wavelength of the oscillations.

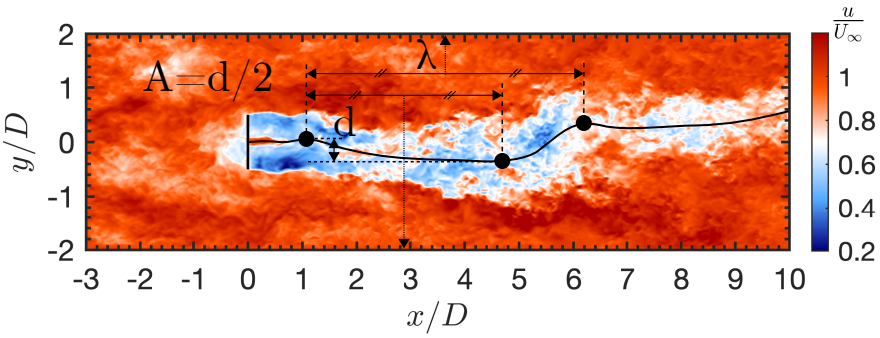



***Figure 4.8:*** *Schematic with the conventions used for the determination of the amplitudes and the wavelengths of the wake centerline oscillations*

For the sake of conciseness, the probability distribution of the wake meandering amplitudes and wavelengths are presented in Appendix B. Figures 4.9(a) and 4.9(b) show the mean amplitude of the wake oscillations as a function of space. This amplitude increases with the distance downwind from the rotor and with the inflow turbulence level. Furthermore, the linear growth of the meandering amplitude with respect to the downwind distance from the rotor is highlighted in Fig. 4.9(c) and 4.9(d), where the amplitude is normalized by the downstream distance. Indeed, the profiles are fairly constant in the central part of Fig. 4.9(c) and 4.9(d). One can observe that the mean binned amplitude of the oscillations obtained with the VPM and FD4 methods are in good agreement for $I = 4.8\%$ and $I = 8.4\%$, the discrepancies being larger for $I = 12.0\%$. As expected with an anisotropic inflow, the wake meandering amplitudes are larger in the horizontal direction ($x - y$ plane) compared to the vertical direction ($x - z$ plane). Since no ground is modeled in the simulations, this difference in wake meandering amplitude is entirely due to the velocity fluctuations that are larger in the horizontal plane than in the vertical plane. Indeed, as stated previously, $\sigma_v = 0.77\,\sigma_u$ and $\sigma_w = 0.54\,\sigma_u$ in the turbulent inflows (regardless of the turbulence intensity) that were generated by the Mann's algorithm. As observed in [16], the ratio between the lateral and vertical wake meandering amplitudes is close to the ratio between the lateral and vertical turbulence intensity components $\sigma_v/\sigma_w$ of the inflow (Fig. 4.10). This is illustrated in Fig. 4.11 where the wake meandering amplitudes in one direction are compared to the wake meandering amplitudes in the other direction, formerly multiplied by the ratio of the turbulence intensity components, i.e $\sigma_v/\sigma_w$ or $\sigma_w/\sigma_v$ depending on the plane considered.

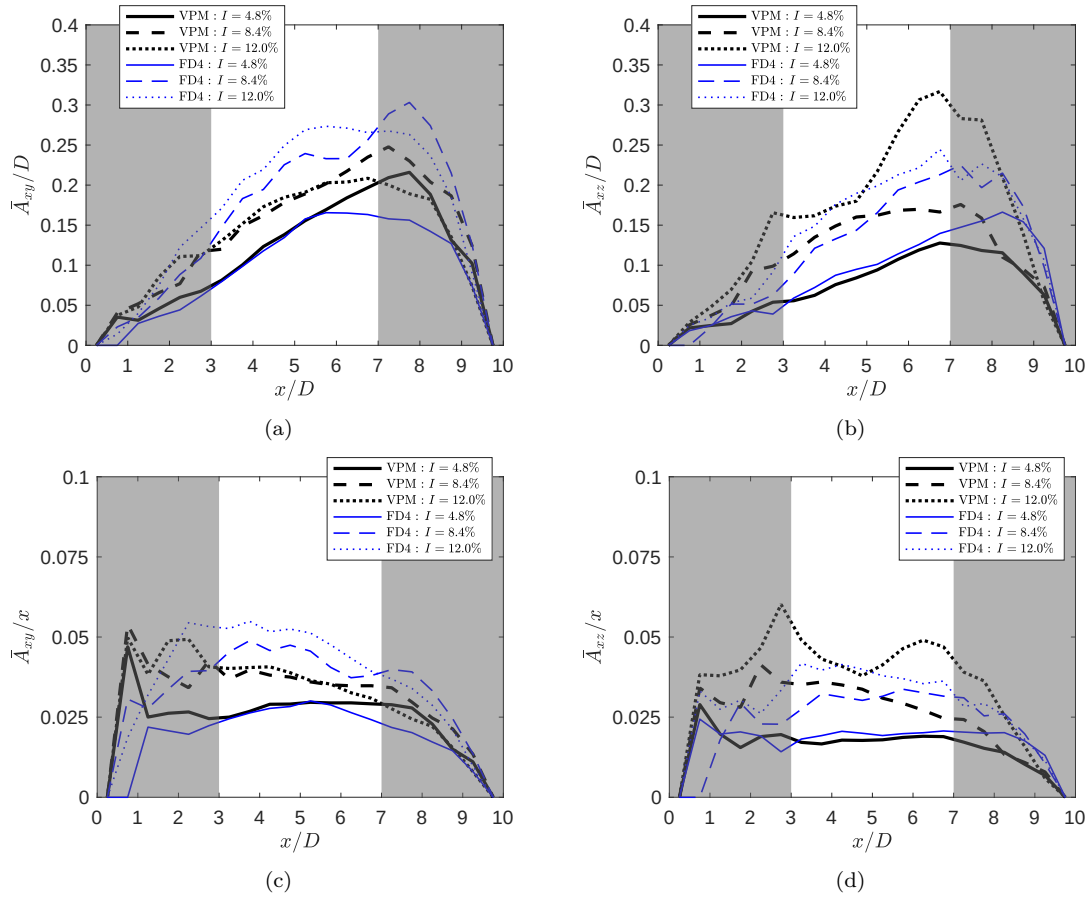



***Figure 4.9:*** *Mean binned wake centerline amplitudes obtained with the VPM and FD4 codes, in the horizontal plane at hub height (a)-(c) and in the vertical plane passing through the hub (b)-(d), normalized by the rotor diameter (a)-(b) and by the downwind distance from the rotor (c)-(d), for several inflow turbulence intensities: $I = 4.8\%$, $I = 8.4\%$, and $I = 12.0\%$; note that the exploitable part of the graphs ranges between $3 \lesssim x/D \lesssim 7$ due to the method used to determine the amplitude and wavelength of the oscillations*

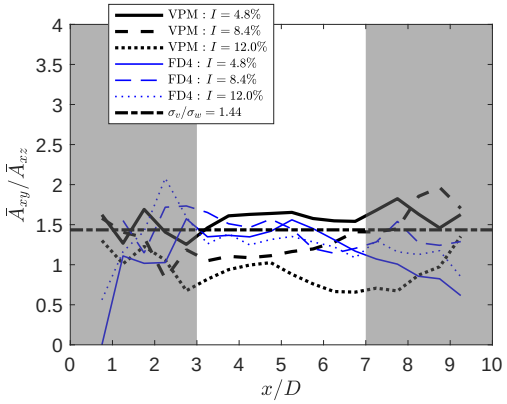



***Figure 4.10:*** *Comparison between ratio of the turbulence intensity components $\sigma_v/\sigma_w = 1.44$ and the ratio of the horizontal and vertical mean binned wake centerline amplitudes obtained with the VPM and FD4 codes; note that the exploitable part of the graphs ranges between $3 \lesssim x/D \lesssim 7$ due to the method used to determine the amplitude and wavelength of the oscillations*

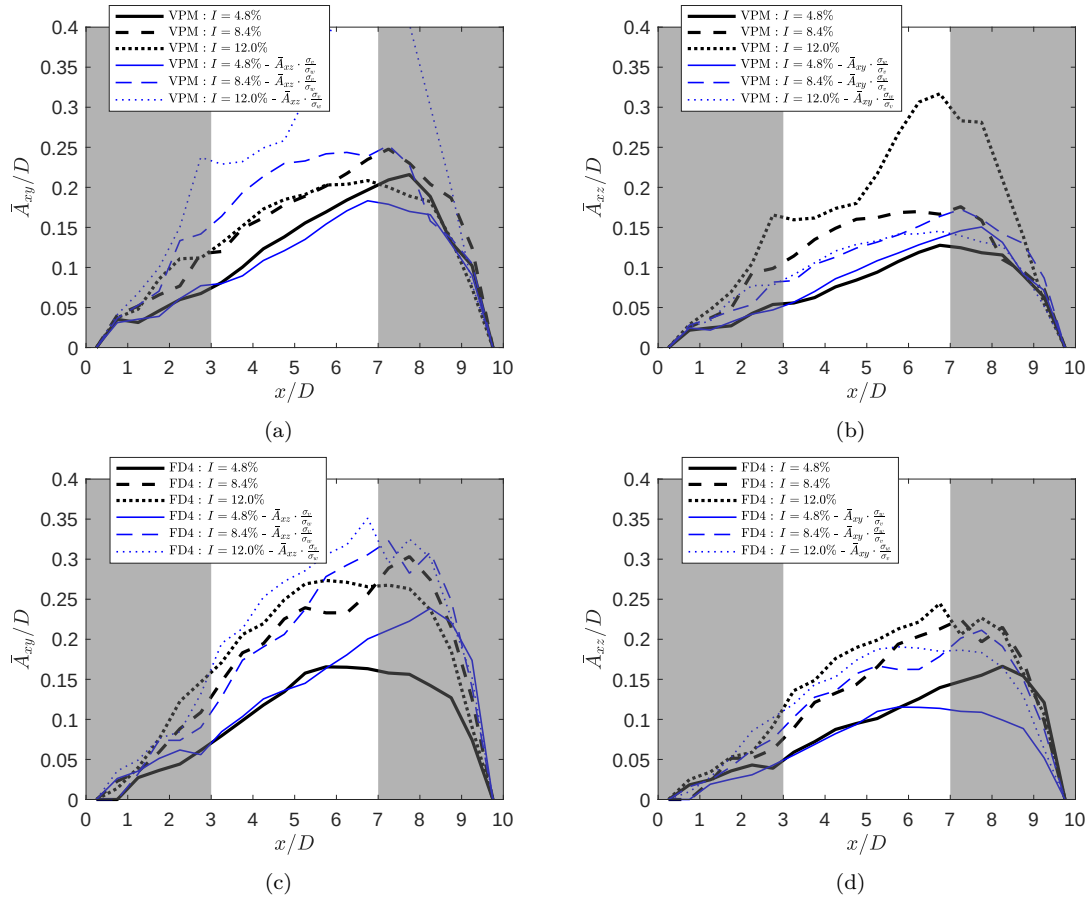
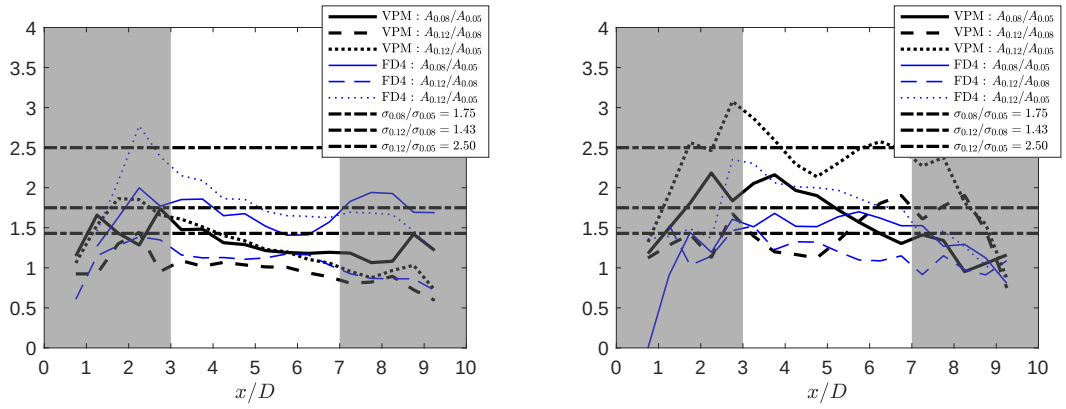



***Figure 4.11:*** *Evidence of the influence of the ratio of the turbulence intensity components ($\sigma_v/\sigma_w$ or $\sigma_w/\sigma_v$) on the mean binned wake centerline amplitudes, normalized by the rotor diameter, obtained with the VPM (a)-(b) and FD4 (c)-(d) codes, in the horizontal plane at hub height (a)-(c) and in the vertical plane passing through the hub (b)-(d) for several inflow turbulence intensities: $I = 4.8\%$, $I = 8.4\%$, and $I = 12.0\%$; note that the exploitable part of the graphs ranges between $3 \lesssim x/D \lesssim 7$ due to the method used to determine the amplitude and wavelength of the oscillations*

In the same vein, the influence, on the wake meandering amplitude, of the ratio of the turbulence intensity components between the inflows was investigated (Table 4.1). The ratio of the turbulence intensity components between the different inflows were therefore computed $\sigma_{i_{0.08}}/\sigma_{i_{0.05}} = 1.75$, $\sigma_{i_{0.12}}/\sigma_{i_{0.08}} = 1.43$, $\sigma_{i_{0.12}}/\sigma_{i_{0.05}} = 2.50$ with $i = u, v, w$ and compared to the ratio of the mean binned wake meandering amplitudes between these inflows (Fig. 4.12). As it can be observed, there is a quite good agreement in the vertical plane and the following trend can be extracted from both planes: the larger the ratio of the turbulence intensity components, the larger the ratio of the amplitudes.




(a) (b)

***Figure 4.12:*** *Comparison between the ratio of the turbulence intensity components $\sigma_{i_{0.08}}/\sigma_{i_{0.05}} = 1.75$, $\sigma_{i_{0.12}}/\sigma_{i_{0.08}} = 1.43$, $\sigma_{i_{0.12}}/\sigma_{i_{0.05}} = 2.50$ with $i = u, v, w$ and the ratio of the mean binned wake centerline amplitudes obtained with the VPM and FD4 codes in the horizontal plane at hub height (a) and in the vertical plane passing through the hub (b); note that the exploitable part of the graphs ranges between $3 \lesssim x/D \lesssim 7$ due to the method used to determine the amplitude and wavelength of the oscillations*

The obtained mean wavelengths of the oscillations are fairly constant for $3 \lesssim x/D \lesssim 7$ and range between $2.75D$ and $4.0D$, except for $I = 12.0\%$ for which the wavelengths obtained with the VPM code can reach $5.75D$ in the vertical plane (Figs. 4.13(a) and 4.13(b)). There is no clear trend concerning the influence of the inflow turbulence level on the wake meandering wavelengths. In the horizontal plane, the wavelengths obtained with the VPM and FD4 codes are equivalent while discrepancies can be observed for $I = 8.4\%$ and $I = 12.0\%$ in the vertical plane. The wavelengths are significantly larger than the mean integral length scales in the three directions. Considering $2.75 \lesssim \lambda/D \lesssim 4.5$, it gives $1.9 \lesssim \lambda/{}^{x}L_u \lesssim 3.1$, $5.6 \lesssim \lambda/{}^{x}L_v \lesssim 9.1$, and $11.8 \lesssim \lambda/{}^{x}L_w \lesssim 19.3$. Similar convective speeds are obtained with the VPM and the FD4 codes from the displacement of the wake centerlines extrema (Figs. 4.13(c) and 4.13(d)). Note that, in order to have the same resolution for the computation of the convective speeds from the VPM and FD4 data, the temporal resolution of the FD4 code is divided by four for the convective speed computation to compensate for the coarser spatial resolution used in the FD4 code. Assuming that Taylor's frozen turbulence hypothesis is applicable, the frequency can be computed from the convective speed $U_c$ and the wavelength $\lambda$

$$f = \frac{U_c}{\lambda}, \tag{4.1}$$

and made dimensionless through the Strouhal number

$$St = \frac{fD}{U_\infty} = \frac{U_c}{U_\infty} \cdot \frac{D}{\lambda}. \tag{4.2}$$

It leads to $0.2 \leqslant St \leqslant 0.3$ for $2.75 \leqslant \lambda/D \leqslant 4.0$ (Figs. 4.13(e) and 4.13(f)).

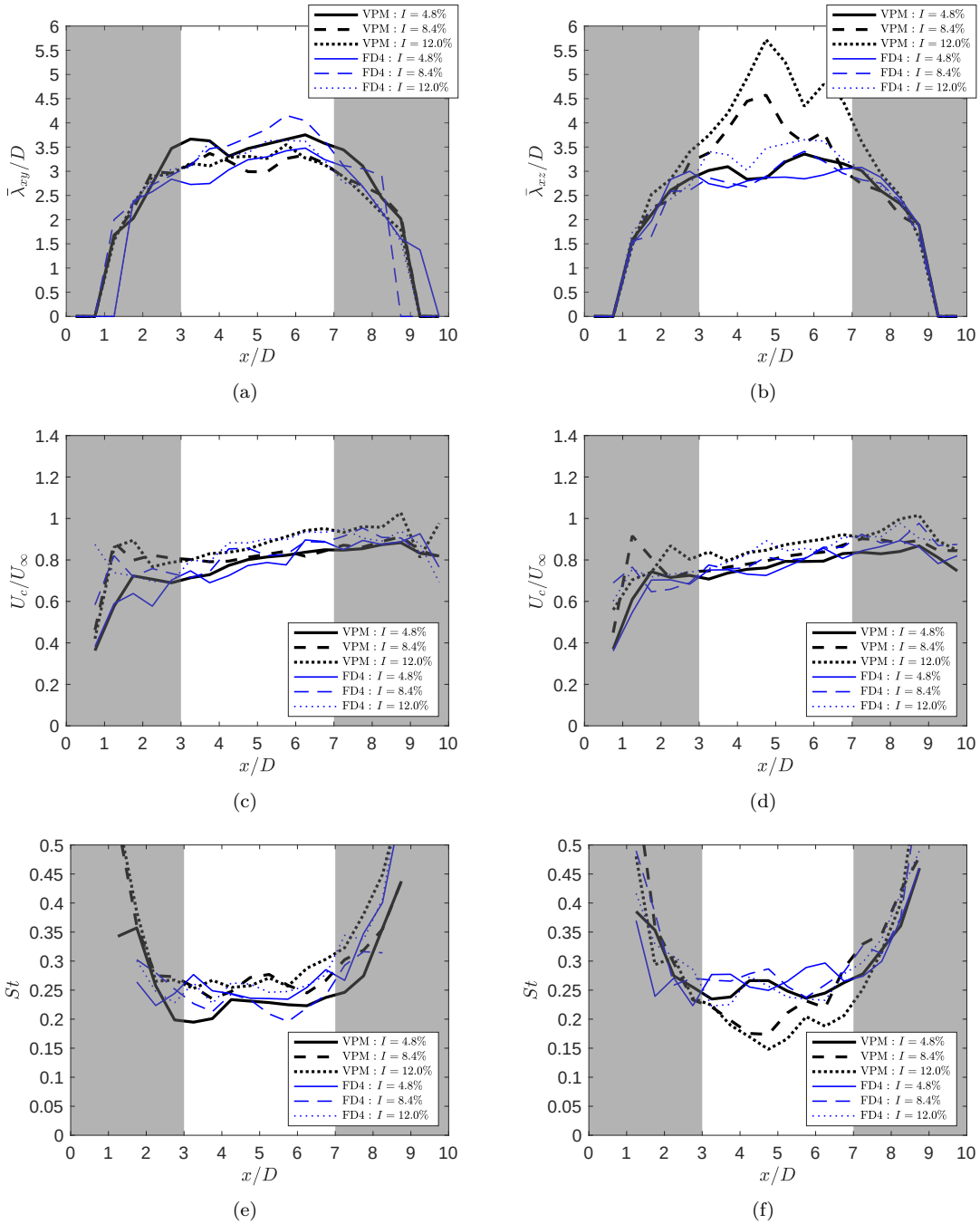
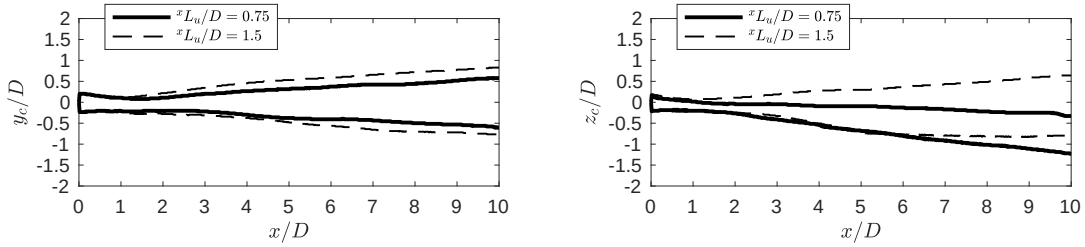



***Figure 4.13:*** *Mean binned wake centerline wavelengths (a)-(b), convective speeds (c)-(d), and Strouhal numbers (e)-(f) obtained with the VPM and FD4 codes, in the horizontal plane at hub height (a)-(c) and in the vertical plane passing through the hub (b)-(d) for several inflow turbulence intensities:* $I = 4.8\%$, $I = 8.4\%$, *and* $I = 12.0\%$*; note that the exploitable part of the graphs ranges between* $3 \lesssim x/D \lesssim 7$ *due to the method used to determine the amplitude and wavelength of the oscillations*

### 4.2.2 Effects of the inflow integral length scales on the wake meandering characteristics

Beside the influence of the turbulence intensity, the influence of the integral length scales was investigated for the case at $I = 8.4\%$. A new inflow with smaller integral length scales was generated to investigate their influence on the wake meandering characteristics. Table 4.2 gathers the integral length scales contained in the inflows as well as the turbulence intensity components. Unfortunately, it was not possible to keep exactly unchanged the turbulence intensity components when varying the size of the integral length scales of the inflow (Table 4.2). The turbulence intensity components remain however close to each other. As it can be observed in Fig. 4.14, the envelopes of the wake centroids are thinner when the integral length scales of the inflow are smaller, especially in the horizontal plane. In terms of wake meandering amplitude (Fig. 4.15), they are also smaller for smaller inflow integral length scales. The size of the inflow integral length scales does not seem to impact significantly the wake meandering wavelengths (Fig. 4.16), and therefore the Strouhal numbers obtained from the convective speeds invoking the Taylor's frozen turbulence hypothesis (Fig. 4.17). Note that the deflections of the envelope in the vertical plane for ${}^{x}L_u/D = 0.75$ is due to an asymmetry in the inflow.




(a) (b)

***Figure 4.14:*** *Dimensionless wake centerline envelopes obtained with the VPM code in the horizontal plane at hub height (a) and in the vertical plane passing through the hub (b) for inflows containing different integral length scales*

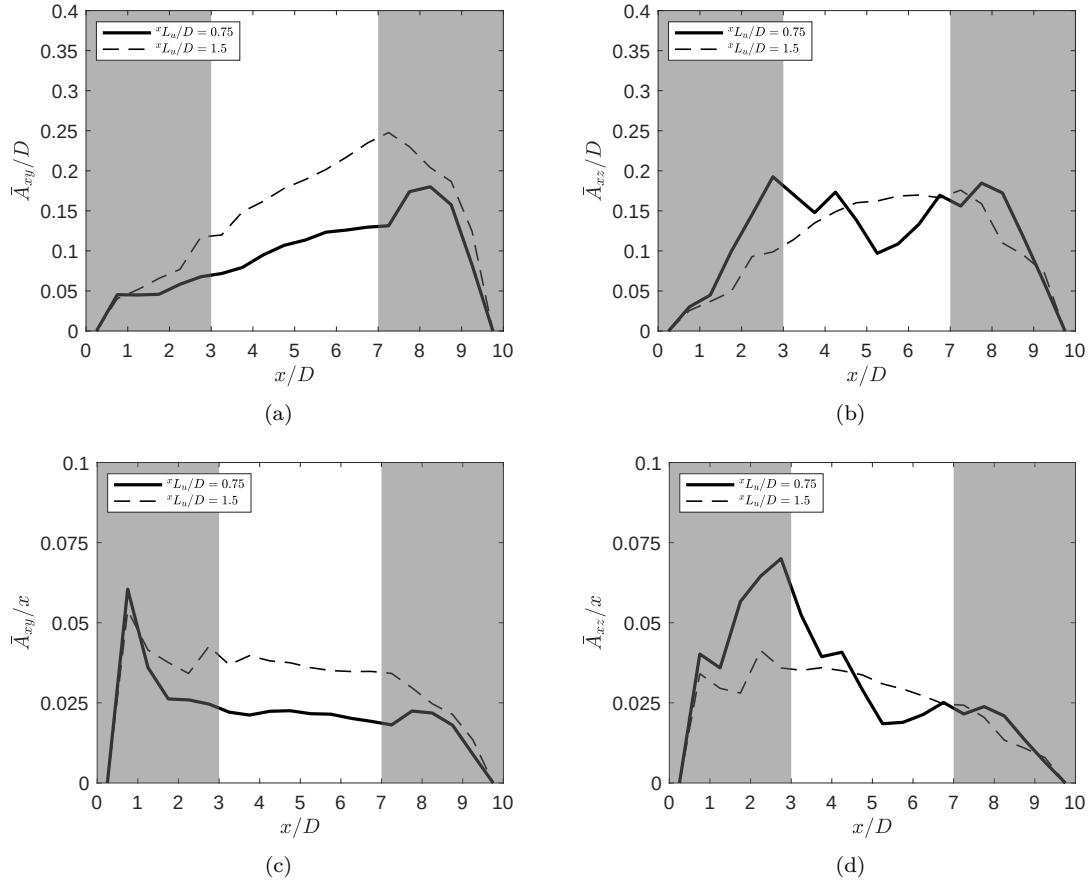



***Figure 4.15:*** *Mean binned wake centerline amplitudes obtained with the VPM code, in the horizontal plane at hub height (a)-(c) and in the vertical plane passing through the hub (b)-(d), normalized by the rotor diameter (a)-(b) and by the downwind distance from the rotor (c)-(d), for inflows containing different integral length scales; note that the exploitable part of the graphs ranges between $3 \lesssim x/D \lesssim 7$ due to the method used to determine the amplitude and wavelength of the oscillations*

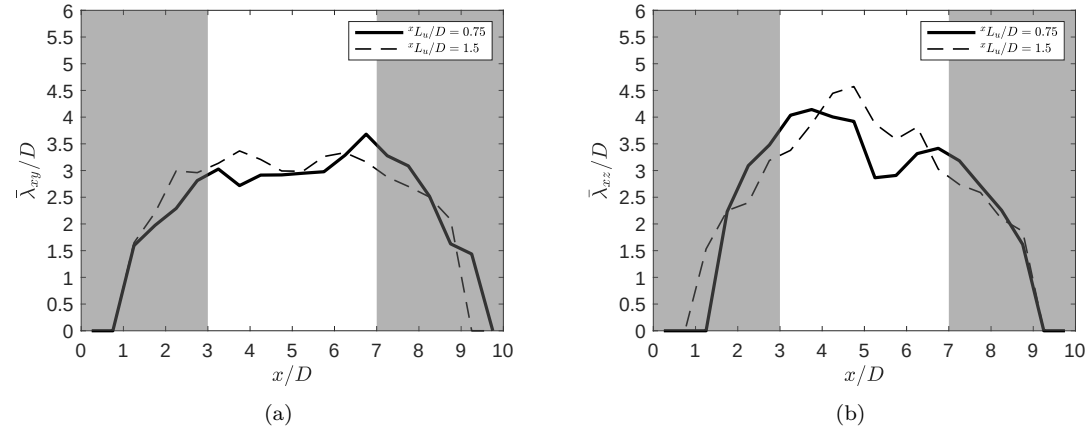



***Figure 4.16:*** *Mean binned wake centerline wavelengths obtained with the VPM code, in the horizontal plane at hub height (a) and in the vertical plane passing through the hub (b), normalized by the rotor diameter for inflows containing different integral length scales; note that the exploitable part of the graphs ranges between $3 \lesssim x/D \lesssim 7$ due to the method used to determine the amplitude and wavelength of the oscillations*

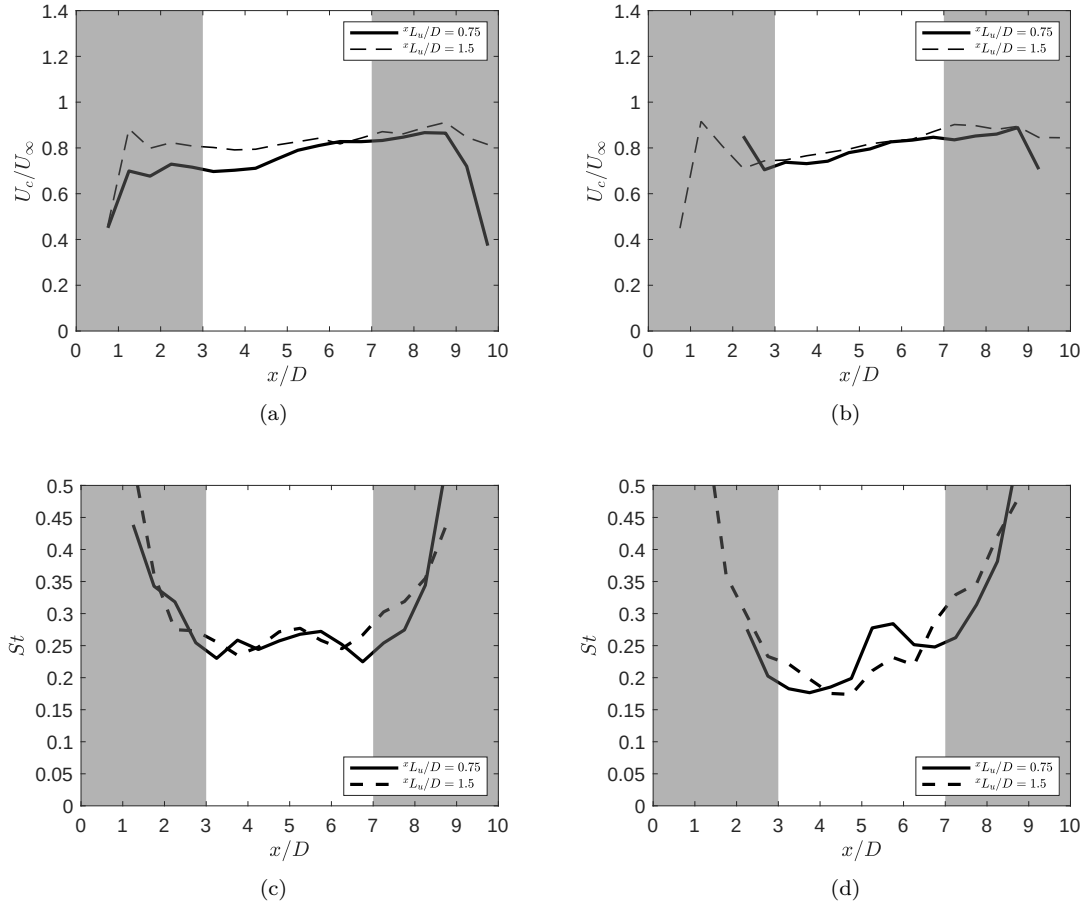



***Figure 4.17:*** *Mean binned wake centerline convective speeds (a)-(b), and Strouhal numbers (c)-(d) obtained with the VPM code, in the horizontal plane at hub height (a)-(c) and in the vertical plane passing through the hub(b)-(d), normalized by the rotor diameter for inflows containing different integral length scales; note that the exploitable part of the graphs ranges between $3 \lesssim x/D \lesssim 7$ due to the method used to determine the amplitude and wavelength of the oscillations*

### 4.2.3 Correlation between inflow, machine loads and wake centroid

#### Correlation between inflow centroid, yaw/tilt moment and lateral/vertical force

Since one of the hypothesis on the wake meandering origin is the influence of large-scale eddies contained in the inflow, the correlation between the inflow, the machine loads and the wake centerline was investigated.

First, the inflow centroid was computed as

$$IC_y = \frac{\int y\, u\, dS}{\int u\, dS}\ ,\ IC_z = \frac{\int z\, u\, dS}{\int u\, dS} \tag{4.3}$$

inside a disk of diameter $D$, centered on the wind turbine rotor axis, and located one rotor diameter upstream of the wind turbine rotor. For clarity, this is illustrated inside a 2D plane in Fig. 4.18. The fact that the inflow centroid computation is performed close to the wind turbine rotor enables to limit the possibility of deformation of the turbulent structures during their advection to the rotor, while the induction created by the turbine has a marginal impact on the centroid computation. Indeed, the inflow centroid is to a certain extent an image of the local inflow shear in the cross-flow directions due to the presence of large eddies. This interpretation is validated when comparing the evolution of the filtered inflow centroid and of the filtered yaw ($YM_z$) and tilt ($TM_y$) moments on the machine as a function of the dimensionless time ($t^* = t \cdot U_\infty/D$) for the three turbulence

intensities tested (Fig. 4.19); the filter cut-off frequency corresponding to one convective time ($t_c = D/U_\infty$). The time-offset used to align the inflow centroid signal with the machine loads was computed from the mean inflow velocity inside a disk of diameter $D$ and located one diameter upstream of the rotor. As expected, there is a strong correlation between the inflow centroid (inflow shear) and the yaw/tilt moments on the machine. In addition, a strong correlation is also observed between these quantities and the lateral ($F_y$) and vertical ($F_z$) forces acting on the machine.

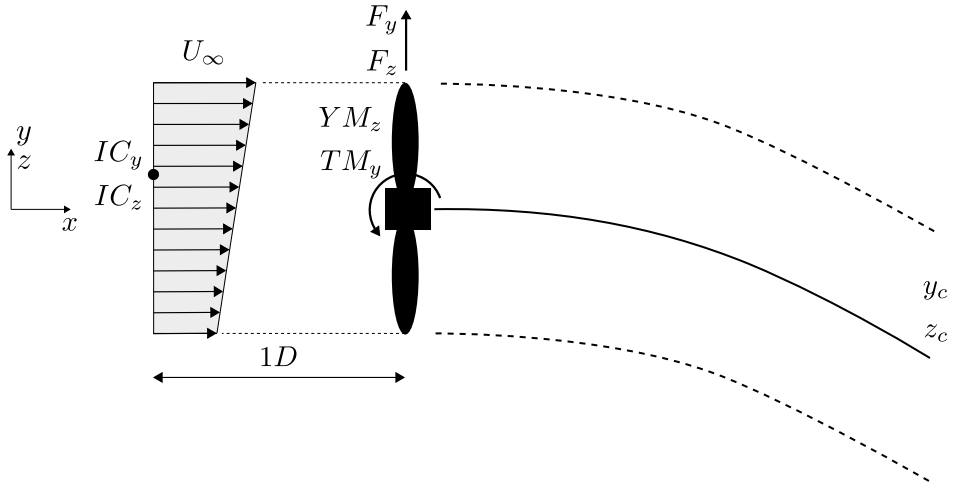



***Figure 4.18:*** *Illustration in a 2D horizontal ($x-y$) or vertical ($x-z$) plane of the inflow centroid ($IC_y$ and $IC_z$), the yaw ($YM_z$) and tilt ($TM_y$) moments, the lateral ($F_y$) and vertical ($F_z$) forces and the wake centerline $y_c$ and $z_c$; the inflow being uniform, the shear represented in this figure corresponds to a local shear due to large eddies contained in the inflow*

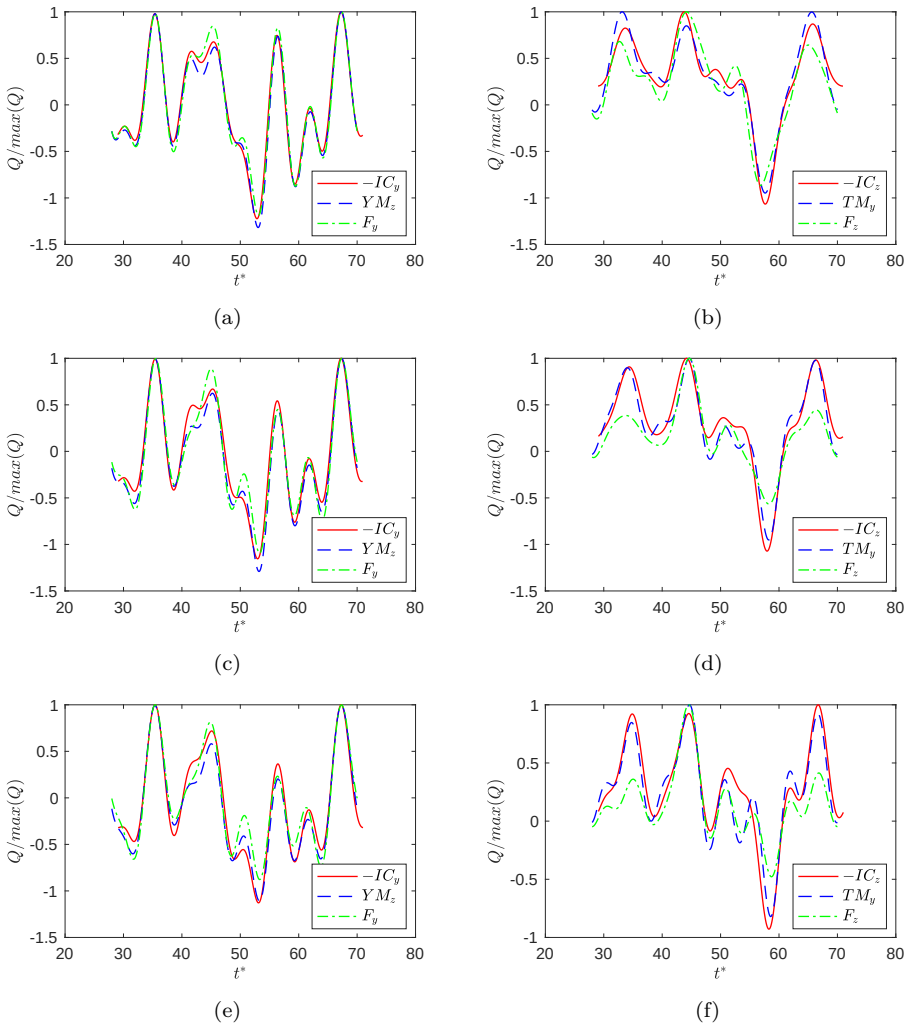



***Figure 4.19:*** *Evidence of the correlation between the inflow centroid ($IC_y$ and $IC_z$), the transverse forces ($F_y$ and $F_z$) and the yaw ($YM_z$) (a)-(c)-(e) and tilt ($TM_y$) (b)-(d)-(f) moments obtained with the VPM code for several inflow turbulence intensities: $I = 4.8\%$ (a)-(b), $I = 8.4\%$ (c)-(d), and $I = 12.0\%$ (e)-(f)*

### Correlation between inflow centroid, yaw/tilt moment, lateral/vertical forces and wake centroid

Figs. 4.20 to 4.22 show, for the three turbulence intensities tested, the evolution of the filtered inflow centroid, machine loads and wake centroid as a function of the dimensionless time ($t^* = t \cdot U_\infty / D$) for several downstream distances ranging from $0.5D$ to $4D$ from the rotor disk; the filter cut-off frequency corresponding to one convective time ($t_c = D/U_\infty$). The time-offset used to align the wake centroid signal with the machine loads was computed from the averaged mean inflow velocities inside disks of diameter $D$ located at the rotor position ($x/D = 0$) and at the position of the wake centroid signal involved. For the three turbulence intensities, the correlations between the signals are unequivocal for $x/D = 0.5$ and $x/D = 1$. The correlations then weaken with the distance to the wind turbine rotor. This clearly highlights the influence of the turbulent scales contained in the inflow on the wake meandering phenomenon and is in good agreement with [25] where it has been shown that the lateral force is a good candidate to predict in real time the wake meandering phenomenon in the horizontal plane.

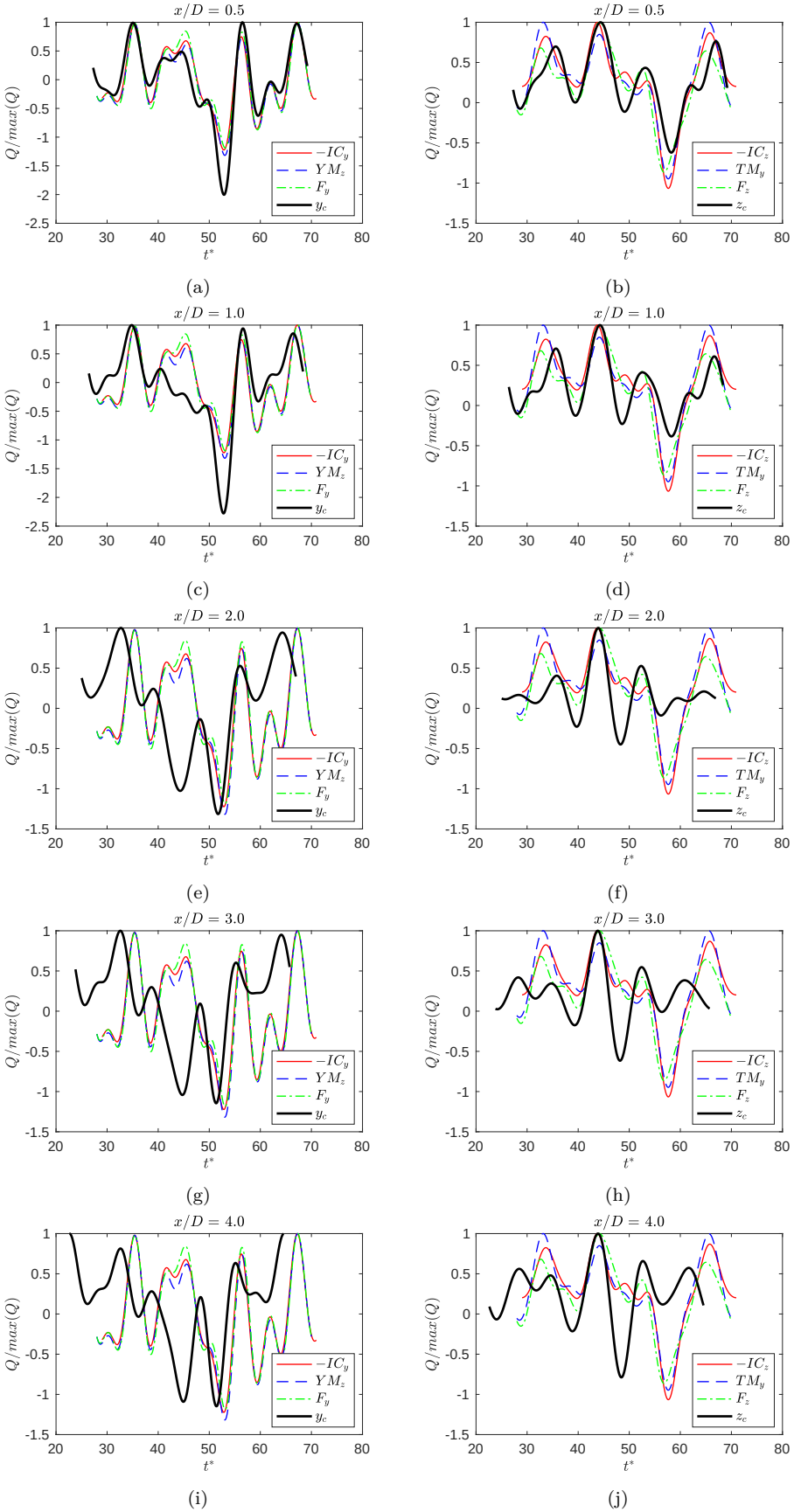



***Figure 4.20:*** *Evidence of the correlation between the inflow centroid ($IC_y$ and $IC_z$), the transverse forces ($F_y$ and $F_z$) and the yaw ($YM_z$) (a)-(c)-(e)-(g)-(i) and tilt ($TM_y$) (b)-(d)-(f)-(h)-(j) moments and the wake centerline obtained with the VPM code for an inflow turbulence intensity $I = 4.8\%$*

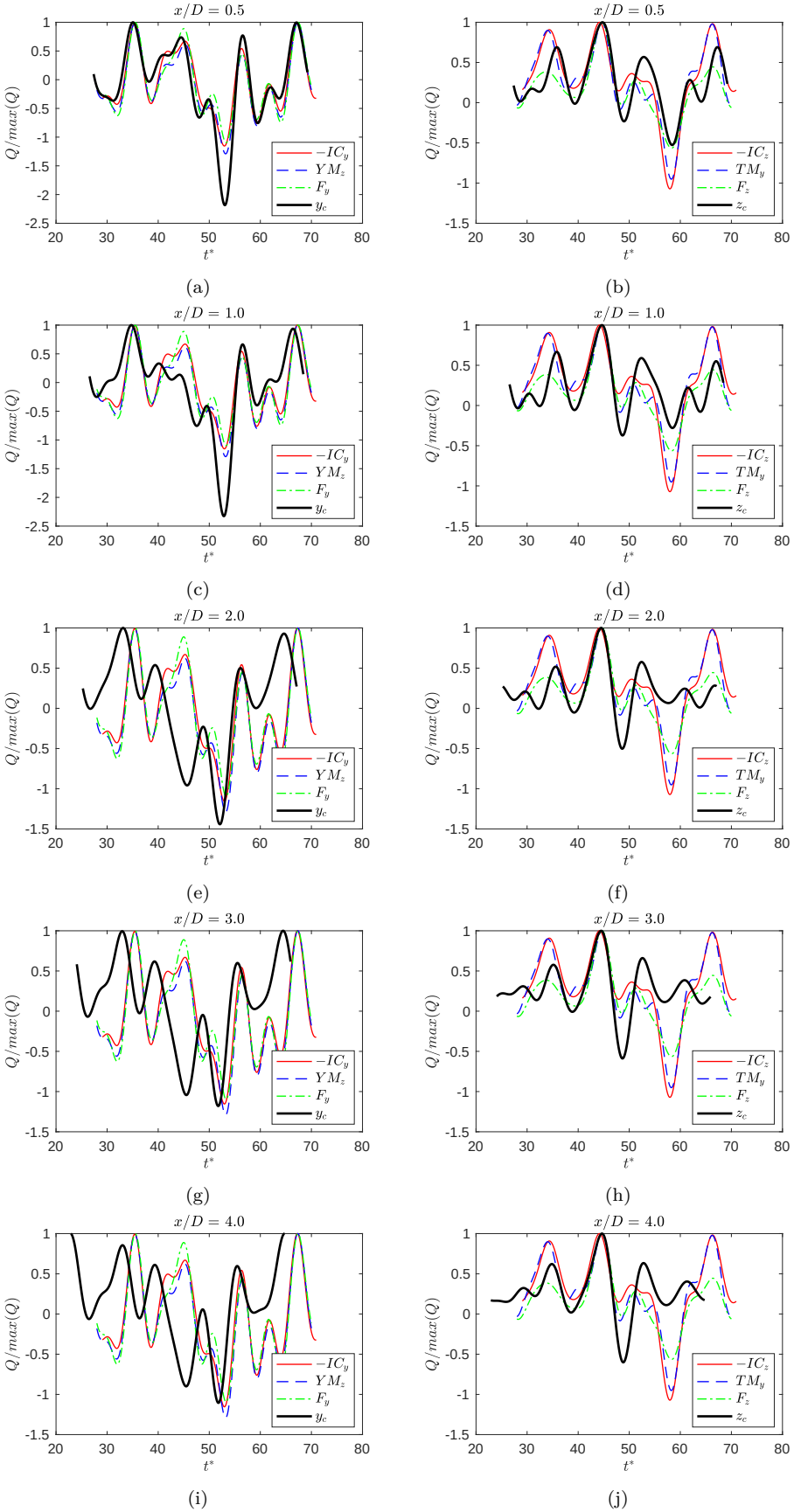



***Figure 4.21:*** *Evidence of the correlation between the inflow centroid ($IC_y$ and $IC_z$), the transverse forces ($F_y$ and $F_z$) and the yaw ($YM_z$) (a)-(c)-(e)-(g)-(i) and tilt ($TM_y$) (b)-(d)-(f)-(h)-(j) moments and the wake centerline obtained with the VPM code for an inflow turbulence intensity $I = 8.4\%$*

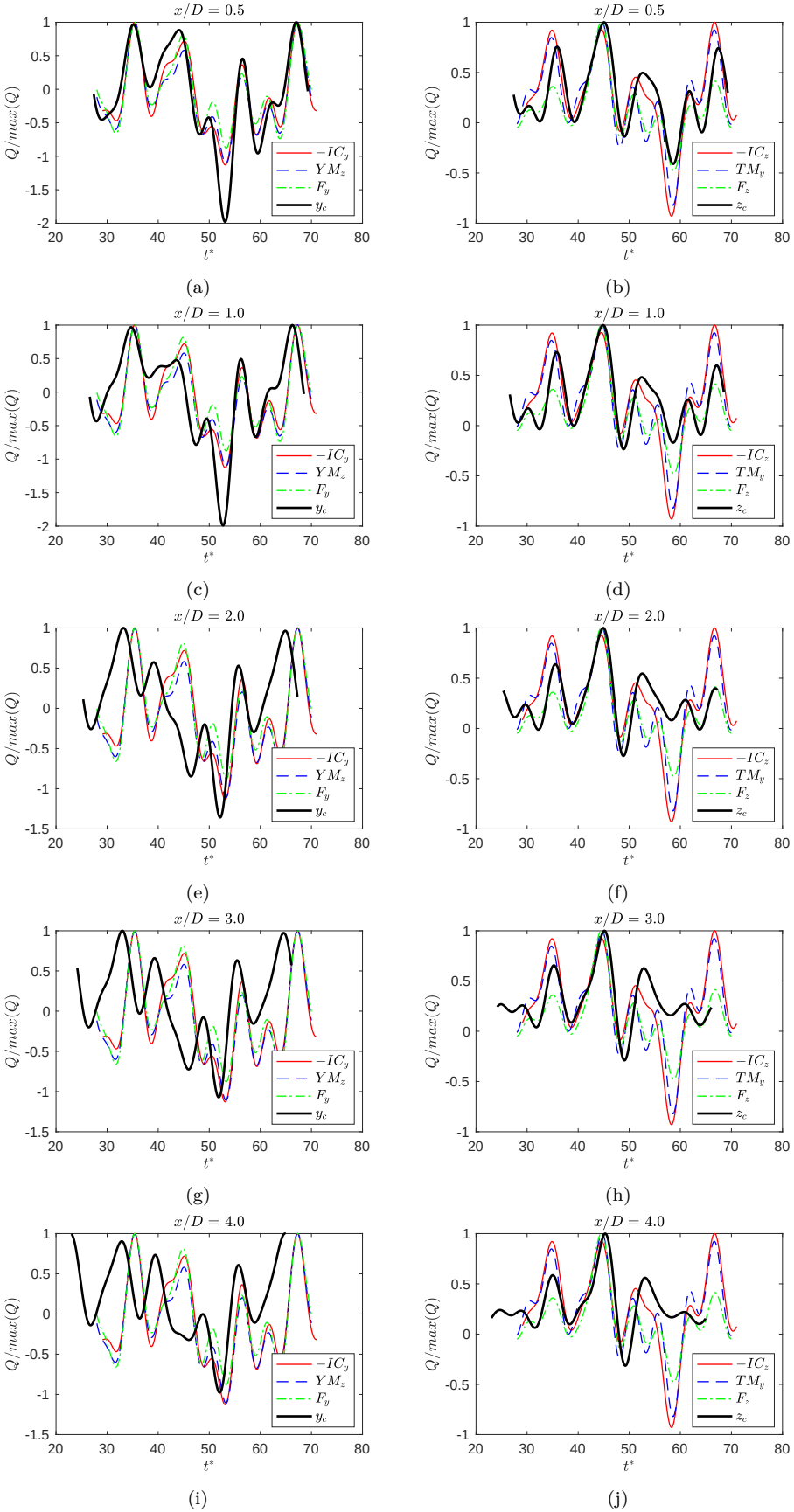



***Figure 4.22:*** *Evidence of the correlation between the inflow centroid ($IC_y$ and $IC_z$), the transverse forces ($F_y$ and $F_z$) and the yaw ($YM_z$) (a)-(c)-(e)-(g)-(i) and tilt ($TM_y$) (b)-(d)-(f)-(h)-(j) moments and the wake centerline obtained with the VPM code for an inflow turbulence intensity $I = 12.0\%$*

## 4.3 Conclusions

The aim of this chapter was to study numerically the wake meandering phenomenon thanks to the VPM code combined with immersed lifting lines and to verify that a modeling approach affordable at wind farm scale, in this case the FD4 code combined with an advanced actuator disk, provides equivalent results in terms of wake meandering compared to a method with a higher fidelity level, i.e. the VPM code.

The numerical simulations were performed with both the VPM and FD4 codes for four inflow turbulence intensities of 0%, 4.8%, 8.4% and 12.0%. Comparing both approaches, it was observed that the FD4 code tends to lead to wake meandering characteristics equivalent to those obtained with the VPM code, especially close to the wind turbine rotor ($x/D \lesssim 4$) or for the lowest inflow turbulence intensities. The discrepancies between the two approaches are more pronounced when the distance from the rotor increases, especially for a higher inflow turbulence level, because of the faster wake recovery. Nevertheless, the very good agreement between the wake meandering characteristics obtained with the VPM and FD4 codes opens the way to study the wake meandering phenomenon inside large wind farms with the FD4 code which is well suited for this kind of application.

First, the focus of this chapter was on the influence of the turbulence intensity on the wake meandering characteristics, independently of the integral length scales contained in the inflow since they were identical whatever the turbulence level. It was observed that a higher inflow turbulence intensity results in larger wake deflections and that the wake meandering starts closer to the rotor when the inflow turbulence level increases. These observations are in good agreement with the results obtained numerically by Foti et al. [37] for a utility scale wind turbine ($D = 90$ m).

Concerning the amplitude of the wake meandering, it ranges within $0.05 \lesssim A/D \lesssim 0.30$. Although larger than what was observed in [37] ($A/D \simeq 0.1$), it also increases linearly with the distance from the rotor and with the inflow turbulence level. Furthermore, a lower amplitude was observed in the vertical plane due to the anisotropic inflow. The ratio of the horizontal and vertical wake centerline amplitudes was incidentally close to the ratio of the turbulence intensity components $\sigma_v/\sigma_w = 1.44$ as observed in [16]. In the same vein, it was observed that the ratio of the turbulence intensity components between the inflows is close to the ratio of the wake centerline amplitudes, mainly in the vertical plane while the following trend can be extracted from both planes: the larger the ratio of the turbulence intensity components, the larger the ratio of the amplitudes. Fairly constant wavelengths mainly ranging between $2.75D$ and $4.0D$ were obtained. These wavelengths are much larger than those reported in [37] ($1.2 \leqslant \lambda/D \leqslant 2.1$). Eventually, Strouhal numbers ranging between 0.2 and 0.3 were computed from the wavelengths using Taylor's frozen turbulence hypothesis. The similar Strouhal numbers reported in [37], which range within $0.25 \leqslant St \leqslant 0.3$, enable to conclude that the difference in wavelengths is due to a difference in the ratio between the convective speed and the incoming wind speed since $St = (U_c/U_\infty)D/\lambda$.

The influence of the integral length scales was then studied for $I = 8.4\%$. It was observed that the extreme wake deflections and the wake meandering amplitudes decrease when the integral lengths scales of the inflow are smaller, while the wavelengths and the Strouhal numbers are essentially unaffected. Finally, because of the influence of the integral length scales, the correlations between the inflow centroid, the machine loads and the wake centroid were investigated for several downstream distances ranging from $0.5D$ to $4D$ from the rotor disk. For the three turbulence intensities, the correlations between the signals were unequivocal for $x/D = 0.5$ and $x/D = 1$, the correlations then weakening with the distance to the wind turbine rotor. This clearly highlights the influence of the turbulent scales contained in the inflow on the wake meandering phenomenon.

Chapter 5

# Wind turbine scale model and ABL modeling in low speed L-1B wind tunnel

The first part of this chapter describes the wind turbine scale model used in the experiments in terms of geometry, control/acquisition system, and electrical and aerodynamic performances. The second part of this chapter is dedicated to the ABL modeling in low speed L-1B wind tunnel.

## 5.1 Three-bladed wind turbine scale model

### 5.1.1 Model description

The three-bladed wind turbine scale model used for the experiments is presented in Fig. 5.1. It has a rotor diameter of 0.15 m and a hub height of 0.13 m. The rotor was designed based on blade-element momentum theory [79], with optimization of the power coefficient $C_p$ for an incoming wind speed of 8 m/s at hub height. To deal with the low Reynolds numbers involved ($Re \leqslant 27 \times 10^3$, based on the chord length and relative velocity for each blade element), the rotor was made of a thin airfoil: the HAM-STD HS1-606 airfoil (Fig. 5.2). The main characteristics of the wind turbine blades can be found in Appendix C and a more detailed overview of the design methodology can be found in [80]. The rotor was manufactured by three-dimensional printing. The rotor is attached to a direct-current motor (Faulhaber 1331T006SR) used as a generator and located inside the nacelle. The generator is connected to a control board with various electrical resistance. By varying the resistance of the circuit, the turbine angular velocity $\omega$ can be controlled, and, therefore, the turbine tip-speed ratio

$$TSR = \frac{\omega \frac{D}{2}}{U_{hub}}, \tag{5.1}$$

where $U_{hub}$ is the mean wind speed at hub height.

The rotor size of the scale-model is representative of a 2-MW offshore wind turbine (e.g. scale 1/440 for a Vestas V66-2MW wind turbine).

Note that for the performance curves determination, the model is equipped with a larger nacelle to accommodate the bearings used in the torque sensor system (see Section 5.1.2.1).

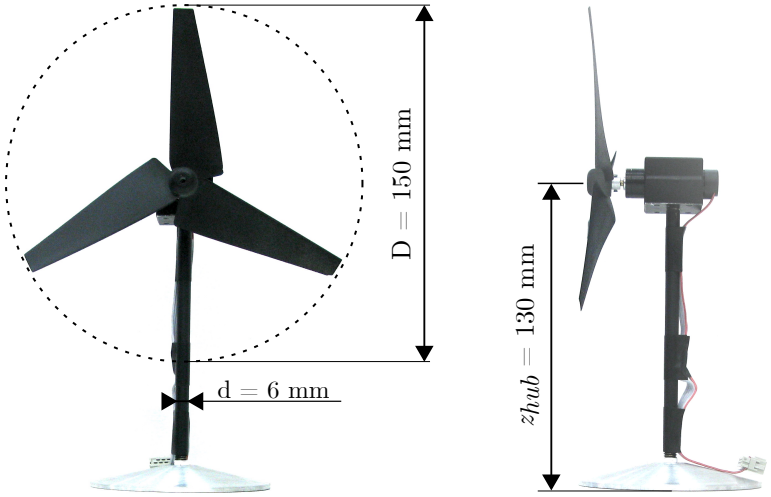



***Figure 5.1:*** *Wind turbine scale model*

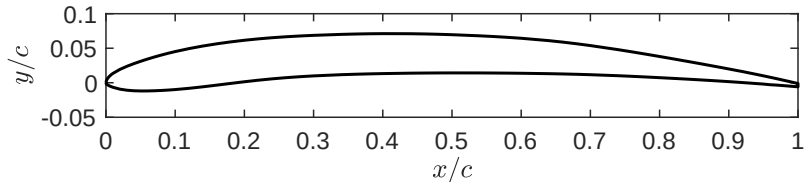



***Figure 5.2:*** *HAM-STD HS1-606 airfoil*

### 5.1.2 Performance curves

The wind turbine characterization was performed inside the L-2B wind tunnel described in Chapter 2. Considering the dimensions of the open test section with underpressure chamber, the blockage factor ($BF$), defined as the ratio between the cross section of the model (the area swept by the rotor blades) and the cross section of the test section, is of the order of 5%:

$$BF = \frac{\pi(\frac{D}{2})^2}{0.65 \cdot 0.50} = 0.054. \tag{5.2}$$

#### 5.1.2.1 Electrical and aerodynamic power measurement

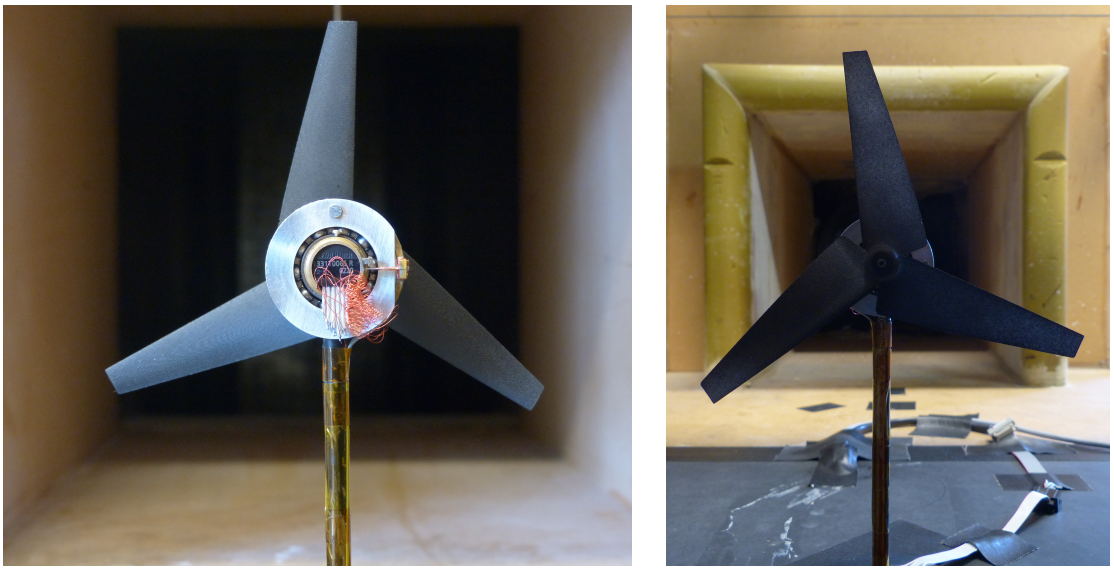
**Electrical vs. aerodynamic power**

Several factors in generators act to significantly decrease the generator efficiency. As stated in [81], these factors are (1) copper losses in the coil winding due to the heat dissipation in the armature copper winding of the generator, (2) magnetic losses which include the hysteresis loss from the magnetic properties of the armature and eddy current losses in the laminated armature, and (3) mechanical losses which consist mainly of the friction losses in bearings and brushes [81]. Therefore, the power computed from the voltage and the current $P^{elec} = VI$ is impacted by these losses and is therefore smaller than the mechanical power extracted by the rotor $P^{aero}$.

The mechanical torque $Q$ applied by the wind to the wind turbine rotor is equal to the difference in the angular momentum of the flow after passing through the rotor. From this mechanical torque and the rotational speed of the rotor, the aerodynamic power can be computed as $P^{aero} = \omega Q$. The benefit of working with this relation is that the results are independent of the characteristics of the generator while it is not the case for $P^{elec} = VI = RI^2$. It is therefore more interesting to compute the power from the torque with the view of comparing the results to other wind tunnel experiments or numerical simulations.

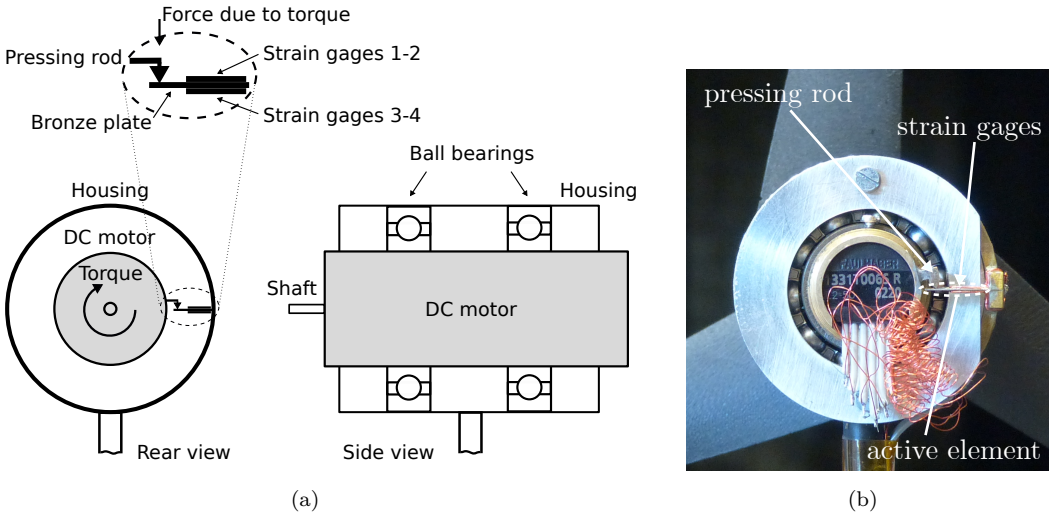
### Torque sensor system

A torque sensor system based on [81] was developed within the framework of this thesis. Photographs of the wind turbine scale model equipped with the torque sensor system are presented in Fig. 5.3. The DC motor is mounted inside the housing through two identical ball bearings (SKF61902) aligned with the hub center (Fig. 5.4). The aim of using ball bearings is to let the DC motor rotate freely in reaction to any applied torque on its shaft. The system is also composed of a small pressing rod with a pin attached to the rear side of the DC motor (cantilever structure). The pin presses against a sensitive active element (a bronze plate) mounted on the housing (Fig. 5.4). This arrangement allows for the deformation of the plate for a large range of torques applied to the motor. On the top and bottom surface of the plate are mounted four strain gauges (two by surface) to form a complete Wheatstone bridge in order to increase the sensitivity of the system. When the wind turbine is subjected to the wind, the rotor angular velocity is counter-clockwise (viewing the wind turbine model from upstream). The torque applied on the blades is transmitted to the generator. Since the generator housing is mounted on ball bearings it has the tendency to rotate, also in counter-clockwise direction. However, the sensitive active element prevents the motor from rotating: the pin presses against the bronze plate and the Wheatstone bridge converts the plate deformation into a voltage signal. This voltage signal, which is amplified, can then be converted into torque via a calibration performed prior to the measurements.



(a) (b)

***Figure 5.3:*** *Photograph of the rear side (a) and front (b) side of the wind turbine equipped with the torque sensor system*




(a) (b)

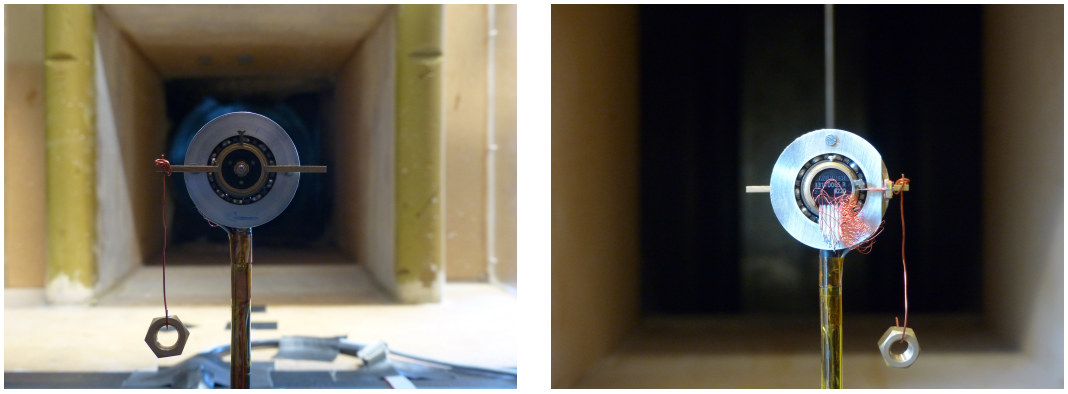
***Figure 5.4:*** *Illustration of the torque sensor system adapted from [81] (a) and photograph (b)*

### Torque sensor system calibration

The torque sensor system is calibrated using a dead weight method. On the front side of the motor, the rotor is replaced by a calibration tool composed of a ring with two square rods welded in alignment with the horizontal direction (Fig. 5.5(a)). The system is fixed to the generator housing with a screw. The two rods present a hole at their extremity, what makes possible to fix a hook-shaped metal wire through one of them in order to hang the weights (Fig. 5.5). Several masses, in a range from 0.5 g to 9.5 g, are attached to the wire. The moment arm length between the center of the motor shaft and the hanging location is 25 mm. Knowing the weight ($M\,g$) and the moment arm ($l$), the torque can be computed as

$$Q = M\,g\,l. \tag{5.3}$$

For each mass, the voltage output from the strain-gauge amplifier is acquired. In this way, a correlation between the torque ($Q$) and the voltage ($V$) from the strain-gauge bridge is obtained (Fig. 5.6). As it can be observed, the linear-fitted line is closed to the calibration data shown with the circles, with a coefficient of determination $R^2 = 0.9995$.



(a) (b)

***Figure 5.5:*** *Photograph of the rear side (b) and front (a) side of the wind turbine equipped with the torque sensor system in calibration configuration*

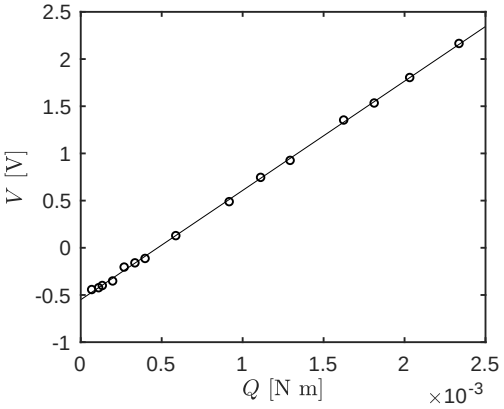
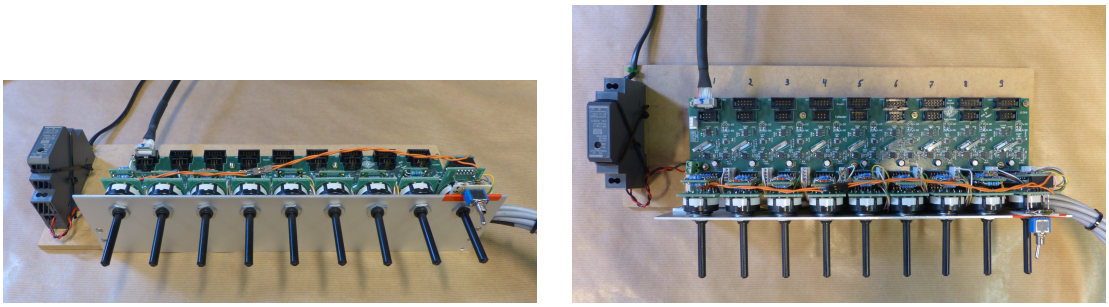



***Figure 5.6:*** *Evolution of the voltage ($V$) output as a function of the torque ($Q$) applied, $R^2 = 0.9995$*

### Methodology

To determine the performance curves of the wind turbine, the voltage ($V$) and current ($I$) produced by the generator as well as the torque ($Q$) and the rotational speed ($\omega$) of the shaft were acquired during ten seconds at a sampling frequency of 100 Hz for several electrical resistances applied to the generator of the wind turbine. The control and acquisition board, allowing for the simultaneous control/acquisition of nine wind turbines, was developed within the framework of this thesis with the *Electronics Laboratory* of the von Karman Institute (Fig. 5.7).



(a) (b)

***Figure 5.7:*** *Photographs of the control and acquisition board, allowing for the simultaneous control/acquisition of nine wind turbines, developed within the framework of this thesis with the* Electronics Laboratory *of the von Karman Institute; the configuration shown was used to perform the wind turbine characterization (canal 9 is modified to provide an extended range of electrical resistances compared to the wind farm configuration)*

For each campaign, the flow velocity was set to a constant value and the resistive load was varied in a range from 1 Ω to 1000 Ω: $[1:1:20, 22:2:30, 40, 51, 101, 151, 251, 501, 751, 1001]$. For each resistance value, the signals were acquired during 10 s at a frequency of 100 Hz. The Pitot-static probe used to determine the free-stream velocity was positioned 520 mm upstream of the wind turbine rotor at a height of 135 mm and at the center of the channel in crosswise direction. The wind speed was acquired with a sampling frequency of 1 kHz and the acquisition time was set to 30 s. Even if the Pitot-static probe was positioned at $\sim 3.5\ D$ in front of the wind turbine rotor, the wind speed measurement was still influenced by the presence of the wind turbine. Therefore, prior to each campaign, the wind speed was measured without and with the wind turbine rotor. The ratio of these two speeds was then used to correct the wind speeds acquired during the campaign. The campaigns were performed at the following corrected mean wind speed : 3.6 m/s, 5.0 m/s, 6.5 m/s, and 8.0 m/s. Two campaigns of measurements were repeated for each wind speed to check the repeatability of the measurements.

**Results**

In this section, the results of the eight campaigns carried out are presented. The data contained on the graphs are the mean value of the signals acquired during 10 s at 100 Hz. For each figure, eight different curves are presented, each pair corresponding to a specific wind speed. To avoid saturating the graphs hereinafter, the symbols are only represented for one campaign for each wind speed and only for some electrical resistance values. Figure 5.8 enables to verify that the wind speed was effectively constant during each campaign. The uncertainty analysis for the wind speed is presented in Appendix D.1.

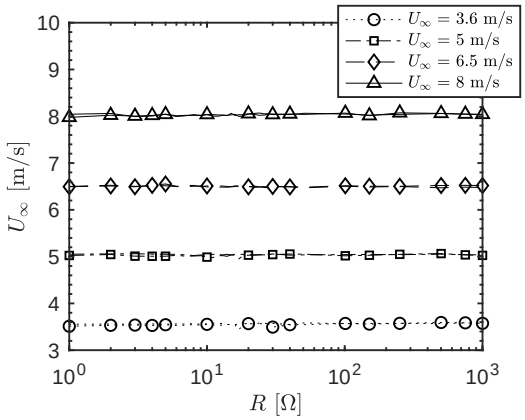
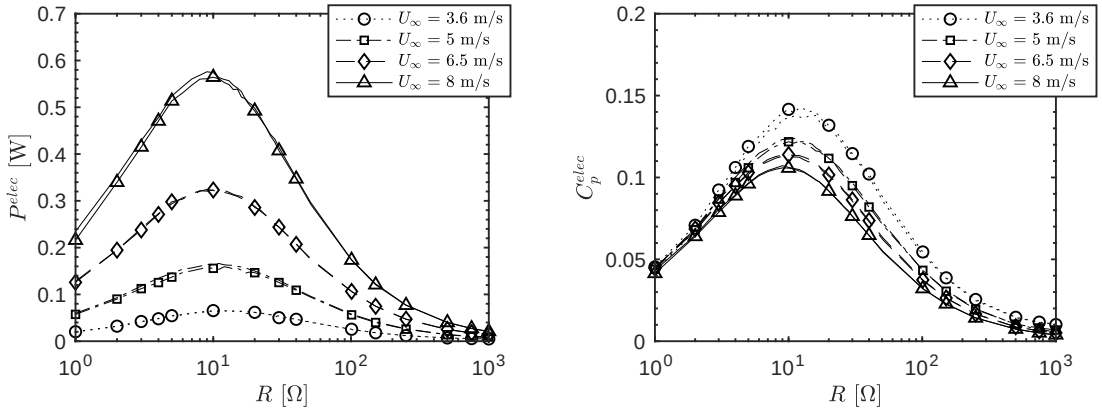



***Figure 5.8:*** *Evolution of the averaged wind speed as a function of the resistive load applied to the generator; lines without symbol correspond to the second set of measurements*

As it can be observed in Fig. 5.9, the power produced by the wind turbine increases with the wind speed. Furthermore, it seems that the value of the resistance corresponding to the maximum power decreases sightly with the wind speed. One can observe that the trend for the power coefficient curves is reversed. Indeed, the higher the wind speed, the lower the power coefficient, with $C_{p_{max}}^{elec} = 0.15$ for $U_\infty = 3.6$ m/s and $C_{p_{max}}^{elec} = 0.11$ for $U_\infty = 8.0$ m/s. It means that the wind turbine scale model is more efficient at lower wind speeds as it extracts a larger part of the available power in the wind.

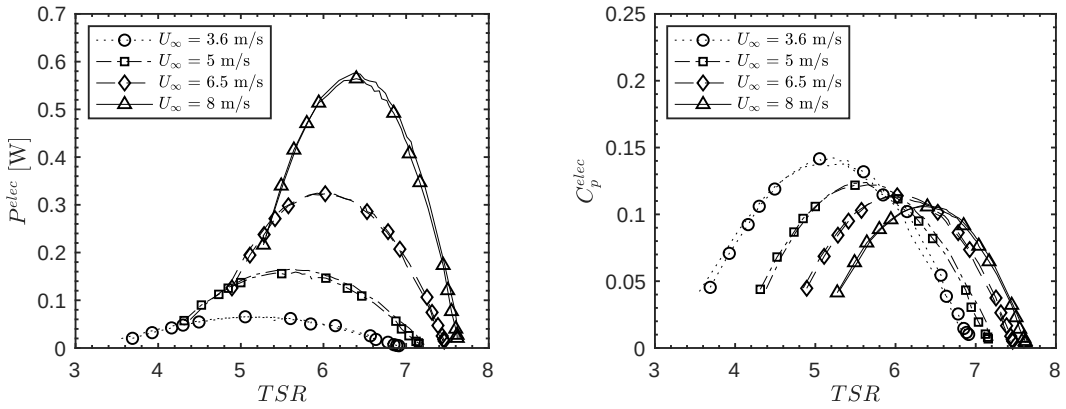
Figure 5.10 shows the variation of the power and the power coefficient as a function of the TSR. It can be observed that the TSR range swepts by the scale model decreases when the wind speed increases. It means that the resistances have less influence on the rotational speed at higher wind speed. Indeed, the TSR value for the curves at 3.6 m/s is bounded between 3.6 and 7 whereas the TSR of the curves at 8.0 m/s ranges from 5.2 to 7.6. The maximum electrical power coefficient occurs at different TSR value depending on the wind speed. The optimum TSR ranges from 5 to 6.4 for the wind speeds tested (Fig. 5.10(b)).

Furthermore, Fig. 5.11 provides essential information for future campaigns of measurement: the resistive load to apply to the wind turbine to obtain a desired TSR at a specific wind speed.




(a) (b)

***Figure 5.9:*** *Evolution of the power (a) and power coefficient (b) as a function of the resistive load applied to the generator; lines without symbol correspond to the second set of measurements*




(a) (b)

***Figure 5.10:*** *Evolution of the power (a) and power coefficient (b) as a function of the tip-speed ratio; lines without symbol correspond to the second set of measurements*

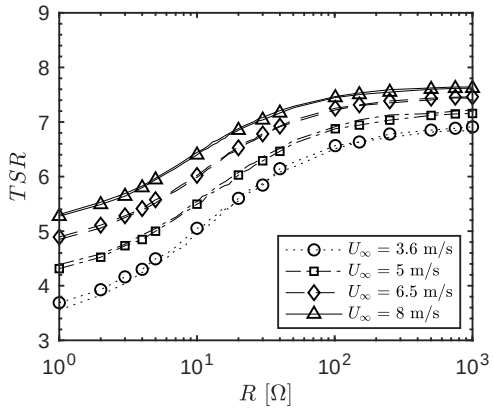



***Figure 5.11:*** *Evolution of the tip-speed ratio as a function of the resistive load applied to the generator; lines without symbol correspond to the second set of measurements*

Figure 5.12(a) presents the evolution of the mechanical torque acting on the generator as a function of the resistive load applied. Globally, the trend is continually decreasing and the torque tends to become constant for the highest resistive loads applied to the generator. Figure 5.12(b) shows the torque with respect to the rotational speed for the four free-stream velocities. Each curve presents a torque decreasing with the rotational speed and shifted to the right considering that the larger the wind speed, the larger the rotational speed.

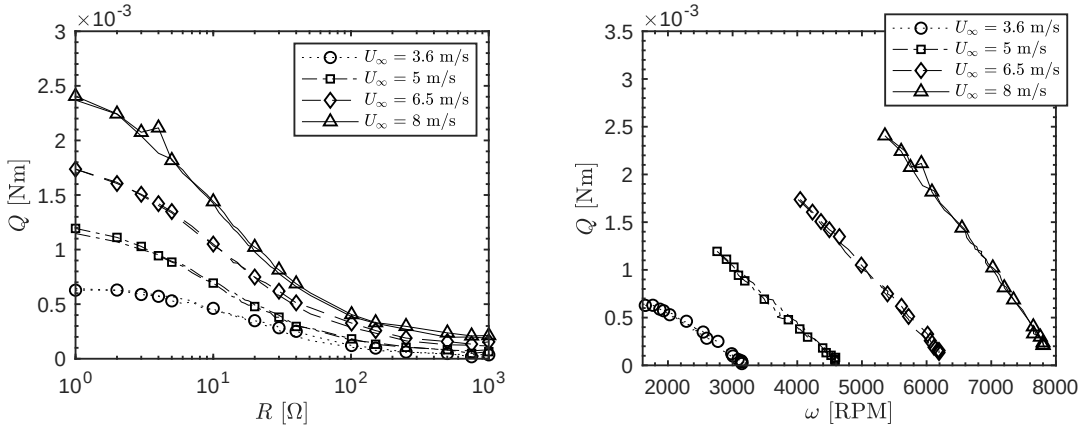



***Figure 5.12:*** *Evolution of the mechanical torque as a function of resistance (a) and as a function of rotational speed (b); lines without symbol correspond to the second set of measurements*

As stated previously, the power extracted by the model wind turbine from the incoming flow can be obtained by multiplying the torque by the rotational speed. A comparison between electrical (thin line) and mechanical (thick line) power and power coefficient obtained for each wind speed is presented in Fig. 5.13. As expected, the power and power coefficient obtained from the mechanical quantities are larger compared to those obtained from the electrical quantities. However, the shape of the aerodynamic curves is different from that of the electrical curves. This is due to a too weak rotation resistance of the generator (too low nominal voltage) and will be discussed in the next section, where the relation between the torque and the current produced by the DC generator is discussed. Table 5.1 enables to compare, for each wind speed, the aerodynamic and the electrical power for the resistance corresponding to the optimal electrical power. Taking the ratio of the two powers shows that around 40% of the aerodynamic power is lost inside the generator. Finally, the evolution of the power and power coefficient as a function of the tip-speed ratio can be observed in Fig. 5.14. The uncertainty on the electrical power can be found in Appendix D.2.

| U [m/s] | $R^{elec}_{max}$ [Ω] | $P^{elec}_{max}$ [W] | $P^{aero}$ [W] | $\frac{P^{elec}}{P^{aero}}$ (%) |
|---|---|---|---|---|
| 3.6 | 11 | 0.065 | 0.101 | 65 |
| 5 | 11 | 0.166 | 0.260 | 64 |
| 6.6 | 9 | 0.324 | 0.560 | 58 |
| 8 | 9 | 0.576 | 1.012 | 57 |

***Table 5.1:*** *Comparison between the optimum electrical power and the corresponding aerodynamic power for the wind speeds tested*

The evolution of the other quantities acquired during the campaigns are presented in Appendix E.1.

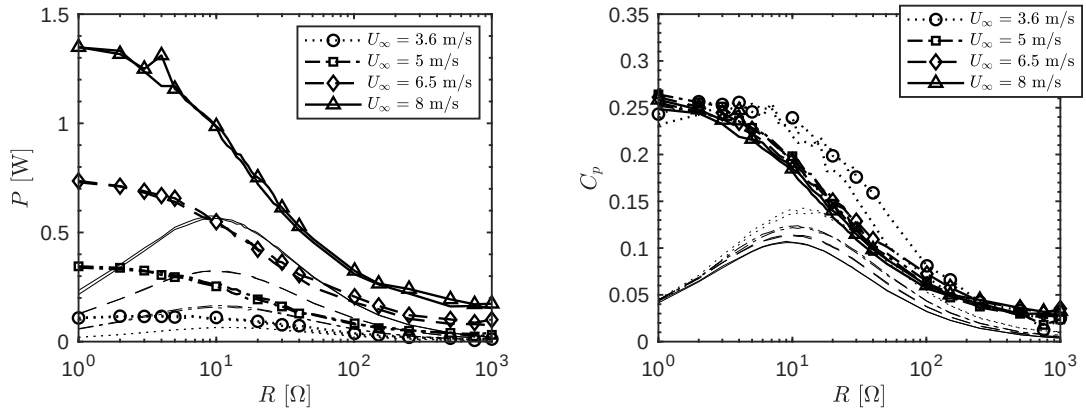



***Figure 5.13:*** *Evolution of the electrical power (thin line) and mechanical power (thick line) as a function of resistance (a); evolution of the electrical power coefficient (thin line) and mechanical power coefficient (thick line) as a function of resistance (b)*

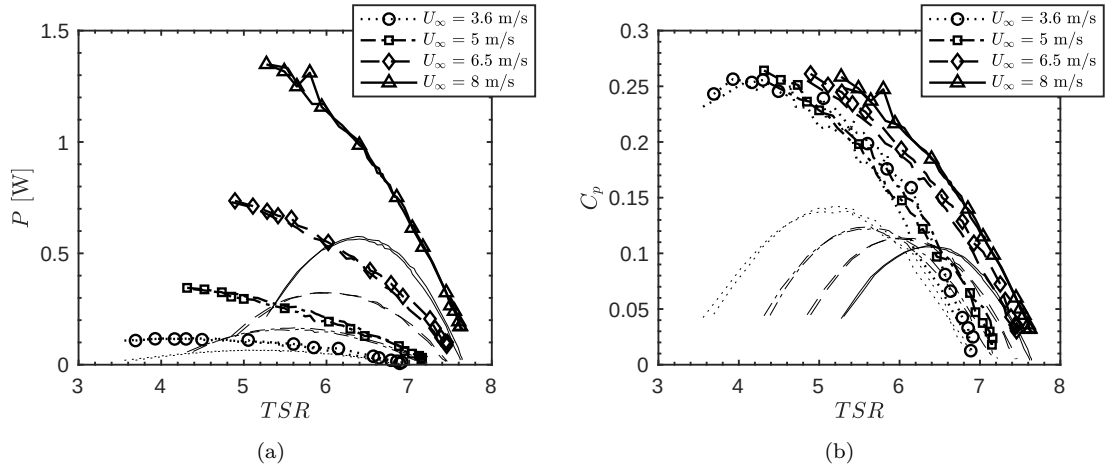



***Figure 5.14:*** *Evolution of the electrical power (thin line) and mechanical power (thick line) as a function of the tip-speed ratio (a); evolution of the electrical power coefficient (thin line) and mechanical power coefficient (thick line) as a function of the tip-speed ratio (b)*

#### 5.1.2.2 Indirect aerodynamic power measurement

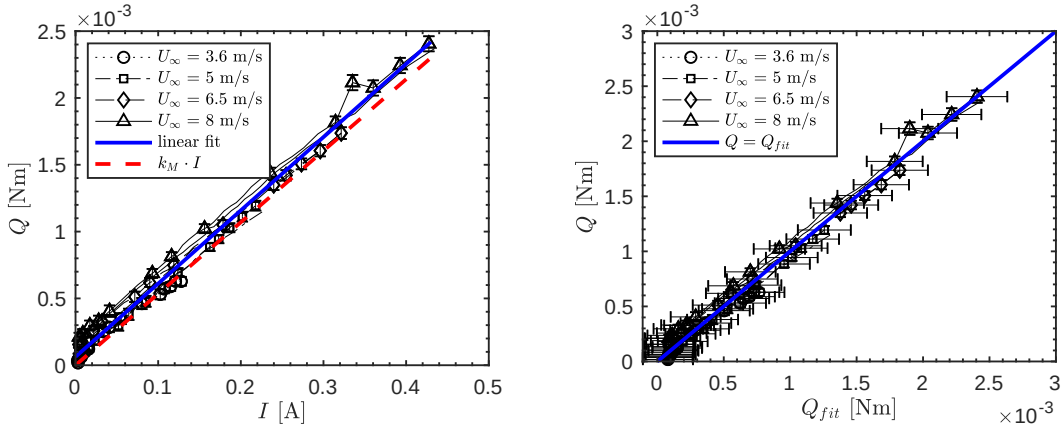
The torque sensor system works fine for an isolated wind turbine but could not be extended to all the machines of a scaled wind farm for practical and financial reasons. Therefore, as in [81], the link between the mechanical torque and the current produced by the generator is investigated in this section. Indeed, within an ideal operating range of a DC motor, the torque is linearly proportional to the current over the resistance.

Figure 5.15(a) shows the mechanical torque as a function of the current over each resistance, for the four wind speeds tested. As expected, the torque is linearly proportional to the current. However, for a given value of the current, the torque appears larger when the wind speed increases. The solid line represents the best fit, in a least-squares sense, between the mechanical torque and the current

$$Q = 0.063 \cdot 10^{-3} + 5.548 \cdot 10^{-3}\, I. \tag{5.4}$$

This fit can be compared to the law $Q = k_M\, I$, where $k_M = 5.350 \cdot 10^{-3}$ Nm/A is the torque constant provided in the datasheet of the motor. While the two slopes are similar, the fit presents

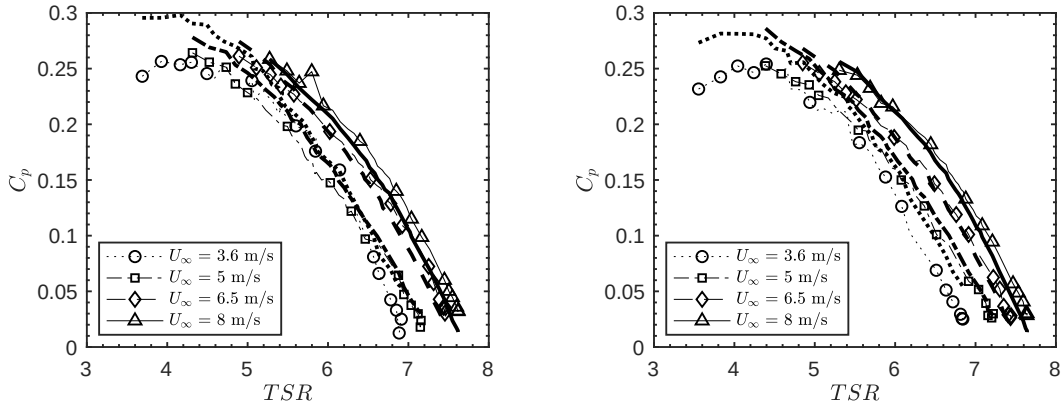
a slight offset towards positive torque values (because of the increase of torque with the incoming wind speed for a given current). Figure 5.15(b) enables to compare the torque computed from the current using Eq. (5.4) to the torque actually measured with the torque sensor system; the errorbars computation are presented in Appendices D.3 and D.4. As it can be observed, the agreement between both torques is very good. It means that, once the generator has been calibrated, it is possible to obtain a very good estimate of the mechanical torque by simply measuring the current produced by the generator.




(a) (b)

***Figure 5.15:*** *Mechanical torque as a function of the current (a), the solid line shows the linear curve fit, $Q = 0.063 \cdot 10^{-3} + 5.548 \cdot 10^{-3} I$; torque measured with the torque sensor system as a function of the torque computed from the current using the linear curve fit (b)*

Finally, Fig. 5.16 shows the evolution, as a function of the tip-speed ratio, of the mechanical power coefficient obtained by computing the torque from the current using Eq. (5.4) (thick line), and of the mechanical power coefficient obtained from the measured torque and the rotational speed (thin line). As it can be observed, there is a good agreement between both curves for the three largest wind speeds tested while the torque determination from the current is less good for $U_\infty = 3.6$ m/s.



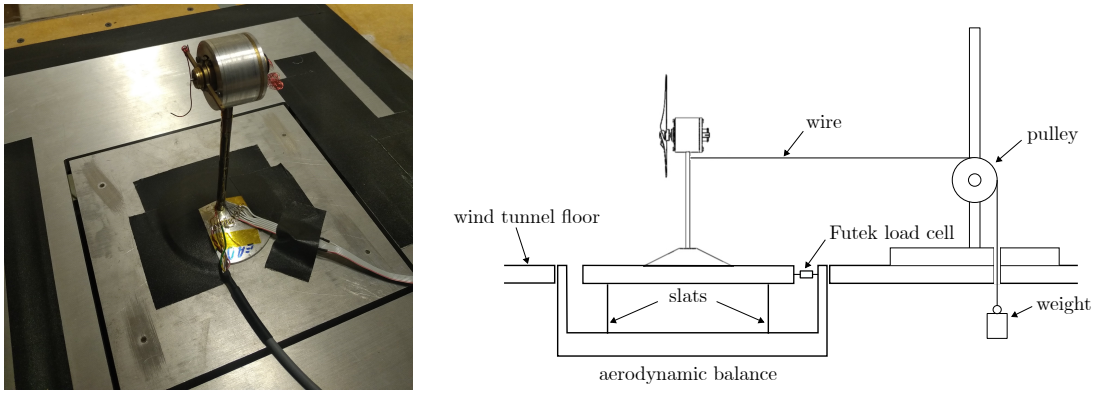

(a) (b)

***Figure 5.16:*** *Evolution, as a function of the tip-speed ratio, of the mechanical power coefficient obtained by computing the torque from the current using Eq. (5.4) (thick line), and of the mechanical power coefficient obtained from the measured torque and the rotational speed (thin line) for the first (a) and the second (b) measurement campaigns*

#### 5.1.2.3 Thrust measurement

In order to measure the thrust of the wind turbine, the balance (described in Section 2.2.2.3) was oriented in such a way that its direction of measurement was aligned with the incoming wind. The wind turbine base was directly fixed to the balance plate which was flush mounted inside the wind tunnel (Fig. 5.17). Prior to the campaigns, the balance was calibrated using a dead weight method. Several weights were attached to one extremity of a wire passing through a pulley, the other extremity being attached to the wind turbine tower as illustrated in Fig. 5.17(b). The calibration line can be found in Appendix E.2.

The trust of the wind turbine was computed by subtracting the drag of the setup without rotor from the drag of the full wind turbine setup. By doing so, it enables to remove the influence of the friction drag on the plate, as well as the drag of the cables, of the tower and of the nacelle (neglecting the influence on the drag of the interaction of the rotor with each of these elements). Due to the unavailability of the balance for the last measurement campaigns whose results were presented up to now, the thrust measurements presented in this section are extracted from previous measurement campaigns, which explains why the lowest speed is now 3.5 m/s. Figure 5.18 enables to verify the stability of the wind speed for each campaign while Fig. 5.19 shows the evolution of the thrust and thrust coefficient as a function of the resistance applied to the generator and the tip-speed ratio, respectively. The thrust of the wind turbine varies slightly with the resistive load applied to the generator and, as expected, the larger the wind speed, the larger the thrust (Fig. 5.19(a)). Concerning the thrust coefficient, it ranges from 0.82 to 1 taking mainly a value around 0.9 for $5 \leqslant TSR \leqslant 8$, which corresponds to a highly loaded wind turbine. Note that the jump in the thrust coefficient for $U_\infty = 5.0$ m/s is due to a small jump in the thrust which should not be present, as shown by the second campaign repeated at the same wind speed. The uncertainty computation for the thrust coefficient is presented in Appendix D.5 and the figures in Appendix E.3.




(a) (b)

***Figure 5.17:*** *Photograph of the aerodynamic balance with the wind turbine model equipped with the torque calibration system (a) and schematic of the calibration setup for the aerodynamic balance (b)*

Note that the characterization of the wind turbine was initially performed with a Maxon DC motor (118516). However, due to delivery time constraints to obtain additional motors for the wind farm, Faulhaber DC motors were selected to performed the experimental campaigns. The characteristics obtained with the Maxon motor can nevertheless be found in Appendix F.

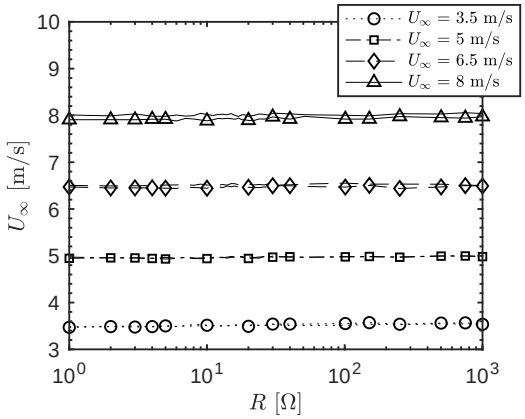
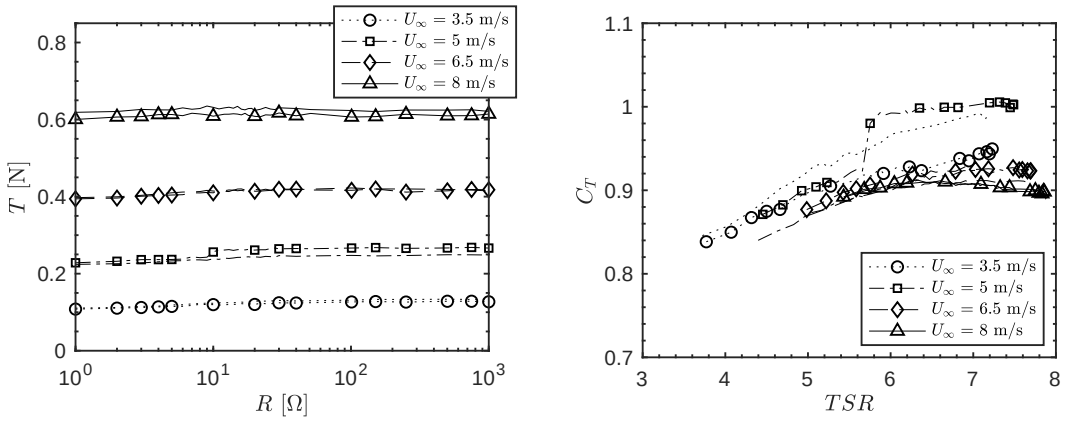



***Figure 5.18:*** *Evolution of the averaged wind speed as a function of the resistive load applied to the generator during the thrust measurements; lines without symbol correspond to the second set of measurements*




(a) (b)

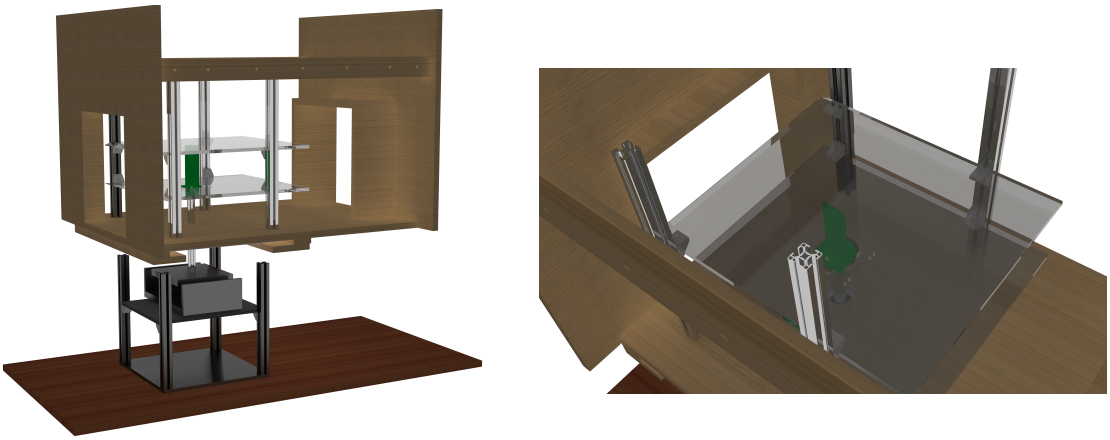
***Figure 5.19:*** *Evolution of the thrust as a function of the resistive load applied to the generator (a) and evolution of the thrust coefficient as a function of the tip-speed ratio (b); lines without symbol correspond to the second set of measurements*

### 5.1.3 Airfoil aerodynamic coefficients

In order to measure the aerodynamic coefficients of the blades airfoil, a scaled-up wing was manufactured by three-dimensional printing. With a chord $c = 49$ mm, the scale is 3.4:1 based on the blade chord at the radius $r = 2R/3$. The span of the wing was set to 116 mm in order to obtain aerodynamic forces that were large enough to be accurately measured while offering a sufficiently rigid model. The experimental setup is presented in Fig. 5.20 and drawings can be found in Appendix G (Figs. G.1 and G.2). As it can be observed, the airfoil was placed between two endplates in order to ensure a 2D flow. The aerodynamic coefficients were measured in the L-2B wind tunnel for 5 flow speeds corresponding to Reynolds numbers $Re_c = U\,c/\nu = 15\,10^3, 20\,10^3, 25\,10^3, 30\,10^3, 35\,10^3$ for angles of attack ranging from $-5^\circ$ to $25^\circ$ by step of $1^\circ$. The flow speed used in the Reynolds number computation is the flow speed between the endplates. This speed is obtained from a Pitot-static probe located upstream in the wind tunnel thanks to a calibration law. This calibration law was build by inserting, before the campaigns, a Pitot-static probe at the location of the airfoil. More details about the calibration can be found in Appendix G. In order to measure the lift and the drag coefficients with the single component balance, the balance was successively rotated by $90^\circ$ (Fig. 5.21). Three campaigns of experiments were conducted to verify the repeatability of the measurements (see Appendix G). Figure 5.22 shows the evolution of the averaged (between the three campaigns) lift and drag coefficients as a function of the angle of attack and Fig. 5.23 shows

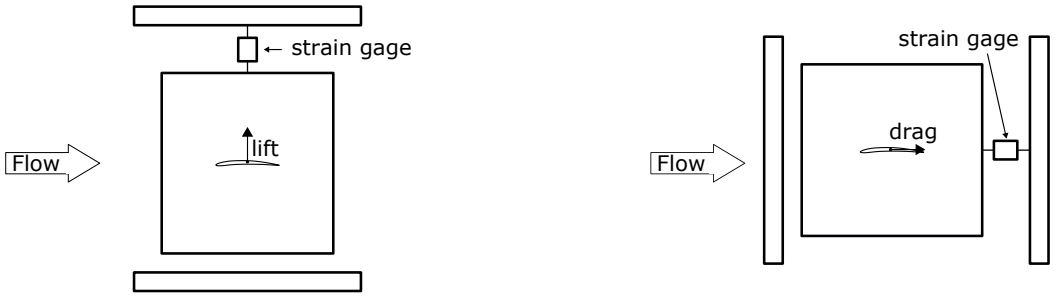
the uncertainties associated with these measurements. The uncertainty analysis is presented in Appendix D.6. Globally, the lift coefficient (Figs. 5.22(a) and 5.23(a)) increases with Reynolds number while the drag coefficient (Figs. 5.22(b) and 5.23(b)) decreases. Furthermore, the lift coefficient saturates from $\alpha = 15°$. Note that the high drag coefficient values are due to the low Reynolds number in play in the experiments, as highlighted in [82]. The standard deviation of the lift and drag coefficients are presented in Appendix G.

Note that additional measurements were performed for the support of the airfoil (without airfoil) in order to subtract the friction drag of the support from the drag measured. The drag presented hereafter is therefore the drag of the "isolated" airfoil.



(a) (b)

***Figure 5.20:*** *CAD of the experimental setup installed in the L-2B wind tunnel for the measurements of the lift and drag coefficients of the airfoil with the single component balance*




(a) (b)

***Figure 5.21:*** *Schematic of the position of the single component balance for the measurements of the lift 5.21(a) and drag 5.21(b) coefficients of the airfoil*

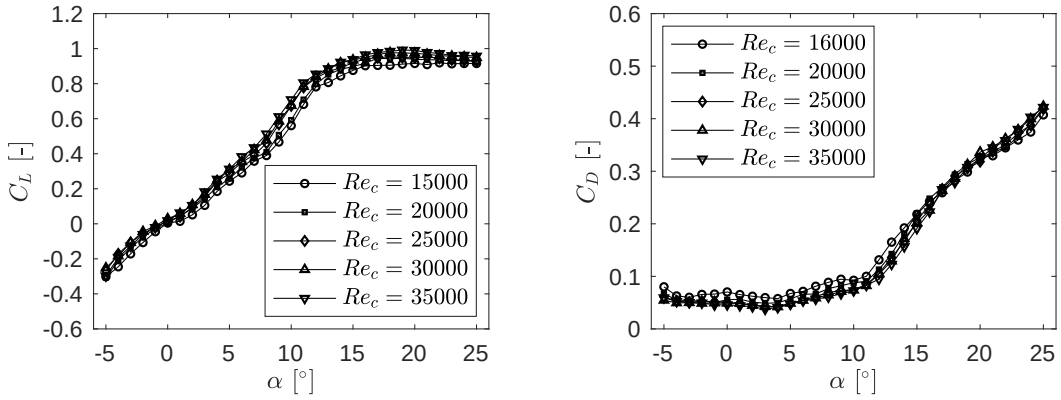



***Figure 5.22:*** *Evolution of the lift (a) and drag (b) coefficients as a function of the angle of attack for* $Re_c = 15000$ *to* $Re_c = 35000$ *by step of* 5000*.*

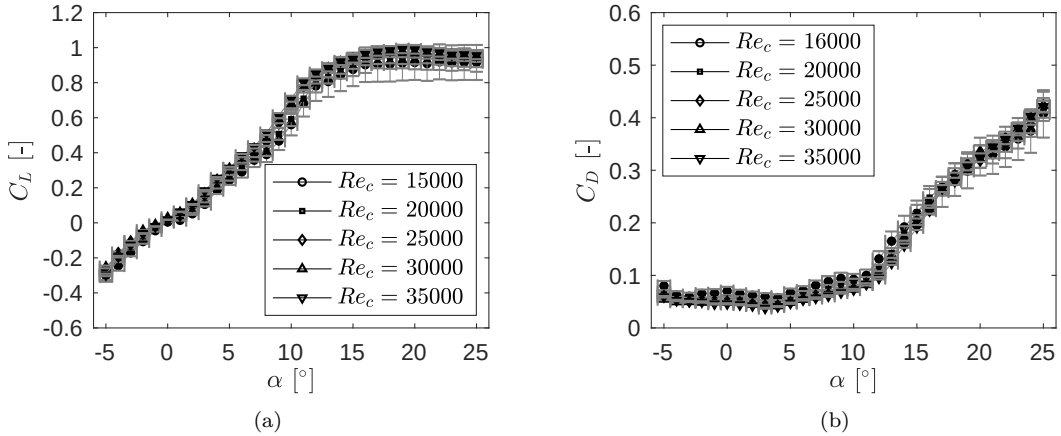



***Figure 5.23:*** *Evolution of the lift (a) and drag (b) coefficients, and the uncertainties associated, as a function of the angle of attack for* $Re_c = 15000$ *to* $Re_c = 35000$ *by step of* 5000*.*

## 5.2 Porous disks

Since porous disks were used as part of another study [83] performed jointly in the L-1B wind tunnel, it was taken advantage of those to study the influence of the rotor geometry on the wake meandering phenomenon. The porous disks have a diameter $D = 0.15$ m, as for the three-bladed wind turbine model, and are made of three different metallic square mesh grids with a wire diameter of 1 mm and a mesh size of 2 mm, 3 mm, and 4 mm, respectively. The disk solidity $\sigma$, defined as the ratio of the solid to the total frontal area of the disk, is therefore of 56%, 44%, and 36%, respectively. These metallic grids were rigid enough to avoid the need for additional reinforcement. The disk properties are presented in Table 5.2. The disks were fixed, via a screw and rubber, to a dummy generator with the same dimensions as those of the three-bladed model generator. The nacelle and the mast were identical to those of the three-bladed model. The models are presented in Fig. 5.24.

As it will be observed in the next chapters, the maximum solidity available ($\sigma = 56\%$) is too low compared to the three-bladed model.

| porous disk | wire diameter [mm] | mesh size [mm] | solidity ($\sigma$) [%] |
|---|---|---|---|
| $\sigma = 56\%$ | 1 | 2 | 56 |
| $\sigma = 44\%$ | 1 | 3 | 44 |
| $\sigma = 36\%$ | 1 | 4 | 36 |

***Table 5.2:*** *Porous disk properties*

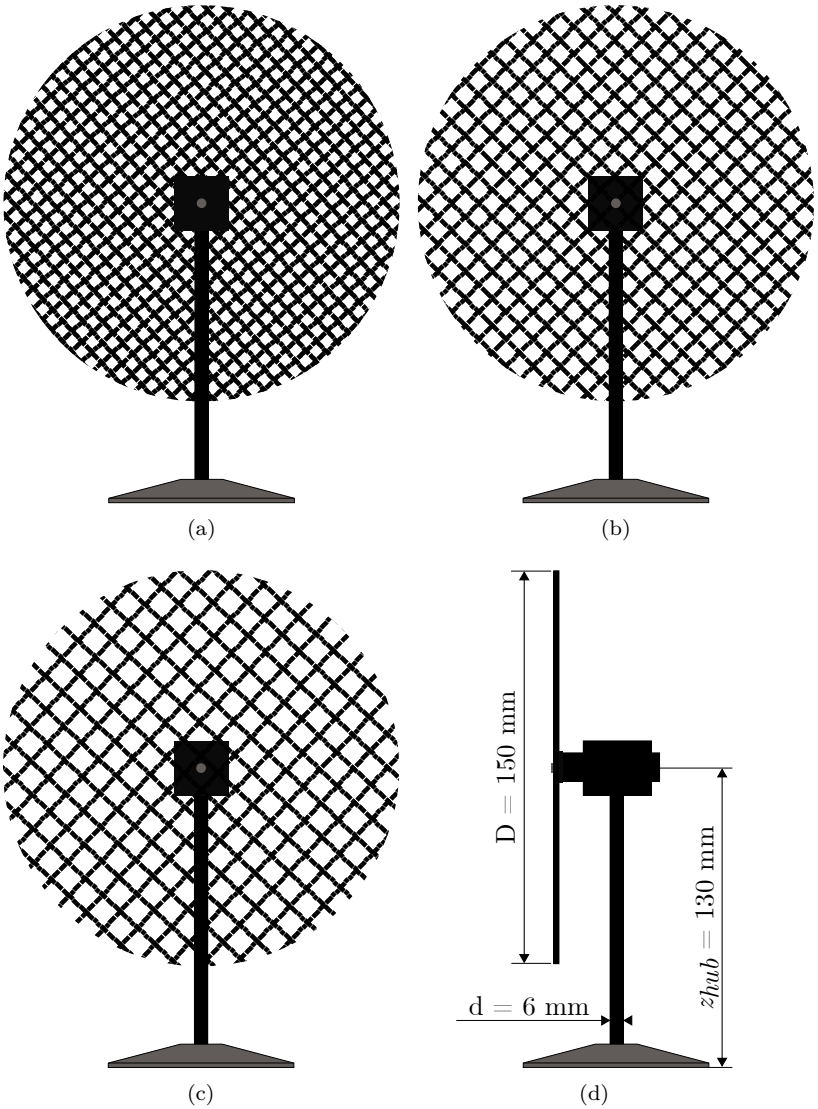



***Figure 5.24:*** *Front view schematics of the porous disk models with several solidities: $\sigma = 56\%$ (a), $\sigma = 44\%$ (b) and $\sigma = 36\%$ (c), and side view schematic of the porous disk models (d)*

## 5.3 ABL modeling in low speed L-1B wind tunnel

### 5.3.1 Atmospheric Boundary Layer (ABL)

The ABL is usually divided in two layers, the inner region and the outer region (Fig. 5.25) [84, 60]. The turbulence intensity is the highest close to the ground and gradually decreases with height. In the inner region, which is called the *surface layer*, the flow mainly depends on the nature of the Earth's surface and not so much on the effects produced by the Earth's rotation. In this layer constituting the lowest 10% of the ABL (100 m to 200 m depending on the surface roughness), the gradient of velocity, turbulence, temperature and humidity is the highest. The outer region is defined from the *surface layer* to the top of the ABL (up to $1-2$ km). This region, where the turbulence in the air keeps decreasing and the Coriolis forces become important, is called the *Ekman layer*.

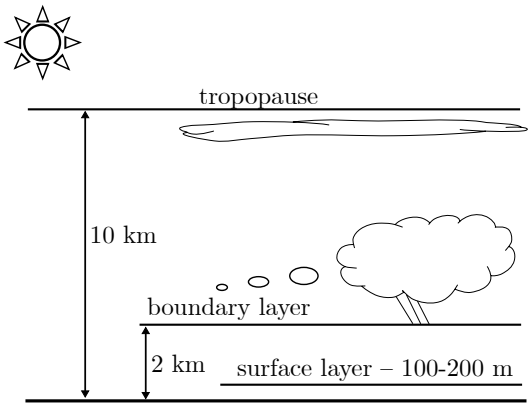



***Figure 5.25:*** *The structure of the atmospheric boundary layer (ABL), adapted from [60]*

For a neutrally stratified ABL (see Section 5.3.2), with no pressure gradient, the average wind speed within the surface layer can be described by the logarithmic law [84, 60]

$$\frac{U}{u_*} = \frac{1}{\kappa} \ln\left(\frac{z-d}{z_0}\right) \tag{5.5}$$

where $u_*$ [m/s] is the friction velocity, $d$ [m] is the displacement height which corrects for the offset of the velocity profile caused by roughness elements (buildings, vegetation), and $z_0$ [m] is the aerodynamic roughness length which is function of the real surface roughness.

An alternative to describe the mean velocity profile inside the ABL is the power law

$$\frac{U}{U_{ref}} = \left(\frac{z-d}{z_{ref}-d}\right)^{\alpha} \tag{5.6}$$

where $\alpha$ [-] is the power law coefficient, $d$ [m] is the displacement height , and $U_{ref}$ [m/s] corresponds to the velocity at a reference height $z_{ref}$ [m]. As stated among others in [60, 84], unlike the logarithmic law, the power law is more a fitting law than a theoretically derived law.

### 5.3.2 Stability of the atmosphere

The height of the atmospheric boundary layer and the turbulence intensity depend on the thermal stratification of the atmosphere [4]. For analyzing atmospheric stability, the concept of the adiabatic lapse rate is useful. The adiabatic lapse rate is the change in temperature with height for a system (an air parcel) with no heat exchange $\left(\frac{dT}{dz}\right)_{ad}$, and is approximately $-1$°C per 100 m. The stability of the atmosphere depends on the actual lapse rate $\frac{dT}{dz}$, which has an average of $-0.65$°C per 100 m in the troposphere (International Standard Atmosphere). Depending on the actual lapse rate, three states of the atmosphere can be distinguished [4]:

- *unstable*: normally during day time, surface heating causes air to rise, forming large convection cells. When the surrounding air is still colder (no thermal equilibrium), this results in large-scale turbulent eddies and a thick boundary layer; the stratification is unstable ($\frac{dT}{dz} < \left(\frac{dT}{dz}\right)_{ad}$).
- *stable*: normally during night time and low winds, surface cooling suppresses vertical motion of the air, leading to a thin boundary layer. Turbulence effects are not caused by large-scale eddies, but are dominated by friction with the ground; the stratification is stable ($\frac{dT}{dz} > \left(\frac{dT}{dz}\right)_{ad}$). Note that the case of $\frac{dT}{dz} > 0$ corresponds to a *temperature inversion*, making the atmosphere even more stable.
- *neutral*: if the air rising from the surface is in thermal equilibrium with the surrounding air, the stratification is said to be neutral ($\frac{dT}{dz} = \left(\frac{dT}{dz}\right)_{ad}$). This happens often in case of strong winds and late in the afternoon. Due to the strong winds this is often the most important situation to consider, but it is also often used because it is an "average condition", between stable and unstable conditions.

### 5.3.3 ABL modeling and characterization

Given that the VKI L-1B wind tunnel does not enable to work with thermally stratified flows, only neutral ABLs were modeled for this work.

In order to model four different neutral ABLs, four boundary layer generation setups were used. The first one is composed of a 0.15 m height fence and a monoplane grid with a mesh size of 0.02 m × 0.02 m that were located at the beginning of the empty test section (Fig. 5.26). This configuration was selected because the wake meandering phenomenon was already observed for the same configuration as part of previous studies performed at VKI [63, 32, 34, 80, 35]. The fence having a large impact on the development of the inflow turbulence [60], the second configuration was obtained by simply removing the fence. From these two setups, two additional configurations were obtained by adding 32-mm height cups inside the previously empty test section. More information concerning the modeling of atmospheric flows in the L-1B wind tunnel can be found in [84, 60]. The four inflow configurations tested are referred to as *grid*, *grid + fence*, *grid + cups*, *grid + fence + cups*.

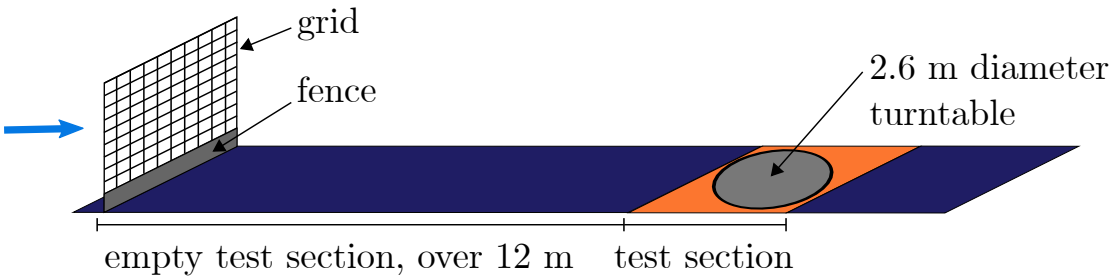



***Figure 5.26:*** *Schematic of the VKI L-1B wind tunnel configuration.*

In order to characterize the various ABLs modeled in the VKI L-1B wind tunnel, three components hot-wire anemometry (3C-HWA) measurements were performed along a vertical line located in the rotor plane of the isolated wind turbine configuration (Section 6.1.2, Fig. 6.3(b)), i.e. at 0.6 m from the beginning of the turntable. For each location, the HWA signal was acquired during 120 s with a sampling frequency of 3 kHz and filtered at 1 kHz.

Note: A spurious peak at the low-pass filtering frequency of the acquisition system ($f = 1$ kHz) was observed in the spectra of the velocity measurements (Fig. 5.27). Since this peak should not be present, it was decided to low-pass filter the velocity components during the post-processing with a cutting frequency of 950 Hz in order to remove the part of the spectra affected. All the results presented in this section were therefore obtained with the low-pass filtered velocity components.

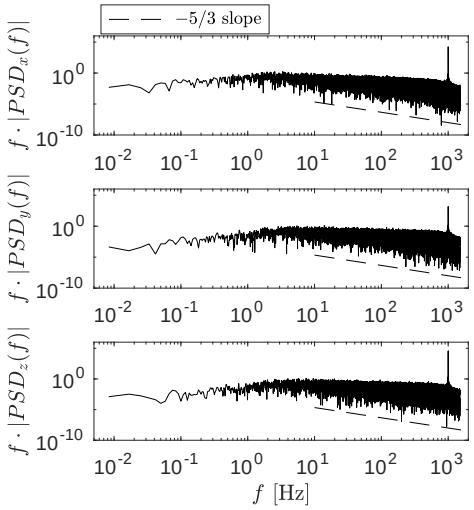



***Figure 5.27:*** *Premultiplied spectra of the velocity fluctuations u, v, w for the configuration grid + fence*

Figure 5.28 presents the normalized velocity profiles, the turbulence intensity profiles and the turbulence intensity components profiles computed from

$$\begin{aligned} I_i(z) &= \frac{\sigma_i(z)}{U(z)}, \\ I(z) &= \frac{\sqrt{\frac{1}{3}\sum_i \sigma_i(z)^2}}{U(z)} \end{aligned} \tag{5.7}$$

where the flow velocity components $i = u, v, w$ are decomposed into two parts, a mean value and a fluctuating part

$$u = U + u' \quad ; \quad v = V + v' \quad ; \quad w = W + w' \tag{5.8}$$

with

$$U = \frac{1}{T}\int_0^T u(t)\,\mathrm{d}t. \tag{5.9}$$

As observed in [60], the fence plays a major role in the boundary layer generation. Therefore, in order to limit the size of the experimental matrix, only two setups were retained to perform the experimental campaigns with the wind turbine scale models: *grid* and *grid + fence*. Furthermore, even if the profiles were measured up to $z/z_{hub} = 10$, the ABL characteristics were only computed for the part of the ABL directly interacting with the wind turbine scale models, i.e. up to $z/z_{hub} = 3.5$. In order to facilitate the interpretation of the next figures, the lower and upper tip heights of the wind turbine rotor are represented by dashed lines. The uncertainty analysis is presented in Appendix D.8.

The determination of the logarithmic law parameters can be performed by fitting the logarithmic equation (Eq. (5.5)) to the logarithmic part of the measured averaged velocity profile. Indeed, by plotting this velocity profile in a semi-logarithmic plot, a linear fit can be performed since the logarithmic part of the profile appears as a line (Fig. 5.29(a)). The friction velocity can then directly be computed from the slope $a$ of the linear fit

$$\begin{aligned} \ln(z) &= \frac{\kappa}{u_*} U + \ln(z_0) \\ &= a\,U + \ln(z_0) \\ u_* &= \frac{\kappa}{a} \end{aligned} \tag{5.10}$$

and the intersection of the linear fit with the vertical axis gives the aerodynamic roughness length $z_0$ ($z = z_0$ for $U = 0$ m/s), see Table 5.3. As it can be observed in Fig. 5.29(a), the $z_0$ obtained with

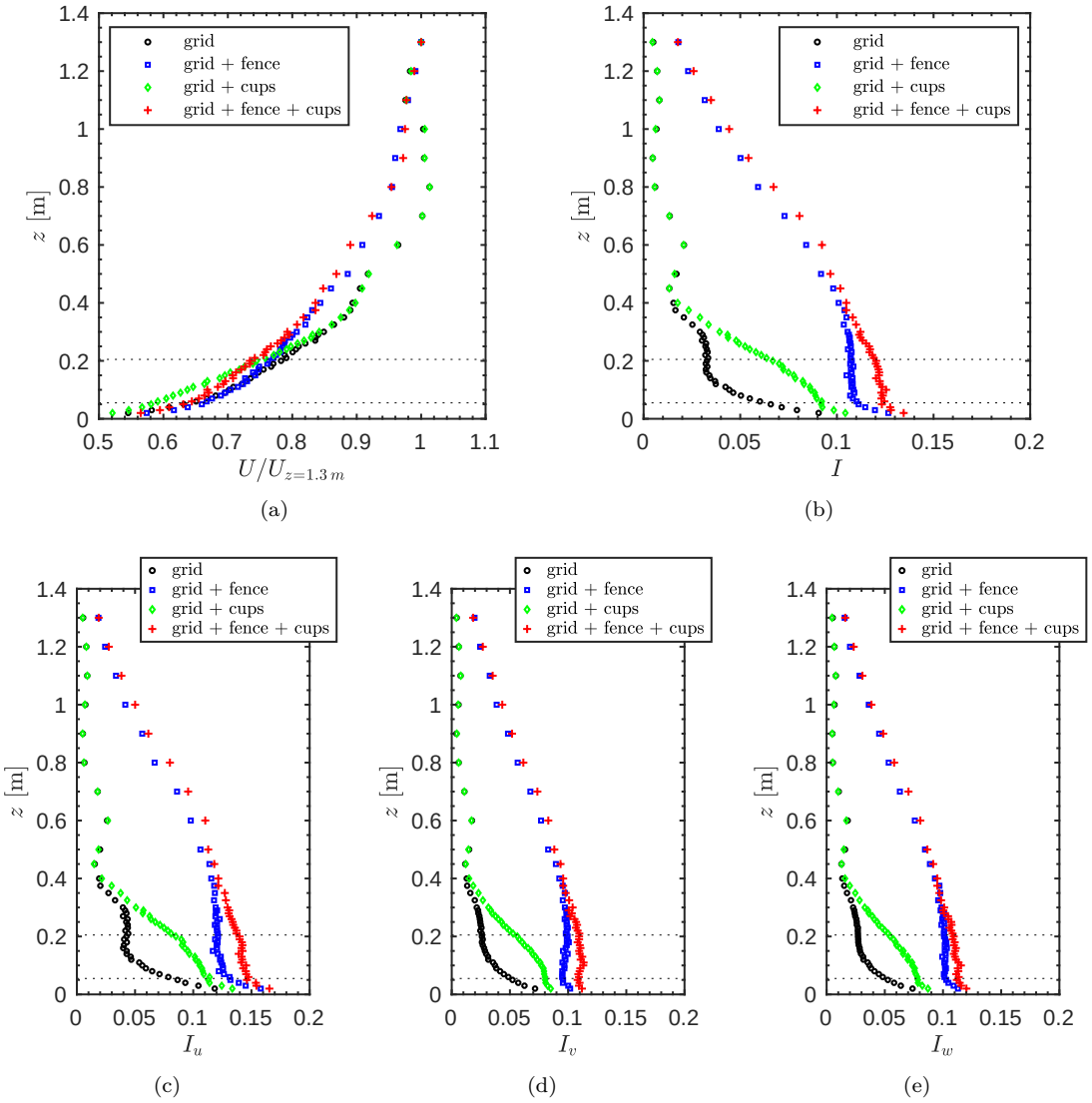



***Figure 5.28:*** *Normalized velocity profiles (a), turbulence intensity profiles (b) and turbulence intensity components profiles (c)-(d)-(e)*

the semi-logarithmic fit depends partly on the inflow speed. Figure 5.29(b) shows the logarithmic law fit for the two ABLs considered.

Concerning the determination of the power coefficient of the power law (Eq. (5.11)), it was determined from the slope $\alpha$ of the linear fit (Fig. 5.30(a)) of the measured velocity profile displayed in a logarithmic-logarithmic plot taking the wind turbine hub height as reference height

$$\ln\left(\frac{U}{U_{ref}}\right) = \alpha \ln\left(\frac{z}{z_{ref}}\right), \tag{5.11}$$

see Table 5.3. Figure 5.30(b) shows the power law fit for the two ABLs. The robustness of this method was assessed by studying the influence of the reference height on the power coefficient computation from Eq. (5.11). As it can be observed, the power coefficient estimation is not significantly impacted by the choice of a specific reference height (Fig. 5.31).

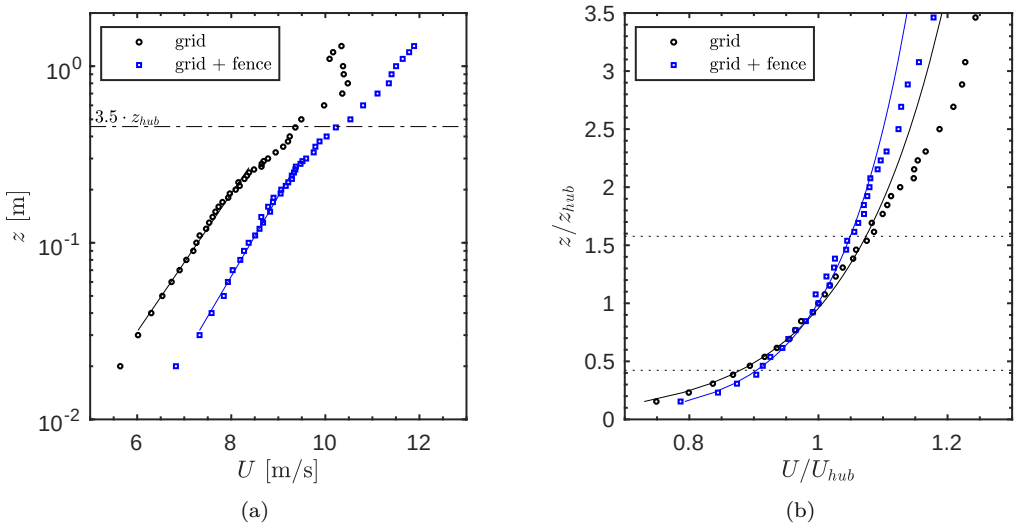



***Figure 5.29:*** *Determination of the ABL logarithmic law parameters (a) and logarithmic law fit (b)*

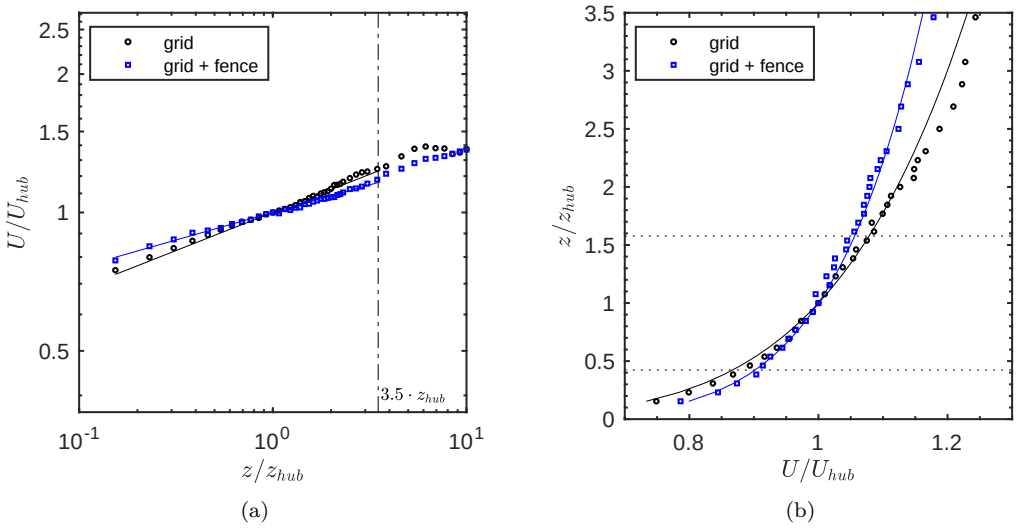



***Figure 5.30:*** *Determination of the ABL power law parameters (a) and power law fit (b)*

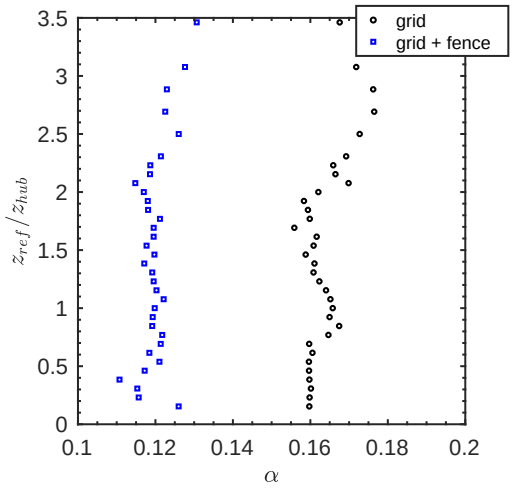



***Figure 5.31:*** *Evolution of the power coefficient as a function of the reference height used in the power law (Eq. (5.11))*

Figure 5.32 enables to compare the logarithmic and the power law fits and shows turbulence intensity profiles while Fig. 5.33 enables to compare the turbulence intensity components profiles for the two configurations. Note that the magnitude of the lateral turbulence intensity component is in good agreement with what is described in the VDI guidelines [78] while the magnitude of the vertical turbulence intensity component is much larger than what is described in these guidelines: $\sigma_v = 0.75\,\sigma_u$ and $\sigma_w = 0.5\,\sigma_u$. Figure 5.34 shows the normalized Reynolds shear stress. In the surface layer, they are expected to be equal to unity, while they are expected to decrease with height above the surface layer.

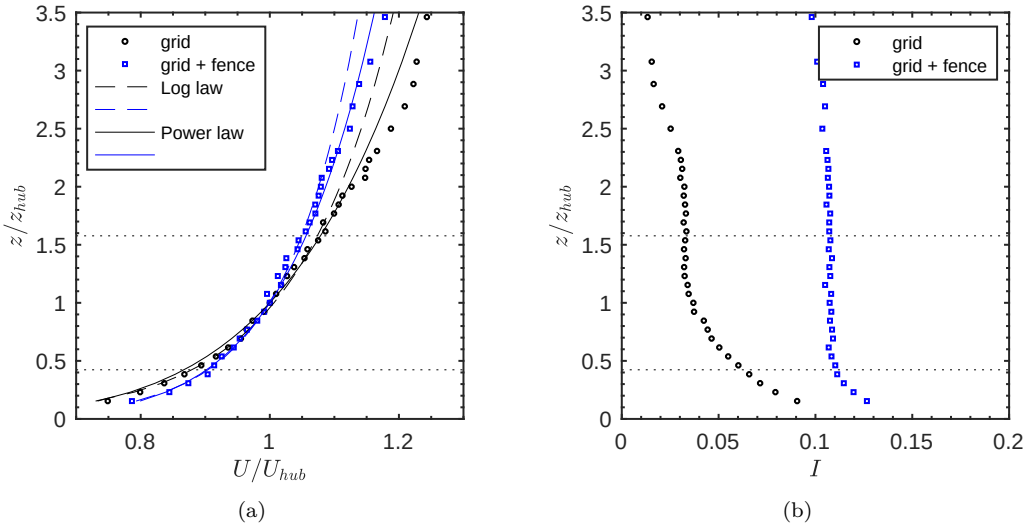



***Figure 5.32:*** *Comparison of the logarithmic law and power law fits (a) and turbulence intensity profile(b)*

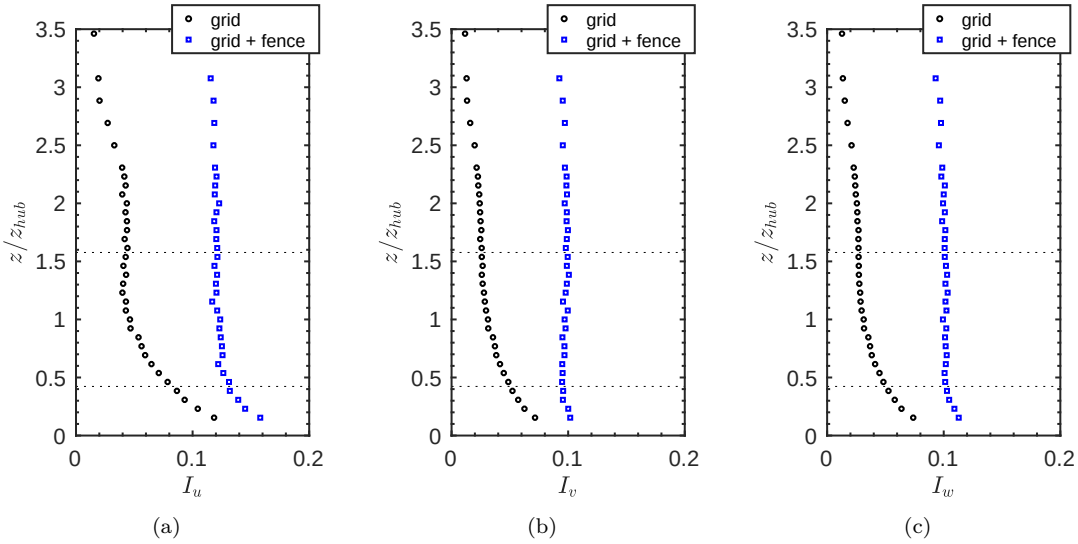



***Figure 5.33:*** *Turbulence intensity components profiles*

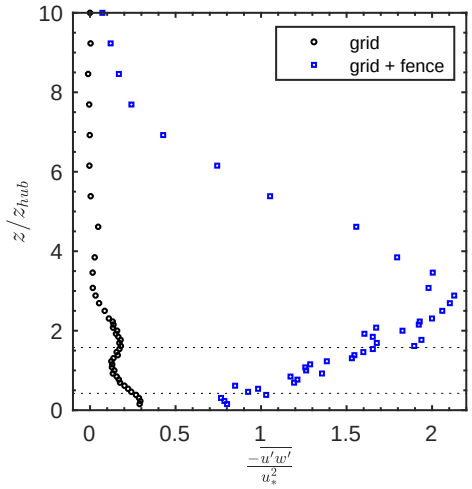



***Figure 5.34:*** *Normalized Reynolds shear stress*

Both the aerodynamic roughness length $z_0$ and the power coefficient $\alpha$ (Table 5.3) reflect the terrain roughness. An empirical relationship between these parameters was proposed by Counihan through a fit of series of field experiments [85]

$$\alpha = 0.096 \ \log_{10} z_0 + 0.016 \ (\log_{10} z_0)^2 + 0.24, \tag{5.12}$$

applicable for $0.001\ m \leqslant z_0 \leqslant 50\ m$. Figure 5.35 presents the Counihan fit as well as the properties of the two ABLs modeled in the L-1B wind tunnel. As $z_0$ and $\alpha$ can be determined independently from each other, and since $\alpha$ is not linked to a scaling factor (it is only a shape parameter) [60], a range of possible scaling factors, from the wind tunnel ABL to the actual (full-scale) ABL, can be obtained from Figure 5.35. Considering the upper and lower bounds of the Couhinan fit, a minimum and a maximum scaling factor achievable for the two ABLs modeled in the L-1B wind tunnel can be determined (Table 5.4).

A scaling factor of 440, corresponding to the scaling of the Vestas V66-2MW rotor diameter, can therefore be selected. Table 5.3 presents the modeled ABL properties obtained with the logarithmic law and the power law, as well as the aerodynamic roughness length scaled to its full scale value.

| | $grid + fence$ | $grid$ |
|---|---|---|
| $u_*$ $[m/s]$ | 0.39 | 0.46 |
| $z_0$ $[m]$ | $1.5 \cdot 10^{-5}$ | $1.4 \cdot 10^{-4}$ |
| $z_{0_{fs}}$ $[m]$ | $7 \cdot 10^{-3}$ | $6 \cdot 10^{-2}$ |
| $\alpha$ | 0.12 | 0.17 |

***Table 5.3:*** *Modeled ABL properties for the logarithmic law and the power law*

| | $grid + fence$ | $grid$ |
|---|---|---|
| min scaling factor | – | 330 |
| max scaling factor | 3700 | 1900 |

***Table 5.4:*** *Minimum and a maximum scaling factors achievable in the L-1B wind tunnel for the two ABLs modeled.*

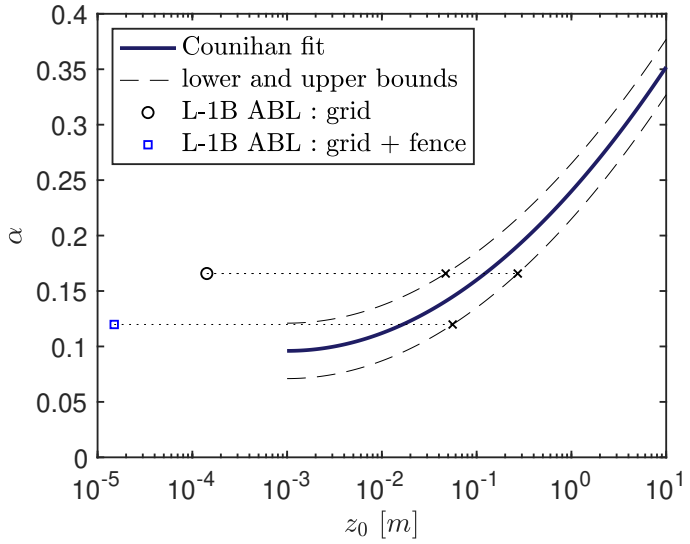



***Figure 5.35:*** *ABL properties and Counihan [85] fit of field data relating $z_0$ and $\alpha$*

These parameters can be compared to the Eurocode and VDI guidelines. According to the Eurocode standard [86], the parameters of the ABL obtained with the *grid + fence* setup correspond to a terrain category of *type 0*, which is defined as a sea or coastal area exposed to the open sea. According to the VDI guidelines [78], these values correspond to the upper limit of the *slightly rough* roughness class representing an ice, snow or water "terrain". Concerning the ABL obtained with the *grid* setup, it corresponds to an ABL developing on a terrain category of *type II*, which is defined as an area with low vegetation such as grass and isolated obstacles (trees, buildings) with separations of at least 20 obstacle heights, according to the Eurocode standard [86]. According to the VDI guidelines [78], these values correspond to the *moderately rough* roughness class representing a grassland or farmland "terrain". It is important to keep in mind that the ABL classification can depend on the standard taken into consideration. The IEC and GL standards, for example, specify an exponent of $\alpha = 0.20$ for normal wind conditions onshore and $\alpha = 0.14$ for normal wind conditions offshore. Both standards specify an exponent of $\alpha = 0.11$ for extreme wind conditions (onshore and offshore) [79].

Due to the presumed important role of large-scale turbulent eddies contained in the ABL on the wake meandering phenomenon, the integral length scales, at each vertical position, were computed from the 3C-HWA measurements. This quantity represents the characteristic size of the energy containing turbulent eddies.

In theory, the integral length scales ($L$) are extracted from the space correlation of the velocity fluctuations. However, using the Taylor's frozen turbulence hypothesis, it can be deduced from a single point measurement over a long time. Indeed, the Taylor's frozen turbulence hypothesis makes the assumption that, while it is convected through a measurement point, an eddy is imperceptibly changed. Then, the time scale and the length scale at a certain height are simply related by

$$L(z) = U(z) \cdot T(z). \tag{5.13}$$

So a good approximation of integral length scale ($L$) is obtained from the integral time scale using Eq. (5.13). The integral time scale ($T$) is calculated as the integral of the auto-correlation coefficient of the time signal of the velocity fluctuations

$$T = \int_0^\infty \rho(\tau) \cdot d\tau \tag{5.14}$$

where the auto-correlation coefficient between two times $t$ and $t + \tau$ is given by

$$\rho(\tau) = \frac{\overline{u'(t) \cdot u'(t+\tau)}}{\overline{u^2}}. \tag{5.15}$$

The integral time scale is therefore representative of the time scale over which the turbulent structures remain correlated. In practice, the value of the integral defined by Eq. (5.14) may vary significantly depending on how the auto-correlation coefficient oscillates around zero. A common approximation of this quantity is however provided by the $1/e$ approximation. This estimation consists in taking the time at which the auto-correlation coefficient equals $1/e \simeq 0.37$ [60] (Fig. 5.36).

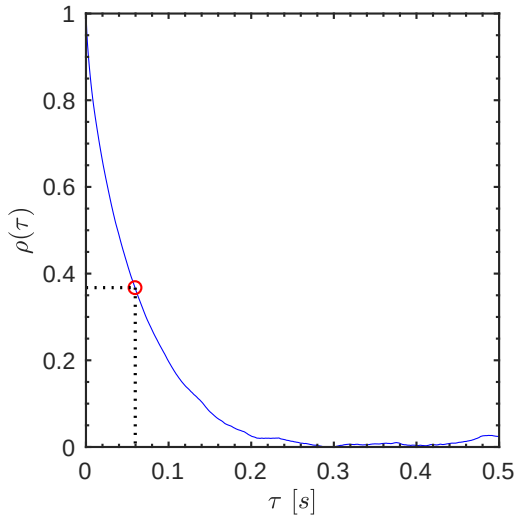



***Figure 5.36:*** *Auto-correlation coefficient at the hub height for the configuration grid + fence*

The integral length scales of the longitudinal, lateral and vertical components in the longitudinal direction at each vertical position are presented in Fig. 5.37. At the heights swept by the wind turbine rotor, the integral length scales of the longitudinal component range from three to four rotor diameters for the *grid + fence* setup and from one to two rotor diameters for the *grid* setup.

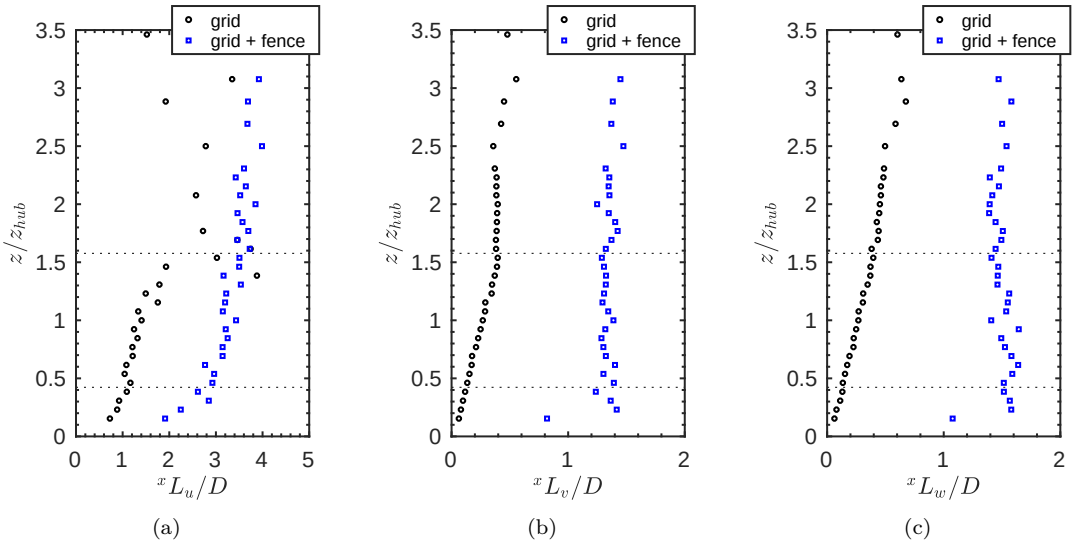



***Figure 5.37:*** *Integral length scales of the longitudinal (a), lateral (b) and vertical (c) components in the longitudinal direction*

A usual representation of the distribution of energy for atmospheric flows is the Kaimal weighted spectrum [87]. It consists in normalizing the energy spectrum by the frequency and the square of the friction velocity ($f \cdot S(f)/u_*^2$) and in plotting it versus a reduced frequency $n$ based on the height $z$ and the mean velocity at that height ($n = (f \cdot z)/U(z)$). In this representation, the $-5/3$ slope turns into a $-2/3$ slope [60]. The Kaimal spectra for the three velocity components are given by [87]

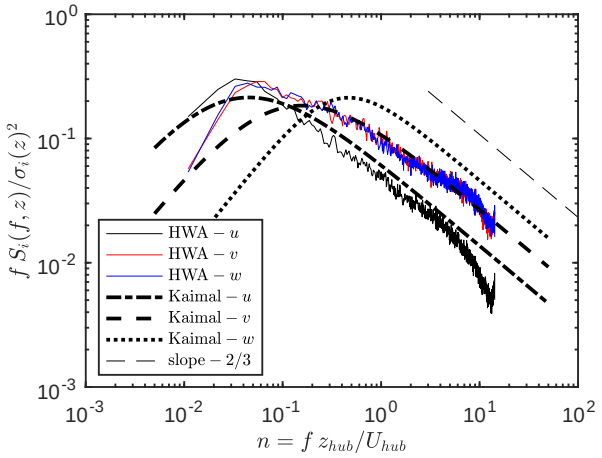
$$\begin{aligned} \frac{fS_u(f)}{u_*^2} &= \frac{102n}{(1+33n)^{5/3}}, \\ \frac{fS_v(f)}{u_*^2} &= \frac{17n}{(1+9.5n)^{5/3}}, \\ \frac{fS_w(f)}{u_*^2} &= \frac{2.1n}{\left(1+5.3n^{5/3}\right)}. \end{aligned} \tag{5.16}$$

From these equations, the conversion from the friction velocity to the standard deviation of the velocity fluctuations, which can be determined more reliably, can be performed using $\sigma_u/u_* = 2.17$, $\sigma_v/u_* = 1.78$, and $\sigma_w/u_* = 1.36$ [87]

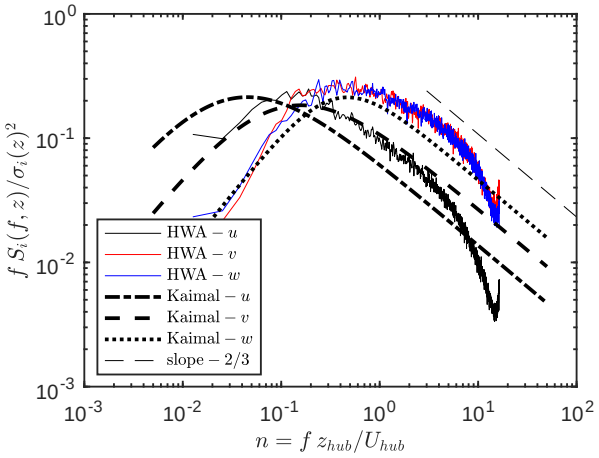
$$\begin{aligned} \frac{fS_u(f)}{\sigma_u^2} &= \frac{102n}{2.17^2\,(1+33n)^{5/3}}, \\ \frac{fS_v(f)}{\sigma_v^2} &= \frac{17n}{1.78^2\,(1+9.5n)^{5/3}}, \\ \frac{fS_w(f)}{\sigma_w^2} &= \frac{2.1n}{1.36^2\,\left(1+5.3n^{5/3}\right)}. \end{aligned} \tag{5.17}$$

The normalized turbulent spectra measured in the L-1B wind tunnel are compared to the Kaimal spectra in Fig. 5.38. For the *grid + fence* configuration, the spectrum obtained for the $u$-component is in good agreement with the corresponding Kaimal spectrum. For the $v$-component, a good agreement can be observed for the higher frequencies while the lower frequencies of the modeled ABL

present more energy than the corresponding Kaimal spectrum. The spectrum of the $w$-component being similar to that of the $v$-component, it presents less energy than the Kaimal spectrum for the high frequencies and more energy for the low frequencies. The large scales of the modeled ABL are therefore more energetic than what is expected based on the Kaimal spectra. Concerning the *grid* setup, the ABL modeled present more energy in the $-2/3$ slope range compared to what is expected from the Kaimal spectra. The large scales of the modeled ABL, however, present a lower energy compared to what is expected from the Kaimal spectra, except for the $w$-component where a good agreement can be observed.




(a)




(b)

***Figure 5.38:*** *L-1B ABL normalized spectra at hub height and Kaimal spectra [87] for the grid + fence (a) and the grid (b) setups*

In order to verify that the boundary layer was fully developed, measurements were performed 1.5 m upstream (P2) of the position considered up to now (P1), for the *grid + fence* setup. Based on the velocity and turbulence intensity profiles (Figs. 5.39 and 5.40), the ABL can be considered fully developed. Indeed, the streamwise velocity profiles are very similar and the maximum deviation in turbulence intensity does not exceed 1%; this difference in turbulence intensity is mainly due to the third component $I_w$.

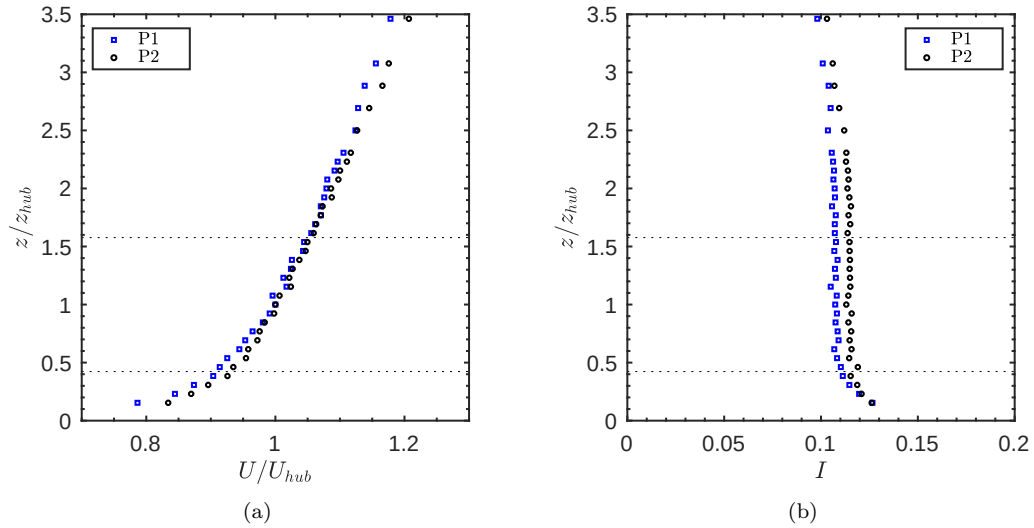



***Figure 5.39:*** *Normalized velocity profiles (a) and turbulence intensity profiles (b) for two positions separated by* 1.5 *m in streamwise direction*

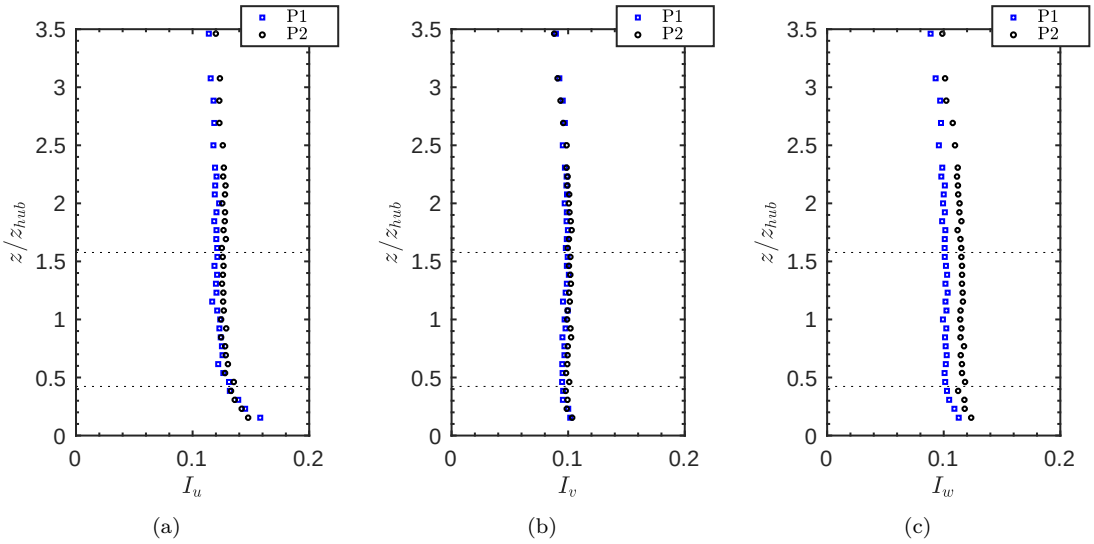



***Figure 5.40:*** *Turbulence intensity components profiles for two positions separated by* 1.5 *m in streamwise direction*

Finally, the dependence on the Reynolds number ($Re = U_{hub}\, D/\nu$) of the velocity and turbulence intensity was investigated. With a maximum deviation of less than 3.2% for the velocity and of less than 0.6% for the turbulence intensity, the influence of the Reynolds number is really weak (Figs. 5.41 and 5.42).

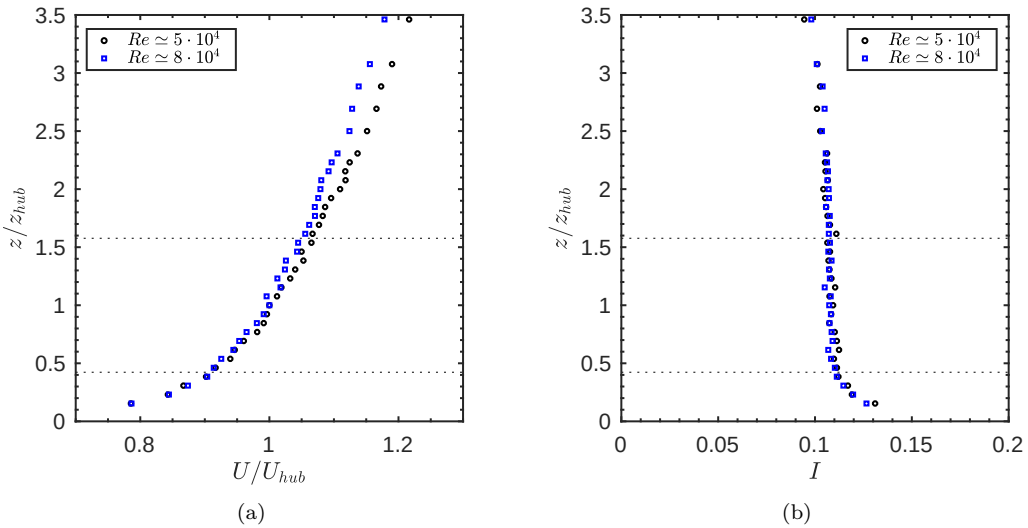



***Figure 5.41:*** *Normalized velocity profiles (a) and turbulence intensity profiles (b) for* $Re = U_{hub}\, D/\nu \simeq 5 \cdot 10^4$ *and* $Re \simeq 8 \cdot 10^4$

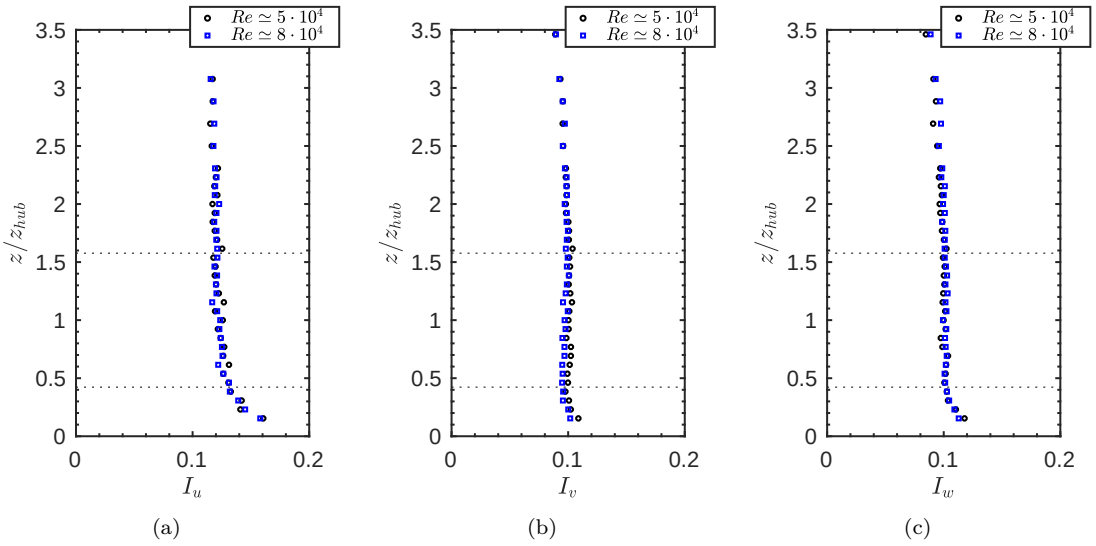



***Figure 5.42:*** *Turbulence intensity components profiles for* $Re = U_{hub}\, D/\nu \simeq 5 \cdot 10^4$ *and* $Re \simeq 8 \cdot 10^4$

## 5.4 Conclusions

The first part of this chapter concerns the wind turbine scale model characterization inside the L-2B wind tunnel via the control and acquisition board developed within the framework of this thesis with the *Electronics Laboratory* of the von Karman Institute. The characterization was performed for four inflow wind speeds: 3.6 m/s, 5.0 m/s, 6.5 m/s, and 8.0 m/s. Via the performance curves based on the electrical quantities, it was observed that while, as expected, the power produced by the wind turbine model increases with the wind speed, the trend is reversed for the power coefficient. Indeed, the higher the wind speed, the lower the power coefficient, with $C_{p_{max}}^{elec} = 0.15$ for $U_\infty = 3.6$ m/s and $C_{p_{max}}^{elec} = 0.11$ for $U_\infty = 8.0$ m/s. It means that the wind turbine scale model is more efficient at lower wind speeds as it extracts a larger part of the available power in the wind. Furthermore, it was observed that the TSR range swepts by the scale model decreases when the wind speed increases. It means that the resistances have less influence on the rotational speed at higher wind speed. Indeed, the TSR value for the curves at 3.6 m/s was bounded between 3.6 and 7 whereas TSR of the curves at 8.0 m/s ranged from 5.2 to 7.6. The maximum electrical power coefficient occurs for $R \approx 9\ \Omega$ and at different TSR value depending on the wind speed. The optimum TSR ranges from 5 to 6.4 for the wind speeds tested.

In addition, the wind turbine performances were determined through mechanical quantities thanks to the torque sensor system developed within the framework of this thesis based on [81]. The power extracted by the model wind turbine from the incoming flow can indeed be obtained by multiplying the torque by the rotational speed. As expected, the aerodynamic power and power coefficient are larger compared to the corresponding electrical quantities. Taking the ratio of the two powers showed that around 40% of the aerodynamic power is lost inside the generator. However, the shape of the aerodynamic curves was different from that of the electrical curves. This is due to a too weak rotation resistance of the generator (too low nominal voltage). The torque sensor system turned out to work fine for an isolated wind turbine but could not be extended to all the machines of a scaled wind farm for practical and financial reasons. Therefore, as in [81], the linear relation between the torque and the current produced by the DC generator was exploited. From the best fit, in a least-squares sense, obtained between the mechanical torque and the current, it is possible to obtain a very good estimate of the mechanical torque by simply measuring the current produced by the generator.

The thrust of the wind turbine was then measured with an aerodynamic balance. The thrust varies slightly with the resistive load applied to the generator and, as expected, increases with the wind speed. Concerning the thrust coefficient, it ranges from 0.82 to 1, which corresponds to a highly loaded wind turbine.

The second part of this chapter focuses on the determination of the aerodynamic coefficients of the airfoil composing the wind turbine blades. The aerodynamic coefficients were measured in the L-2B wind tunnel on a scaled-up wing based on the blades airfoil for 5 flow speeds corresponding to Reynolds numbers $Re_c = U\,c/\nu = 15\,10^3, 20\,10^3, 25\,10^3, 30\,10^3, 35\,10^3$ for angles of attack ranging from $-5^\circ$ to $25^\circ$ by step of $1^\circ$. These aerodynamic coefficients were then used to set up numerical simulations at wind tunnel scale (see Section 7.2.2).

Finally, the last part of this chapter focuses on the ABL modeling the low speed L-1B wind tunnel. Four inflow configurations referred to as *grid*, *grid + fence*, *grid + cups*, and *grid + fence + cups* were tested in the L-1B wind tunnel. Based on their main characteristics, two configurations were chosen: *grid* and *grid + fence*. The ABL resulting from these two configurations were then entirely characterized in terms of velocity profile, turbulence intensity components, integral length scales and spectra. For the *grid + fence* configuration, it was verified that the ABL was fully developed and that there was no longer a Reynolds number dependency. In the next chapters, the ABL corresponding to the *grid + fence* configuration is referred to as ABL1 and the ABL corresponding to the *grid* configuration to as ABL2.

Chapter 6

# Wind turbine wake characteristics at wind tunnel scale

This chapter presents time-resolved PIV measurements performed for an isolated wind turbine, a row of three wind turbines, a three-row three-column wind farm, and isolated porous disks with several solidities, all subjected to two incoming ABLs, namely ABL1 and ABL2. As stated in Section 5.3, ABL1 and ABL2 correspond to the ABL developing in the L-1B wind tunnel with the *grid + fence* configuration (i.e. high turbulence level) and the *grid* configuration (low turbulence level), respectively. The mean streamwise velocity, the turbulence intensity and the electrical and aerodynamic powers are compared for the various configurations tested.

## 6.1 Experimental setup

### 6.1.1 Time-resolved PIV setup

The 2D2C TR-PIV technique was used to perform measurements in the horizontal plane at hub height in the wake of the wind turbine scale models. Therefore, the laser was positioned on one side of the test section, with the cameras (Phantom Miro LAB140 12GB) located on the roof of the wind tunnel where two drilled holes allow for optical access (Fig. 6.1). The cameras have a spatial resolution of four megapixels and were equipped with 50-mm Nikkor lenses. The resolution of the cameras was reduced from $2560 \times 1600$ px to $2560 \times 1536$ px in order to be able to store 1000 pairs of images in the buffer of each camera, and therefore to acquire 1000 pairs of images per set (and per camera). The cameras were located at $\sim 1.87$ m from the laser sheet to obtain a field-of-view as large as ten rotor diameters in the streamwise direction when stitching the field-of-view of the two cameras (Fig. 6.2). The calibration was performed with a wooden plate on which was pasted a 2 m $\times$ 0.9 m paper sheet with a doted pattern (radius of 5 mm and center-to-center spacing of 15 mm). The calibration sheet was located at hub height and was covering the entire field-of-view of the two cameras. After the calibration using a third order polynomial fit, the averaged deviation from the marks was 0.134 px for camera 1 and 0.125 px for camera 2, which validates the calibration process since the fit can be considered as excellent when the deviation is smaller than 0.3 pixel [88]. Based on this setup, the magnification factor obtained was 0.362 mm/px. To collect a large amount of light scattered by the seeding particles, the aperture was set to $f_{\#} = 1.4$. The seeding particles are oil droplets of diameter of 1-5 $\mu$m, produced by a smoke generator composed of a plate heated at 180°C on which oil (Shell Ondina Oil 917) is vaporized. To obtain a uniform seeding, the oil particles were injected into the end of the test section so that mixing aided by

the counter-rotating fans occurs in the return circuit of the wind tunnel. The measurements were performed using the time-resolved PIV system of UMONS (LaVision's DAVIS 8 system). Two cavities of a Nd:Yag pulsed laser system (Litron Lasers Ltd. LPY 704-100PIV) were used to obtain two flashes of light, those being synchronized with the cameras. The separation time between two images of a pair was adapted based on the inflow wind speed and the configuration investigated to obtain particle displacements of about eight pixels (see Table 6.1). For each measurement, 1000 image pairs were acquired per camera at a frequency of 100 Hz. Two examples of the PIV images obtained can be visualized in Fig. 6.2. The processing of the images was carried out using the Davis 8.3.0 software with 128 x 128-pixel initial interrogation areas, an overlap of 50%, one refinement step, and multi-pass processing. Between each pass, spurious vectors were removed from the vectors field before using it as a reference in the next pass. Vectors derived from a cross-correlation with a signal-to-noise ratio smaller than 1.3 were deleted and a median filter in the version *strongly remove & iteratively replace* [89] was also applied to remove spurious vectors or groups of spurious vectors. The median filter compares the middle vector of a group of neighboring vectors to the median vector of the group and rejects the middle vector if the deviation is too large. The rejected vector may then be replaced by a vector that corresponds to the second, third or fourth highest correlation peak detected in this interrogation window if it fits into the group of neighboring vectors or otherwise be interpolated from the neighboring vectors. Furthermore, the images were corrected for distortions during the processing and the models were masked prior to the vectors field computation. More detailed information about the processing can be found in the *FlowMaster* manual [89].

| | $\Delta t$ [$\mu$s] | |
|---|---|---|
| | $U_{hub} \simeq 5$ m/s | $U_{hub} \simeq 8$ m/s |
| configurations w/o wind turbine | 700 | 380 |
| configurations w wind turbine(s) | 800 | 530 |

***Table 6.1:*** *Separation times used for the time-resolved PIV measurements for the configurations without and with wind turbine(s)*

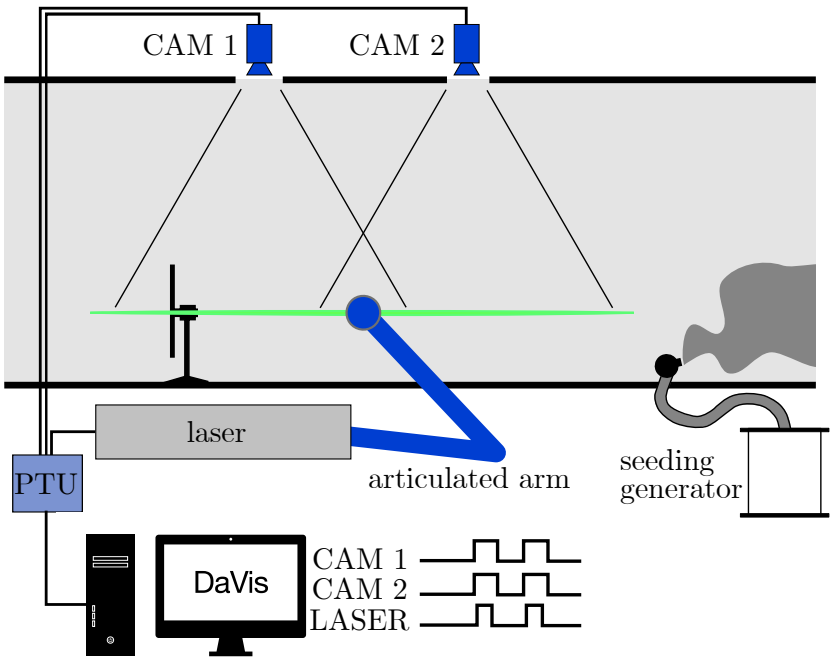
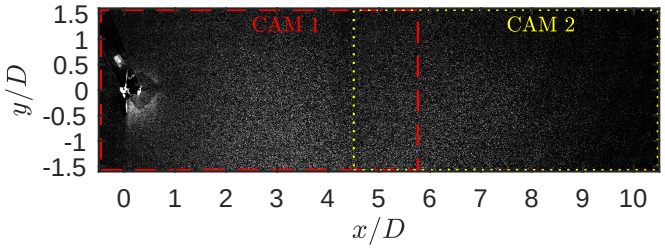
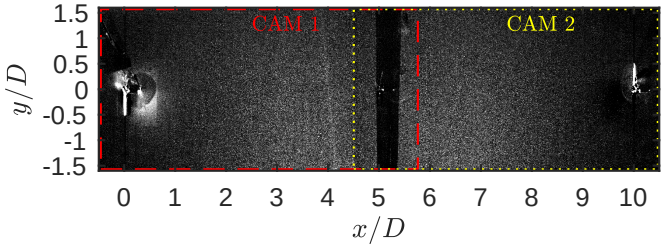



***Figure 6.1:*** *Schematic of the PIV setup in L-1B wind tunnel*




(a)




(b)

***Figure 6.2:*** *Examples of PIV images for the isolated wind turbine (a) and for the middle row of the three-row three-column wind farm (b) inside ABL1, the rectangles represent the field-of-view of camera 1 (CAM 1) and camera 2 (CAM 2) and enable to visualize the overlapping region*

### 6.1.2 Wind turbine configurations and design of experiments

The wind turbines were located at the end of the test section of the L-1B wind engineering facility. Several configurations were tested. First, the measurements were performed without model (Fig. 6.3(a)) in order to characterize the incoming flow. Then the isolated wind turbine was installed at the beginning of the TR-PIV field of view to capture the wake over the longest possible distance (Fig. 6.3(b)). A row of three wind turbines (Fig. 6.3(c) to 6.3(e)) separated by $5D$ was then installed inside the wind tunnel to be able to study the influence of the lateral rows when comparing with the wind farm configuration. Due to the limitations in the positioning of the TR-PIV cameras on the roof of the wind tunnel (see Section 6.1.1), the TR-PIV system remained stationary while the wind turbines row was progressively shifted upstream to study the wakes of the first and second wind turbines (Fig. 6.3(c)), of the second and third wind turbines (Fig. 6.3(d)), and of the third wind turbine (Fig. 6.3(e)). These changes in the wind turbines positioning have a negligible influence on the reliability of the results, since the entire testing area is contained within a fully-developed boundary layer (see Section 5.3). Furthermore, since the PIV system remains in the same position, the comparison of the wind turbine wakes is not affected by changes in the TR-PIV set-up. A three-row three-column wind farm was then installed in the wind tunnel and was progressively shifted upstream in the same way as for the row of wind turbines (Fig. 6.3(f) to 6.3(h)). For the wind farm configurations, the wind turbine scale models were separated by distances of $3D$ and $5D$ in the spanwise and streamwise directions, respectively. These distances make possible to fit a three-row three-column wind farm inside the wind tunnel test section while being representative of a full-scale wind farm. Figure 6.4 shows photographs of the wind farm in configuration 1. Finally, the isolated wind turbine was replaced by different isolated porous disks with various solidities (Fig. 6.3(b)).

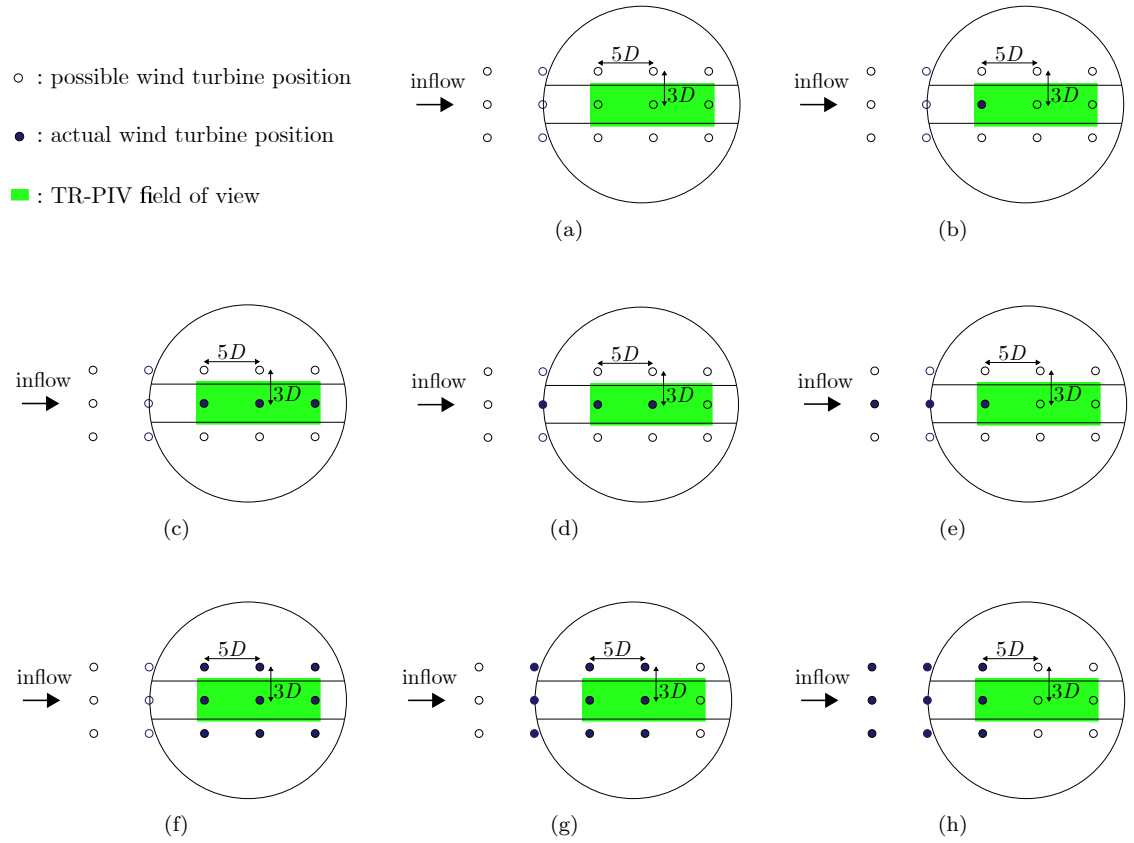



***Figure 6.3:*** *Schematics of the configurations used for the TR-PIV campaign in the L-1B wind engineering facility: inflow (a), isolated wind turbine (b), row of wind turbines in configuration 1 (c), row of wind turbines in configuration 2 (d) and row of wind turbines in configuration 3 (e), wind farm in configuration 1 (f), wind farm in configuration 2 (g), wind farm in configuration 3 (h)*




***Figure 6.4:*** *Photographs of the three-row three-column wind farm in configuration 1 seen from upstream (a) and downstream (b) in the L-1B wind tunnel*

The design of experiments for the TR-PIV measurements performed in the L-1B wind tunnel is presented in Table 6.2. The measurements were performed for ABL1 and ABL2 which were characterized in Section 5.3.3. In order to characterize the incoming flow, the measurements were first performed without model (0WT) for $Re = U_{hub}\, D/\nu \simeq 8 \cdot 10^4$ and $Re \simeq 5 \cdot 10^4$. The measurements were then performed for the isolated wind turbine (1WT) with different operating conditions; R9 corresponding to the electrical optimal operating conditions when $R = 9\,\Omega$ (see Section 5.1.2) and R3 and R150 corresponding to $R = 3\,\Omega$ and $R = 150\,\Omega$, respectively. For the optimal operating point, the measurements were performed for both Reynolds numbers in order to study its influence on the wind turbine wake. A row of three wind turbines (3WT) working at their optimal operating point (R999, i.e. $R = 9\,\Omega$ for the three wind turbines) was then installed inside the wind tunnel to be able to study the influence of the lateral rows when comparing with the wind farm configuration (9WT). For the wind farm setup, TR-PIV measurements were only performed for the central row while power measurements were performed for the entire farm. The influence of power mitigation of the upstream turbines was investigated by mitigating the power of the first line (R399, i.e. $R = 3\,\Omega$ for first line and $R = 9\,\Omega$ for the second and third lines) and of the first two lines (R339, i.e. $R = 3\,\Omega$ for first two lines and $R = 9\,\Omega$ for the third line) of the wind farm. Finally, the influence of the bladed model was investigated by replacing it by three porous disks with a solidity $\sigma = 56\%$, $\sigma = 44\%$, and $\sigma = 36\%$. Furthermore, each set of measurements was performed twice to verify the repeatability of the measurements. These second sets are represented in dashed line in all the velocity and turbulence intensity profiles that will be presented hereafter.

| | | 0WT | 1WT | | | 3WT | 9WT | | | 1PD | | |
|---|---|---|---|---|---|---|---|---|---|---|---|---|
| | | | | | | WT1-WT2-WT3 | WT1-WT2-WT3 | | | | | |
| | | | R3 | R9 | R150 | R999 | R999 | R399 | R339 | $\sigma$56 | $\sigma$44 | $\sigma$36 |
| $Re \simeq 8 \cdot 10^4$ | ABL1 | x | x | x | x | x | x | x | x | x | x | x |
| | ABL2 | x | x | x | x | x | x | x | x | x | x | x |
| $Re \simeq 5 \cdot 10^4$ | ABL1 | x | | x | | | | | | | | |
| | ABL2 | x | | x | | | | | | | | |

***Table 6.2:*** *Design of experiments for the TR-PIV measurements performed in L-1B wind tunnel*

### 6.1.3 Quality assessment of the TR-PIV measurements

The signal-to-noise ratio (S/N) enables to assess the confidence in the velocity fields obtained from PIV measurements. In DaVis [89], it is defined as

$$S/N = \frac{P_1 - C_{min}}{P_2 - C_{min}} > 1 \tag{6.1}$$

where $P1$ and $P2$ are the first and second highest peak of the correlation matrix, and $C_{min}$ is the lowest value of the correlation matrix. For the "extreme" PIV setup (very large field-of-view) used in this work, the signal-to-noise ratio was mainly between 2 and 5 (Fig. 6.5), which are typical values for good quality PIV measurements. As it can be observed on the averaged signal-to-noise ratio field, the S/N is weaker at the beginning ($x/D < 1$) and at the end ($X/D > 9$) of the field-of-view, as well as for $y/D > 0$. All these areas correspond to regions where the laser light was less powerful because of the larger distance from the laser light source. Furthermore, it can be observed that, because of the higher complexity of the flow, the S/N is weaker in the wake of the wind turbine than in the inflow (no wind turbine).

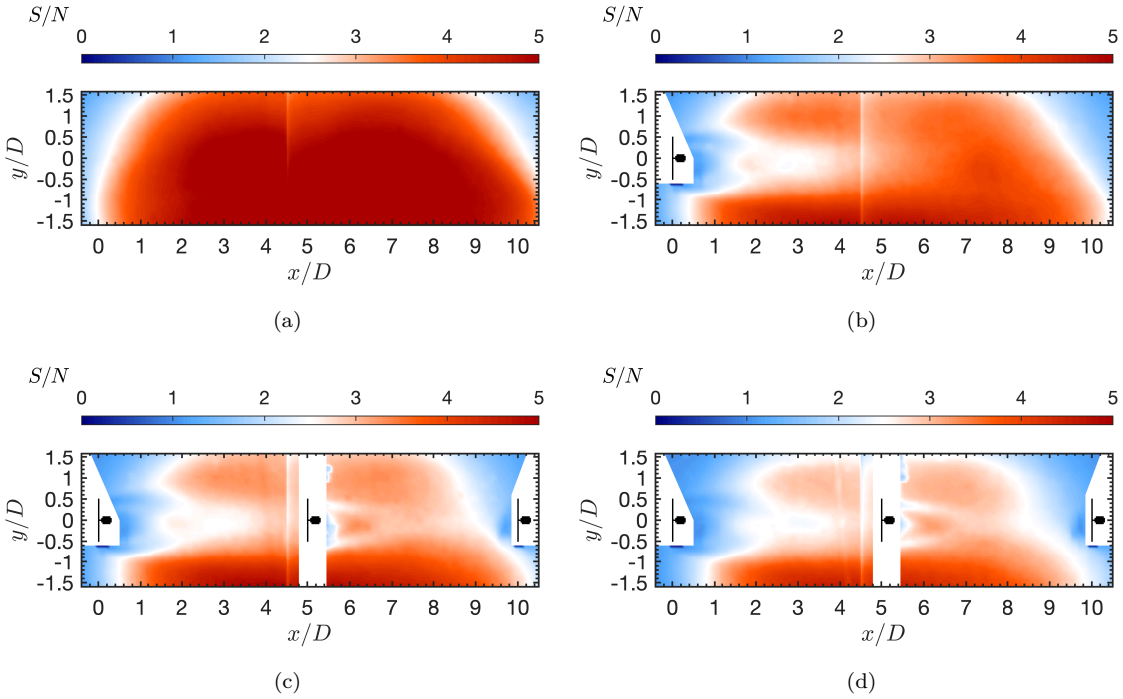



***Figure 6.5:*** *Signal-to-noise ratio fields for the inflow (a), the isolated wind turbine (b), the row of wind turbines (c), and the middle row of the wind farm (d) within ABL1*

For each measurement, 1000 image pairs were acquired at a frequency of 100 Hz. The dependence on the number of images of each component of the mean velocity and of the standard deviation are presented in Figs. 6.6 and 6.7 for the three-row three-column wind farm configuration inside ABL1 and ABL2, respectively. As it can be observed, 1000 images are clearly enough to obtain converged quantities.

Based on the uncertainty analysis procedure proposed in [66], and considering a confidence interval of 95%, the uncertainty (see Appendix D.7) on the velocity does not exceed 1.5%.

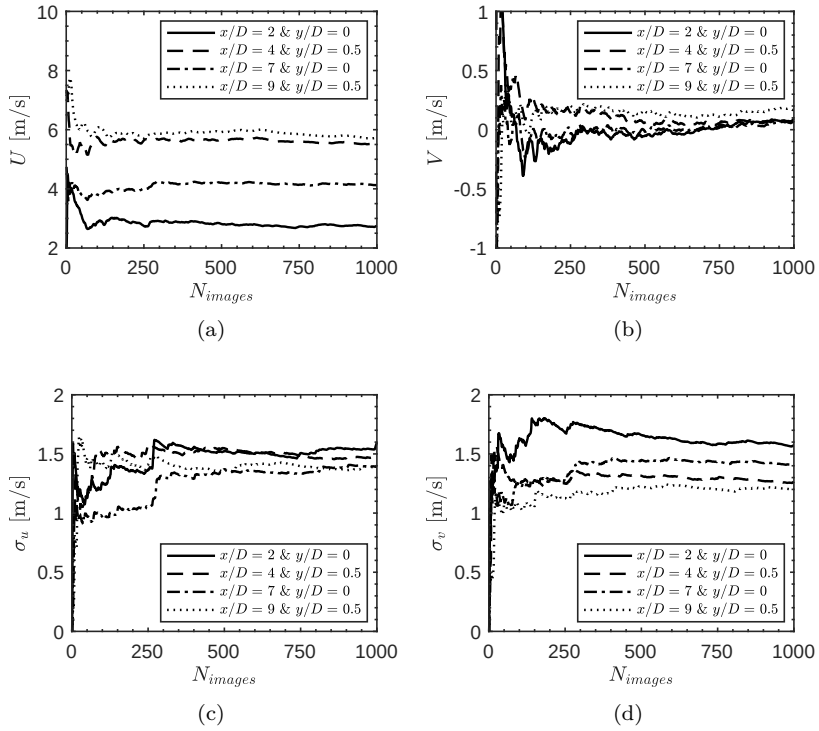



***Figure 6.6:*** *Dependence on the number of images of each component of the mean velocity (a)-(b) and of the standard deviation (c)-(d) for the first and second wind turbines of the wind farm located inside ABL1*

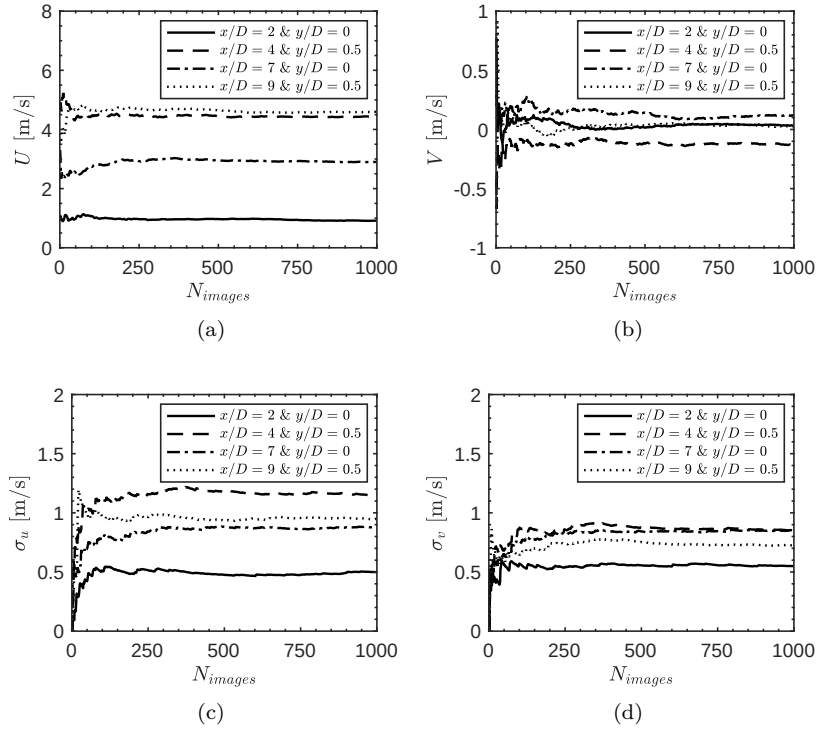



***Figure 6.7:*** *Dependence on the number of images of each component of the mean velocity (a)-(b) and of the standard deviation (c)-(d) for the first and second wind turbines of the wind farm located inside ABL2*

The "extreme" configuration used to capture the wakes on a very long distance (very long field-of-view) leads to particles materialized by $\sim 2$ pixels on the PIV images, which is smaller than the optimal value of 3 pixels. This smaller representation of the particles on the PIV images can lead to an effect commonly referred to as peak locking. The effect originates from the fact that the displacement-correlation peak increasingly deviates from its assumed Gaussian shape for decreasing size of the image of the tracer particles, which enhances biasing towards integer pixel displacements [65]. This effect, when occurring, is apparent in the displacement histogram of PIV data. Figure 6.8 shows that the displacements are not locked at integer values and that therefore peak locking is not occurring for the measurements. Note that the peak at zero displacement is due to the presence of the mask covering the model (solid object) and where the velocity, and therefore the displacement, is set to zero for the processing of the PIV images.

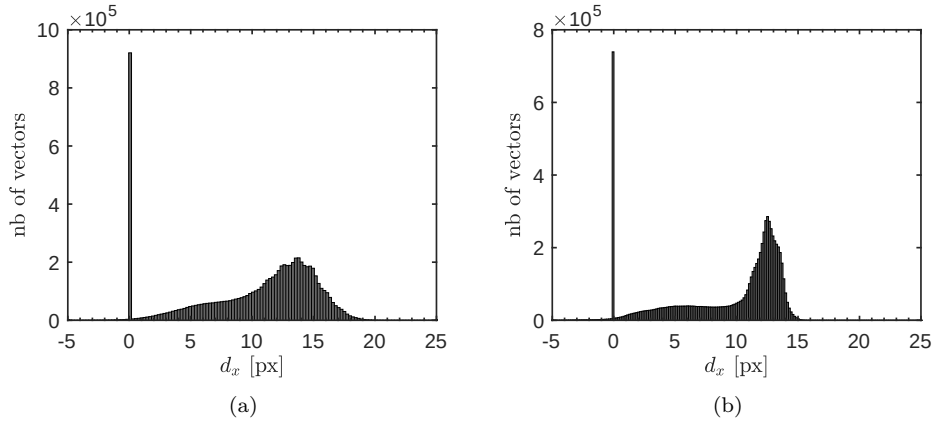



***Figure 6.8:*** *Averaged particules displacement at hub height for the first and second wind turbines of the central row of the wind farm located inside ABL1 (a) and ABL2 (a)*

## 6.2 Inflow

In addition to the 3C-HWA measurements presented in Section 5.3.3, the inflow was measured with the time-resolved PIV system in the horizontal plane at hub height; the inflow corresponding to a configuration without wind turbine. Since the inflow fields are used to normalize all the measurements presented in the next sections, combined statistics were computed from the two sets of 1000 image pairs for each configuration.

Figures 6.9 and 6.10 show the inflow streamwise velocity component and turbulence intensity in the horizontal plane at hub height for ABL1 and ABL2 at $Re \simeq 8 \cdot 10^4$ and $Re \simeq 5 \cdot 10^4$.

As it can be observed in Tables 6.3 and 6.4, the inflow streamwise velocity component and the turbulence intensities obtained from the TR-PIV measurements at hub height are in good agreement with the results obtained during the 3C-HWA campaign performed to characterize the incoming ABLs. Note that the differences are not due to the measurement techniques but mainly to the fact the wind speeds were set up independently for the 3C-HWA and the TR-PIV campaigns from a Pitot-static probe located at hub height in the L-1B wind tunnel.

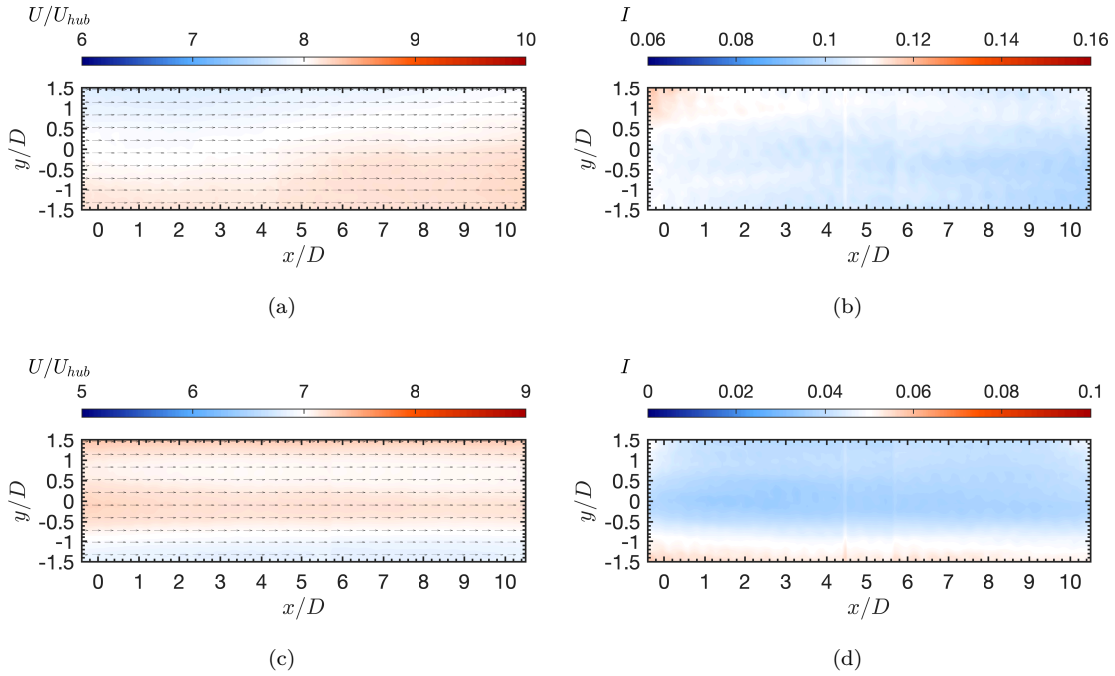



***Figure 6.9:*** *Inflow streamwise velocity component (a)-(c) and turbulence intensity (b)-(d) for ABL1 (a)-(b) and ABL2 (c)-(d) at* $Re \simeq 8 \cdot 10^4$

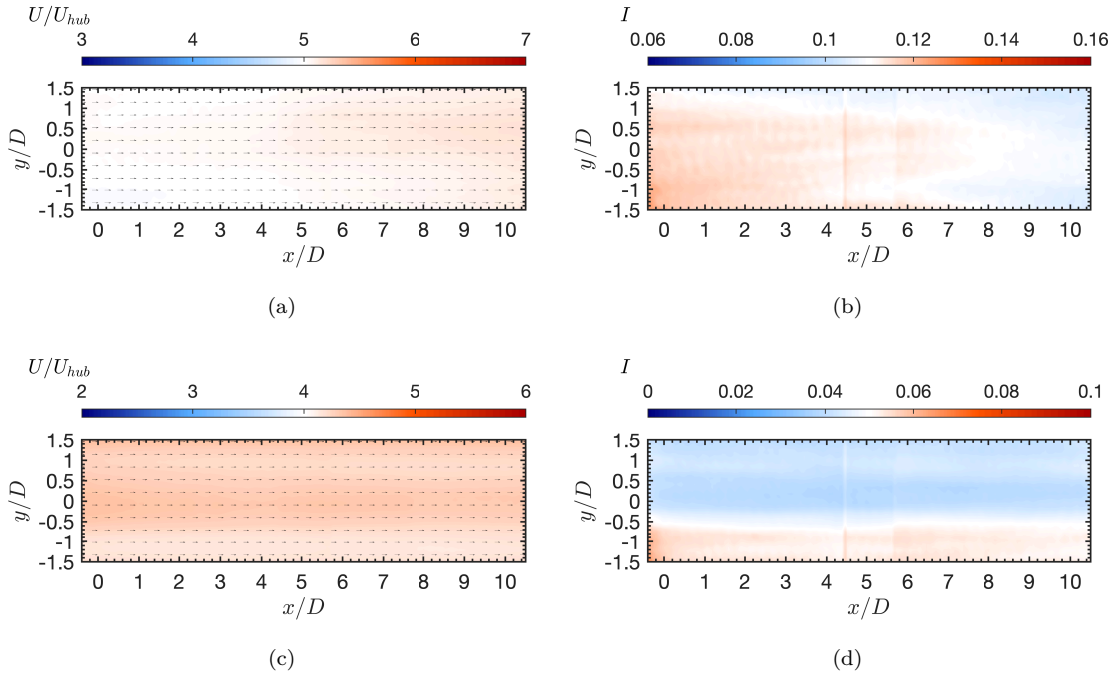



***Figure 6.10:*** *Inflow streamwise velocity component (a)-(c) and turbulence intensity (b)-(d) for ABL1 (a)-(b) and ABL2 (c)-(d) at* $Re \simeq 5 \cdot 10^4$

| | ABL1 | | ABL2 | |
|---|---|---|---|---|
| | $U_{hub}$ [m/s] | $I$ [-] | $U_{hub}$ [m/s] | $I$ [-] |
| TR-PIV | 8.02 | 0.106 | 7.10 | 0.043 |
| 3C-HWA | 8.68 | 0.107 | 7.53 | 0.037 |

***Table 6.3:*** *Comparison of streamwise velocity component and turbulence intensity obtained from the TR-PIV measurements and 3C-HWA at hub height for* $Re \simeq 8 \cdot 10^4$

| | ABL1 | | ABL2 | |
|---|---|---|---|---|
| | $U_{hub}$ [m/s] | $I$ [-] | $U_{hub}$ [m/s] | $I$ [-] |
| TR-PIV | 5.06 | 0.111 | 4.27 | 0.046 |
| 3C-HWA | 5.49 | 0.109 | - | - |

***Table 6.4:*** *Comparison of streamwise velocity component and turbulence intensity obtained from the TR-PIV measurements and 3C-HWA at hub height for* $Re \simeq 5 \cdot 10^4$

## 6.3 Isolated wind turbine

### 6.3.1 Influence of the incoming ABL

Due to the large impact of the incoming ABL on the wake characteristics, it was decided to present the influence of various parameters/configurations on the wake for the two ABLs modeled in the wind tunnel. The influence of the incoming ABL is therefore discussed within each of the following sections.

### 6.3.2 Influence of Reynolds number

Figures 6.11 and 6.12 show the influence of the ABL and of the Reynolds number on the averaged streamwise velocity component. As it can be observed, the wake is much shorter for the wind turbine located inside ABL1 than ABL2. This can be explained by the increased mixing in the wake of the wind turbine within ABL1 because of the much higher turbulence intensity (Figs. 6.13 and 6.14).

The influence of the Reynolds number itself is very limited. According to [90], the Reynolds-number independence for low-order statistics, e.g. the mean-velocity deficit, starts at $Re \simeq 4.8 \times 10^4$, while high-order statistics, e.g. the turbulence intensity and kinematic shear stress, become insensitive to Reynolds-number effects at $Re \simeq 9.3 \times 10^4$. The weak influence of the Reynolds number on the streamwise velocity component and on the turbulence intensity enable to expect that, for the highest $Re$ reached during these experiments ($Re \simeq 8 \cdot 10^4$), $Re$ independence is reached for the main flow statistics. In the following sections, results are therefore presented for $Re \simeq 8 \cdot 10^4$ only.

Focusing on the turbulence intensity, the shear layers, which thicken when moving downstream, are clearly visible on the fields (Fig. 6.13) and on the profiles (Fig. 6.14). Furthermore, a peak of turbulence intensity is visible just behind the nacelle of the wind turbine. This peak is partly due to the presence of the nacelle itself but mainly to the root vortices coming from the blades of the wind turbine. This can be confirmed by comparing the turbulence intensity behind the isolated wind turbine and behind the porous disks (Figs. 6.43 and 6.44 of Section 6.6). The turbulence intensity fields are not perfectly symmetric inside ABL2. One shear layer is more developed than the other (Figs. 6.13 and 6.14). While it could have been hypothesized that this asymmetry is linked to the direction of rotation of the wind turbine model, it is not the case since it is also present for the porous disks (see Section 6.6).

Figures 6.12 and 6.14 also highlight the good repeatability of the measurements, the second sets of data being represented by dashed lines.

This good repeatability of the measurements is also confirmed by examining the power extracted by the isolated wind turbine (Fig. 6.15). Figure 6.15 shows the electrical power, represented by an empty bar, and the aerodynamic power, represented by the entire bar; the losses occurring inside the generator correspond therefore to the colored part of the bar. For reminder, the electrical power is simply computed as $P = U \cdot I$, while the aerodynamic power is computed from $P = Q \cdot \omega$, where $Q$ is the torque determined directly from the current using Eq. (5.4) established in Chapter 5. The power, whether electrical or aerodynamic, is higher for ABL1 than for ABL2 whether for $Re \simeq 8 \cdot 10^4$ or $Re \simeq 5 \cdot 10^4$. As expected, the power production is larger for $Re \simeq 8 \cdot 10^4$, since the inflow wind speed is larger.

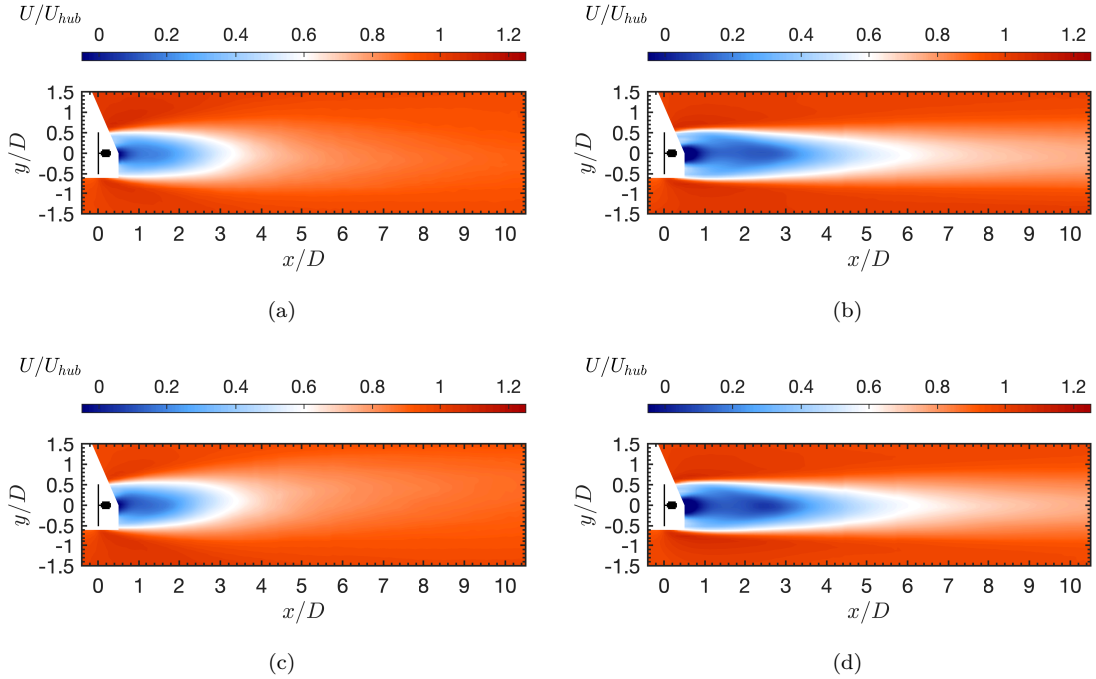



***Figure 6.11:*** *Normalized averaged velocity fields in the horizontal plane at hub height for the isolated wind turbine subjected to ABL1 (a)-(c) and ABL2 (b)-(d) at* $Re \simeq 8 \cdot 10^4$ *(a)-(b) and* $Re \simeq 5 \cdot 10^4$ *(c)-(d)*

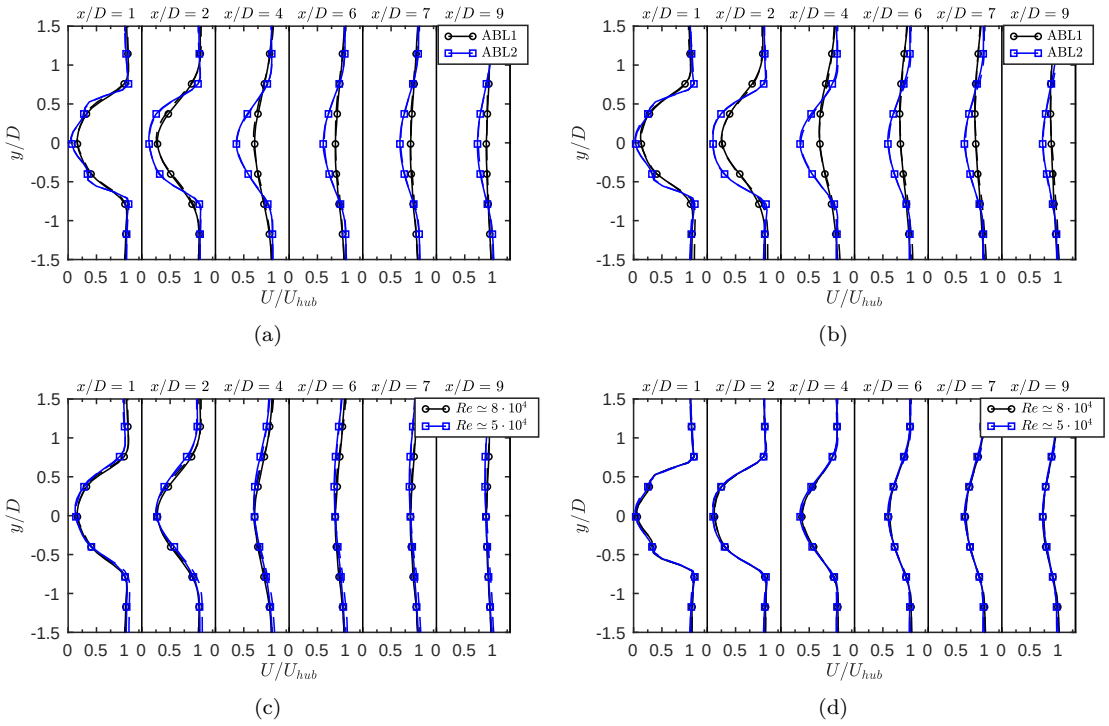



***Figure 6.12:*** *Normalized averaged velocity profiles for $Re \simeq 8 \cdot 10^4$ (a) and $Re \simeq 5 \cdot 10^4$ (b) at several downstream locations in the wake of the isolated wind turbine subjected to ABL1 (c) and ABL2 (d); dashed lines without symbol correspond to the second set of measurements*

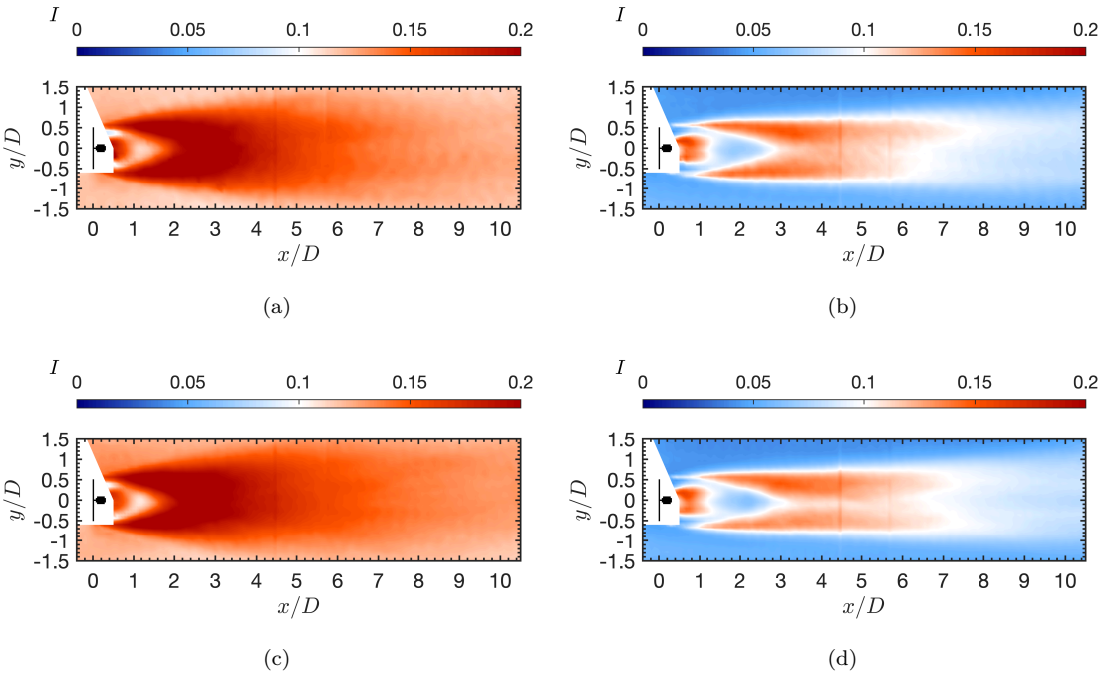



***Figure 6.13:*** *Turbulence intensity field in the horizontal plane at hub height for the isolated wind turbine subjected to ABL1 (a)-(c) and ABL2 (b)-(d) at $Re \simeq 8 \cdot 10^4$ (a)-(b) and $Re \simeq 5 \cdot 10^4$ (c)-(d)*

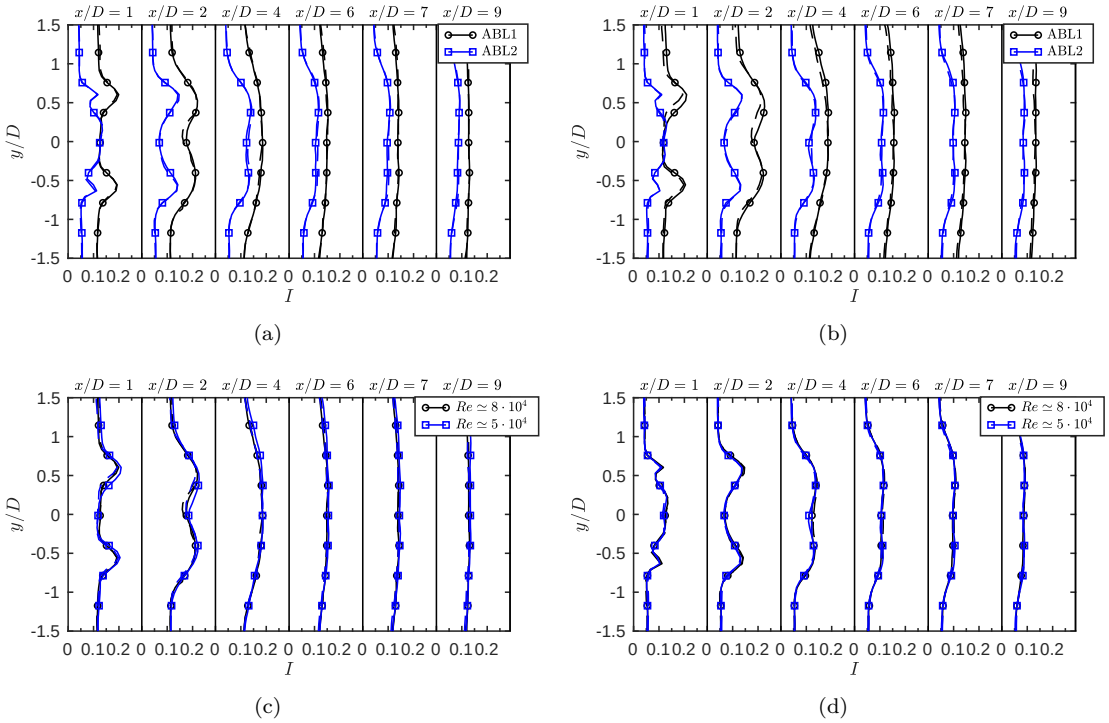



***Figure 6.14:*** *Turbulence intensity profiles for $Re \simeq 8 \cdot 10^4$ (a) and $Re \simeq 5 \cdot 10^4$ (b) at several downstream locations in the wake of the isolated wind turbine subjected to ABL1 (c) and ABL2 (d); dashed lines without symbol correspond to the second set of measurements*

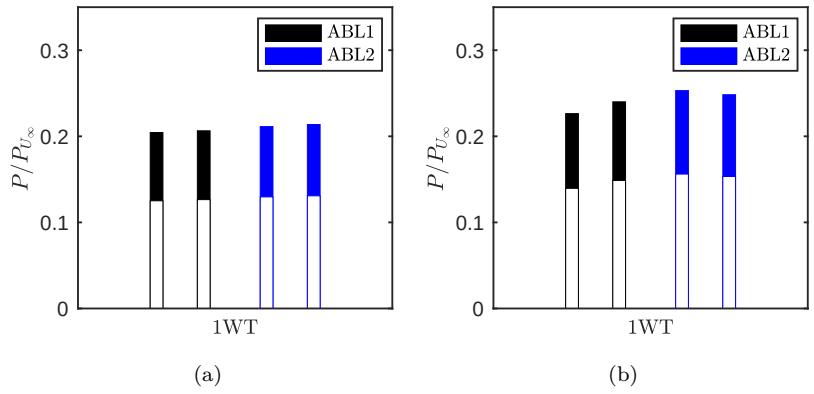



***Figure 6.15:*** *Electrical (empty bar) and aerodynamic (entire bar) power produced by the isolated wind turbine subjected to ABL1 and ABL2 at $Re \simeq 8 \cdot 10^4$ (a) and $Re \simeq 5 \cdot 10^4$ (b); the second bar of each case corresponds to the second set of measurements*

### 6.3.3 Influence of the wind turbine operating conditions

For both ABL1 and ABL2, the changes in operating conditions, i.e. mainly in the tip-speed ratios since the thrust coefficient of the scale model involved in this study varies little with respect to the tip-speed ratio ($0.88 \leqslant C_T \leqslant 0.94$ for $5 \leqslant TSR \leqslant 8$, see Fig. 5.19(b)), mainly affect the near wake. The velocity deficit (Figs. 6.16 and 6.17) is less pronounced when the electrical resistance increases, i.e. when the tip-speed ratio increases. The link between the electrical resistance applied to the generator of the isolated wind turbine and the tip-speed ratio obtained within ABL1 and ABL2 is presented in Table 6.5. The similarity of the profiles evidences the interest of repeating the measurements twice since it ensures that the variation in the profiles are actually due to a change in operating conditions, and not to any variation in the measurements. Concerning the turbulence intensity (Figs. 6.18 and 6.19), the differences are more pronounced for ABL1 than ABL2.

| | $TSR$ | |
|---|---|---|
| | ABL1 | ABL2 |
| $R = 3\,\Omega$ | 6.1 | 5.8 |
| $R = 9\,\Omega$ | 7.0 | 6.7 |
| $R = 150\,\Omega$ | 8.0 | 7.9 |

***Table 6.5:*** *Link between the electrical resistance applied to the generator of the isolated wind turbine and the tip-speed ratio ($TSR$) obtained during the time-resolved PIV measurements*

For both ABL1 or ABL2, the electrical power produced by the isolated wind turbine is the highest for $R = 9\,\Omega$ (Fig. 6.20) since this electrical resistance corresponds to the optimal operating conditions (see Section 5.1.2). However, the maximum aerodynamic power occurs for $R = 3\,\Omega$. The losses inside the generator are the highest for $R = 3\,\Omega$ and the lowest for $R = 150\,\Omega$, since they are proportional to the current which decreases with the resistance (see Appendix E).

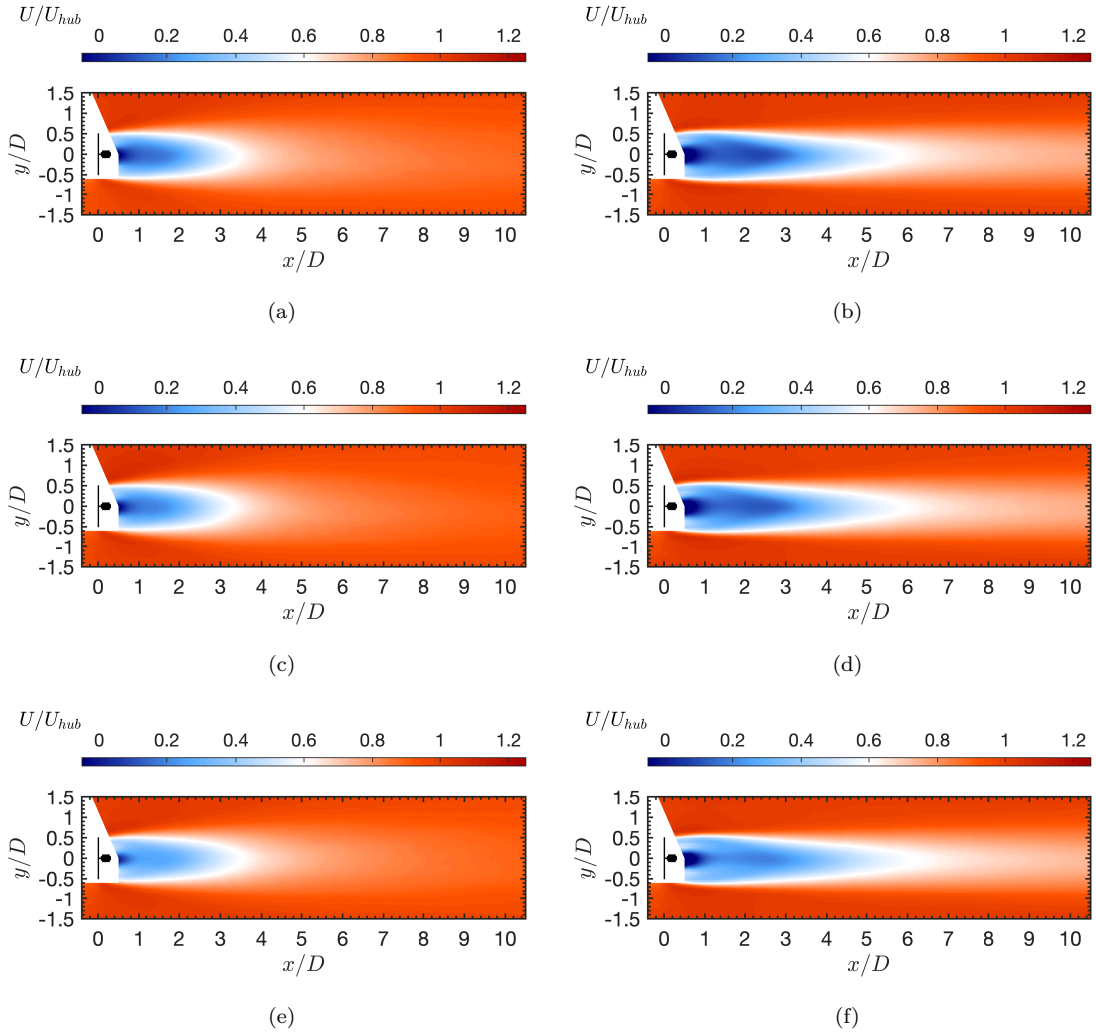



***Figure 6.16:*** *Normalized averaged velocity fields in the horizontal plane at hub height for the isolated wind turbine subjected to ABL1 (a)-(c)-(e) and ABL2 (b)-(d)-(f) at for $R = 3\,\Omega$ (a)-(b), $R = 9\,\Omega$ (c)-(d), $R = 150\,\Omega$ (e)-(f)*

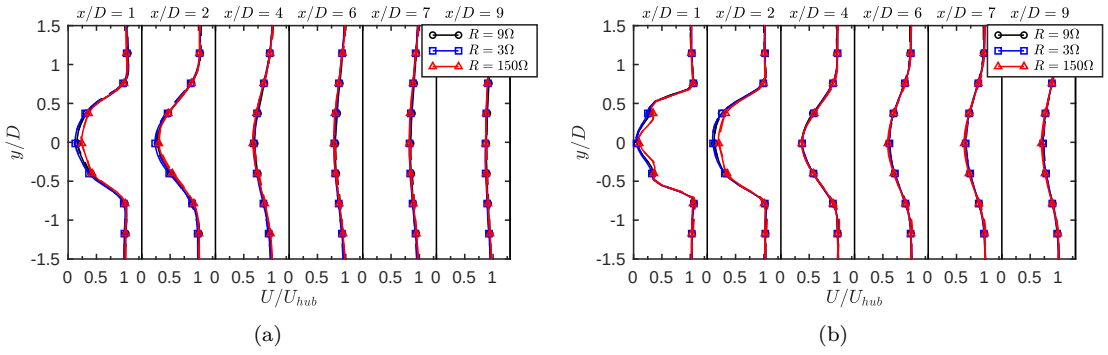



***Figure 6.17:*** *Normalized averaged velocity profiles at several downstream locations in the wake of the wind turbine subjected to ABL1 (a) and ABL2 (b), and operating in different conditions; dashed lines without symbol correspond to the second set of measurements*

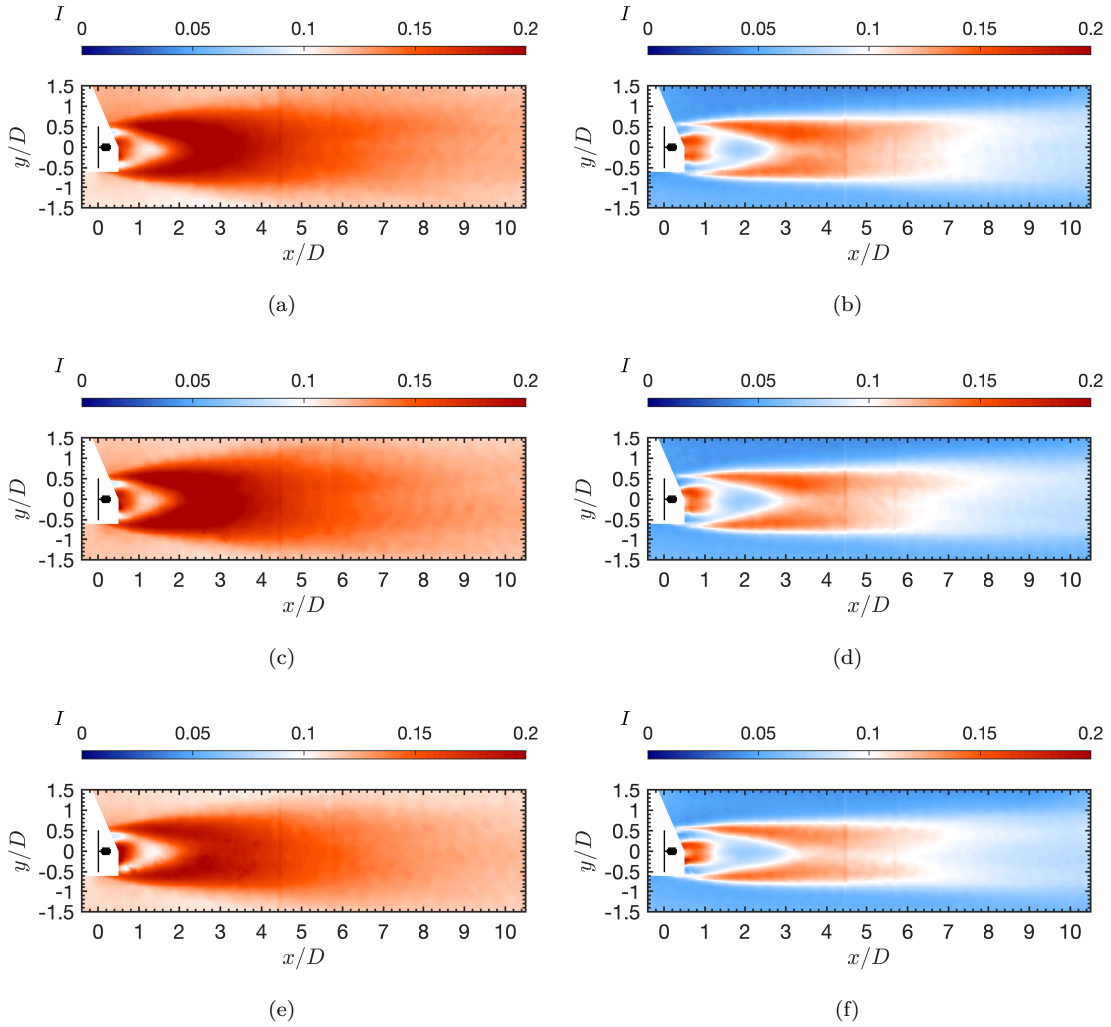



***Figure 6.18:*** *Turbulence intensity field in the horizontal plane at hub height for the isolated wind turbine subjected to ABL1 (a)-(c)-(e) and ABL2 (b)-(d)-(f) at for $R = 3\,\Omega$ (a)-(b), $R = 9\,\Omega$ (c)-(d), $R = 150\,\Omega$ (e)-(f)*

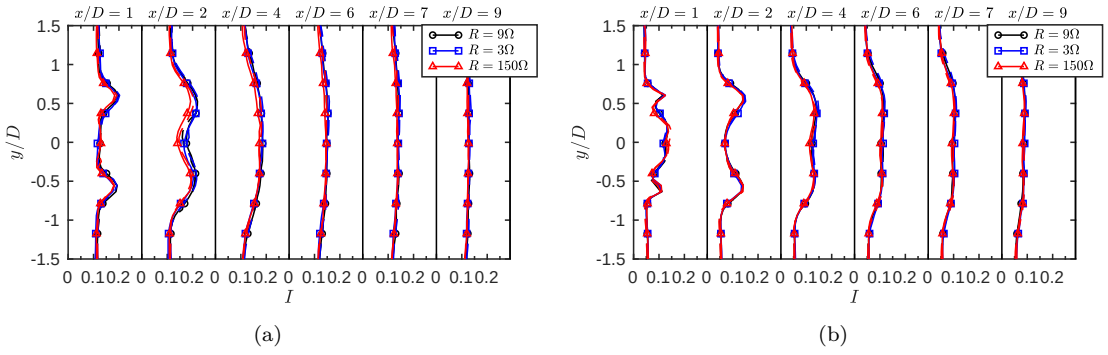



***Figure 6.19:*** *Turbulence intensity profiles at several downstream locations in the wake of the wind turbine subjected to ABL1 (a) and ABL2 (b), and operating in different conditions; dashed lines without symbol correspond to the second set of measurements*

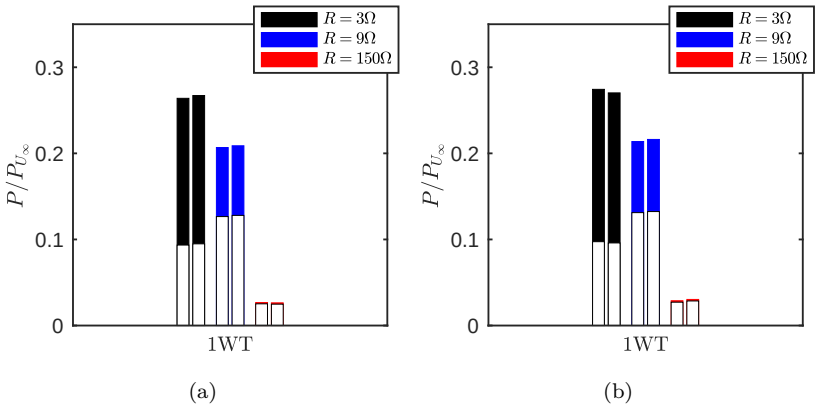



***Figure 6.20:*** *Electrical (empty bar) and aerodynamic (entire bar) power produced by the wind turbine subjected to ABL1 (a) and ABL2 (b) for different operating conditions; the second bar of each case corresponds to the second set of measurements*

## 6.4 Row of three wind turbines

### 6.4.1 Isolated wind turbine vs. first and second wind turbines

For both ABLs, the near wake of the first wind turbine of the row is similar to the near wake of the isolated wind turbine in terms of mean streamwise velocity component (slightly larger velocity deficit) and turbulence intensity (Figs. 6.21 to 6.24). When getting closer to the second wind turbine ($x/D \simeq 4$), its influence starts to be clearly visible; the velocity deficit becomes larger for the first wind turbine of the row. It can be explained by the induction zone upstream of the downstream turbine.

When comparing the wake of the first and second wind turbines of the row, one can observe a smaller velocity deficit and a smoother velocity profile for the second wind turbine (Figs. 6.21 and 6.22). It is due to the increased turbulence intensity (Figs. 6.23 and 6.24) created by the upstream turbine. Furthermore, the wakes of the first and second wind turbines present a clear difference in turbulence intensity just behind the nacelle (Figs. 6.23 and 6.24). There is a peak of turbulence intensity just behind the nacelle for the first wind turbine but not for the second wind turbine of the row. Finally, the shear layers behind the second wind turbine of the row are much shorter than behind the isolated wind turbine or the first wind turbine of the row. These differences can also be explained by the increased incoming turbulence intensity created by the upstream turbine.

The power produced by the isolated wind turbine is larger compared to the power produced by the first wind turbine of the row whether for ABL1 or ABL2 (Fig. 6.25). This can be explained by the induction effect following from the row of wind turbines when compared to the isolated wind turbine. The wake extension has a direct impact on the power produced by the wind turbines. Indeed, the faster wake recovery behind the second wind turbine compared with that behind the first turbine results in a larger power production for the third wind turbine than for the second wind turbine of the row. This is consistent with other wind tunnel [34] and field [29] experiments.

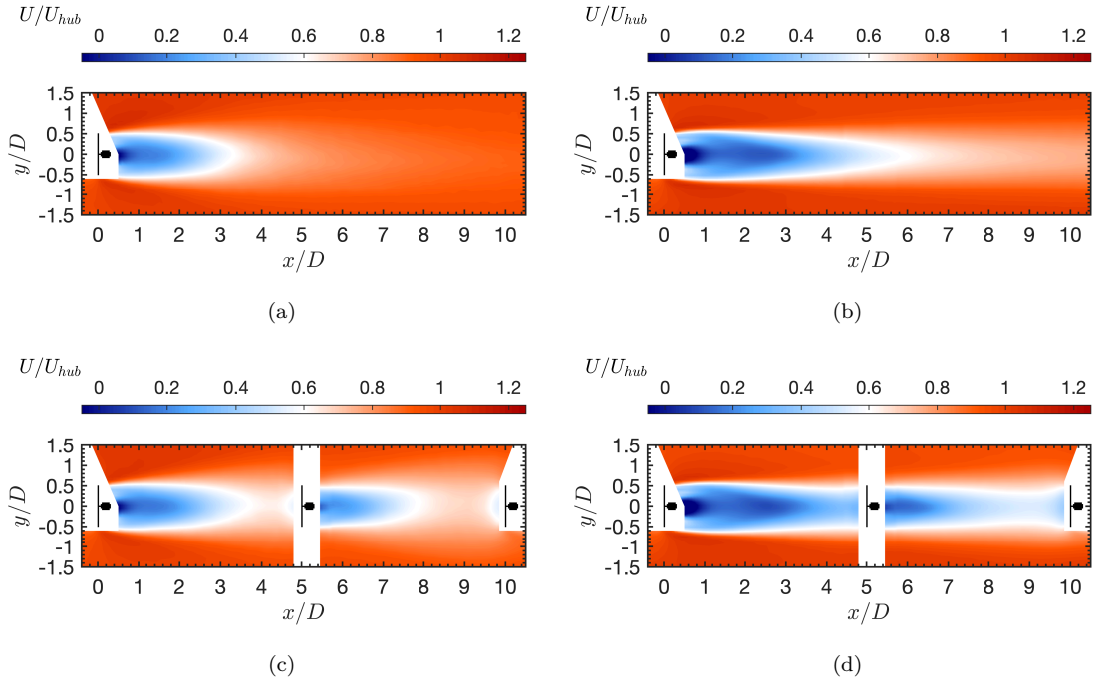



***Figure 6.21:*** *Normalized averaged velocity fields in the horizontal plane at hub height for the isolated wind turbine (a)-(b) and the first and second wind turbines of the row of three wind turbines (c)-(d) subjected to ABL1 (a)-(c) and ABL2 (b)-(d)*

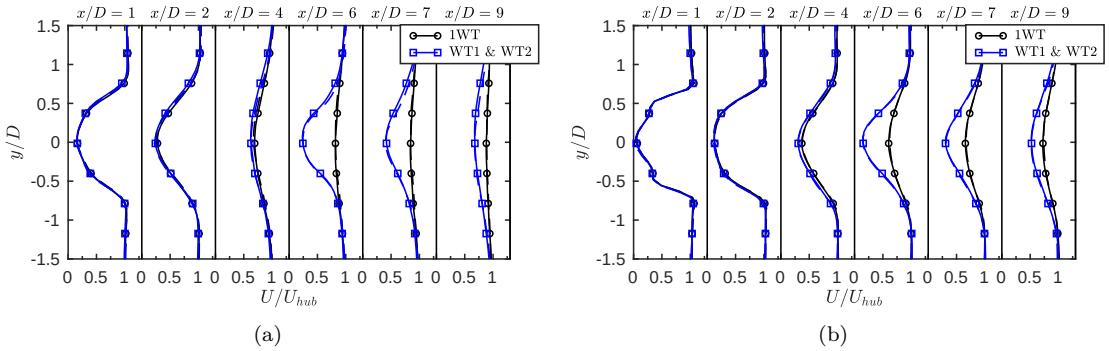



***Figure 6.22:*** *Normalized averaged velocity profiles at several downstream locations in the wake of the isolated wind turbine and the first and second wind turbines of the row of wind turbines subjected to ABL1 (a) and ABL2 (b); dashed lines without symbol correspond to the second set of measurements*

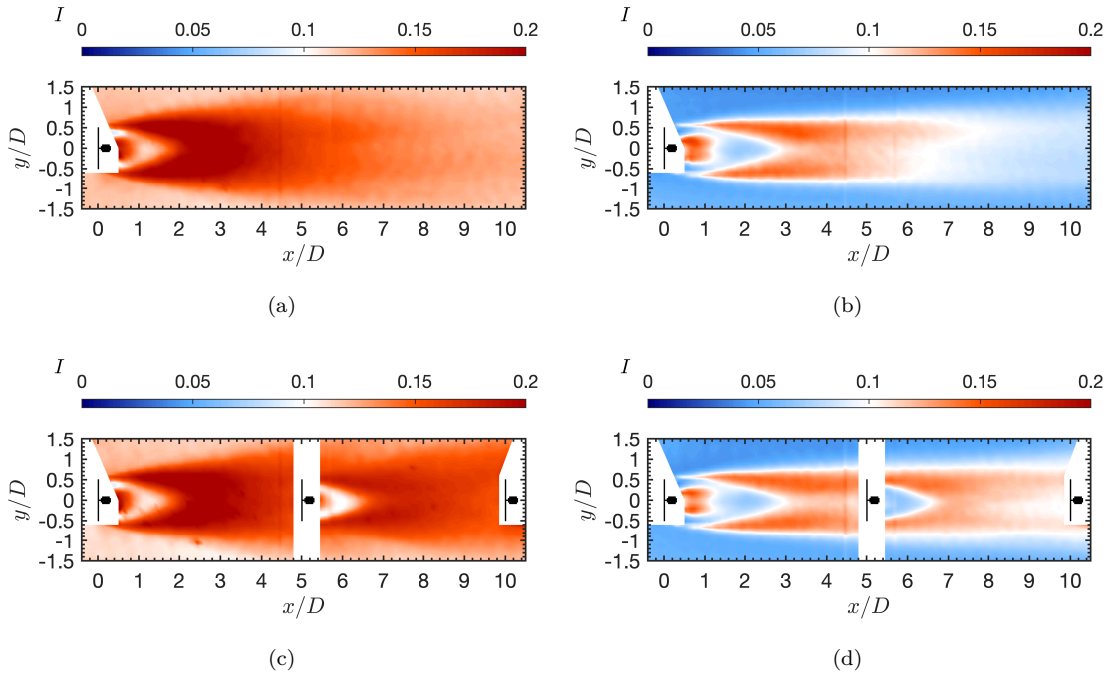



***Figure 6.23:*** *Turbulence intensity field in the horizontal plane at hub height for the isolated wind turbine (a)-(b) and the first and second wind turbines of the row of three wind turbines (c)-(d) subjected to ABL1 (a)-(c) and ABL2 (b)-(d)*

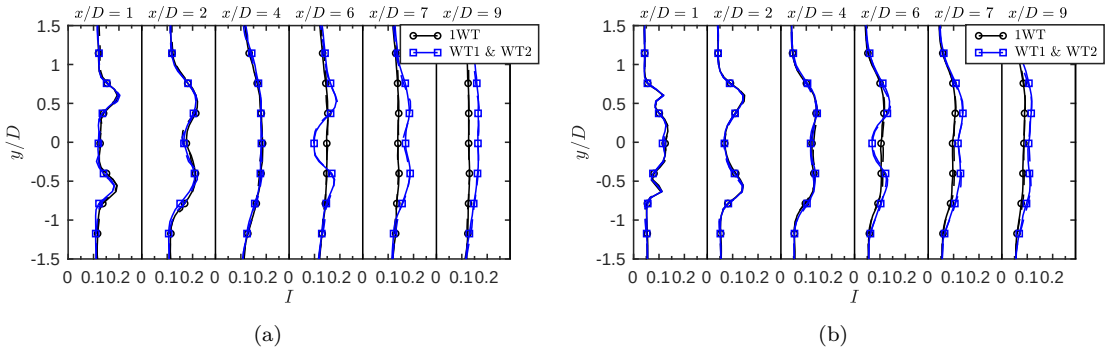



***Figure 6.24:*** *Turbulence intensity profiles at several downstream locations in the wake of the isolated wind turbine and the first and second wind turbines of the row of wind turbines subjected to ABL1 (a) and ABL2 (b); dashed lines without symbol correspond to the second set of measurements*

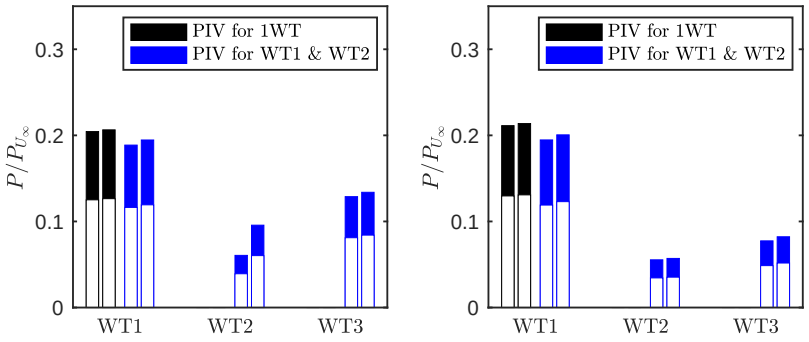



***Figure 6.25:*** *Electrical (empty bar) and aerodynamic (entire bar) power produced by the isolated wind turbine and the row of three wind turbines subjected to ABL1 (a) and ABL2 (b); the second bar of each case corresponds to the second set of measurements*

### 6.4.2 Isolated wind turbine vs. third wind turbine

Figures 6.26 and 6.27 make possible to compare the wakes behind the isolated wind turbine and behind the third wind turbine of the row of three wind turbines. The wake is less pronounced and the velocity profiles are smoother for the wake of the third wind turbine, whether for ABL1 or ABL2. This is due to the larger turbulence level in the wake because of the higher incoming turbulence intensity created by the upstream turbine(s) (Figs. 6.28 and 6.29). In the near wake, the velocity deficit is larger for the isolated wind turbine across the rotor width ($-0.5 \leqslant y/D \leqslant 0.5$). Since the velocity profiles of the isolated wind turbine wake are also sharper compared to the third wind turbine wake, the profiles intersect around $|y/D| = 0.5$. Because of the higher turbulence intensity within ABL1, the wakes of the third wind turbine and of the isolated one become similar more quickly for ABL1 than for ABL2.

For this configuration, the power production of the third wind turbine is equivalent to that of the second wind turbine when subjected to ABL1 (Fig. 6.30). Comparing with Fig. 6.25 shows that this equivalence is mainly due to an increase in power production for the second wind turbine, the cause of this power rise remaining unknown. For ABL2, the power is nevertheless higher for the third wind turbine than for the second wind turbine of the row, as observed previously.

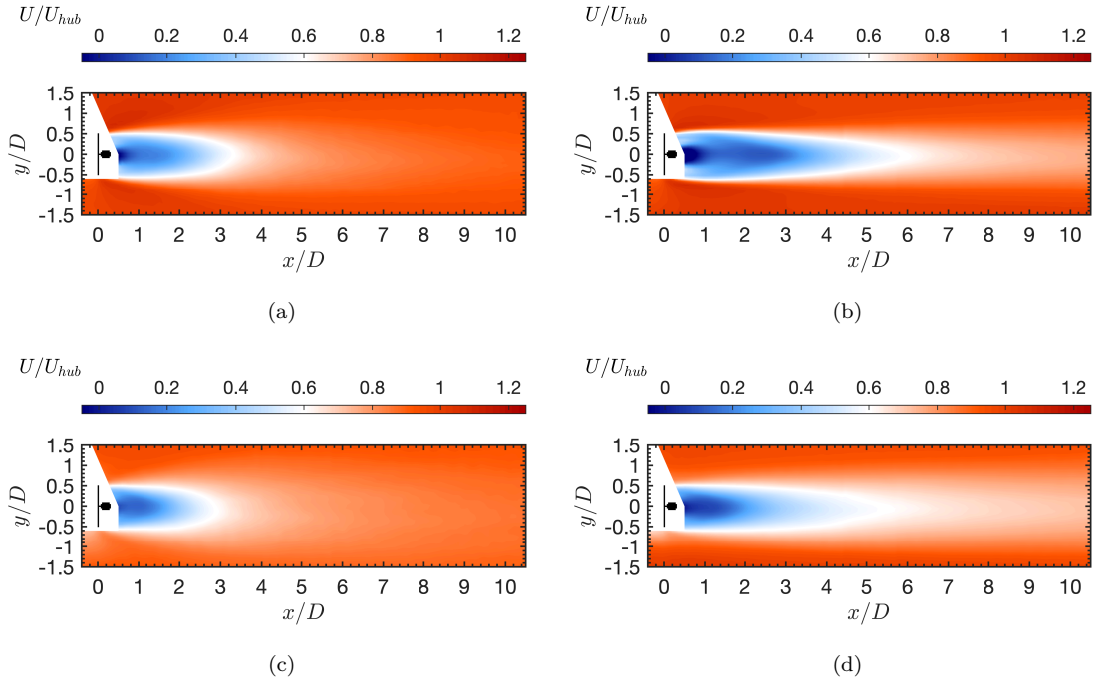



***Figure 6.26:*** *Normalized averaged velocity fields in the horizontal plane at hub height for the isolated wind turbine (a)-(b) and the third wind turbine of the row of three wind turbines (c)-(d) subjected to ABL1 (a)-(c) and ABL2 (b)-(d)*

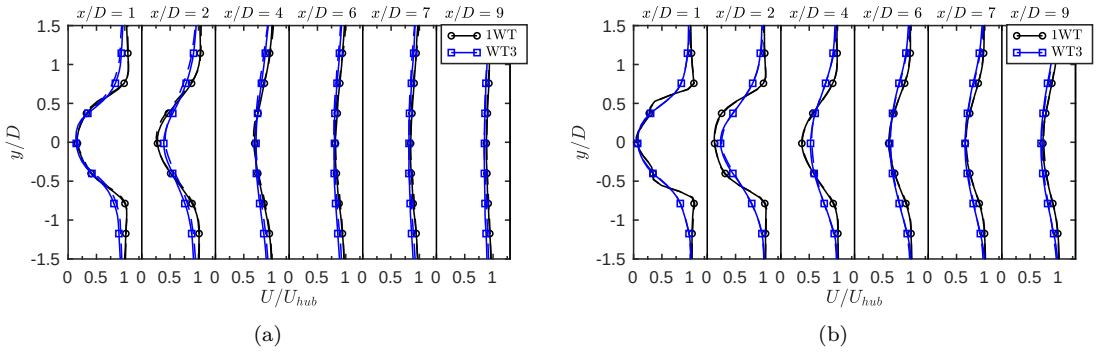



***Figure 6.27:*** *Normalized averaged velocity profiles at several downstream locations in the wake of the isolated wind turbine and the third wind turbine of the row of wind turbines subjected to ABL1 (a) and ABL2 (b); dashed lines without symbol correspond to the second set of measurements*

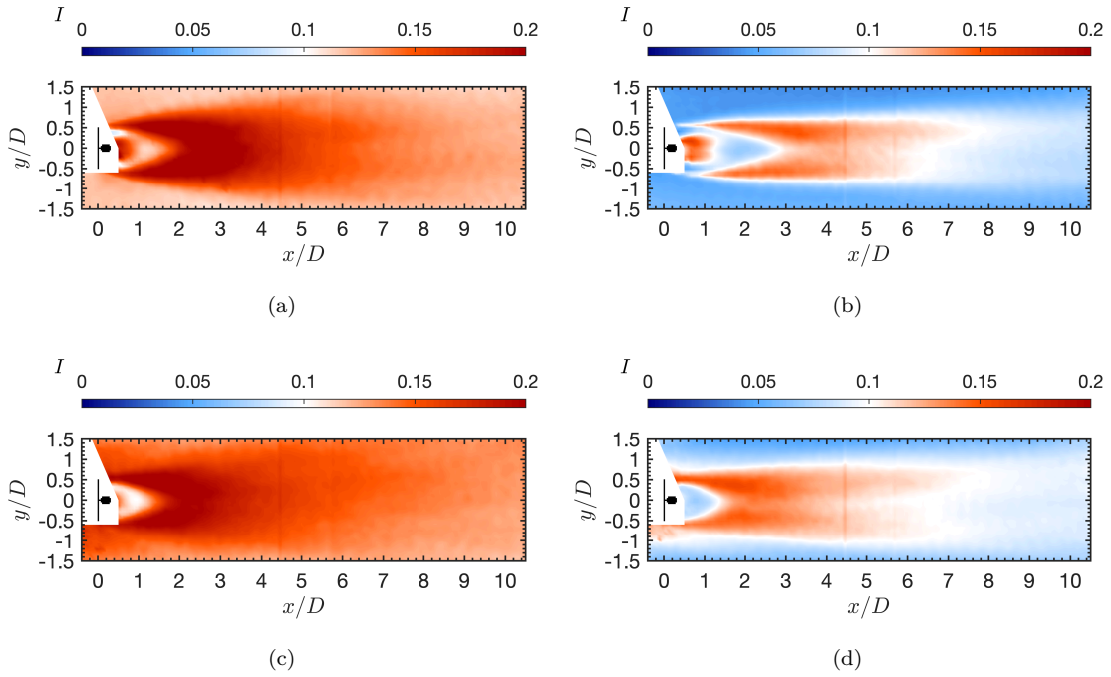



***Figure 6.28:*** *Turbulence intensity field in the horizontal plane at hub height for the isolated wind turbine (a)-(b) and the third wind turbine of the row of three wind turbines (c)-(d) subjected to ABL1 (a)-(c) and ABL2 (b)-(d)*

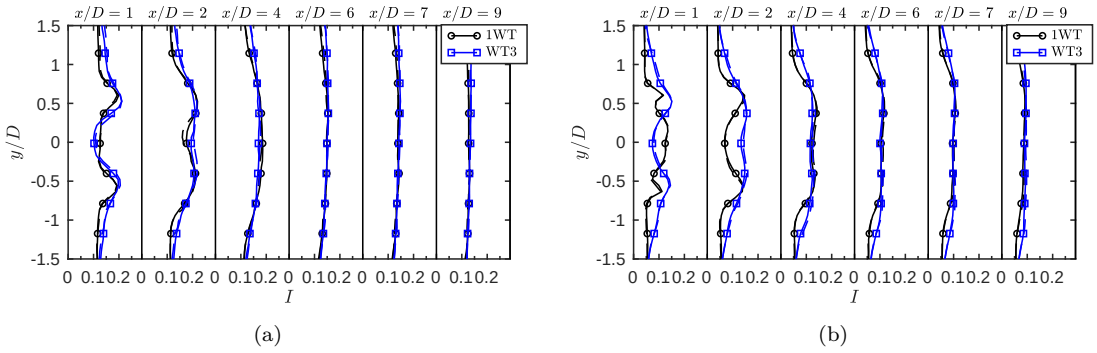



***Figure 6.29:*** *Turbulence intensity profiles at several downstream locations in the wake of the isolated wind turbine and the third wind turbine of the row of wind turbines subjected to ABL1 (a) and ABL2 (b); dashed lines without symbol correspond to the second set of measurements*

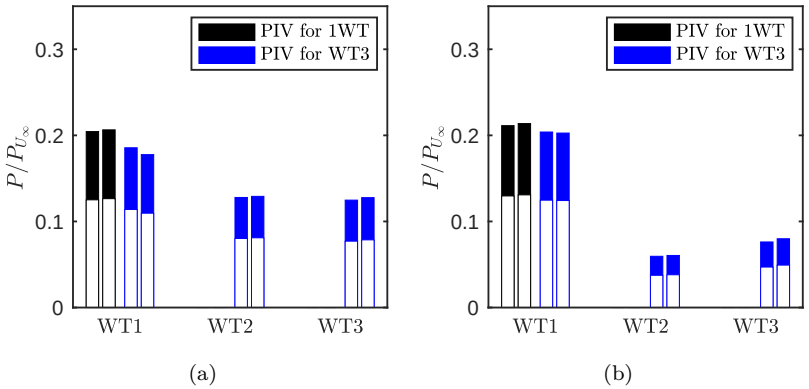



***Figure 6.30:*** *Electrical (empty bar) and aerodynamic (entire bar) power produced by the isolated wind turbine and the row of three wind turbines subjected to ABL1 (a) and ABL2 (b); the second bar of each case corresponds to the second set of measurements*

## 6.5 Wind farm

### 6.5.1 Row vs. wind farm: first and second wind turbines

As it can be observed in Figs. 6.31 to 6.34, there is no major influence of the lateral rows of wind turbines on the wakes of the wind turbines composing the central row. Concerning the power production (Fig. 6.35), it is similar for the two configurations and there is not a clear trend in favor of one of the two configurations.

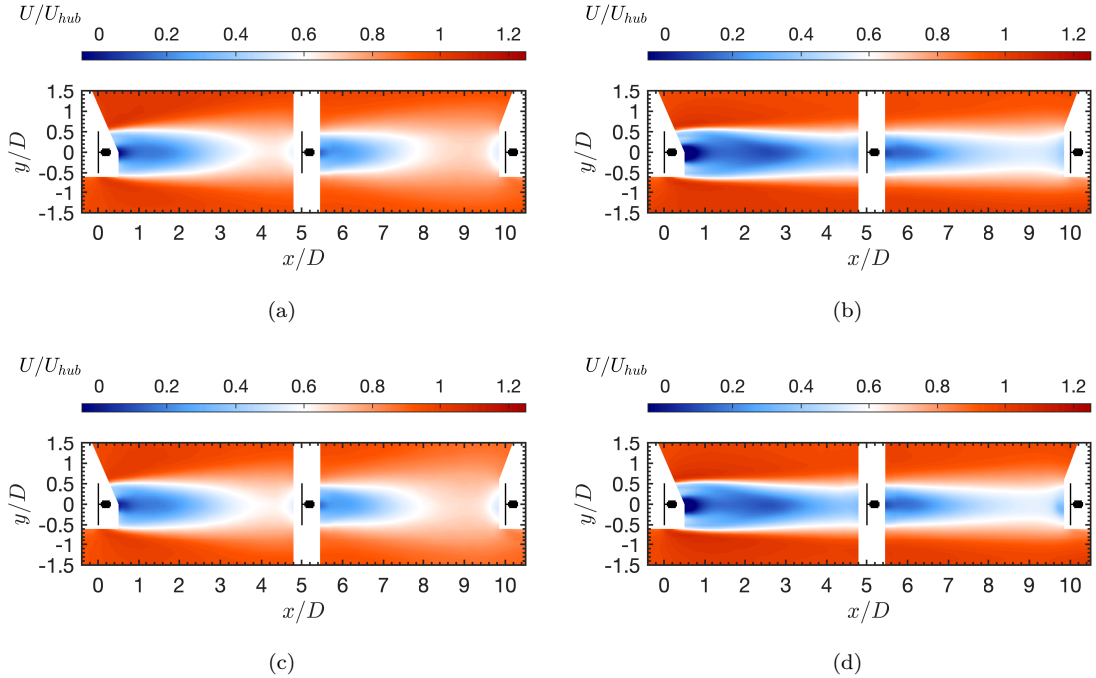



***Figure 6.31:*** *Normalized averaged velocity fields in the horizontal plane at hub height for the first and second wind turbines of the row of three wind turbines (a)-(b) and of the central row of the wind farm (c)-(d) subjected to ABL1 (a)-(c) and ABL2 (b)-(d)*

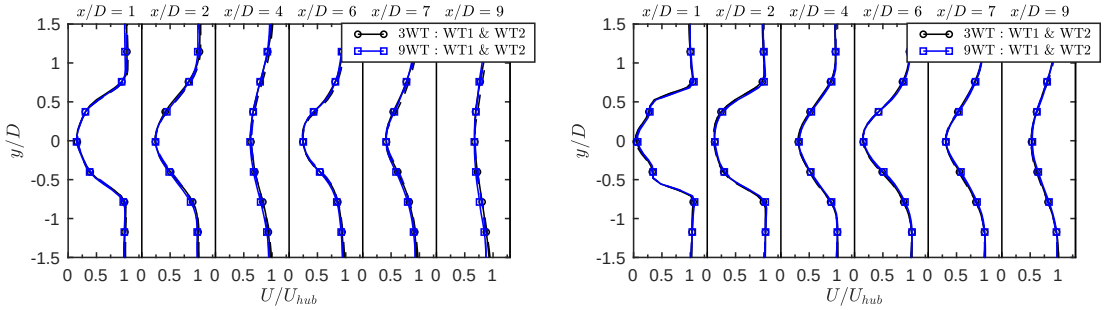



***Figure 6.32:*** *Normalized averaged velocity profiles at several downstream locations in the wake of the first and second wind turbines of the row of three wind turbines and of the central row of the wind farm subjected to ABL1 (a) and ABL2 (b); dashed lines without symbol correspond to the second set of measurements*

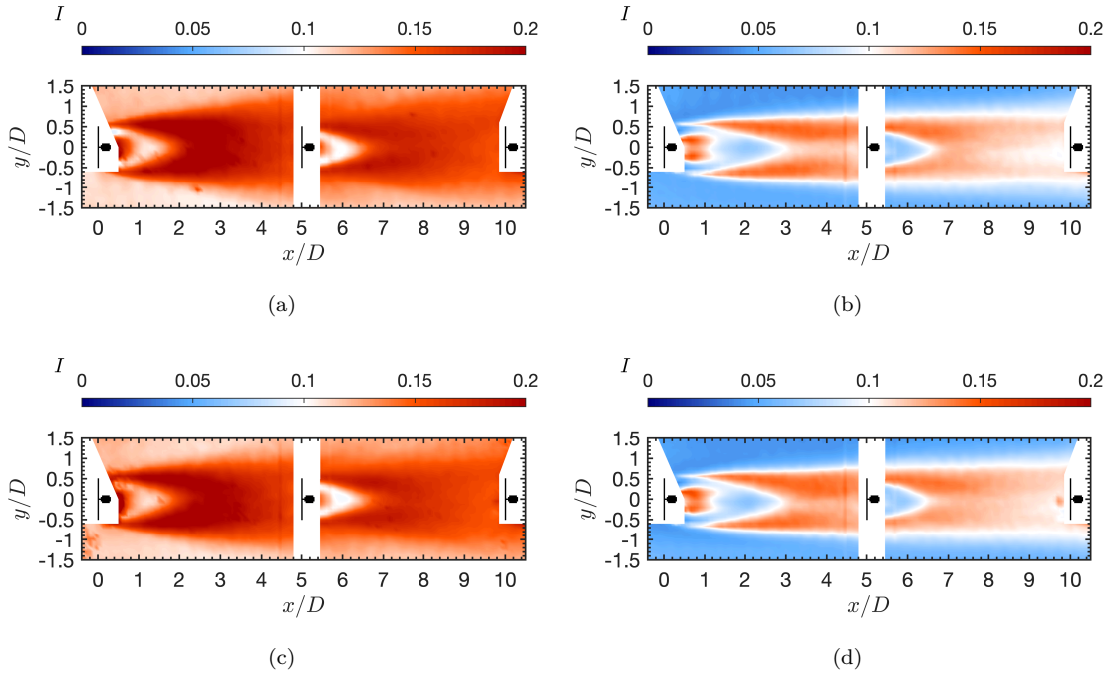



***Figure 6.33:*** *Normalized averaged velocity fields in the horizontal plane at hub height for the first and second wind turbines of the row of three wind turbines (a)-(b) and of the central row of the wind farm (c)-(d) subjected to ABL1 (a)-(c) and ABL2 (b)-(d)*

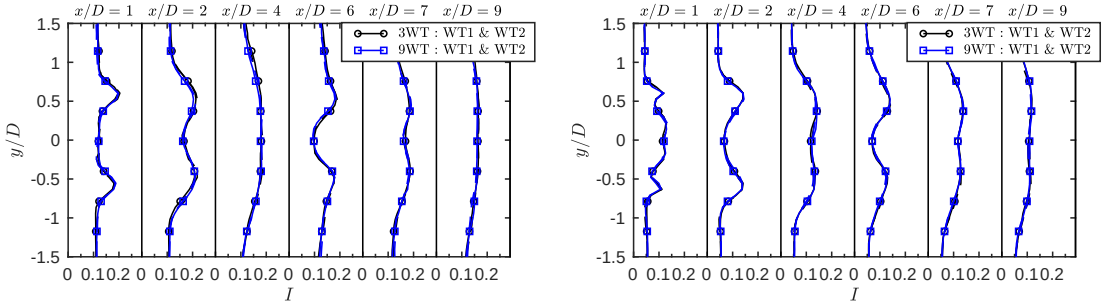



***Figure 6.34:*** *Normalized averaged velocity profiles at several downstream locations in the wake of the first and second wind turbines of the row of three wind turbines and of the central row of the wind farm subjected to ABL1 (a) and ABL2 (b); dashed lines without symbol correspond to the second set of measurements*

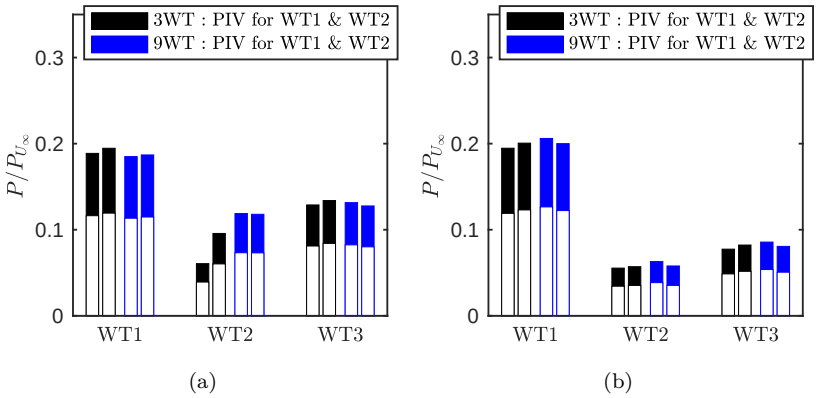



***Figure 6.35:*** *Electrical (empty bar) and aerodynamic (entire bar) power produced by the row of wind turbines and the central row of the wind farm subjected to ABL1 (a) and ABL2 (b); the second bar of each case corresponds to the second set of measurements*

### 6.5.2 Row vs. wind farm: third wind turbine

As for the first and second wind turbine wakes, there is no influence of the lateral rows on the wake of the third wind turbine of the central row of the wind farm (Figs. 6.36 to 6.39). Furthermore, the power production is similar for the two configurations (Fig. 6.40). As already observed in Fig. 6.30, the power production of the second wind turbine is equivalent to the power production of the third wind turbine for ABL1.

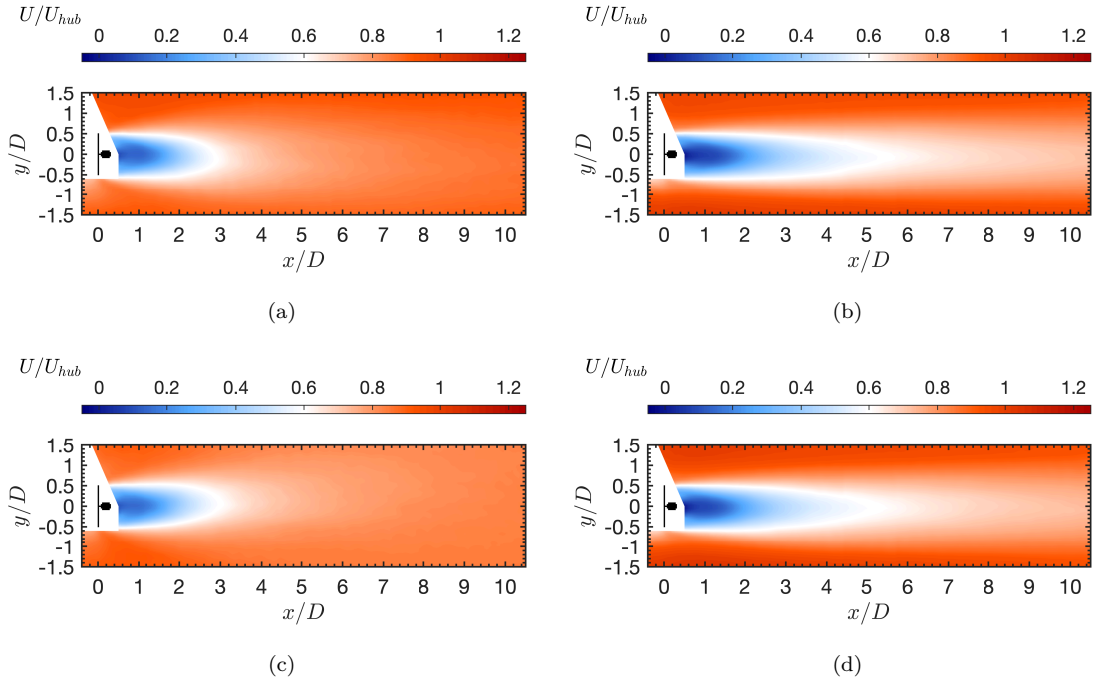



***Figure 6.36:*** *Normalized averaged velocity fields in the horizontal plane at hub height for the third wind turbine of the row of three wind turbines (a)-(b) and of the wind farm (c)-(d) subjected to ABL1 (a)-(c) and ABL2 (b)-(d)*

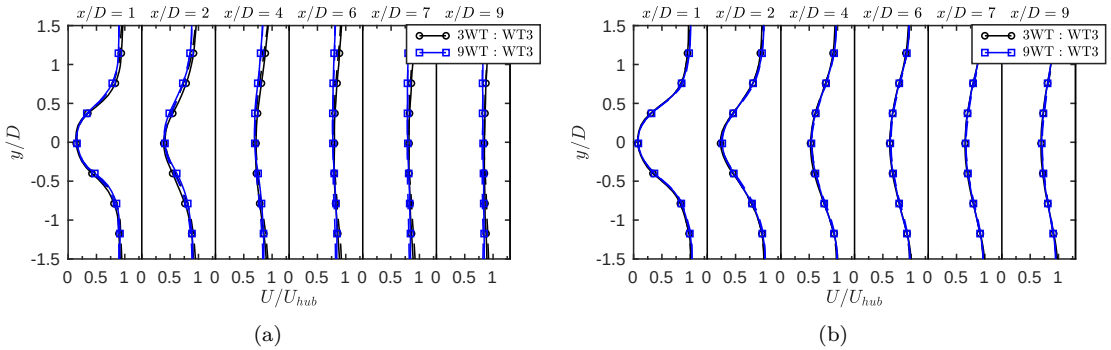



***Figure 6.37:*** *Normalized averaged velocity profiles at several downstream locations in the wake of the first and second wind turbines of the row of three wind turbines and of the wind farm subjected to ABL1 (a) and ABL2 (b); dashed lines without symbol correspond to the second set of measurements*

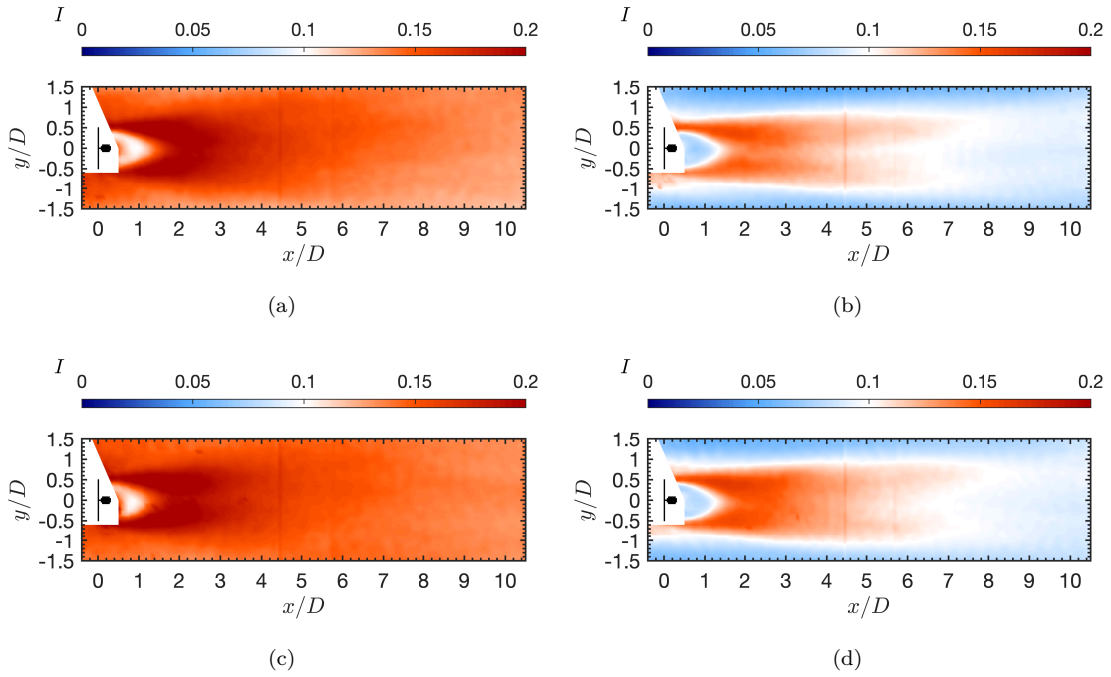



***Figure 6.38:*** *Turbulence intensity field in the horizontal plane at hub height for the third wind turbine of the row of three wind turbines (a)-(b) and of the wind farm (c)-(d) subjected to ABL1 (a)-(c) and ABL2 (b)-(d)*

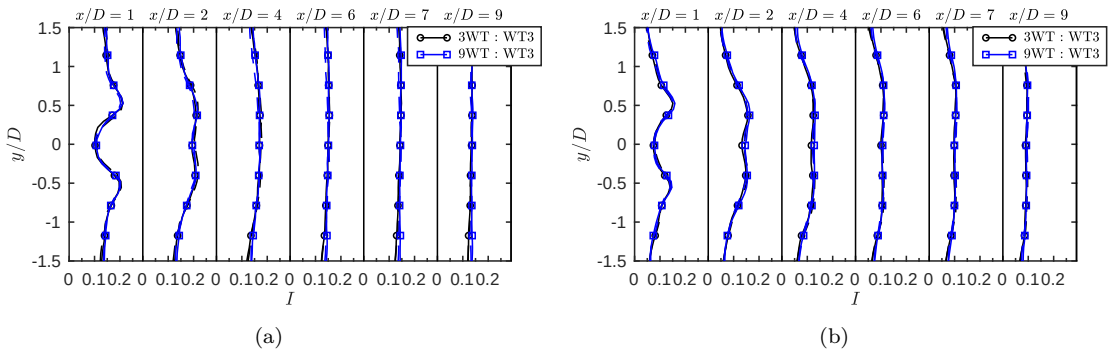



***Figure 6.39:*** *Turbulence intensity profiles at several downstream locations in the wake of the first and second wind turbines of the row of three wind turbines and of the wind farm subjected to ABL1 (a) and ABL2 (b); dashed lines without symbol correspond to the second set of measurements*

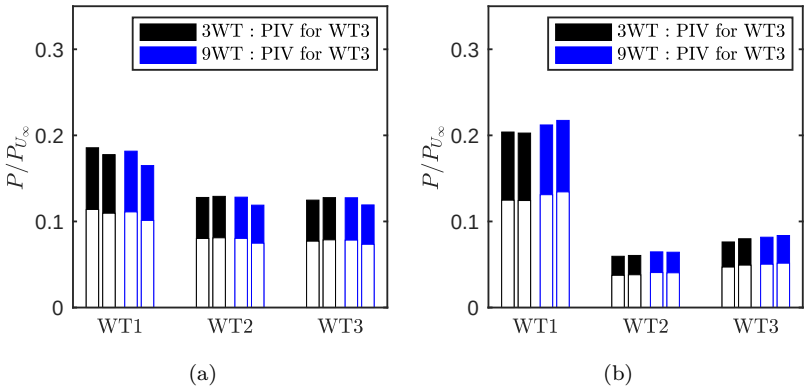



***Figure 6.40:*** *Electrical (empty bar) and aerodynamic (entire bar) power produced by the row of wind turbines and the central row of the wind farm subjected to ABL1 (a) and ABL2 (b); the second bar of each case corresponds to the second set of measurements*

## 6.6 Porous disks

In this section, the wake of the isolated three-bladed wind turbine model is compared to the wake of porous disks with several solidities: $\sigma = 56\%$, $\sigma = 44\%$, and $\sigma = 36\%$. As expected, the wake is less pronounced when the solidity decreases (Figs. 6.41 and 6.42). Note that the largest solidity is still too weak to mimic the three-bladed wind turbine model. The wake is much shorter for ABL1 because of the higher incoming turbulence intensity. Due to the larger turbulence level of ABL1, the velocity profiles become similar around $x/D = 6$, while it is not yet the case for ABL2 at $x/D = 9$. The turbulence intensity in the shear layers is lower for the porous disks (Figs. 6.43 and 6.44) and a weak asymmetry of the shear layers is also visible as for the rotating models. Furthermore, the peak of turbulence intensity visible just behind the nacelle of the isolated wind turbine is also present for the porous disks. This peak is much weaker for the porous disks (Figs. 6.43 and 6.44) since it is only due to the presence of the nacelle and not to the root vortices coming from the blades as for the three-bladed model.

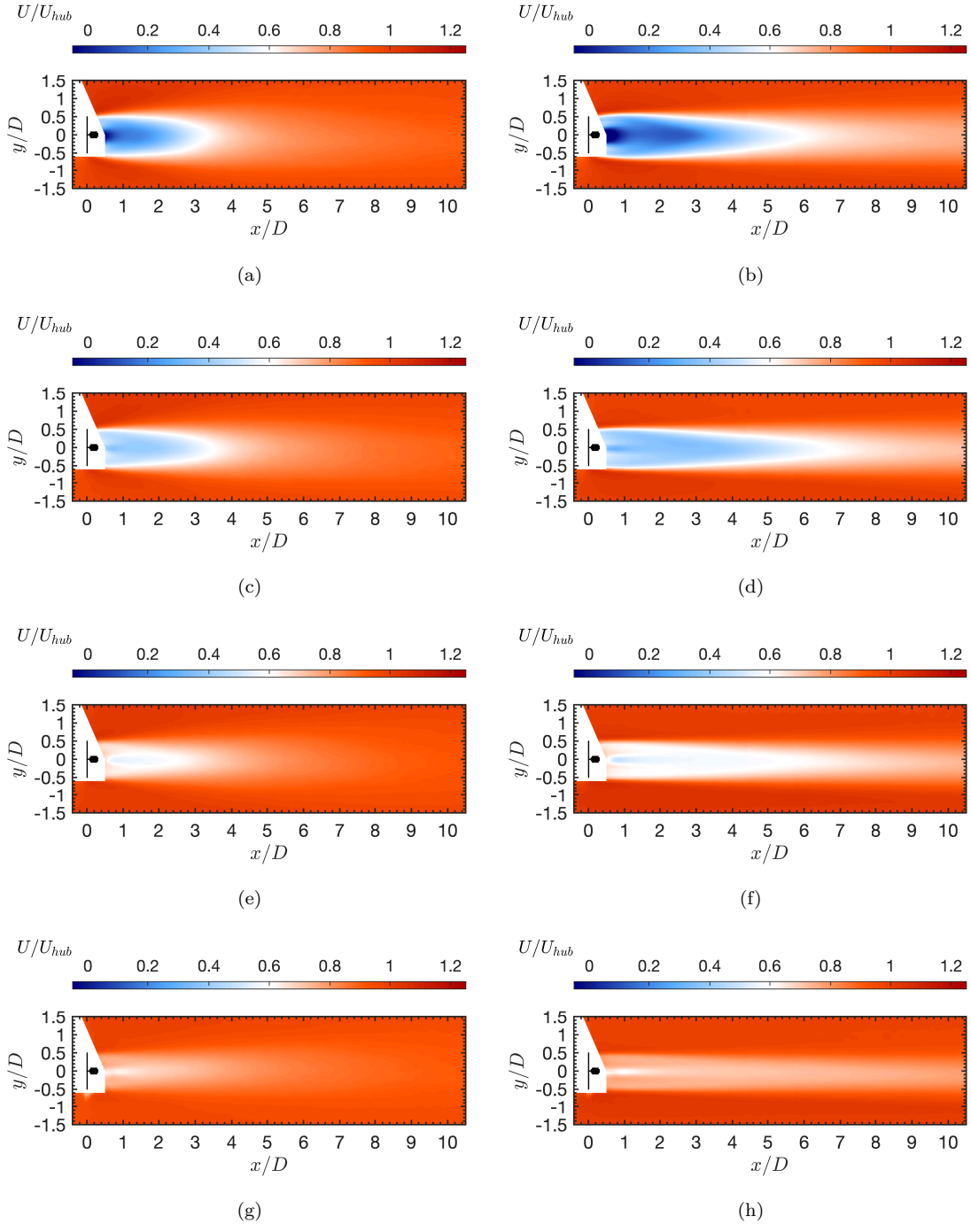



***Figure 6.41:*** *Normalized averaged velocity fields in the horizontal plane at hub height for the isolated wind turbine (a)-(b) and the porous disks with a solidity $\sigma = 56\%$ (c)-(d), $\sigma = 44\%$ (e)-(f), $\sigma = 36\%$ (g)-(h) subjected to ABL1 (a)-(c)-(e)-(g) and ABL2 (b)-(d)-(f)-(h)*

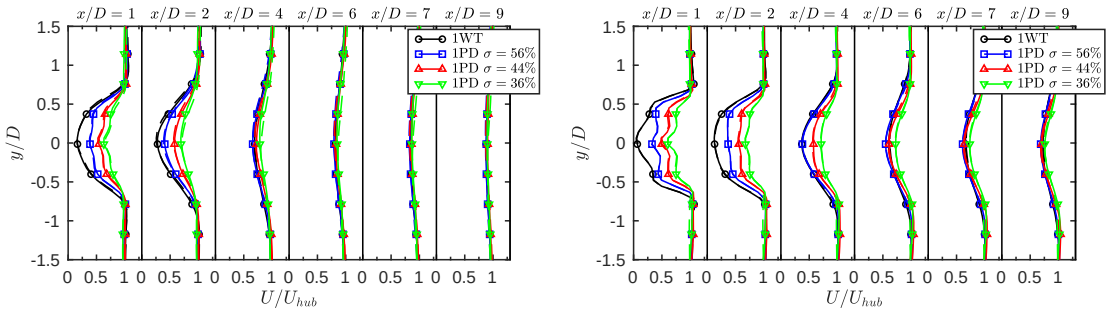



***Figure 6.42:*** *Normalized averaged velocity profiles at several downstream locations in the wake of the isolated wind turbine and of the porous disks with several solidities subjected to ABL1 (a) and ABL2 (b); dashed lines without symbol correspond to the second set of measurements*

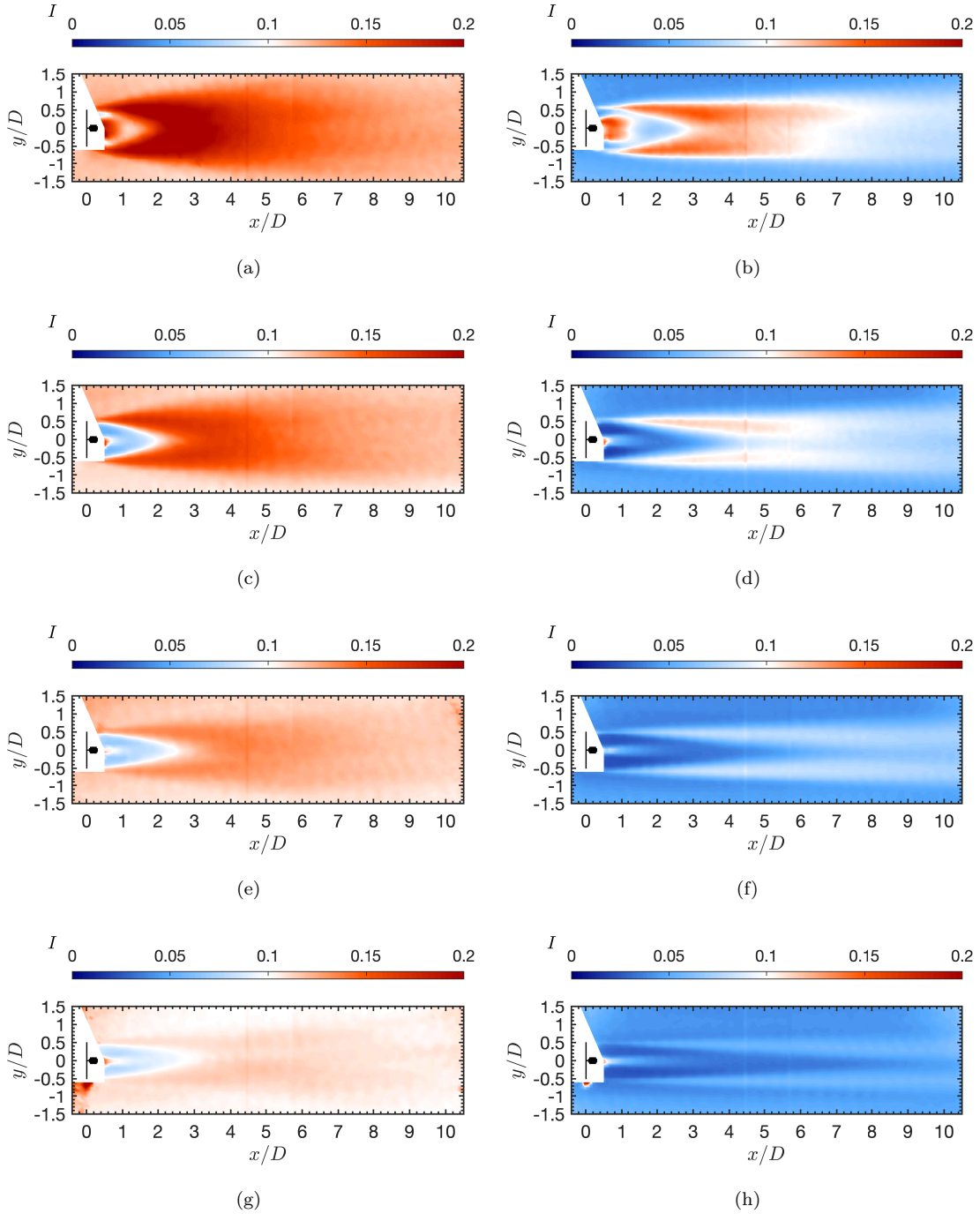



***Figure 6.43:*** *Normalized averaged velocity fields in the horizontal plane at hub height for the isolated wind turbine (a)-(b), the porous disks with a solidity $\sigma = 56\%$ (c)-(d), $\sigma = 44\%$ (e)-(f), $\sigma = 36\%$ (g)-(h) subjected to ABL1 (a)-(c)-(e)-(g) and ABL2 (b)-(d)-(f)-(h)*

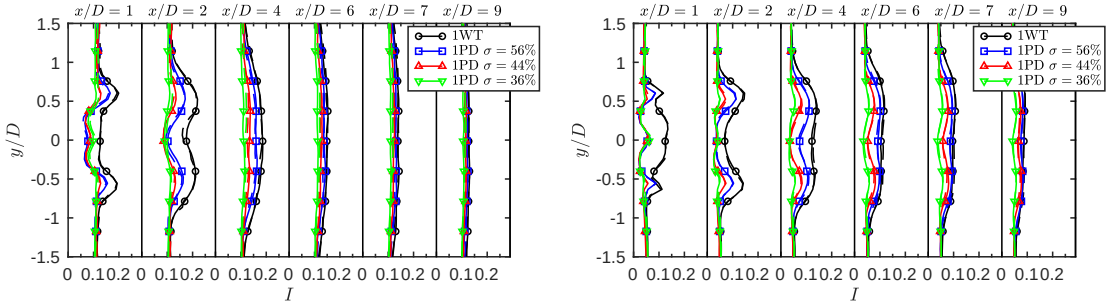



***Figure 6.44:*** *Turbulence intensity profiles at several downstream locations in the wake of the isolated wind turbine and of the porous disks with several solidities subjected to ABL1 (a) and ABL2 (b); dashed lines without symbol correspond to the second set of measurements*

## 6.7 Conclusions

The influence of the Reynolds number, the incoming ABL, the wind turbine operating conditions, and the wind turbine(s) arrangement on the wake characteristics and on the power production was investigated over this chapter. The influence of the Reynolds number has proved to be very limited on the isolated wind turbine configuration. The weak influence of the Reynolds number on the wake characteristics enables to expect that, for the highest Reynolds number reached during these experiments ($Re \simeq 8 \times 10^4$), $Re$ independence was reached for the main flow statistics. As it could be observed over this chapter, the incoming ABL had a large impact on the wake characteristics. Concerning the changes in operating conditions of the isolated wind turbine, they turned out to mainly affect the near wake, whatever the ABL.

The interaction between wind turbines was then investigated for a row of three wind turbines. For both ABLs, it was observed that the near wake of the first wind turbine of the row is similar to the near wake of the isolated wind turbine in terms of mean streamwise velocity component (slightly larger velocity deficit) and turbulence intensity. Closer to the second wind turbine, its induction effect starts to be felt and the velocity deficit becomes larger for the first wind turbine of the row compared to the isolated one. Because of the higher incoming turbulence intensity created by the upstream turbine(s), the wakes of the second and third wind turbines are less pronounced and their velocity profiles smoother compared to the first or isolated wind turbine.

Because of the induction effect following from the row of wind turbines, the power produced by the isolated wind turbine is larger compared to the power produced by the first wind turbine of the row for both ABLs. Furthermore, compared to the second wind turbine of the row, a larger power production was observed for the third wind turbine. This is due to the faster wake recovery behind the second wind turbine compared with that behind the first turbine. This is consistent with other wind tunnel [34] and field [29] experiments. However, for the configuration 3 subjected to ABL1, the power production of the third wind turbine is equivalent to that of the second wind turbine; this equivalence is mainly due to an increase, whose cause remains unknown, in the power production of the second wind turbine.

A wind farm was then set up in the wind tunnel. Compared to the row of wind turbines, no major influence of the lateral rows of wind turbines was observed for the wakes of the wind turbines composing the central row. Concerning the power production, it was similar for the two configurations and there was not a clear trend in favor of one of the two configurations.

Isolated porous disks with various solidities were then tested. As expected, the wake is less pronounced when the solidity of the disk decreases. Compared to the isolated three-bladed wind turbine model, the turbulence intensity in the shear layers is lower for the porous disks. Furthermore, the peak of turbulence intensity visible just behind the nacelle of the isolated wind turbine was also

present for the porous disks. This peak being partly due to the presence of the nacelle itself, but mainly to the root vortices coming from the blades of the wind turbine, is much weaker for the porous disks.

With the view of future studies concerning wind farm optimization, the power production of the upstream turbines was decreased to study the impact of power mitigation on the global wind farm power production. It is however not discussed here as the converging physics was such that the electrical and mechanical optimum were quite different; the mitigation leading to a mechanical power degradation. For the sake of completeness, the results are presented in Appendix H.

Chapter 7

# Wind turbine wake meandering characteristics at wind tunnel scale

The wake meandering characteristics (amplitude, wavelength, and frequency) obtained at wind tunnel scale from the time-resolved PIV measurements presented in Chapter 6 are studied in this chapter. These results are then compared with numerical simulations performed at wind tunnel scale with the FD4 code.

## 7.1 Experimental results

The results presented hereafter were obtained from the tracking of the wake centerline using the 2D convolution method, in the horizontal plane at hub height, supplemented with a wake centroid predictor, the quantity used for the tracking being the available power in the flow (see Chapter 3). The quantitative analysis of the wake centerline characteristics performed is based on the work of Foti et al. [37]. First, each wake centerline is low-pass filtered spatially with a cut-off length $L_{cut-off} = 1D$. The amplitude of wake meandering is then computed as half the cross-wind distance between consecutive maximum-minimum of the wake centerline while the wavelength is computed as the streamwise distance between two consecutive maxima or minima (Fig. 7.1). The downstream position of these quantities was set to the intermediate position of the two points involved in the computation. The quantities were then binned, with respect to the downwind distance from the rotor, into half-diameter bins and the mean values were computed. Note that, for the sake of transparency, the amplitudes and wavelength are presented over downwind distances ranging from $0D$ to $10D$, even if the exploitable part of the graphs is for $3 \lesssim x/D \lesssim 7.5$ due to the method used to determine the amplitude and wavelength of the oscillations. Concerning the convective speed presented hereafter, it is computed from the displacement of the extrema or minima between consecutive velocity fields. For the sake of conciseness, the probability distribution of the wake meandering amplitudes and wavelengths are presented in Appendix I.

As in Chapter 6, the results obtained from the second sets of measurements are represented in dashed line in the figures that will be presented hereafter.

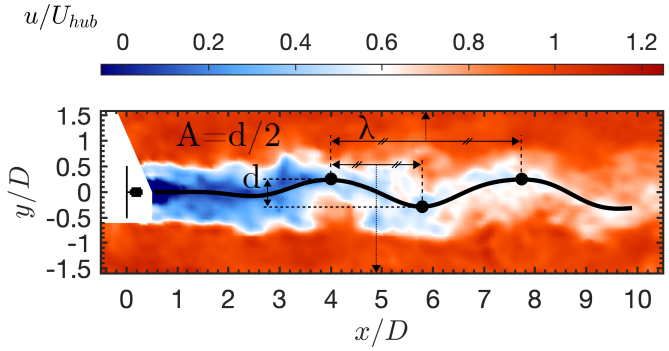



***Figure 7.1:*** *Conventions used for the determination of the amplitudes and the wavelengths of the wake centerline oscillations*

### 7.1.1 Isolated wind turbine

#### 7.1.1.1 Influence of the incoming ABL

Due to the large impact of the incoming ABL on the wake meandering characteristics, it was decided to present the influence of various parameters/configurations for both ABL modeled in the wind tunnel. The influence of the incoming ABL is therefore discussed within each of the following sections.

#### 7.1.1.2 Influence of Reynolds number

Figure 7.2 shows, for a specific instant, the wake centerline superimposed on the streamwise velocity field for the isolated wind turbine subjected to ABL1 and ABL2 at $Re \simeq 8 \cdot 10^4$ and $Re \simeq 5 \cdot 10^4$. As it can be observed, the wake deflections are larger for ABL1 than for ABL2. Figure 7.3 is more complete and shows the wake centerline position for the entire acquisition time, i.e. the wake centroid position as a function of space and time. It shows that, for ABL1, the wake centroid deflections are smaller at $Re \simeq 5 \cdot 10^4$ than at $Re \simeq 8 \cdot 10^4$, which is not the case for ABL2. Furthermore, one can observe that the pattern of peaks and valleys is wider for $Re \simeq 5 \cdot 10^4$, leading to oscillations that are more gradual. Comparing ABL1 and ABL2, it is clear that the wake centroid deflections are larger for ABL1. Moreover, large wake deflections, that sightly increase with the downstream distance, are rapidly observed for ABL1, while the wake deflections increase very progressively with the downstream distance for ABL2.

These observations are confirmed by examining at the probability distribution of the wake centroid position as a function of the streamwise position (Fig. 7.4) and at the wake centerline envelopes (Fig. 7.5). Indeed, Fig. 7.4 shows that the distribution of the wake centroid position is larger at $Re \simeq 8 \cdot 10^4$ than at $Re \simeq 5 \cdot 10^4$ for ABL1, while it is very similar for ABL2. Concerning the wake centerline envelopes, they are slightly wider at $Re \simeq 8 \cdot 10^4$ than at $Re \simeq 5 \cdot 10^4$ from $x/D \simeq 4.5$ for ABL1, while they are similar for ABL2 (Fig. 7.5). A wider wake centerline envelope reflects larger extreme wake centroid deflections.

While the extreme wake deflections are slightly larger at higher Reynolds number for ABL1, there is no clear influence of the Reynolds number on the mean binned wake meandering amplitude, whether for ABL1 or ABL2 (Fig. 7.6). For ABL1, the amplitude does not vary much for $3 \lesssim x/D \lesssim 7.5$ and is of the order of $0.3D$. For ABL2, the amplitude of the wake meandering increases linearly with the downstream distance to reach a maximum of $0.22D$. The linear increase is evidenced in Fig. 7.6(d) where the amplitude is normalized by the downstream distance from the wind turbine rotor. In such a graph, a linear increase of the amplitude results in a constant value for the normalized amplitude. Regarding the mean binned wavelengths (Fig. 7.7), they are slightly longer at $Re \simeq 5 \cdot 10^4$, for both ABL1 and ABL2. When comparing ABL1 and ABL2, the wavelengths are slightly larger for ABL1 ($2.75 \lesssim \lambda/D \lesssim 3.5$) than for ABL2 ($2.5 \lesssim \lambda/D \lesssim 3.25$) for $3 \lesssim x/D \lesssim 7.5$. Concerning the averaged convective speeds, they are slightly larger at $Re \simeq 5 \cdot 10^4$ (Fig. 7.7), whether for ABL1

or ABL2. This explains the slightly longer wavelengths obtained at $Re \simeq 5 \cdot 10^4$. Assuming that Taylor's frozen turbulence hypothesis is applicable, the frequency can be computed from convective speed $U_c$ and the wavelength $\lambda$

$$f = \frac{U_c}{\lambda}, \tag{7.1}$$

and made dimensionless through the Strouhal number

$$St = \frac{fD}{U_{hub}} = \frac{U_c}{U_{hub}} \cdot \frac{D}{\lambda}. \tag{7.2}$$

It leads to $0.21 \lesssim St \lesssim 0.27$ for ABL1 and to $0.22 \lesssim St \lesssim 0.29$ for ABL2 (Figs. 7.7(e) and 7.7(f)).

The Reynolds number has therefore a very limited influence on the wake meandering characteristics. In the following sections, results are therefore presented for $Re \simeq 8 \cdot 10^4$ only.

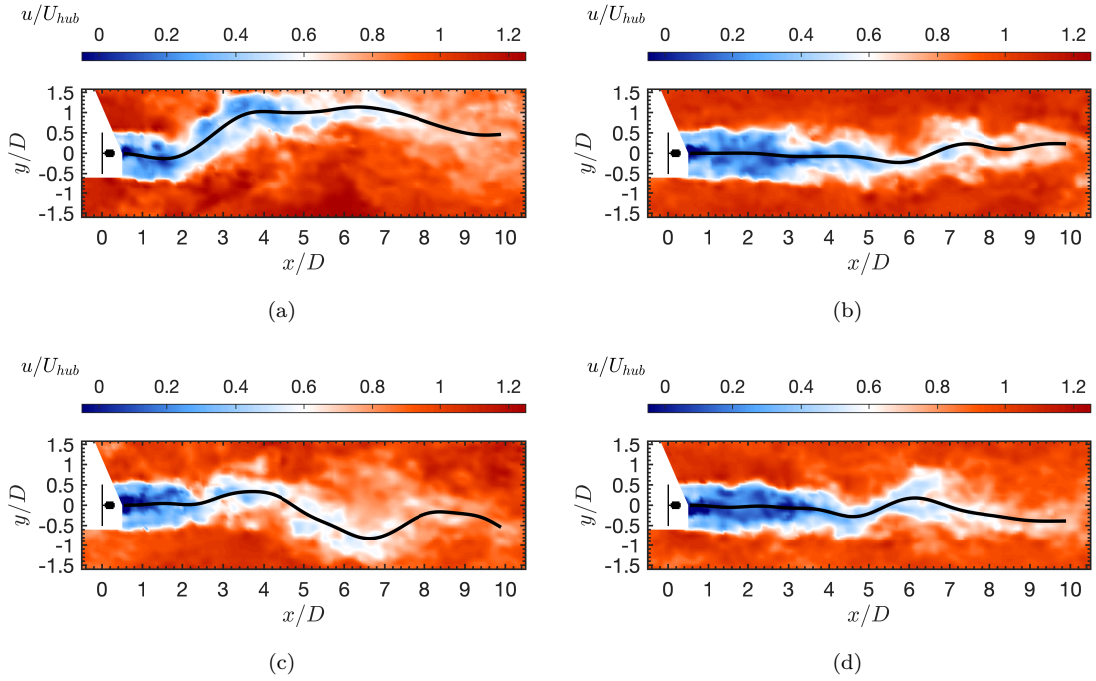



***Figure 7.2:*** *Wake centerline superimposed on the instantaneous streamwise velocity field for the isolated wind turbine subjected to ABL1 (a)-(c) and ABL2 (b)-(d) at* $Re \simeq 8 \cdot 10^4$ *(a)-(b) and* $Re \simeq 5 \cdot 10^4$ *(c)-(d)*

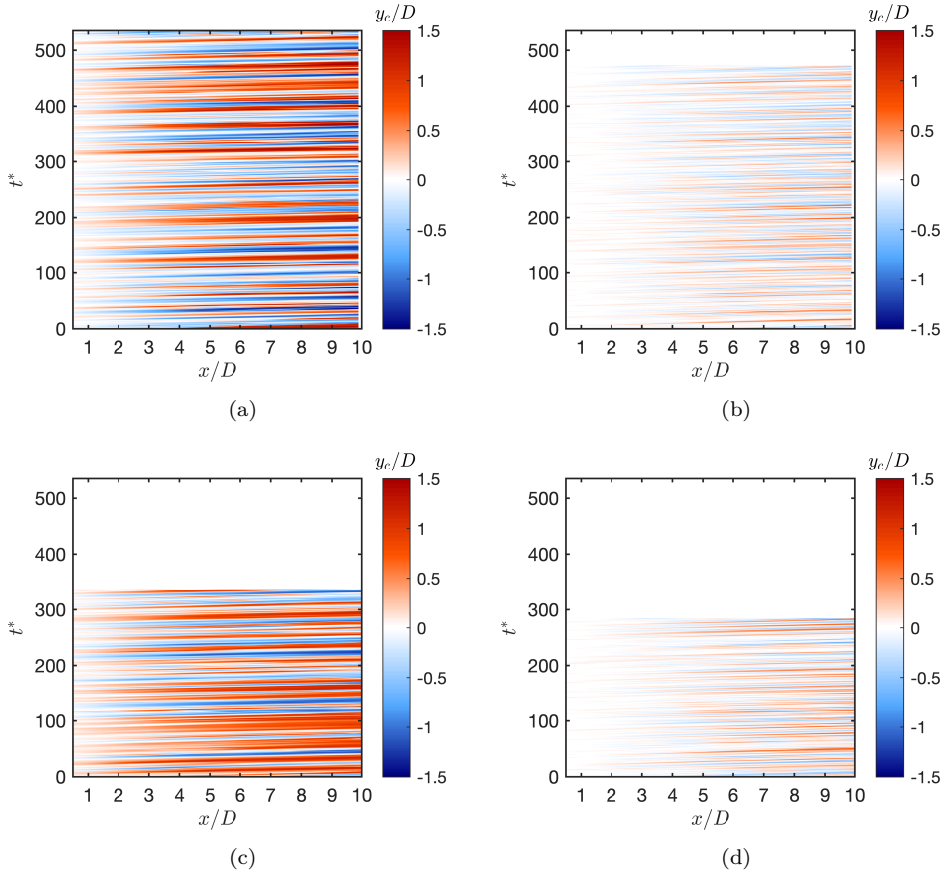



***Figure 7.3:*** *Dimensionless wake centroid position as a function of space and time for the isolated wind turbine subjected to ABL1 (a)-(c) and ABL2 (b)-(d) at* $Re \simeq 8 \cdot 10^4$ *(a)-(b) and* $Re \simeq 5 \cdot 10^4$ *(c)-(d)*

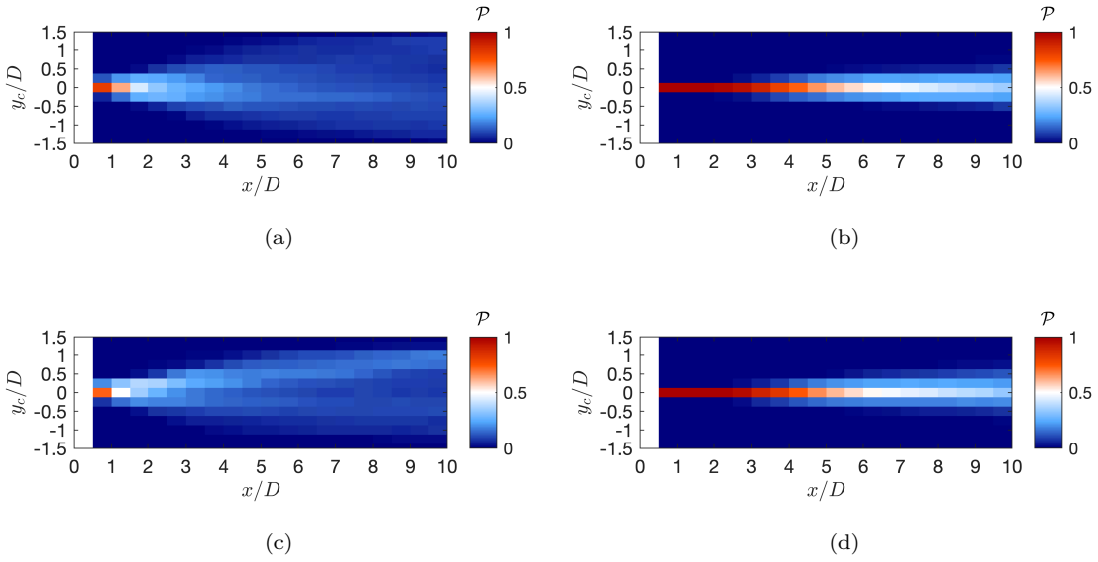



***Figure 7.4:*** *Probability distribution of the binned wake centroid position as a function of space for ABL1 (a)-(c) and ABL2 (b)-(d) at* $Re \simeq 8 \cdot 10^4$ *(a)-(b) and* $Re \simeq 5 \cdot 10^4$ *(c)-(d), the bins width is* $D/4$

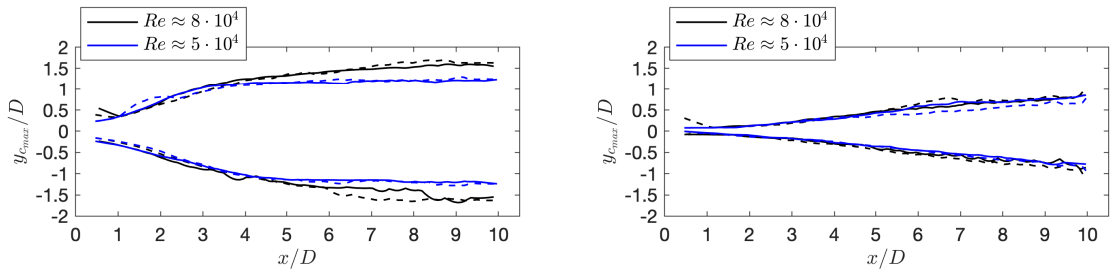



***Figure 7.5:*** *Dimensionless wake centerline envelopes for ABL1 (a) and ABL2 (b) at* $Re \simeq 8 \cdot 10^4$ *and* $Re \simeq 5 \cdot 10^4$*; dashed lines correspond to the second set of measurements*

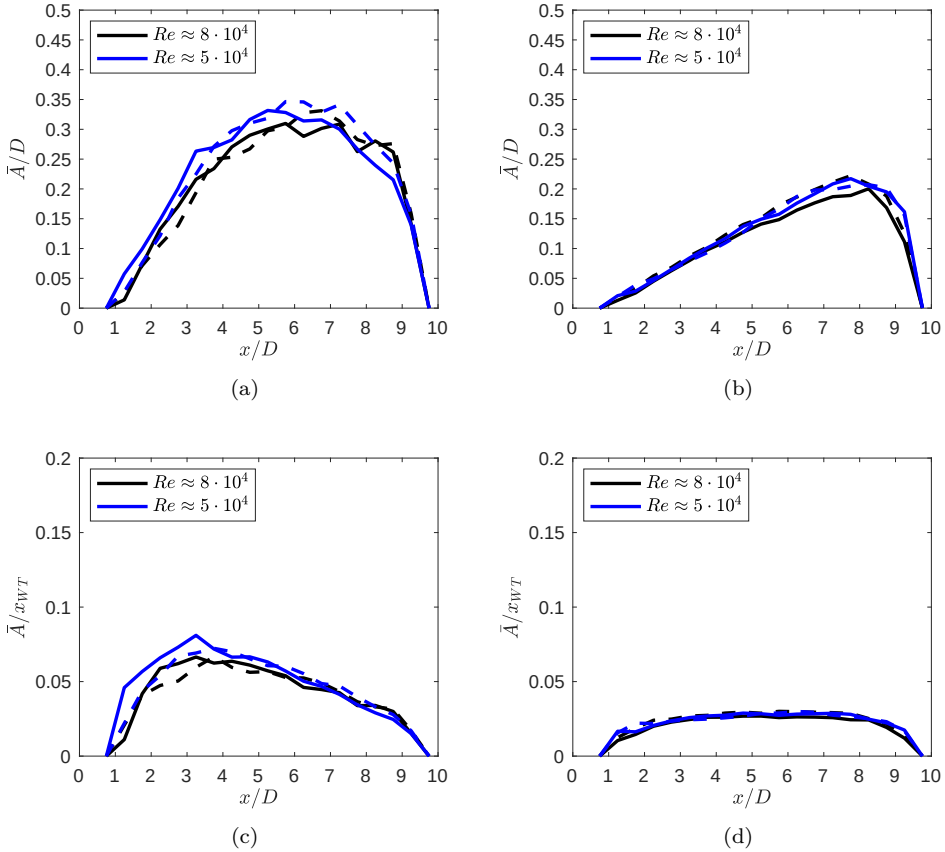



***Figure 7.6:*** *Mean binned wake centerline amplitudes for ABL1 (a)-(c) and ABL2 (b)-(d) at* $Re \simeq 8 \cdot 10^4$ *and* $Re \simeq 5 \cdot 10^4$*; dashed lines correspond to the second set of measurements*

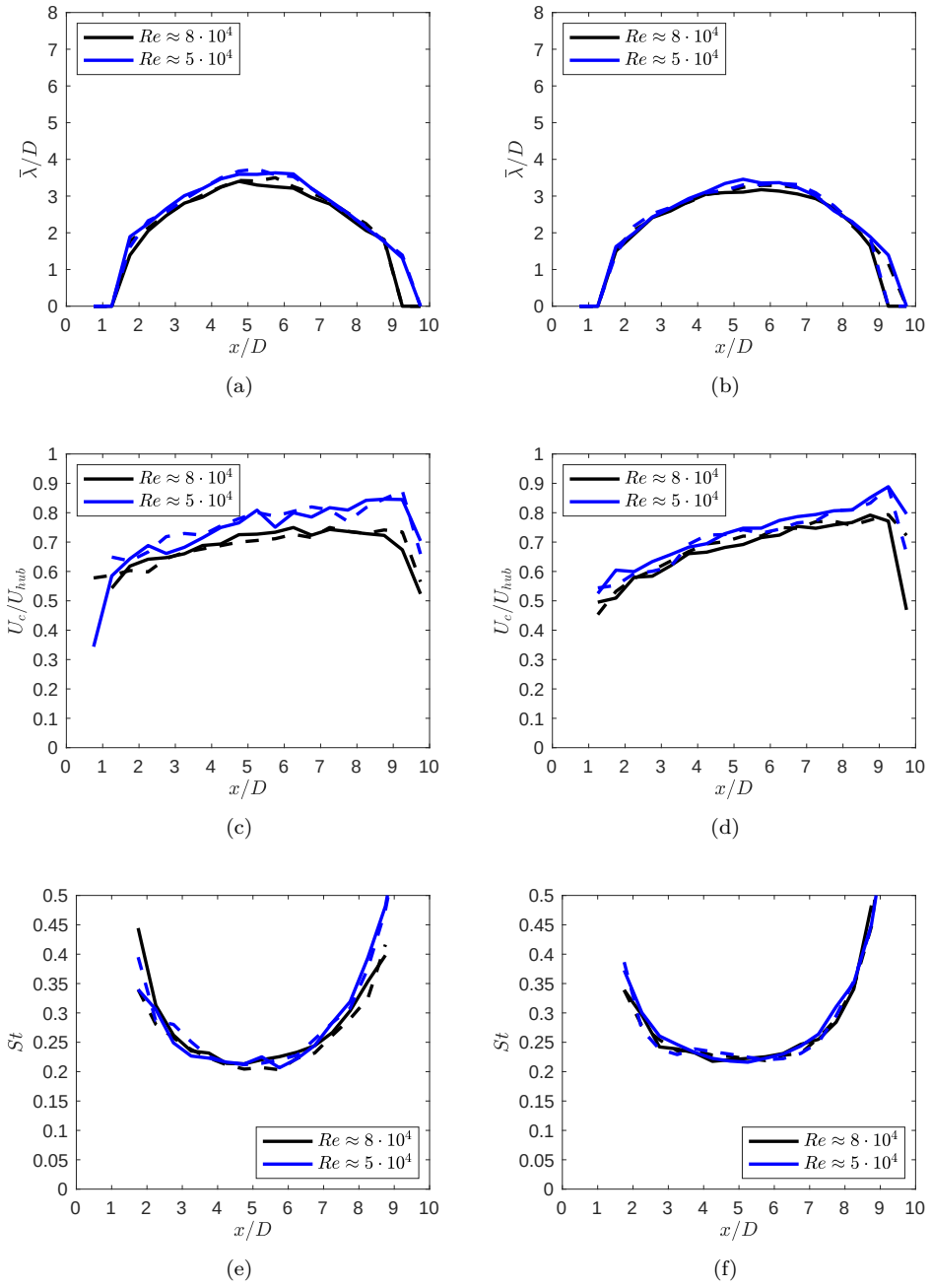



***Figure 7.7:*** *Mean binned wake centerline wavelengths, convective speeds and Strouhal numbers for ABL1 (a)-(c)-(e) and ABL2 (b)-(d)-(f) at $Re \simeq 8 \cdot 10^4$ and $Re \simeq 5 \cdot 10^4$; dashed lines correspond to the second set of measurements*

#### 7.1.1.3 Influence of wind turbine operating conditions

Whatever the operating conditions (Table 7.1), the wake deflections are larger for ABL1 than for ABL2 (Fig. 7.8). Figure 7.9 shows that the wake centroid deflections are weaker for $R = 150\,\Omega$ than for $R = 3\,\Omega$ and $R = 9\,\Omega$, $R = 9\,\Omega$ corresponding to the maximum electrical power production (see Section 5.1.2). Furthermore, it is clear that the wake centroid deflections are larger for ABL1 than for ABL2, whatever the instant considered.

| | $TSR$ | |
|---|---|---|
| | ABL1 | ABL2 |
| $R = 3\,\Omega$ | 6.1 | 5.8 |
| $R = 9\,\Omega$ | 7.0 | 6.7 |
| $R = 150\,\Omega$ | 8.0 | 7.9 |

***Table 7.1:*** *Link between the electrical resistance applied to the generator of the isolated wind turbine and the tip-speed ratio ($TSR$) obtained during the time-resolved PIV measurements*

Concerning the probability distribution of the wake centroid as a function of space (Fig. 7.10), the probability to observe strong wake deflections within ABL1 is larger for $R = 9\,\Omega$ than for the two other operating conditions. For ABL2, the probability distributions of the wake centroid position show that the wake centerlines stay closer to $y/D = 0$ over a longer distance for larger resistive loads, i.e. higher rotation speed. All this reflects in similar wake centerline envelopes for ABL1 and in a slightly narrower wake centerline envelope with $R = 150\,\Omega$ for ABL2 (Fig. 7.11).

As it can be observed in Figs. 7.12 and 7.13, the operating conditions, i.e. the tip-speed ratios since the thrust coefficient of the scale model involved in this study varies little with respect to the tip-speed ratio ($0.88 \leqslant C_T \leqslant 0.94$ for $5 \leqslant TSR \leqslant 8$, see Fig. 5.19(b)), do not have a clear impact on the wake meandering characteristics, whether in terms of amplitudes (Fig. 7.12) or wavelengths (Figs. 7.13(a) and 7.13(b)). Concerning the convective speeds, they are also very similar (Figs. 7.13(c) and 7.13(d). Overall, this results in similar Strouhal numbers (Figs. 7.13(e) and 7.13(f)) regardless of the operating conditions.

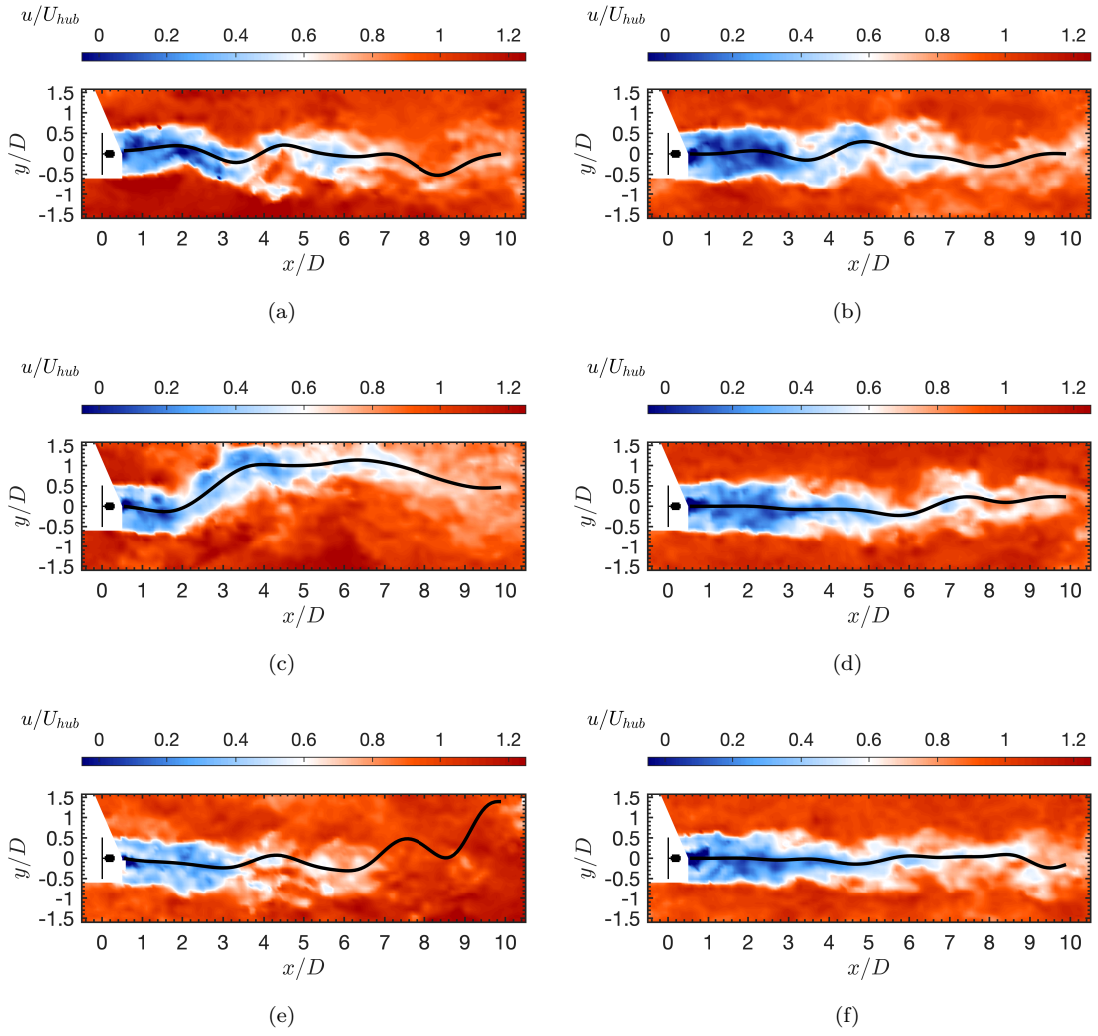



***Figure 7.8:*** *Wake centerline superimposed on the instantaneous streamwise velocity field for the isolated wind turbine subjected to ABL1 (a)-(c)-(e) and ABL2 (b)-(d)-(f) for different operating conditions:* $R = 3\,\Omega$ *(a)-(b),* $R = 9\,\Omega$ *(c)-(d),* $R = 150\,\Omega$ *(e)-(f)*

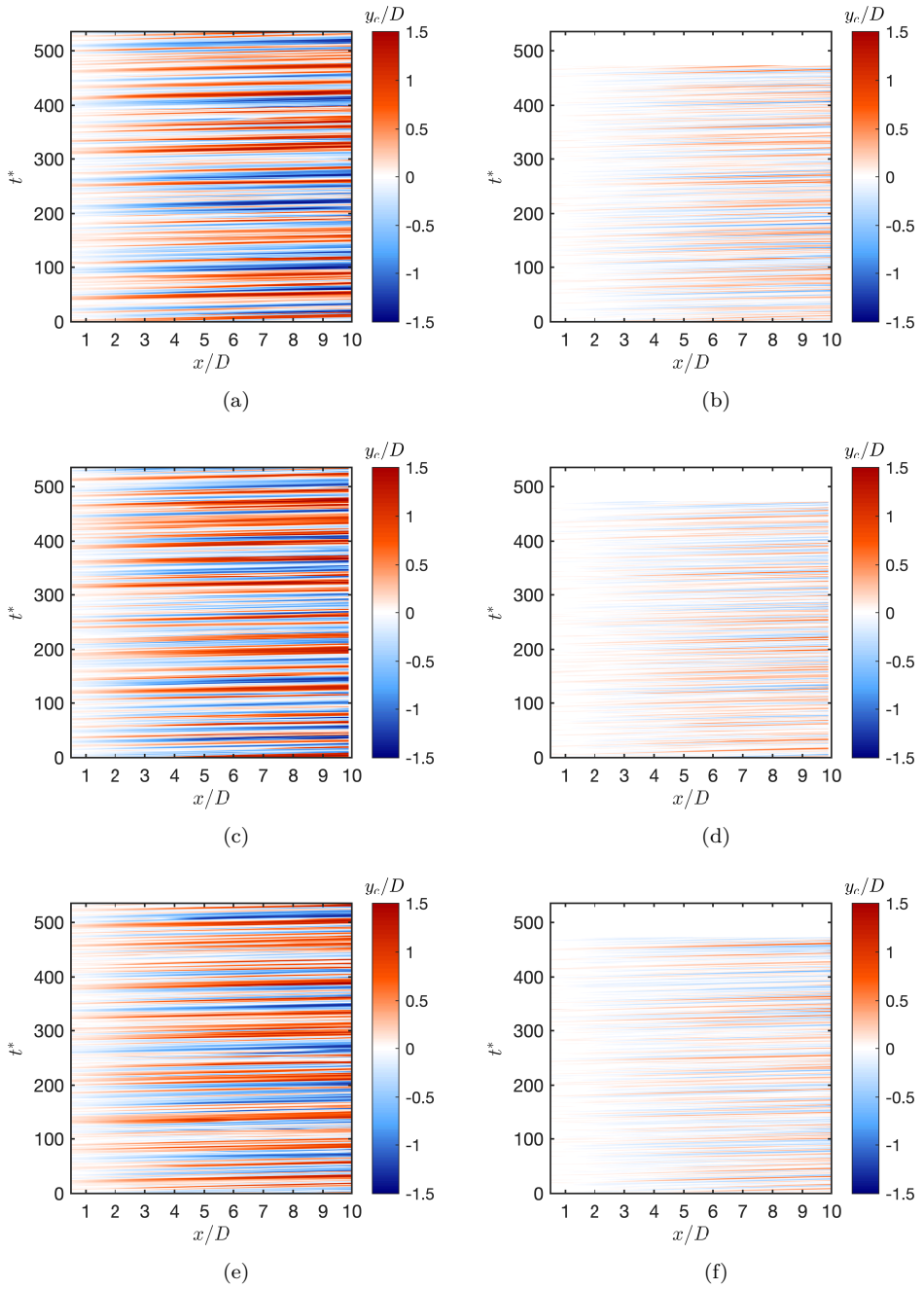



***Figure 7.9:*** *Dimensionless wake centroid position as a function of space and time for the isolated wind turbine subjected to ABL1 (a)-(c)-(e) and ABL2 (b)-(d)-(f) for different operating conditions:* $R = 3\,\Omega$ *(a)-(b),* $R = 9\,\Omega$ *(c)-(d),* $R = 150\,\Omega$ *(e)-(f)*

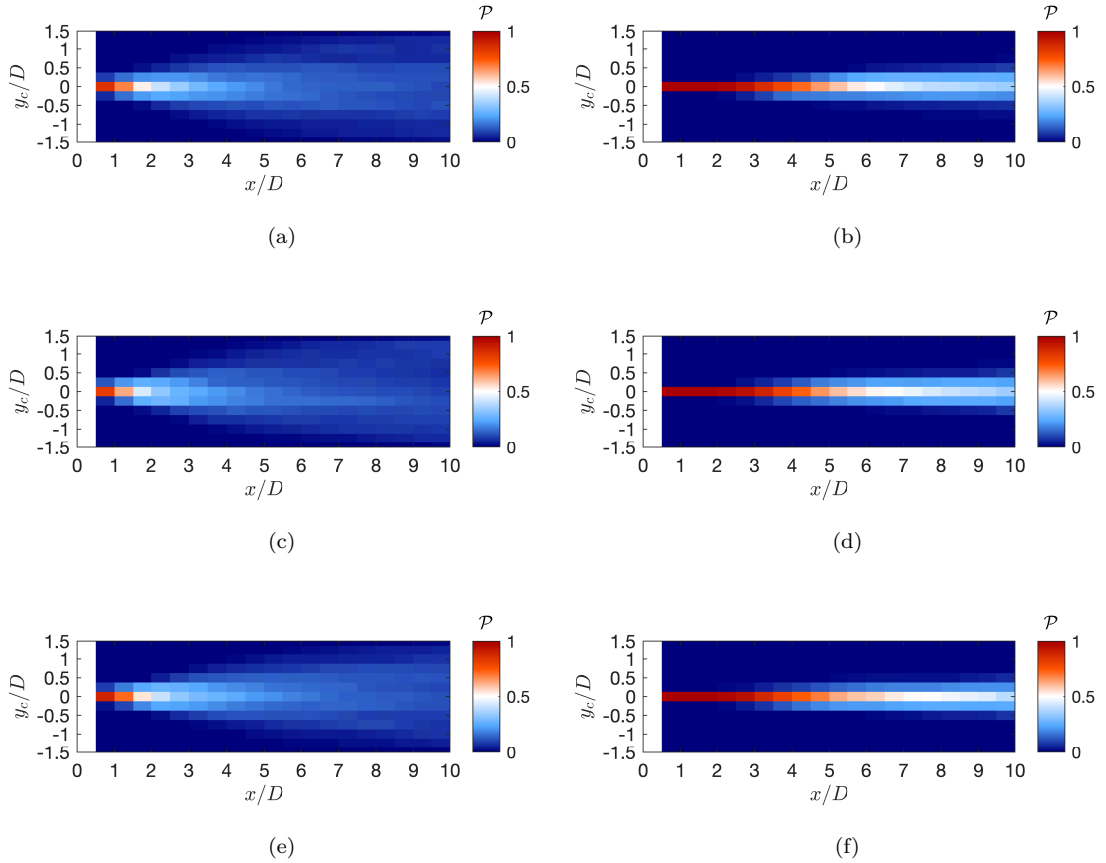



***Figure 7.10:*** *Probability distribution of the binned wake centroid position as a function of space for ABL1 (a)-(c)-(e) and ABL2 (b)-(d)-(f) for different operating conditions: $R = 3\,\Omega$ (a)-(b), $R = 9\,\Omega$ (c)-(d), $R = 150\,\Omega$ (e)-(f), the bins width is $D/4$*

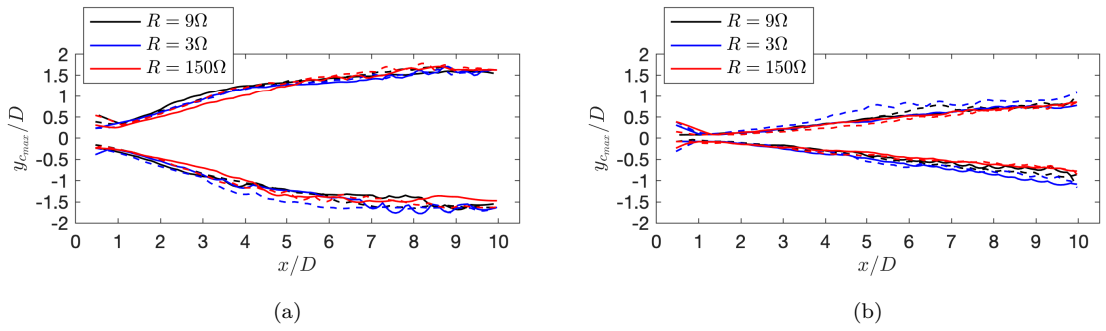



***Figure 7.11:*** *Dimensionless wake centerline envelopes for ABL1 (a) and ABL2 (b) for different operating conditions: $R = 3\,\Omega$, $R = 9\,\Omega$, and $R = 150\,\Omega$; dashed lines correspond to the second set of measurements*

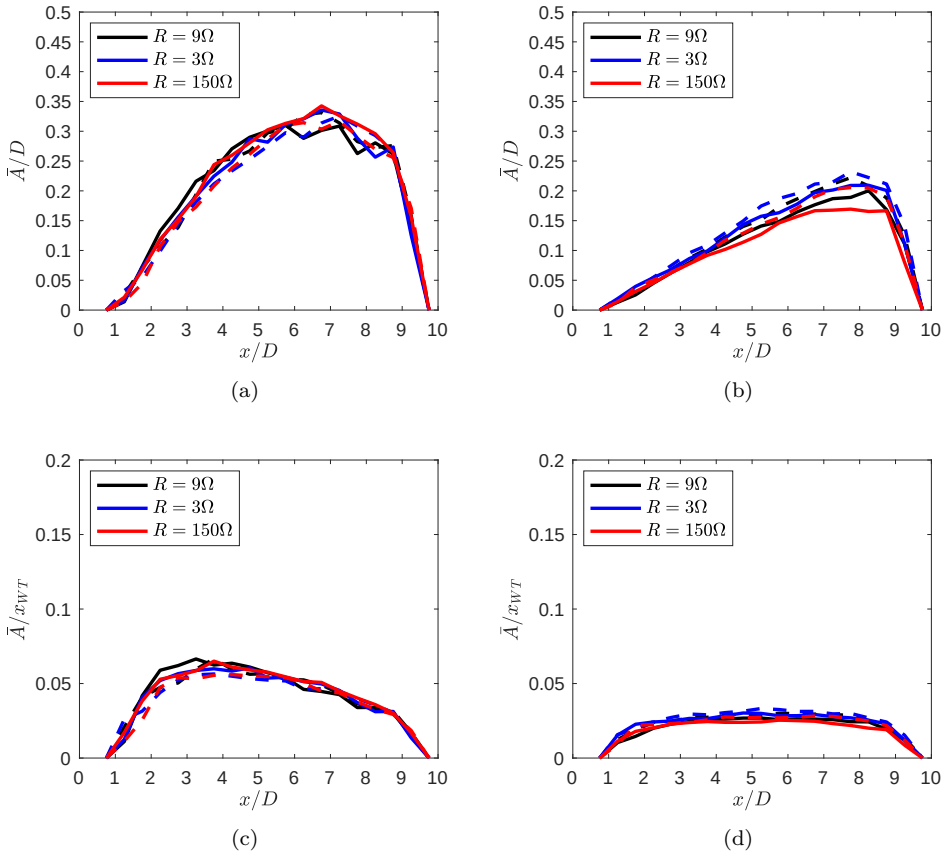



***Figure 7.12:*** *Mean binned wake centerline amplitudes for ABL1 (a)-(c) and ABL2 (b)-(d) for different operating conditions: $R = 3\,\Omega$, $R = 9\,\Omega$, and $R = 150\,\Omega$; dashed lines correspond to the second set of measurements*

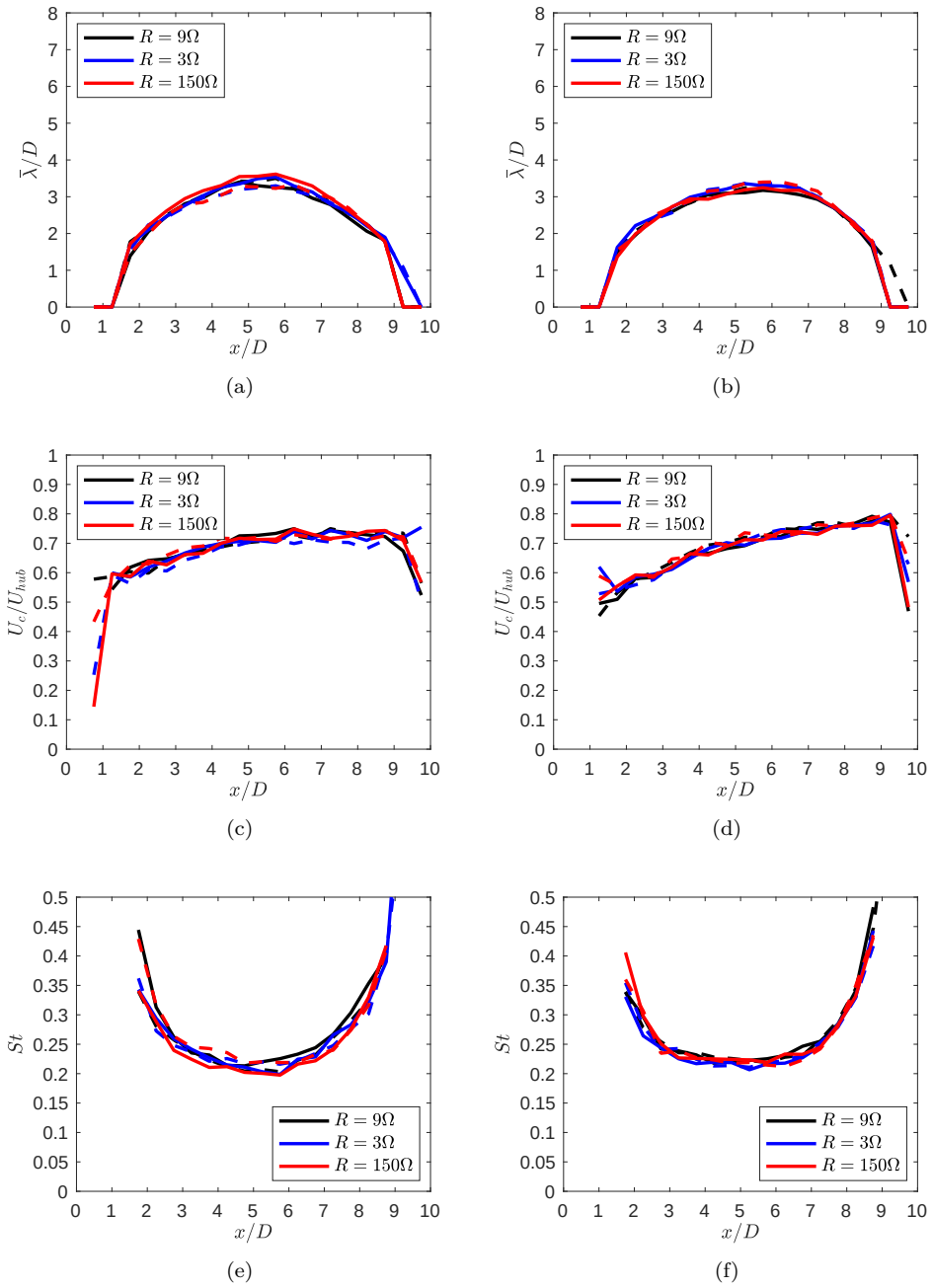



***Figure 7.13:*** *Mean binned wake centerline wavelengths, convective speeds, and Strouhal numbers for ABL1 (a)-(c)-(e) and ABL2 (b)-(d)-(f) for different operating conditions: $R = 3\,\Omega$, $R = 9\,\Omega$, and $R = 150\,\Omega$; dashed lines correspond to the second set of measurements*

## 7.1.2 Row of three wind turbines

### 7.1.2.1 Isolated wind turbine vs. first and second wind turbines

For ABL1, the deviations of the wake centerline are larger for the isolated wind turbine than for the first and second wind turbines of the row (Fig. 7.14). For ABL2, the deviations of the wake centerline seem similar for the isolated wind turbine and for the wind turbines of the row. Comparing ABL1 and ABL2, the deflections are much larger for ABL1. This is confirmed in Fig. 7.15 and also reflects in the probability distribution of the binned wake centroid position as a function of space (Fig. 7.16). In comparison with the isolated wind turbine, the presence of the second wind turbine increases the probability of finding the wake centroid around $y/D = 0$ for $x/D > 5.5$.

The maximum wake centerline deflections are slightly larger for the isolated wind turbine than for the first wind turbine of the row when subjected to ABL1, while they are similar when subjected to ABL2 (Fig. 7.17). Furthermore the presence of a second turbine limits the maximum deflections of the wake centerlines for $x/D > 5$. However, when compared at similar distances from the rotor, the envelopes of the wake centerline of the second wind turbine are larger than those of the first wind turbine wake (Fig. 7.17). The upstream turbine is therefore responsible for an increase in the extreme wake deflections.

The mean binned wake centerline amplitudes are equivalent for the isolated wind turbine and for the first wind turbine of the row (Fig. 7.18). When compared to the case of the isolated wind turbine, the presence of the second wind turbine reduces the amplitude of the wake meandering in the region of the wake of the second wind turbine. The fact that the amplitude normalized by the downstream distance is larger for the second wind turbine, when compared to the isolated wind turbine (Fig. 7.18(c) and 7.18(d)), is caused by the normalization itself: $x_{WT}$ corresponding to the distance from the closest upstream rotor, this distance being much shorter when the second wind turbine is present than for the isolated wind turbine. However, when comparing the turbines of the row, the amplitudes are larger for the second wind turbine than for the first wind turbine, evidencing the influence of an upstream turbine on the wake meandering amplitude. Concerning the mean binned wake centerline wavelengths, they are equivalent for the isolated wind turbine and the wind turbines of the row, whether for ABL1 or ABL2 (Fig. 7.19). The reduced mean binned wake centerline amplitudes and wavelength around $x/D = 5$ are inherent to the methodology used to compute these quantities, as explained previously. Concerning the convective speeds, they are similar for the isolated wind turbine and the first wind turbine of the row. For $x/D > 5$, the convective speed is lower for the second wind turbine compared to the isolated wind turbine. This difference is due to the fact that for $x/D > 5$, there is a smaller velocity deficit for the isolated wind turbine because of the wake recovery, while there is a strong velocity deficit just behind the second wind turbine.

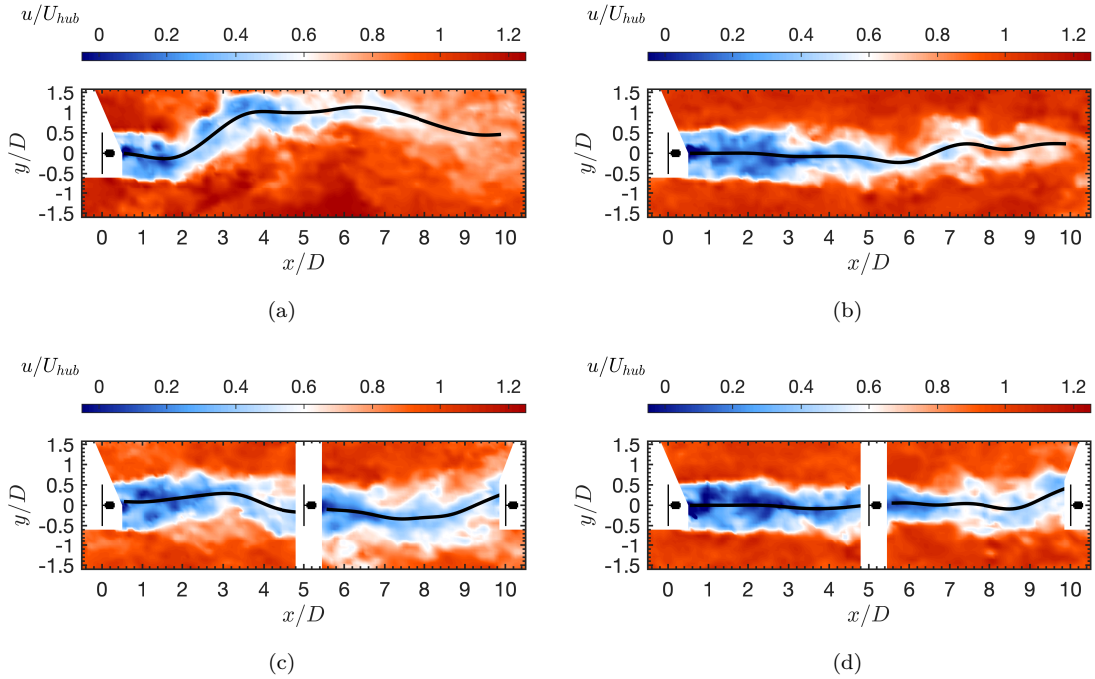



***Figure 7.14:*** *Wake centerline superimposed on the instantaneous streamwise velocity field for the isolated wind turbine (a)-(b) and the first and second wind turbines (c)-(d) of the row for ABL1 (a)-(c) and ABL2 (b)-(d)*

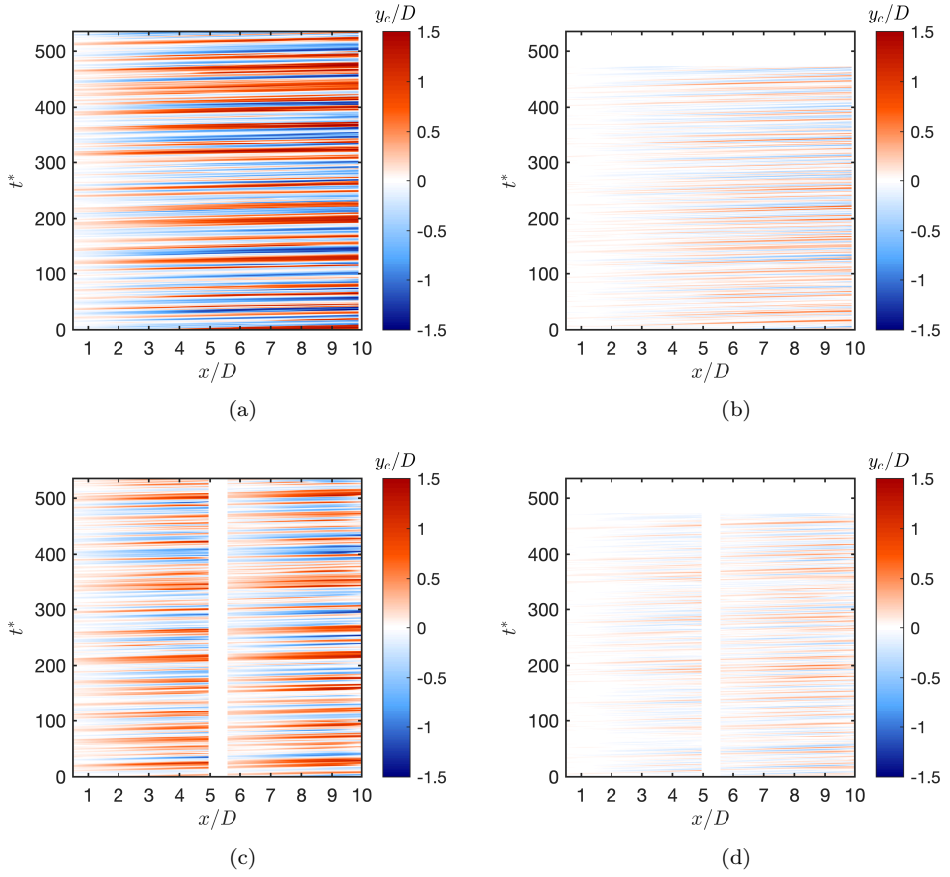



***Figure 7.15:*** *Dimensionless wake centroid position as a function of space and time for the isolated wind turbine (a)-(b) and the first and second wind turbines (c)-(d) of the row for ABL1 (a)-(c) and ABL2 (b)-(d)*

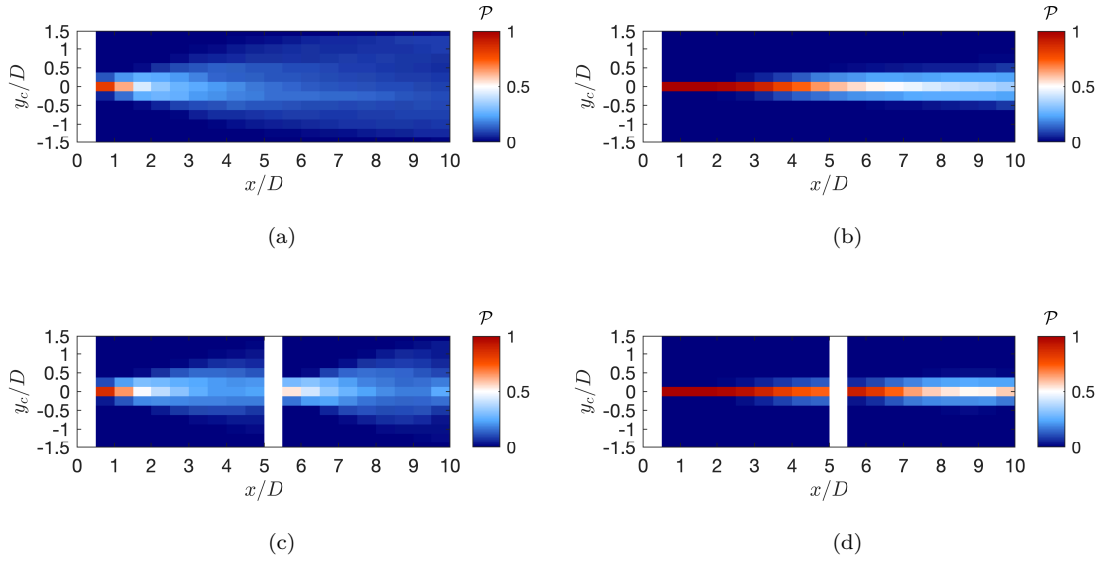



***Figure 7.16:*** *Probability distribution of the binned wake centroid position as a function of space for the isolated wind turbine (a)-(b) and the third wind turbine (c)-(d) of the row for ABL1 (a)-(c) and ABL2 (b)-(d), the bins width is $D/4$*

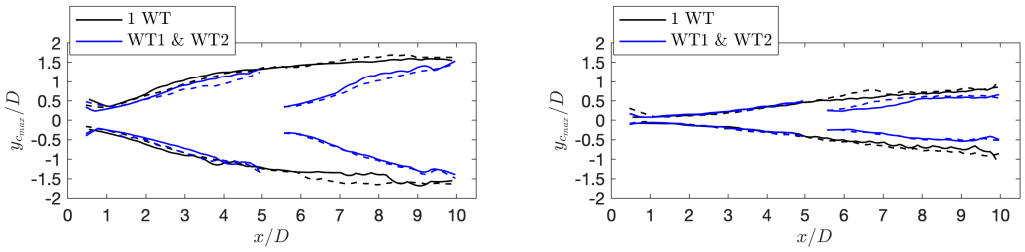



***Figure 7.17:*** *Dimensionless wake centerline envelopes for the isolated wind turbine and the first and second wind turbines of the row for ABL1 (a) and ABL2 (b); dashed lines correspond to the second set of measurements*

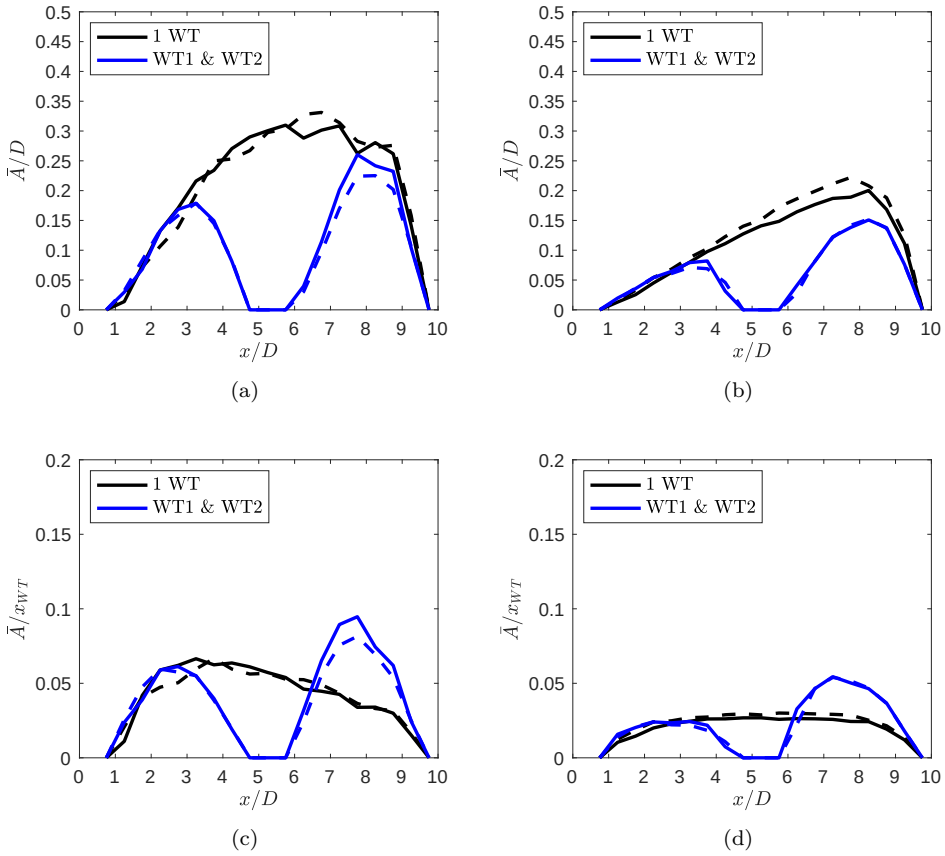



***Figure 7.18:*** *Mean binned wake centerline amplitudes obtained for the isolated wind turbine and the first and second wind turbines of the row for ABL1 (a)-(c) and ABL2 (b)-(d); dashed lines correspond to the second set of measurements*

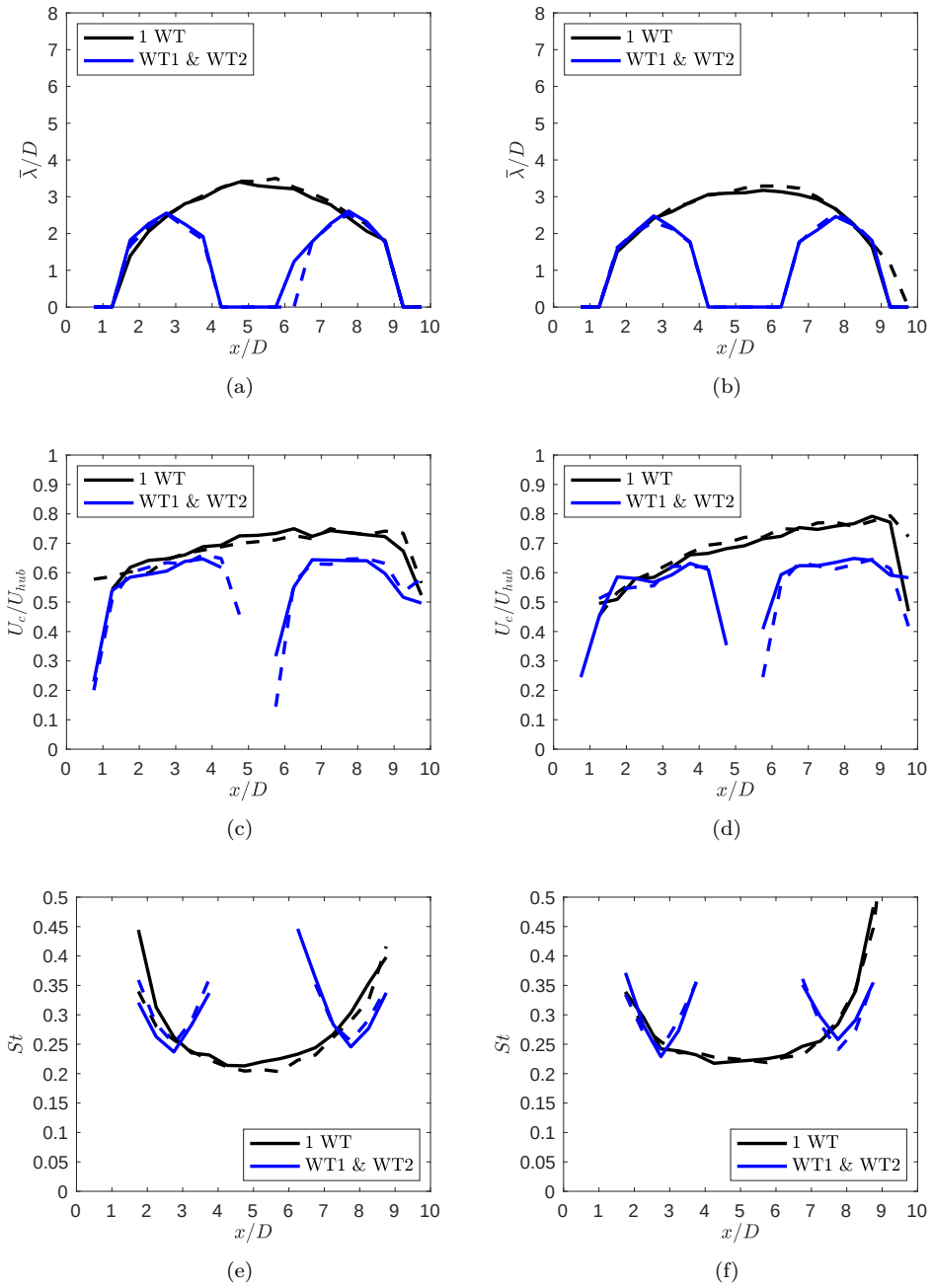



***Figure 7.19:*** *Mean binned wake centerline wavelengths, convective speeds, and Strouhal numbers obtained for the isolated wind turbine and the first and second wind turbines of the row for ABL1 (a)-(c)-(e) and ABL2 (b)-(d)-(f); dashed lines correspond to the second set of measurements*

#### 7.1.2.2 Isolated wind turbine vs. third wind turbine

From the wake centerline deflections for the isolated wind turbine and the third wind turbine of the row at a specific time (Fig. 7.20), it is difficult to extract a clear trend. However, when considering the wake deflections over the entire acquisition time, it is clear that the deviations of the wake centroids are larger for the third wind turbine of the row than for the isolated wind turbine (Fig. 7.21), especially for ABL2. Comparing ABL1 and ABL2, the deflections are much larger for ABL1.

As it can be observed in Fig. 7.22, the wake centroid deviates sooner from $y/D = 0$ for the third wind turbine of the row compared to the isolated wind turbine. Furthermore, the maximum wake centroid deflections are larger for the third wind turbine of the row than for the isolated wind turbine, especially for ABL2 (Fig. 7.23).

The mean binned wake centerline amplitudes (Fig. 7.24) are much larger for the third wind turbine of the row than for the isolated wind turbine wake, whether for ABL1 ($0.25 \lesssim A/D \lesssim 0.38$) or ABL2 ($0.20 \lesssim A/D \lesssim 0.27$). It means that the amplitude of the wake meandering increases within the wind farm. While the amplitude increases linearly with the downstream distance for the isolated wind turbine within ABL2, it is not the case anymore for the third wind turbine of the row: the amplitude increases much faster with the downstream distance up to $x/D = 4$ and then increases slightly beyond this distance. The mean binned wake centerline wavelengthsare equivalent for ABL1 and range within $2.75 \lesssim \lambda/D \lesssim 3.5D$ (Fig. 7.25). For ABL2, they are slightly larger for the third wind turbine ($2.75 \lesssim \lambda/D \lesssim 3.5$) compared to the isolated wind turbine ($2.5 \lesssim \lambda/D \lesssim 3.25$). As expected, the convective speed is smaller for the third wind turbine compared to the isolated machine (Fig. 7.25). Assuming that the Taylor's frozen turbulence hypothesis is applicable, it leads to $0.19 \lesssim St \lesssim 0.27$ for the third wind turbine in ABL1 or ABL2 (Figs. 7.25(e) and 7.25(f)).

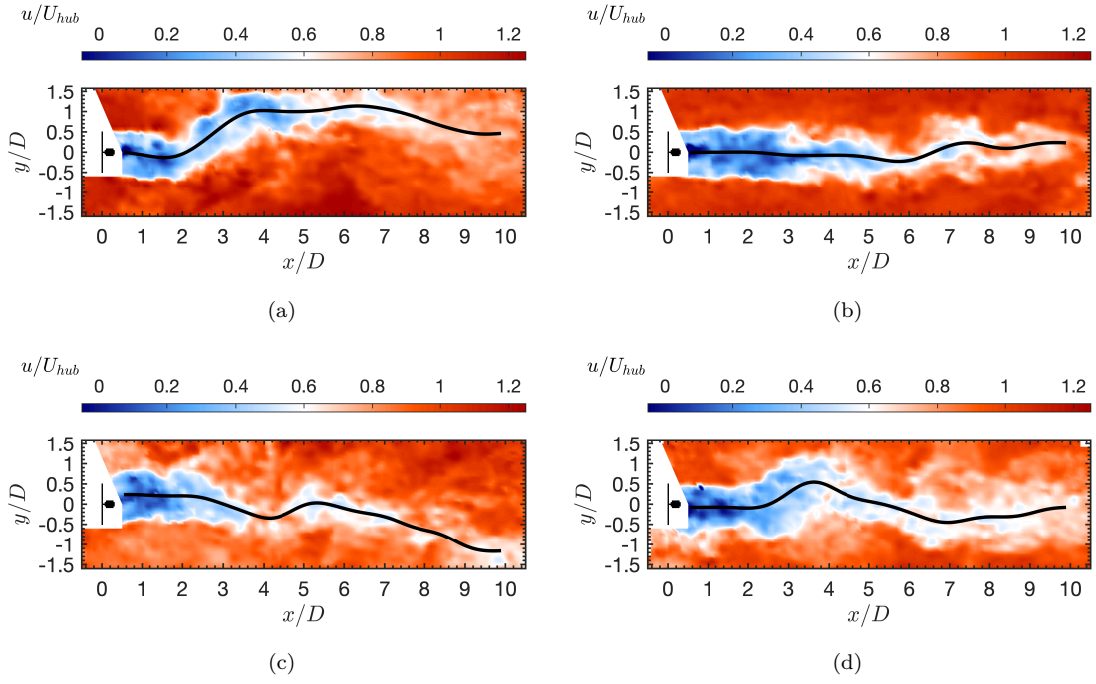



***Figure 7.20:*** *Wake centerline superimposed on the instantaneous streamwise velocity field for the isolated wind turbine (a)-(b) and the third wind turbine (c)-(d) of the row for ABL1 (a)-(c) and ABL2 (b)-(d)*

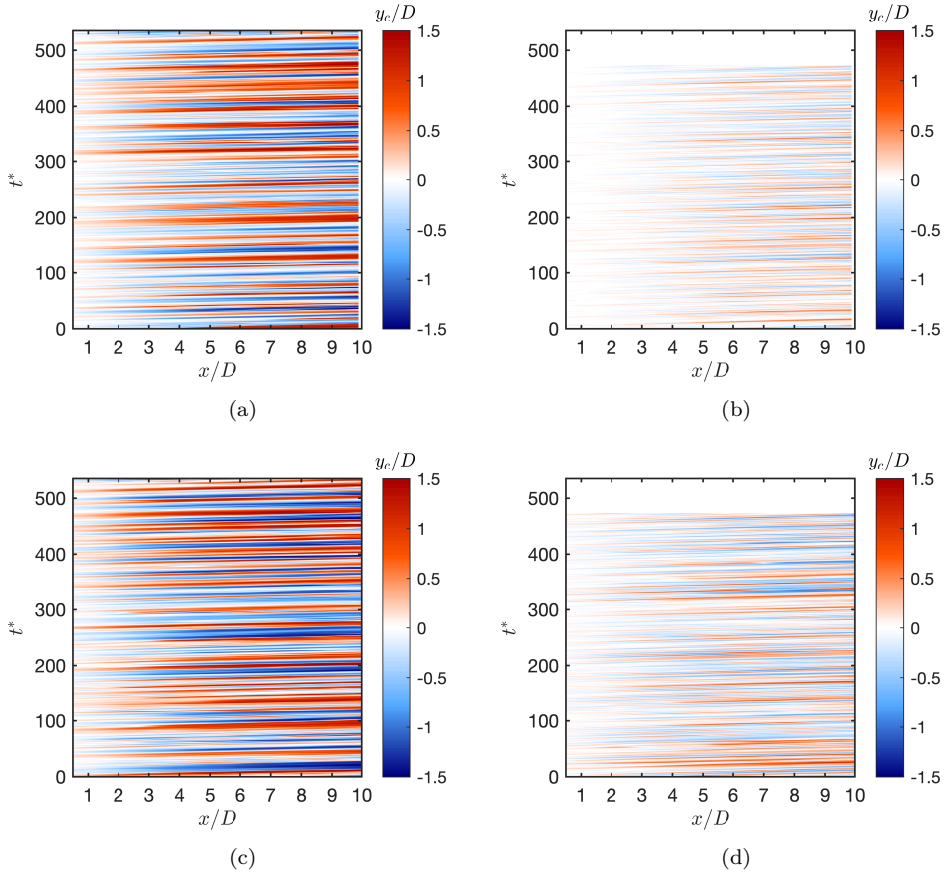



***Figure 7.21:*** *Dimensionless wake centroid position as a function of space and time for the isolated wind turbine (a)-(b) and the third wind turbine (c)-(d) of the row for ABL1 (a)-(c) and ABL2 (b)-(d)*

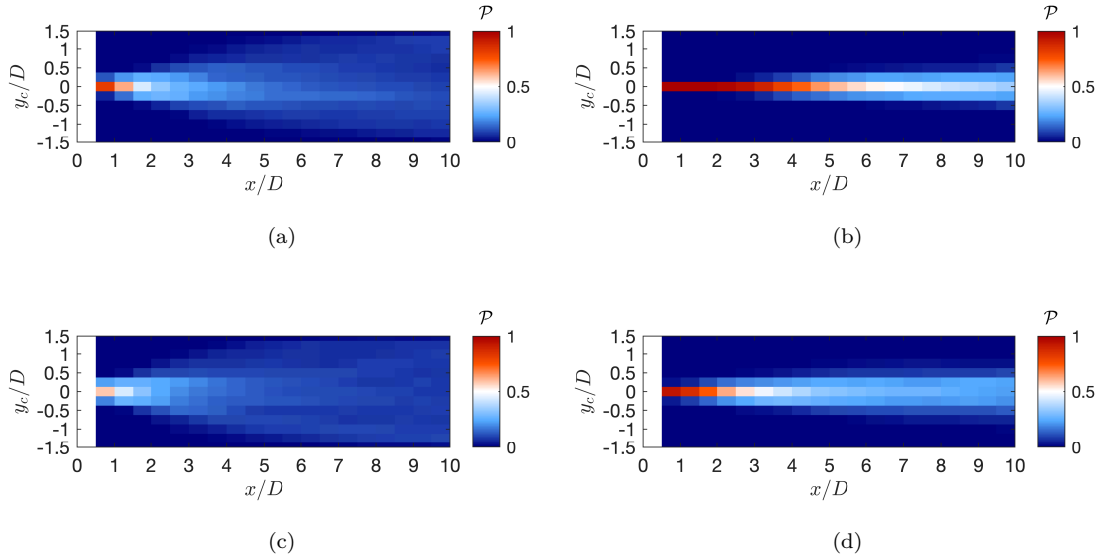



***Figure 7.22:*** *Probability distribution of the binned wake centroid position as a function of space for the isolated wind turbine (a)-(b) and the third wind turbine (c)-(d) of the row for ABL1 (a)-(c) and ABL2 (b)-(d), the bins width is $D/4$*

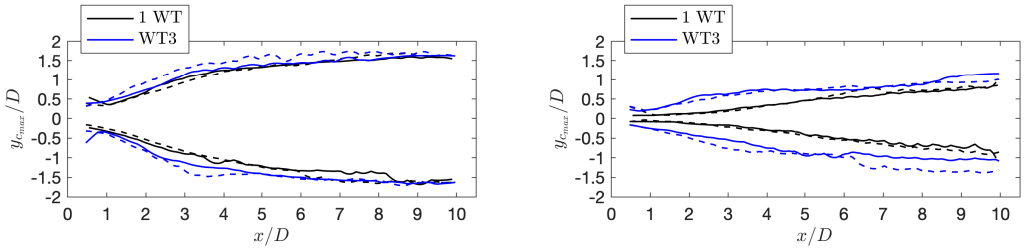



***Figure 7.23:*** *Dimensionless wake centerline envelopes for the isolated wind turbine and the third wind turbine of the row for ABL1 (a) and ABL2 (b); dashed lines correspond to the second set of measurements*

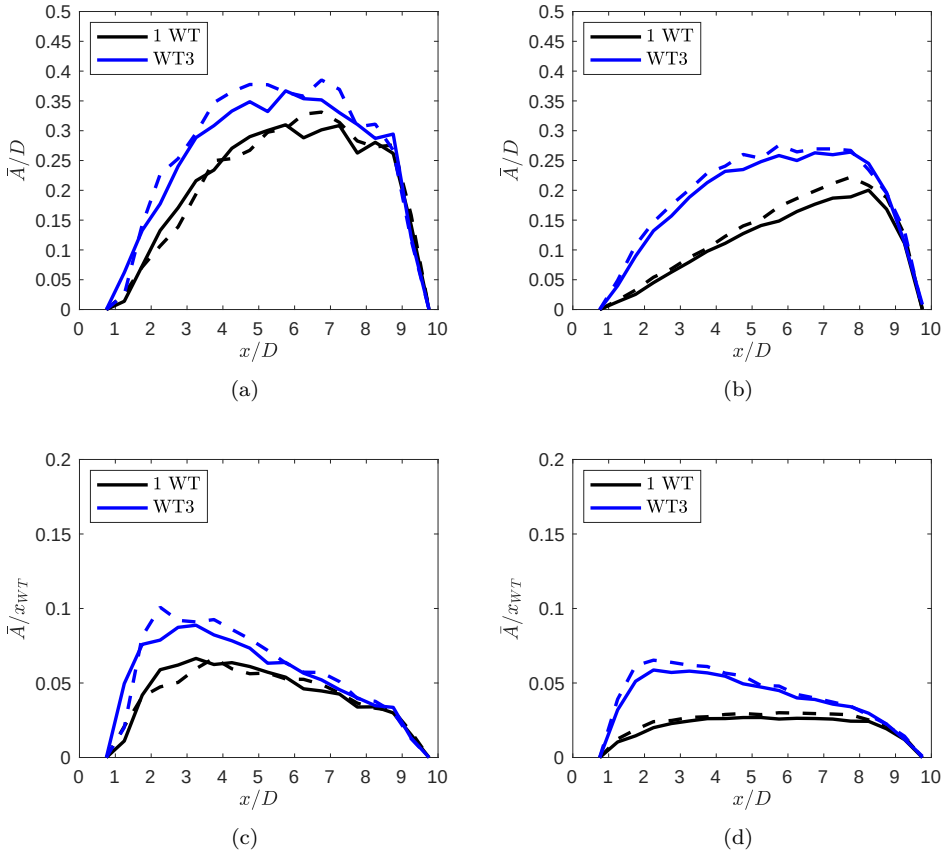



***Figure 7.24:*** *Mean binned wake centerline amplitudes obtained for the isolated wind turbine and the third wind turbine of the row for ABL1 (a)-(c) and ABL2 (b)-(d); dashed lines correspond to the second set of measurements*

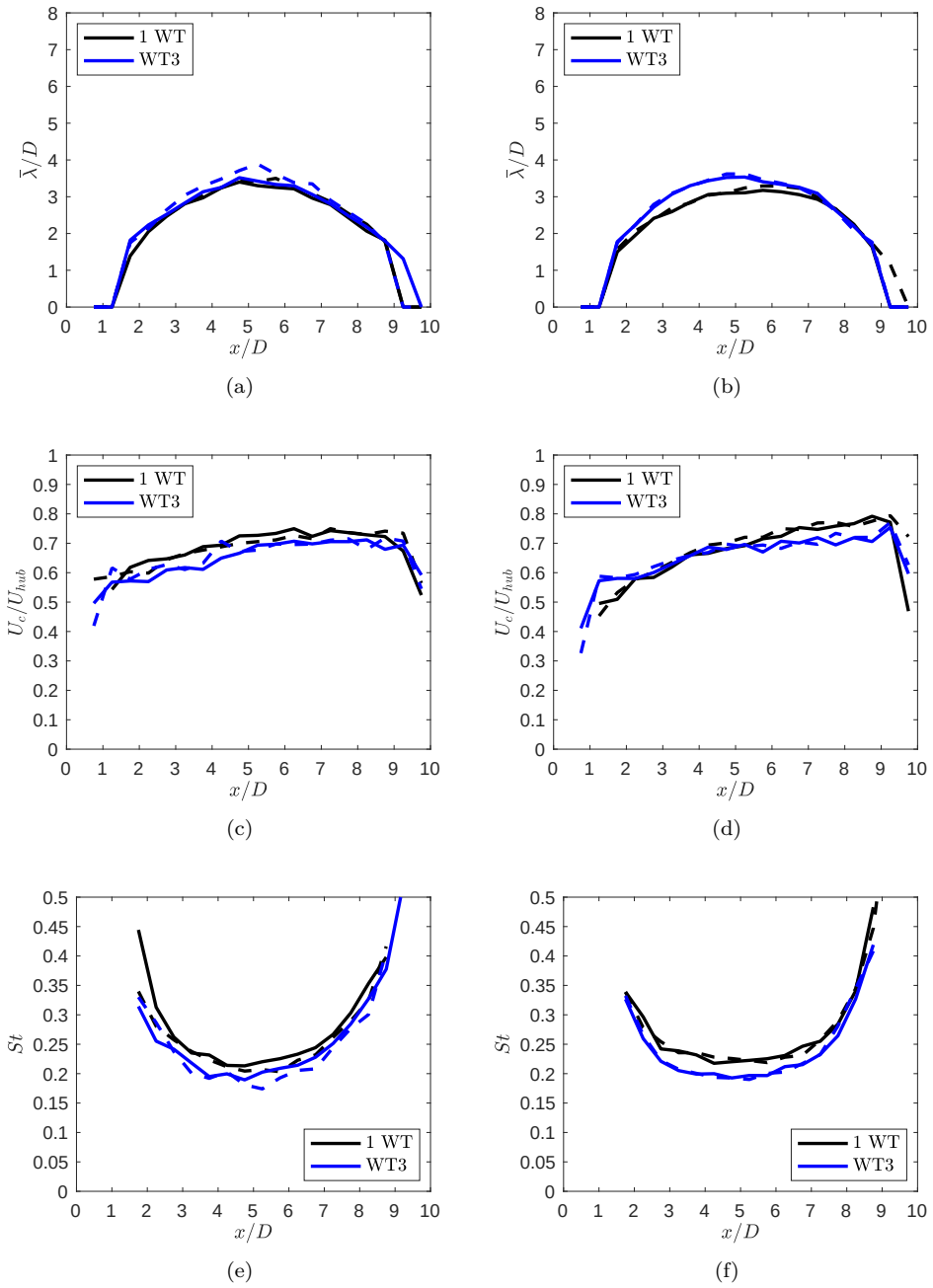



***Figure 7.25:*** *Mean binned wake centerline wavelengths, convective speeds, and Strouhal numbers obtained for the isolated wind turbine and the third wind turbine of the row for ABL1 (a)-(c)-(e) and ABL2 (b)-(d)-(f); dashed lines correspond to the second set of measurements*

### 7.1.3 Wind farm

#### 7.1.3.1 Row vs. wind farm: first and second wind turbines

The aim of this section is to investigate the influence of the lateral rows on the central row of the wind farm. To this end, the characteristics of the central row of the wind farm are compared to those of the row of three wind turbines. The lateral rows do not seem to limit the wake deflections of the central row of the wind farm, especially when examining Fig. 7.26(c) where an extreme wake deflection can be observed for the second wind turbine. As it can be observed in Figs. 7.27 to 7.31, the lateral rows of the wind farm do not impact the wake meandering characteristics, whether for ABL1 or ABL2 . The wake meandering characteristics are therefore the same than for the row of three wind turbines.

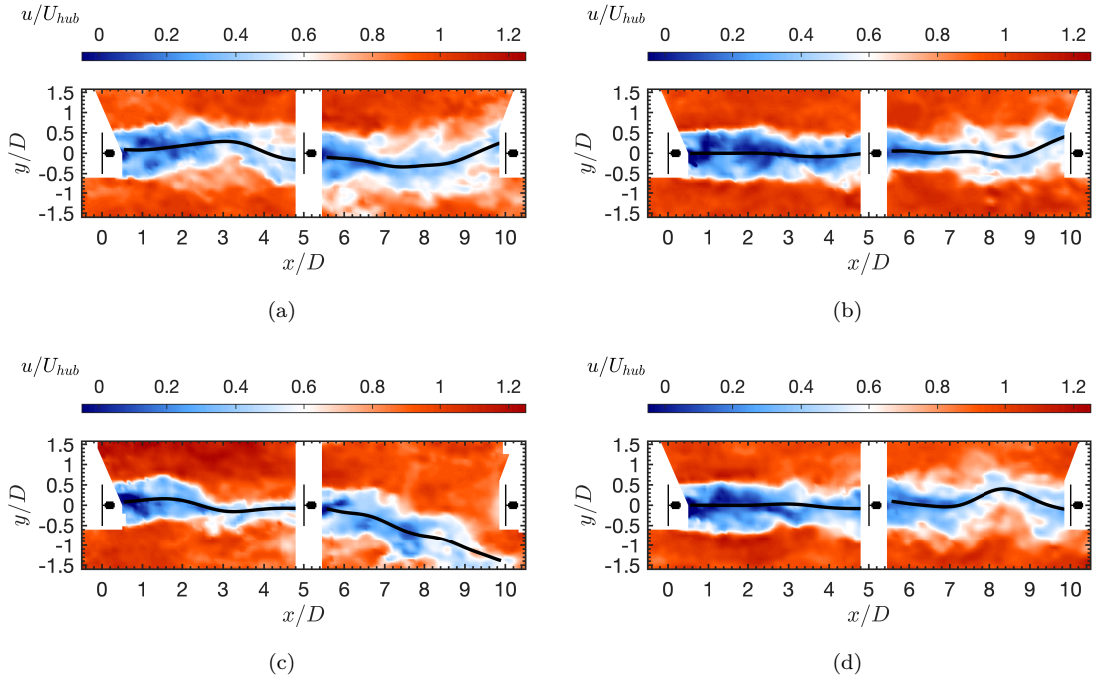



***Figure 7.26:*** *Wake centerline superimposed on the instantaneous streamwise velocity field for the first and second wind turbines of the row (a)-(b) and for the first and second wind turbines of the central row of the wind farm (c)-(d) within ABL1 (a)-(c) and ABL2 (b)-(d)*

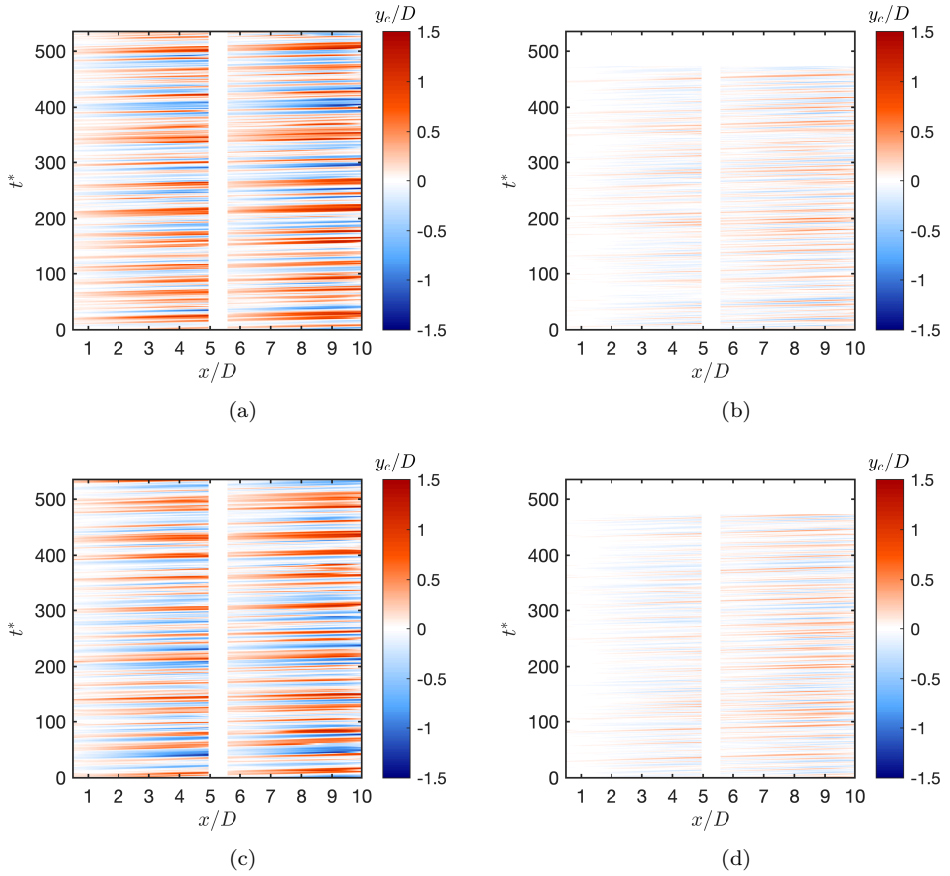



***Figure 7.27:*** *Dimensionless wake centroid position as a function of space and time for the first and second wind turbines of the row (a)-(b) and for the first and second wind turbines of the central row of the wind farm (c)-(d) within ABL1 (a)-(c) and ABL2 (b)-(d)*

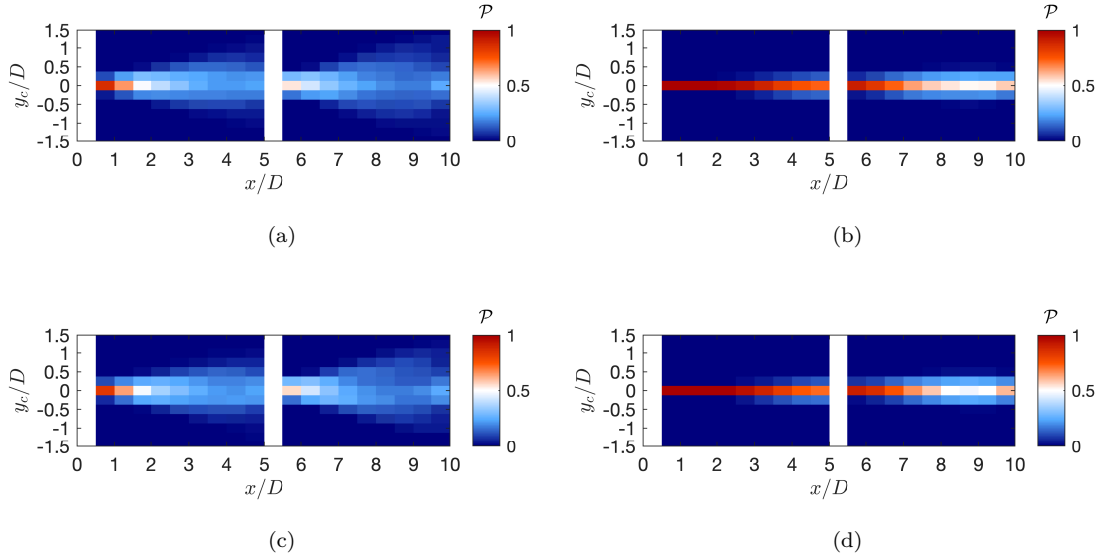



***Figure 7.28:*** *Probability distribution of the binned wake centroid position as a function of space for the first and second wind turbines of the row (a)-(b) and for the first and second wind turbines of the central row of the wind farm (c)-(d) of the row for ABL1 (a)-(c) and ABL2 (b)-(d), the bins width is $D/4$*

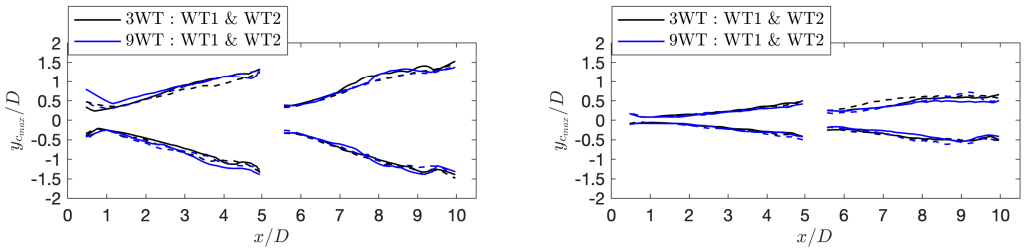



***Figure 7.29:*** *Dimensionless wake centerline envelopes for the first and second wind turbines of the row and of the central row of the wind farm for ABL1 (a) and ABL2 (b); dashed lines correspond to the second set of measurements*

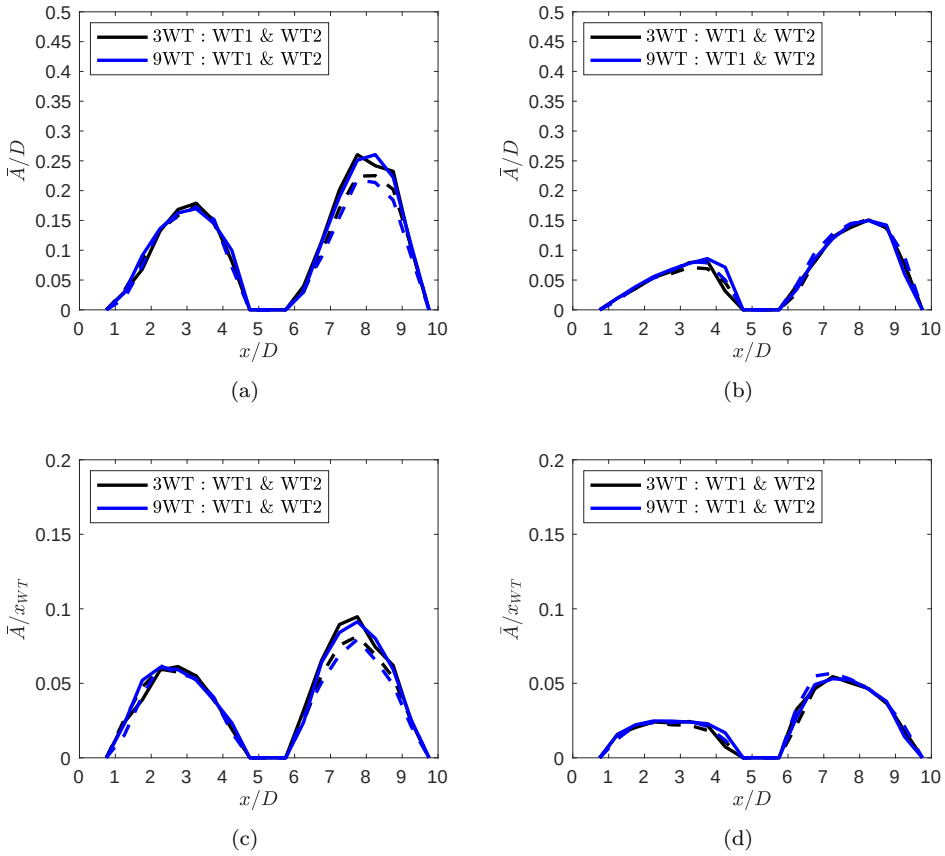



***Figure 7.30:*** *Mean binned wake centerline amplitudes obtained for the first and second wind turbines of the row and of the central row of the wind farm for ABL1 (a)-(c) and ABL2 (b)-(d); dashed lines correspond to the second set of measurements*

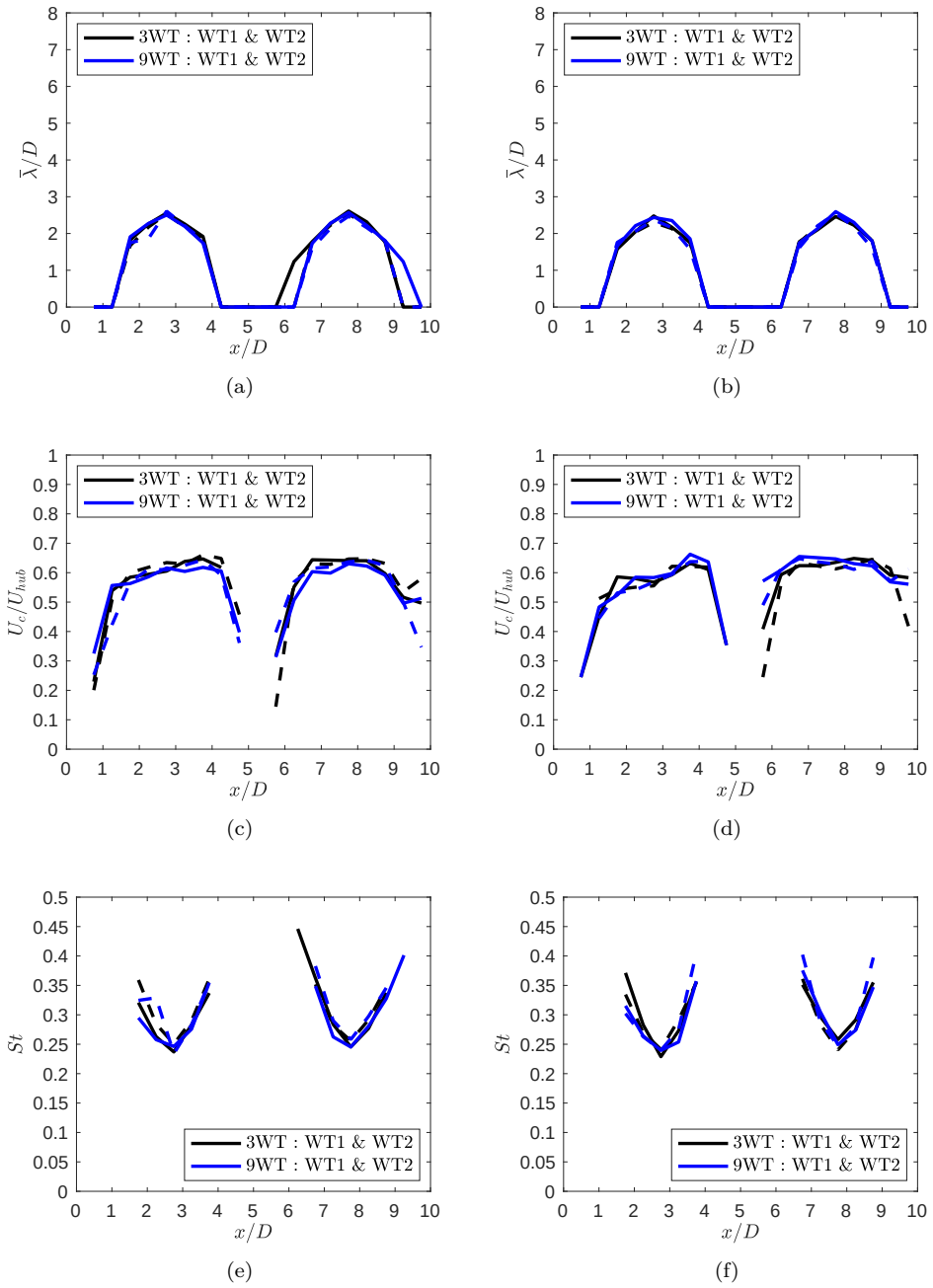



***Figure 7.31:*** *Mean binned wake centerline wavelengths, convective speeds, and Strouhal numbers obtained for the first and second wind turbines of the row and of the central row of the wind farm for ABL1 (a)-(c)-(e) and ABL2 (b)-(c)-(f); dashed lines correspond to the second set of measurements*

#### 7.1.3.2 Row vs. wind farm: third wind turbine

As for the first and second wind turbines of the central row, the lateral rows of the wind farm do not impact the wake meandering characteristics of the third wind turbine (Figs. 7.32 to 7.37).

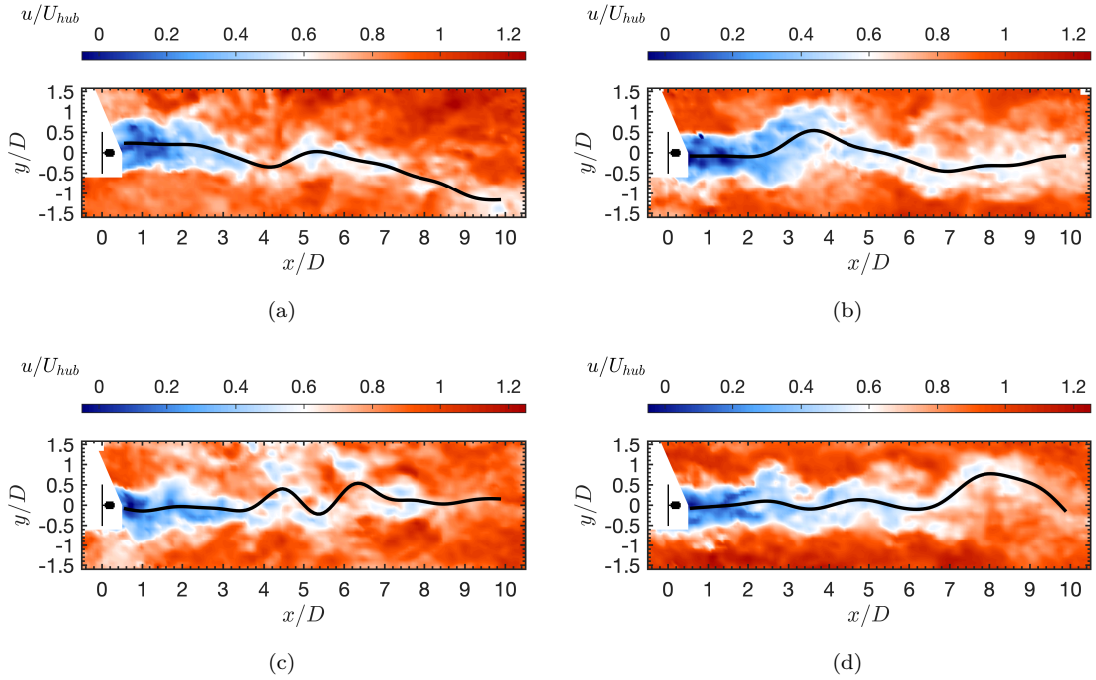



***Figure 7.32:*** *Wake centerline superimposed on the instantaneous streamwise velocity field for the third wind turbine of the row (a)-(b) and for the third wind turbine of the central row of the wind farm (c)-(d) within ABL1 (a)-(c) and ABL2 (b)-(d)*

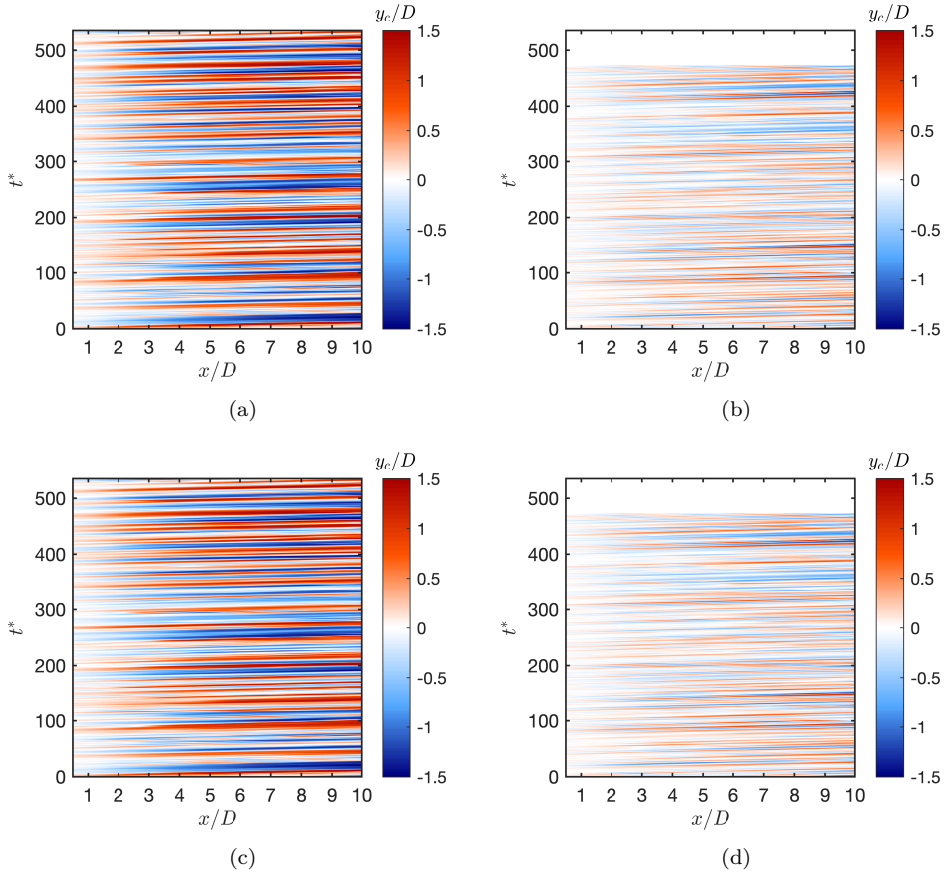



***Figure 7.33:*** *Dimensionless wake centroid position as a function of space and time for the third wind turbine of the row (a)-(b) and for the third wind turbine of the central row of the wind farm (c)-(d) within ABL1 (a)-(c) and ABL2 (b)-(d)*

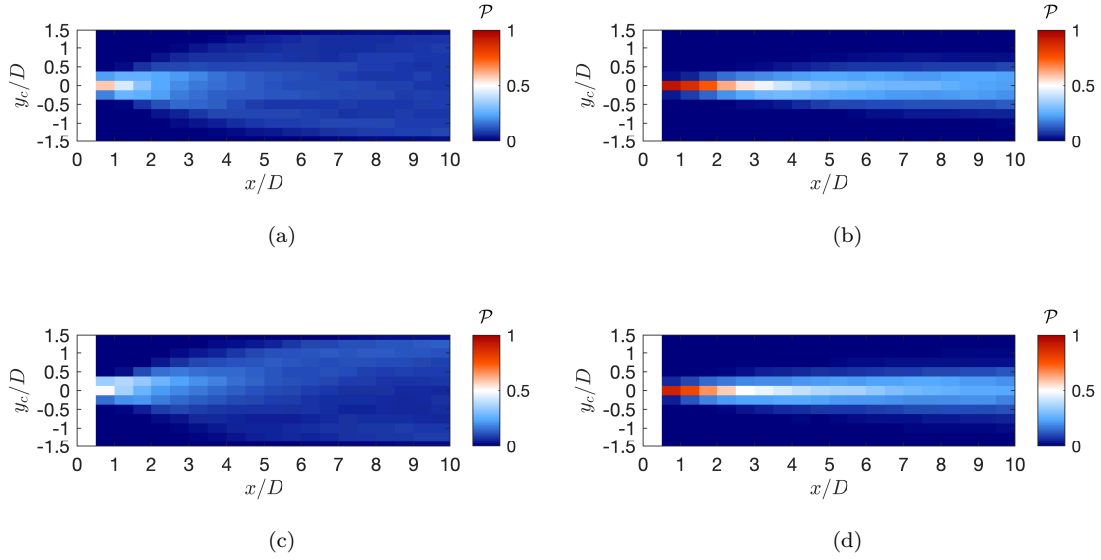



***Figure 7.34:*** *Probability distribution of the binned wake centroid position as a function of space for the third wind turbine of the row (a)-(b) and for the third wind turbine of the central row of the wind farm (c)-(d) of the row for ABL1 (a)-(c) and ABL2 (b)-(d), the bins width is $D/4$*

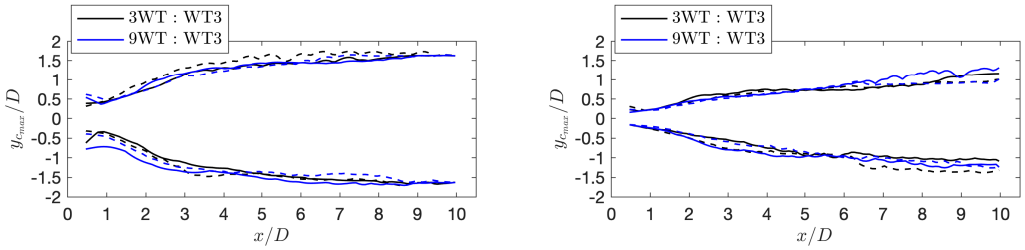



***Figure 7.35:*** *Dimensionless wake centerline envelopes for the third wind turbine of the row for ABL1 (a) and ABL2 (b); dashed lines correspond to the second set of measurements*

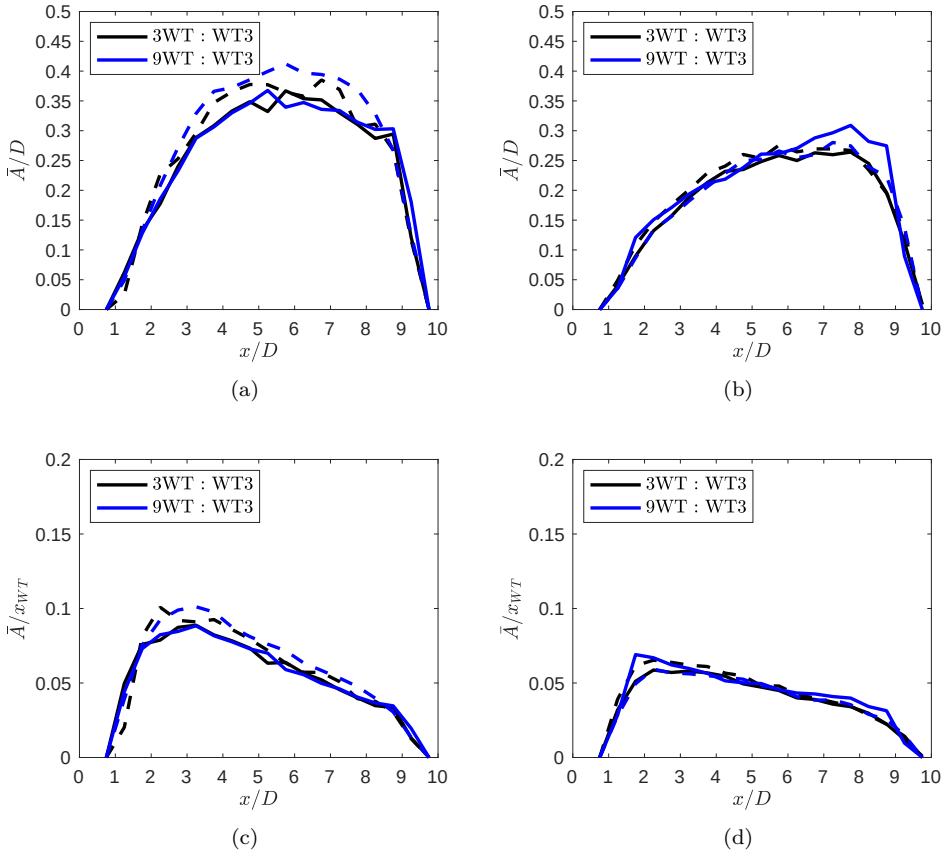



***Figure 7.36:*** *Mean binned wake centerline amplitudes obtained for the third wind turbine of the row and of the central row of the wind farm for ABL1 (a)-(c) and ABL2 (b)-(d); dashed lines correspond to the second set of measurements*

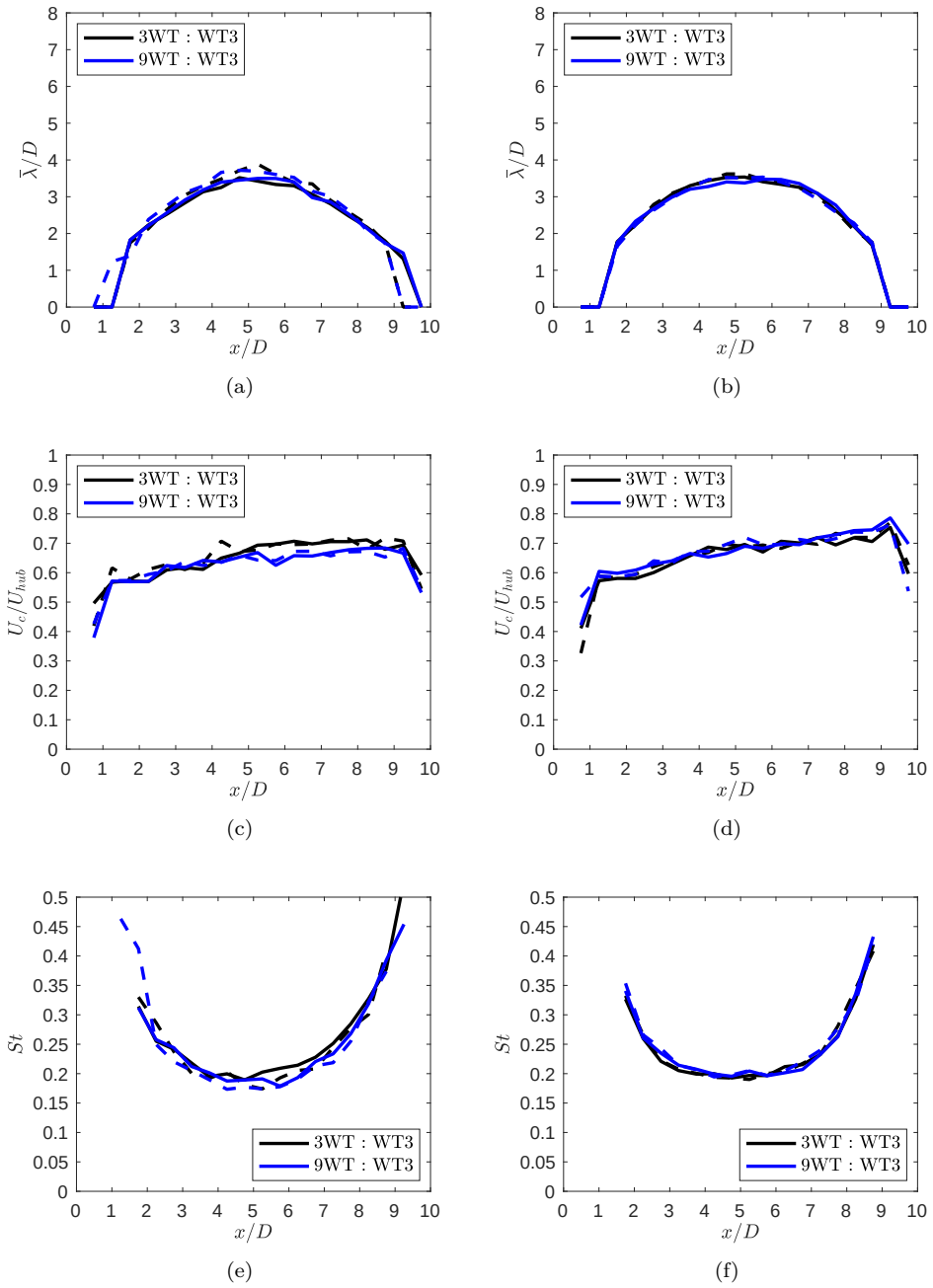



***Figure 7.37:*** *Mean binned wake centerline wavelengths, convective speeds, and Strouhal numbers obtained for the third wind turbine of the row and of the central row of the wind farm for ABL1 (a)-(c)-(e) and ABL2 (b)-(d)-(f); dashed lines correspond to the second set of measurements*

### 7.1.4 Porous disks

After studying the influence of the operating conditions for an isolated wind turbine in Section 7.1.1.3, this section covers the influence of the scale model itself. For the sake of practicality and cost reduction, the rotor of the isolated wind turbine was substituted by several porous disk with solidities $\sigma = 56\%$, $\sigma = 44\%$, and $\sigma = 36\%$. Figure 7.38 shows that even with the smallest solidity of $\sigma = 36\%$, the wake meandering is still present. The wake centroid deflections decrease when the solidity decreases for the porous disks within ABL2, while there is no clear trend for ABL1 (Fig. 7.39). While the probability distributions of the wake centroid position are very similar for ABL1, they show that, within ABL2, the wake centroids stay over a longer distance around $y/D = 0$ when the solidity is smaller (Fig. 7.40).

For ABL1, there is no clear trend concerning the effect of solidity on the extreme deflections of the wake while they decrease when the solidity decreases for ABL2 (Fig. 7.41). In terms of wake meandering amplitude, the influence of the solidity is not clear for ABL1, while the amplitude clearly decreases when the solidity of the disks decreases for ABL2 (Fig. 7.42). As for the isolated bladed model, the wake meandering amplitude of the porous disk with a solidity $\sigma = 56\%$ increases linearly with the downstream distance from the rotor. For the lower solidities, this increase is weaker.

Concerning the wavelengths (Fig. 7.43), they are of the same size ($2.75 \lesssim \lambda/D \lesssim 3.5$ for ABL1 and $2.5 \lesssim \lambda/D \lesssim 3.25$ for ABL2) whether for the rotating model or the porous disks with $\sigma = 56\%$ and $\sigma = 44\%$, and are larger ($2.75 \lesssim \lambda/D \lesssim 3.75$ for ABL1 and $2.5 \lesssim \lambda/D \lesssim 3.5$ for ABL2) for the porous disk with $\sigma = 36\%$. Concerning the convective speeds, they are smaller for the isolated wind turbine and then increase when the solidity decreases. This is clear in the near wake while the differences are reduced in the far wake, especially for ABL1 because of the larger mixing due to the higher turbulence intensity. Assuming that the Taylor's frozen turbulence hypothesis is applicable, it leads to $0.20 \lesssim St \lesssim 0.27$ for the porous disks within ABL1 and to $0.22 \lesssim St \lesssim 0.27$ within ABL2 (Figs. 7.43(e) and 7.43(f)).

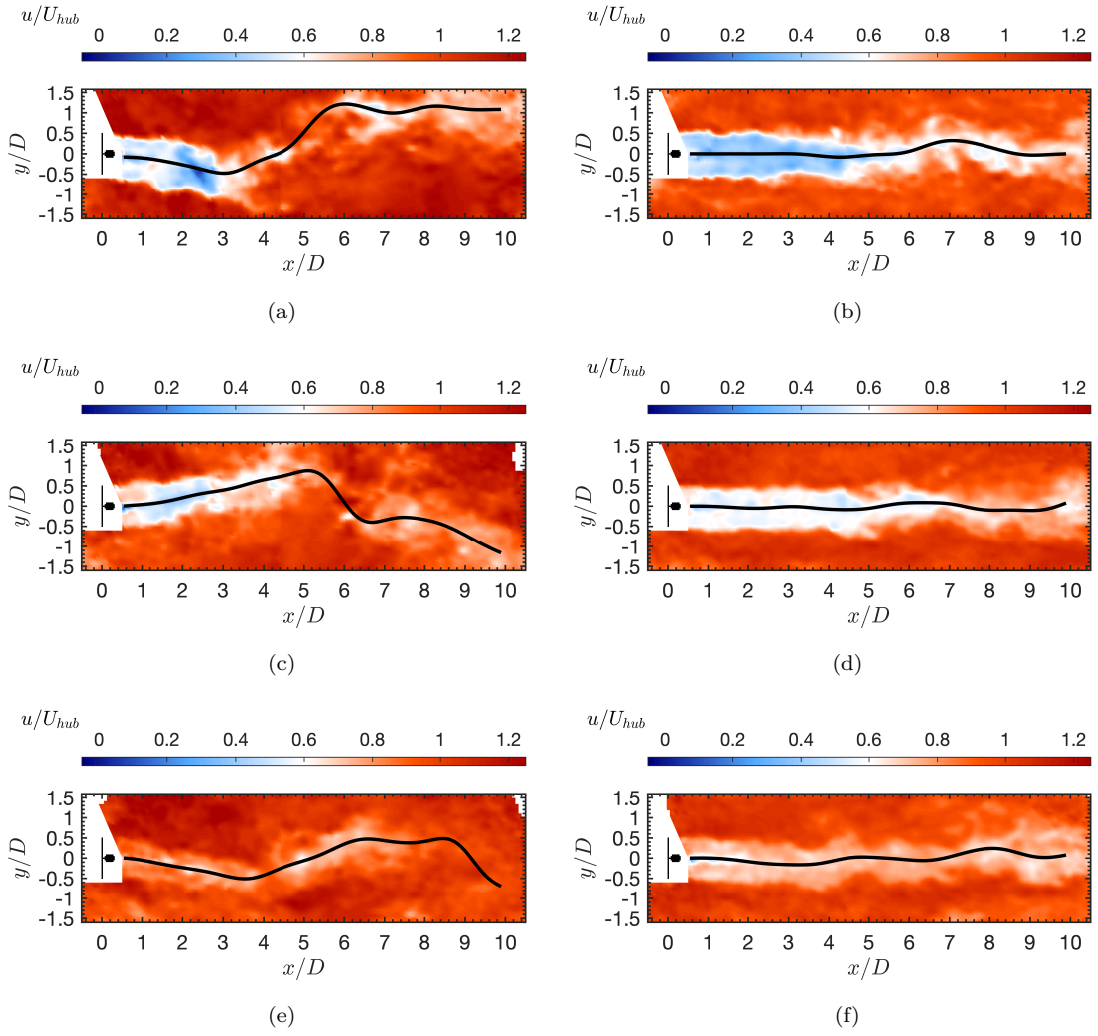



***Figure 7.38:*** *Wake centerline superimposed on the instantaneous streamwise velocity field for the porous disk subjected to ABL1 (a)-(c)-(e) and ABL2 (b)-(d)-(f) for different disk solidities: $\sigma$ = 56% (a)-(b), $\sigma$ = 44% (c)-(d), $\sigma$ = 36% (e)-(f)*

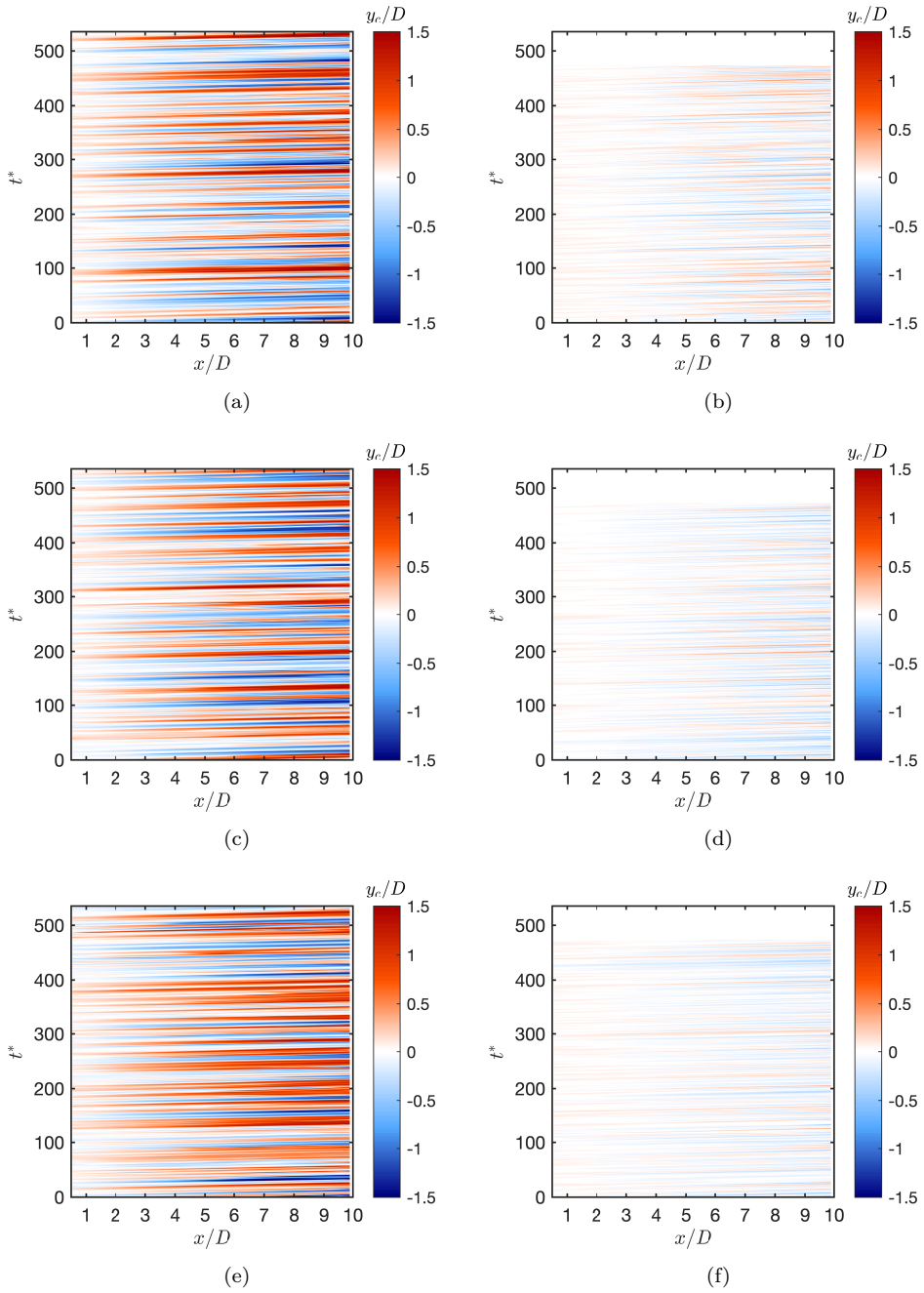



***Figure 7.39:*** *Dimensionless wake centroid position as a function of space and time for the porous disk subjected to ABL1 (a)-(c)-(e) and ABL2 (b)-(d)-(f) for different disk solidities: $\sigma = 56\%$ (a)-(b), $\sigma = 44\%$ (c)-(d), $\sigma = 36\%$ (e)-(f)*

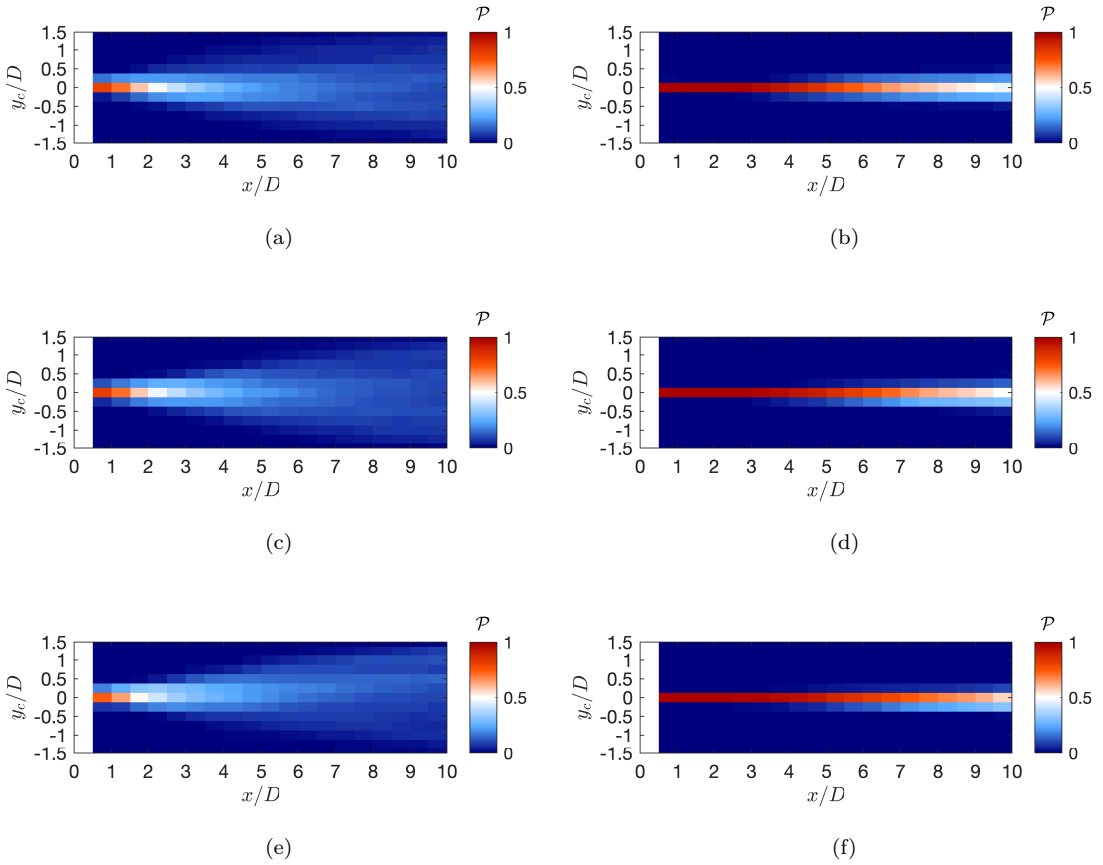



***Figure 7.40:*** *Probability distribution of the binned wake centroid position as a function of space for ABL1 (a)-(c)-(e) and ABL2 (b)-(d)-(f) for different disk solidities: $\sigma = 56\%$ (a)-(b), $\sigma = 44\%$ (c)-(d), $\sigma = 36\%$ (e)-(f), the bins width is $D/4$*

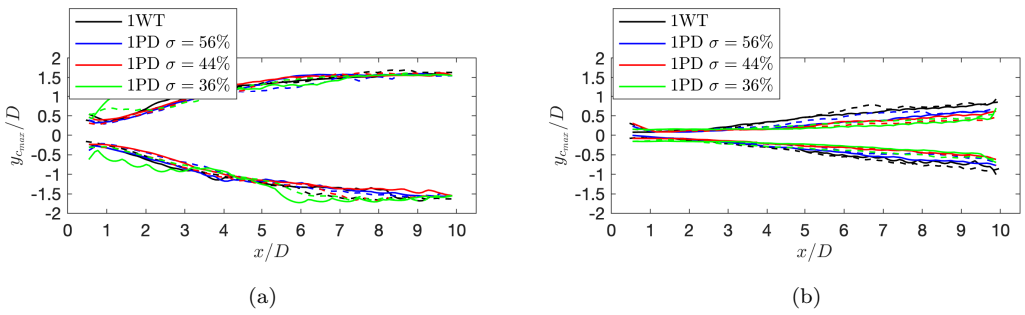



***Figure 7.41:*** *Dimensionless wake centerline envelopes for ABL1 (a) and ABL2 (b) for different disk solidities: $\sigma = 56\%$, $\sigma = 44\%$, and $\sigma = 36\%$; dashed lines correspond to the second set of measurements*

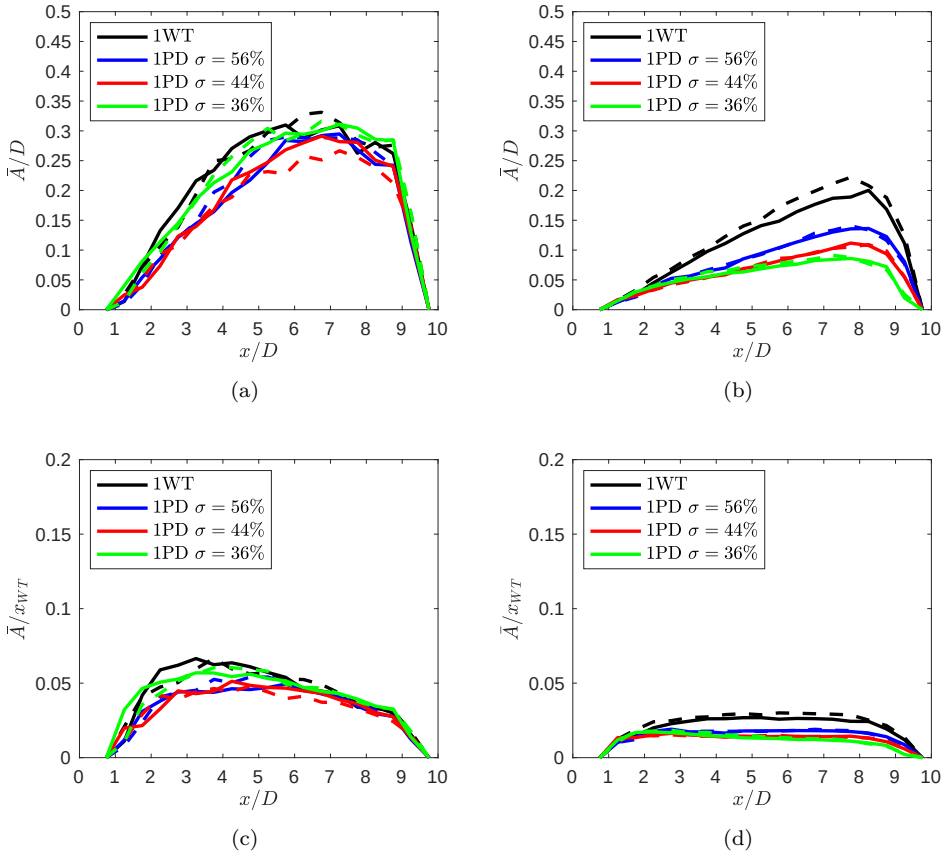



***Figure 7.42:*** *Mean binned wake centerline amplitudes for ABL1 (a)-(c) and ABL2 (b)-(d) for different disk solidities: $\sigma = 56\%$, $\sigma = 44\%$, and $\sigma = 36\%$; dashed lines correspond to the second set of measurements*

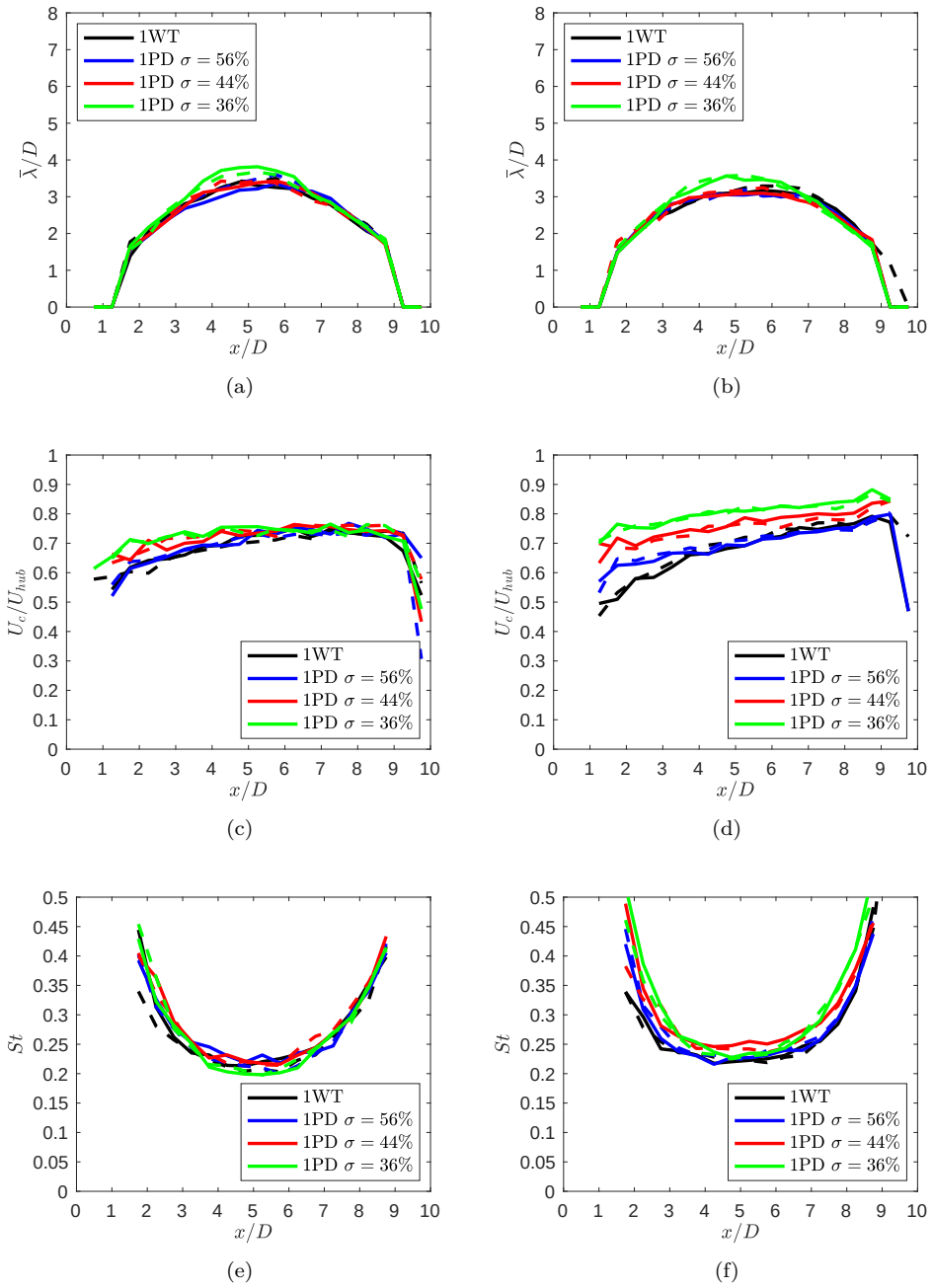



***Figure 7.43:*** *Mean binned wake centerline wavelengths, convective speeds, and Strouhal numbers for ABL1 (a)-(c)-(e) and ABL2 (b)-(d)-(f) for different disk solidities: $\sigma = 56\%$, $\sigma = 44\%$, and $\sigma = 36\%$; dashed lines correspond to the second set of measurements*

## 7.2 Numerical results

### 7.2.1 Numerical setup

Numerical simulations were performed at wind tunnel scale in order to be able to perform a direct comparison between the experimental and the numerical results. The configuration simulated is the isolated wind turbine subjected to ABL1 and ABL2. The numerical simulations were performed with the FD4 code which enables to model ABL flows. The computational domain size is $14D \times 8D \times 8D$. The rotor of the wind turbine scale model was modeled using the advanced actuator disk presented in Section 2.1.2 with a resolution of 16 points per rotor diameter. The wind turbine scale model data provided to the FD4 code are the geometrical properties of the blades that were already presented in Appendix C, the aerodynamic coefficients of the blade profile, presented in Section 5.1.3, and the rotational speed of the rotor. The rotational speed of the rotor was extracted from the TR-PIV measurements campaigns performed for the isolated wind turbine. It was set up to 7154 RPM for the ABL1 case and to 6048 RPM for the ABL2 case, what corresponds to $TSR = 7.0$ and $TSR = 6.7$, respectively. The time step was set up such that $\Delta t \cdot \frac{U_{hub}}{D} = 5 \cdot 10^{-3}$, leading to $CFL \simeq 0.1$.

Concerning the inflow, the strategy employed consists in superimposing a logarithmic velocity profile on the turbulence box generated with the Mann's algorithm. The parameters used for the logarithmic law were obtained from the 3C-HWA measurements presented in Section 5.3. Since the laws of the wall implemented in the FD4 code use $\kappa = 0.38$, the same value of $\kappa$ was used for the logarithmic law (Eq. (5.5)) for consistency reasons. Therefore, the logarithmic-law parameters that were used for the numerical simulations are not those presented in Table 5.3 but in Table 7.2.

| | ABL1 | ABL2 |
|---|---|---|
| $\kappa$ | 0.38 | 0.38 |
| $d$ | 0 | 0 |
| $u_*$ $[m/s]$ | 0.36 | 0.42 |
| $z_0$ $[m]$ | $1.5 \cdot 10^{-5}$ | $1.4 \cdot 10^{-4}$ |

***Table 7.2:*** *ABL properties used in the FD4 code for the logarithmic law (Eq. (5.5))*

Concerning the parameters used to generate the turbulent boxes, they were adapted in order to obtain a numerical inflow matching as good as possible with the experimental inflow. While the experimental data were acquired during ten seconds, only one passage of the turbulent inflow box through the computational domain was used, i.e. $t = 32D/U_\infty$ equals to 0.60 s for ABL1 and to 0.68 s for ABL2. The acquisition of the numerical data was started after two flow-through times to ensure that the flow was developed.

In the next figures, the numerical and experimental inflows are compared in terms of velocity (Fig. 7.44(a) and 7.44(b)), turbulence intensity (Figs. 7.44(c), 7.44(d) and 7.45) and integral length scales (Fig. 7.46) profiles. The experimental inflows correspond to the 3C-HWA measurements presented in Section 5.3 while the numerical inflows were extracted from the computational domain at $x/D = -2.5$ in the vertical plane passing through the hub. The numerical velocity profiles match very well with the experimental data, especially in the rotor region (Fig. 7.44(a) and 7.44(b)). The logarithmic law fit described in Section 5.3 was indeed performed such as to obtain the best fit between the logarithmic law and the experimental data in the region close to the rotor. Concerning the turbulence intensities (Figs. 7.44(c), 7.44(d) and 7.45), several trials of inflow settings revealed the importance of the horizontal turbulence intensity component ($I_v$) on the wake meandering characteristics. Therefore, the parameters of the inflows were set up to obtain, for this component, the best match possible with the experimental data. A very good agreement could be obtained for ABL1 but not for ABL2 because of some restriction in the generation of the turbulent inflow with the Mann's algorithm. Concerning the integral length scales, the parameters were set up to obtain

a good agreement for the streamwise integral length scales (Fig. 7.46).

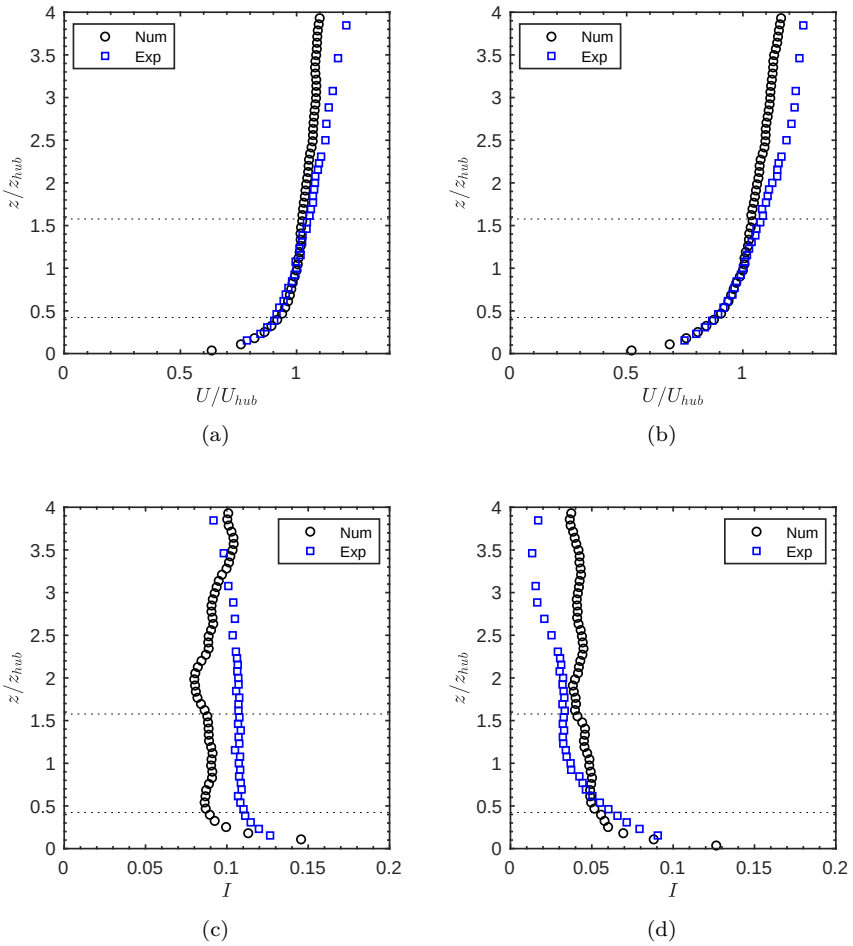



***Figure 7.44:*** *Velocity (a)-(b) and turbulence intensity (c)-(d) profiles for ABL1 (a)-(c) and ABL2 (b)-(d)*

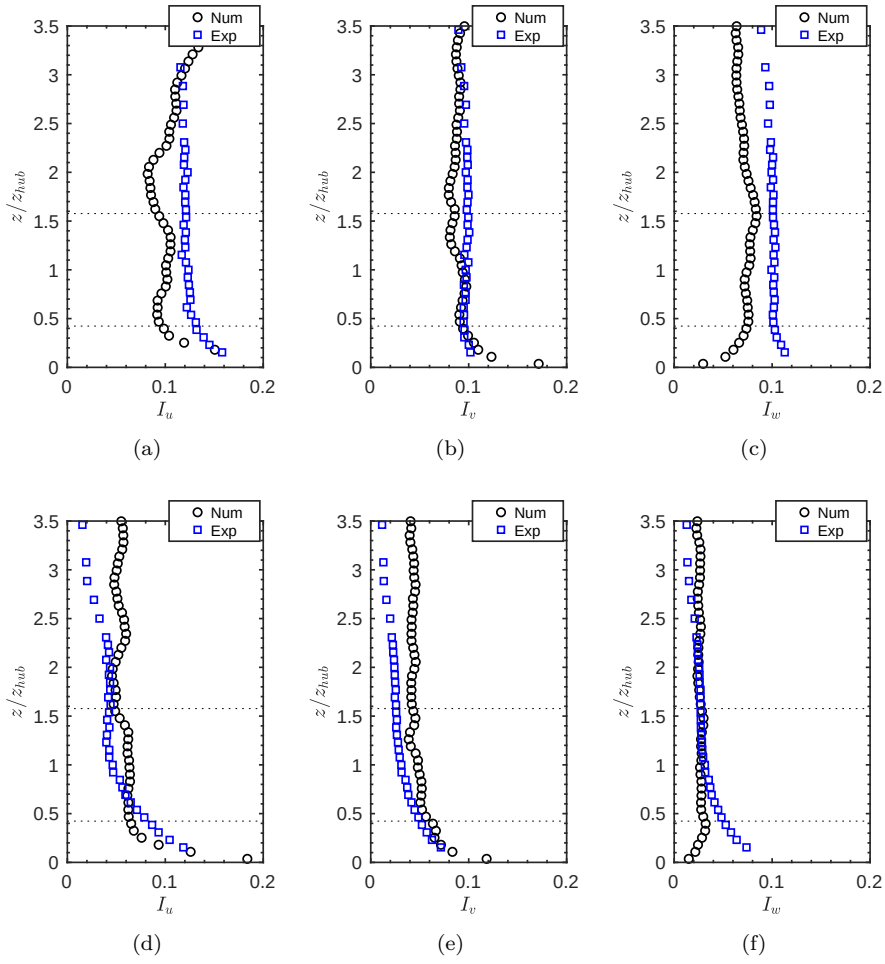



***Figure 7.45:*** *Profiles of the turbulence intensity components contained in the inflow for ABL1 (a)-(b)-(c) and ABL2 (d)-(e)-(f)*

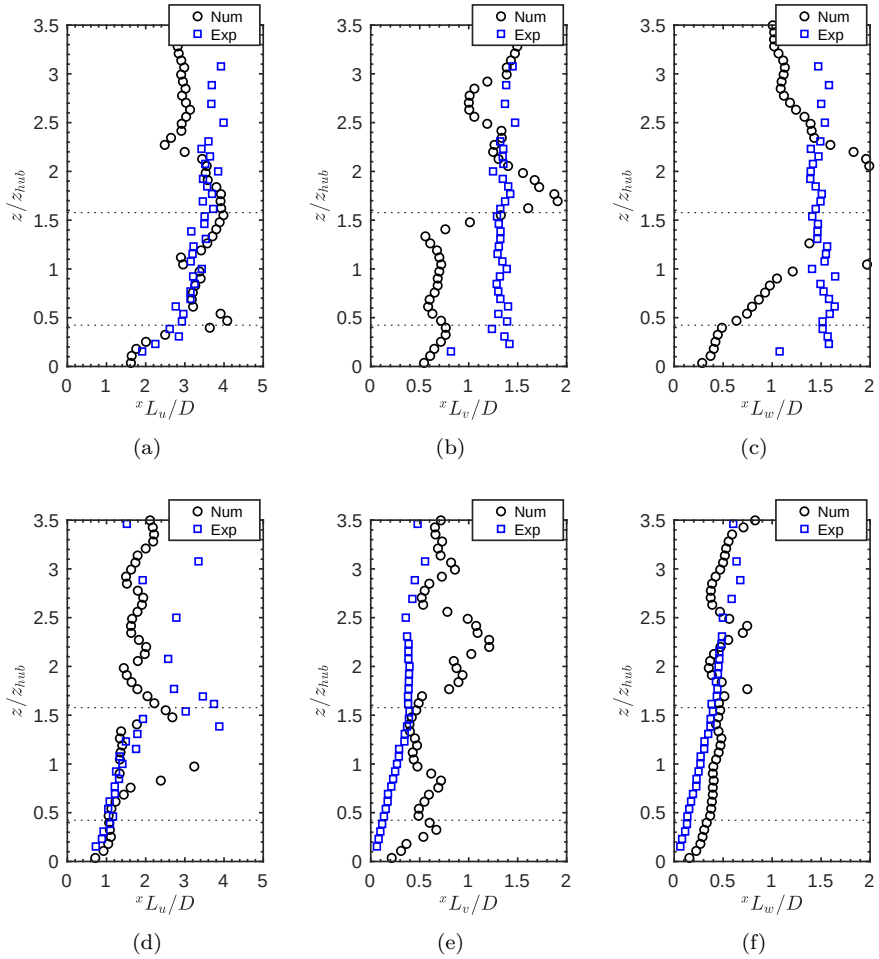



***Figure 7.46:*** *Integral length scales of the longitudinal (a)-(d), lateral (b)-(e) and vertical (c)-(f) components in the longitudinal direction for ABL1 (a)-(b)-(c) and ABL2 (d)-(e)-(f)*

### 7.2.2 Comparison between numerical and experimental results

The statistics of the numerical and experimental wakes are compared in terms of averaged streamwise velocity components (Figs. 7.47 and 7.48) and turbulence intensity (Figs. 7.49 and 7.50). As it can be observed, the wakes present similar shapes but different velocity deficits, especially in the near wake (Figs. 7.47 and 7.48). The velocity deficits are indeed much weaker for the numerical cases, whatever the ABL. This is most probably due to the modeling of the wind turbine scale model rotor, the rotor extracting less energy from the wind in the numerical simulations. The wind turbine rotor was indeed modeled based on the aerodynamic coefficients determined experimentally on a scaled up airfoil, scale 3.4:1 based on the blade chord at $2R/3$. Nevertheless, the 2D aerodynamic coefficients measured on this airfoil can vary from the actual aerodynamic coefficients of the blades because of 3D and rotational effects [91]. Concerning the turbulence intensity (Figs. 7.49 and 7.50), the increase in turbulence intensity in the wake of the wind turbine is much weaker for the numerical cases; the shear layers are particularly much weaker for the numerical cases, whatever the ABL.

Even if the wakes obtained numerically are weaker compared to the wakes obtained experimentally, the wake meandering phenomenon was nevertheless studied for the numerical cases and compared to the experimental data. As for the experimental data, the tracking of the wake centerline was performed in the horizontal plane at hub height for the numerical cases. Figure 7.51 shows instantaneous streamwise velocity fields on which the wake centerlines are superimposed. As it can

be observed, the wake meandering is clearly present for the numerical simulations. Concerning the wake centroids deflections (Fig. 7.52), the numerical results show larger wake centroids deflections for ABL1 than for ABL2, as it was also observed experimentally. Furthermore, the intensity of the deflections obtained from the numerical data are in good agreement with the experimental results. The probability distributions of the binned wake centroid positions as a function of space (Fig. 7.53) show that, for ABL1, the wake has the tendency to remain longer around $y = 0$ in the numerical simulations than for the experiments. For ABL2, there is a pretty good agreement in the probability distribution of the binned wake centroid positions obtained numerically and experimentally. Note that the asymmetry observed for the numerical results is due to very large integral length scales contained in the long turbulent boxes generated with the Mann's algorithm. In terms of wake centerline envelopes (Fig. 7.54), there is an underestimation of the maximal wake centerline deflections obtained numerically with ABL1 up to $x/D = 7$, while there is a good agreement between the numerical and experimental data beyond $x/D = 7$. Concerning ABL2, there is a very good match in the wake centerline envelopes. As it can be observed in Figs. 7.55(a) and 7.55(b), there is a good agreement between the numerical and experimental mean binned wake centerline amplitudes. The fact that the wake meandering amplitude obtained numerically is slightly larger for ABL2 can be justified by the larger turbulence intensity component $I_v$ contained in the numerical inflow representing ABL2. Regarding the mean binned wake centerline wavelengths (Fig. 7.55(c)), they are larger for the numerical simulations, which is consistent with the convective speeds (Fig. 7.7) that are also larger for the numerical cases since the velocity deficit are weaker. It results therefore in weaker Strouhal numbers ($0.16 \lesssim St \lesssim 0.22$) from the numerical simulations (Fig. 7.55(e)).

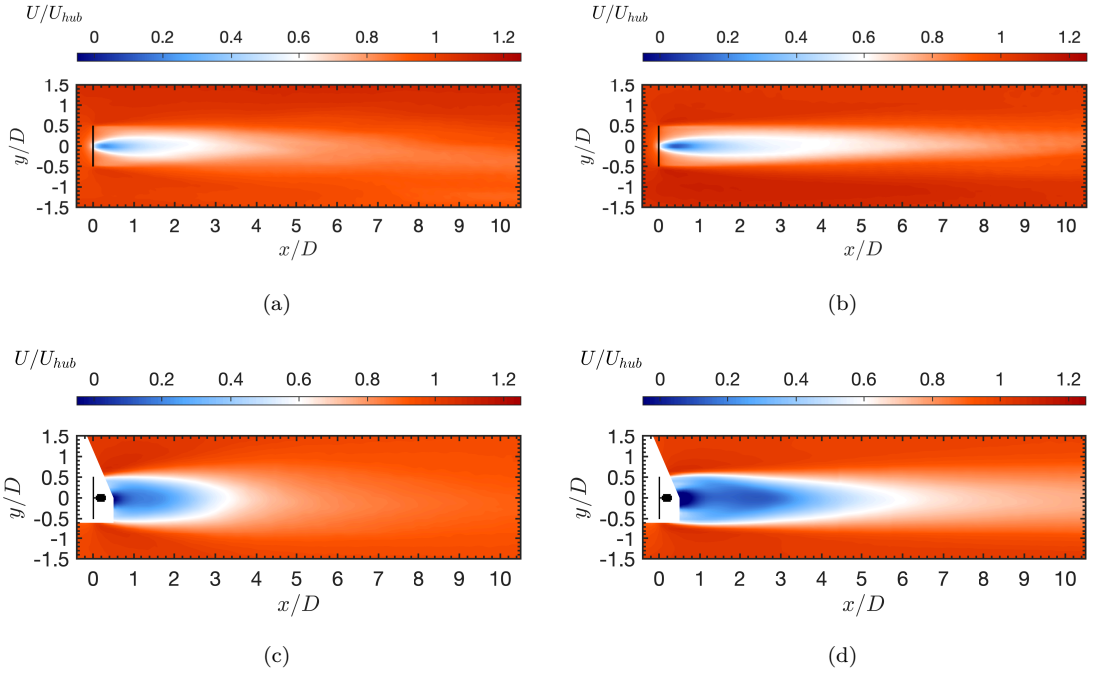



***Figure 7.47:*** *Normalized averaged velocity field in the horizontal plane located at hub height obtained with the FD4 code (a)-(b) and experimentally (c)-(d) for the isolated wind turbine subjected to ABL1 (a)-(c) and ABL2 (b)-(d)*

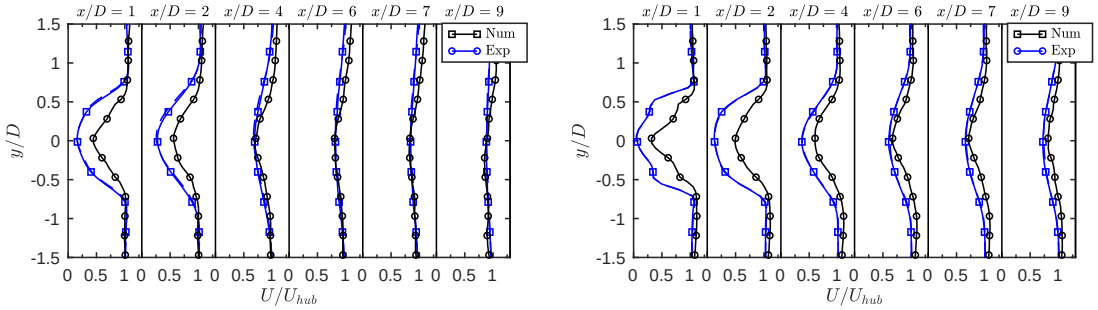



***Figure 7.48:*** *Normalized velocity profiles at several downstream locations in the wake of the isolated wind turbine subjected to ABL1 (a) and ABL2 (b); dashed lines without symbol correspond to the second set of measurements*

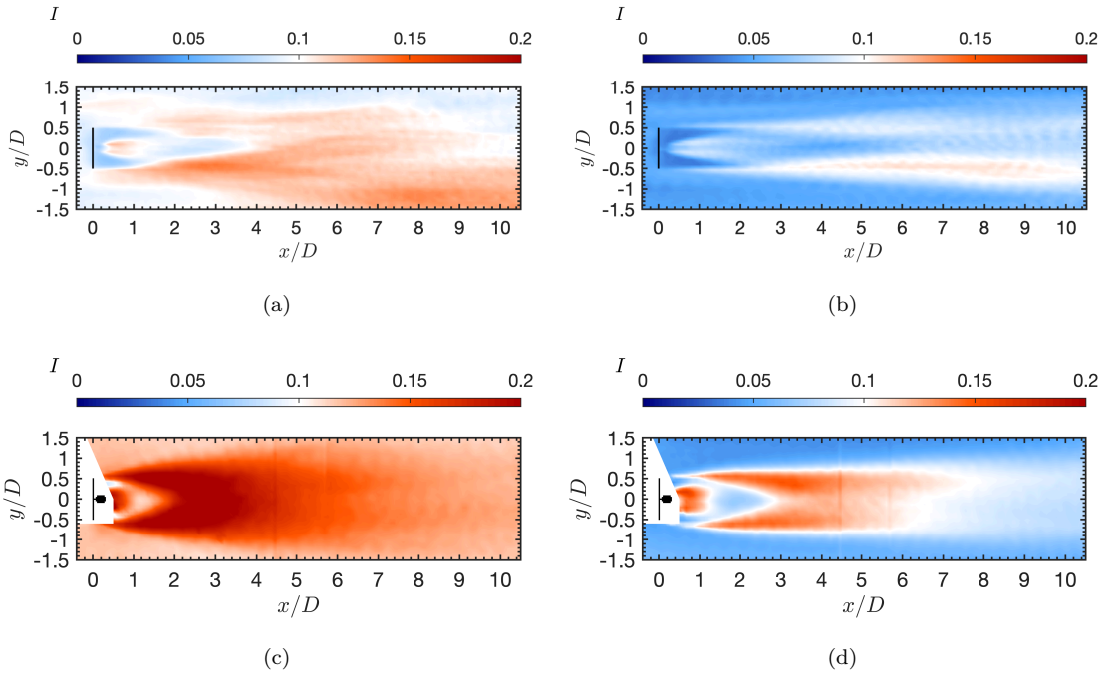



***Figure 7.49:*** *Turbulence intensity field in the horizontal plane located at hub height obtained with the FD4 code (a)-(b) and experimentally (c)-(d) for the isolated wind turbine subjected to ABL1 (a)-(c) and ABL2 (b)-(d)*

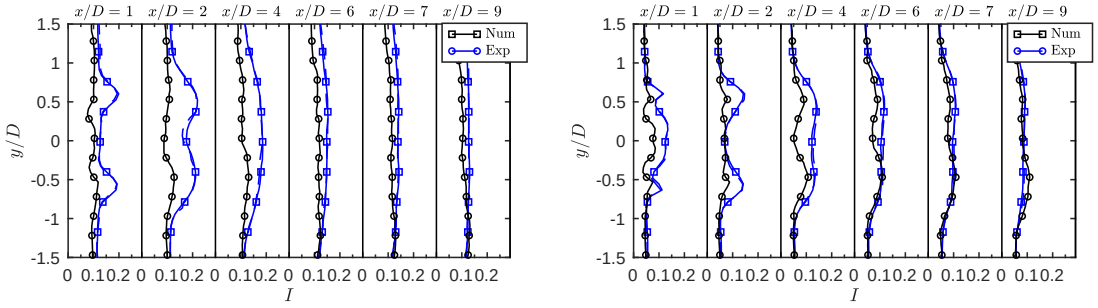



***Figure 7.50:*** *Turbulence intensity (a)-(b) profiles at several downstream locations in the wake of the isolated wind turbine subjected to ABL1 (a) and ABL2 (b); dashed lines without symbol correspond to the second set of measurements*

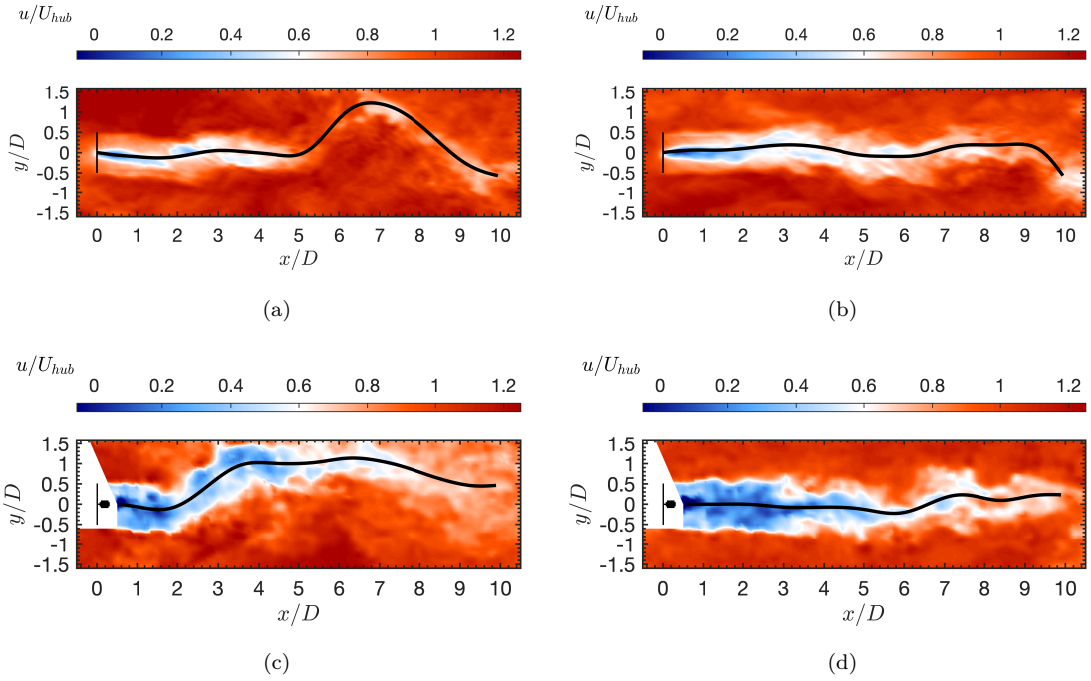



***Figure 7.51:*** *Wake centerline superimposed on the instantaneous streamwise velocity field obtained with the FD4 code (a)-(b) and experimentally (c)-(d) for the isolated wind turbine subjected to ABL1 (a)-(c) and ABL2 (b)-(d)*

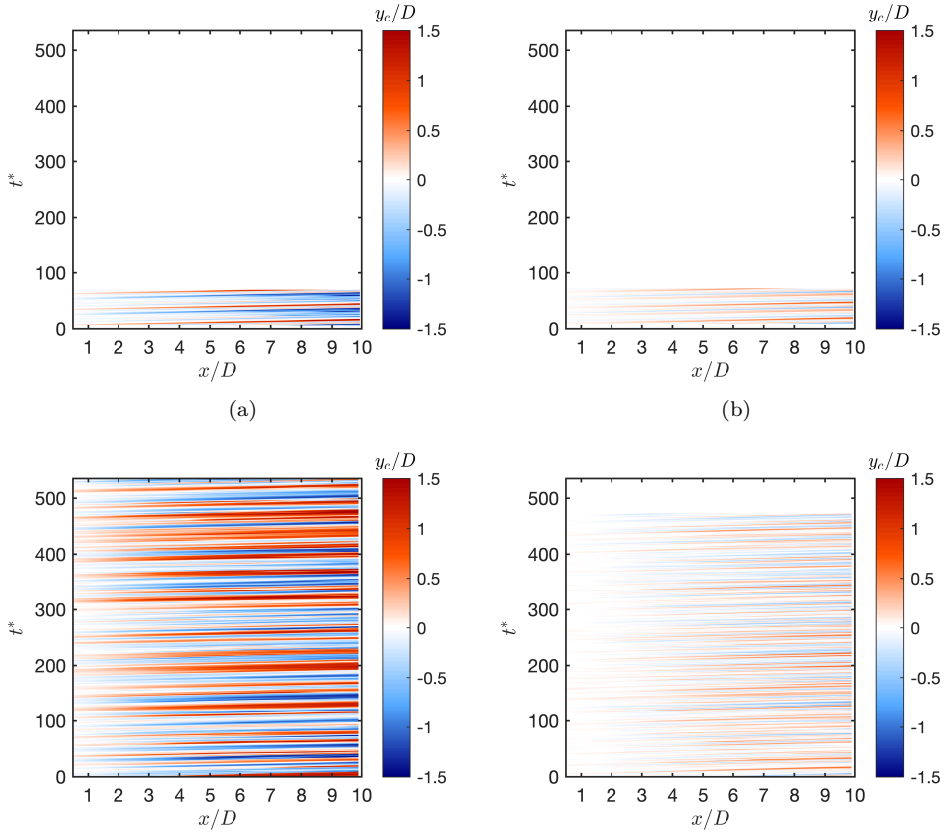



***Figure 7.52:*** *Dimensionless wake centroid position as a function of space and time obtained with the FD4 code (a)-(b) and experimentally (c)-(d) for the isolated wind turbine subjected to ABL1 (a)-(c) and ABL2 (b)-(d)*

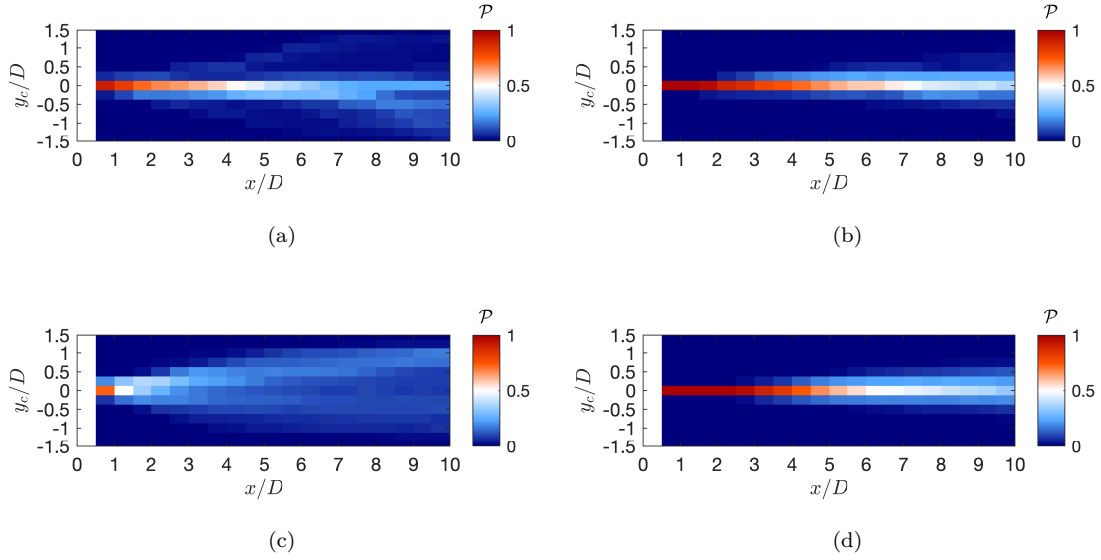



***Figure 7.53:*** *Probability distribution of the binned wake centroid position as a function of space obtained with the FD4 code (a)-(b) and experimentally (c)-(d) for the isolated wind turbine subjected to ABL1 (a)-(c) and ABL2 (b)-(d), the bins width is $D/4$*

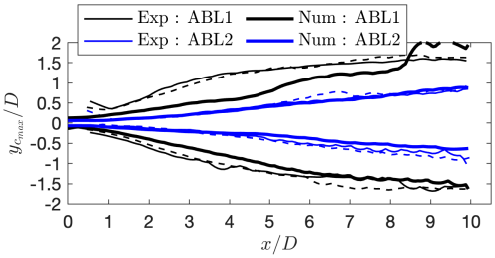



***Figure 7.54:*** *Dimensionless wake centerline envelopes obtained with the FD4 code and experimentally for ABL1 and ABL2; dashed lines without symbol correspond to the second set of measurements*

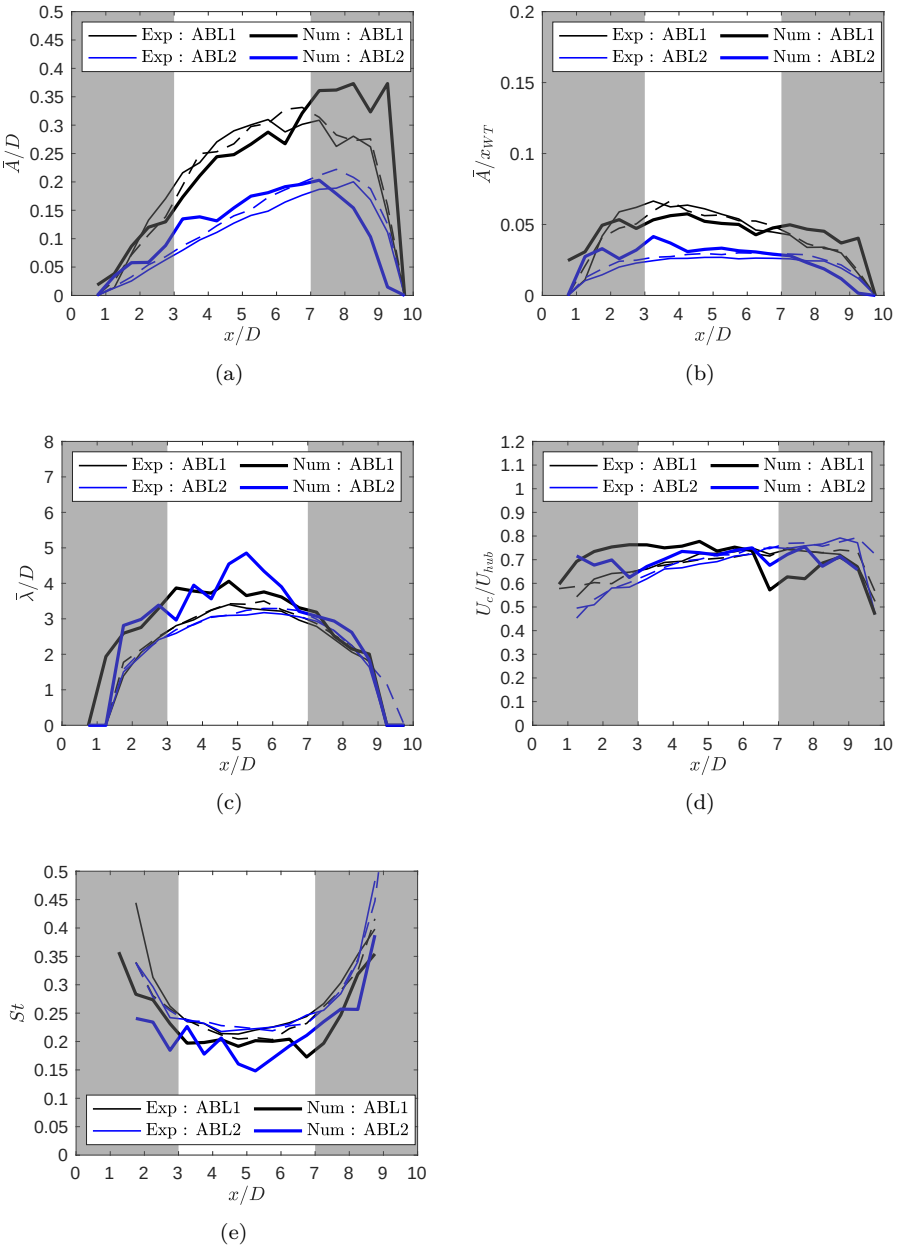



***Figure 7.55:*** *Mean binned wake centerline amplitudes (a)-(b), wavelength (c), convective speeds (d), and Strouhal numbers (e) obtained with the FD4 code and experimentally for ABL1 and ABL2; dashed lines without symbol correspond to the second set of measurements*

## 7.3 Conclusions

In this chapter, the wake meandering characteristics were investigated for various configurations including an isolated wind turbine, a row of three wind turbines, a three-row three-column wind farm, and isolated porous disks with several solidities. Overall, the large influence of the ABL on the wake meandering characteristics could be observed. ABL1 leading, amongst others, to much larger wake deflections.

For the isolated wind turbine, it was observed that the extreme wake deflections and the averaged meandering amplitude were much larger for ABL1 ($0.15 \lesssim A/D \lesssim 0.35$) than ABL2 ($0.075 \lesssim A/D \lesssim 0.22$). Furthermore, a linear increase of the wake meandering amplitude with the downstream distance from the rotor was observed for ABL2, while almost constant amplitudes ($A/D \simeq 0.3$) over a large section of the downstream distance were observed for ABL1. Regarding the wavelengths, they were slightly larger for ABL1 ($2.75 \lesssim \lambda/D \lesssim 3.5$) than for ABL2 ($2.5 \lesssim \lambda/D \lesssim 3.25$), what results in $0.21 \lesssim St \lesssim 0.27$ for ABL1 and in $0.22 \lesssim St \lesssim 0.29$ for ABL2 using Taylor's frozen turbulence hypothesis and the convective speeds of the wakes, $0.65 \lesssim U_c/U_{hub} \lesssim 0.75$ and $0.6 \lesssim U_c/U_{hub} \lesssim 0.75$ for ABL1 and ABL2, respectively. Furthermore, a very limited influence of the Reynolds number on the wake meandering characteristics was observed. Concerning the operating conditions (influence of tip-speed ratio mainly since the thrust coefficient of the scale model varies little with respect to the tip-speed ratio), they did not show a clear impact on the wake meandering characteristics, whether in terms of amplitudes, wavelengths or Strouhal numbers.

The results obtained for the isolated wind turbine are in quite good agreement with experimental [30] and numerical [31] results obtained for a three-bladed scale model wind turbine with a diameter $D = 0.128$ m, subjected to a turbulent boundary layer ($I_u = 7.5\%$ at hub height), and operating at its optimum tip-speed ratio ($TSR = 3.2$). Indeed, the experimental study revealed a mean amplitude of $A/D \simeq 0.14$, wavelengths ranging within $1 \lesssim \lambda/D \lesssim 1.5$, a convective speed of $U_c/U_{hub} \simeq 0.5$, and a characteristic frequency corresponding to $St = 0.3$. The numerical study [31, 37] led to amplitudes such that $A/D \simeq 1$ and wavelengths within the range $1 \lesssim \lambda/D \lesssim 3.5$ with higher probability densities around $\lambda/D = 1.5$ and $\lambda/D = 2.0$. They observed that wake meandering appears in the far wake ($x/D > 4$) within a low frequency range such that $0.15 \leqslant St \leqslant 0.3$. The weaker amplitude observed in [30, 31, 37] can be explained by a weaker thrust coefficient ($C_T = 0.4$) compared to $0.88 \leqslant C_T \leqslant 0.94$ within $5 \leqslant TSR \leqslant 8$ for the scale model involved in this study. Foti et al. have indeed shown in [37, 39] that a larger thrust coefficient results in larger wake meandering amplitudes. The larger wavelengths obtained in this study can be explained by the larger convective speeds involved. Overall, it leads to similar Strouhal numbers since $St = (U_c/U_\infty)D/\lambda$.

Concerning the influence of the operating conditions, no clear impact on the wake meandering characteristics was observed, while an increase of amplitude and wavelength was observed in [30] when the machine was operating freely (no external load applied). Nevertheless, it is shown in [37] that the tip-speed ratio has a secondary effect on the wake meandering characteristics compared to the turbine thrust, what confirms the observations concerning the influence of the operating conditions since the thrust coefficient of the scale model involved in this study varies little with respect to the tip-speed ratio ($0.88 \leqslant C_T \leqslant 0.94$ for $5 \leqslant TSR \leqslant 8$).

The wake meandering characteristics of the isolated wind turbine were then compared to the characteristics of the row of three wind turbines. For ABL1, the extreme deviations of the wake centerline are slightly larger for the isolated wind turbine than for the first wind turbine of the row, while they are similar for ABL2. Comparing ABL1 and ABL2, the extreme deflections were much larger for ABL1. Compared to the case with the isolated wind turbine, the presence of a second wind turbine reduces the amplitude of the wake meandering in the wake region of this second wind turbine. However, when comparing the turbines of the row, the amplitudes are larger for the second and third wind turbines than for the first wind turbine. Amplitudes ranging within $0.25 \lesssim A/D \lesssim 0.38$ and $0.20 \lesssim A/D \lesssim 0.27$ were obtained for the third wind turbine inside ABL1 and ABL2, respectively. It means that the amplitude of the wake meandering increases within the row of wind turbines. The amplification of the meandering process by the presence of an upstream wake was also reported in [25] for two porous disks ($D = 0.2$ m) subjected to an ABL

and separated by $5D$ in streamwise direction. It is however interesting to note that the opposite behavior was observed in [30] for two three-bladed wind turbine scale models ($D = 0.128$ m) with the same spacing of $5D$ in streamwise direction: a slight decrease of the wake meandering amplitude and wavelength being observed for the downstream turbine. Concerning the mean binned wake centerline wavelengths, they are equivalent for the isolated wind turbine and the first and second wind turbines of the row, whether for ABL1 or ABL2. Concerning the third wind turbine, the mean binned wake centerline wavelengths are also equivalent for ABL1, while they are slightly larger for ABL2 ($2.75 \lesssim \lambda/D \lesssim 3.50$). Strouhal numbers ranging between 0.19 and 0.27 were obtained within both ABLs.

When comparing the wake characteristics of the row of three wind turbines to those of a three-row three-column wind farm, it was observed that the lateral rows of the wind farm do not impact the wake meandering characteristics of the central row.

The influence of the wind turbine model was then investigated by substituting the three-bladed rotor by three porous disks with solidities $\sigma = 56\%$, $\sigma = 44\%$, and $\sigma = 36\%$. Whatever the solidity of the disk, the wake meandering was still present. It was observed that the extreme wake centroid deflections decrease when the solidity of the porous disks decreases within ABL2, while no clear trend could be extracted for ABL1. Furthermore, the probability distributions of the wake centroid position were very similar for ABL1, while they showed that, within ABL2, the wake centroids stay over a longer distance around $y/D = 0$ when the solidity decreases. Whether for ABL1 or ABL2, the averaged wake meandering amplitudes were larger for the bladed model than for the porous disks; one has however to keep in mind that the largest solidity of the disk was still too weak to mimic the bladed wind turbine rotor. Concerning the influence of the disk solidity, no clear trend could be extracted for ABL1, while a decrease in the meandering amplitude was observed for ABL2 when the solidity was lower. Furthermore, as for the isolated bladed model, a linear increase of the wake meandering amplitude with the downstream distance was observed for the porous disk with $\sigma = 56\%$, while this increase was weaker for the two lower solidities. Regarding the wavelengths, they were of the same size whether for the rotating model or the porous disks with $\sigma = 56\%$ and $\sigma = 44\%$, and were larger for the porous disk with $\sigma = 36\%$ ($2.75 \lesssim \lambda/D \lesssim 3.75$ for ABL1 and $2.5 \lesssim \lambda/D \lesssim 3.5$ for ABL2). Concerning the convective speeds, they were smaller for the isolated wind turbine and were increasing with a decrease of the solidity. This was clear in the near wake while the differences were reduced in the far wake, especially for ABL1 because of the larger mixing due to the higher turbulence intensity. Finally, Strouhal numbers such that $0.20 \lesssim St \lesssim 0.27$ and $0.22 \lesssim St \lesssim 0.27$ were obtained within ABL1 and ABL2, respectively. While it is reported in [37] that the incoming turbulence has a secondary effect on the wake meandering characteristics compared to the turbine thrust, the fact the influence of the disk solidity, and therefore of the thrust, depends on the incoming ABL shows that the incoming flow characteristics (turbulence intensity and integral length scales) have a larger impact on the meandering dynamics than the turbine thrust.

Even if the numerical simulations at wind tunnel scale result in weaker wakes compared to the experimental data, most probably due to the modeling of the wind turbine rotor, wake meandering characteristics close to those obtained experimentally could be extracted.

The symmetry of the flow being affected for too long turbulent boxes generated with the Mann's algorithm (due to very large integral length scales), an alternative to be able to study numerically the wake meandering over a longer time (without periodicity) would be to run precursor simulations to obtain inflows representing ABL1 and ABL2. The great interest of obtaining numerically wake meandering characteristics that are similar to those obtained experimentally results in the possibilities to vary easily the inflow of the numerical simulations. While the study of the influence of the ABL stability would run into a lot of practical problems for an experimental study, this could be performed more easily numerically.

Chapter 8

# Modal analysis of wind turbine wakes

In this chapter, a modal analysis, developed at the von Karman Institute and referred to as multi-scale Proper Orthogonal Decomposition (mPOD), is applied to the time-resolved PIV data presented in Chapter 6. As a reminder, the theoretical aspects of the mPOD analysis can be found in Section 2.3.

In the literature, the Strouhal number associated with the wind turbine wake meandering phenomenon usually ranges between 0.1 and 0.3, or between 0.1 and 0.5 when considering a wider range of frequencies (see Chapter 1). Therefore, in order to study the wake meandering mechanisms involved inside this wide range of frequencies, the multi-scale Proper Orthogonal Decomposition (mPOD) developed by Mendez [40] was used. Indeed, with the classical POD analysis, exclusively based on energy optimality, phenomena having comparable energy content share the same POD structure even if they are occurring at largely different scales. Therefore, classical POD can merge the dynamics of different phenomena within the same modes and makes their respective contributions indistinguishable. This problem was referred to as spectral mixing ([92, 93]). The mPOD, described in Section 2.3, enables to avoid this spectral mixing by splitting the correlation matrix $K$ into the contributions of different scales (Eq. (2.34)). It is important to remind that the spectral constraints associated with the mPOD only impose that a mode having a frequency content in one scale does not have a frequency content in others. Each scale is then equipped with its own POD, and the final mPOD basis is constructed by sorting these POD modes from various scales by energy contribution.

The filter bank used for the mPOD performed in this work is characterized by the frequency splitting vector $St_V = [0, 0.1, 0.2, 0.3, 0.5]$. Indeed, the use of such a filter bank enables to separate the wake meandering dynamics into several scales in order to understand the contribution of each scale. The choice of this splitting vector will become clearer in the following sections.

The mPOD analysis inside the horizontal plane at hub height is first applied for ABL1 and ABL2 without wind turbine. The mPOD analysis is then applied to the isolated wind turbine, to a row of three wind turbines, to a three-row three-column wind farm, and to three porous disks, all located inside ABL1 and ABL2. The mPOD modes obtained enable to study the influence of the wind turbine(s) parameters/configurations on the wake meandering dynamics.

## 8.1 Inflow

First, the mPOD was applied to the flow without wind turbine to study the inflow content in terms of spatial structures and frequencies, and this for the two ABLs.

Figure 8.1 (a) shows, for ABL1, the normalized frequency content of the diagonal of the temporal correlation matrix $K$ on which the filter bank, with frequency splitting vector $St_V = [0, 0.1, 0.2, 0.3, 0.5]$, is superimposed. As it can be observed, the dominant frequencies are present for the largest scales, i.e. $St \leqslant 0.1$. Figure 8.1 (b) shows the energy contributions ($diag(\Sigma_{\mathcal{M}})$) of the first fifty mPOD modes. The first three modes have a significantly larger energy contribution compared to the other modes.

The spatial structures and the spectral content of the associated temporal structures are presented in Figs. 8.2 to 8.3 for the main modes of ABL1. Modes 1 and 2 (Fig. 8.2(a) to 8.2(d)) are quite symmetric in space and describe very large-scale spatial structures, whose size is comparable to the entire field of view, that they cross laterally. Modes 3, 4 and 5 (Fig. 8.2(e) to 8.2(j)) show vortices (visible in mode 3 and mode 5) alternating with saddle points (visible in mode 4 and mode 5). These modes are therefore linked to traveling structures similar to the shedding mode observed in the wake of a cylinder [94]. The flow topology of the saddle pattern results of the interaction between phase-shifted counter-rotating vortices (see Fig. 15 in [95]). The structures corresponding to modes 3, 4 and 5 appear like traveling, although not perfectly, in the streamwise direction because of the lateral deflection induced by modes 1 and 2 by which they are strongly influenced (they share the same scale in the frequency domain but not in the spatial domain). These structures are intermediate structures with a wavelength of the order of 5 to $10D$. Smaller-scale structures, with wavelengths of the order of about $4D$, appear in modes 8, 9, 12 and 14. Modes 8 and 9 correspond to second harmonic corrections for the intermediate structures while mode 12 and 14 originate from the breaking of larger structures.

For ABL2, Fig. 8.4(a) shows that the dominant frequencies are still contained in the largest scales and evidences a stronger frequency content for $0.1 \leqslant St \leqslant 0.3$ than for ABL1. The dominance of the first modes, in terms of energy, is less marked than for ABL1 (Fig. 8.4(b)). Concerning the spatial structures (Figs. 8.5 to 8.7), modes 1 to 3 are similar to modes 1 and 2 of ABL1, the spatial structures appearing nonetheless very elongated compared to ABL1. Mode 4 corresponds to mode 4 of ABL1. Modes 9,10, 11, 12 are similar to modes 8 and 9 of ABL1 but present smaller spatial structures of the order of $3D$. These smaller-scale structures have more importance, comparatively to the structures of the first modes, in ABL2 than in ABL1 since the energy contributions of the modes of ABL2 decays less vigorously than for ABL1 (Fig. 8.4(b)).

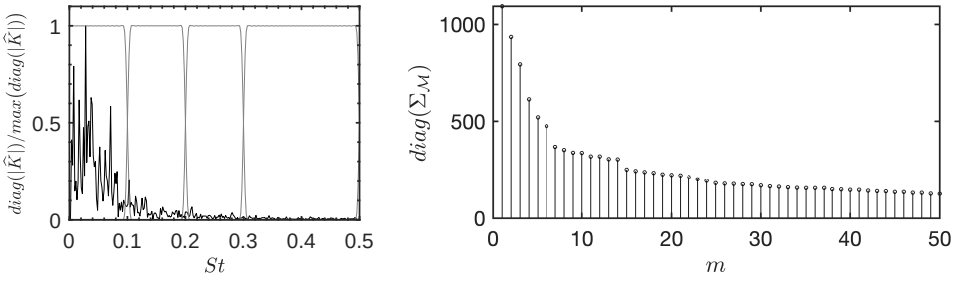



***Figure 8.1:*** *Normalized frequency content of the diagonal of the temporal correlation matrix $K$ on which the filter bank with the frequency splitting vector $St_V = [0, 0.1, 0.2, 0.3, 0.5]$ is superimposed (a) and energy contributions of the first fifty mPOD modes (b) obtained for ABL1*

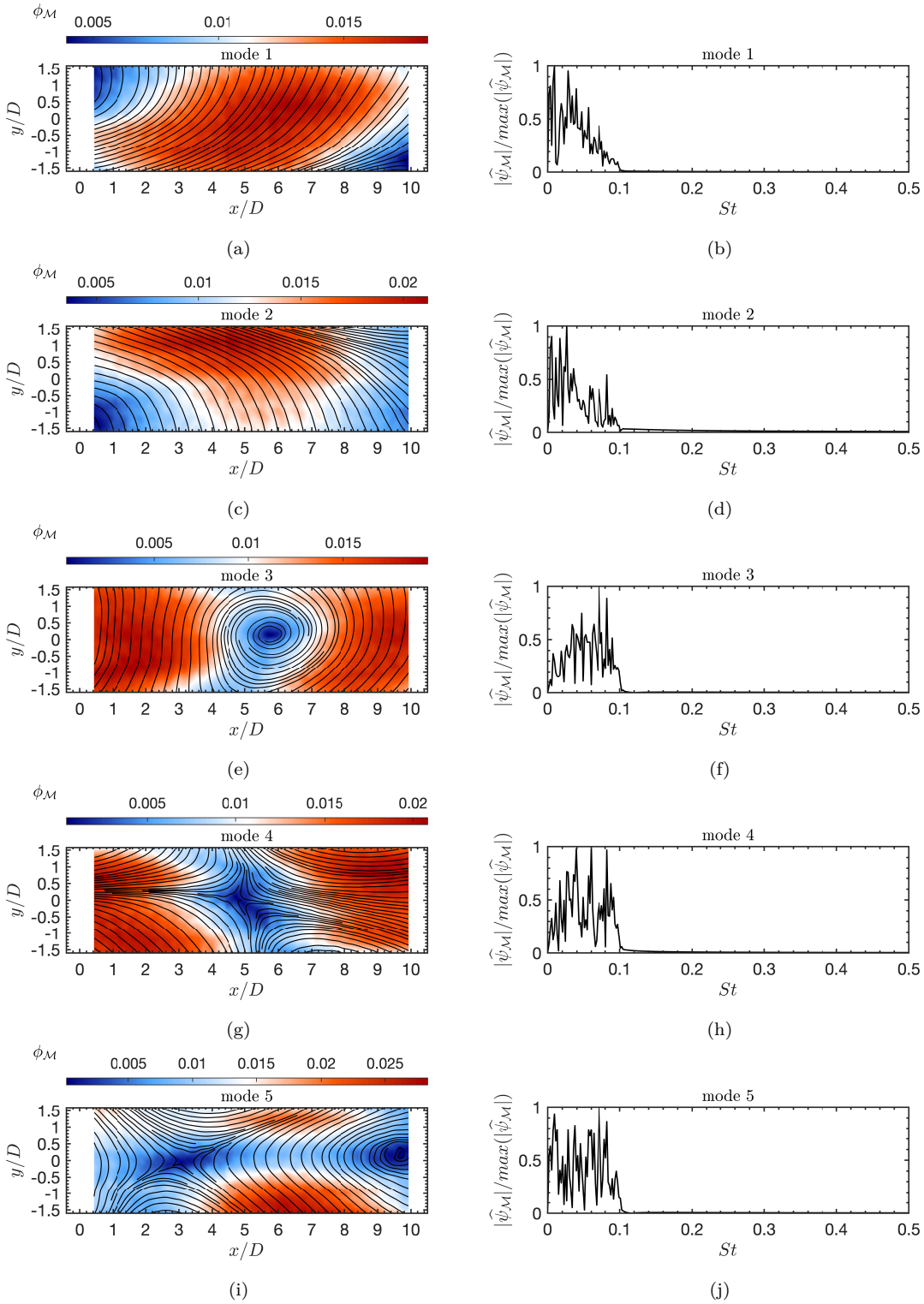



***Figure 8.2:*** *Spatial structures (left) and spectral content of temporal structures (right) obtained from the mPOD analysis of the ABL1 without wind turbine*

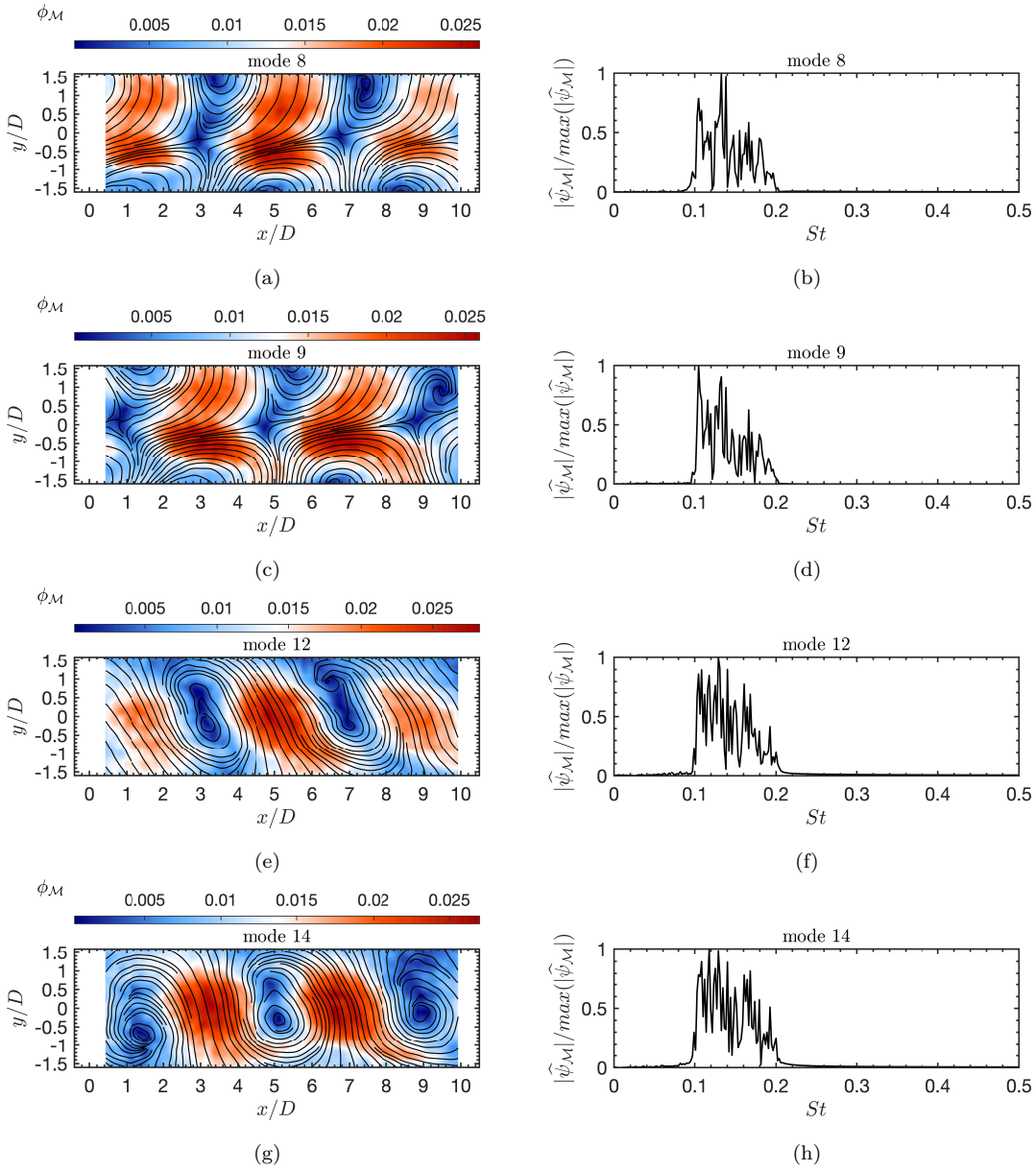



***Figure 8.3:*** *Spatial structures (left) and spectral content of temporal structures (right) obtained from the mPOD analysis of the ABL1 without wind turbine (continued)*

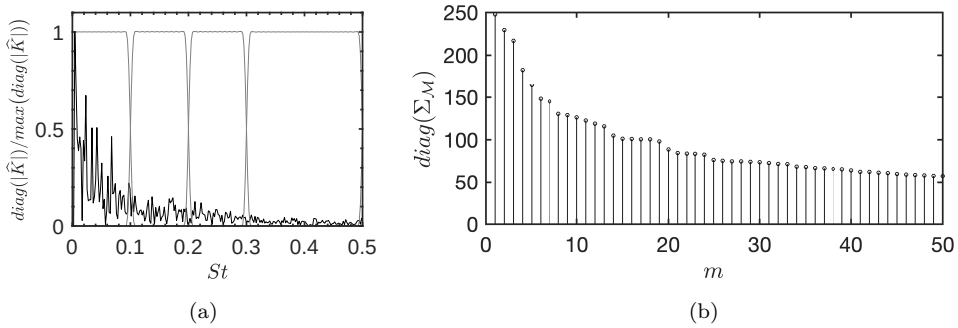



***Figure 8.4:*** *Normalized frequency content of the diagonal of the temporal correlation matrix $K$ on which the filter bank with the frequency splitting vector $St_V = [0, 0.1, 0.2, 0.3, 0.5]$ is superimposed (a) and energy contributions of the first fifty mPOD modes (b) obtained for ABL2*

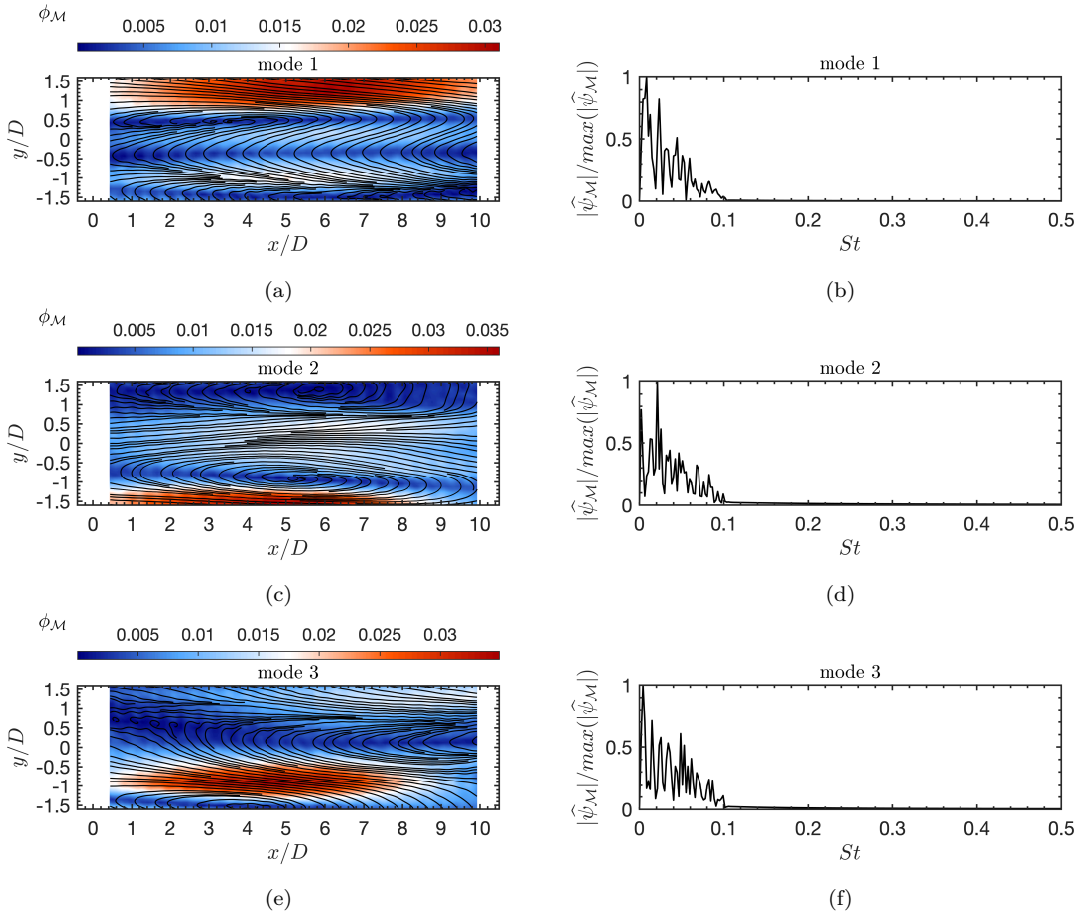



***Figure 8.5:*** *Spatial structures (left) and spectral content of temporal structures (right) obtained from the mPOD analysis of the ABL2 without wind turbine*

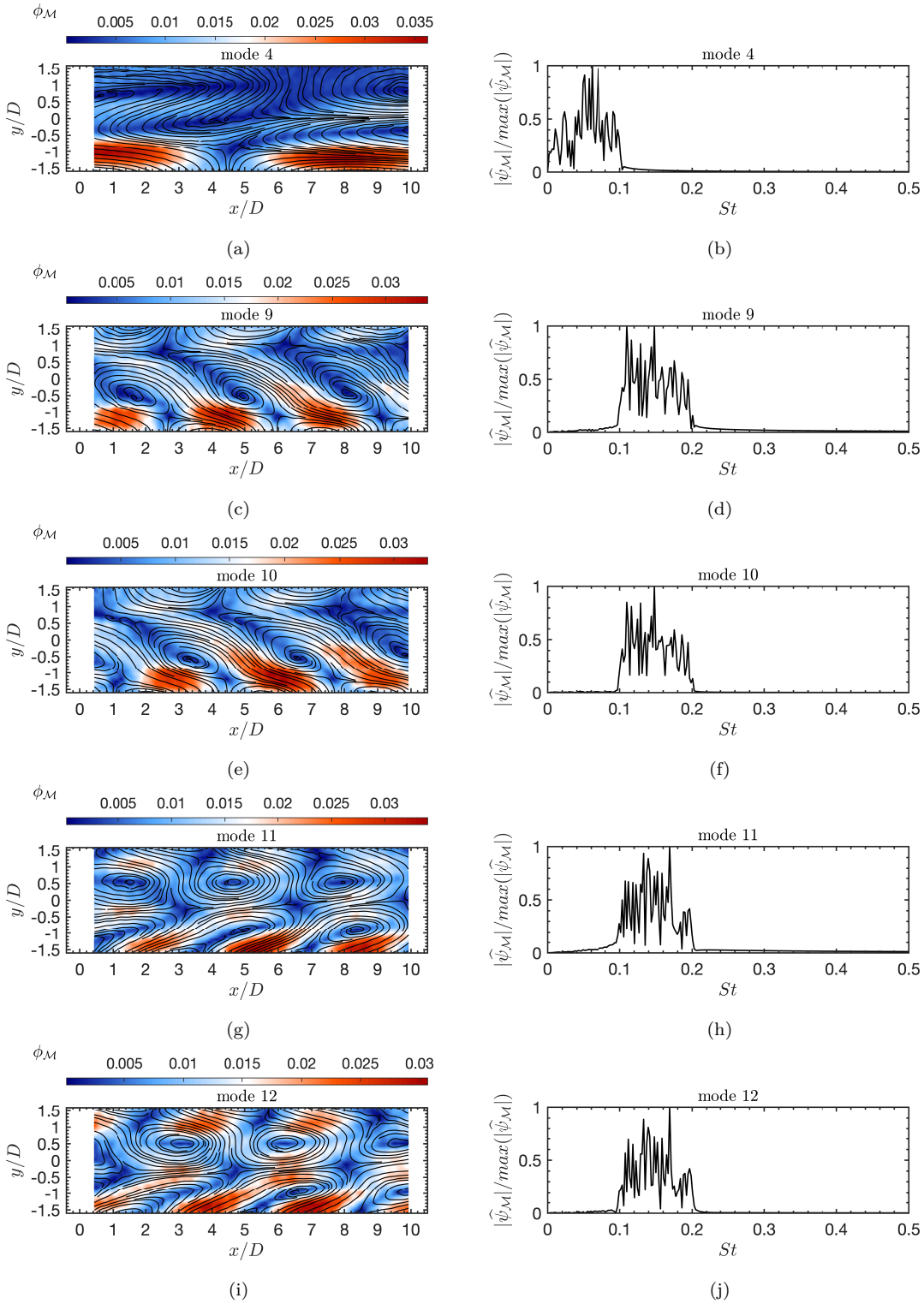



***Figure 8.6:*** *Spatial structures (left) and spectral content of temporal structures (right) obtained from the mPOD analysis of the ABL2 without wind turbine (continued)*

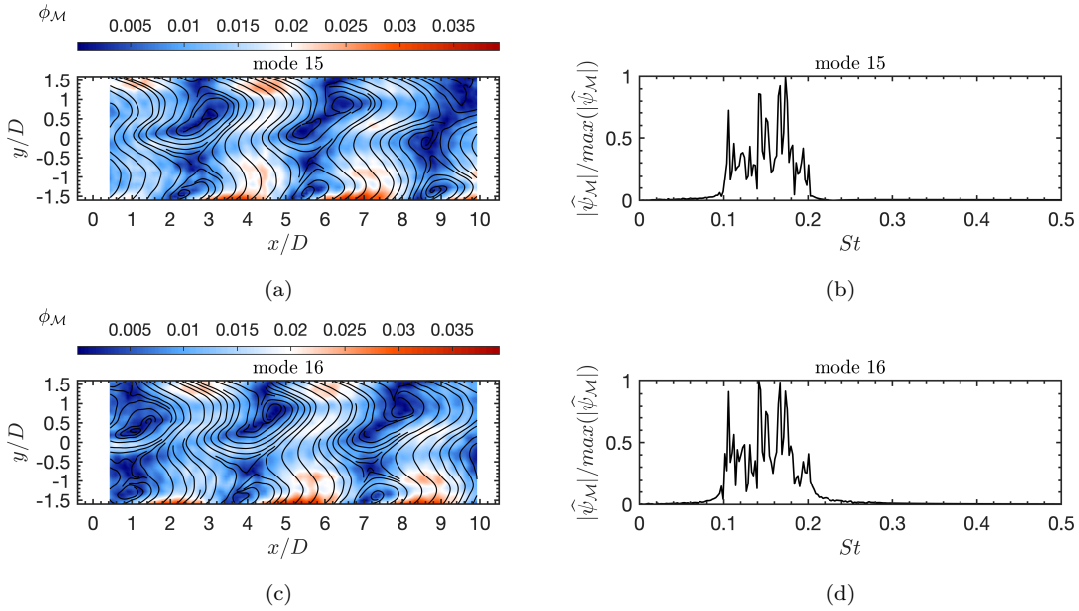



***Figure 8.7:*** *Spatial structures (left) and spectral content of temporal structures (right) obtained from the mPOD analysis of the ABL2 without wind turbine (continued)*

## 8.2 Isolated wind turbine

### 8.2.1 mPOD analysis

In this section, the mPOD analysis of the wake of an isolated wind turbine subjected to ABL1 and ABL2 is presented.

Concerning the wind turbine subjected to ABL1, Fig. 8.8 (a) shows the normalized frequency content of the diagonal of the temporal correlation matrix $K$ on which the filter bank, with frequency splitting vector $St_V = [0, 0.1, 0.2, 0.3, 0.5]$, is superimposed. As it was the case for the inflow, the dominant frequencies are present at the largest scales. The other scales present less pronounced peaks around $St = 0.14$ and $St = 0.25$. Figure 8.8 (b) shows the energy contributions ($diag(\Sigma_{\mathcal{M}})$) of the first fifty mPOD modes. The first two modes have a significantly larger energy contribution compared to the other modes.

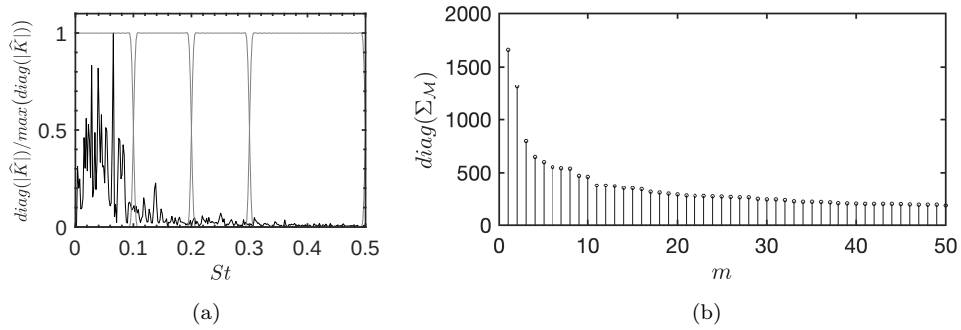



***Figure 8.8:*** *Normalized frequency content of the diagonal of the temporal correlation matrix $K$ on which the filter bank with the frequency splitting vector $St_V = [0, 0.1, 0.2, 0.3, 0.5]$ is superimposed (a) and energy contributions of the first fifty mPOD modes (b) obtained for the isolated wind turbine subjected to ABL1*

Figures 8.9 to 8.11 show the spatial structures, in the horizontal plane, of the first mPOD modes and the frequency content of the corresponding temporal structures. Each of these modes represent

specific dynamics of the wake which can be visualized in Figs. 8.12 and 8.13, where the instantaneous velocity field, reconstructed from the mean flow and each mode (recalling that the mPOD analysis was applied on the mean-subtracted velocity field), is represented at two specific instants selected to evidence the mechanism involved.

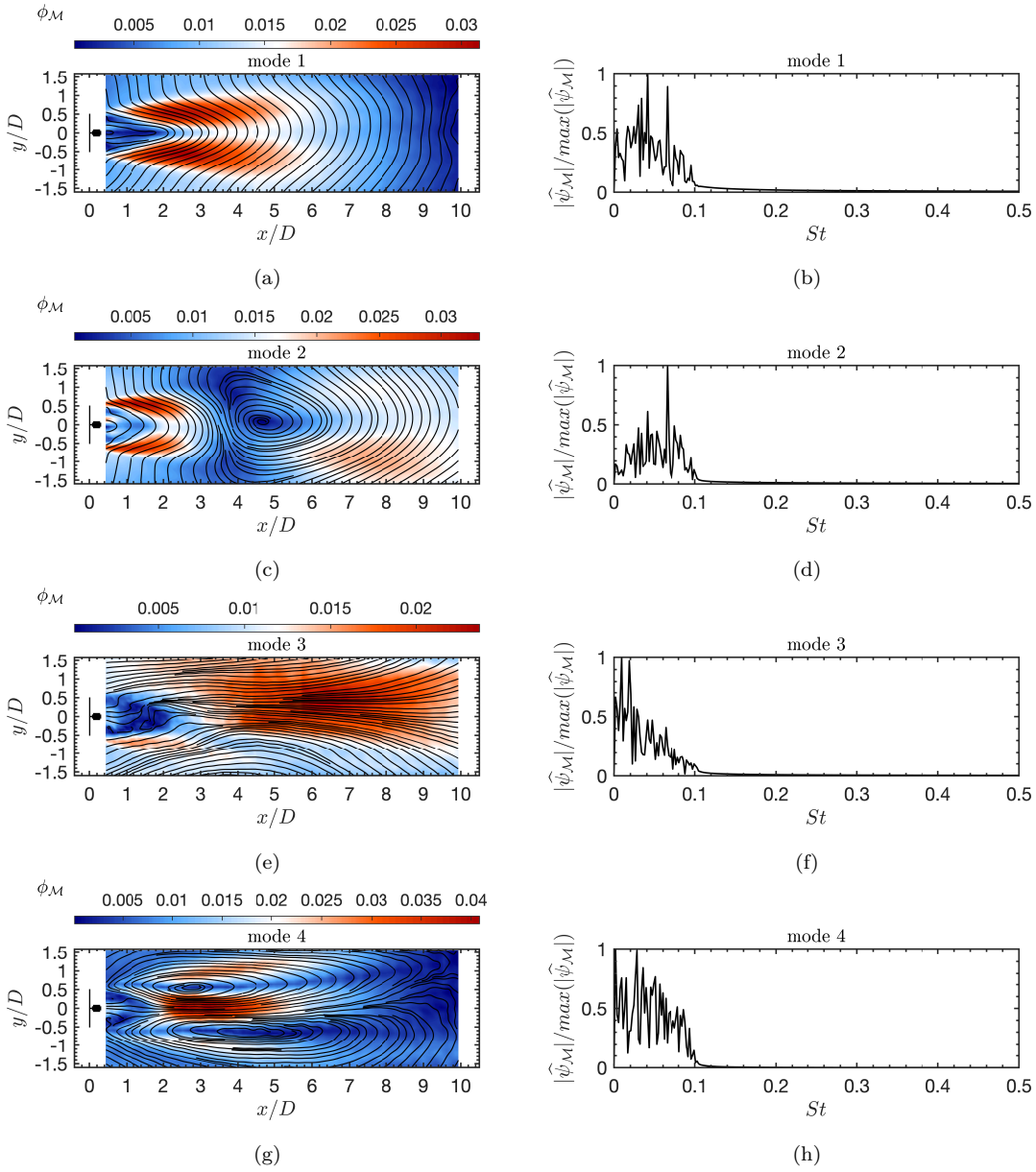



***Figure 8.9:*** *Spatial structures (left) and spectral content of temporal structures (right) obtained from the mPOD analysis of the wake of an isolated wind turbine subjected to ABL1*

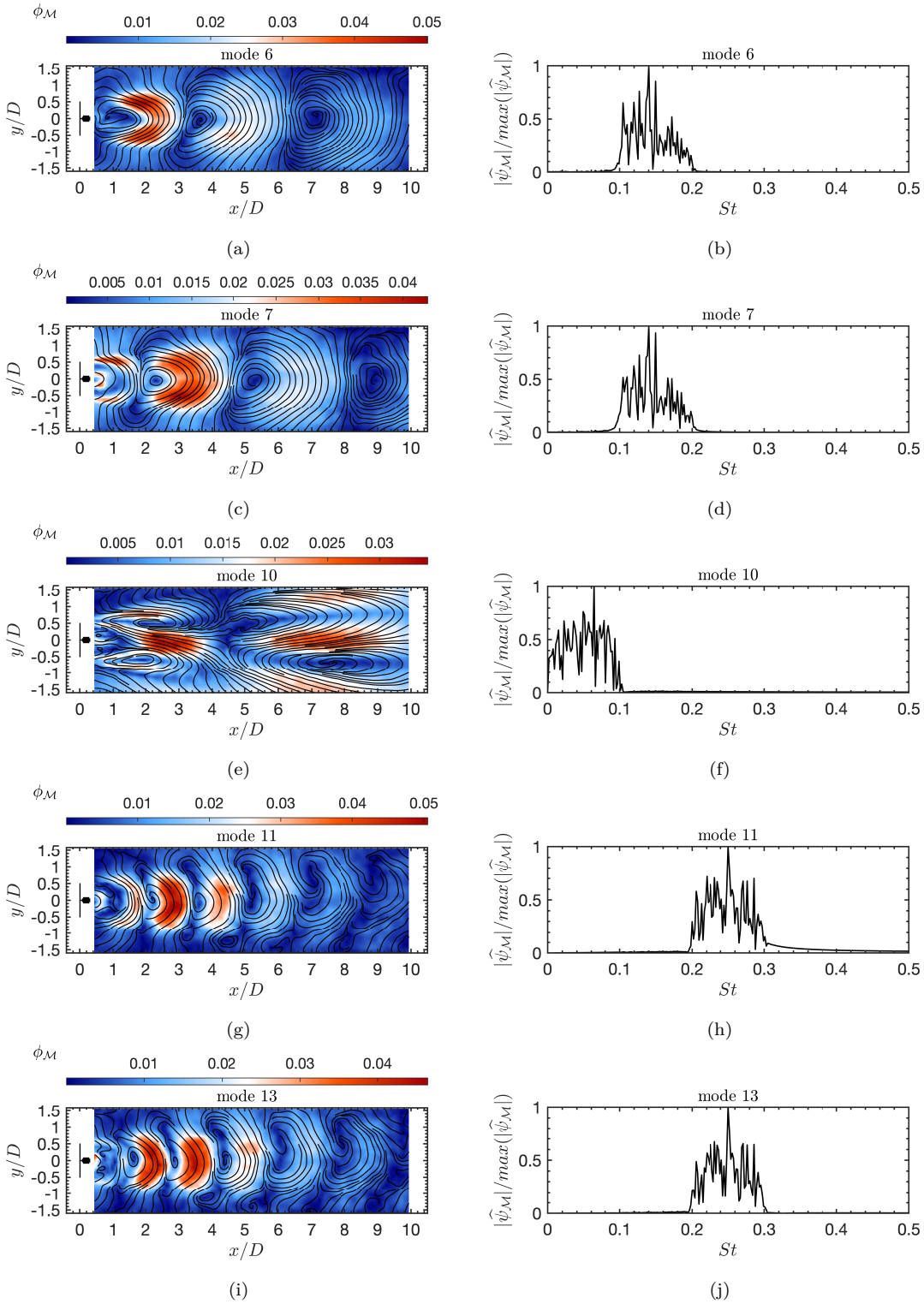



***Figure 8.10:*** *Spatial structures (left) and spectral content of temporal structures (right) obtained from the mPOD analysis of the wake of an isolated wind turbine subjected to ABL1 (continued)*

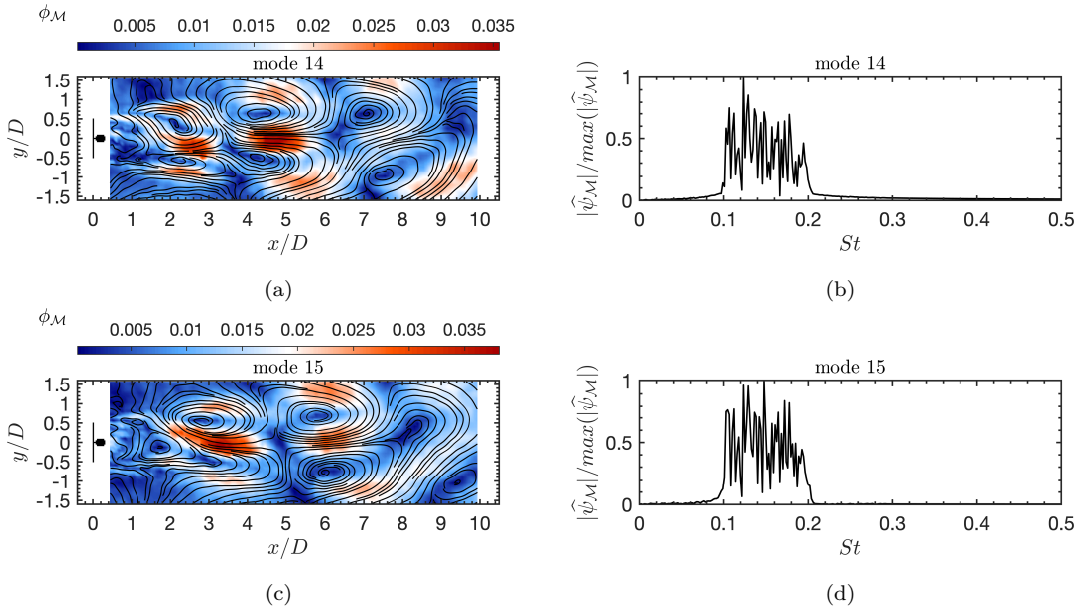



***Figure 8.11:*** *Spatial structures (left) and spectral content of temporal structures (right) obtained from the mPOD analysis of the wake of an isolated wind turbine subjected to ABL1 (continued)*

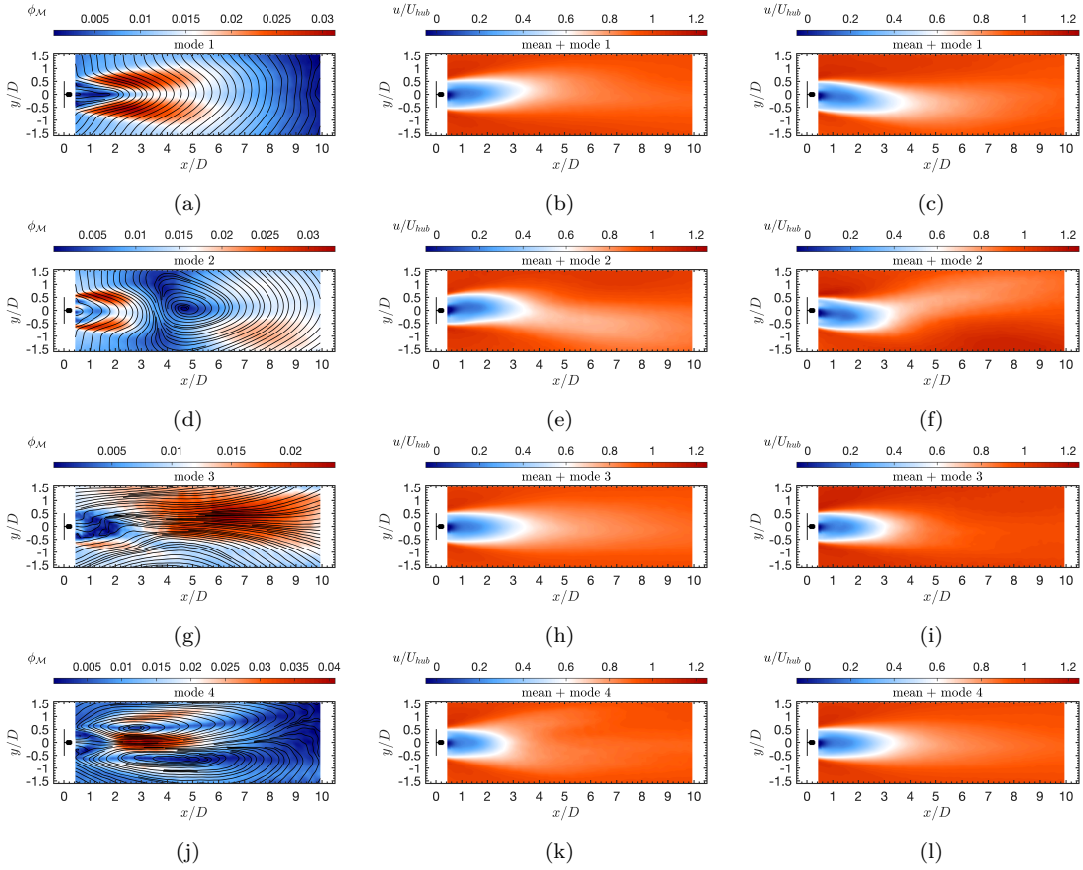



***Figure 8.12:*** *Spatial structures (left) and instantaneous reconstructed field at two different times (middle and right) obtained from the mPOD analysis of the wake of an isolated wind turbine subjected to ABL1*

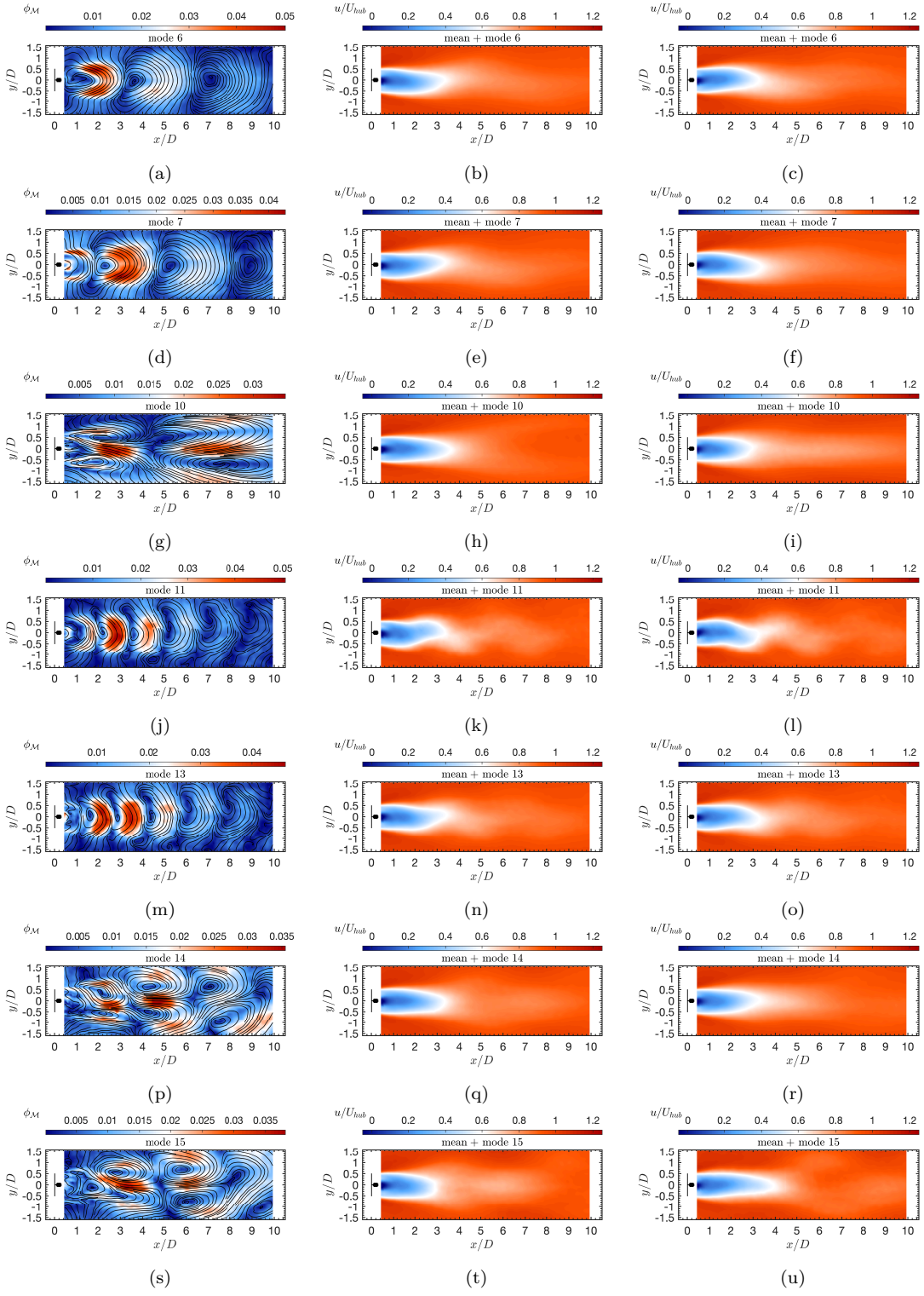



***Figure 8.13:*** *Spatial structures (left) and instantaneous reconstructed field at two different times (middle and right) obtained from the mPOD analysis of the wake of an isolated wind turbine subjected to ABL1 (continued)*

Mode 1 (Fig. 8.9(a) and 8.9(b)) corresponds to a low-frequency flapping of the near wake, i.e. the wake moving from left to right, in the horizontal plane, as a rigid body. This flapping of the wake occurring at $St \leqslant 0.1$ is schematically represented in Fig. 8.14 and can be visualized in Fig. 8.12(b) and 8.12(c). This mode is most probably influenced by modes 1 and 2 of the inflow.

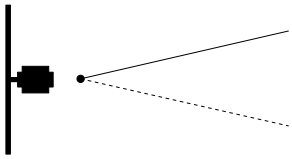


***Figure 8.14:*** *Schematic of the near wake flapping mechanism corresponding to mode 1*

Mode 2 (Fig. 8.9(c) and 8.9(d)) presents a vortical structure at $x/D \simeq 4.6$ which represents a pivotal point. Therefore mode 2 corresponds to a low-frequency long-wavelength oscillatory mechanism, as schematically represented in Fig. 8.15, and as it can be visualized in Fig. 8.12(e) and 8.12(f). Note that this mode highlights the strong link between the wake dynamics and the structures of the inflow. Mode 2 is clearly influenced by mode 3 of the inflow, the large-scale structures of the inflow imposing therefore the wake dynamics.

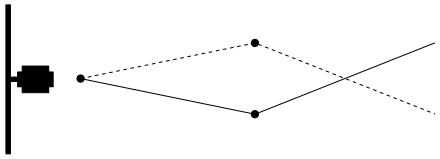


***Figure 8.15:*** *Schematic of the long-wavelength oscillatory mechanism corresponding to mode 2*

Modes 3, 4, 10, 14, and 15 (Figs. 8.9 to 8.11) do not correspond to oscillatory mechanisms but represent the shortening and lengthening of the wake at different frequencies due to the wake breakdown (Fig. 8.16). The presence of mode 3 is certainly due to mode 1 and 2 contained in the inflow.



***Figure 8.16:*** *Schematic of the wake shortening and lengthening mechanism due to wake breakdown as in mode 3*

Modes 6 (Fig. 8.10(a) and 8.10(b)) and 7 (Fig. 8.10(c) and 8.10(d)) present several vortical structures and correspond to standing waves; mode 6 being schematically represented in Fig. 8.17 for the sake of clarity. The vortical structures of mode 6 are located around $x/D = 3.6D$ and $x/D = 7.2D$, while they are located around $x/D = 2.3D$, $x/D = 5.3D$ and $x/D = 8.9D$ for mode 7. From the spatial structures of these two modes, a streamwise wavelength of the order of $3.6D$ can be extracted. As it can be observed, the centers of the vortical structures are shifted in space between mode 6 and mode 7, and these two modes present a similar spectral content. These two modes are therefore in quadrature and, while they correspond to standing waves (Fig. 8.13(b), 8.13(c), 8.13(e) and

8.13(f)) when taken independently, they represent a traveling wave when paired together. The spectral content of these modes reveals that the oscillations occur for $0.1 \leqslant St \leqslant 0.2$ (Fig. 8.10(b) and 8.10(d)) and shows distinctive peaks around $St = 0.14$.

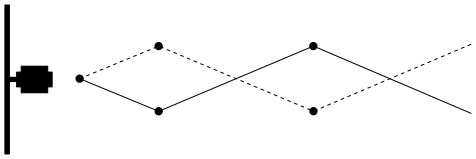


***Figure 8.17:*** *Schematic of the standing wave mechanism corresponding to mode 6*

As modes 6 and 7, modes 11 and 13 (Fig. 8.10(g), 8.10(h), 8.10(i) and 8.10(j)) correspond to standing waves but with an even shorter wavelength ranging between $\sim 1.2D$ and $\sim 1.8D$, the wavelength increasing with the downstream distance since the velocity increases due to the wake recovery. These two modes also share a similar frequency content and are in quadrature. Mode 11 is schematically represented in Fig. 8.18. Therefore, they also represent a traveling wave (Fig. 8.13(k), 8.13(l), 8.13(n) and 8.13(o)) but with a shorter wavelength than for mode 6 and 7. The spectral contents of modes 11 and 13 reveal a distinct peak at $St = 0.25$.

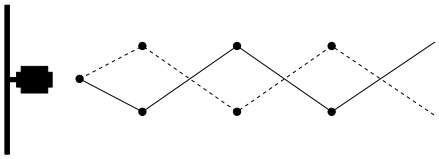


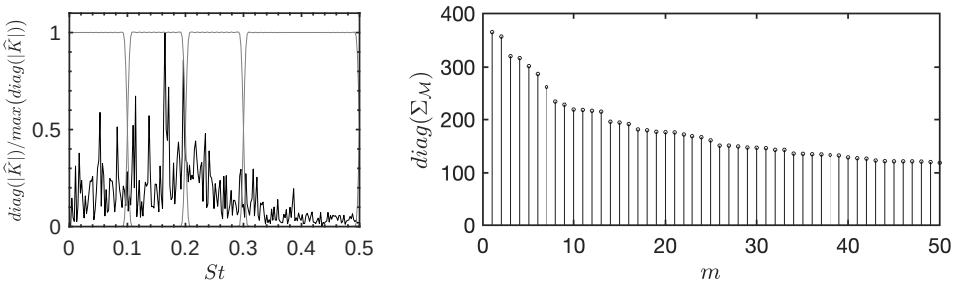
***Figure 8.18:*** *Schematic of the standing wave mechanism for mode 11*

The other modes, not mentioned above, correspond to some corrections for the modes previously discussed or to high order modes, and are not included in this thesis for the sake of conciseness.

Based on the mPOD analysis, the wake meandering for the isolated wind turbine located in ABL1 can be seen as a combination of a low-frequency flapping and low-frequency long-wavelength oscillations on which higher-frequency oscillations are superimposed. A mechanism corresponding to the wake breakdown, due to the large-scale incoming structures, completes the wake dynamics.

The influence of the ABL on the wake dynamics is now investigated by considering the wind turbine subjected to ABL2. While the dominant frequencies were gathered in the range $0 \leqslant St \leqslant 0.1$ for the wind turbine subjected to ABL1, they are this time in the range $0.1 \leqslant St \leqslant 0.2$ (Fig. 8.19(a)). Furthermore, the other scales also show a rich spectral content compared to what was observed for the wind turbine inside ABL1. Regarding the energy contributions of the first fifty mPOD modes (Fig. 8.19(b)), the decrease of energy within the first modes is quite gradual compared to the wind turbine subjected to ABL1.

The energy dominant modes are different (Figs. 8.20 to 8.22) compared to the case within ABL1. In this case, the first four modes correspond to wake oscillations with a spectral content beyond $St = 0.1$; within the range $0.1 \leqslant St \leqslant 0.2$ for the first two modes (Fig. 8.20(a) to 8.20(d)), and within $0.2 \leqslant St \leqslant 0.3$ for the third and fourth modes (Fig. 8.20(e) to 8.20(h)). This change in the frequency content of the dominant mPOD modes, when compared to the inflow, shows that the wind turbine is transferring the energy from the large-scale structures of the inflow ($St \leqslant 0.1$) to the smaller scales inside the wake ($0.1 \leqslant St \leqslant 0.2$).




(a) (b)

***Figure 8.19:*** *Normalized frequency content of the temporal correlation matrix $K$ on which the filter bank with the frequency splitting vector $St_V = [0, 0.1, 0.2, 0.3, 0.5]$ is superimposed (a) and energy contribution of the first fifty mPOD modes (b) for the wind turbine subjected to ABL2*

Modes 1 and 2 represent standing waves when considered separately, as illustrated in Fig. 8.23(b) to 8.23(f). However, since they share a similar spectral content and are in quadrature, they represent a traveling wave when paired. Wavelengths ranging between $1.4 \leqslant \lambda/D \leqslant 2.5$ can be extracted from the spatial structures of these modes, which present a spectral content within $0.1 \leqslant St \leqslant 0.2$ with a peak around $St = 0.17$. Similar comments can be made for modes 3 and 4 (Fig. 8.23(h) to 8.23(l)) which present a spectral content within $0.2 \leqslant St \leqslant 0.3$ with a peak around $St = 0.24$, and for which wavelengths ranging within $1.1 \leqslant \lambda/D \leqslant 1.8$ can be extracted from the spatial structures.

The mode corresponding to the flapping of the near wake is only the sixth mode (Figs. 8.20(i), 8.20(j), 8.24(b), 8.24(c)), which has much less energy than the corresponding mode for the case inside ABL1 (mode 3). Modes 8 and 11 have a spectral content within $0.1 \leqslant St \leqslant 0.2$ and correspond to oscillations with wavelengths within $2.3 \leqslant \lambda/D \leqslant 2.8$. In addition, mode 9 (Fig. 8.21(c) and 8.21(d)) corresponds to the flapping of the far wake as visible in Fig. 8.24(h) and 8.24(i), and schematically represented in Fig. 8.25.

Compared to the wind turbine within ABL1, the mPOD modes have globally higher frequencies. Oscillations at $0.3 \leqslant St \leqslant 0.5$ can even be observed for modes 10 and 12 (Fig. 8.21(e), 8.21(f), 8.21(i), and 8.21(j)). This highlights the large influence of the ABL on the wake meandering dynamics.

The other modes, not mentioned above, correspond to some corrections for the modes previously discussed or to high order modes, and are not shown here for the sake of conciseness.

These observations support that the frequency content of wake meandering is already present within the inflow with a lower energy content.

Based on the mPOD analysis, the wake meandering for the isolated wind turbine located in ABL2 can be seen as a combination of oscillations and a low-frequency flapping of the near and far wake. The low-frequency long-wavelength oscillations and the wake breakdown observed for ABL1 are not involved in the wake dynamics of the wind turbine within ABL2. This evidences the large influence of the inflow on the wake dynamics.

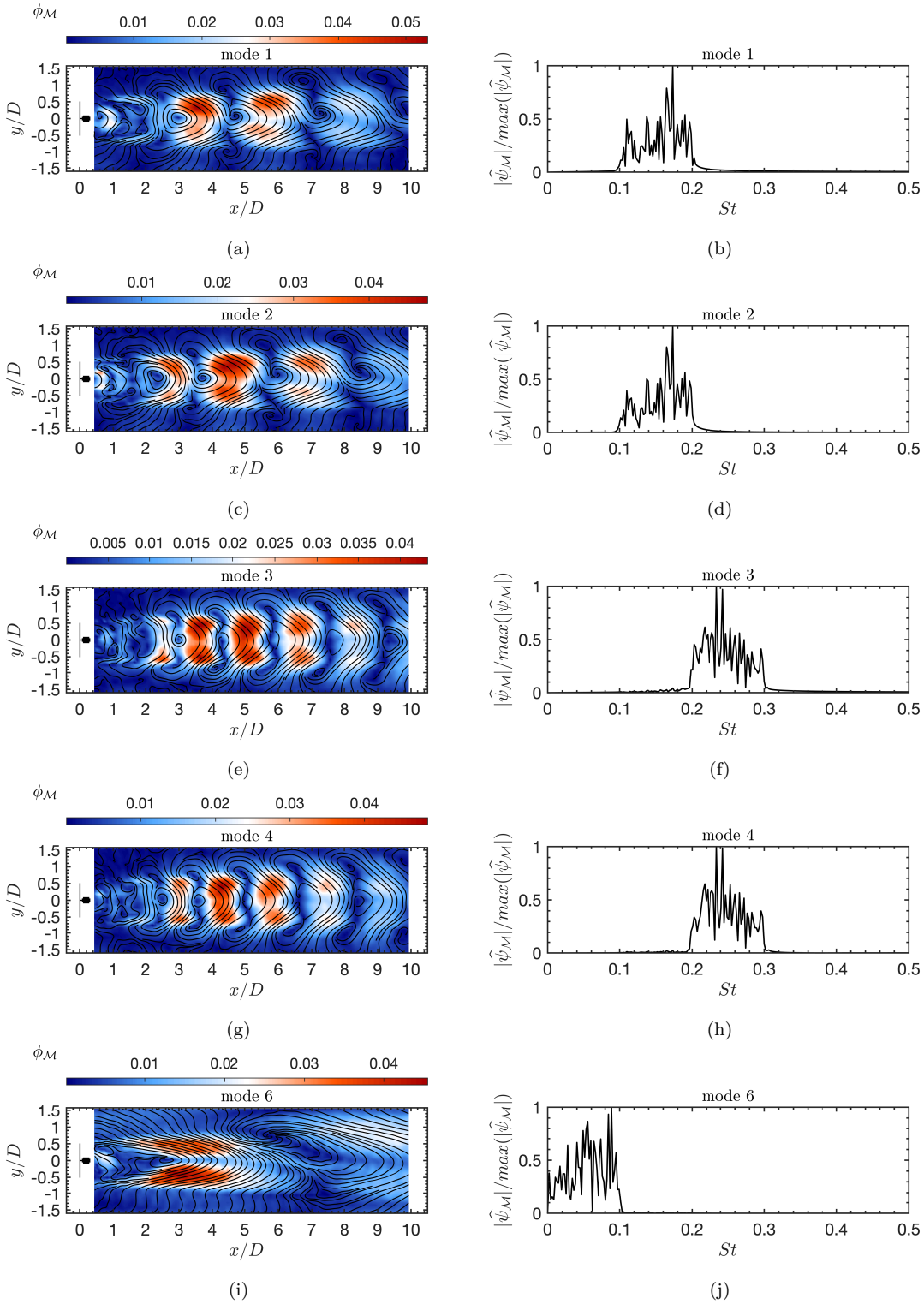



***Figure 8.20:*** *Spatial structures (left) and spectral content of temporal structures (right) obtained from the mPOD analysis of the wake of an isolated wind turbine subjected to ABL2*

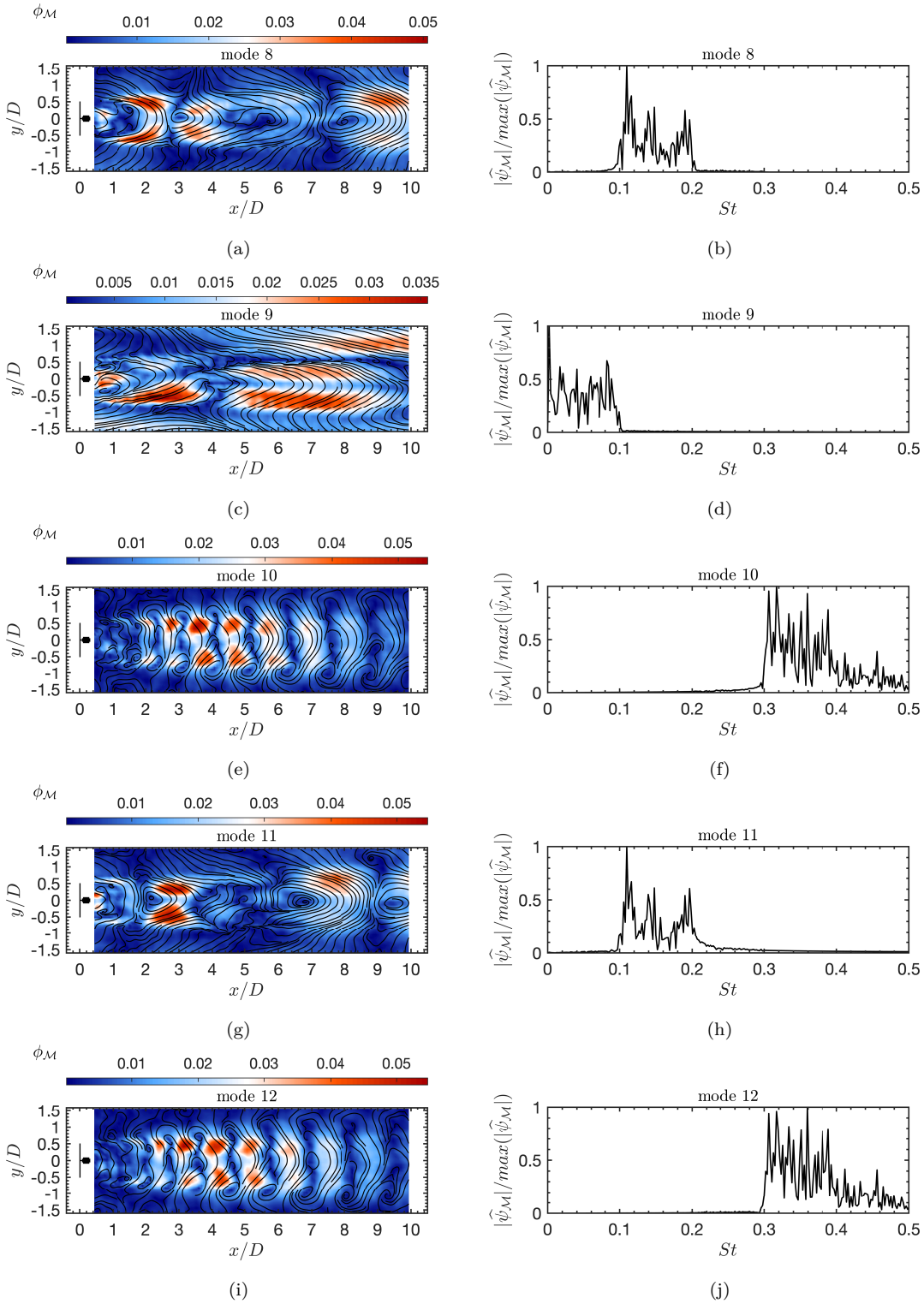



***Figure 8.21:*** *Spatial structures (left) and spectral content of temporal structures (right) obtained from the mPOD analysis of the wake of an isolated wind turbine subjected to ABL2 (continued)*

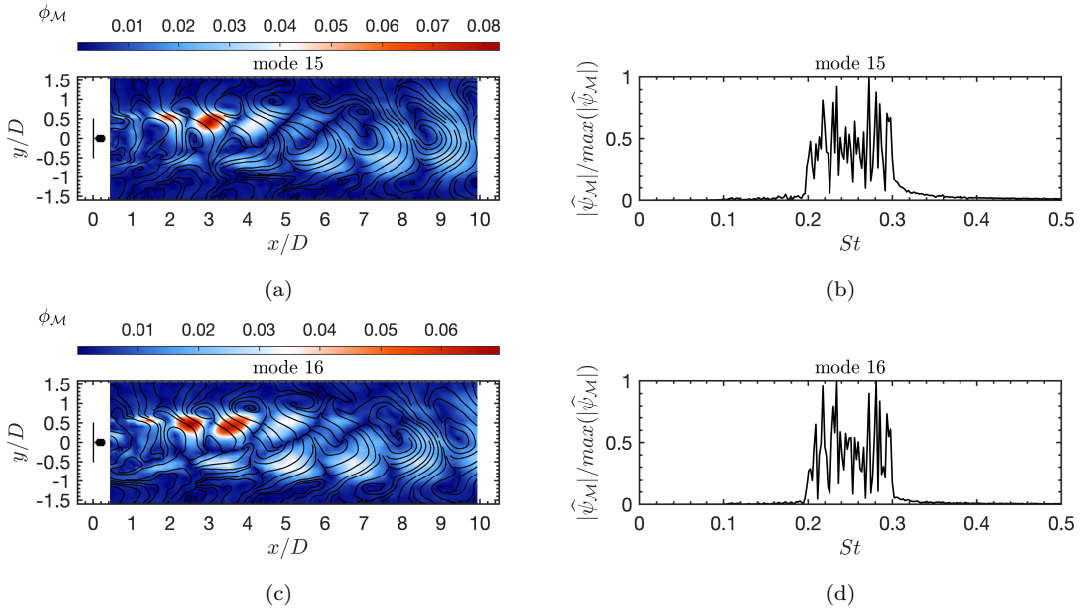



***Figure 8.22:*** *Spatial structures (left) and spectral content of temporal structures (right) obtained from the mPOD analysis of the wake of an isolated wind turbine subjected to ABL2 (continued)*

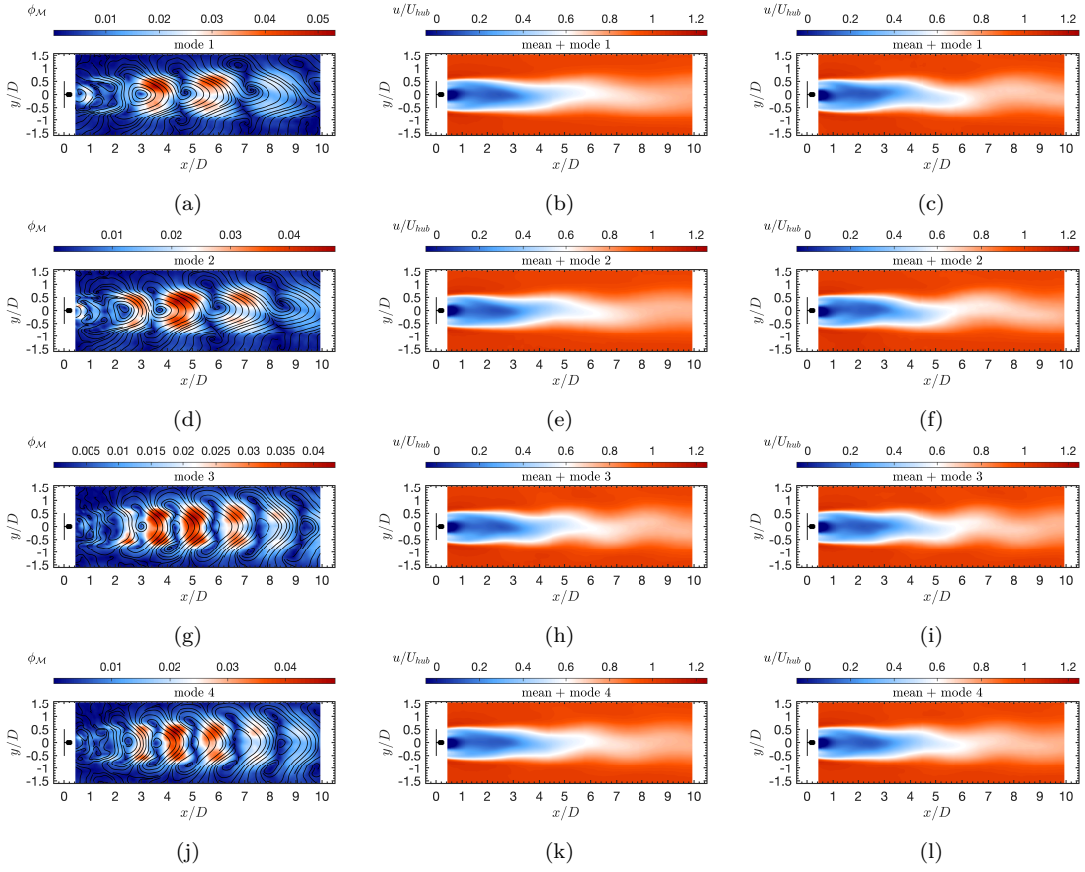



***Figure 8.23:*** *Spatial structures (left) and instantaneous reconstructed field at two different times (middle and right) obtained from the mPOD analysis of the wake of an isolated wind turbine subjected to ABL2*

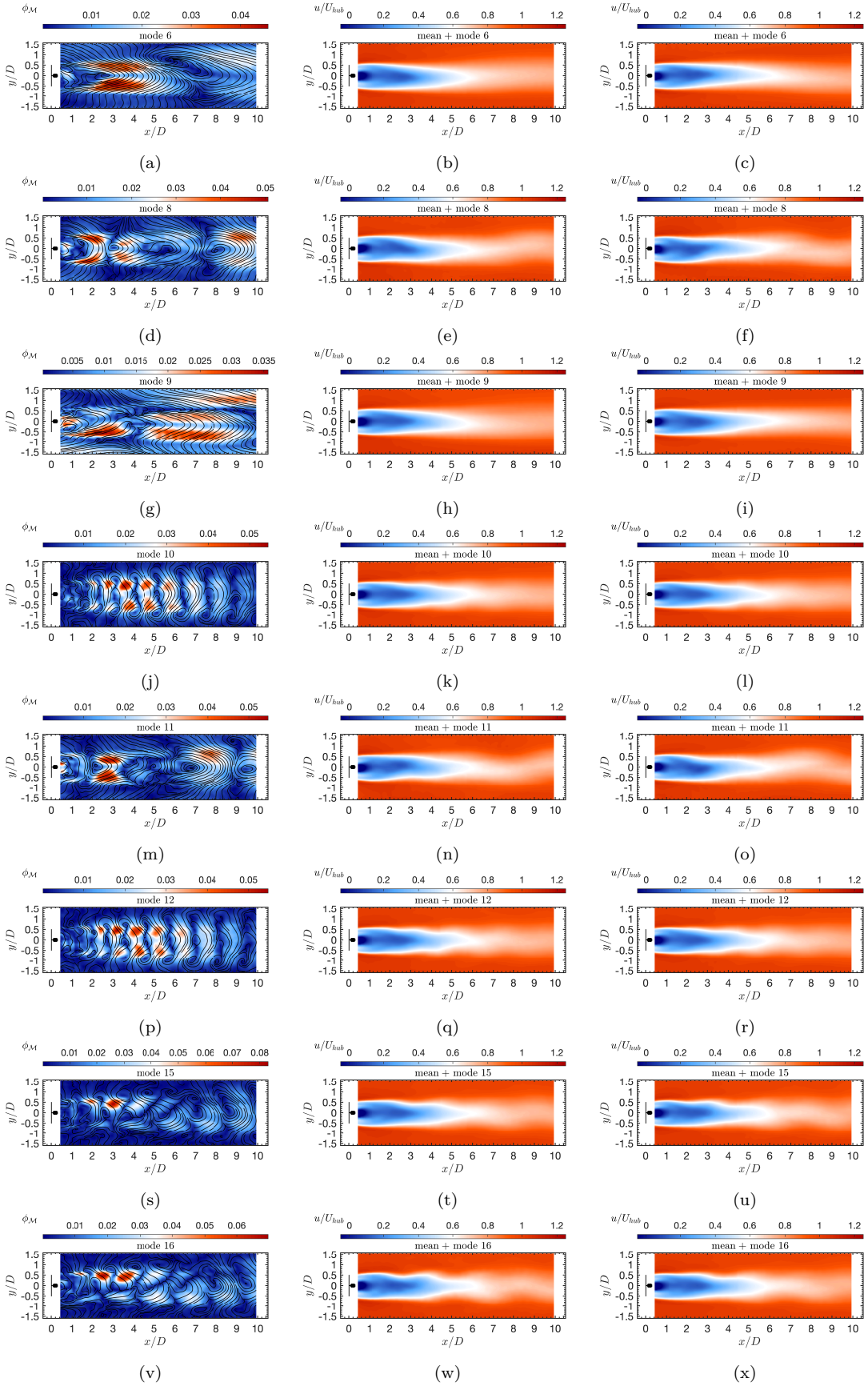



***Figure 8.24:*** *Spatial structures (left) and instantaneous reconstructed field at two different times (middle and right) obtained from the mPOD analysis of the wake of an isolated wind turbine subjected to ABL2 (continued)*

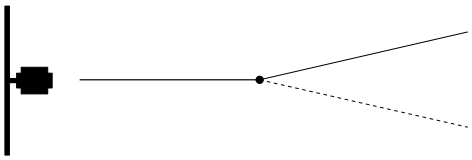


***Figure 8.25:*** *Schematic of the far-wake flapping mechanism*

### 8.2.2 Wake tracking from mPOD field

Since the velocity field can be reconstructed from the mPOD modes, the wake centerline tracking was applied to reconstructed velocity fields from $m$ mPOD modes. The wake centerlines obtained are compared to those resulting from the tracking applied to the actual velocity field obtained from the PIV measurements (Figs. 8.26 and 8.27). As expected, the wake tracking improves when the number of modes considered increases. This could be expected since, when applying the modal analysis, the reconstructed field is closer to the actual field as the rank (number of modes exploited) increases (Figs. 8.28 and 8.29). However, a good approximation of the wake centerline can be obtained for the first part of the wake ($x/D \leqslant 5$) even with a reduced number of modes. This is due to the fact that the near wake is well structured, and can therefore be represented with less mPOD modes than the far wake that is more complex.

Concerning the wind turbine within ABL1, sixteen modes enable to obtain a fairly good approximation of the wake centerline up to $x/D = 5$ while fifty modes provide a very good approximation up to $x/D = 7$. The number of modes required for the case with ABL2 is more limited since only twelve modes are required to end up with a good approximation of the wake centerline up to $x/D = 5$, and only sixteen to obtain a good approximation over the entire wake. The larger number of modes required for ABL1 can be justified by the fact that the first modes of the case within ABL1 have a limited frequency range ($St \leqslant 0.2$), and capture therefore well some mechanism of the wake dynamics but not others. For the case within ABL2, the flow is less complex because of the lower incoming turbulence intensity, and the first modes cover the entire frequency range up to $St = 0.5$, which enables to obtain a good approximation of the velocity field with a reduced number of modes.

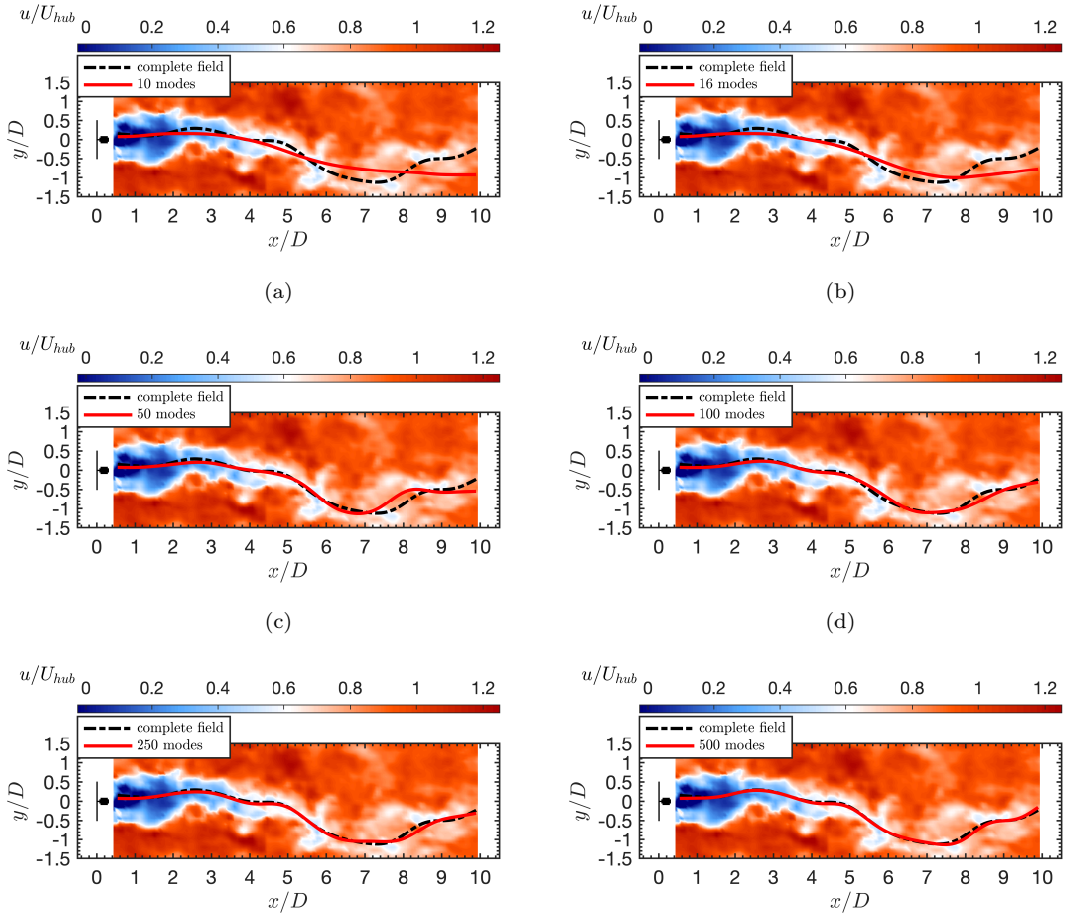



***Figure 8.26:*** *Streamwise velocity field on which is superimposed the wake centerline obtained from the tracking on the complete flow field and on the reconstructed field up to m modes for the isolated wind turbine located in ABL1*

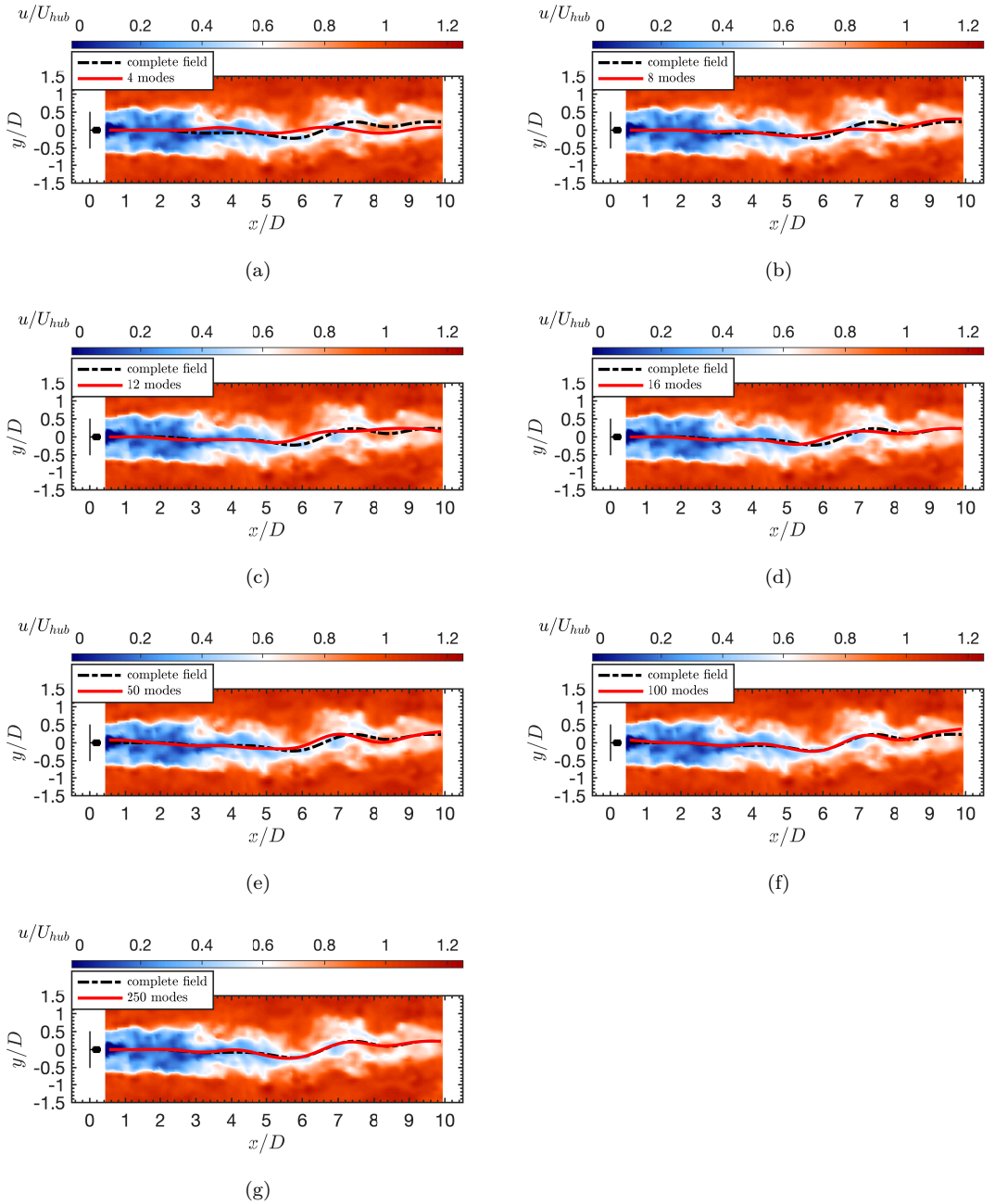



***Figure 8.27:*** *Streamwise velocity field on which is superimposed the wake centerline obtained from the tracking on the complete flow field and on the reconstructed field up to m modes for the isolated wind turbine located in ABL2*

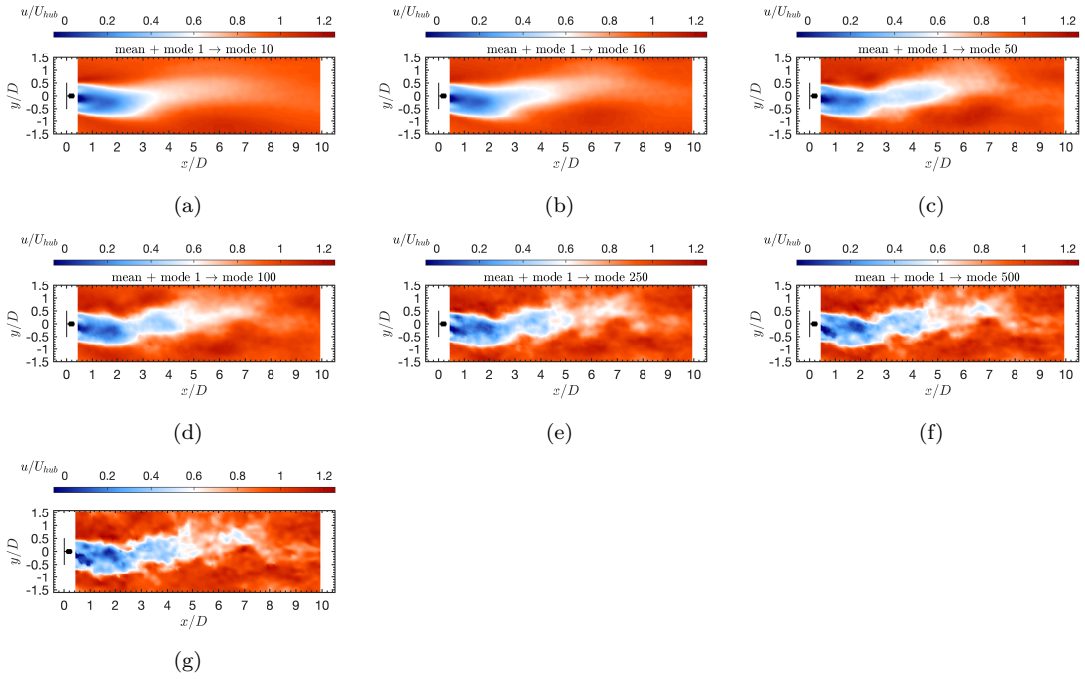



***Figure 8.28:*** *Instantaneous streamwise velocity field reconstructed from m modes for the isolated wind turbine subjected to ABL1 (a)-(f) and actual velocity field (g)*

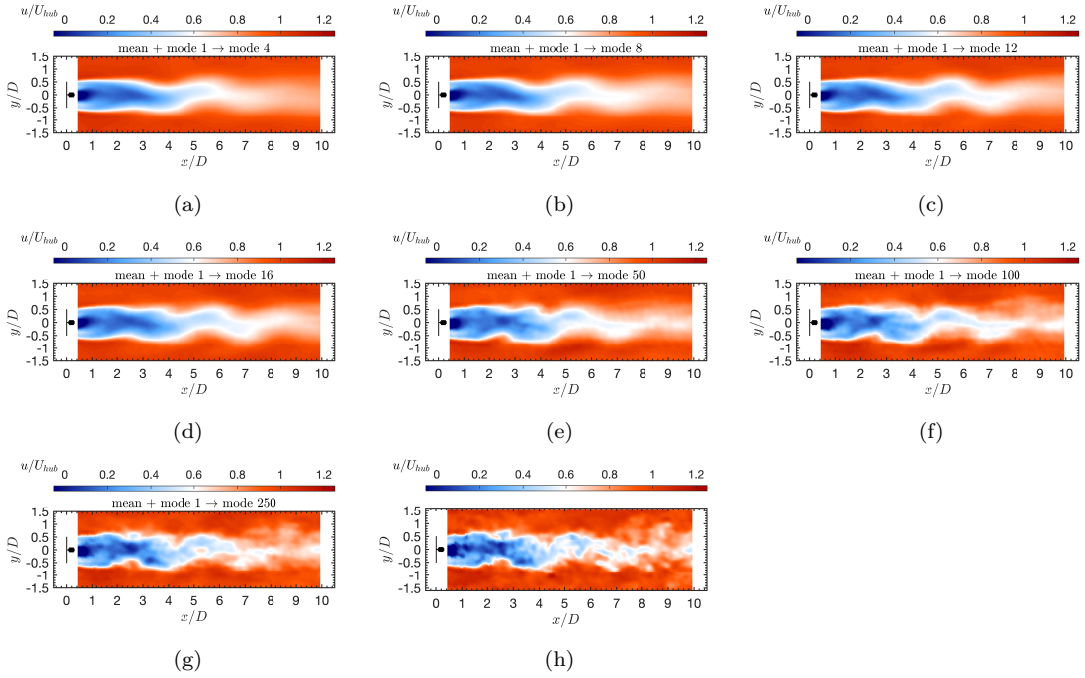



***Figure 8.29:*** *Instantaneous streamwise velocity field reconstructed from m modes for the isolated wind turbine subjected to ABL2 (a)-(g) and actual velocity field (h)*

## 8.3 Wind turbine row

### 8.3.1 Isolated wind turbine vs. first and second wind turbines

Except for the very first mPOD modes, the difference of energy between consecutive modes is not substantial. Since the modes are sorted based on their energy contributions, it can therefore lead to some swaps between modes representing the wake of the upstream or downstream wind turbine. In order to ease the comparison between the modes of the upstream and downstream wind turbines contained in the same field of view, the ordering of the modes based on their energy contribution was strictly followed only for the upstream turbine. For the downstream turbine, the modes were initially sorted based on their energy contribution and then their ordering was slightly adapted to coincide with the corresponding modes of the upstream wind turbine. The modes whose ordering was adapted are represented by dashed stem in the figures representing the energy contribution of each mode (e.g. Fig. 8.31(b)).

Figure 8.30 shows that the frequency content of the temporal correlation matrices $K$ is quite similar for the first and second wind turbines of the row, and for the isolated wind turbine subjected to ABL1. The energy contributions of the mPOD modes of the first and second wind turbines of the row subjected to ABL1 are presented in Fig. 8.31 where they can be compared to that of the isolated wind turbine. As it can be observed, the energy contributions are similar except for the second mode, corresponding to the long-wavelength oscillatory mechanism, which is much less energetic for the first and second wind turbines of the row of wind turbines.

Dominant modes (Figs. 8.32 to 8.35) correspond to large-scale motion of the wake influenced by the large-scale structures contained in the inflow. For the row of wind turbines, mode 1, corresponding to the flapping of the wake, is clearly the dominant mode in term of energy. The three first modes, corresponding to the flapping, the long-wavelength oscillatory mechanism, and the shortening/lengthening of the wake are very similar. Starting from mode 4, there is a shift in the ordering of the modes. For example, the equivalent of mode 4 for the row of wind turbines can be found at mode 6 for the isolated wind turbine. Despite the similarity between the modes of the isolated turbine and of the wind turbines composing the row, it can be observed that the presence of a downstream turbine influences slightly the wake dynamics, especially for mode 2 which shows a lower energy contribution in the wind turbine row than for the isolated wind turbine.

Within ABL2, the normalized frequency content of the temporal correlation matrix $K$ of the first wind turbine of the row is similar to that of the isolated wind turbine, while it is much stronger in the range $0 \leqslant St \leqslant 0.3$ for the second wind turbine of the row (Fig. 8.36). Compared to the isolated wind turbine in ABL2, the energy distribution (Fig. 8.37) changes leading to three dominant modes for the row of wind turbines. For ABL2, the two first modes are similar (Fig. 8.38). Then, there are some shifts in the ordering of the modes (Figs. 8.39 and 8.40) starting from mode 3. In particular, mode 3 of the row of wind turbines, which represents the flapping of the wake, is now a dominant mode while it was only mode 6 for the isolated wind turbine. The other modes are quite similar.

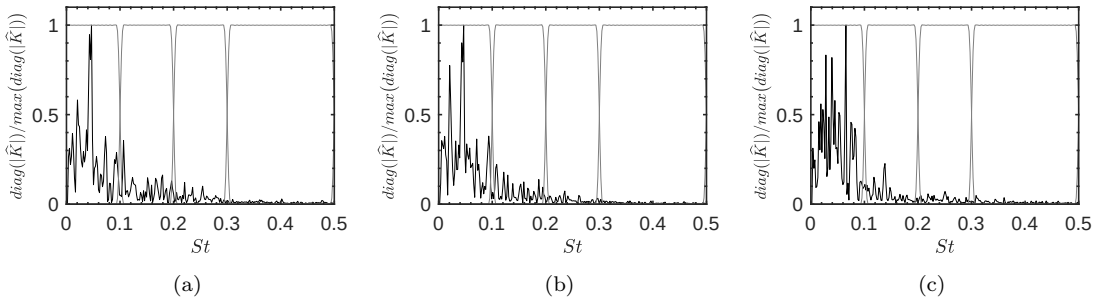



***Figure 8.30:*** *Normalized frequency content of the temporal correlation matrix $K$ on which the filter bank with the frequency splitting vector $St_V = [0, 0.1, 0.2, 0.3, 0.5]$ is superimposed for the first (a) and the second (b) wind turbines of the row, and for the isolated wind turbine (c) in ABL1*

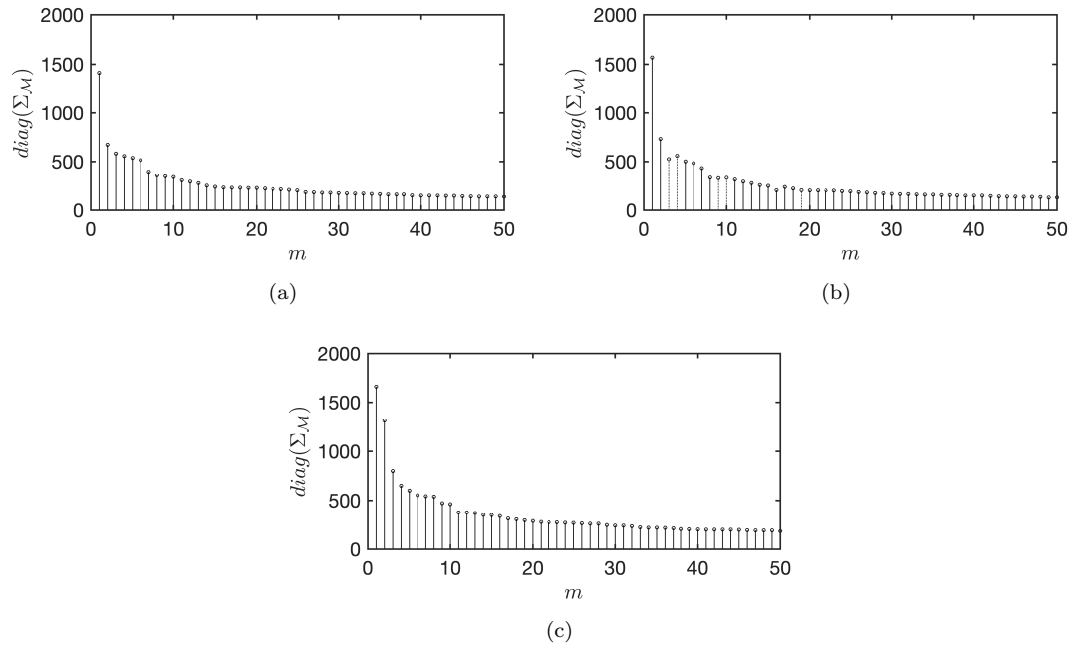



***Figure 8.31:*** *Energy contribution of the first fifty mPOD modes for the first (a) and the second (b) wind turbines of the row, and for the isolated wind turbine (c) in ABL1; dashed stems indicate modes for which the ordering was adapted*

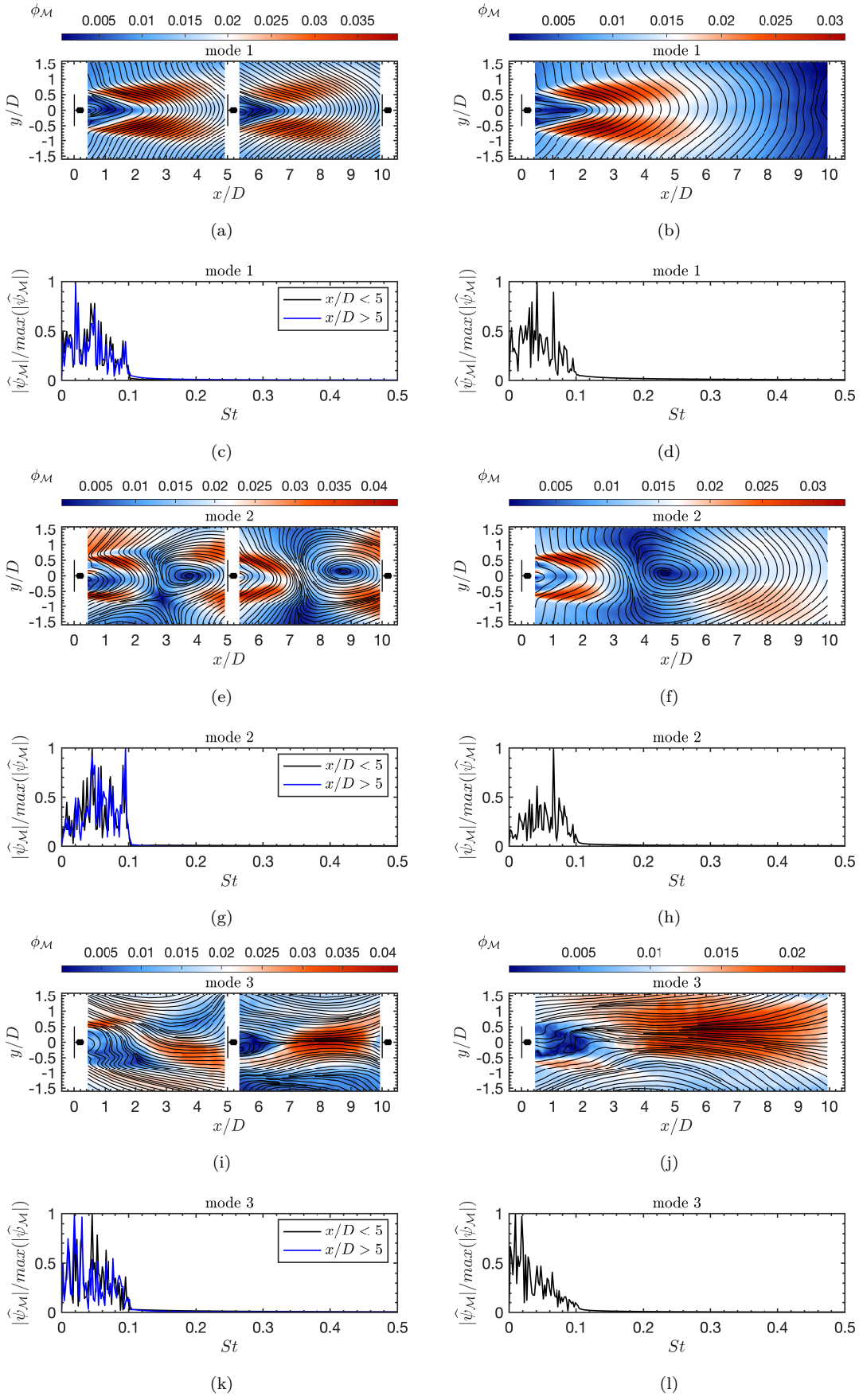



***Figure 8.32:*** *Spatial structures and spectral content of temporal structures obtained from the mPOD analysis of the wake of the first and second wind turbines (left) and of the isolated wind turbine (right) subjected to ABL1*

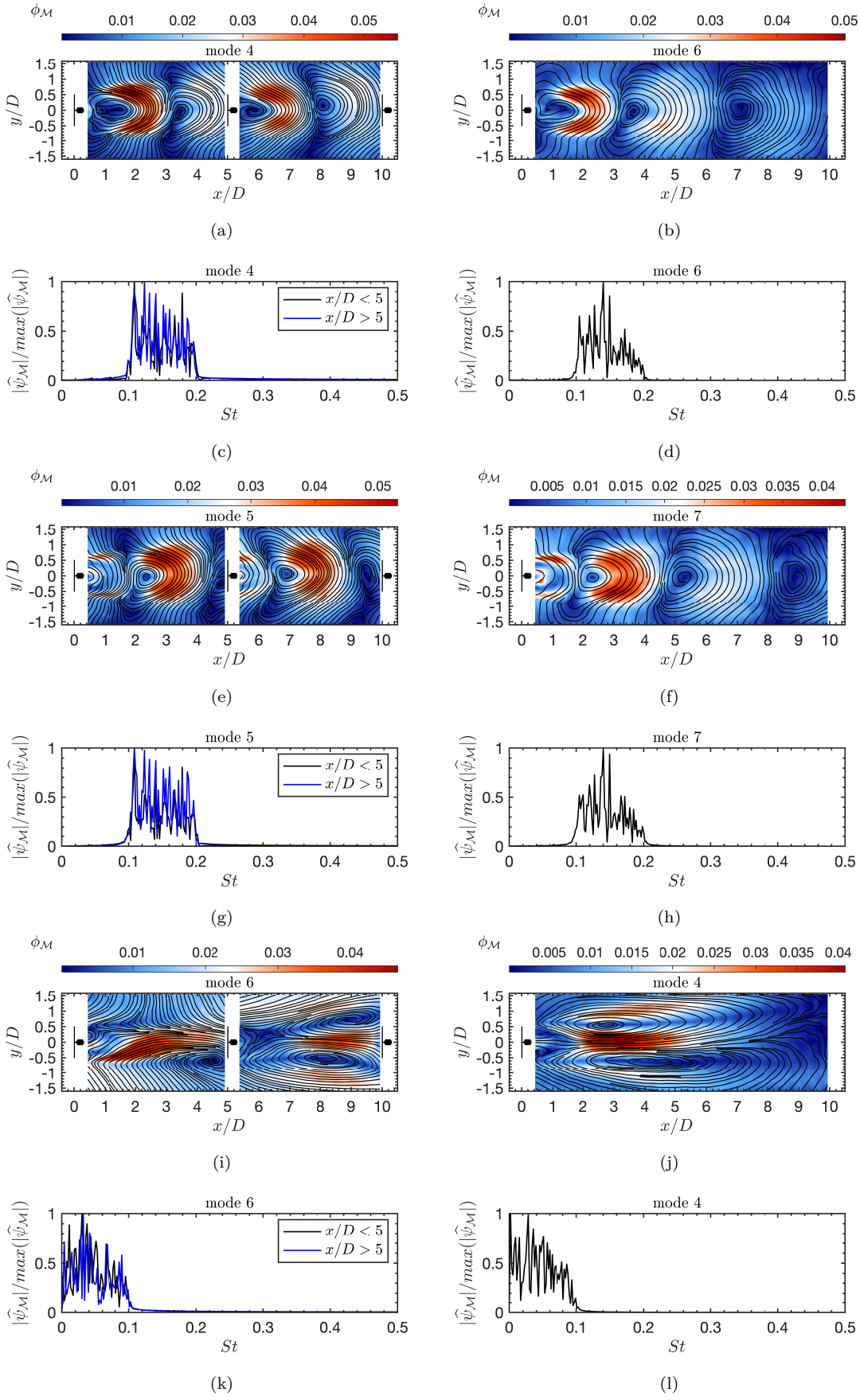



***Figure 8.33:*** *Spatial structures and spectral content of temporal structures obtained from the mPOD analysis of the wake of the first and second wind turbines (left) and of the isolated wind turbine (right) subjected to ABL1 (continued)*

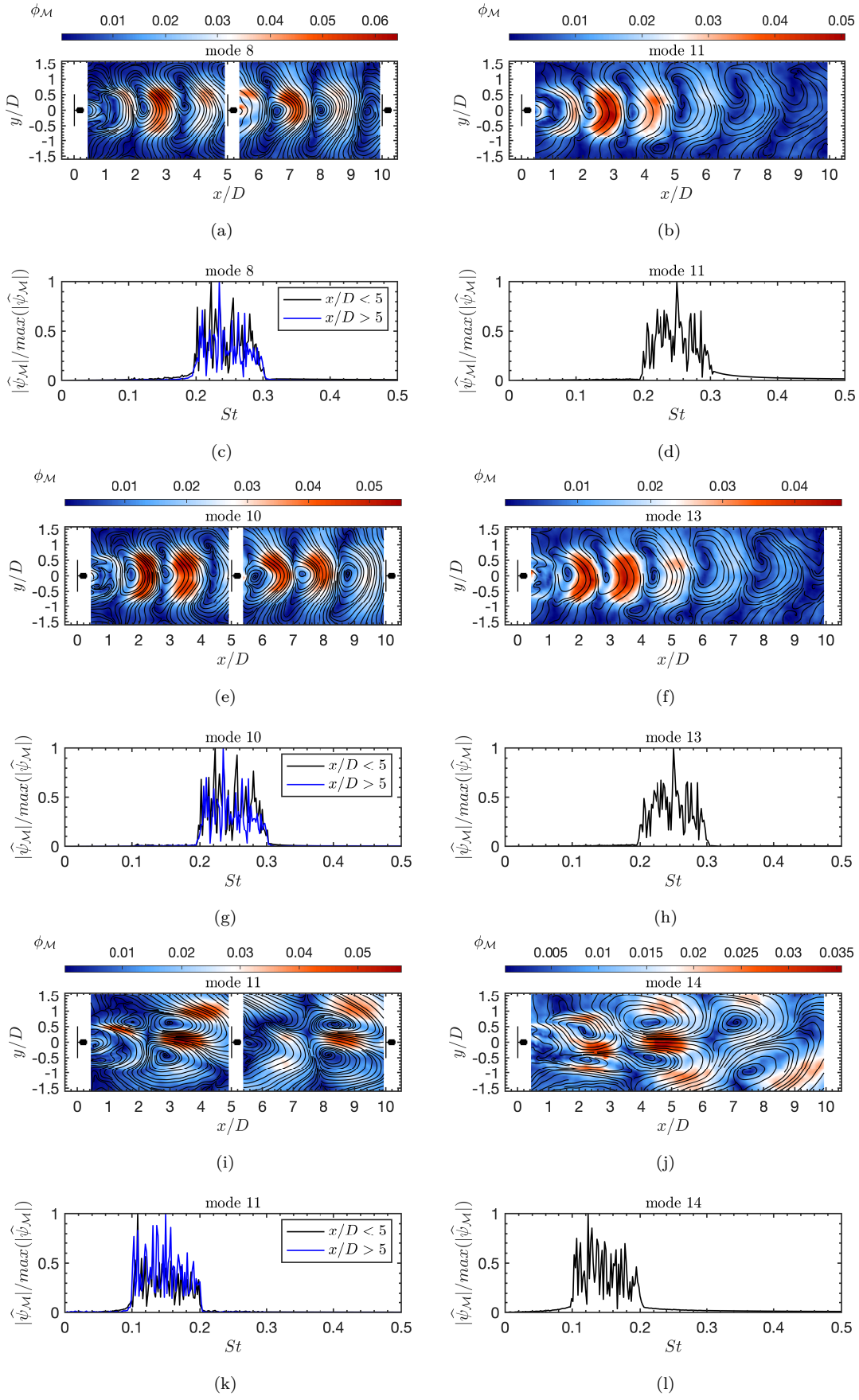



***Figure 8.34:*** *Spatial structures and spectral content of temporal structures obtained from the mPOD analysis of the wake of the first and second wind turbines (left) and of the isolated wind turbine (right) subjected to ABL1 (continued)*

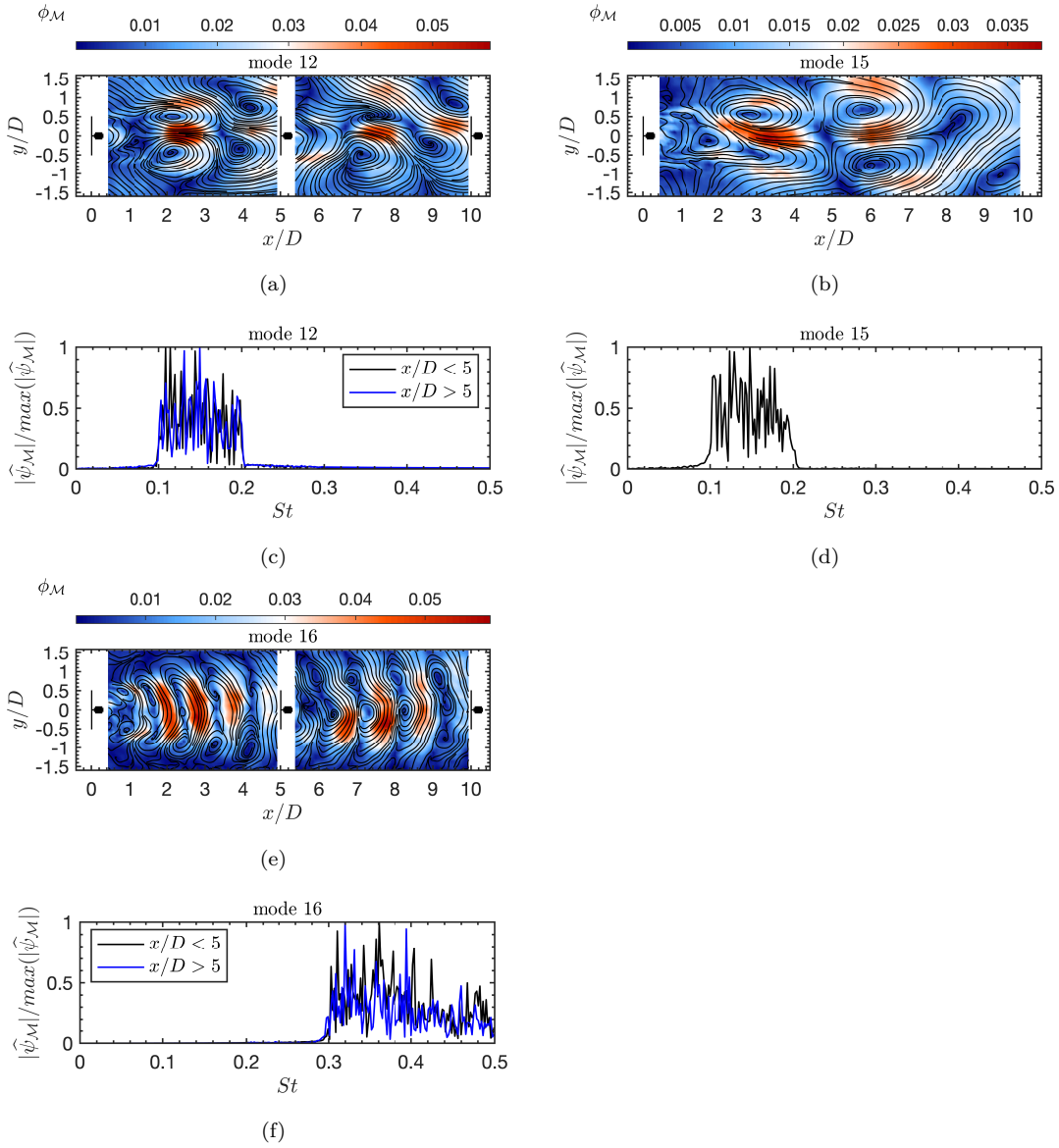



***Figure 8.35:*** *Spatial structures and spectral content of temporal structures obtained from the mPOD analysis of the wake of the first and second wind turbines (left) and of the isolated wind turbine (right) subjected to ABL1 (continued)*

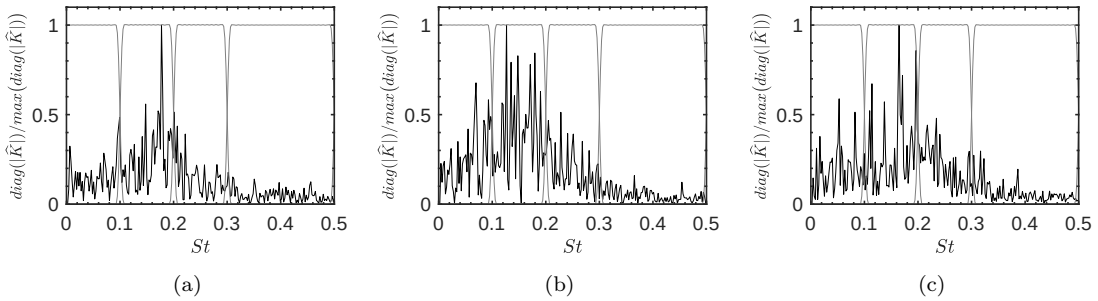



***Figure 8.36:*** *Normalized frequency content of the temporal correlation matrix $K$ on which the filter bank with the frequency splitting vector $St_V = [0, 0.1, 0.2, 0.3, 0.5]$ is superimposed for the first (a) and the second (b) wind turbines of the row, and for the isolated wind turbine (c) in ABL2*

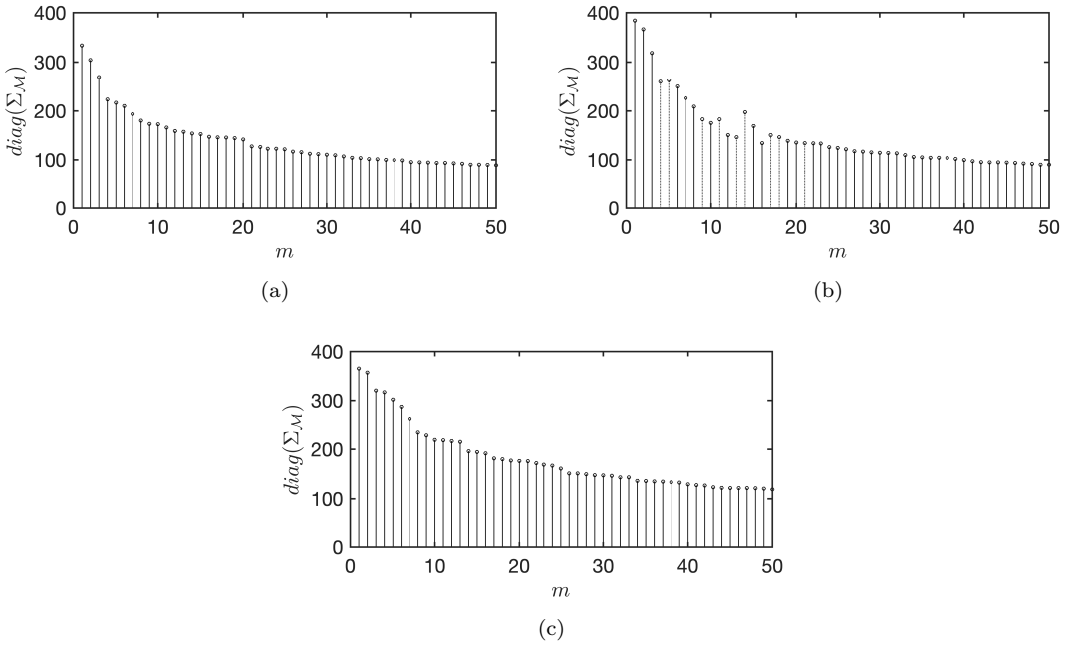



***Figure 8.37:*** *Energy contribution of the fifty first mPOD modes for the first (a) and the second (b) wind turbines of the row, and for the isolated wind turbine (c) in ABL2; dashed stems indicate modes for which the ordering was adapted*

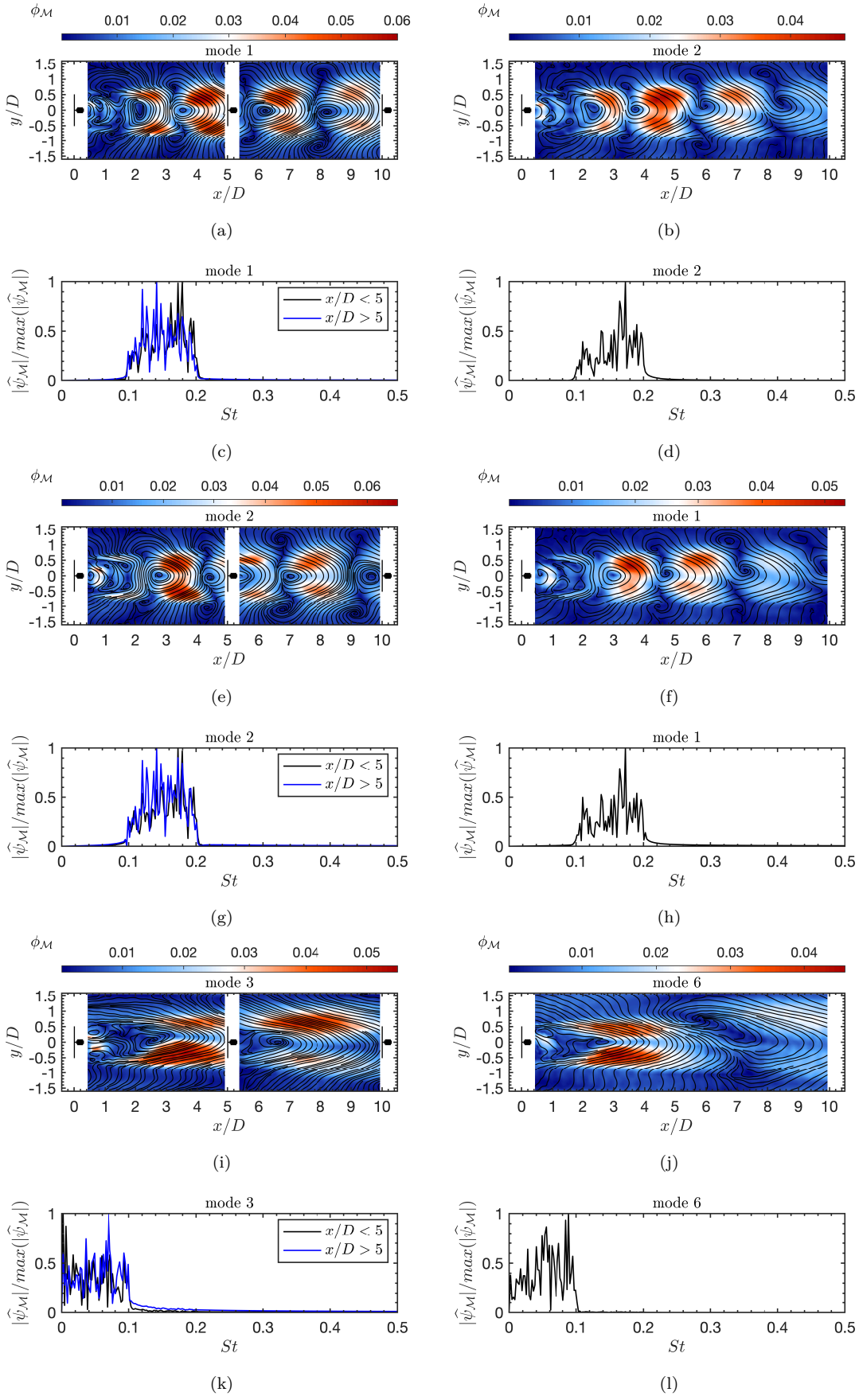



***Figure 8.38:*** *Spatial structures and spectral content of temporal structures obtained from the mPOD analysis of the wake of the first and second wind turbines (left) and of the isolated wind turbine (right) subjected to ABL2*

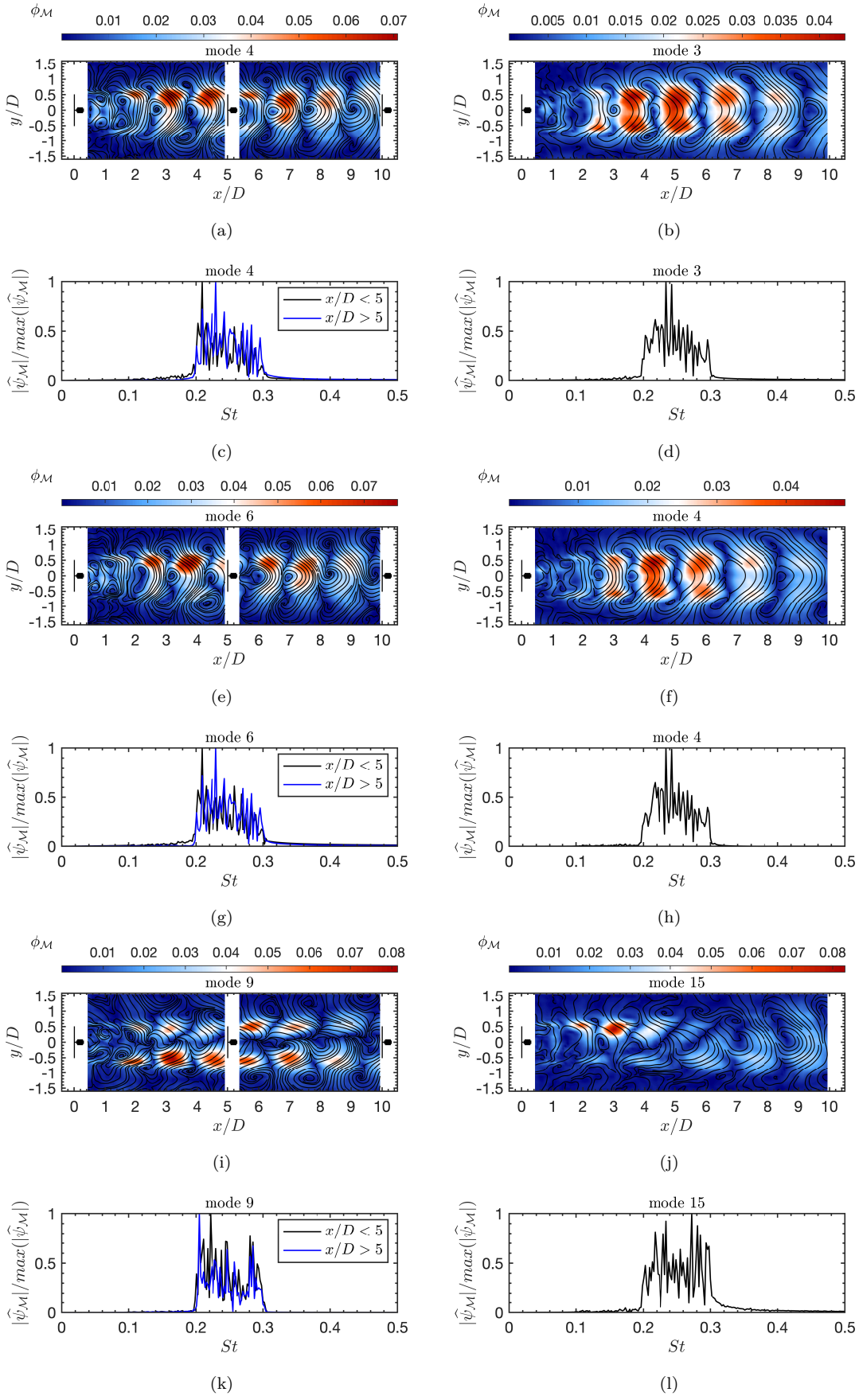



***Figure 8.39:*** *Spatial structures and spectral content of temporal structures obtained from the mPOD analysis of the wake of the first and second wind turbines (left) and of the isolated wind turbine (right) subjected to ABL2 (continued)*

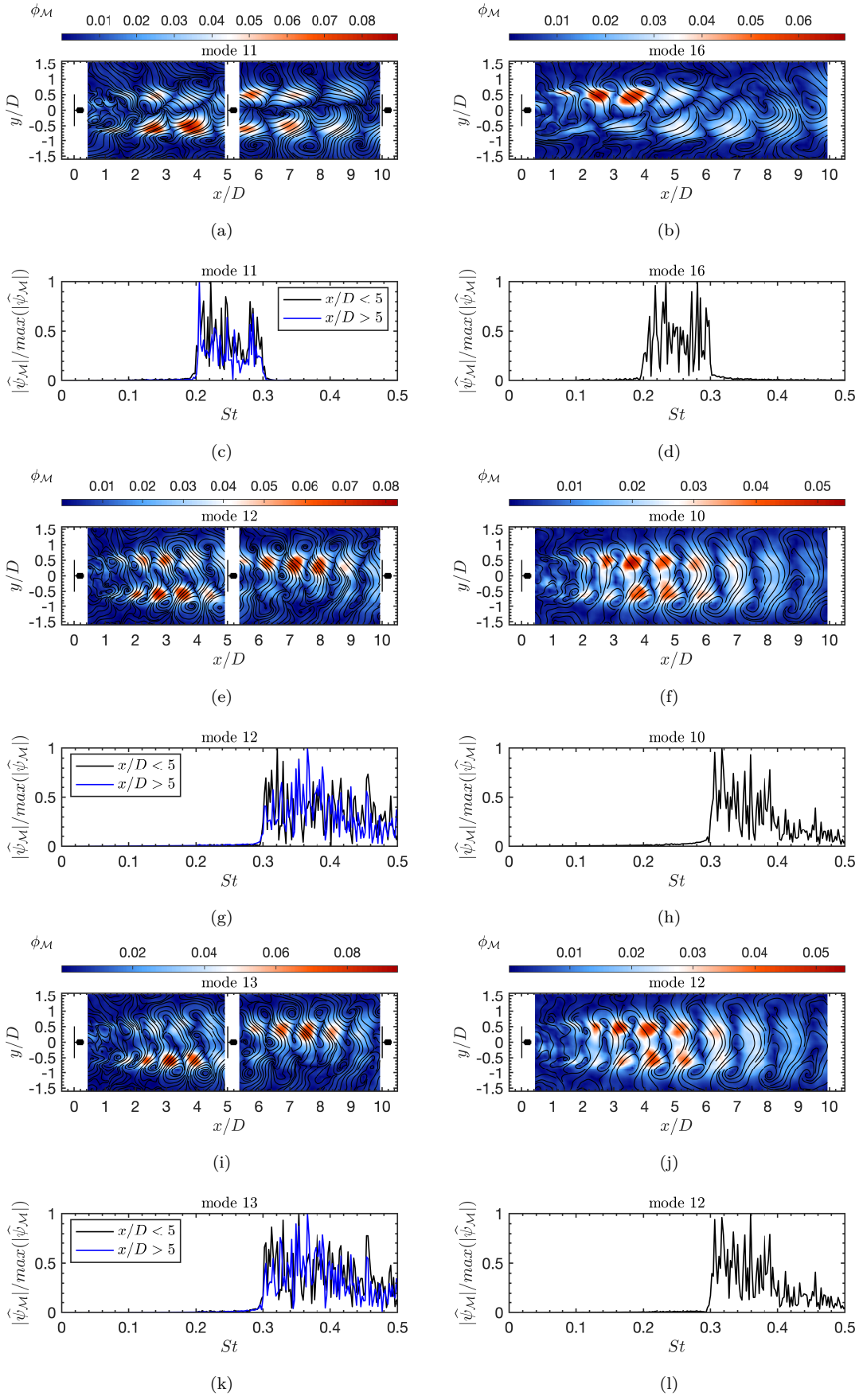



***Figure 8.40:*** *Spatial structures and spectral content of temporal structures obtained from the mPOD analysis of the wake of the first and second wind turbines (left) and of the isolated wind turbine (right) subjected to ABL2 (continued)*

### 8.3.2 Isolated wind turbine vs. third wind turbine

In this section, the mPOD modes obtained in the wake of the third wind turbine of the row of wind turbines are compared to the mPOD modes obtained in the wake of the isolated wind turbine for ABL1 and ABL2.

For ABL1, the dominant frequency content of both temporal correlation matrices $K$ ranges in $0 \leqslant St \leqslant 0.1$ (Fig. 8.41). Figure 8.42 shows that the energy contribution of the modes is slightly larger for the third wind turbine of the row than for the isolated wind turbine. All the mPOD modes presented (Figs. 8.43 to 8.45) are also very similar; taking into account that the ordering of the mode is slightly shifted beyond mode 3. Modes 1, 2, 5, and 6 of the third wind turbine appear nevertheless stronger than the corresponding modes of the isolated wind turbine. Furthermore, the wavelengths extracted from the spatial structures of modes 5 and 6 range within $2.9 \leqslant \lambda/D \leqslant 3.3$ and are slightly shorter than those obtained for the isolated wind turbine ($3.0 \leqslant \lambda/D \leqslant 3.7$). The pronounced similarity between the mPOD modes of the third wind turbine and of the isolated wind turbine highlights the fact that the upstream wind turbines do not modify drastically the wake meandering dynamics of the downstream turbine. However, the strength of the mPOD modes of the third wind turbine shows that the wake dynamics is amplified for the downstream turbine.

For ABL2, the normalized frequency content of the temporal correlation matrix $K$ (Fig. 8.46) are quite similar in the range $0 \leqslant St \leqslant 0.2$ while the frequency content is poorer in the range $0.2 \leqslant St \leqslant 0.5$ for the third wind turbine of the row compared to the isolated one. This will reflect on the mPOD modes obtained for the third wind turbine, as discussed later in this paragraph. Regarding the energy contributions of the mPOD modes, it is much higher for the third wind turbine of the row of wind turbines than for the isolated wind turbine (Fig. 8.47). Furthermore, an important change in the ordering of the modes, much more pronounced than for ABL1, can be observed in Figs. 8.48 to 8.51; the low-frequency modes gaining in energy (or the high-frequency modes loosing in energy). Indeed, for the third wind turbine, the low-frequency modes corresponding to the flapping of the far wake (mode 3) and the long-wavelength oscillatory mechanism (mode 4) have more energy than the corresponding modes for the isolated wind turbine (modes 9 and 6, respectively). Note that, since the vortical structure of mode 6 of the isolated wind turbine is not well defined, this mode represents more strictly the flapping of the wake even if it is visually very close to mode 4. Modes 5 and 6 correspond then to modes 8 and 11 of the isolated wind turbine. The higher frequency modes ($0.2 \leqslant St \leqslant 0.3$) only appear as eighth and ninth mode while they were third and fourth for the isolated wind turbine. This important gain of energy for the low-frequency modes of the third wind turbine can be explained by the interaction of its wake with the wakes of the upstream turbines. Furthermore, the wavelengths extracted from the spatial structures of the modes corresponding to an oscillatory mechanism appear globally larger for the third wind turbine of the row than for the isolated one, especially for modes 1 and 2 for which $1.9 \leqslant \lambda/D \leqslant 2.7$ compared to $1.4 \leqslant \lambda/D \leqslant 2.5$ for the isolated wind turbine.

Finally, modes 13 and 14 correspond to wake dynamics not observed yet. They correspond to an alternate thickening and slimming of the wake as evidenced in Fig. 8.52.

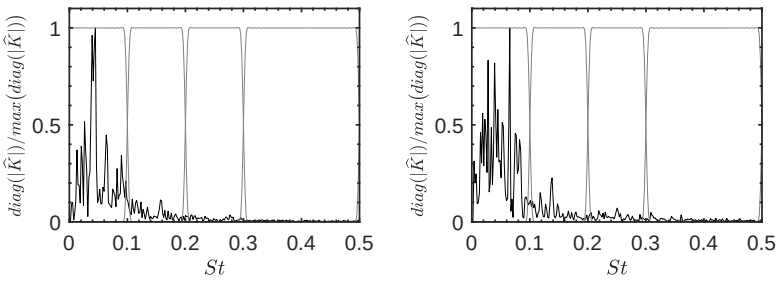



***Figure 8.41:*** *Normalized frequency content of the temporal correlation matrix $K$ on which the filter bank with the frequency splitting vector $St_V = [0, 0.1, 0.2, 0.3, 0.5]$ is superimposed for the third wind turbine (a) of the row and for the isolated wind turbine (b) within ABL1*

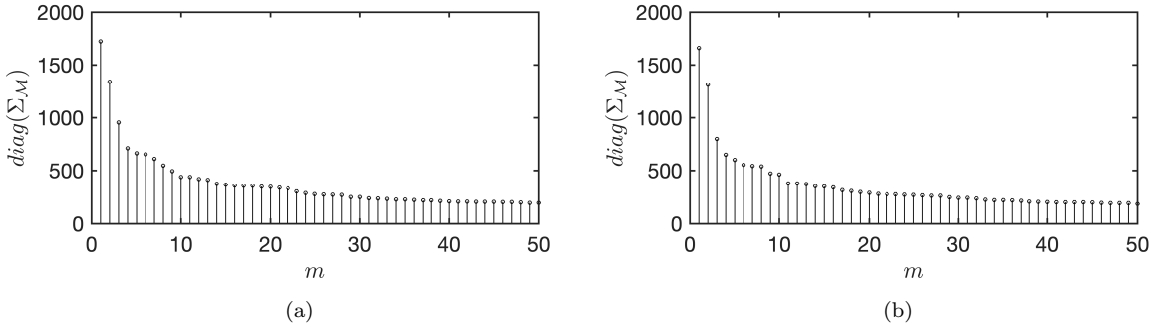



***Figure 8.42:*** *Energy contribution of the fifty first mPOD modes for the third wind turbine (a) of the row and for the isolated wind turbine (b) within ABL1*

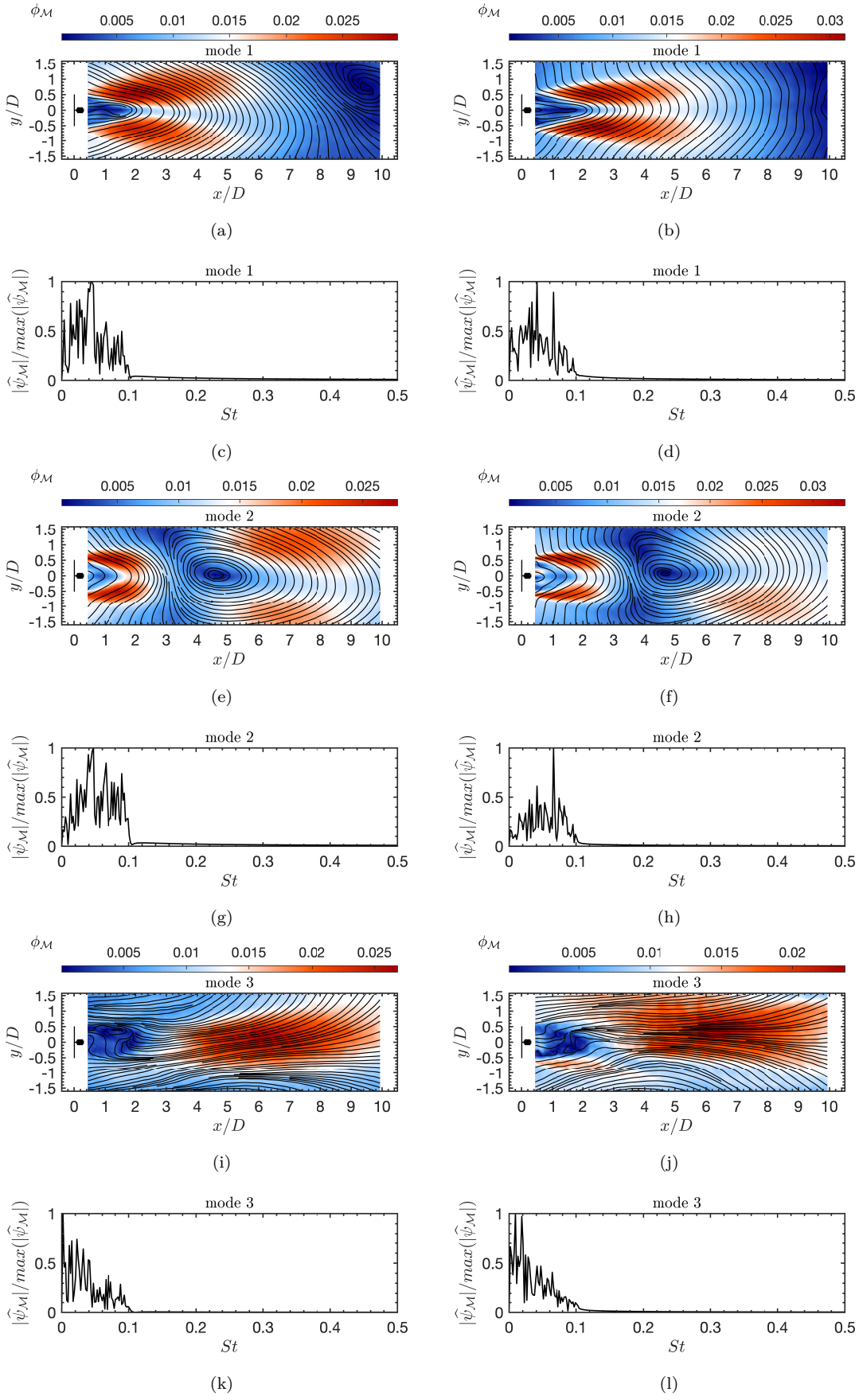



***Figure 8.43:*** *Spatial structures and spectral content of temporal structures obtained from the mPOD analysis of the wake of the third wind turbine (left) of the row and of the isolated wind turbine (right) subjected to ABL1*

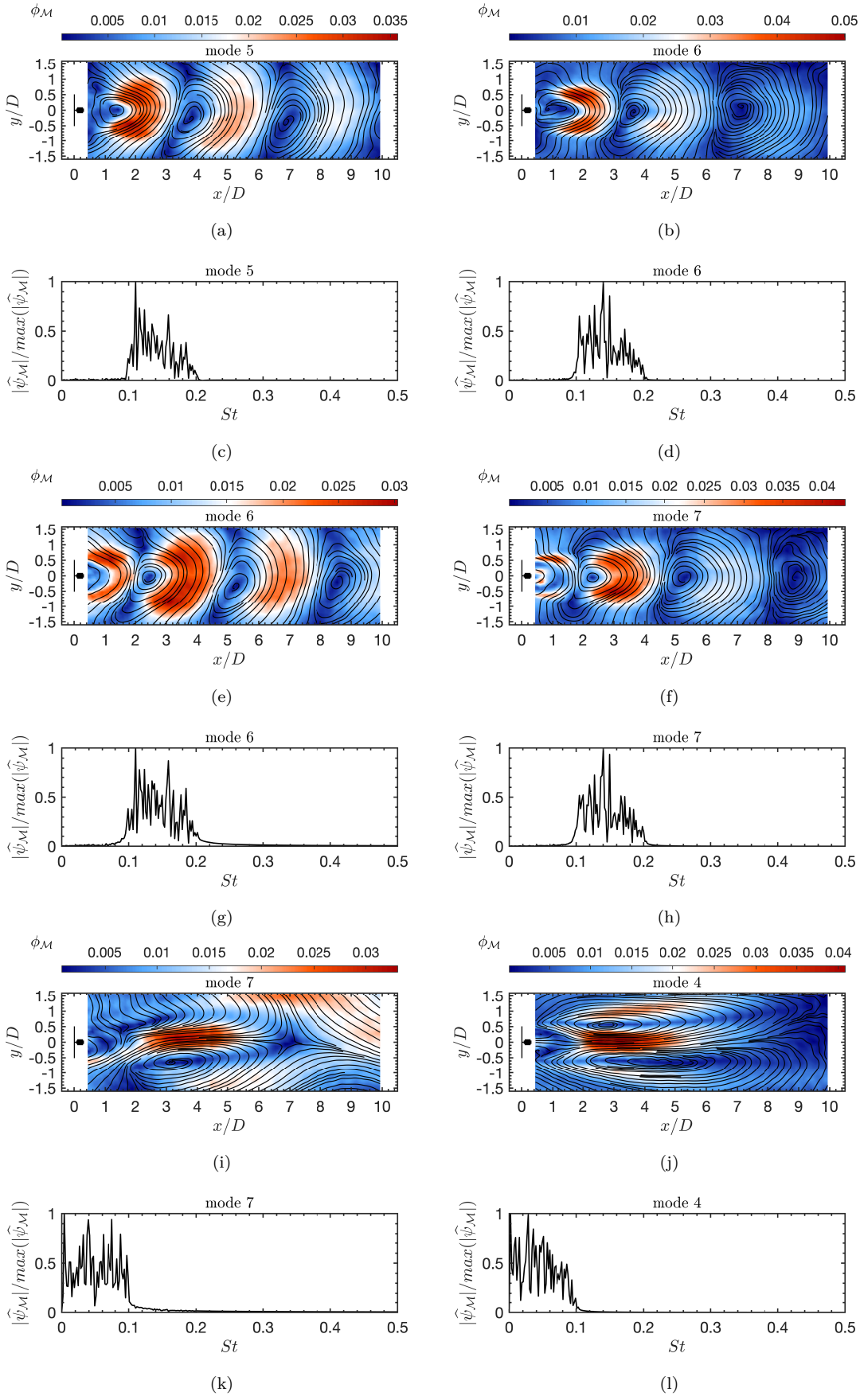



***Figure 8.44:*** *Spatial structures and spectral content of temporal structures obtained from the mPOD analysis of the wake of the third wind turbine (left) of the row and of the isolated wind turbine (right) subjected to ABL1 (continued)*

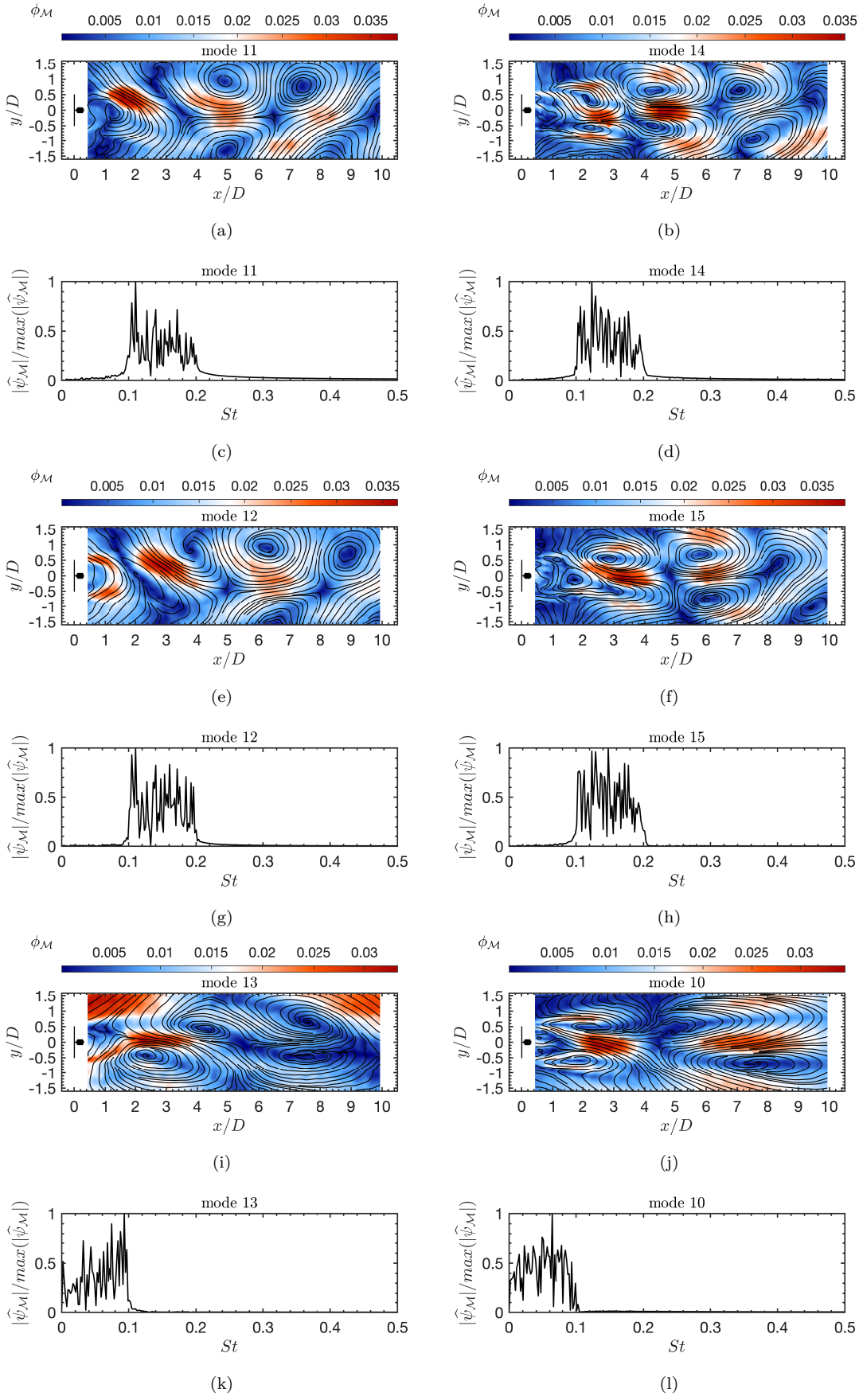



***Figure 8.45:*** *Spatial structures and spectral content of temporal structures obtained from the mPOD analysis of the wake of the third wind turbine (left) of the row and of the isolated wind turbine (right) subjected to ABL1 (continued)*

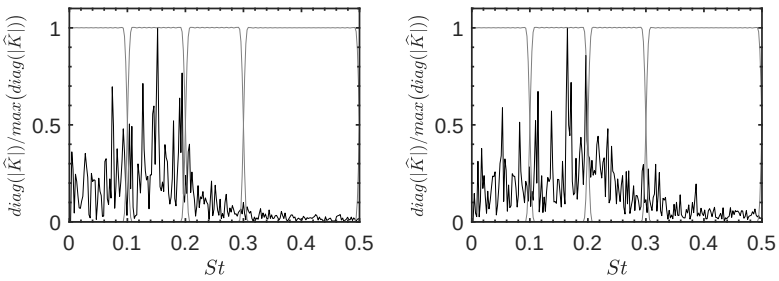



***Figure 8.46:*** *Normalized frequency content of the temporal correlation matrix $K$ on which the filter bank with the frequency splitting vector $St_V = [0, 0.1, 0.2, 0.3, 0.5]$ is superimposed for the third wind turbine (a) of the row and for the isolated wind turbine (b) within ABL2*

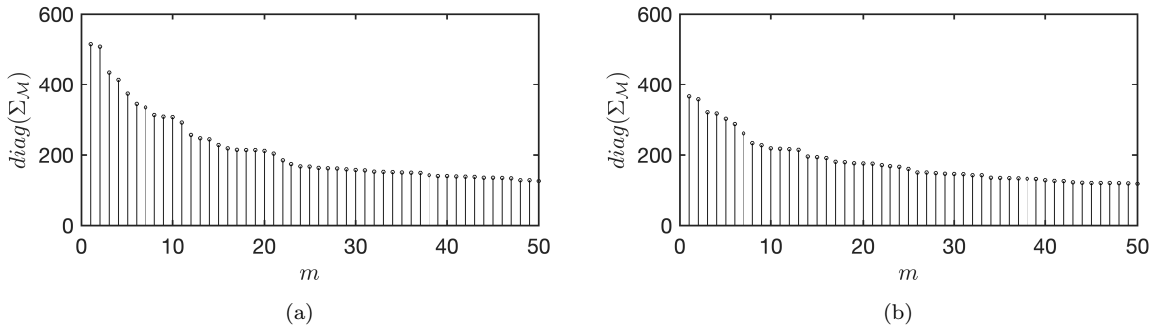



***Figure 8.47:*** *Energy contribution of the fifty first mPOD modes for the third wind turbine (a) and for the isolated wind turbine (b) in ABL2*

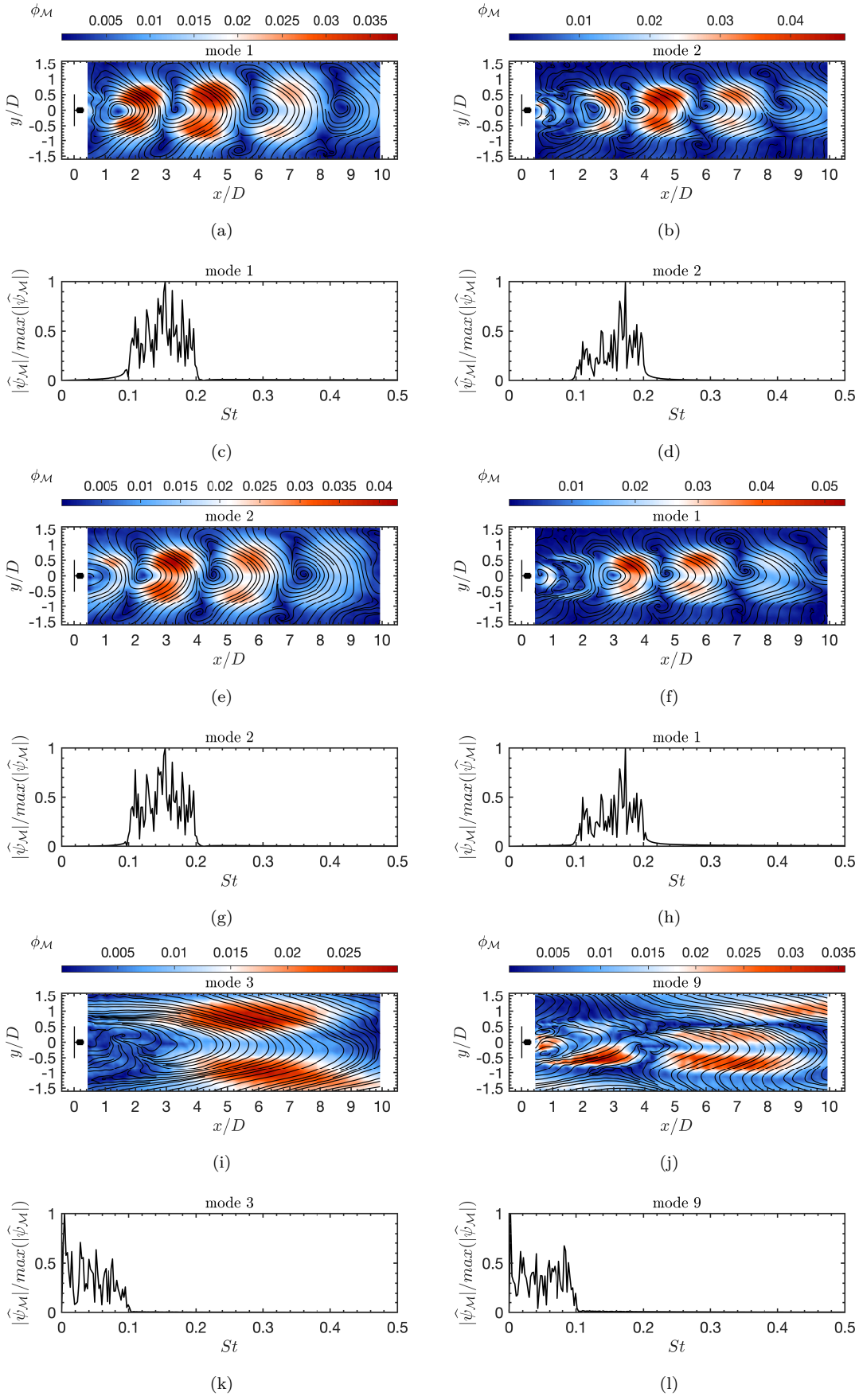



***Figure 8.48:*** *Spatial structures and spectral content of temporal structures obtained from the mPOD analysis of the wake of the third wind turbine (left) of the row and of the isolated wind turbine (right) subjected to ABL2*

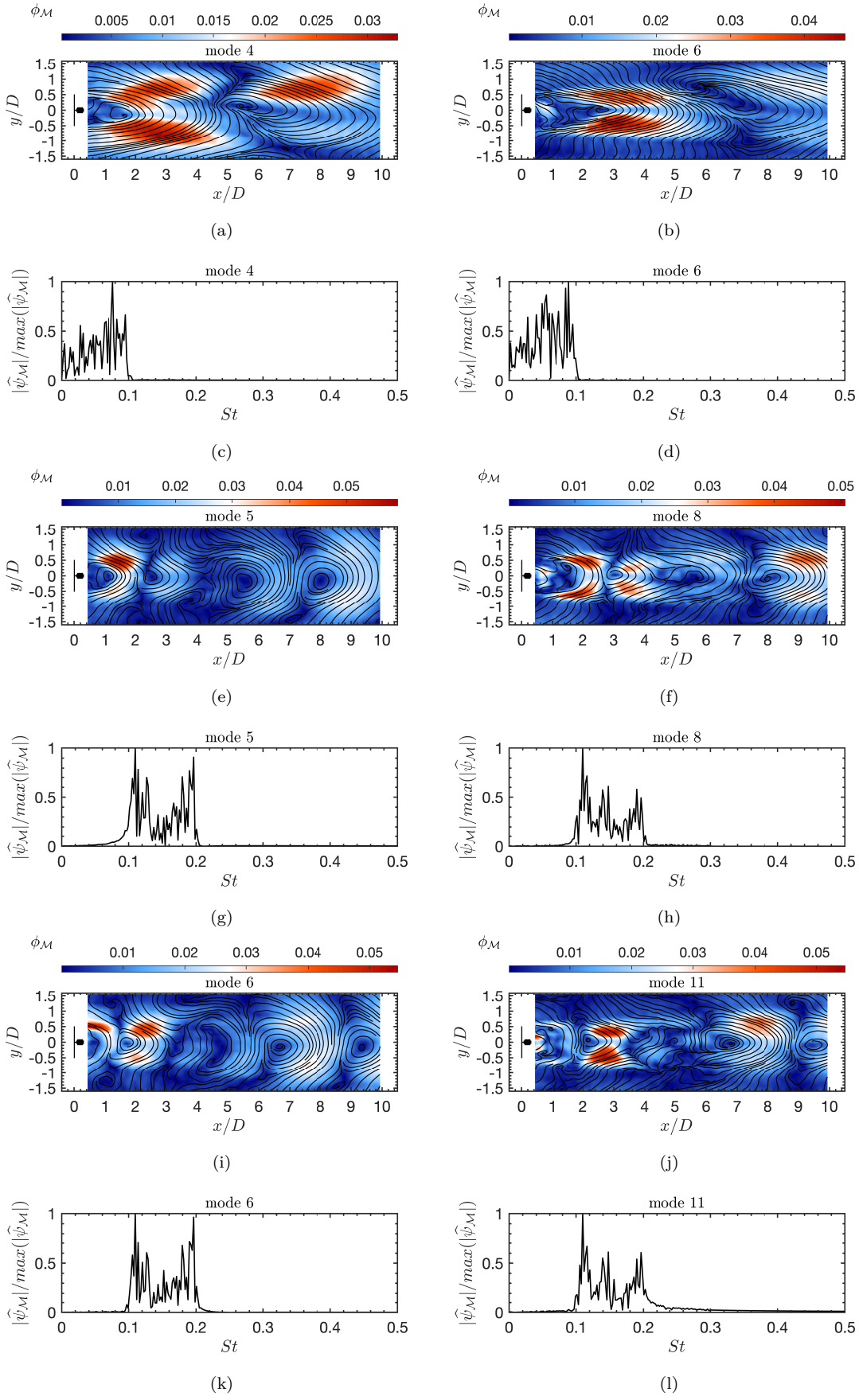



***Figure 8.49:*** *Spatial structures and spectral content of temporal structures obtained from the mPOD analysis of the wake of the third wind turbine (left) of the row and of the isolated wind turbine (right) subjected to ABL2 (continued)*

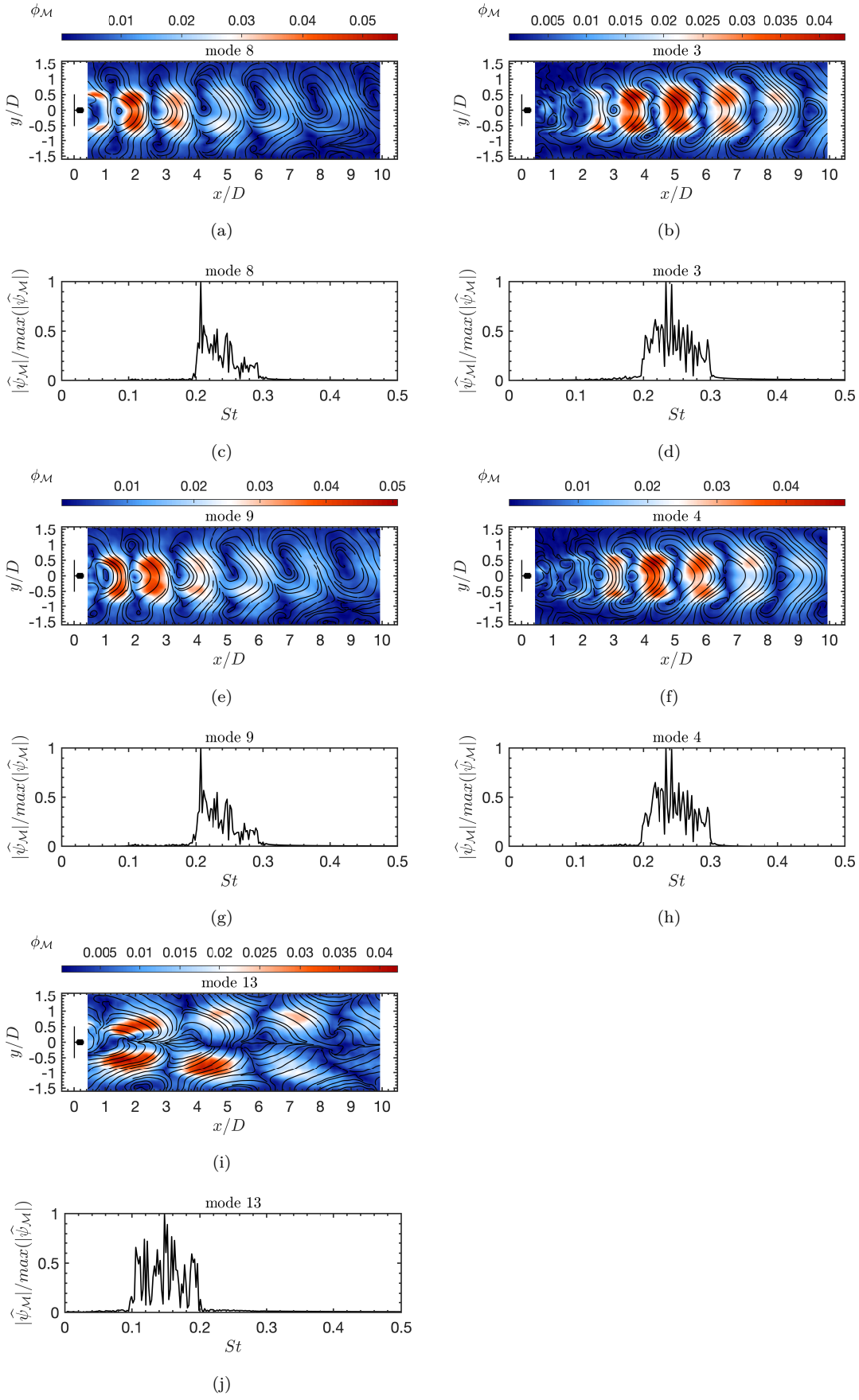



***Figure 8.50:*** *Spatial structures and spectral content of temporal structures obtained from the mPOD analysis of the wake of the third wind turbine (left) of the row and of the isolated wind turbine (right) subjected to ABL2 (continued)*

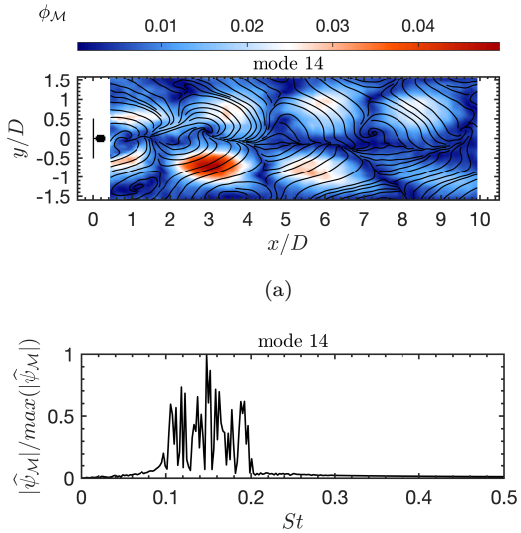



***Figure 8.51:*** *Spatial structures and spectral content of temporal structures obtained from the mPOD analysis of the wake of the third wind turbine (left) of the row and of the isolated wind turbine (right) subjected to ABL2 (continued)*

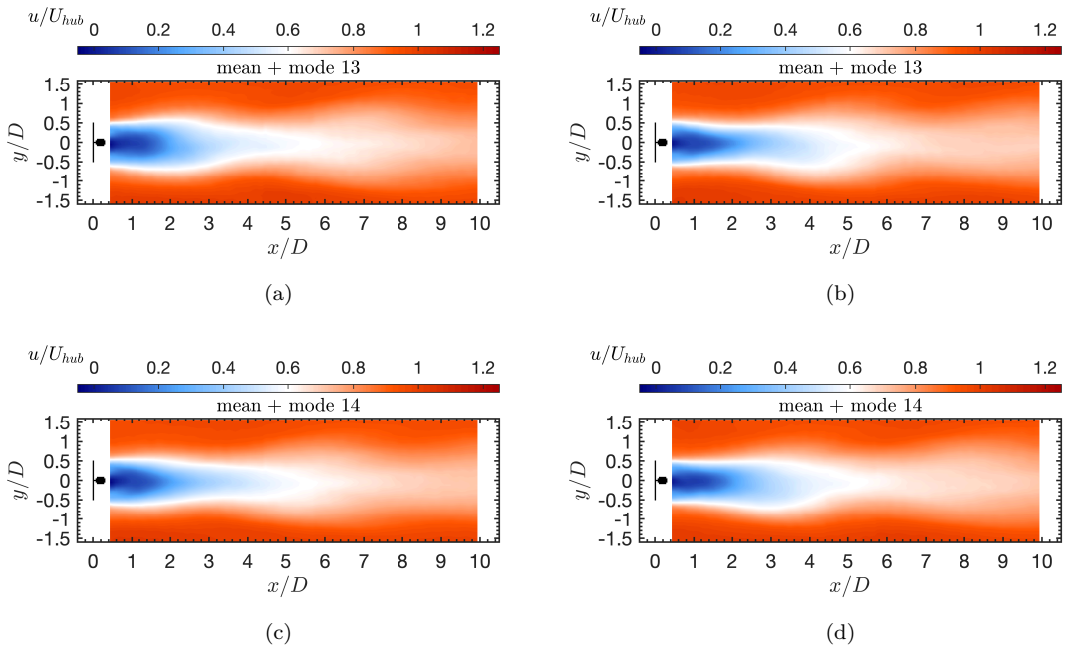



***Figure 8.52:*** *Instantaneous reconstructed field at two different times (left and right) obtained from the mPOD analysis of the wake of the third wind turbine of the row subjected to ABL2*

## 8.4 Wind farm

For ABL1 and ABL2, the mPOD modes obtained for the wind turbines composing the central row of the wind farm are very similar to those of the isolated row, they only present some minor changes in their ordering. For the sake of conciseness, they are therefore presented in Appendix J (Figs. J.1 to J.16).

## 8.5 Porous disks

In order to understand the importance of the wind turbine model on the wake meandering phenomenon, the isolated three-bladed model was successively replaced by three porous disks with a solidity of 56%, 44% and 36%, respectively. The modal analysis is performed in the wake of the porous disks for ABL1 and ABL2.

### 8.5.1 Porous disk vs. three-bladed wind turbine model

In this section, the mPOD results obtained for the porous disk with a solidity $\sigma = 56\%$ are compared to those of the isolated three-bladed wind turbine.

For ABL1, the dominant frequency content of the temporal correlation matrix $K$ ranges in $0 \leqslant St \leqslant 0.1$ for both the porous disk with a solidity $\sigma = 56\%$ and the bladed model (Fig. 8.53). The evolution of the energy contribution (Fig. 8.54) of the modes obtained in the wake of the porous disk is quite similar to that obtained for the bladed model. Even if the modes are similar, they are less energetic in the case of the porous disk, which results overall in a smaller amplitude of the wake meandering. Considering the energy contribution of the first modes, the relative contribution of mode 3 compared to mode 1 and 2 is larger for the porous disk than for the bladed model. The modes obtained for the porous disk are very similar to the modes obtained for the bladed model (Figs. 8.55 to 8.57), considering the small shift in the ordering for modes 5, 6 and 7. In general, it can be observed that the spatial structures extend or are located further downstream for the porous disk than for the rotating model. This can be justified by the fact that the velocity deficit is smaller for the porous disk. Furthermore, the spatial structures corresponding to an oscillatory mechanism of the wake (Figs 8.56(e) and 8.56(i)) present wavelengths similar to those of the three-bladed model.

For ABL2, the dominant frequency content of the temporal correlation matrix $K$ present over $0.1 \leqslant St \leqslant 0.2$ for the bladed model has disappeared and is spread all over $0 \leqslant St \leqslant 0.3$ for the porous disk with a solidity $\sigma = 56\%$ (Fig. 8.58). The evolution of the energy contribution (Fig. 8.59) of the modes obtained in the wake of the porous disk is similar to that obtained for the bladed model. However, they are also less energetic in the case of the porous disk, what results overall in a smaller amplitude of the wake meandering. As it can be observed in Figs. 8.60 to 8.63, the ordering of the modes is largely affected. The low-frequency flapping of the wake represented by modes 1 and 2 for the porous disk corresponds to modes 13 and 9 for the bladed model. It means that the mechanisms that are the most energetic are different for the porous disk compared to the bladed model. Concerning the other modes, they are quite similar considering a slight shift in the ordering, and the wavelengths extracted from the spatial structures are similar to those of the bladed model, as for ABL1.

In particular, it is interesting to compare the second mode obtained in the wake of the porous disk for ABL1 and ABL2. Both modes present a vortex around $x/D \simeq 5$ but, while the structures represented in red are located just behind the rotor for ABL1, they are located right after the vortex for ABL2. In terms of wake dynamics, it translates into a long-wavelength oscillatory motion of the wake for ABL1 while the wake starts to move laterally only at $x/D \simeq 5$ for ABL2.

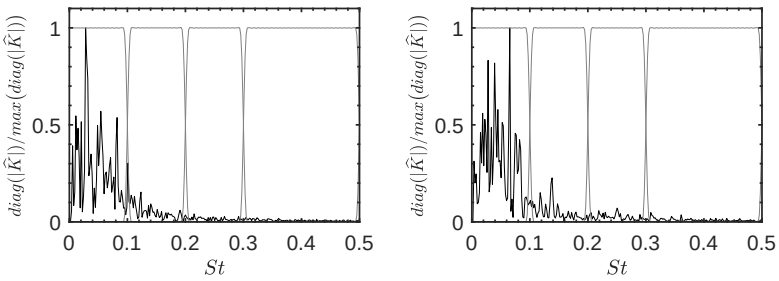



***Figure 8.53:*** *Normalized frequency content of the temporal correlation matrix $K$ on which the filter bank with the frequency splitting vector $St_V = [0, 0.1, 0.2, 0.3, 0.5]$ is superimposed for the porous disk with a solidity $\sigma = 56\%$ (a) and for the isolated wind turbine (b) within ABL1*

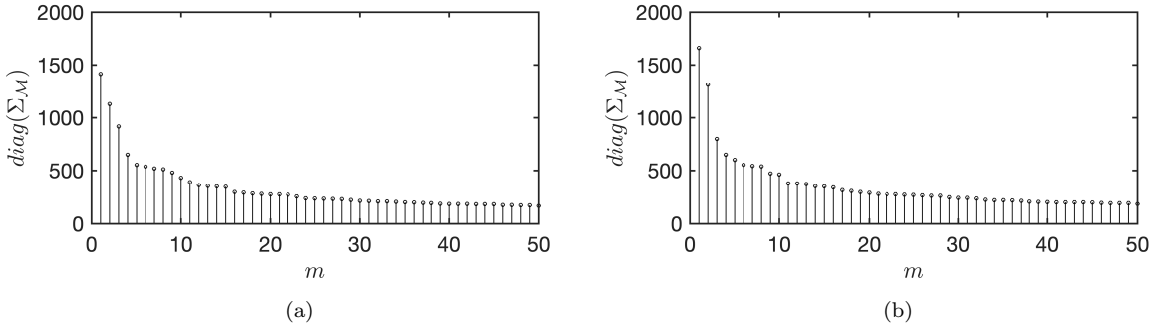



***Figure 8.54:*** *Energy contribution of the fifty first mPOD modes for the porous disk with a solidity $\sigma = 56\%$ (a) and for the bladed wind turbine model (b) within ABL1*

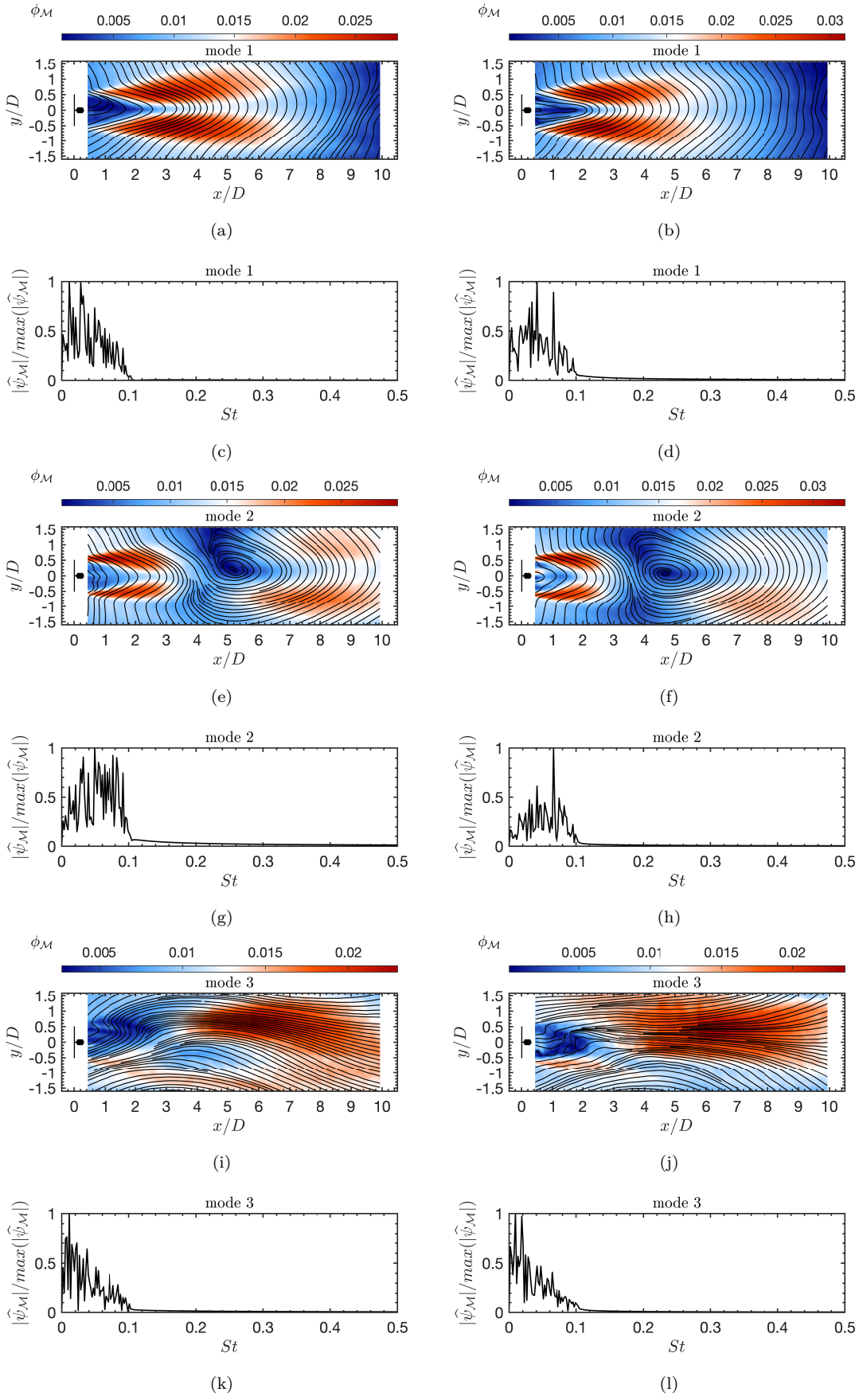



***Figure 8.55:*** *Spatial structures and spectral content of temporal structures obtained from the mPOD analysis of the wake of the porous disk with a solidity $\sigma = 56\%$ (left) and of the isolated bladed wind turbine model (right) subjected to ABL1*

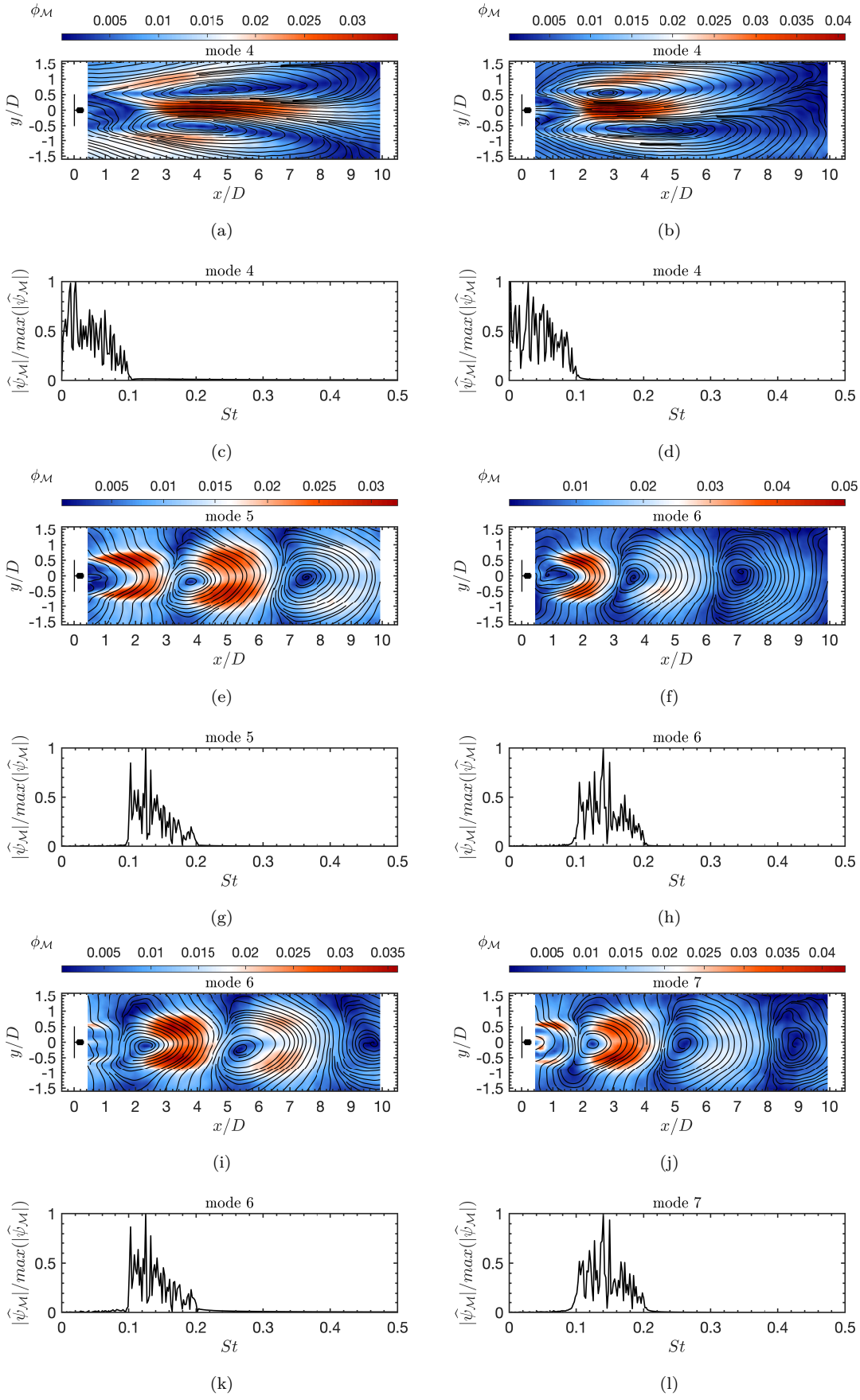



***Figure 8.56:*** *Spatial structures and spectral content of temporal structures obtained from the mPOD analysis of the wake of the porous disk with a solidity $\sigma = 56\%$ (left) and of the isolated bladed wind turbine model (right) subjected to ABL1 (continued)*

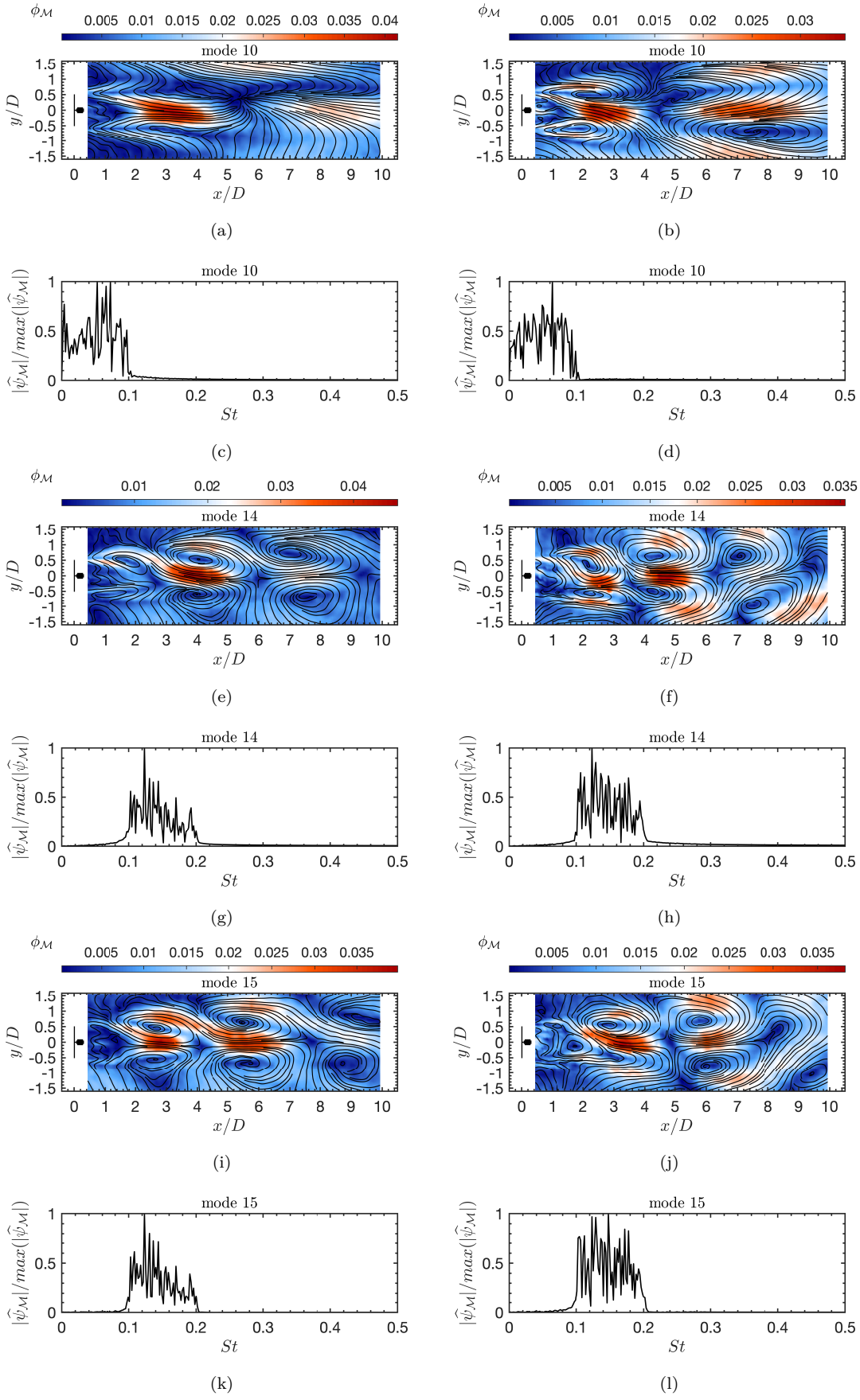



***Figure 8.57:*** *Spatial structures and spectral content of temporal structures obtained from the mPOD analysis of the wake of the porous disk with a solidity $\sigma = 56\%$ (left) and of the isolated bladed wind turbine model (right) subjected to ABL1 (continued)*

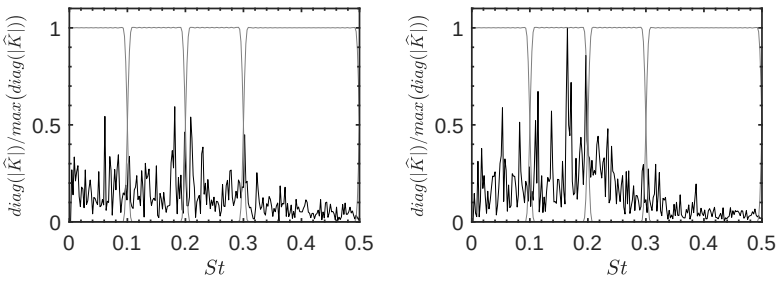



***Figure 8.58:*** *Normalized frequency content of the temporal correlation matrix $K$ on which the filter bank with the frequency splitting vector $St_V = [0, 0.1, 0.2, 0.3, 0.5]$ is superimposed for the porous disk with a solidity $\sigma = 56\%$ (a) and for the isolated wind turbine (b) within ABL2*

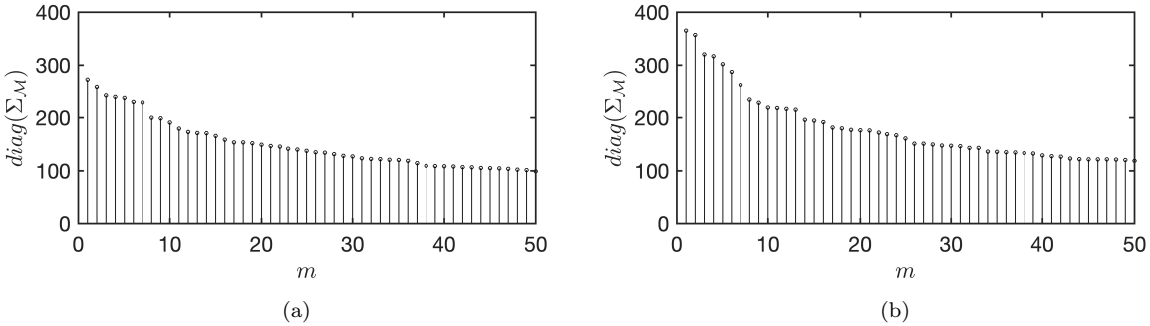



***Figure 8.59:*** *Energy contribution of the fifty first mPOD modes for the porous disk with a solidity $\sigma = 56\%$ (a) and for the bladed wind turbine model (b) within ABL2*

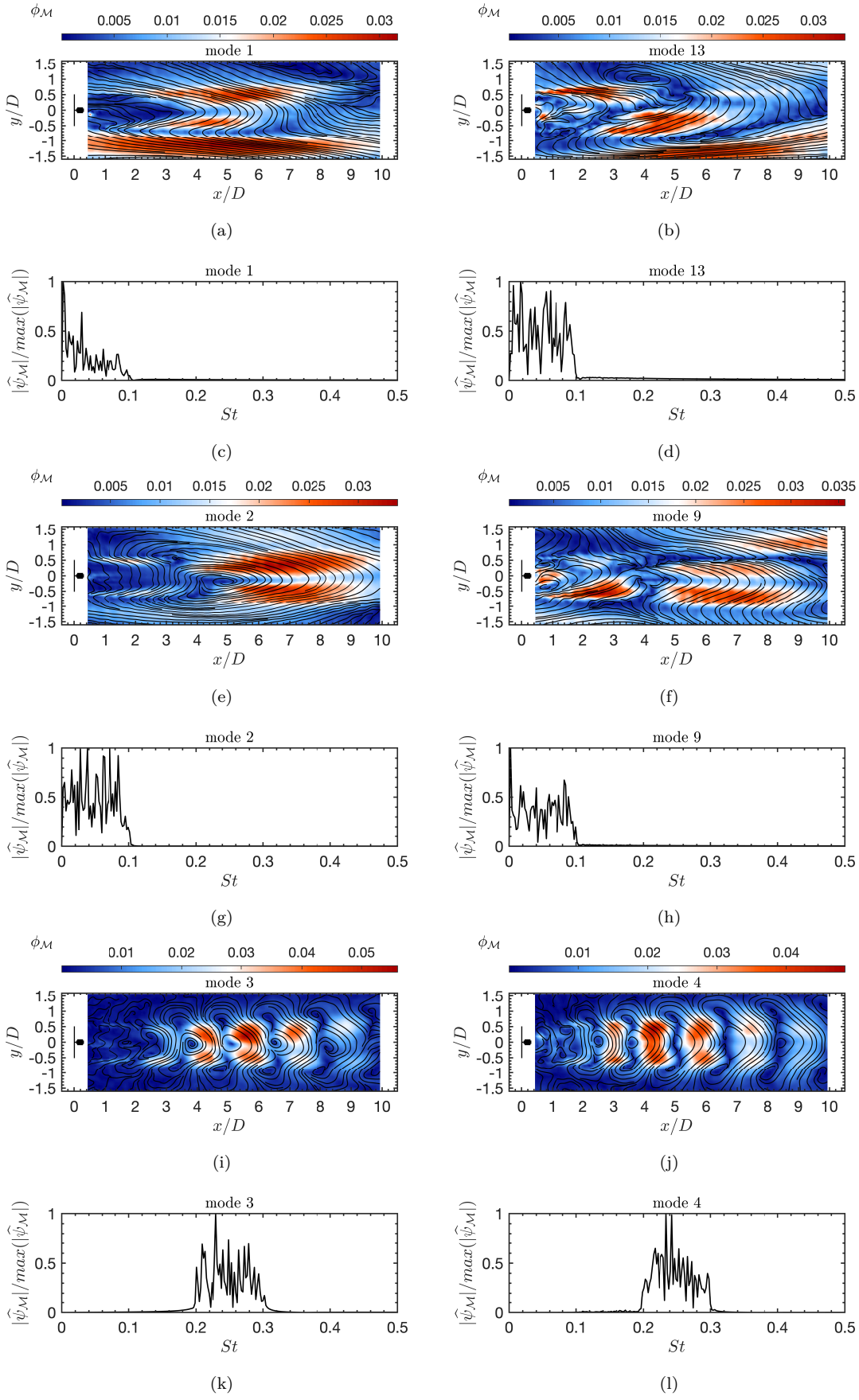



***Figure 8.60:*** *Spatial structures and spectral content of temporal structures obtained from the mPOD analysis of the wake of the porous disk with a solidity $\sigma = 56\%$ (left) and of the isolated bladed wind turbine model (right) subjected to ABL2*

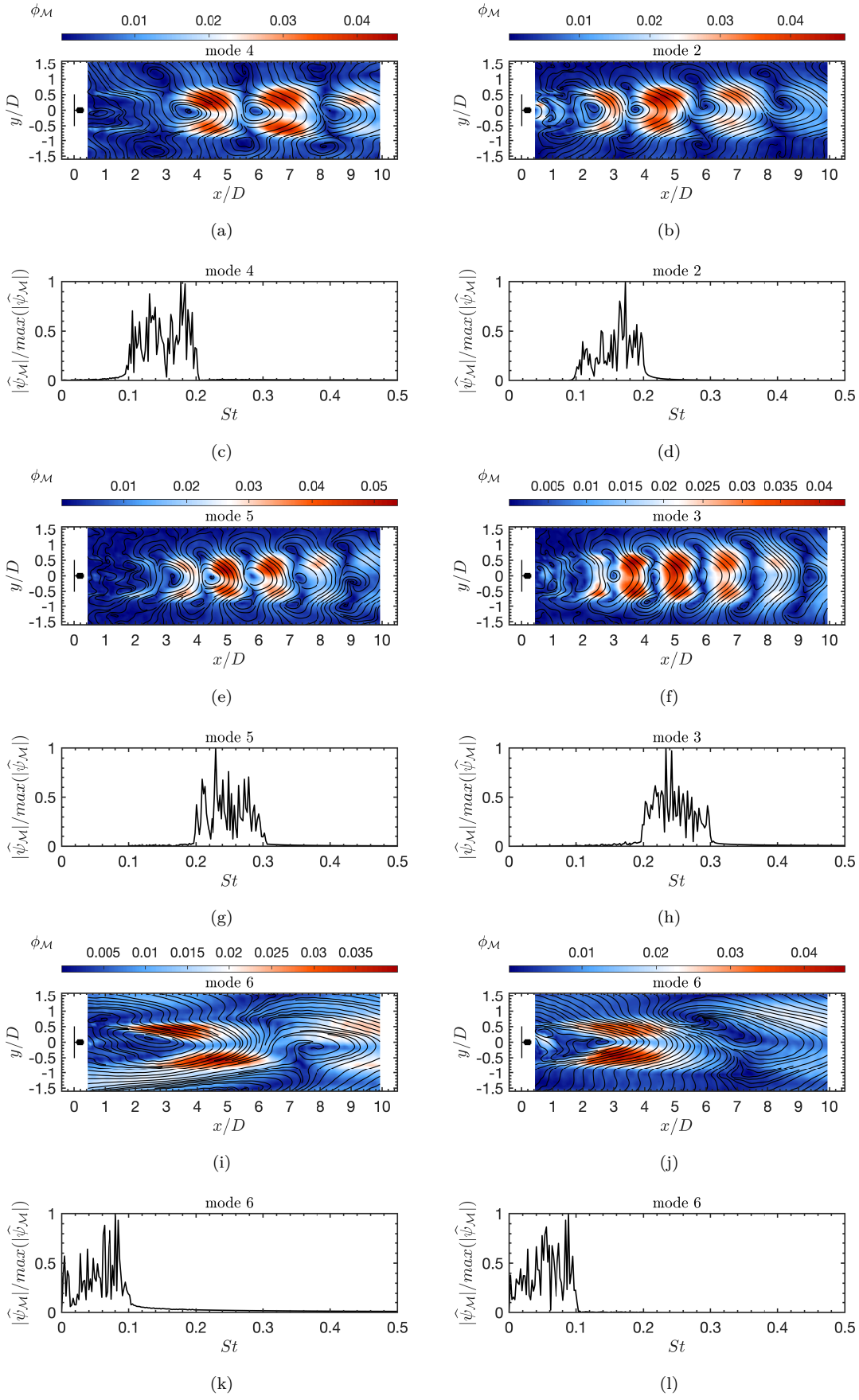



***Figure 8.61:*** *Spatial structures and spectral content of temporal structures obtained from the mPOD analysis of the wake of the porous disk with a solidity $\sigma = 56\%$ (left) and of the isolated bladed wind turbine model (right) subjected to ABL2 (continued)*

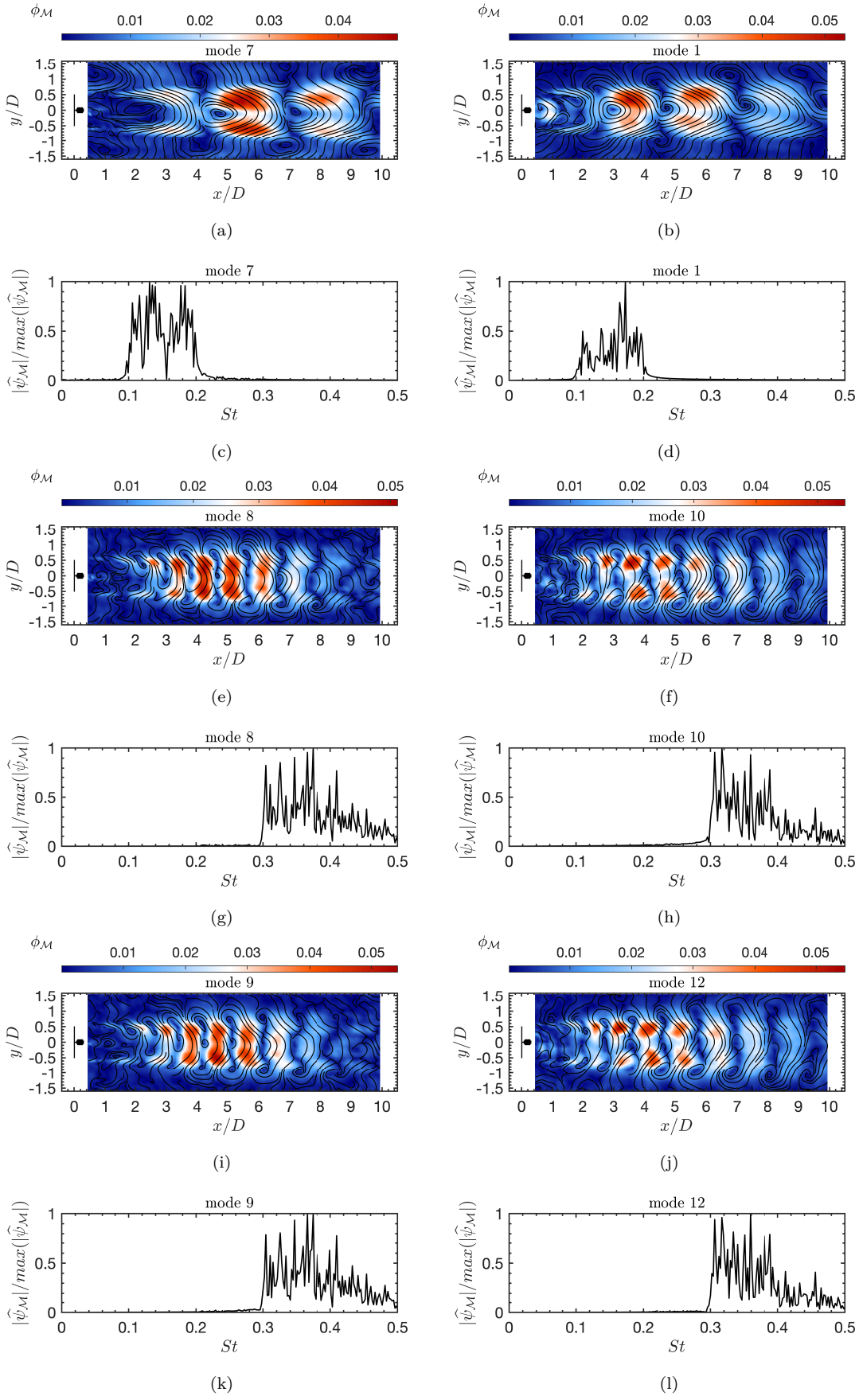



***Figure 8.62:*** *Spatial structures and spectral content of temporal structures obtained from the mPOD analysis of the wake of the porous disk with a solidity $\sigma = 56\%$ (left) and of the isolated bladed wind turbine model (right) subjected to ABL2 (continued)*

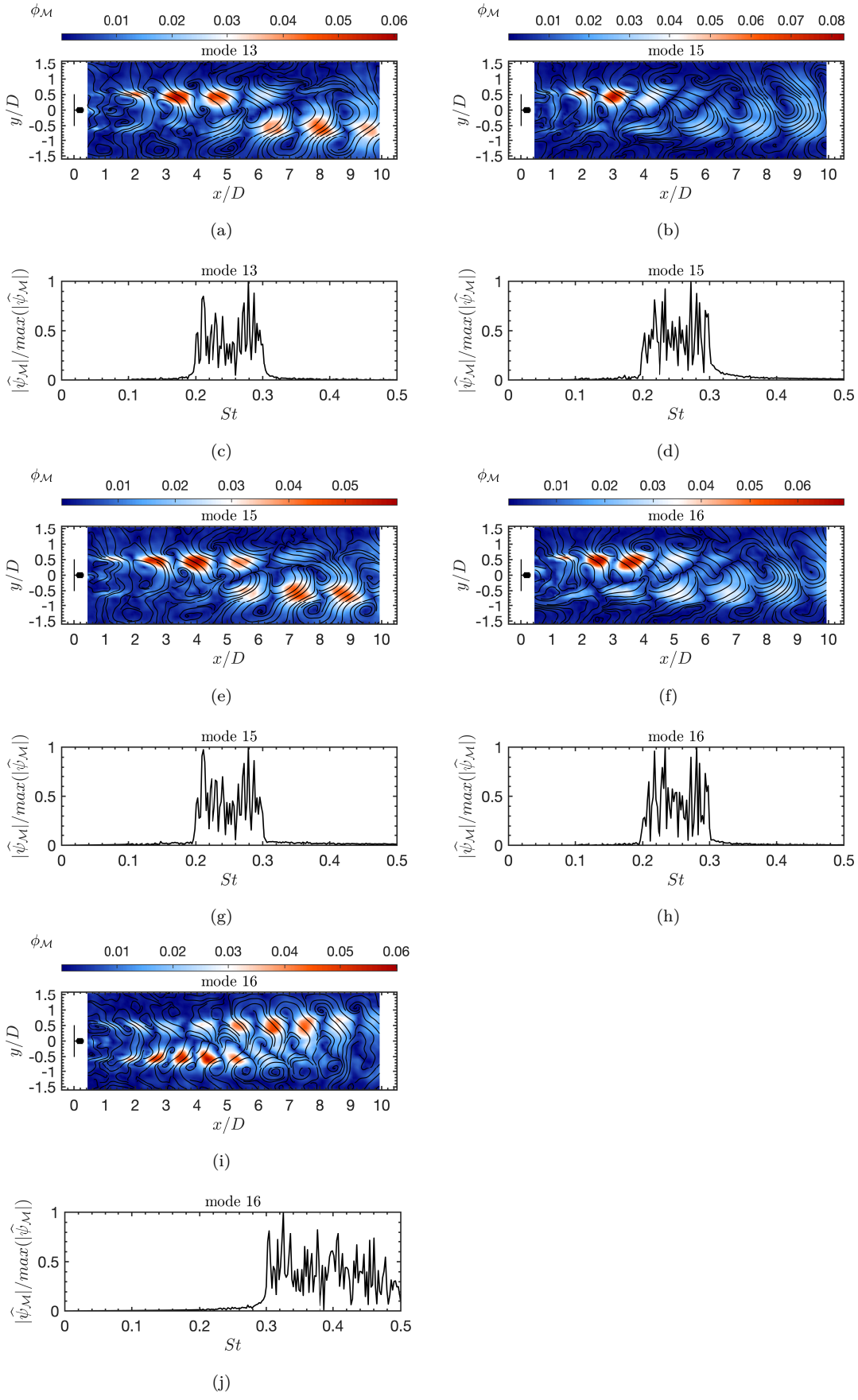



***Figure 8.63:*** *Spatial structures and spectral content of temporal structures obtained from the mPOD analysis of the wake of the porous disk with a solidity $\sigma = 56\%$ (left) and of the isolated bladed wind turbine model (right) subjected to ABL2 (continued)*

### 8.5.2 Influence of the porous disk solidity

For ABL1, the normalized frequency content of the temporal correlation matrix $K$ is dominant for $0 \leqslant St \leqslant 0.1$ whatever the solidity of the porous disk (Fig. 8.64). Furthermore, the modes obtained in the wake of the porous disks with a solidity of 56%, 44%, and 36% present an energy distribution (Fig. 8.65) that is similar, the energy increasing slightly with the solidity.

The modes obtained are quite similar even if the ordering is different (Fig 8.66 to 8.68). The vortical structure of mode 2 ($\sigma = 56\%$ and $\sigma = 44\%$) or mode 3 ($\sigma = 36\%$) moves downstream (Fig. 8.66) when the solidity decreases since the velocity deficit becomes smaller. Similarly to mode 2, the spatial structures have the tendency to move downstream when the solidity decreases. Furthermore, the influence of the solidity can be observed on the spatial structures. Indeed, even if they represent the same wake dynamics, their shape for each specific mode varies clearly between the disks with $\sigma = 56\%$ and $\sigma = 36\%$. Concerning the wavelengths present on the spatial structures of the modes corresponding to an oscillatory motion of the wake, they are similar regardless of the solidity.

For ABL2, the frequency content of the temporal correlation matrix $K$ (Fig. 8.69) is weaker when the solidity decreases. Regarding the energy distribution, it globally decreases when the solidity decreases (Fig. 8.70), as observed for ABL1. Concerning the modes ordering (Fig 8.71 to 8.73), it can be observed that the higher the solidity and the more modes with a higher spectral content are present within the most energetic ones. Indeed, within the nine first modes, the porous disk with $\sigma = 56\%$ has modes corresponding to $0.3 \leqslant St \leqslant 0.5$ (high frequency oscillations) while the porous disk with $\sigma = 36\%$ has only modes corresponding to the maximum range of $0.1 \leqslant St \leqslant 0.2$ (wake expansion and slimming). Concerning the wavelengths that can be extracted from the spatial structures of the modes corresponding to an oscillatory motion of the wake, they are similar regardless of the solidity.

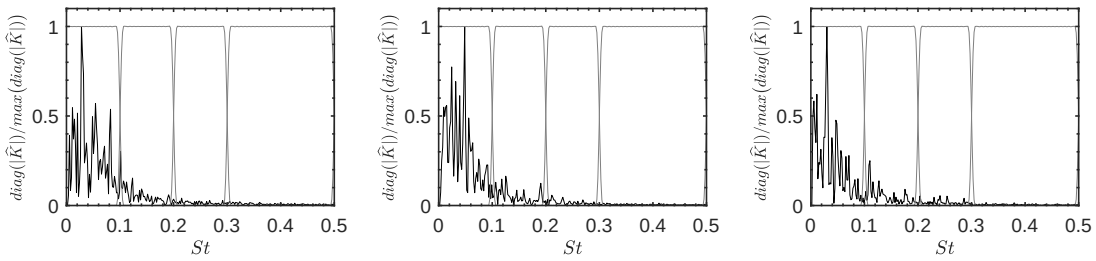



***Figure 8.64:*** *Normalized frequency content of the temporal correlation matrix $K$ on which the filter bank with the frequency splitting vector $St_V = [0, 0.1, 0.2, 0.3, 0.5]$ is superimposed for the porous disks with various solidity: $\sigma = 56\%$ (a), $\sigma = 44\%$ (b) and $\sigma = 36\%$ (c) within ABL1*

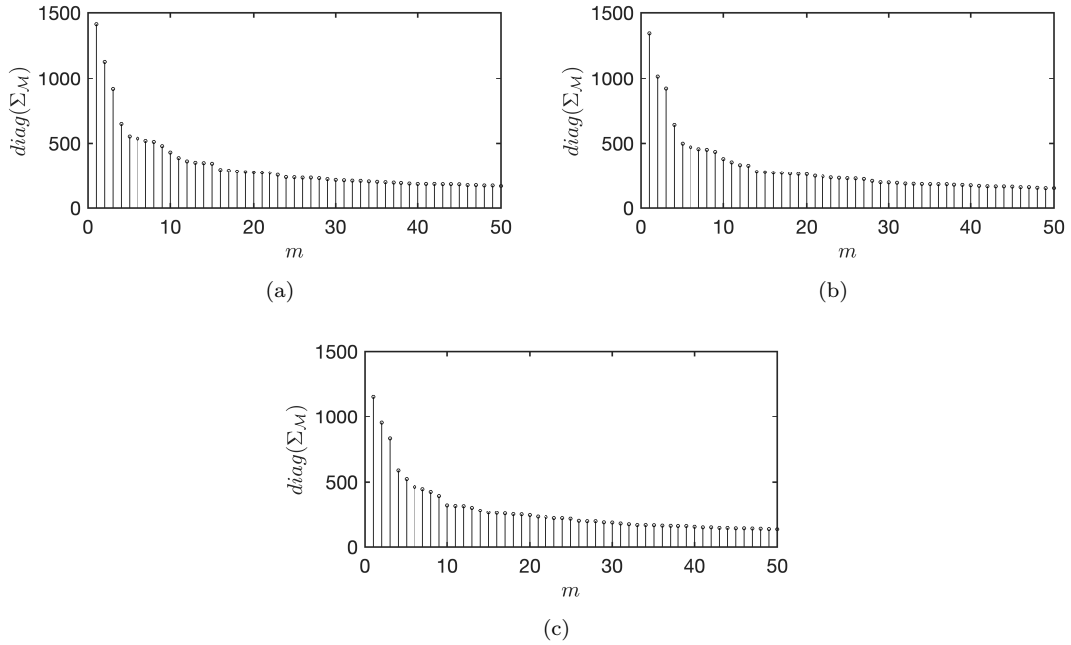



***Figure 8.65:*** *Energy contribution of the fifty first mPOD modes for the porous disks with various solidity: $\sigma = 56\%$ (a), $\sigma = 44\%$ (b) and $\sigma = 36\%$ (c) in ABL1*

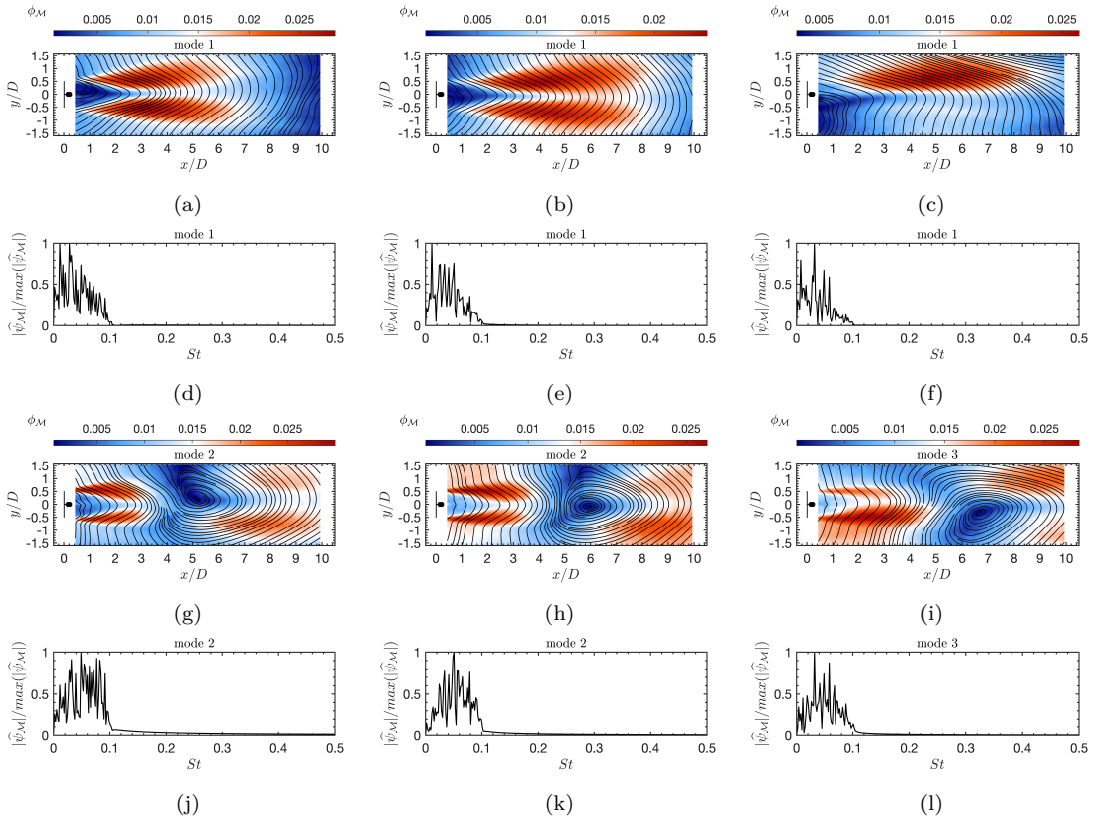



***Figure 8.66:*** *Spatial structures and spectral content of temporal structures obtained from the mPOD analysis of the wake of the porous disks with various solidity: $\sigma = 56\%$ (left), $\sigma = 44\%$ (middle) and $\sigma = 36\%$ (right) in ABL1*

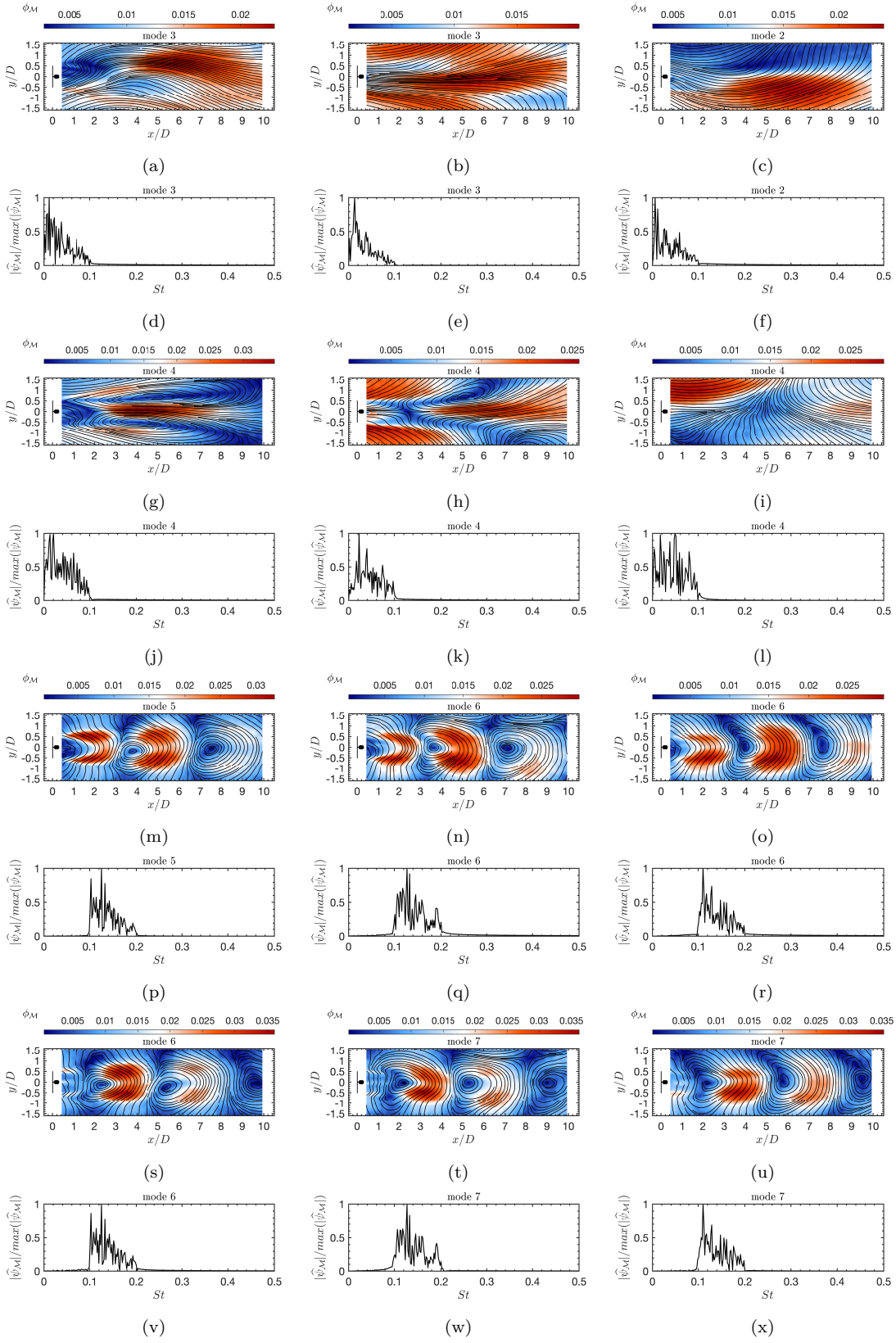



***Figure 8.67:*** *Spatial structures and spectral content of temporal structures obtained from the mPOD analysis of the wake of the porous disks with various solidity: $\sigma$ = 56% (left), $\sigma$ = 44% (middle) and $\sigma$ = 36% (right) in ABL1 (continued)*

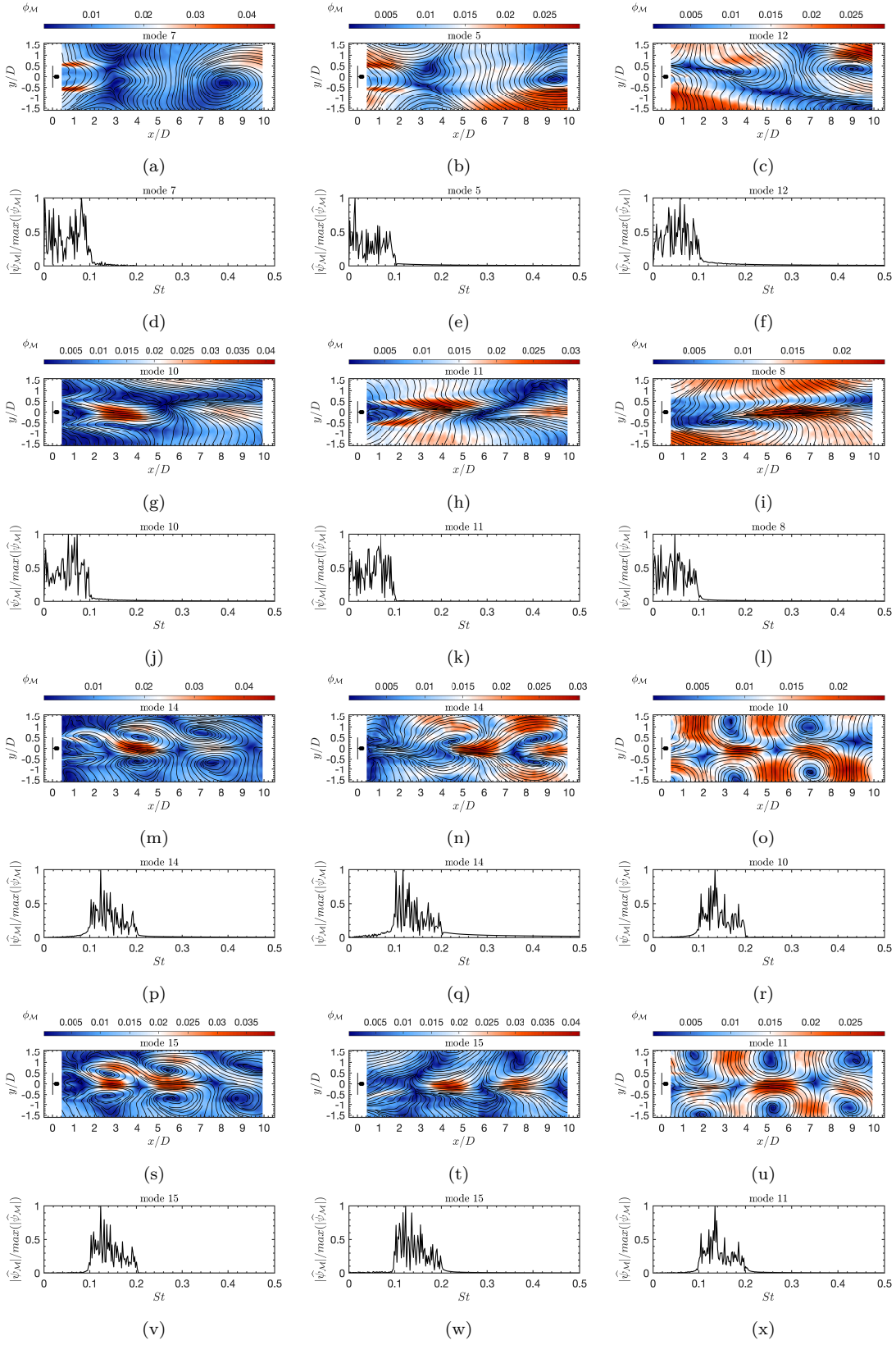



***Figure 8.68:*** *Spatial structures and spectral content of temporal structures obtained from the mPOD analysis of the wake of the porous disks with various solidity: $\sigma$ = 56% (left), $\sigma$ = 44% (middle) and $\sigma$ = 36% (right) in ABL1 (continued)*

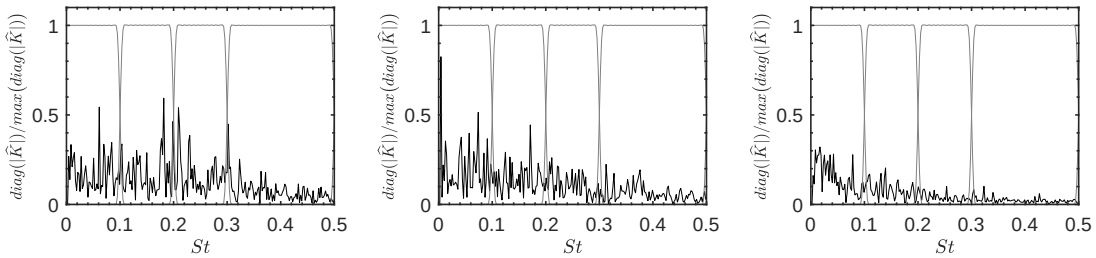



***Figure 8.69:*** *Normalized frequency content of the temporal correlation matrix $K$ on which the filter bank with the frequency splitting vector $St_V = [0, 0.1, 0.2, 0.3, 0.5]$ is superimposed for the porous disks with various solidity: $\sigma = 56\%$ (a), $\sigma = 44\%$ (b) and $\sigma = 36\%$ (c) within ABL2*

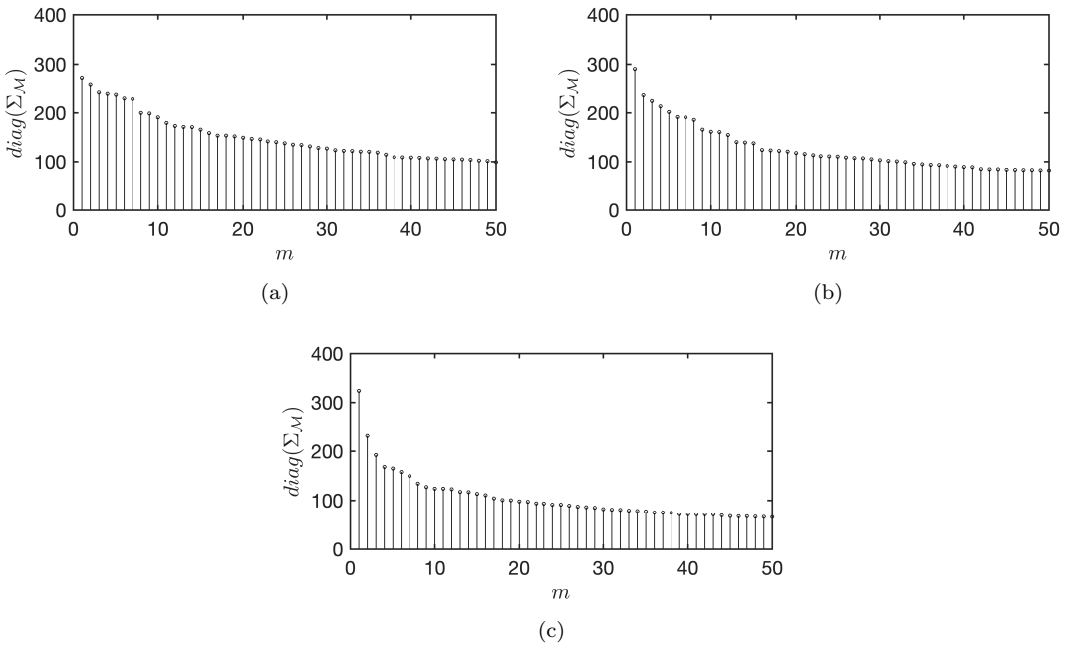



***Figure 8.70:*** *Energy contribution of the fifty first mPOD modes for the porous disks with various solidity: $\sigma = 56\%$ (a), $\sigma = 44\%$ (b) and $\sigma = 36\%$ (c) in ABL2*

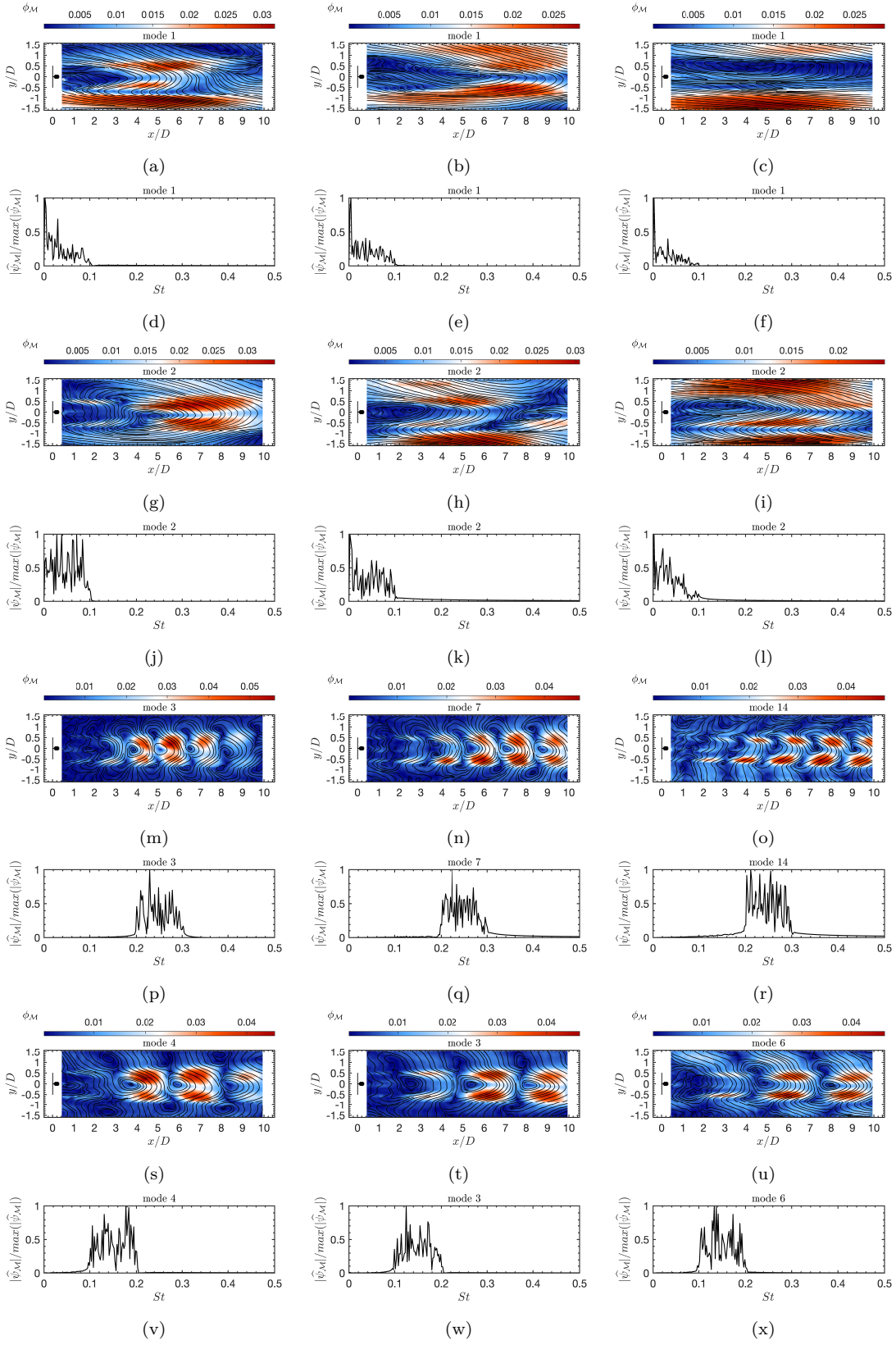



***Figure 8.71:*** *Spatial structures and spectral content of temporal structures obtained from the mPOD analysis of the wake of the porous disks with various solidity: $\sigma$ = 56% (left), $\sigma$ = 44% (middle) and $\sigma$ = 36% (right) in ABL2*

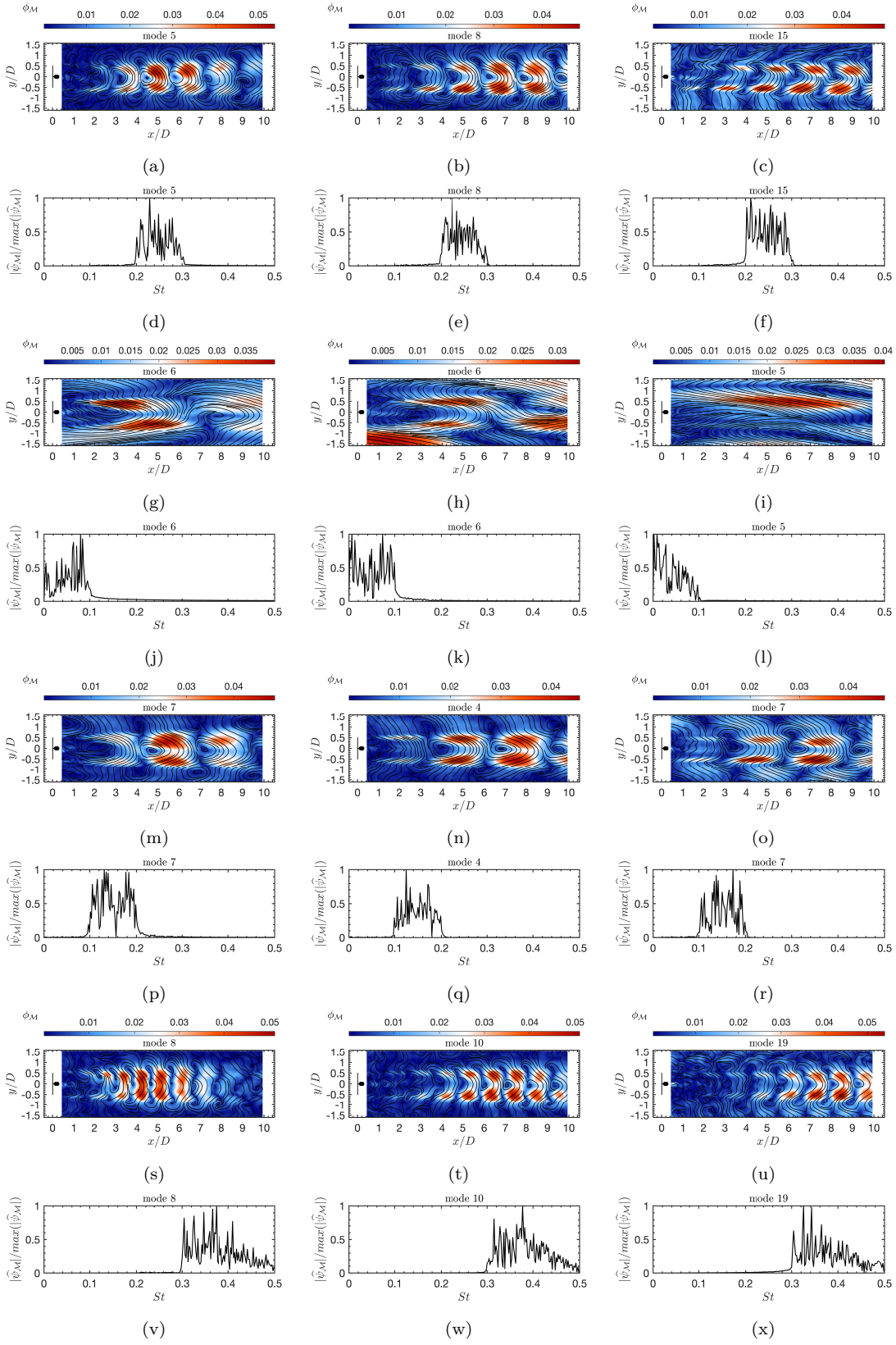



***Figure 8.72:*** *Spatial structures and spectral content of temporal structures obtained from the mPOD analysis of the wake of the porous disks with various solidity: $\sigma$ = 56% (left), $\sigma$ = 44% (middle) and $\sigma$ = 36% (right) in ABL2 (continued)*

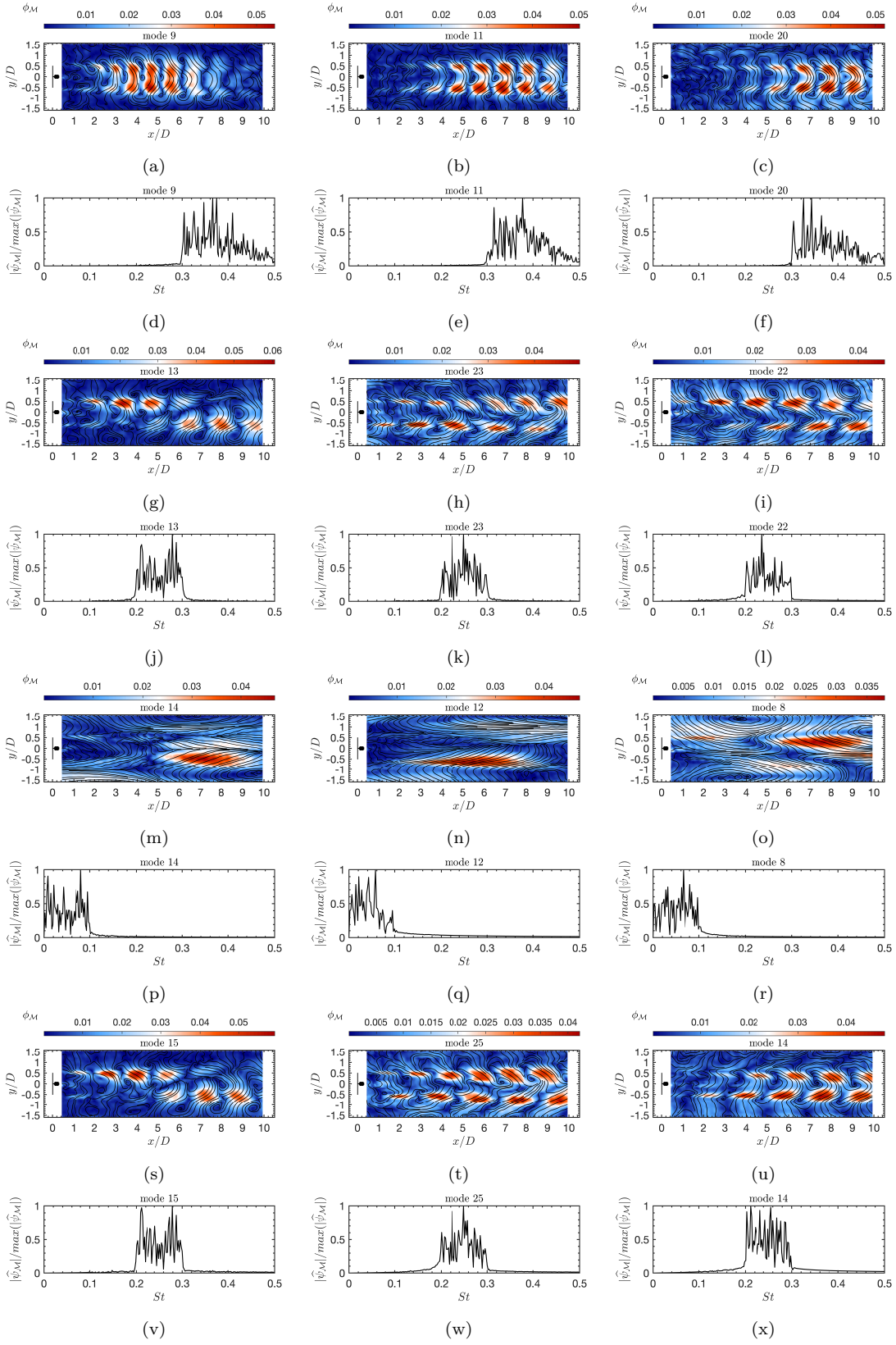



***Figure 8.73:*** *Spatial structures and spectral content of temporal structures obtained from the mPOD analysis of the wake of the porous disks with various solidity: $\sigma$ = 56% (left), $\sigma$ = 44% (middle) and $\sigma$ = 36% (right) in ABL2 (continued)*

## 8.6 Conclusions

The mPOD analysis conducted for the isolated wind turbine subjected to ABL1 and ABL2 reveals the large influence of the inflow on the wake meandering dynamics. For ABL1, the wake meandering can be seen as a combination of a low-frequency ($St \leqslant 0.1$) flapping and low-frequency ($St \leqslant 0.1$) long-wavelength oscillations on which higher-frequencies ($0.1 \leqslant St \leqslant 0.3$) oscillations are superimposed; a mechanism corresponding to the wake breakdown because of large-scale incoming structures completing the wake dynamics. For ABL2, the wake meandering can be seen as a combination of oscillations ($0.1 \leqslant St \leqslant 0.5$) and a low-frequency ($St \leqslant 0.1$) flapping of the near and far wake; the low-frequency long-wavelength oscillations and the wake breakdown observed for ABL1 being not involved in the wake dynamics of the wind turbine within ABL2.

For the isolated wind turbine within ABL1, wavelengths ranging within $1.2 \lesssim \lambda/D \lesssim 3.6$ were extracted from the spatial structures of the modes corresponding to an oscillatory mechanism and presenting a spectral content such that $0.1 \leqslant St \leqslant 0.3$. For the isolated wind turbine within ABL2, smaller wavelengths ranging within $1.1 \lesssim \lambda/D \lesssim 2.8$ were obtained, the spectral content being also such that $0.1 \leqslant St \leqslant 0.3$. Despite shorter wavelengths, these values are in good agreement with the spatial analysis of the wake centerlines performed in Chapter 7 from which wavelengths ranging within $2.75 \lesssim \lambda/D \lesssim 3.5$ and $2.5 \lesssim \lambda/D \lesssim 3.25$, and Strouhal numbers ranging within $0.21 \lesssim St \lesssim 0.27$ and $0.22 \lesssim St \lesssim 0.29$ were obtained for ABL1 and ABL2, respectively. Shorter wavelengths are however visible on the probability distribution of the wavelengths obtained from the spacial analysis performed in Chapter 7 (see Appendix I), the mean binned wavelengths being however longer. Furthermore, the oscillations corresponding to $St < 0.1$ that were observed in this chapter could not be obtained from the spatial analysis carried out in Chapter 7 since $St \simeq 0.1D$ corresponds to a wavelength of the order of 10 rotor diameters, what correspond to the length of the wake centerline that could be extracted from the TR-PIV measurements.

The mPOD analysis applied to the inflow has shown that the frequency content of wake meandering is already present within the inflow with a lower energy content, the wind turbine transferring energy from the large scales contained in the inflow to smaller scales in the wake. The wake meandering behavior depending largely on the inflow, the conclusions are presented separately for ABL1 and ABL2.

The pronounced similarity between the mPOD modes of the isolated turbine and of the row of wind turbines subjected to ABL1 highlights the fact that the wake meandering dynamics is not significantly modified for the turbines composing the row, the spacing between wind turbines being such that it limits the interactions between them. Nevertheless, some differences were observed. Especially concerning the mode corresponding to the long-wavelength oscillatory mechanism which was weaker for the first and second wind turbines of the row than for the isolated wind turbine. The fact that this mode was not weaker for the third wind turbine evidences the influence of the downstream turbine on this particular mechanism. Furthermore, an increase in the strength of the mPOD modes was observed for the third wind turbine. It shows that the wake dynamics is amplified for the downstream turbine.

For ABL2, the mPOD modes of the first and second wind turbines are quite similar to the modes of the isolated wind turbine. Mode 3, corresponding to the flapping of the wake, gains however in energy in the row of turbines. Concerning the third wind turbine, the low-frequency mPOD modes gain clearly in energy compared to the isolated wind turbine. It is particularly the case for the mode corresponding to the flapping of the far wake and for the mode corresponding to the long-wavelength oscillatory mechanism. The gain of energy for the low-frequency modes of the third turbine can be explained by the interaction with the wake of the upstream turbine(s). Furthermore, the wavelengths extracted from the spatial structures of the modes corresponding to an oscillatory mechanism appear globally larger for the third wind turbine of the row.

This evolution of the wake dynamics observed within the row of wind turbines for ABL1 and ABL2 was reflected in Chapter 7, in particular by an increase of the wake meandering amplitude within the row of wind turbines and by slightly larger wavelengths for the third wind turbine of the row.

Finally, no major change in the mPOD modes has been observed between the row of the turbines and the wind farm configuration. It shows that the lateral rows of wind turbines do not impact the wake meandering dynamics of the central row of wind turbines, as observed in Chapter 7 from the spatial analysis of the wake centerlines.

In order to understand the importance of the wind turbine model on the wake meandering phenomenon, the isolated three-bladed model was successively replaced by three porous disks with a solidity of 56%, 44% and 36%, respectively. For ABL1, it can be observed that the spatial structures extend or are located further downstream for the porous disks than for the rotating model. This can be justified by the fact that the velocity deficit is smaller for the porous disks. Moreover, the vortical structure of the mode representing the long-wavelength oscillatory mechanism moves downstream when the solidity decreases. This downstream displacement of the pivotal point of the wake is due to the decrease of the velocity deficit when the solidity decreases. For ABL2, the low-frequency mechanism corresponding to the far-wake flapping appears in a more energetic mode for the porous disk than for the bladed model. Furthermore, it was observed that the higher the solidity of the porous disk and the more modes with a higher spectral content are present within the most energetic ones. Whatever the ABL, similar wavelengths were observed on the spatial structures of the modes corresponding to an oscillatory mechanism, regardless of the solidity. This is in agreement with the results of Chapter 7 where only a slight increase in the wavelengths was observed for the porous disk with $\sigma = 56\%$, regardless of the ABL.

Chapter 9

# Conclusions & Perspectives

The general objective of this thesis was to investigate the wake meandering physics through the combination of LES computations of the NREL 5-MW wind turbine subjected to turbulent inflows and TR-PIV measurements of scale-model wind turbines subjected to two different ABLs. The original aspects of this thesis are

- the proposition, validation and comparison of several wake centerline tracking algorithms for HAWT;
- the study of the influence of the inflow turbulence intensity and inflow integral length scales on the wake meandering characteristics obtained from LES simulations with the VPM and FD4 codes, and therefore the study of the effects of the fidelity level of numerical simulations on the wake meandering characteristics;
- the implementation of TR-PIV measurements in an "extreme" configuration making possible to cover simultaneously the wake of scale-model wind turbines over a distance slightly larger than ten rotor diameters;
- the study of wake meandering for a row of three scale-model wind turbines and for the central row of a three-row three-column scale-model wind farm within two different ABLs;
- the application of mPOD analysis to scale-model wind turbine wakes.

## 9.1 Summary of investigations and major contributions

Several algorithms to track the wake centerline of horizontal axis wind turbines are proposed in Chapter 3. The tracking algorithms, applied to the cross-flow planes, were validated using LES computations of the NREL 5-MW wind turbine subjected to a synthetic turbulent inflow. Once supplemented with a wake centroid predictor, the 2D convolution in a cross-flow plane between the available power in the flow and a Gaussian masking function has proved to be the most robust and modular technique for wake centroid tracking. In order to extend the application of the tracking to a wider range of data, and in particular to the TR-PIV measurements performed in a horizontal plane, the 2D convolution technique was also adapted so as to be applicable in a 2D horizontal plane.

In Chapter 4, the 2D convolution supplemented with a predictor of the wake centroid is used to track the wake centerline for LES computations performed with both the VPM and FD4 codes using four synthetic turbulent inflows ($I$ = 0%, 4.8%, 8.4%, and 12.0%). It was observed that a higher inflow turbulence intensity results in larger wake deflections and that the wake meandering

starts closer to the rotor when the inflow turbulence level increases. Concerning the amplitude of the wake meandering, it was found that it increases linearly with the distance from the rotor and also with the inflow turbulence level, as also reported in [37]. Furthermore, a lower amplitude was observed in the vertical plane due to the anisotropic inflow, the ratio of the horizontal and vertical wake centerline amplitudes being close to the ratio of the turbulence intensity components in the transverse and vertical directions $\sigma_v/\sigma_w = 1.44$, as observed in [16]. Concerning the wavelengths, they are fairly constant and mainly range between $2.75D$ and $4.0D$, what is larger compared to what was reported in [37]. Eventually, Strouhal numbers ranging between 0.2 and 0.3 were obtained from the wavelengths using Taylor's frozen turbulence hypothesis. Despite the differences observed for the wavelengths, these Strouhal numbers are similar to those reported in [37] ($0.25 \leqslant St \leqslant 0.3$) because of the difference in the ratio between the convective speed and the incoming wind speed since $St = (U_c/U_\infty)D/\lambda$.

Furthermore, it was observed that the FD4 code provides equivalent results in terms of wake meandering characteristics compared to the VPM code (higher fidelity level); especially close to the wind turbine rotor ($x/D \lesssim 4$) or for the lowest inflow turbulence intensities. It opens the way to study the wake meandering phenomenon inside large wind farms with the FD4 code, which is well suited for this kind of application.

In addition, it was observed that the extreme wake deflections and the wake meandering amplitudes decrease when the inflow presents smaller integral length scales, while the wavelengths and the Strouhal numbers are essentially unaffected. Finally, strong correlations between the inflow centroid, the machine loads and the wake centroid were observed in the near wake of the wind turbine, the correlations then weakening with the distance to the wind turbine rotor.

The wind turbine scale model characteristics are presented in Chapter 5. The electric and aerodynamic performance curves of the scale model were obtained in the L-2B wind tunnel thanks to the control/acquisition board and to the torque sensor system [81] developed within the framework of this thesis. Comparing those curves revealed losses of around 40% of the aerodynamic power inside the generator. Furthermore, the shape of the aerodynamic curves was different from that of the electrical curves due to a too weak rotation resistance of the generator (too low nominal voltage). In addition, given the linear proportionality between the torque and the current produced by a DC generator, a very good estimate of the mechanical torque could be obtained through the measure of the current produced by the generator, once calibrated using the torque sensor system. Finally, thrust measurements with an aerodynamic balance have shown that the thrust varies slightly with the resistive load applied to the generator and that the thrust coefficients range from 0.82 to 1 taking mainly a value around 0.9 for $5 \leqslant TSR \leqslant 8$, which corresponds to a highly loaded wind turbine. The developed control/acquisition chain has proved to be successful and could be used for future studies.

Prior to the time-resolved PIV measurements on the wind turbine scale models, two ABLs modeled in the low speed L-1B wind tunnel were fully characterized in terms of velocity profile, turbulence intensity components, integral length scales and spectra. ABL1 corresponds to an inflow with a turbulence intensity $I = 10.7\%$ and longitudinal integral length scales of the order of $3D$ at hub height, while ABL2 has a turbulence intensity $I = 3.7\%$ and longitudinal integral length scales of the order of $1D$ at hub height.

Chapter 3 presents TR-PIV measurements performed in the VKI L-1B wind tunnel for the various configurations subjected to ABL1 and ABL2, i.e. the isolated wind turbine, a row of three wind turbines, a three-row three-column wind farm, and isolated porous disks with several solidities. First, it was shown that Reynolds independence was reached for the main flow statistics. On the other hand, the incoming ABL has proved to have a large impact on the wake characteristics. Concerning the changes in operating conditions of the isolated wind turbine, they turned out to mainly affect the near wake, regardless of the ABL.

The investigations on the interactions between wind turbines composing a row of three wind turbines have shown, for both ABLs, that the presence of the downstream turbines mainly affects the far wake of the first wind turbine, when compared to the wake of the isolated wind turbine. Concerning the downstream turbines, the wake recovery of these machines is faster compared to the first wind

turbine because of the increased incoming turbulence level created by the upstream turbine(s). The power production of the machines was in line with these observations.

The comparison between the row of three wind turbines and the central row of a three-row three-column wind farm has shown that there is no significant influence of the lateral rows on the wakes and power production of the machines composing the central row. The substitution of the isolated wind turbine by porous disks with several solidities made possible to study the effect of the scale model on the wake characteristics. It was confirmed that the wake is less pronounced and that the shear layers are weaker for the disks with a smaller solidity.

The wake meandering characteristics extracted from the TR-PIV measurements performed for the various configurations mentioned above are presented in Chapter 7. For the isolated wind turbine, a very limited influence of the Reynolds number on the wake meandering characteristics was observed; this confirms the Reynolds independence already observed for the main flow statistics. The extreme wake deflections and the meandering amplitude turned out to be much larger for ABL1 than for ABL2. Furthermore, a linear increase in the wake meandering amplitude with the downstream distance from the rotor was observed for ABL2, while large and almost constant amplitudes over the downstream distance were observed for ABL1. Regarding the wavelengths, they were slightly larger for ABL1 ($2.75 \lesssim \lambda/D \lesssim 3.5$) than ABL2 ($2.5 \lesssim \lambda/D \lesssim 3.25$), what results in $0.21 \lesssim St \lesssim 0.27$ for ABL1 and $0.22 \lesssim St \lesssim 0.29$ for ABL2 using Taylor's frozen turbulence hypothesis and the convective speeds of the wakes. As for the main flow statistics, the changes in the operating conditions, i.e. in the tip-speed ratio since the thrust coefficient of the scale model involved in this study varies little with respect to the tip-speed ratio ($0.88 \leqslant C_T \leqslant 0.94$ for $5 \leqslant TSR \leqslant 8$), have a negligible impact on the wake meandering characteristics, as also reported in [37].

For ABL1, the extreme deviations of the wake centerline were slightly larger for the isolated wind turbine than for the first wind turbine of the row of three wind turbines, while they were similar for ABL2. Comparing ABL1 and ABL2, the extreme deflections of the wake were much larger for ABL1. Furthermore, an increase in the wake meandering amplitude was observed within the row of wind turbines, as reported in [25] for porous disks. Concerning the wake centerline wavelengths, they were equivalent for the isolated wind turbine and the first and second wind turbines of the row, whether for ABL1 or ABL2. Concerning the third wind turbine, the wake centerline wavelengths were also equivalent for ABL1, while they were slightly larger for ABL2 ($2.75 \lesssim \lambda/D \lesssim 3.50$), resulting in $0.19 \lesssim St \lesssim 0.27$ for both ABLs.

Comparing the wake characteristics of the row of three wind turbines to those of the three-row three-column wind farm has shown that the lateral rows of the wind farm do not impact the wake meandering characteristics of the central row. Furthermore, the successive substitution of the three-bladed rotor by three porous disks with various solidities made possible to investigate the influence of the wind turbine model on the wake meandering characteristics. It was observed that the extreme wake centroid deflections decrease and that the wake centroids stay over a longer distance around $y/D = 0$ when the solidity of the porous disk located within ABL2 decreases, while no clear trend could be extracted for ABL1. Regardless of the ABL, the wake meandering amplitudes were larger for the bladed model than for the porous disks; one has however to keep in mind that the largest solidity of the disk was still too weak to mimic the bladed wind turbine model. Concerning the influence of the disk solidity, no clear trend could be extracted for ABL1, while a decrease in the meandering amplitude was observed for ABL2 when the solidity was lower. Furthermore, as for the isolated bladed model, an increase in the wake meandering amplitude with the downstream distance was observed for the porous disks. Regarding the wavelengths, they were of the same size than for the rotating model, except for the porous disk with the lowest solidity for which they were larger ($2.75 \lesssim \lambda/D \lesssim 3.75$ for ABL1 and $2.5 \lesssim \lambda/D \lesssim 3.5$ for ABL2) because of the much weaker velocity deficit, resulting in $0.20 \lesssim St \lesssim 0.27$ within ABL1 and in $0.22 \lesssim St \lesssim 0.27$ within ABL2.

Even if the numerical simulations performed at wind tunnel scale resulted in weaker wakes compared to the experimental data, wake meandering characteristics close to those obtained experimentally could be extracted. This is very encouraging since it opens the way to many investigations as it

will be discussed in the perspectives.

Chapter 8 covers the multi-scale Proper Orthogonal Decomposition (mPOD) applied to the time-resolved PIV data presented in Chapter 7. The mPOD analysis conducted for the isolated wind turbine subjected to ABL1 and ABL2 reveals the large influence of the inflow on the wake meandering dynamics. For ABL1, the wake meandering can be seen as a combination of a low-frequency ($St \leqslant 0.1$) flapping and low-frequency ($St \leqslant 0.1$) long-wavelength oscillations on which higher-frequencies ($0.1 \leqslant St \leqslant 0.3$) oscillations are superimposed; a mechanism corresponding to the wake breakdown because of large-scale incoming structures completing the wake dynamics. For ABL2, the wake meandering can be seen as a combination of oscillations ($0.1 \leqslant St \leqslant 0.5$) and a low-frequency ($St \leqslant 0.1$) flapping of the near and far wake; the low-frequency long-wavelength oscillations and the wake breakdown observed for ABL1 being not involved in the wake dynamics of the wind turbine within ABL2.

Wavelengths ranging within $1.2 \lesssim \lambda/D \lesssim 3.6$ and $1.1 \lesssim \lambda/D \lesssim 2.8$ were extracted from the spatial structures of the modes corresponding to an oscillatory mechanism of the wake for the isolated wind turbine within ABL1 and ABL2, respectively. The Strouhal numbers are such that $0.1 \leqslant St \leqslant 0.3$. These values are in good agreement with the spatial analysis of the wake centerlines performed in Chapter 7.

The mPOD analysis applied to the inflow has shown that the frequency content of wake meandering is already present within the inflow with a lower energy content, the wind turbine transferring energy from the large scales contained in the inflow to smaller scales in the wake.

The pronounced similarity between the mPOD modes of the isolated turbine and of the row of wind turbines subjected to ABL1 and ABL2 highlights the fact that the wake meandering dynamics is not significantly modified for the turbines composing the row. The most striking difference is the higher energy of the low-frequency modes of the third wind turbine of the row, what can be explained by the interaction with the wake of the upstream turbine(s).

Finally, no major change in the mPOD modes has been observed between the row of the turbines and the wind farm configuration. It shows that the lateral rows of wind turbines do not impact the wake meandering dynamics of the central row of wind turbines. In order to understand the importance of the wind turbine model on the wake meandering phenomenon, the isolated three-bladed model was successively replaced by three porous disks with various solidities. For ABL1, it was observed that the spatial structures extend or are located further downstream for the porous disks than for the rotating model. This can be justified by a smaller velocity deficit for the porous disks. Moreover, the vortical structure of the mode representing the long-wavelength oscillatory mechanism moves downstream when the solidity decreases, because of a weaker velocity deficit. For ABL2, the low-frequency mechanism corresponding to the far-wake flapping appears in a more energetic mode for the porous disk than for the bladed model. Furthermore, it was observed that higher is the solidity of the porous disk and more modes with a higher spectral content are present within the most energetic ones.

## 9.2 Major findings

From the numerical and experimental results obtained at very different scales during this thesis, some conclusions can be drawn regarding the scale effect on the wake meandering phenomenon. Maximum amplitudes of the order of $0.325D$ and $0.2D$ were obtained from the measurements performed for the isolated wind turbine scale model located inside ABL1 and ABL2, respectively. The numerical simulations performed at full scale led on their side to maximum amplitudes that range, in the horizontal plane, between $0.175D$ and $0.3D$ depending on the inflow and the numerical code. Regarding the wavelengths, the experimental study gives $2.75 \lesssim \lambda/D \lesssim 3.5$ and $2.5 \lesssim \lambda/D \lesssim 3.25$ for the isolated wind turbine scale model located inside ABL1 and ABL2, respectively. Applying Taylor frozen turbulence hypothesis, it corresponds to $0.21 \lesssim St \lesssim 0.27$ and $0.22 \lesssim St \lesssim 0.29$. Numerically, in the horizontal plane and at full scale, the wavelengths were comprised between $2.75D$ and $5.75D$ but mainly ranging within $2.75 \lesssim \lambda/D \lesssim 4.0$; what results in $0.2 \lesssim St \lesssim 0.3$. Despite the large difference in scale (1:840) between the wind tunnel tests and the numerical

simulations, the obtained wake meandering amplitudes, wavelengths and Strouhal number are equivalent, what is an important point with regard to experimental studies. These similarities in the wake meandering characteristics regardless of the scale was also observed in [37] for different wind turbine designs for different scales going from wind tunnel scale ($D = 0.128$ m) to utility scale ($D = 96$ m). The similar wind turbine wake meandering characteristics obtained in [37] regardless of the wind turbine size and design are such that $0.07 \leqslant A/D \leqslant 0.15$, $1.2 \leqslant \lambda/D \leqslant 2.1$, and $0.25 \leqslant St \leqslant 0.3$.

Concerning the increase of the wake meandering amplitude with the inflow turbulence intensity that was observed in this work at both wind tunnel and full scale, it is interesting to remind that no wake meandering was observed in [34] for an isolated wind turbine scale model ($D = 0.15$ m) subjected to an ABL with a very high turbulence level ($I = 17.5\%$ at hub height). Indeed, the mixing in the wake is very large for such a high turbulence level, what results in an unstructured wake that recovers rapidly.

The findings of this thesis enable to sharpen the conclusions concerning the different factors causing or influencing the wind turbine wake meandering that were presented in the introduction:

- *a periodic vortex shedding within the wake, the rotor swept disk of the wind turbine acting as a porous bluff body with decreasing permeability as the tip-speed ratio increases [9, 10];*

  The wake meandering observed in this work does not correspond to a periodic vortex shedding within the wake since the phenomenon observed in this work rather presents a broad frequency content.

- *the effects of the large-scale turbulent eddies contained in the ABL as observed for plume-dispersion analysis [7, 12, 15, 16, 36];*

  This work also reveals the major influence of the large-scale turbulent eddies contained in the inflow on the wake meandering dynamics. There is however a nuance to be brought concerning the definition of the large-scale eddies. As stated in [12], the limit between the turbulent structures contributing mainly to wake meandering and mainly to the turbulent expansion of the wake, respectively, is not well defined and does not correspond to a sharp limit; this limit corresponds rather to a frequency range than to a distinct frequency. The limit suggested in [12] is two times the wake deficit diameter, what is slightly larger than two times the rotor diameter. In this work, wake meandering was however observed for numerical simulations performed with an inflow containing longitudinal integral length scales of $\sim 1.5D$ and even of $\sim 0.75D$. Furthermore, the ABLs modeled in the L-1B wind tunnel contained, at hub height, longitudinal integral length scales of $\sim 3D$ for ABL1 and of $\sim 1D$ for ABL2. Wake meandering was observed for both ABLs and presented clearly different characteristics. From this work, it seems that the limit suggested in [12] could be at least reduced to $\sim 0.75D$. It is however clear that the amplitude of wake meandering depends on the size of the turbulent structures contained in the inflow; the larger the integral length scale, the larger the wake meandering amplitude.

- *the instability of the tip vortices [21] as observed for a propeller wake [22];*

  Even if the instability of the tip vortices could influence the wake meandering dynamics, this is clearly not the a major cause since wake meandering characteristics similar to those obtained for an isolated three-bladed wind turbine were observed for porous disks from which tip vortices are not shed.

- *the spiral instability (precessing motion) of the hub vortex, the meandering of the wake being initiated close to the location where the hub vortex intercepts the outer shear layer [23, 24, 31];*

  Even if the spiral instability of the hub vortex influences the wake meandering dynamics, this is clearly not the a major cause since the wake meandering was observed in the LES simulations performed during this study, and for which the nacelle was not modeled; only the rotor was modeled using immersed lifting lines or an advanced actuator disk. Furthermore, the wake meandering characteristics obtained from these simulations without nacelle are similar to those obtained from the experimental campaigns for which the nacelle was present.

- *the amplification of large-scale inflow perturbations by the shear in the wake, and then the inclination and distortion of the large coherent vortex structures in the wake by the amplified perturbations to induce meandering [38].*

  The amplification of large-scale inflow perturbations by the shear in the wake was not investigated in this study which does not enable to conclude about this point.

In addition to these findings, the major conclusions about wind turbine wake meandering that can be drawn from this thesis are gathered hereafter.

- The wake meandering characteristics are not influenced by the scale effect.
- The wake meandering amplitude increases with the downstream distance from the rotor and depends on the characteristics of the inflow: it increases with the inflow turbulence intensity and integral length scales. On the contrary, the wake meandering wavelengths are essentially constant whatever the inflow characteristics and mainly range within $2.5 \lesssim \lambda/D \lesssim 4.0$.
- The wake meandering amplitude increases within a row of wind turbine while the wavelength, and therefore $St$, remain constant.
- The wake meandering characteristic frequencies, obtained from the wavelengths invoking the Taylor frozen turbulence hypothesis, are such that $0.2 \lesssim St \lesssim 0.3$ what is in good agreement with previous findings [32, 35] and the literature presented in the introduction.
- The wake meandering characteristics of a row are not impacted by the neighboring rows inside a wind farm.
- The wake meandering dynamics strongly depends on the inflow.

Based on all the previous observations, it is clear that the wake meandering strongly depends on the characteristics of the inflow and secondarily on the characteristics of the wind turbine, what makes it a challenging topic for the wind energy community.

## 9.3 Perspectives

The results obtained during this thesis open the way to numerous possible studies.

The wake meandering data obtained with the VPM code combined with immersed lifting lines constitute a very good starting point to build a wake meandering model. Such a wake meandering model is currently developed by Lejeune [96] from the set of data obtained during this thesis.

The very good agreement between the wake meandering characteristics obtained with the fourth-order FD4 code combined with an advanced actuator disk and the VPM code combined with immersed lifting lines opens the way to study the wake meandering phenomenon inside large wind farms with the FD4 code, which is well suited for this kind of application. Preliminary studies have been carried out by Moens [97, 98] for a five-row three-column wind farm. In addition, the use of FD4 code makes it possible to study numerically the impact of the ABL stability on the wake meandering phenomenon.

It would also be interesting to model the mast and the nacelle in the numerical simulations. Indeed, from LES of a wind turbine scale model ($D = 1.1$ m) [39], it was reported that the wake meandering amplitude is larger if the nacelle is modeled because of the existence of an unstable hub vortex (the absence of the nacelle leading to a stable and columnar hub vortex); the wavelengths being similar regardless of the presence of the nacelle.

Even if the FD4 code can reproduce properly what happens experimentally in terms of wake meandering characteristics, the numerical setup could be further improved. The differences observed in the wake statistics between the numerical and the experimental data seem to result from the modeling of the wind turbine rotor, which was based on the aerodynamic coefficients determined experimentally on the scaled-up airfoil. The 2D aerodynamic coefficients measured on this wing could be corrected to account for 3D and rotational effects. A totally different approach, consisting in imposing in the numerical simulations a thrust coefficient similar to the experimental one, could

also be adopted. Furthermore, the inflow could be improved. The symmetry of the flow being affected for too long turbulent boxes generated with the Mann's algorithm (due to very large integral length scales), an alternative to be able to study numerically the wake meandering over a longer time (without periodicity) would be to run precursor simulations to obtain inflows representing ABL1 and ABL2. It would also enable to further study the correlation between the inflow centroid, the machine loads and the wake centroid. Once these points are addressed, the FD4 code could be used extensively to investigate the wake meandering phenomenon at wind tunnel scale. Indeed, this could help to further understand the phenomena occurring at wind tunnel scale and help to better understand the experimental results presented in the literature.

While the tracking algorithms are implemented within the VPM code to perform run-time tracking of the wake centerline, it is not yet the case for the FD4 code. The implementation of the algorithms within the FD4 code would enable to perform run-time tracking of the wake centerline, avoiding therefore the need to store a large amount of data necessary for the tracking as a post-processing step, and opening a door towards real-time alleviation control of the wake meandering within wind farms.

Concerning the experimental part, it would be very interesting to design a new wind turbine mast supplemented with strain gages to measure the thrust force, the lateral force and the yaw moment acting on the wind turbine. It would make it possible to correlate the wake centerline with these forces/moment. It has indeed been shown in [25] that the lateral force is a good candidate to predict in real time the wake meandering process. The strong correlation between the lateral force and the wake centroid position has also been observed from the numerical data obtained in this work. With the view of alleviating this phenomenon, it is clear that the use of common sensors, that are or could be found in full-scale wind turbines, to predict in real time the wake meandering phenomenon would be a real plus.

Furthermore, the selection of a generator with a larger rotation resistance (higher nominal voltage) would enable to vary more significantly the operating conditions of the machines, which would also make it possible to further investigate the power optimization inside the experimental wind farm.

# Bibliography


[1] G. Corbetta, A. Mbistrova, A. Ho, I. Pineda, and K. Ruby. Wind in power - 2015 European statistics. http://www.ewea.org/fileadmin/files/library/ publications/statistics/EWEA-Annual-Statistics-2015.pdf, February 2016. The European Wind Energy Association.

[2] I. Komusanac, G. Brindley, D. Fraile, C. Walsh, and L. Van de Velde. Wind energy in Europe in 2019 - Trends and statistics, February 2020. The European Wind Energy Association.

[3] G. Corbetta, A. Ho, I. Pineda, K. Ruby, and L. Van de Velde. Wind energy scenarios for 2030. http://www.ewea.org/fileadmin/files/library/publications/ reports/EWEA-Wind-energy-scenarios-2030.pdf, August 2015. The European Wind Energy Association.

[4] B. Sanderse. Aerodynamics of wind turbine wakes - literature review. Technical report, Energy research Centre of the Netherlands (ECN), 2009.

[5] F. Porté-Agel, M. Bastankhah, and S. Shamsoddin. Wind-turbine and wind-farm flows: A review. *Boundary-Layer Meteorology*, Sep 2019. ISSN 1573-1472. doi: 10.1007/s10546-019-00473-0. URL `https://doi.org/10.1007/s10546-019-00473-0`.

[6] P. B. S. Lissaman. Energy Effectiveness of Arbitrary Arrays of Wind Turbines. *Journal of Energy*, 3(6):323–328, 1979.

[7] G. España, S. Aubrun, S. Loyer, and P. Devinant. Wind tunnel study of the wake meandering downstream of a modelled wind turbine as an effect of large scale turbulent eddies. *J Wind Eng Ind Aerodyn*, pages 24–33, 2012.

[8] J.-J. Trujillo and M. Kühn. Wake Meandering Modeling for Wind Turbine Loading and Performance. Endowed Chair of Wind Energy and Universität Stuttgart. Offshore Wind Farms Workshop - Roskilde 25-26.02.2009.

[9] D. Medici and P. H. Alfredsson. Measurements on a wind turbine wake: 3D effects and bluff-body vortex shedding. In *The science of making torque from wind. Special Topic Conference*, pages 155–165, Delft, 19–21 April 2004.

[10] D. Medici and P. H. Alfredsson. Measurements on a wind turbine wake: 3D effects and bluff body vortex shedding. *Wind Energy*, 9(3):219–236, 2006.

[11] V. L. Okulov and J. N. Sørensen. Stability of helical tip vortices in a rotor far wake. *J Fluid Mech*, 576:1–25, 2007.

[12] G. C. Larsen, H. Aa. Madsen, K. Thomsen, and T. J. Larsen. Wake meandering: A Pragmatic Approach. *Wind Energy*, 11(4):377–395, 2008.

[13] D. Medici and P. H. Alfredsson. Measurements behind model wind turbines: further evidence of wake meandering. *Wind Energy*, 11(2):211–217, 2008. ISSN 1099-1824.

[14] G. C. Larsen, H. A. Madsen, F. Bingöl, J. Mann, S. Ott, J. N. Sørensen, V. Okulov, N. Troldborg, M. Nielsen, K. Thomsen, T. J. Larsen, and R. Mikkelsen. Dynamic Wake Meandering Modeling. Tech. Rep. R-1607(EN), Risø National Laboratory, Technical University of Denmark, 2007.

[15] S. Aubrun, S. Loyer, G. España, P. Hayden, and P. Hancock. Experimental study on the wind turbine wake meandering with the help of a non-rotating simplified model and of a rotating model. Number AIAA 2011-0460, 49th AIAA Aerospace Sciences Meeting, Orlando, FL, January 2011.

[16] G. España, S. Aubrun, S. Loyer, and P. Devinant. Spatial study of the wake meandering using modelled wind turbines in a wind tunnel. *Wind Energy*, 14(7):923–937, 2011.

[17] M. Bastankhah and F. Porté-Agel. A new miniature wind turbine for wind tunnel experiments. part ii: Wake structure and flow dynamics. *Energies*, 10:923, 07 2017. doi: 10.3390/en10070923.

[18] N. Hutchins and Ivan Marusic. Evidence of very long meandering features in the logarithmic region of turbulent boundary layers. *Journal of Fluid Mechanics*, 579:1–28, 2007. doi: 10.1017/S0022112006003946.

[19] N. Hutchins, K. Chauhan, I. Marusic, J. Monty, and J. Klewicki. Towards reconciling the large-scale structure of turbulent boundary layers in the atmosphere and laboratory. *Boundary-Layer Meteorology*, 145(2):273–306, Nov 2012. ISSN 1573-1472. doi: 10.1007/s10546-012-9735-4. URL `https://doi.org/10.1007/s10546-012-9735-4`.

[20] S. J. Andersen, J. N. Sørensen, and R. Mikkelsen. Simulation of the inherent turbulence and wake interaction inside an infinitely long row of wind turbines. *Journal of Turbulence*, 14(4): 1–24, 2013. doi: 10.1080/14685248.2013.796085. URL `https://doi.org/10.1080/14685248.2013.796085`.

[21] L. P. Chamorro, C. Hill, S. Morton, C. Ellis, R. E. A. Arndt, and F. Sotiropoulos. On the interaction between a turbulent open channel flow and an axial-flow turbine. *J Fluid Mech*, 716:658–670, 002 2013.

[22] M. Felli, R. Camussi, and F. Di Felice. Mechanisms of evolution of the propeller wake in the transition and far fields. *J Fluid Mech*, 682:5–53, 009 2011.

[23] S. Kang, X. Yang, and F. Sotiropoulos. On the onset of wake meandering for an axial flow turbine in a turbulent open channel flow. *J Fluid Mech*, 744:376–403, 005 2014.

[24] V. L. Okulov, I. V. Naumov, R. F. Mikkelsen, I. K. Kabardin, and J. N. Sørensen. A regular strouhal number for large-scale instability in the far wake of a rotor. *J Fluid Mech*, 747: 369–380, 005 2014.

[25] Y.-A. Muller, S. Aubrun, and C. Masson. Determination of real-time predictors of the wind turbine wake meandering. *Exp Fluids*, 56(3):1–11, 2015.

[26] S. Aubrun, Y. A. Muller, and C. Masson. Predicting wake meandering in real-time through instantaneous measurements of wind turbine load fluctuations. *Journal of Physics: Conference Series*, 625:012005, jun 2015. doi: 10.1088/1742-6596/625/1/012005. URL `https://doi.org/10.1088%2F1742-6596%2F625%2F1%2F012005`.

[27] Y.-A. Muller, C. Masson, and S. Aubrun. Turbulent large-scale structure effects on wake meandering. *Journal of Physics: Conference Series*, 625:012038, jun 2015. doi: 10.1088/1742-6596/625/1/012038. URL `https://doi.org/10.1088%2F1742-6596%2F625%2F1%2F012038`.

[28] T. J. Larsen, H. Aa. Madsen, G. C. Larsen, and K. S. Hansen. Validation of the dynamic wake meander model for loads and power production in the Egmond aan Zee wind farm. *Wind Energy*, 16(4):605–624, 2013.

[29] M. J. Churchfield, S. Lee, P. J. Moriarty, Y. Hao, M. A. Lackner, R. Barthelmie, J. K. Lundquist, and G. Oxley. A Comparison of the Dynamic Wake Meandering Model, Large-Eddy Simulation, and Field Data at the Egmond aan Zee Offshore Wind Plant. Number AIAA 2015-0724, 33rd Wind Energy Symposium, AIAA SciTech, Kissimmee, FL, January 2015.

[30] K. B. Howard, A. Singh, F. Sotiropoulos, and M. Guala. On the statistics of wind turbine wake meandering: An experimental investigation. *Phys Fluids*, 27(7), 2015.

[31] D. Foti, X. Yang, M. Guala, and F. Sotiropoulos. Wake meandering statistics of a model wind turbine: Insights gained by large eddy simulations. *Phys. Rev. Fluids*, 1:044407, Aug 2016. doi: 10.1103/PhysRevFluids.1.044407. URL `https://link.aps.org/doi/10.1103/PhysRevFluids.1.044407`.

[32] E. Barlas, S. Buckingham, and J. van Beeck. Roughness Effects on Wind-Turbine Wake Dynamics in a Boundary-Layer Wind Tunnel. *Boundary-Layer Meteorol*, 158(1):27–42, 2016.

[33] B. M. Sumer and J. Fredsøe. *Hydrodynamics Around Cylindrical Structures*. World Scientific Publishing Co Pte Ltd, 1997.

[34] E. Barlas, S. Buckingham, G. Glabeke, and J. van Beeck. Offshore and onshore wind turbine wake meandering studied in an ABL wind tunnel, International Workshop on Physical Modeling of Flow and Dispersion Phenomena (PHYSMOD). Zürich, September 2015.

[35] N. Coudou, S. Buckingham, L. Bricteux, and J. van Beeck. Experimental study on the wake meandering within a scale model wind farm subject to a wind-tunnel flow simulating an atmospheric boundary layer. *Boundary-Layer Meteorology*, 167(1):77–98, Apr 2018. ISSN 1573-1472. doi: 10.1007/s10546-017-0320-8. URL `https://doi.org/10.1007/s10546-017-0320-8`.

[36] M. Bastankhah and F. Porté-Agel. Wind tunnel study of the wind turbine interaction with a boundary-layer flow: Upwind region, turbine performance, and wake region. *Physics of Fluids*, 29(6):18. 065105, 2017. doi: 10.1063/1.4984078. URL `http://infoscience.epfl.ch/record/230117`.

[37] D. Foti, X. Yang, and F. Sotiropoulos. Similarity of wake meandering for different wind turbine designs for different scales. *Journal of Fluid Mechanics*, 842:5–25, 2018. doi: 10.1017/jfm.2018.9.

[38] X. Mao and J. N. Sørensen. Far-wake meandering induced by atmospheric eddies in flow past a wind turbine. *Journal of Fluid Mechanics*, 846:190–209, 2018. doi: 10.1017/jfm.2018.275.

[39] D. Foti, X. Yang, F. Campagnolo, D. Maniaci, and F. Sotiropoulos. Wake meandering of a model wind turbine operating in two different regimes. *Phys. Rev. Fluids*, 3:054607, May 2018. doi: 10.1103/PhysRevFluids.3.054607. URL `https://link.aps.org/doi/10.1103/PhysRevFluids.3.054607`.

[40] M. A. Mendez, M. Balabane, and J.-M. Buchlin. Multi-scale proper orthogonal decomposition of complex fluid flows. *Journal of Fluid Mechanics*, 870:988–1036, May 2019. ISSN 1469-7645. doi: 10.1017/jfm.2019.212. URL `http://dx.doi.org/10.1017/jfm.2019.212`.

[41] P. Chatelain, A. Curioni, M. Bergdorf, D. Rossinelli, W. Andreoni, and P. Koumoutsakos. Billion vortex particle direct numerical simulations of aircraft wakes. *Computer Methods in Applied Mechanics and Engineering*, 197(13):1296–1304, Feb 2008.

[42] P. Chatelain, S. Backaert, G. Winckelmans, and S. Kern. Large eddy simulation of wind turbine wakes. In Wolfgang Rodi, editor, *Proceedings of The 9th International Symposium on Engineering Turbulence Modelling and Measurements (ETMM-9), June 6–8, 2012, Thessaloniki, Greece*, volume 91 of *Flow, Turbulence and Combustion*, pages 587–605. ERCOFTAC, Springer, Jun 2013. doi: 10.1007/s10494-013-9474-8.

[43] S. Backaert, P. Chatelain, and G. Winckelmans. Vortex particle-mesh with immersed lifting lines for aerospace and wind engineering. In Jens Honoré Walther, editor, *Symposium on Particle Methods in Fluid Dynamics, October 15-17 2012, DTU Copenhagen*, volume 18 of *Procedia IUTAM*, pages 1–7. IUTAM, 2015. doi: 10.1016/j.piutam.2015.11.001.

[44] G. Winckelmans. Vortex methods. In Erwin Stein, René De Borst, and Thomas J.R. Hughes, editors, *Encyclopedia of Computational Mechanics*, volume 3. John Wiley and Sons, 2004.

[45] R. W. Hockney and J. W. Eastwood. *Computer Simulation Using Particles*. Taylor & Francis, Inc., USA, 1988. ISBN 0852743920.

[46] P. Chatelain and P. Koumoutsakos. A fourier-based elliptic solver for vortical flows with periodic and unbounded directions. *Journal of Computational Physics*, 229(7):2425 – 2431, 2010. ISSN 0021-9991. doi: https://doi.org/10.1016/j.jcp.2009.12.035. URL `http://www.sciencedirect.com/science/article/pii/S0021999110000021`.

[47] H. Jeanmart and G. Winckelmans. Investigation of eddy-viscosity models modified using discrete filters: A simplified "regularized variational multiscale model" and an "enhanced field model". *Phys. Fluids*, 19(5):055110, May 2007. ISSN 1070-6631. doi: 10.1063/1.2728935.

[48] P. Chatelain, Y. Marichal, M. Duponcheel, M. Moens, and G. Winckelmans. Vortex methods applied to the large eddy simulation of wind turbine flows. *Journal of Computational Physics*. Preprint submitted to Journal of Computational Physics.

[49] R. Cocle, L. Bricteux, and G. Winckelmans. Scale dependence and asymptotic very high reynolds number spectral behavior of multiscale subgrid models. *Phys. Fluids*, 21(8):085101, Aug 2009. ISSN 1070-6631. doi: 10.1063/1.3194302.

[50] J. Mann. Wind field simulation. *Probabilistic Engineering Mechanics*, 13(4):269–282, 10 1998. URL http://www.sciencedirect.com/science/article/pii/S0266892097000362.

[51] L. Georges. *Development and validation of a LES methodology for complex wall-bounded flows - Application to high-order structured and industrial unstructured solvers*. PhD thesis, Université catholique de Louvain, 6 2008.

[52] L. Bricteux. *Simulation of turbulent aircraft wake vortex flows and their impact on the signals returned by a coherent Doppler LIDAR system*. PhD thesis, Université catholique de Louvain, 4 2008.

[53] M. Duponcheel. *Direct and large-eddy simulation of turbulent wall-bounded flows : further development of a parallel solver, improvement of multiscale subgrid models and investigation of vortex pairs in ground effect*. PhD thesis, Université catholique de Louvain, 10 2009.

[54] M. Duponcheel, P. Orlandi, and G. Winckelmans. Time-reversibility of the euler equations as a benchmark for energy conserving schemes. *Journal of Computational Physics*, 227(19): 8736 – 8752, 2008. ISSN 0021-9991. doi: https://doi.org/10.1016/j.jcp.2008.06.020. URL http://www.sciencedirect.com/science/article/pii/S0021999108003422.

[55] M. Duponcheel, L. Bricteux, M. Manconi, G. Winckelmans, and Y. Bartosiewicz. Assessment of RANS and improved near-wall modeling for forced convection at low Prandtl numbers based on LES up to $Re_\tau = 2000$. *Int. J. Heat Mass Transf.*, 75:470–482, 2014. ISSN 0017-9310. doi: http://dx.doi.org/10.1016/j.ijheatmasstransfer.2014.03.080. URL http://www.sciencedirect.com/science/article/pii/S0017931014002865.

[56] M. Moens, M. Duponcheel, G. Winckelmans, and P. Chatelain. An actuator disk method with tip-loss correction based on local effective upstream velocities. *Wind Energy*, 21(9): 766–782, 2018. doi: 10.1002/we.2192. URL https://onlinelibrary.wiley.com/doi/abs/10.1002/we.2192.

[57] M. Moens. *Large eddy simulation of wind farm flows : improved Actuator Disk model and investigations of wake phenomena*. PhD thesis, Université catholique de Louvain, 9 2018.

[58] Von Karman Institute Website. Low speed wind tunnel l-2b. https://www.vki.ac.be/index.php/facilities-other-menu-148/low-speed-wind-tunnels/48-research-and-consulting/facilities/low-speed-wind-tunnels/60-low-speed-wind-tunnel-l-2b, consulted 04/09/2020.

[59] E. Krause. *Fluid Mechanics: With Problems and Solutions, and an Aerodynamics Laboratory*. Springer London, Limited, 2005. ISBN 9783540272236. URL https://books.google.be/books?id=lbhEAAAAQBAJ.

[60] B. Conan. *Wind resource accessment in complex terrain by wind tunnel modelling*. PhD thesis, Université d'Orléans - von Karman Institute for Fluid Dynamics, VKI PHDT 2013-04, 2012.

[61] Von Karman Institue for Fluids Dynamics. TEST FACILITIES and TECHNICAL SUPPORT, 2003.

[62] Von Karman Institute Website. Low speed wind tunnel l-1b. https://www.vki.ac.be/index.php/facilities-other-menu-148/low-speed-wind-tunnels/48-research-and-consulting/facilities/low-speed-wind-tunnels/57-3-meter-diameter-wind-tunnel-l-1a, consulted 04/09/2020.

[63] E. Barlas. Experimental investigation of wind turbine/farm wakes in an atmospheric boundary layer wind tunnel. PR 2014-01, von Karman Institute for Fluid Dynamics, 2014.

[64] J. Anthoine, J. Arts, and et al. Measurements techniques in Fluid Dynamics: An Introduction. Number Reprint of VKI LS 1994-01, Third revised edition, Von Karman Institute for Fluid Dynamics, 1994.

[65] C. Tropea, A.L. Yarin, and J.F. Foss. *Springer Handbook of Experimental Fluid Mechanics*. Springer Handbook of Experimental Fluid Mechanics. Springer, 2007. ISBN 9783540251415.

[66] International Towing Tank Conference. Recommended Procedures and Guidelines : Uncertainty Analysis - Particle Image Velocimetry. Number 7.5-01-03-03, 2008.

[67] F. Jørgensen. How to measure turbulence with hot-wire anemometers - a practical guide. 2002.

[68] F.E Jørgensen. Directional Sensitivity of Wire and Fibre-Film Probes. Number DISA Information No. 11, 1971.

[69] S.M. Aminossadati. *A Technique for Calibration a Triple Hot-wire Probe (DANTEC Type 55P91)*. Report (University of Queensland. Dept. of Mechanical Engineering). Mechanical Engineering Department, The University of Queensland, 1998. URL `https://books.google.be/books?id=uIfhNQAACAAJ`.

[70] S. Vandenbussche. Etude aérodynamique du nouveau véhicule Eco-marathon ECAM. Final year thesis, ECAM, 2012-2013.

[71] J.-J. Trujillo, F. Bingöl, G. C. Larsen, J. Mann, and M. Kühn. Light detection and ranging measurements of wake dynamics. part ii: two-dimensional scanning. *Wind Energy*, 14(1):61–75, 2011. ISSN 1099-1824. doi: 10.1002/we.402. URL `http://dx.doi.org/10.1002/we.402`.

[72] S. Aubrun, T. F. Tchouaké, G. España, G. Larsen, J. Mann, and F. Bingöl. *Progress in Turbulence and Wind Energy IV: Proceedings of the iTi Conference in Turbulence 2010*. Springer Berlin Heidelberg, Berlin, Heidelberg, 2012. ISBN 978-3-642-28968-2.

[73] L. Vollmer, G. Steinfeld, D. Heinemann, and M. Kühn. Estimating the wake deflection downstream of a wind turbine in different atmospheric stabilities: an LES study. *Wind Energy Science*, 1(2):129–141, 2016.

[74] M. F. Howland, J. Bossuyt, L. A. Martínez-Tossas, J. Meyers, and C. Meneveau. Wake structure in actuator disk models of wind turbines in yaw under uniform inflow conditions. *Journal of Renewable and Sustainable Energy*, 8(4):043301, 2016. doi: 10.1063/1.4955091.

[75] J. Jonkman, S. Butterfield, W. Musial, and G. Scott. Definition of a 5-mw reference wind turbine for offshore system development. Technical Report NREL/TP-500-38060, National Renewable Energy Laboratory (NREL), February 2009.

[76] S.B. Pope. *Turbulent Flows*. Cambridge University Press, 2000. ISBN 9780521598866. URL `https://books.google.be/books?id=HZsTw9SMx-0C`.

[77] J. Counihan. Adiabatic atmospheric boundary layers: A review and analysis of data from the period 1880–1972. *Atmospheric Environment (1967)*, 9(10):871 – 905, 1975. ISSN 0004-6981. doi: https://doi.org/10.1016/0004-6981(75)90088-8. URL `http://www.sciencedirect.com/science/article/pii/0004698175900888`.

[78] VDI Guidelines 3783/12. Physical modelling of flow and dispersion processes in the atmospheric boundary layer - Application for wind tunnels. Beuth Verlag, 2000.

[79] T. Burton, D. Sharpe, N. Jenkins, and E. Bossanyi. *Wind Energy Handbook*. John Wiley & Sons, 2001. ISBN 9780471489979.

[80] N. Coudou. Wind turbine / farm wake(s) meandering study in an abl wind tunnel. PR 2016-05, von Karman Institute for Fluid Dynamics, 2016.

[81] H. S. Kang and C. Meneveau. Direct mechanical torque sensor for model wind turbines. *Measurement Science and Technology*, 21(10):105206, sep 2010. doi: 10.1088/0957-0233/21/10/105206. URL `https://doi.org/10.1088%2F0957-0233%2F21%2F10%2F105206`.

[82] J. Winslow, H. Otsuka, B. Govindarajan, and I. Chopra. Basic understanding of airfoil characteristics at low reynolds numbers (104–105). *Journal of Aircraft*, 55(3):1050–1061, 2018. doi: 10.2514/1.C034415. URL `https://doi.org/10.2514/1.C034415`.

[83] T. Osswald. Study of wind turbine loads through wind tunnel testing with a porous disc model. PR 2019-20, von Karman Institute for Fluid Dynamics, 2020.

[84] S. Buckingham. Wind park siting in complex terrains assessed by wind tunnel simulations. PR 2010-04, von Karman Institute for Fluid Dynamics, 2010.

[85] J. Counihan. Adiabatic atmospheric boundary layers : a review and analysis of data from the period 1880-1972. *Atmospheric environment*, 9:871–905, 1975.

[86] Eurocode. EN 1991-1-4:2005 : Actions on structures - Part 1-4: General actions - Wind actions. CEN, 2005.

[87] J.C. Kaimal and J.J. Finnigan. *Atmospheric Boundary Layer Flows: Their Structure and Measurement*. Oxford University Press, 1994. ISBN 9780195362770.

[88] LaVision GmbH. Imaging tools. Product-Manual Item-Number(s): 1005xxx, LaVision GmbH, 2015.

[89] LaVision GmbH. Flowmaster. Product-Manual for DaVis 8.3 Item-Number(s): 1105011-4, LaVision GmbH, 2016.

[90] Leonardo P. Chamorro, R.E.A Arndt, and F. Sotiropoulos. Reynolds number dependence of turbulence statistics in the wake of wind turbines. *Wind Energy*, 15(5):733–742, 2012. doi: 10.1002/we.501.

[91] Z. Du and M. S. Selig. A 3-d stall-delay model for horizontal axis wind turbine performance prediction. pages 9–19, January 1998. AIAA/ASME Wind Energy Symposium, 1998 ; Conference date: 12-01-1998 Through 15-01-1998.

[92] B. R. Noack. From snapshots to modal expansions – bridging low residuals and pure frequencies. *Journal of Fluid Mechanics*, 802:1–4, 2016. doi: 10.1017/jfm.2016.416.

[93] M.A. Mendez, M.T. Scelzo, and J.-M. Buchlin. Multiscale modal analysis of an oscillating impinging gas jet. *Experimental Thermal and Fluid Science*, 91:256 – 276, 2018. ISSN 0894-1777. doi: https://doi.org/10.1016/j.expthermflusci.2017.10.032. URL `http://www.sciencedirect.com/science/article/pii/S0894177717303370`.

[94] M. A. Mendez, D. Hess, B. B. Watz, and J.-M. Buchlin. Multiscale proper orthogonal decomposition (mPOD) of TR-PIV data—a case study on stationary and transient cylinder wake flows. *Measurement Science and Technology*, 31(9):094014, jun 2020. doi: 10.1088/1361-6501/ab82be. URL `https://doi.org/10.1088%2F1361-6501%2Fab82be`.

[95] J. G. Chen, Y. Zhou, R. A. Antonia, and T. M. Zhou. Characteristics of the turbulent energy dissipation rate in a cylinder wake. *Journal of Fluid Mechanics*, 835:271–300, 2018. doi: 10.1017/jfm.2017.765.

[96] M. Lejeune, M. Moens, M. Coquelet, N. Coudou, and P. Chatelain. Data assimilation for the prediction of wake trajectories within wind farms. *Journal of Physics: Conference Series*, 1618:062055, sep 2020. doi: 10.1088/1742-6596/1618/6/062055. URL `https://doi.org/10.1088%2F1742-6596%2F1618%2F6%2F062055`.

[97] N. Coudou, M. Moens, Y. Marichal, J. van Beeck, L. Bricteux, and P. Chatelain. Development of wake meandering detection algorithms and their application to large eddy simulations of an isolated wind turbine and a wind farm. *Journal of Physics: Conference Series*, 1037: 072024, jun 2018. doi: 10.1088/1742-6596/1037/7/072024. URL `https://doi.org/10.1088%2F1742-6596%2F1037%2F7%2F072024`.

[98] M. Maud, N. Coudou, and P. Chatelain. A numerical study of correlations between wake meandering and loads within a wind farm. *Journal of Physics: Conference Series*, 1256: 012012, jul 2019. doi: 10.1088/1742-6596/1256/1/012012. URL `https://doi.org/10.1088%2F1742-6596%2F1256%2F1%2F012012`.

[99] CECI-hpc Website. http://www.ceci-hpc.be/clusters.html. consulted the 07/09/2020.

[100] K. Siddharth. Random error. https://explorable.com/random-error, 2009. URL `https://explorable.com/random-error`. Retrieved May 21, 2016.

[101] F. Scarano. *Particle Image Velocimetry - Development and Application*. PhD thesis, von Karman Institute for Fluid Dynamics, VKI PHDT 2000-06, 2000.

[102] Litron Lasers. Lasers for piv applications. Product-datasheet, Litron Lasers.

Appendix A

# Computational aspects

## A.1 Tier-1 facilities

The numerical simulations were performed on the Tier-1 supercomputer of Wallonia, *Zenobe*, hosted and operated by the Cenaero. The main characteristics of this cluster can be found in Table A.1.

| Cluster | Host | CPU type | CPU count* | RAM/node | Max time |
|---|---|---|---|---|---|
| Zenobe | Cenaero | Haswell 2.5 GHz | 5760 (240 × 24) | 64..256 GB | 24 hours |
| | | IvyBridge 2.7 GHz | 8208 (342 × 24) | 64 GB | - |

***Table A.1:*** *Main characteristics of the* Zenobe *cluster [99]; *in this context, a CPU has to be understood as a core or a hardware thread: count = number of nodes × CPU/node*

## A.2 Computational costs

| | VPM | | | | |
|---|---|---|---|---|---|
| | ${}^{x}L_u/D = 1.50$ | | | | ${}^{x}L_u/D = 0.75$ |
| | $I = 0\%$ | $I = 4.8\%$ | $I = 8.4\%$ | $I = 12.0\%$ | $I = 8.4\%$ |
| Number of CPUs | 512 | 512 | 512 | 512 | 512 |
| Memory used [Gb] | $\simeq 460$ | $\simeq 710$ | $\simeq 816$ | $\simeq 955$ | $\simeq 822$ |
| CPUs-hours/$(D/U_\infty)$ | $\simeq 501$ | $\simeq 760$ | $\simeq 900$ | $\simeq 1124$ | $\simeq 1110$ |
| Wall-hours/$(D/U_\infty)$ | $\simeq 1$ | $\simeq 1.5$ | $\simeq 1.8$ | $\simeq 2.2$ | $\simeq 2.2$ |

***Table A.2:*** *Computational costs of the VPM simulations for five flow-through times including three with tracking; initial domain size* $[L_x \times L_y \times L_z] = [14D \times 4D \times 4D]$

| | FD4 | | | |
|---|---|---|---|---|
| | $I = 0\%$ | $I = 4.8\%$ | $I = 8.4\%$ | $I = 12.0\%$ |
| Number of CPUs | 32 | 32 | 32 | 32 |
| Memory used [Gb] | $\simeq 4$ | $\simeq 5$ | $\simeq 5$ | $\simeq 5$ |
| CPUs-hours/$(D/U_\infty)$ | $\simeq 2.6$ | $\simeq 3.7$ | $\simeq 4$ | $\simeq 4$ |
| Wall-hours/$(D/U_\infty)$ | $\simeq 0.09$ | $\simeq 0.12$ | $\simeq 0.13$ | $\simeq 0.13$ |

***Table A.3:*** *Computational costs of the FD4 simulations for five flow-through times; domain size* $[L_x \times L_y \times L_z] = [14D \times 9D \times 9D]$

Appendix B

# Probability distribution of the wake meandering amplitudes and wavelengths obtained from numerical simulations

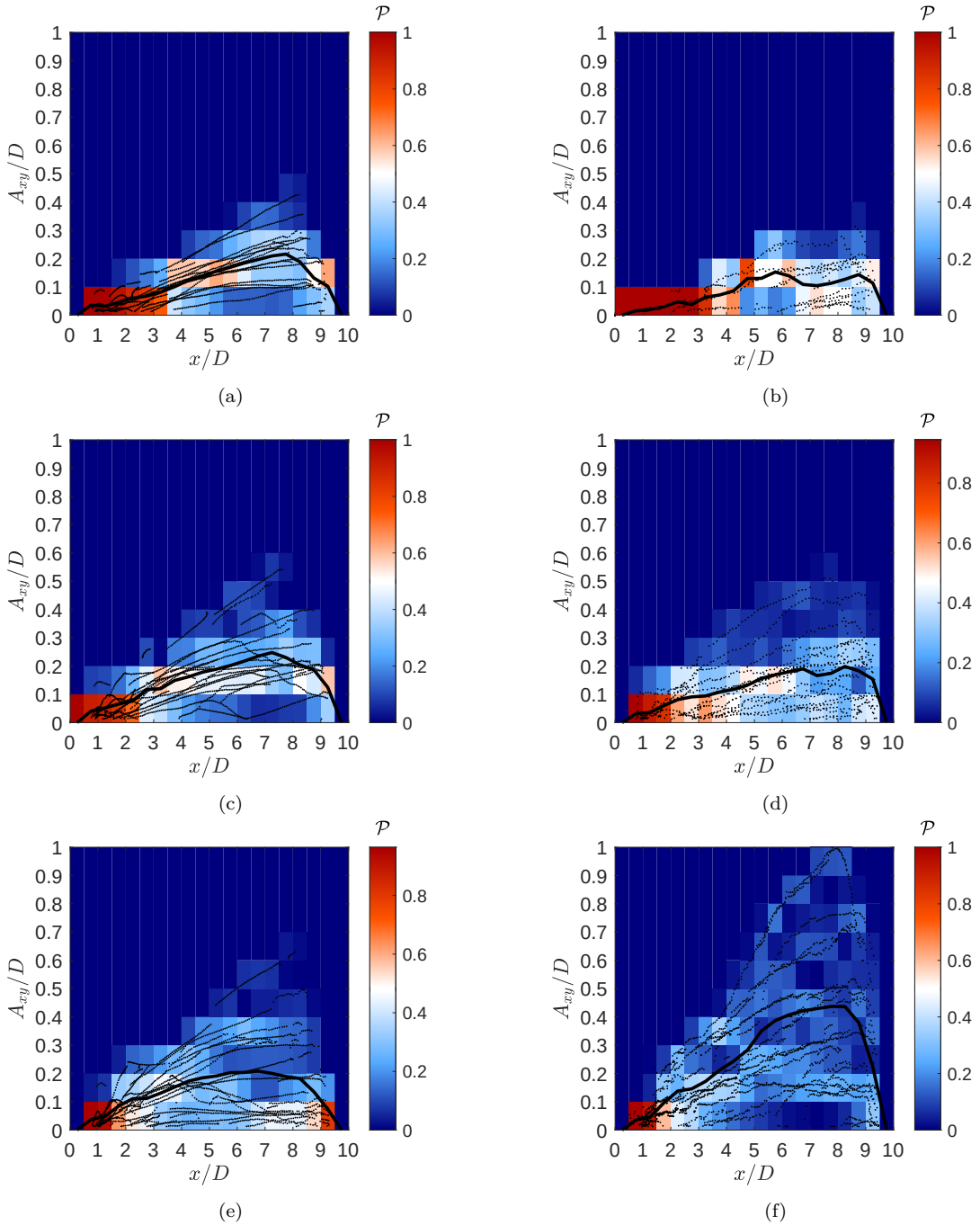



***Figure B.1:*** *Probability distribution of the wake meandering amplitudes and mean binned wake centerline amplitude as a function of the streamwise position obtained with the VPM (a)-(c)-(e) and FD4 (b)-(d)-(f) codes, in the horizontal plane at hub height, normalized by the rotor diameter for several inflow turbulence intensities:* $I = 4.8\%$ *(a)-(b),* $I = 8.4\%$ *(c)-(d), and* $I = 12.0\%$ *(e)-(f)*

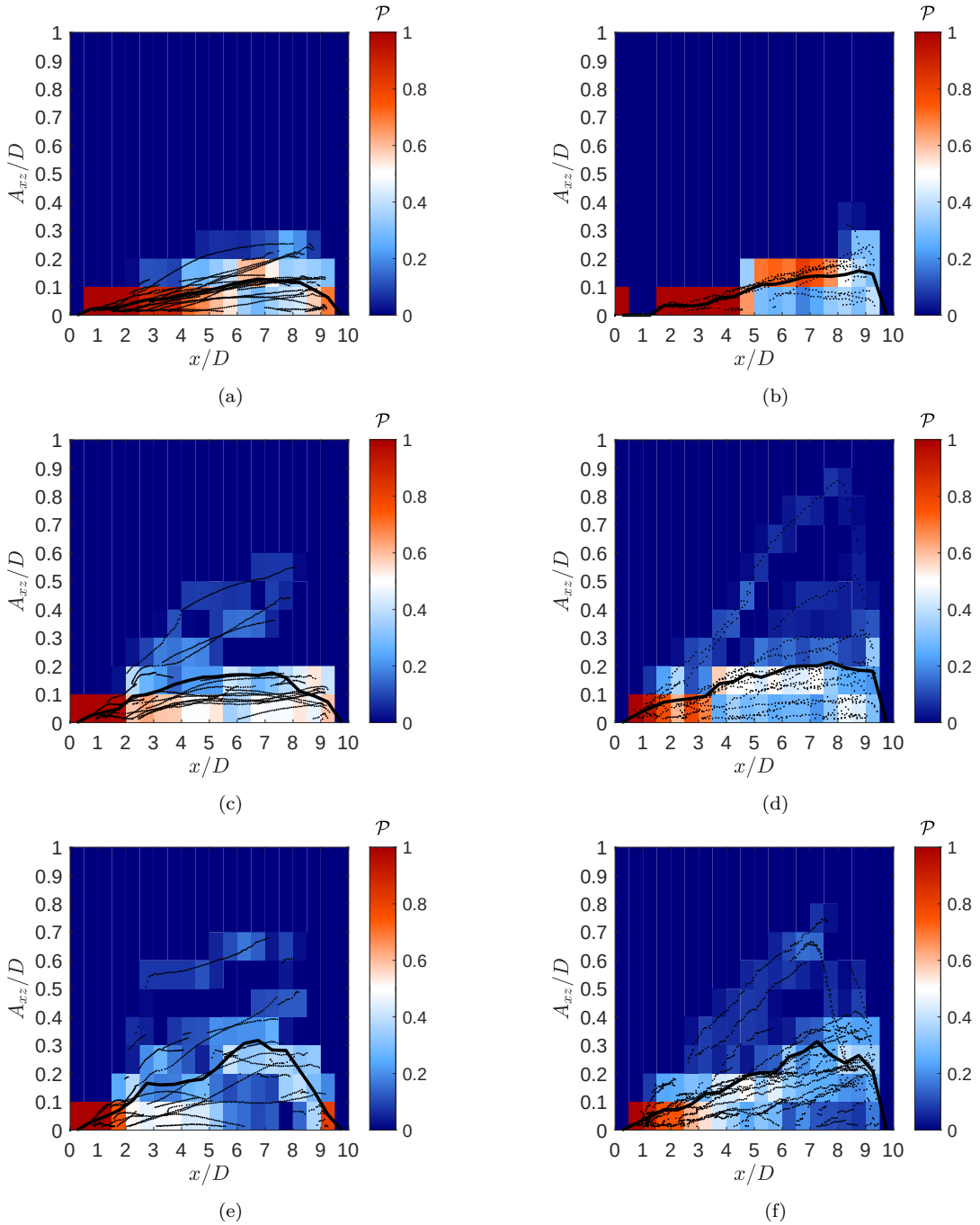



***Figure B.2:*** *Probability distribution of the wake meandering amplitudes and mean binned wake centerline amplitude as a function of the streamwise position obtained with the VPM (a)-(c)-(e) and FD4 (b)-(d)-(f) codes, in the vertical plane passing through the hub, normalized by the rotor diameter for several inflow turbulence intensities:* $I = 4.8\%$ *(a)-(b),* $I = 8.4\%$ *(c)-(d), and* $I = 12.0\%$ *(e)-(f)*

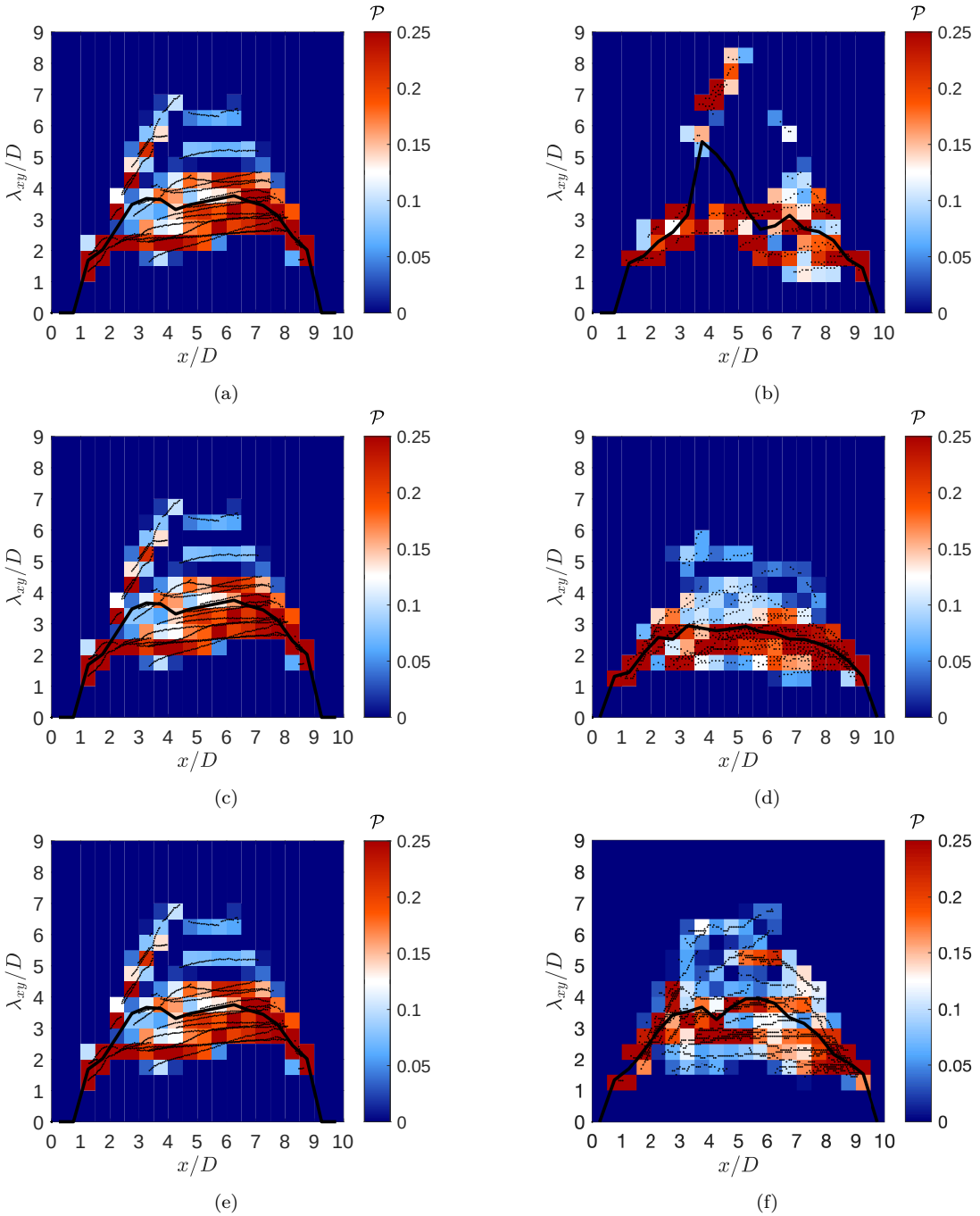



***Figure B.3:*** *Probability distribution of the wake meandering wavelengths and mean binned wake centerline wavelengths as a function of the streamwise position obtained with the VPM (a)-(c)-(e) and FD4 (b)-(d)-(f) codes, in the horizontal plane at hub height, normalized by the rotor diameter for several inflow turbulence intensities:* $I = 4.8\%$ *(a)-(b),* $I = 8.4\%$ *(c)-(d), and* $I = 12.0\%$ *(e)-(f)*

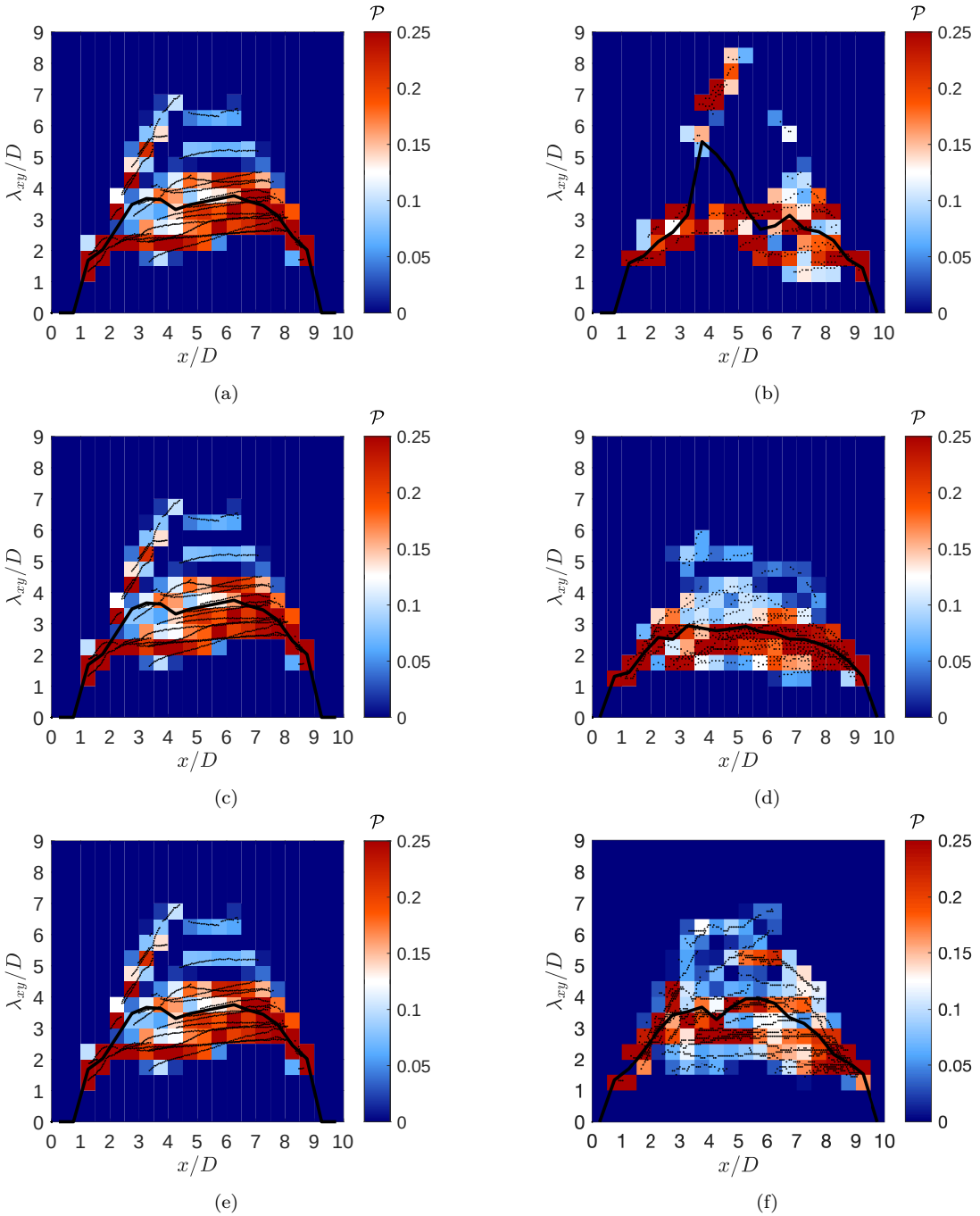



***Figure B.4:*** *Probability distribution of the wake meandering wavelengths and mean binned wake centerline wavelengths as a function of the streamwise position obtained with the VPM (a)-(c)-(e) and FD4 (b)-(d)-(f) codes, in the vertical plane passing through the hub, normalized by the rotor diameter for several inflow turbulence intensities: $I = 4.8\%$ (a)-(b), $I = 8.4\%$ (c)-(d), and $I = 12.0\%$ (e)-(f)*

APPENDIX C

# Wind turbine blade characteristics

| $r/R$ | 0.067 | 0.100 | 0.133 | 0.167 | 0.200 | 0.233 | 0.267 | 0.300 | 0.333 | 0.367 |
|---|---|---|---|---|---|---|---|---|---|---|
| $c/R$ | 0.334 | 0.326 | 0.319 | 0.311 | 0.303 | 0.295 | 0.287 | 0.279 | 0.271 | 0.263 |
| $\beta$ [$\circ$] | 21.1 | 21.7 | 20.3 | 19.0 | 17.8 | 16.7 | 15.6 | 14.7 | 13.8 | 12.9 |

| | 0.400 | 0.433 | 0.467 | 0.500 | 0.533 | 0.567 | 0.600 | 0.633 | 0.667 | 0.700 |
|---|---|---|---|---|---|---|---|---|---|---|
| | 0.256 | 0.248 | 0.240 | 0.232 | 0.224 | 0.216 | 0.208 | 0.201 | 0.193 | 0.185 |
| | 12.1 | 11.4 | 10.7 | 10.1 | 9.5 | 9.0 | 8.4 | 8.0 | 7.5 | 7.0 |

| | 0.733 | 0.767 | 0.800 | 0.833 | 0.867 | 0.900 | 0.933 | 0.967 | 1.000 |
|---|---|---|---|---|---|---|---|---|---|
| | 0.177 | 0.169 | 0.161 | 0.153 | 0.146 | 0.138 | 0.130 | 0.122 | 0.114 |
| | 6.6 | 6.2 | 5.7 | 5.3 | 4.9 | 4.5 | 4.0 | 3.6 | 3.1 |

***Table C.1:*** *Wind turbines blade characteristics for the chord length (c) and pitch angle ($\beta$) as a function of the distance from the turbine axis (r); $R = D/2$*

APPENDIX D

# Uncertainty analysis

## D.1 Uncertainty on wind speed from Pitot-static

The velocity can be computed as

$$U = \sqrt{\frac{2\,\Delta p}{\rho}} \tag{D.1}$$

Based on Eq. (D.1), the uncertainty on the velocity is defined as

$$\delta U = \sqrt{\left(\frac{\partial U}{\partial \Delta p}\delta\Delta p\right)^2 + \left(\frac{\partial U}{\partial \rho}\delta\rho\right)^2}. \tag{D.2}$$

After applying the partial derivatives, Eq. (D.2) leads to

$$\frac{\delta U}{U} = \sqrt{\left(\frac{\delta\Delta p}{2\,\Delta p}\right)^2 + \left(\frac{\delta\rho}{2\,\rho}\right)^2}. \tag{D.3}$$

- Uncertainty on the dynamic pressure:

  The uncertainty on the dynamic pressure can be computed as

  $$\delta\Delta p = \sqrt{\delta\Delta p_{device}^2 + \delta\Delta p_{reading}^2} \tag{D.4}$$

  where

  - $\delta\Delta p_{device}$ is the uncertainty on the pressure sensor (AMS5812) computed as

    $$\delta\Delta p_{device} = m_{PS} \cdot \frac{1.5}{100} \cdot FSO, \tag{D.5}$$

    where $m_{PS}$ is the slope obtained from the calibration of the pressure sensor, and $FSO$ is the Full Span Output, i.e. the algebraic difference between the output signal at the minimum pressure and the output signal at the maximum pressure used during the experiments;

– $\delta\Delta p_{reading}$ is the reading uncertainty coming from the calibration of the pressure sensor with the water manometer, and defined as

$$\delta\Delta p_{reading} = \delta H_{mm_{H20}}, \tag{D.6}$$
$$\delta\Delta p_{reading} = 0.980665\,\text{Pa}. \tag{D.7}$$

The water manometer having a resolution of 0.2 $\text{mm}_{H2O}$, the error $\delta H_{mm_{H20}}$ is of 0.1 $\text{mm}_{H2O}$, i.e. 0.980665 Pa.

- Uncertainty on the density:

The density can be obtained from the Ideal Gas Law

$$\rho = \frac{p}{RT}. \tag{D.8}$$

Based on Eq. (D.8), the uncertainty on the density is defined by

$$\delta\rho = \sqrt{\left(\frac{\partial\rho}{\partial p}\delta p\right)^2 + \left(\frac{\partial\rho}{\partial T}\delta T\right)^2}. \tag{D.9}$$

After applying the partial derivatives, Eq. (D.9) leads to

$$\frac{\delta\rho}{\rho} = \sqrt{\left(\frac{\delta p}{p}\right)^2 + \left(\frac{\delta T}{T}\right)^2} \tag{D.10}$$

where

– $\delta p$ is the error on the barometric pressure of the *Druck DPI 150 Precision Pressure Indicator* of the von Karman institute, i.e. $\Delta p = 0.15$ mbar = 15 Pa;

– $\delta T$ is the error on the temperature of the weather station used, i.e. $\Delta T = 1$ K.

The evolution of the uncertainty on the velocity, which depends on the wind speed, is presented in Fig. D.1 considering a slope $m_{PS} = 52.07$ Pa/V, a FSO of 1.62 V, an atmospheric pressure of 101325 Pa and a temperature of 20°C.

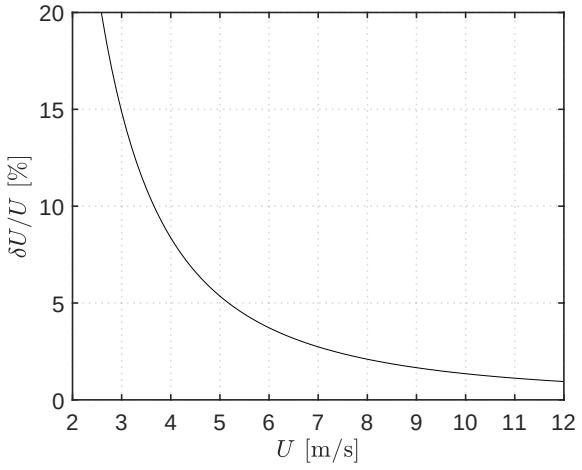



***Figure D.1:*** *Uncertainty on the velocity obtained from the Pitot-static as a function of the wind speed*

## D.2 Uncertainty on electrical power

The electrical power coefficient can be computed as

$$C_p^{elec} = \frac{V \cdot I}{0.5\,\rho\,U_\infty^3\,A}. \tag{D.11}$$

Based on Eq. (D.11), the uncertainty on the electrical power is defined as

$$\delta\,C_p^{elec} = \sqrt{\left(\frac{\partial C_p^{elec}}{\partial V}\delta V\right)^2 + \left(\frac{\partial C_p^{elec}}{\partial I}\delta I\right)^2 + \left(\frac{\partial C_p^{elec}}{\partial \rho}\delta \rho\right)^2 + \left(\frac{\partial C_p^{elec}}{\partial U_\infty}\delta U_\infty\right)^2 + \left(\frac{\partial C_p^{elec}}{\partial A}\delta A\right)^2}. \tag{D.12}$$

After applying the partial derivatives, Eq. (D.12) leads to

$$\frac{\delta Cp^{elec}}{C_p^{elec}} = \sqrt{\left(\frac{\delta V}{V}\right)^2 + \left(\frac{\delta I}{I}\right)^2 + \left(\frac{\delta \rho}{\rho}\right)^2 + \left(\frac{-3\delta U_\infty}{U_\infty}\right)^2 + \left(\frac{\delta A}{A}\right)^2}. \tag{D.13}$$

- Uncertainty on the voltage:

  The uncertainty on the voltage can be computed as

  $$\frac{\delta V}{V} = \sqrt{\epsilon_{gain\ error}^2 + \epsilon_{offset\ error}^2} = 0.0071 \tag{D.14}$$

  where the gain error is 0.6% and the offset error is 0.38% based on the datasheet of the NI9215 acquisition board.

- Uncertainty on the current:

  The current $I$ is obtained from measuring the voltage ($V_{shunt}$) over the resistance $R_{shunt}$

  $$I = \frac{V_{shunt}}{R_{shunt}}. \tag{D.15}$$

  Based on Eq. (D.15), the relative uncertainty on the current is defined as

  $$\delta\,I = \sqrt{\left(\frac{\partial I}{\partial V_{shunt}}\delta V shunt\right)^2 + \left(\frac{\partial I}{\partial R_{shunt}}\delta R_{shunt}\right)^2}. \tag{D.16}$$

  After applying the partial derivatives, Eq. (D.16) leads to

  $$\frac{\delta I}{I} = \sqrt{\left(\frac{\delta V_{shunt}}{V_{shunt}}\right)^2 + \left(\frac{\delta R_{shunt}}{R_{shunt}}\right)^2} = 0.0505 \tag{D.17}$$

  where

  - $\delta V_{shunt}$ is the uncertainty on the voltage measured, i.e. $\delta V_{shunt}/V_{shunt} = 0.0071$;
  - $\delta R_{shunt}$ is the uncertainty on the resistance, $\delta R_{shunt}/R_{shunt} = 5\%$ according to the manufacturer specifications.

- Uncertainty on the density:

  see Appendix D.1

- Uncertainty on the velocity:

  see Appendix D.1

- Uncertainty on the surface:

  Considering an error $\delta R = 0.5$ mm on the blade length, the uncertainty on the swept area ($A = \pi R^2$) is

$$\delta A = 2\pi R\,\delta R \tag{D.18}$$
$$\frac{\delta A}{A} = \frac{2\,\delta R}{R} \tag{D.19}$$
$$\frac{\delta A}{A} = 1.33\%. \tag{D.20}$$

## D.3 Uncertainty on mechanical power

The following uncertainty analysis is based on the uncertainty analysis proposed in [81]. The mechanical power coefficient can be computed as

$$C_p^{aero} = \frac{Q \cdot \omega}{0.5\,\rho\,U_\infty^3\,A}. \tag{D.21}$$

Based on Eq. (D.21), the uncertainty on the mechanical power is defined as

$$\delta\,C_p^{aero} = \sqrt{\left(\frac{\partial C_p^{aero}}{\partial Q}\right)^2 \delta Q^2 + \left(\frac{\partial C_p^{aero}}{\partial \omega}\right)^2 \delta\omega^2 + \left(\frac{\partial C_p^{aero}}{\partial \rho}\right)^2 \delta\rho^2 + \left(\frac{\partial C_p^{aero}}{\partial U_\infty}\right)^2 \delta U_\infty^2 + \left(\frac{\partial C_p^{aero}}{\partial A}\right)^2 \delta A^2}. \tag{D.22}$$

After applying the partial derivatives, Eq. (D.22) leads to

$$\frac{\delta Cp^{aero}}{C_p^{aero}} = \sqrt{\left(\frac{\delta Q}{Q}\right)^2 + \left(\frac{\delta\omega}{\omega}\right)^2 + \left(\frac{\delta\rho}{\rho}\right)^2 + \left(\frac{-3\delta U_\infty}{U_\infty}\right)^2 + \left(\frac{\delta A}{A}\right)^2}. \tag{D.23}$$

- Uncertainty on the mechanical torque:

  In order to find the overall uncertainty on the mechanical torque as evaluated from the measure voltage using a fitting linear function, individual uncertainties of the torque measurement and calibration must be documented. Following the approach of Meneveau's article, the output voltages from the torque-sensor system ($\delta Q_V$) can be defined as

$$\frac{\delta Q}{Q} = \sqrt{\left(\frac{\delta Q_{ref}}{Q_{ref}}\right)^2 + \left(\frac{\delta V_{rep}}{V_{rep}}\right)^2 + \left(\frac{\delta Q_{fit:V-Q}}{Q_{fit:V-Q}}\right)^2}, \tag{D.24}$$

  where

  - $\frac{\delta Q_{ref}}{Q_{ref}}$ is the relative uncertainty on the reference torque;
  - $\frac{\delta V_{rep}}{V_{rep}}$ is the relative uncertainty on the reproducibility of the output voltage;
  - $\frac{\delta Q_{fit:V-Q}}{Q_{fit:V-Q}}$ is the relative uncertainty on the linear curve fitting of Q as a function of V.

  Considering

$$Q_{ref} = m\,g\,l, \tag{D.25}$$

  the relative uncertainty on the reference torque can be expressed as

$$\delta Q_{ref} = \sqrt{\left(\frac{\partial Q_{ref}}{\partial m}\right)^2 \delta m^2 + \left(\frac{\partial Q_{ref}}{\partial l}\right)^2 \delta l^2} \tag{D.26}$$

  where

  - $m$ is the mass of the weight;

– $g$ is the gravitational acceleration (9.81 m/s$^2$);

– $l$ is the arm from the center of the motor to the weight (0.025 m).

After applying the partial derivatives, Eq. (D.26) leads to

$$\frac{\delta Q_{ref}}{Q_{ref}} = \sqrt{\left(\frac{\delta m}{m}\right)^2 + \left(\frac{\delta l}{l}\right)^2} \tag{D.27}$$

where

– $\delta m$ is the uncertainty of the mass. The weights were measured using a precision balance (*Adventurer Pro AS214*), the error on the weights mass is given by

$$\begin{aligned} \delta m &= \sqrt{\epsilon^2_{non-linearity} + \epsilon^2_{precision} + \epsilon^2_{reproducibility}} && \text{(D.28)} \\ &= \sqrt{0.0002^2 + 0.0001^2 + 0.0001^2} \cdot 10^{-3}\,\text{kg} && \text{(D.29)} \\ &= 0.24 \cdot 10^{-6}\,\text{kg}. && \text{(D.30)} \end{aligned}$$

– $\delta l$ is the uncertainty of the length. The drilling position on the calibration part has been measured with a caliper with a precision of 0.5 mm.

The uncertainty on the reproducibility of the output voltage is determined by measuring the output voltage from the torque sensor ten times for each weight. The uncertainty on the reproducibility is defined as

$$\frac{\delta V_{\text{rep}}}{V_{\text{rep}}} = C_t \frac{\sigma_V}{\bar{V}} = C_t \frac{1}{\bar{V}} \sqrt{\frac{\sum_{i=1}^{N} \left(V_i - \bar{V}\right)^2}{N-1}} \tag{D.31}$$

where $N$ is the number of samples, $C_t$ is the confidence limit factor of 2.131 for the 95% confidence interval and $N = 15$ (t-distribution), and $\bar{V}$ is the mean value of the output voltage $V$. The evolution of the uncertainty on the reproducibility as a function of the reference torque is shown in Fig. D.2.

The relative uncertainty on the linear curve fitting between the torque and the output voltage ($\delta Q_{fit:V-Q}$) is defined as

$$\frac{\delta Q_{\text{fit:}V-Q}}{Q_{\text{fit:}V-Q}} = C_t \frac{1}{Q} \sqrt{\frac{\sum_{i=1}^{N} \left(Q_i - m_V V_i - b_V\right)^2}{N-2}} \tag{D.32}$$

where $C_t = 2.131$ for the 95% confidence interval and $N = 15$ (t-distribution), $m_V = 8.3113 \cdot 10^{-4}$ and $b_V = -6.6272 \cdot 10^{-5}$. $N-2$ is used because the degree of freedom decreases by 2 in obtaining the slope $m_V$ and offset $b_V$. The absolute uncertainty on the linear curve fitting is $19.1619 \cdot 10^{-6}$ Nm. The relative uncertainty varies from 28.4% for $67.5188 \cdot 10^{-6}$ Nm and 0.8% for $2.3362 \cdot 10^{-3}$ Nm, which dominates the overall relative uncertainty on the torque calibration. The evolution of the uncertainty on the linear curve fitting as a function of the reference torque is shown in Fig. D.2.

- Uncertainty on the rotational speed:

The rotational speed is measured using an encoder. Its pulse lengths may vary due to mechanical tolerances. As a result the measured position deviates from the real position in a periodic way over one motor revolution. The encoder used for our application has 50 cpt (count or pulses per turn). This setting allows the detection of the direction of motor rotation and gives 4 distinct states per pulse. The Integrated Non-linearity (INL) can be computed as

$$\begin{aligned} INL &= \frac{360^\circ}{4 \cdot 50} && \text{(D.33)} \\ &= 1.8^\circ && \text{(D.34)} \\ &= 0.005\,\text{tr}. && \text{(D.35)} \end{aligned}$$

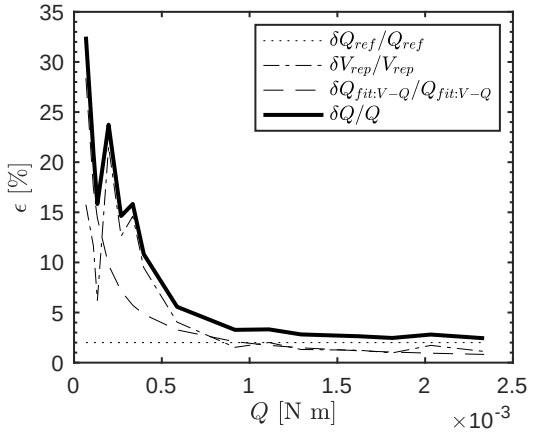



***Figure D.2:*** *Relative uncertainty on the calibration of the torque-sensor system*

The uncertainty on the rotational speed $\delta\omega$ is therefore equal to 0.005 tr/min. Indeed, the error is the same for each turn.

- Uncertainty on the density:

  see Appendix D.1

- Uncertainty on the velocity:

  see Appendix D.1

- Uncertainty on the surface:

  see Appendix D.2

## D.4 Uncertainty on mechanical power measured from current

The relative uncertainty on the mechanical torque, computed indirectly from the measured current over the resistance using a linear fitting function (Eq. (5.4)), depends on the relative uncertainty on the direct torque measurement using the torque-sensor system, on the relative uncertainty on the current, and on the relative uncertainty on the curve fitting using Eq. (5.4). The relative uncertainty on the mechanical torque can therefore be estimated as

$$\frac{\delta Q_{Q-I}}{Q_{Q-I}} = \sqrt{\left(\frac{\delta Q}{Q}\right)^2 + \left(\frac{\delta I}{I}\right)^2 + \left(\frac{\delta Q_{\text{fit:}Q-I}}{Q_{\text{fit:}Q-I}}\right)^2} \tag{D.36}$$

- Uncertainty on the mechanical torque:

  see Appendix D.3

- Uncertainty on the current:

  see Appendix D.3

- Uncertainty on the linear curve fitting between the torque and the current:

  The relative uncertainty on the linear curve fitting between the torque and the current ($\delta Q_{fit:Q-I}$) can be computed as

$$\frac{\delta Q_{\text{fit:}Q-I}}{Q_{\text{fit:}Q-I}} = C_t \frac{1}{Q} \sqrt{\frac{\sum_{i=1}^{N} \left(Q_i - m_I I_i - b_I\right)^2}{N-2}} \tag{D.37}$$

where $C_t = 1.980$ for the 95% confidence interval and $N = 328$ (t-distribution), $m_I = 1.2032 \cdot 10^3$ and $b_I = -0.079738$. $N - 2$ is used because the degree of freedom decreases by 2 in obtaining the slope $m_I$ and offset $b_I$. The absolute uncertainty on the linear curve fitting is $1.8498 \cdot 10^{-4}$ Nm.

## D.5 Uncertainty on the thrust coefficient

The aerodynamic thrust coefficient can be computed as

$$C_T = \frac{T}{0.5\,\rho\,U_{ref}^2\,A} \tag{D.38}$$

$$= \frac{T}{\Delta p\,A} \qquad \text{since} \quad U_{ref} = \sqrt{\frac{2\,\Delta p}{\rho}}. \tag{D.39}$$

Based on Eq. (D.39), the uncertainty on the thrust coefficient is defined as

$$\delta C_T = \sqrt{\left(\frac{\partial C_T}{\partial T}\delta T\right)^2 + \left(\frac{\partial C_T}{\partial \Delta p}\delta \Delta p\right)^2 + \left(\frac{\partial C_T}{\partial A}\delta A\right)^2}. \tag{D.40}$$

After applying the partial derivatives, Eq. (D.40) leads to

$$\frac{\delta C_T}{C_T} = \sqrt{\left(\frac{\delta T}{T}\right)^2 + \left(\frac{\delta \Delta p}{\Delta p}\right)^2 + \left(\frac{\delta A}{A}\right)^2}. \tag{D.41}$$

- Uncertainty on the thurst:

$$\delta T = \sqrt{\delta T_{weights}^2 + \delta T_{load\ cell}^2 + \delta T_{random}^2} \tag{D.42}$$

  - $\delta T_{weights}$:

    The weights were measured using an *Adventurer Pro AS214* balance, the error on the weights mass is given by

$$\epsilon_{weights} = \sqrt{\epsilon_{non-linearity}^2 + \epsilon_{precision}^2 + \epsilon_{reproducibility}^2} \tag{D.43}$$

$$= \sqrt{0.0002^2 + 0.0001^2 + 0.0001^2} \cdot 10^{-3}\,\text{kg} \tag{D.44}$$

$$= 0.24 \cdot 10^{-6}\,\text{kg} \tag{D.45}$$

    and the error on the reference thrust by

$$\delta T_{weights} = g \cdot \epsilon_{weights} \tag{D.46}$$

$$= 2.4 \cdot 10^{-6}\,\text{N} \tag{D.47}$$

    where $g = 9.80665$ m/s$^2$ is the gravity force.

  - $\delta T_{load\ cell}$:

    Neglecting the temperature related errors, since the temperature was stable during the tests, the load cell error is given by

$$\epsilon_{load\ cell} = \sqrt{\epsilon_{non-linearity}^2 + \epsilon_{hysteresis}^2 + \epsilon_{repeatability}^2} \tag{D.48}$$

$$\epsilon_{load\ cell} = \sqrt{\left(\frac{0.1}{100}RO\right)^2 + \left(\frac{0.1}{100}RO\right)^2 + \left(\frac{0.05}{100}RO\right)^2} \tag{D.49}$$

$$\epsilon_{load\ cell} = 0.0015RO \tag{D.50}$$

and the error on the thrust due to the load cell error by

$$\delta T_{load\ cell} = m_{balance} \cdot \epsilon_{load\ cell} \quad (D.51)$$
$$= 1.89 \cdot 10^{-6}\,\mathrm{N} \quad (D.52)$$

where $m_{balance} = 0.126$ N/V is the slope of the calibration curve of the balance and $RO$ is the Rated Output of the load cell, which is 10 mV with an excitation voltage of 5 V (2 mV/V · 5 V = 10 mV).

– $\delta T_{random}$:

Assuming a Gaussian distribution of the measurement and a confidence interval of 95%, the random uncertainty on the measurements can be computed in the following way

$$\delta T_{random} = z_\alpha \cdot \frac{\sigma}{\sqrt{N}} \quad (D.53)$$

where $z_\alpha = 1.96$ and $N = f_s \cdot T_{acq.} = 100 \cdot 10 = 1000$.

- Uncertainty on the dynamic pressure:

  See Appendix D.1 for the detailed analysis.

$$\delta\Delta p = \sqrt{\delta\Delta p^2_{device} + \delta\Delta p^2_{reading}} \quad (D.54)$$
$$\delta\Delta p = \sqrt{\left(m_{PS} \cdot \frac{1.5}{100} \cdot FSO\right)^2 + \left(0.980665\right)^2} \quad (D.55)$$
$$\delta\Delta p = \sqrt{\left(53.023 \cdot \frac{1.5}{100} \cdot 1.612\right)^2 + \left(0.980665\right)^2} \quad (D.56)$$
$$\delta\Delta p = 1.614\ \mathrm{Pa} \quad (D.57)$$

- Uncertainty on the surface:

  see Appendix D.2

## D.6 Uncertainty on airfoil lift/drag coefficients

The uncertainty analysis presented hereafter is for the drag coefficient. The uncertainty on the lift coefficient can be obtained by simply replacing the drag force by the lift force.

The aerodynamic drag coefficient can be computed as

$$C_D = \frac{D}{0.5\,\rho\,U^2_{ref}\,A} \quad (D.58)$$
$$= \frac{D}{\Delta p\,A} \qquad \text{since} \quad U_{ref} = \sqrt{\frac{2\,\Delta p}{\rho}}. \quad (D.59)$$

Based on Eq. (D.59), the uncertainty on the drag coefficient is defined as

$$\delta C_D = \sqrt{\left(\frac{\partial C_D}{\partial D}\delta D\right)^2 + \left(\frac{\partial C_D}{\partial \Delta p}\delta\Delta p\right)^2 + \left(\frac{\partial C_D}{\partial A}\delta A\right)^2}. \quad (D.60)$$

After applying the partial derivatives, Eq. (D.60) leads to

$$\frac{\delta C_D}{C_D} = \sqrt{\left(\frac{\delta D}{D}\right)^2 + \left(\frac{\delta\Delta p}{\Delta p}\right)^2 + \left(\frac{\delta A}{A}\right)^2}. \quad (D.61)$$

- Uncertainty on the drag:

$$\delta D = \sqrt{\delta D^2_{weights} + \delta D^2_{load\ cell} + \delta D^2_{random}} \tag{D.62}$$

  - $\delta D_{weights}$:

    see Appendix D.5

  - $\delta D_{load\ cell}$:

    Neglecting the temperature related errors, since the temperature was stable during the tests, the load cell error is given by

$$\epsilon_{load\ cell} = \sqrt{\epsilon^2_{non-linearity} + \epsilon^2_{hysteresis} + \epsilon^2_{repeatability}} \tag{D.63}$$

$$\epsilon_{load\ cell} = \sqrt{\left(\frac{0.1}{100}RO\right)^2 + \left(\frac{0.1}{100}RO\right)^2 + \left(\frac{0.05}{100}RO\right)^2} \tag{D.64}$$

$$\epsilon_{load\ cell} = 0.0015RO \tag{D.65}$$

    and the error on the drag due to the load cell error by

$$\delta D_{load\ cell} = m_{balance} \cdot \epsilon_{load\ cell} \tag{D.66}$$

$$= 1.85 \cdot 10^{-6}\,\text{N} \tag{D.67}$$

    where $m_{balance} = 0.123$ N/V is the slope of the calibration curve of the balance and $RO$ is the Rated Output of the load cell, which is 10 mV with an excitation voltage of 5 V (2 mV/V $\cdot$ 5 V = 10 mV).

  - $\delta D_{random}$:

    Assuming a Gaussian distribution of the measurement and a confidence interval of 95%, the random uncertainty on the measurements can be computed in the following way

$$\delta D_{random} = z_\alpha \cdot \frac{\sigma}{\sqrt{N}} \tag{D.68}$$

    where $z_\alpha = 1.96$ and $N = f_s \cdot T = 30000$.

- Uncertainty on the dynamic pressure:

  See Appendix D.1 for the detailed analysis.

$$\delta\Delta p = \sqrt{\delta\Delta p^2_{device} + \delta\Delta p^2_{reading}} \tag{D.69}$$

$$\delta\Delta p = \sqrt{\left(m_{PS} \cdot \frac{1.5}{100} \cdot FSO\right)^2 + \left(0.980665\right)^2} \tag{D.70}$$

$$\delta\Delta p = \sqrt{\left(52.065 \cdot \frac{1.5}{100} \cdot 1.637\right)^2 + \left(0.980665\right)^2} \tag{D.71}$$

$$\delta\Delta p = 1.611\ \text{Pa} \tag{D.72}$$

- Uncertainty on the surface:

  Considering an error of 0.5 mm on the blade chord ($c$) and blade height ($h$), the uncertainty on the surface is

$$\frac{\delta A}{A} = \sqrt{\left(\frac{\delta h}{h}\right)^2 + \left(\frac{\delta c}{c}\right)^2} \tag{D.73}$$

$$\frac{\delta A}{A} = \sqrt{\left(\frac{5 \cdot 10^{-4}}{0.116}\right)^2 + \left(\frac{5 \cdot 10^{-4}}{0.049}\right)^2} \tag{D.74}$$

$$\frac{\delta A}{A} = 1.11\%. \tag{D.75}$$

## D.7 Uncertainty analysis for PIV

Since the PIV measurement system consists of several sub-systems, and the evaluation of the uncertainty on the measurements needs to consider the coupling between the sub-systems. The uncertainty analysis developed below is based on the procedure proposed in [66].

In the following analysis, the uncertainty is considered to be due to a systematic error or bias error ($\epsilon_{bias}$) and a random error ($\epsilon_{rnd}$). The first one is the error committed in each measurement and is inherent in the calibration errors, in the equipment, in the experimenter, etc. The latter occurs because there are a very large number of parameters beyond the control of the experiment that may interfere with the results of the experiment [100], and is therefore due to the variability of the studied phenomenon, to electronic noise in the circuit of an electrical instrument, etc. The uncertainty on the measurements is therefore defined as

$$\epsilon_{tot} = \sqrt{\epsilon_{bias}^2 + \epsilon_{rnd}^2}. \tag{D.76}$$

### D.7.1 Systematic error or bias error

As stated formerly, the systematic error is inherent in the calibration errors, in the equipment, in the experimenter, etc. Once the magnification factor $M$ [mm/pixel] is determined through calibration, PIV measurements enable to detect the flow velocity $u$ [mm/s] by means of the displacement of the particle images $d$ [pixel] and the time interval $\Delta t$ [s] between successive images constituting a pair. The flow velocity can indeed be computed by

$$u = M\frac{d}{\Delta t} + \Delta u \tag{D.77}$$

where $\Delta u$ is a parameter which takes into account that the information of the image differs from the flow field due to the velocity lag of the tracer particle from acceleration and projection procedure from 3-D physical space to 2-D image plane [66]. Following the classical error analysis procedure [64] and neglecting the term $\Delta u$ ($\Delta u = 0$), the bias error associated with the velocity $u$ is

$$\epsilon_{bias} = \delta u = \sqrt{\Big(\frac{\partial u}{\partial M}\delta M\Big)^2 + \Big(\frac{\partial u}{\partial d}\delta d\Big)^2 + \Big(\frac{\partial u}{\partial \Delta t}\delta \Delta t\Big)^2} \tag{D.78}$$

which, after applying the partial derivatives, yields to

$$\frac{\delta u}{u} = \sqrt{\Big(\frac{\delta M}{M}\Big)^2 + \Big(\frac{\delta d}{d}\Big)^2 + \Big(\frac{\delta \Delta t}{\Delta t}\Big)^2}. \tag{D.79}$$

Since $M$ and $\Delta t$ are constant through the whole investigated area, this equation enables to conclude that the percentage error made on the velocity $u$ increases for decreasing values of $d$, i.e. for weaker velocities. The three error sources of Eq. (D.79) are analyzed in the following sections.

- Uncertainty on the magnification factor:

  The magnification factor is determined by positioning a calibration board, of size 2000 mm × 900 mm mm and composed of 10 mm diameter printed black circles spaced by a distance of 15 mm, at the same position as the laser light sheet. Defining $L_{mm}$ [mm] the physical length and $L_{px}$ [pixel] the related length in the image, the expression of the magnification factor is

  $$M = \frac{L_{mm}}{L_{pxl}} \cdot cos\theta_1 \simeq \frac{L_{mm}}{L_{pxl}}\Big(1 - \frac{\theta_1^2}{2}\Big) \tag{D.80}$$

  where $\theta_1$ is the small angle between the laser light sheet and the calibration board (Fig. D.3).

The uncertainties which affect the magnification factor are:

- uncertainty with regard to the physical length ($\delta L_{mm}$) of the calibration target. $\delta L_{mm} = 1\ mm$, considering an error of 0.5 mm for each extremity of the reference segment.
- uncertainty on the length of the calibration target on the display ($\delta L_{px}$) due to image resolution. $\delta L_{px} = 1$ pixel, considering an error of 0.5 pixel on the location of each extremity of the reference segment on the display.
- uncertainty with regard to image distortion due to the aberration of lenses. This uncertainty is neglected in the present analysis.
- uncertainty due to error sources of CMOS. This uncertainty is usually small and can be neglected.
- uncertainty on the alignment of the calibration board with the laser light sheet (Fig. D.3). The misalignment angle can be estimated as $\theta_1 = 2^\circ = 0.035$ rad.

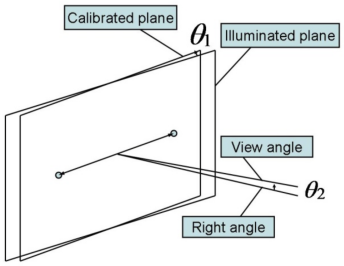



***Figure D.3:*** *Possible misalignment of the calibration plane with the illuminated plane and of the camera with the illuminated plane [66]*

Neglecting the impact of image distortion and the error sources of CMOS, the expression of the error on the magnification factor is

$$\delta M = \sqrt{\left(\frac{\partial M}{\partial L_{mm}}\delta L_{mm}\right)^2 + \left(\frac{\partial M}{\partial L_{px}}\delta L_{px}\right)^2 + \left(\frac{\partial^2 M}{\partial \theta_1^2}\delta\theta_1^2\right)^2}. \tag{D.81}$$

Note that the effect of misalignment has to be taken into account using a second order derivative, since the first order derivative ($\frac{\partial M}{\partial \theta} = -\frac{L_{mm}}{L_{px}}\theta_1$) equals zero because the nominal value of $\theta_1$ is zero. Applying the partial derivatives yields to

$$\frac{\delta M}{M} = \sqrt{\left(\frac{\delta L_{mm}}{L_{mm}}\right)^2 + \left(\frac{\delta L_{px}}{L_{px}}\right)^2 + \left(\frac{\delta\theta_1^2}{(1-\frac{\theta_1^2}{2})}\right)^2}. \tag{D.82}$$

- Uncertainty on the displacement of particles image:

  The real displacement $\Delta x$ [pixel] of the particles can be different from the one measured by the camera $d$ because the latter can be affected by a misalignment of the camera compared to the laser light sheet

  $$d = \Delta x \cdot cos\theta_2. \tag{D.83}$$

  The main error sources on the displacement of particles image are due to:

  - Laser intensity fluctuations. This uncertainty is neglected in the present analysis.
  - Image distortion. This uncertainty is neglected in the present analysis.
  - Misalignment of the camera with the laser light sheet (Fig. D.3). This angle can be estimated as $\theta_2 = 2^\circ = 0.035$ rad.

– The error coming from the PIV processing software. This error $\delta\Delta x$ can be estimated to be about 0.1 pixel [101].

The error on the displacement is therefore

$$\delta d = \sqrt{\left(\frac{\partial d}{\partial \Delta x}\delta\Delta x\right)^2 + \left(\frac{\partial^2 d}{\partial \theta_2^2}\delta\theta_2^2\right)^2} \tag{D.84}$$

which, after applying the partial derivatives, yields to

$$\frac{\delta d}{d} = \sqrt{\left(\frac{\delta\Delta x}{\Delta x}\right)^2 + \left(\frac{\delta\theta_2^2}{1-\frac{\theta_2^2}{2}}\right)^2}. \tag{D.85}$$

- Uncertainty on the time interval:

  The error on the time interval is due to two parameters [66]:

  – the delay of the synchronizer, approximately of 1 ns,

  – the pulse timing accuracy of the lasers (timing jitter) which is smaller than 0.5 ns [102].

The systematic error was computed based on the analysis presented above and from the parameters and error values presented in Tables D.1 and D.2. The results obtained are presented in Table D.3.

| | w/o wind turbine | | w/ wind turbine | |
|---|---|---|---|---|
| Parameters | $U_{hub}$ = 5.06 m/s | $U_{hub}$ = 8.02 m/s | $U_{hub}$ = 4.27 m/s | $U_{hub}$ = 7.10 m/s |
| $L_{mm}$ [mm] | 915.74 | 915.74 | 915.74 | 915.74 |
| $L_{px}$ [pixel] | 2528 | 2528 | 2528 | 2528 |
| $M$ [mm/pixel] | 0.362239 | 0.362239 | 0.362239 | 0.362239 |
| $d$ [pixel] | 8 | 8 | 8 | 8 |
| $\Delta t$ [s] | $700 \cdot 10^{-6}$ | $380 \cdot 10^{-6}$ | $800 \cdot 10^{-6}$ | $530 \cdot 10^{-6}$ |
| $\theta_1$ [°] | 0 | 0 | 0 | 0 |
| $\theta_2$ [°] | 0 | 0 | 0 | 0 |

***Table D.1:*** *Parameters used to compute the systematic error*

| Errors | |
|---|---|
| $\delta L_{mm}$ [mm] | 1 |
| $\delta L_{px}$ [pixel] | 1 |
| $\delta\Delta x$ [pixel] | 0.1 |
| $\delta\Delta t$ [s] | $1 \cdot 10^{-9}$ |
| $\delta\theta_1$ [°] | 2 |
| $\delta\theta_2$ [°] | 2 |

***Table D.2:*** *Errors used to compute the systematic error*

| | w/o wind turbine | | w/ wind turbine | |
|---|---|---|---|---|
| Relative error | $U_{hub} = 5.06$ m/s | $U_{hub} = 8.02$ m/s | $U_{hub} = 4.27$ m/s | $U_{hub} = 7.10$ m/s |
| $\delta M/M$ [%] | 0.17 | 0.17 | 0.17 | 0.17 |
| $\delta d/d$ [%] | 1.26 | 1.26 | 1.26 | 1.26 |
| $\delta \Delta t/\Delta t$ [%] | 0.0002 | 0.0003 | 0.0001 | 0.0002 |
| $\epsilon_{bias} = \delta u/u$ [%] | 1.27 | 1.27 | 1.27 | 1.27 |

***Table D.3:*** *Systematic error*

### D.7.2 Random error

The random error occurs because there are a very large number of parameters beyond the control of the experiment that may interfere with the results of the experiment. This error is linked to the physics of the flow and to the characteristics of the phenomena. The expression of the random error is

$$\epsilon_{rnd} = \frac{z_\alpha I}{\sqrt{N}} \tag{D.86}$$

where $z_\alpha$ is the coefficient depending on the confidence interval, $I$ the turbulence intensity ($I = \frac{\sigma_u}{U_{hub}}$), and $N$ the total number of samples, i.e. the number of pair images. Eq. (D.86) highlights the fact the random error can be reduced by increasing the number of samples, i.e. the number of pair images.

Considering a confidence interval of 95% ($z_\alpha = 1.96$) and 1000 samples, the random error (Table D.4) was computed considering the turbulence intensities specified in Table D.4.

| | ABL1 | | ABL2 | |
|---|---|---|---|---|
| Parameters / Relative error | $U_{hub} = 5.06$ m/s | $U_{hub} = 8.02$ m/s | $U_{hub} = 4.27$ m/s | $U_{hub} = 7.10$ m/s |
| $I$ | 0.12 | 0.109 | 0.058 | 0.054 |
| $\epsilon_{rnd}$ [%] | 0.74 | 0.68 | 0.36 | 0.33 |

***Table D.4:*** *Random error*

### D.7.3 Uncertainty on the measurements

The uncertainty on the measurements, which is due to a bias error and the random error (Eq. (D.76)) is presented in Table D.5.

| | ABL1 | | ABL2 | |
|---|---|---|---|---|
| Relative error | $U_{hub} = 5.06$ m/s | $U_{hub} = 8.02$ m/s | $U_{hub} = 4.27$ m/s | $U_{hub} = 7.10$ m/s |
| $\epsilon_{bias}$ [%] | 1.27 | 1.27 | 1.27 | 1.27 |
| $\epsilon_{rnd}$ [%] | 0.74 | 0.68 | 0.36 | 0.33 |
| $\epsilon_{tot}$ [%] | 1.47 | 1.44 | 1.32 | 1.31 |

***Table D.5:*** *Uncertainty on the PIV measurements considering a confidence level of* 95%

## D.8 Uncertainty analysis for 3C-HWA

As for the PIV uncertainty analysis (Appendix D.7), the uncertainty is considered to be due to a systematic error or bias error ($\epsilon_{bias}$) and a random error ($\epsilon_{rnd}$). The uncertainty on the measurements is therefore defined as

$$\epsilon_{tot} = \sqrt{\epsilon_{bias}^2 + \epsilon_{rnd}^2}. \tag{D.87}$$

### D.8.1 Systematic error or bias error

For the calculation of the bias error of the hot wire anemometer, the calibration procedure is taken into account. As stated previously, the hot-wire probe is placed in the core of a nozzle of which velocity is calculated from the difference between the ambient pressure and the pressure in the settling chamber using the Bernoulli's equation

$$U = \sqrt{\frac{2\,\Delta p}{\rho}} \tag{D.88}$$

where $\Delta p$ is the pressure difference between the settling chamber of the nozzle and the ambient pressure. Therefore, applying the classical error analysis leads to

$$\delta U = \sqrt{\left(\frac{\partial U}{\partial \Delta p}\delta\Delta p\right)^2 + \left(\frac{\partial U}{\partial \rho}\delta\rho\right)^2}. \tag{D.89}$$

Applying the partial derivatives, Eq. (D.89) becomes

$$\frac{\delta U}{U} = \sqrt{\left(\frac{\delta\Delta p}{2\,\Delta p}\right)^2 + \left(\frac{\delta\rho}{2\,\rho}\right)^2} \tag{D.90}$$

- Uncertainty on the dynamic pressure:

  The uncertainty on the dynamic pressure can be computed as (see Appendix D.1 for the detailed analysis)

$$\delta\Delta p = \sqrt{\delta\Delta p_{device}^2 + \delta\Delta p_{reading}^2} \tag{D.91}$$

$$\delta\Delta p = \sqrt{\left(m_{PS}\cdot\frac{1.5}{100}\cdot FSO\right)^2 + \left(0.980665\right)^2} \tag{D.92}$$

$$\delta\Delta p = \sqrt{\left(51.668\cdot\frac{1.5}{100}\cdot 1.890\right)^2 + \left(0.980665\right)^2} \tag{D.93}$$

$$\delta\Delta p = 1.763 \text{ Pa} \tag{D.94}$$

  where $m_{PS}$ is the slope obtained from the calibration of the pressure sensor and $FSO$ is the Full Span Output, i.e. the algebraic difference between the output signal at the minimum pressure and the output signal at the maximum pressure used during the experiments.

- Uncertainty on the density:

  Considering the perfect gas law, the uncertainty on the density can be computed as (see Appendix D.1 for the detailed analysis)

$$\frac{\delta\rho}{\rho} = \sqrt{\left(\frac{\delta p}{p}\right)^2 + \left(\frac{\delta T}{T}\right)^2} \tag{D.95}$$

  where

  – $\delta p$ is the error on the barometric pressure of the *Druck DPI 150 Precision Pressure Indicator* of the von Karman institute: $\Delta p = 0.15$ mbar = 15 Pa;

  – $\delta T$ is the error on the temperature of the weather station used: $\Delta T = 1$ K.

  This yields to $\frac{\delta p}{p} = \frac{15}{100610} = 0.015\%$ and $\frac{\delta T}{T} = \frac{1}{294.15} = 0.34\%$.

Since the dynamic pressure $\Delta p$ depends on the velocity, the error is function of the velocity and can be expressed as

$$\frac{\delta U}{U} = \sqrt{\left(\frac{1}{2}\frac{1.645736}{U^2}\right)^2 + \left(\frac{1}{2}0.169981\right)^2 + \left(\frac{1}{2}0.000149\right)^2}. \tag{D.96}$$

Finally, the error due to the fitting by a fourth order polynomial has to be added. It is estimated with the RMSE (Root Mean Square Error) of the fitting, equals to 1.05% in this case. Table D.6 sums up the different contribution to the bias error while Figure D.4 represents the evolution of the bias error with the velocity.

| | ABL1 | | ABL2 |
|---|---|---|---|
| Relative error | $U_{hub} = 5.49$ m/s | $U_{hub} = 8.68$ m/s | $U_{hub} = 7.53$ m/s |
| $0.5 \cdot \delta\Delta p/\Delta p$ [%] | 4.907 | 1.963 | 2.609 |
| $0.5 \cdot \delta T/T$ [%] | 0.170 | 0.170 | 0.170 |
| $0.5 \cdot \delta p/p$ [%] | 0.007 | 0.007 | 0.007 |
| $\epsilon_{fit}$ [%] | 1.048 | 1.048 | 1.048 |
| $\epsilon_{bias}$ [%] | 7.02 | 2.98 | 3.84 |

***Table D.6:*** *Systematic error*

## D.8.2 Random error

Due to the high acquisition frequency of the HWA, a large number of samples are available to compute average quantities. However, the statistical average is based on the mean of independent samples. As stated in [60], to be statistically independent, two measurements must be separated by at least two characteristic times $T$ (integral time scale) of the flow. The number of independent sample during the observation time is therefore $N = T_{obs}/(2 \cdot T_{hub}) = 120/(2 \cdot 0.06) = 1000$ for ABL1 and $N = T_{obs}/(2 \cdot T_{hub}) = 120/(2 \cdot 0.03) = 2000$ for. ABL2. The random error, computed in the same manner as for the PIV random error using Eq. (D.86), is presented in Table D.7.

## D.8.3 Uncertainty on the measurements

The global uncertainty on the measurements, which is due to the bias error and the random error is presented in Table D.8.

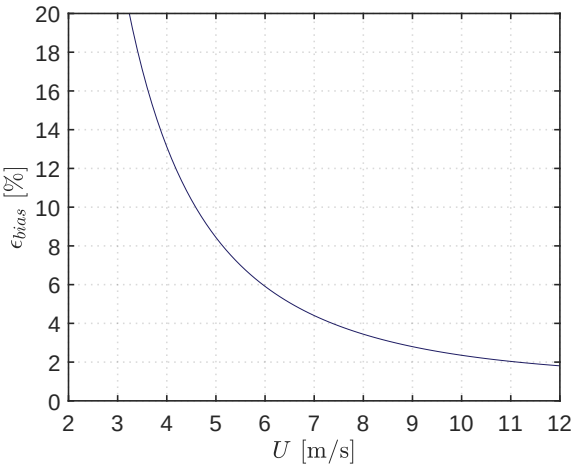



***Figure D.4:*** *Bias error in function of the velocity*

| | ABL1 | | ABL2 |
|---|---|---|---|
| Parameters / Relative error | $U_{hub}$ = 5.49 m/s | $U_{hub}$ = 8.68 m/s | $U_{hub}$ = 7.53 m/s |
| $I$ | 0.126 | 0.124 | 0.046 |
| $N$ | 1000 | 1000 | 2000 |
| $\epsilon_{rnd}$ [%] | 0.78 | 0.77 | 0.20 |

***Table D.7:*** *Random error*

| | ABL1 | | ABL2 |
|---|---|---|---|
| Relative error | $U_{hub}$ = 5.49 m/s | $U_{hub}$ = 8.68 m/s | $U_{hub}$ = 7.53 m/s |
| $\epsilon_{bias}$ [%] | 7.02 | 2.98 | 3.84 |
| $\epsilon_{rnd}$ [%] | 0.78 | 0.77 | 0.20 |
| $\epsilon_{tot}$ [%] | 7.07 | 3.07 | 3.85 |

***Table D.8:*** *Uncertainty on the HWA measurements considering a confidence level of* 95%

APPENDIX E

# Faulhaber generator

## E.1 Evolution of electrical and mechanical quantities

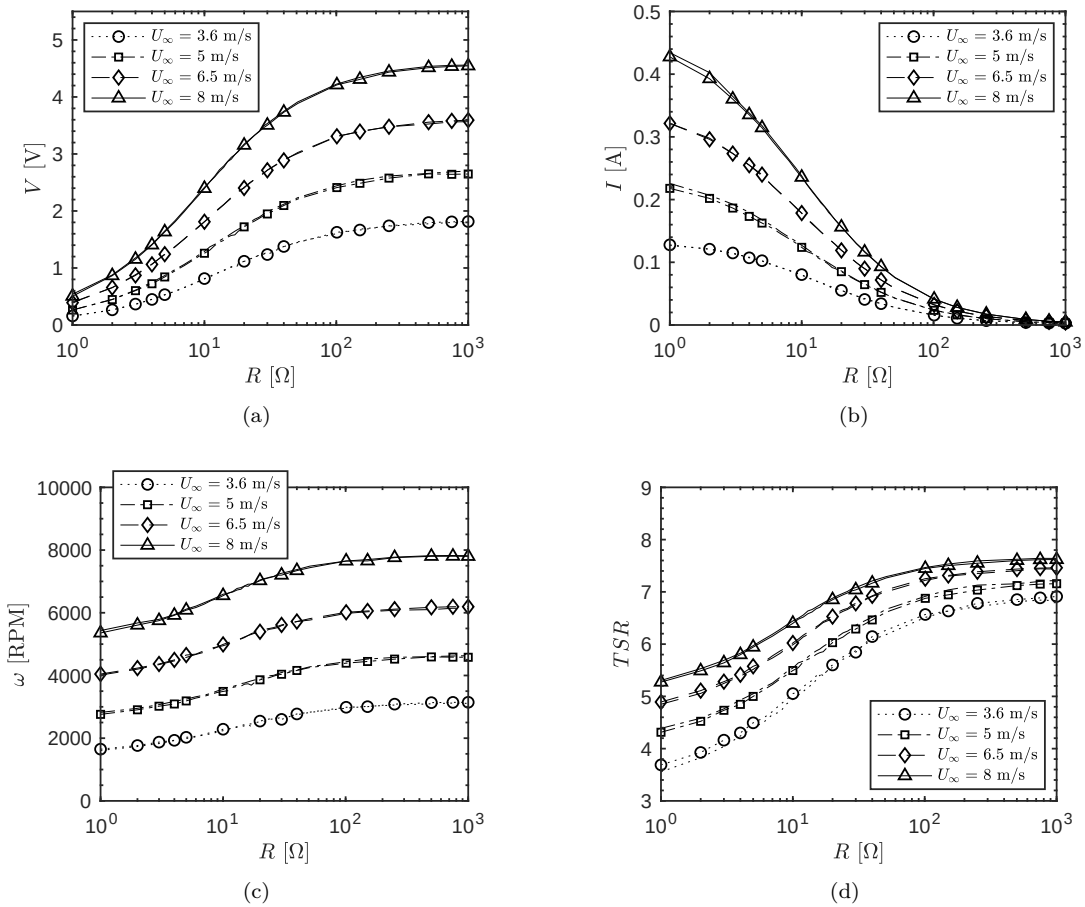



***Figure E.1:*** *Evolution of the voltage (a), current (b), rotational speed (c), and tip-speed ratio (d) as a function of the resistive load applied to the generator*

## E.2 Calibration of the balance for the thrust measurements

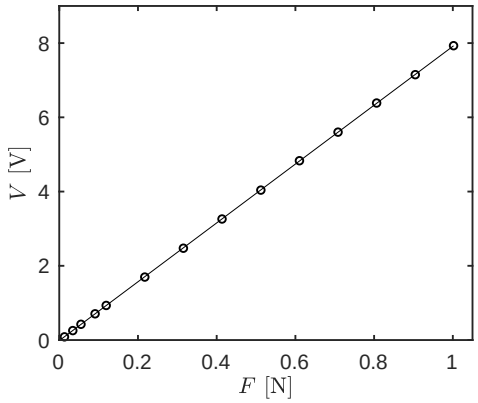
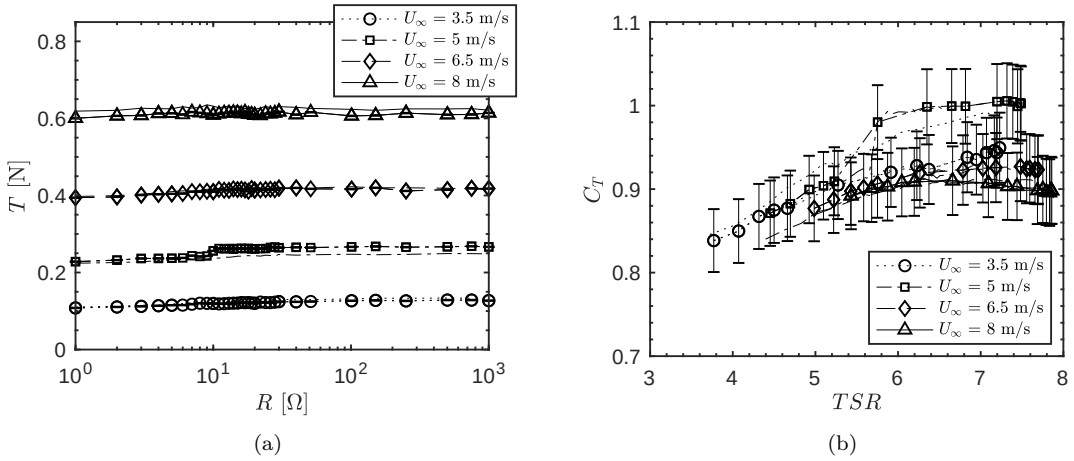



***Figure E.2:*** *Evolution of the voltage ($V$) output as a function of the force ($F$) applied on the wind turbine tower, $R^2 = 0.999994$*

## E.3 Uncertainty on the thrust




(a) (b)

***Figure E.3:*** *Evolution, with uncertainties, of the thrust as a function of the resistive load applied to the generator (a) and evolution of the thrust coefficient as a function of the tip-speed ratio (b)*

APPENDIX F

# Wind turbine characteristics with 118516 Maxon generator

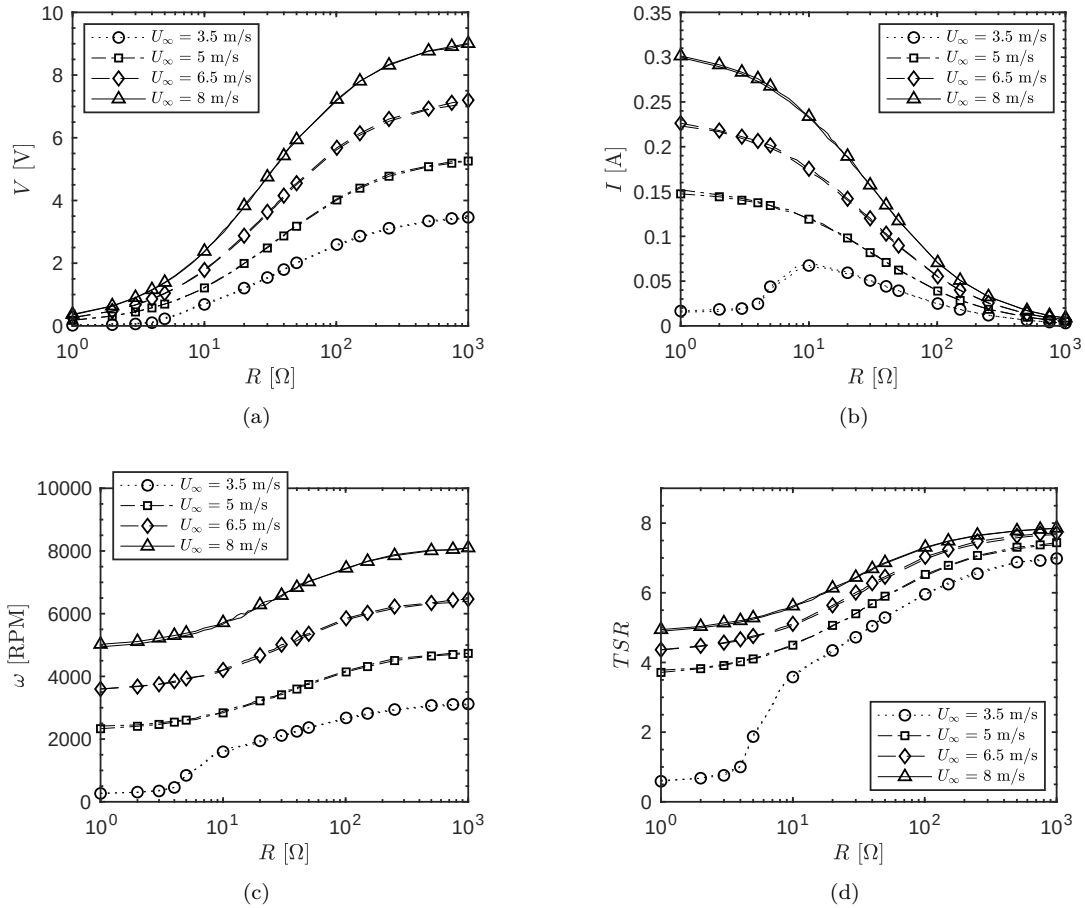



***Figure F.1:*** *Evolution of the voltage (a), current (b), rotational speed (c), and tip-speed ratio (d) as a function of the resistive load applied to the generator*

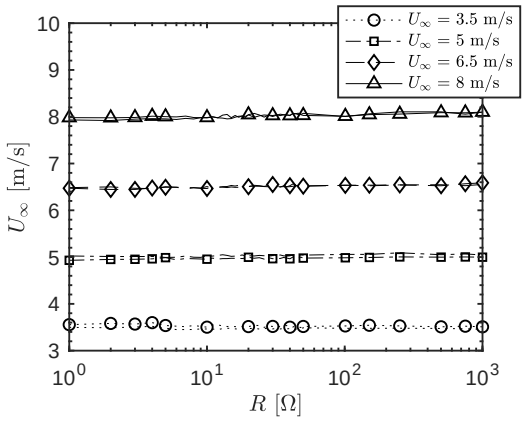
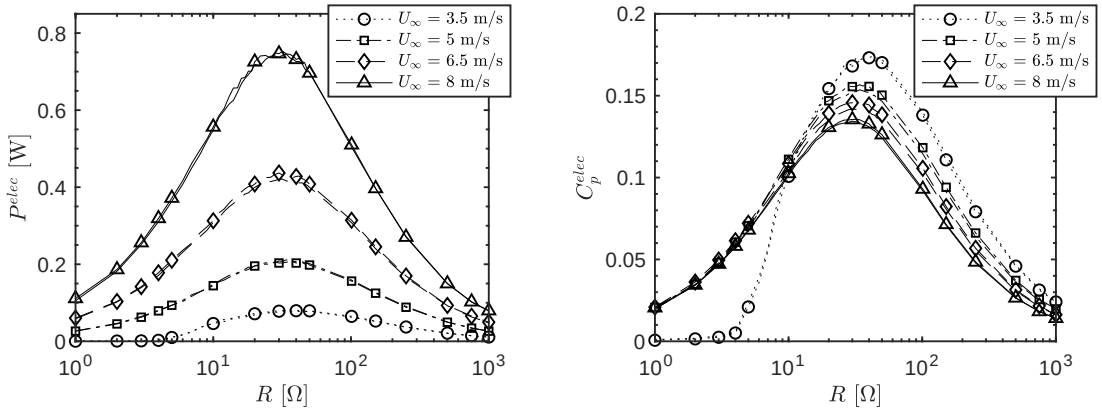
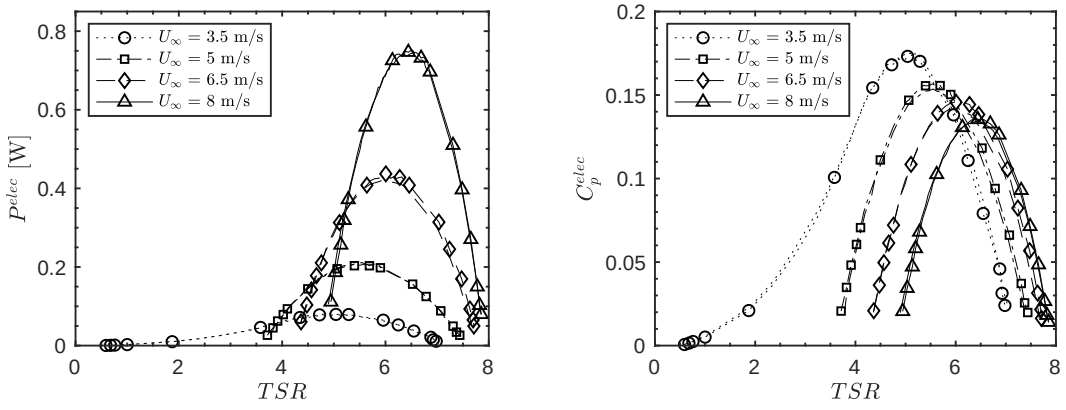



***Figure F.2:*** *Evolution of the wind speed as a function of the resistive load applied to the generator*




(a) (b)

***Figure F.3:*** *Evolution of the power (a) and power coefficient (b) as a function of the resistive load applied to the generator*




(a) (b)

***Figure F.4:*** *Evolution of the power (a) and power coefficient (b) as a function of the tip-speed ratio*

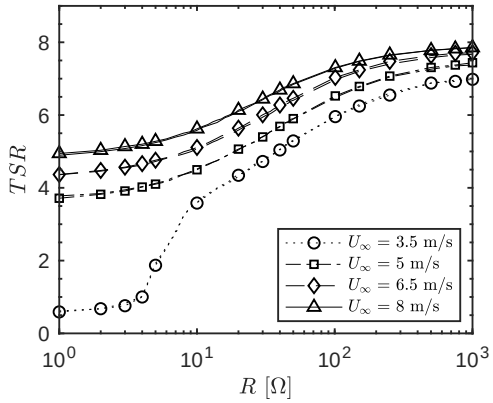



***Figure F.5:*** *Evolution of the tip-speed ratio as a function of the resistive load applied to the generator*

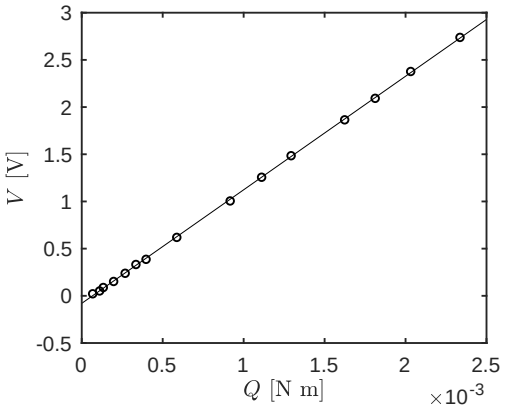
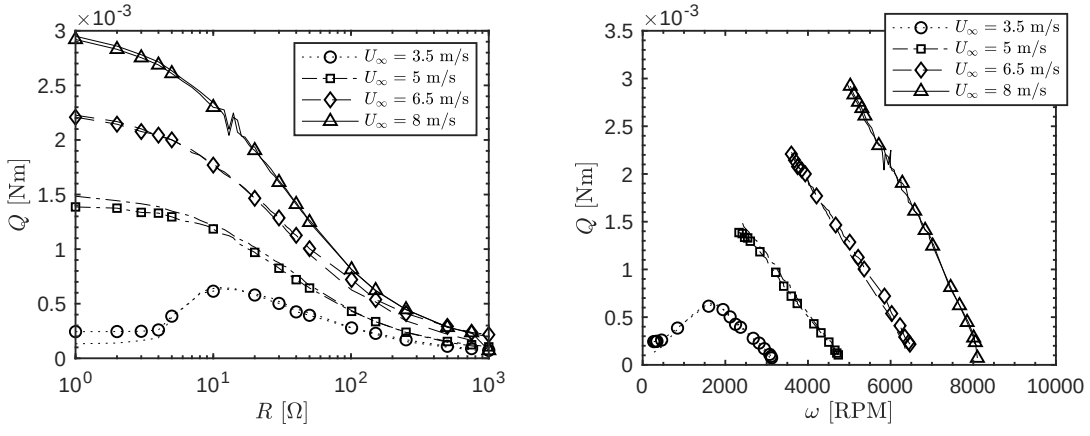
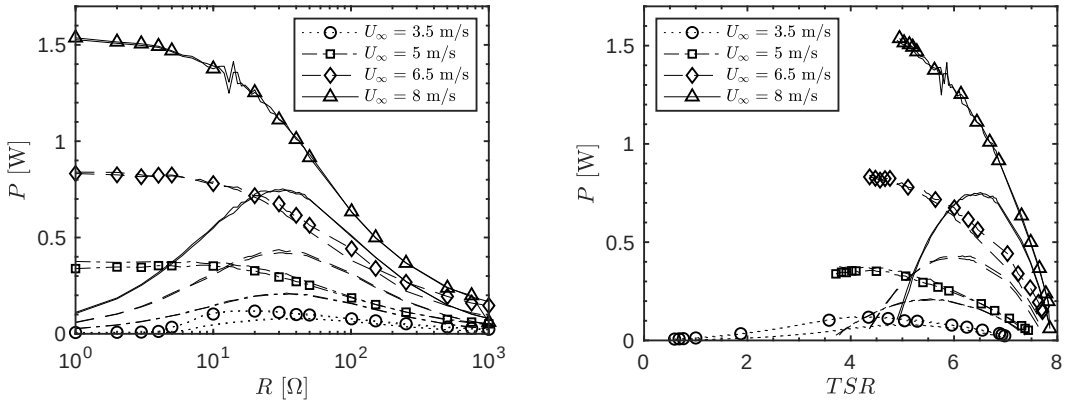



***Figure F.6:*** *Evolution of the voltage ($V$) output as a function of the torque ($Q$) applied*



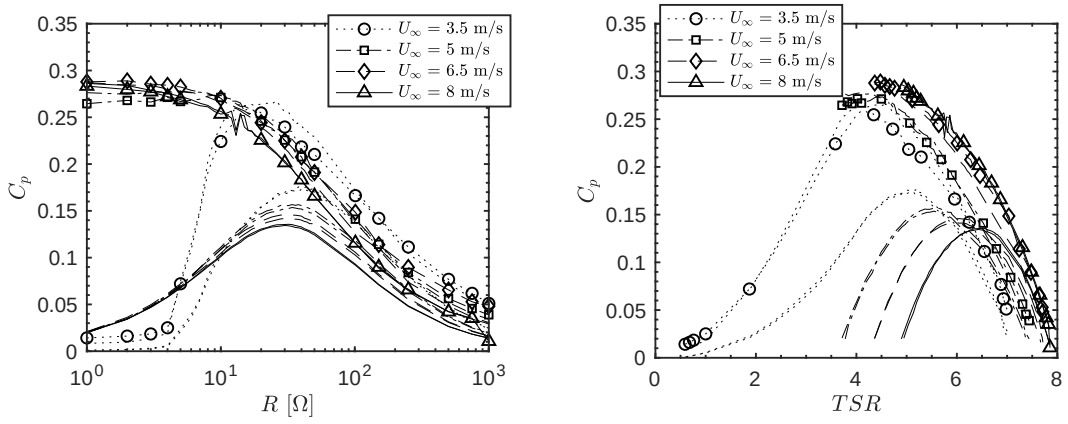

(a) (b)

***Figure F.7:*** *Evolution of the mechanical torque as a function of resistance (a) and rotational speed (b)*



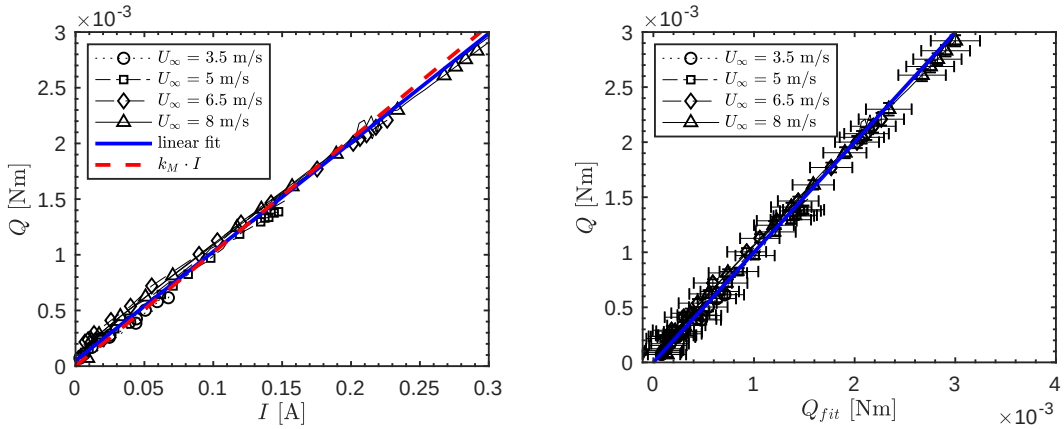

(a) (b)

***Figure F.8:*** *Evolution of the electrical power (dashed line with symbol) and mechanical power (solid line with symbol) as a function of resistance (a); evolution of the electrical power coefficient (dashed line with symbol) and mechanical power coefficient (solid line with symbol) as a function of resistance (b)*



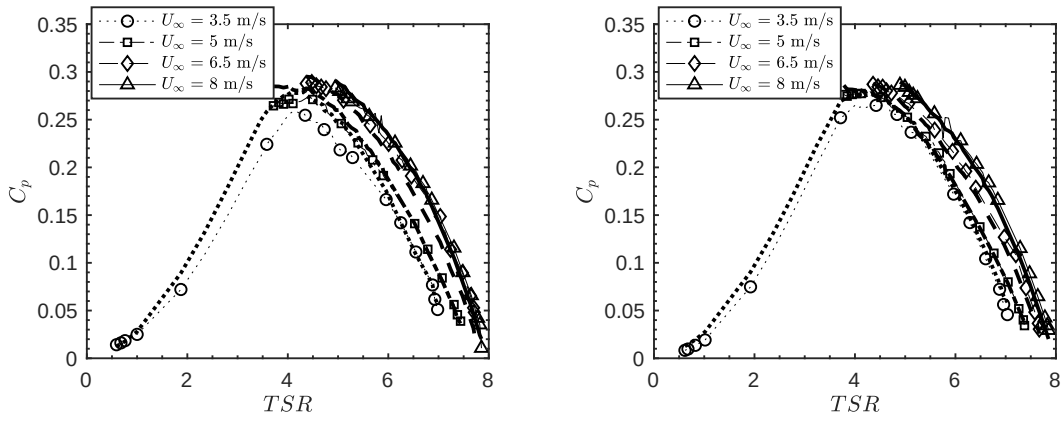

(a) (b)

***Figure F.9:*** *Evolution of the electrical power coefficient (dashed line with symbol) and mechanical power coefficient (solid line with symbol) as a function of R and TSR*



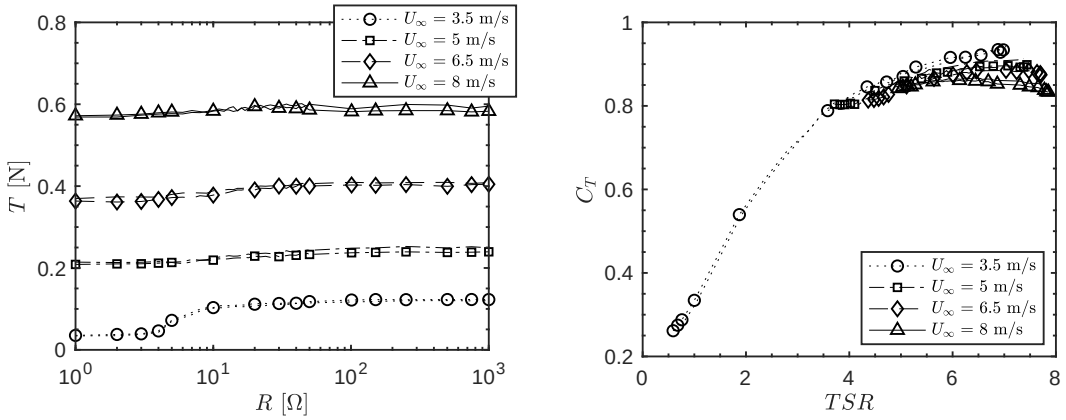

(a) (b)

***Figure F.10:*** *Mechanical torque as a function of the current (a), the solid line shows the linear curve fit,* $Q = 0.0489 \cdot 10^{-3} + 9.7954 \cdot 10^{-3}\, I$*; torque measured with the torque sensor system as a function of the torque computed from the current using the linear curve fit (b)*




(a) (b)

***Figure F.11:*** *Evolution, as a function of the tip-speed ratio, of the mechanical power coefficient obtained by computing the torque from the current using Eq. (5.4) (thick line), and of the mechanical power coefficient obtained from the measured torque and the rotational speed (line with symbols) for the first (a) and the second (b) measurement campaigns*




(a) (b)

***Figure F.12:*** *Evolution of the thrust as a function of the resistive load applied to the generator (a) and evolution of the thrust coefficient as a function of the tip-speed ratio (b)*

Appendix G

# Aerodynamic coefficients of wind turbine airfoil

## G.1 Drawings

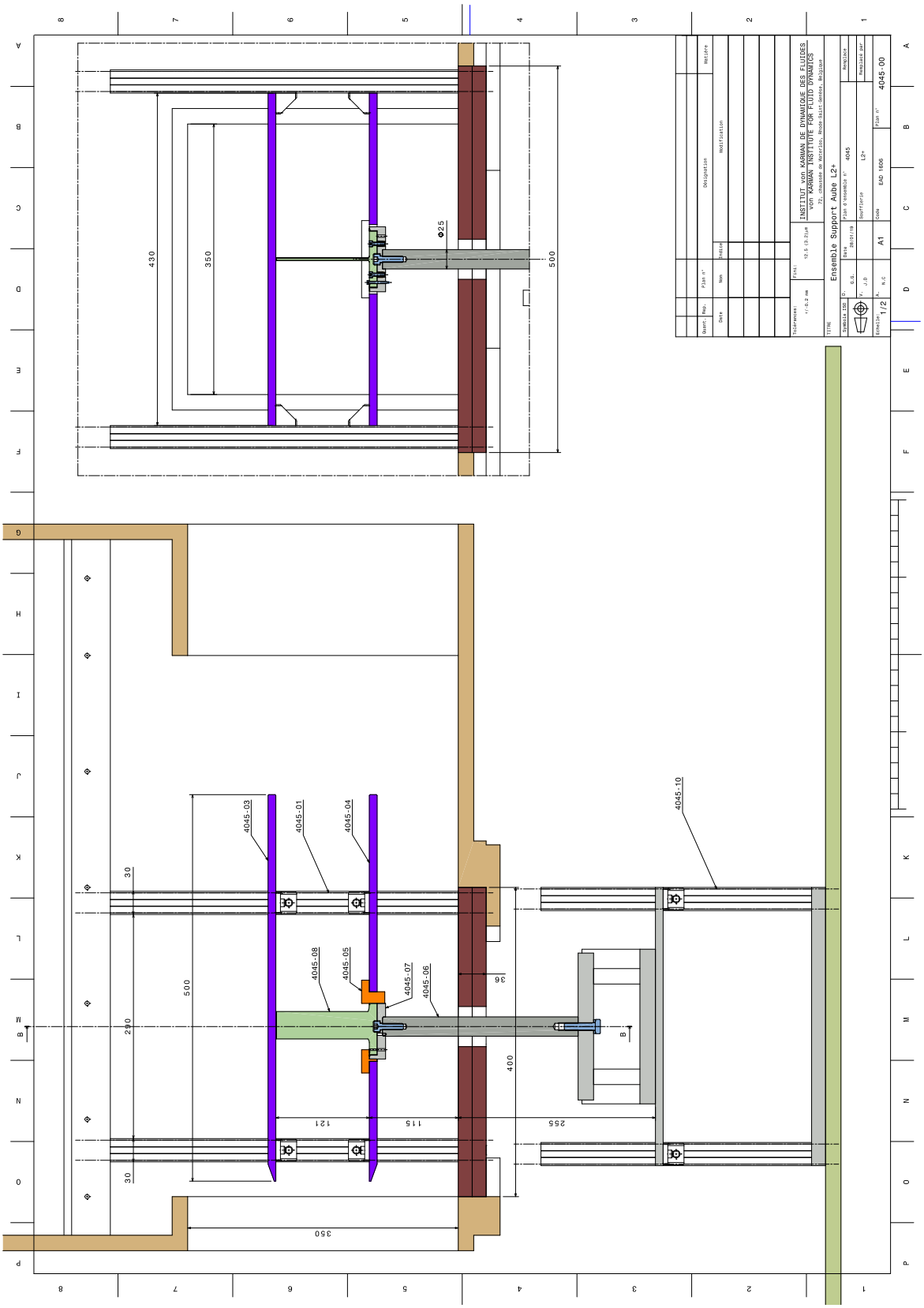



***Figure G.1:*** *Drawing of the experimental setup installed in the L-2B wind tunnel for the measurements of the lift and drag coefficients of the airfoil with the single component balance*

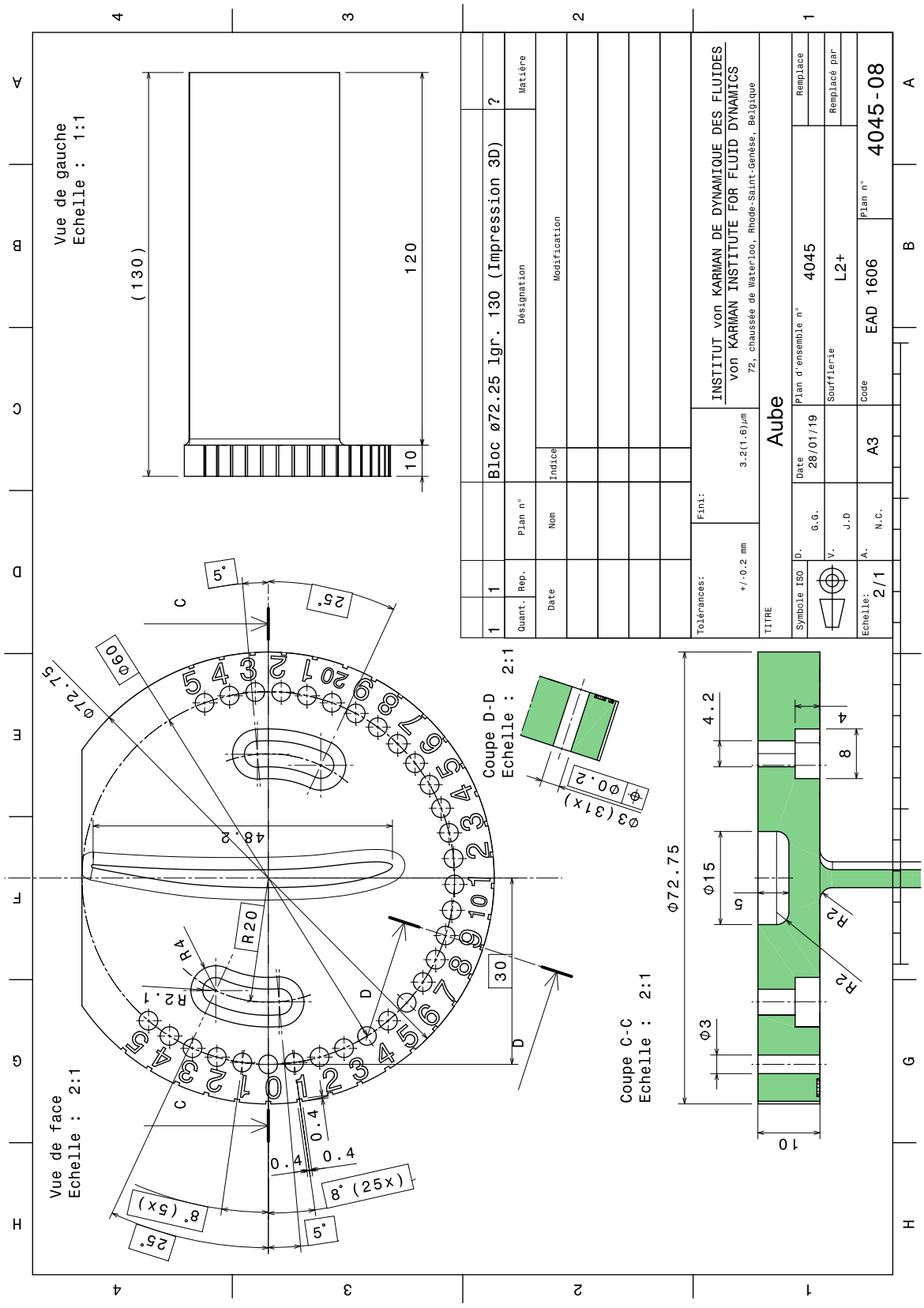



***Figure G.2:*** *Drawing of the component used to vary the angle of attack of the airfoil for the measurements of the lift and drag coefficients*

## G.2 Calibrations

### G.2.1 Balance

Typical calibration curves of the balance for lift and drag measurements are presented in Fig. G.3. The balance was calibrated in traction-compression for the lift measurements and only in compression for the drag measurements.

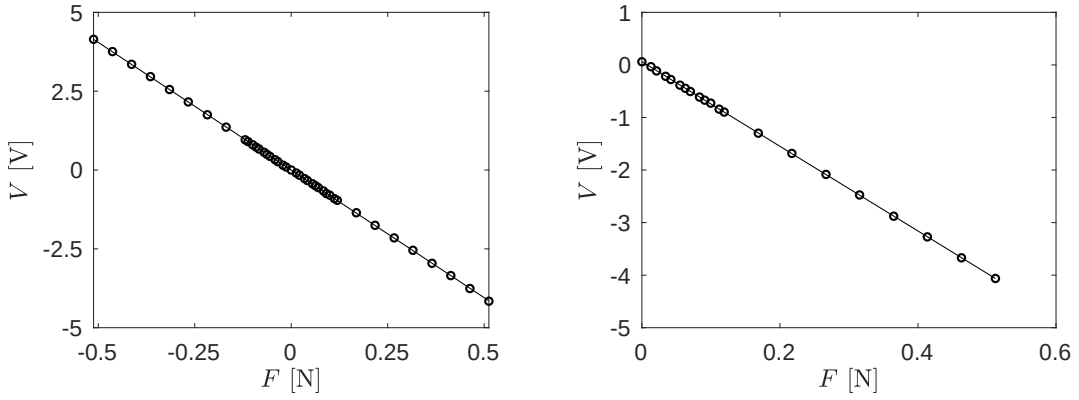



***Figure G.3:*** *Typical calibration curve of the balance for lift (a) and and drag (b) measurements;* $R^2 = 0.999977$ *and* $R^2 = 0.999986$*, respectively*

### G.2.2 Pitot static

Typical calibration curves of the pressure sensor used for flow speed measurements with a Pitot-static probes located between the end plates and upstream in the wind tunnel are presented in Fig. G.4.

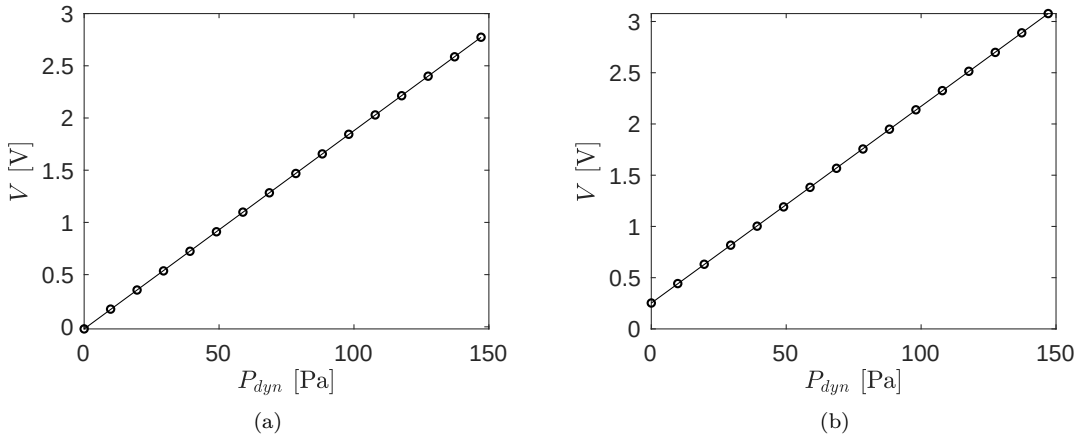



***Figure G.4:*** *Calibration curve of the pressure sensor used to measure the flow speed between the end plates (a) and upstream in the wind tunnel (b);* $R^2 = 0.999997$ *and* $R^2 = 0.999995$*, respectively*

In order to correct the flow speed by taking into account the acceleration of the flow between the end plates, a calibration linking the pressure measured by a Pitot-static probe positioned at the airfoil location and a Pitot-static probe located upstream of the test section was performed prior to the campaigns. Figure G.5 shows the calibration curves in terms of dynamic pressure and flow speed.

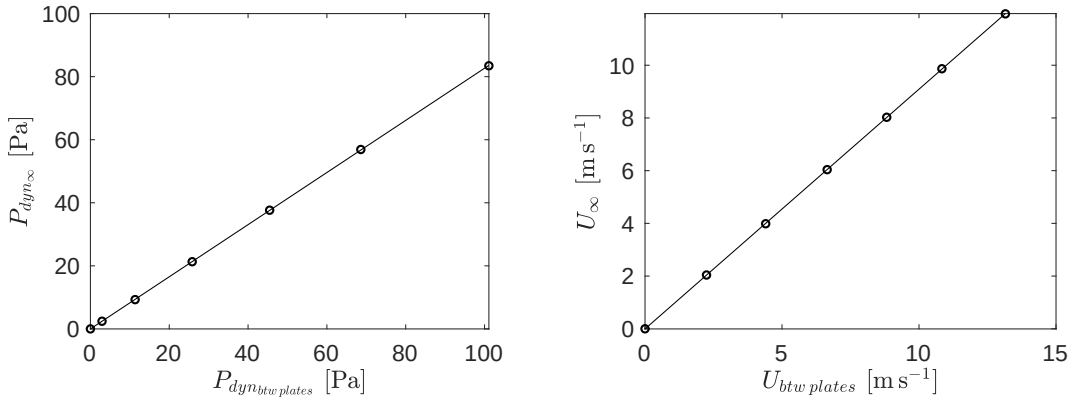



***Figure G.5:*** *Link between the dynamic pressure (a) and the flow speed (a) obtained from the two Pitot-static probes;* $R^2 = 0.999990$ *and* $R^2 = 0.999994$*, respectively*

## G.3 Results

The aerodynamics coefficients of the airfoil were measured in L-2B wind tunnel for 5 inflow velocities corresponding to $Re_c = U_\infty\, c/\nu = 15000, 20000, 25000, 30000, 35000$ and for angles of attack going from $-5^\circ$ to $25^\circ$ by step of $1^\circ$. The results of three campaigns of experiments, conducted to verify the repeatability of the measurements, are presented in Fig. G.6 and the uncertainties associated with these measurements in Fig. G.7 .

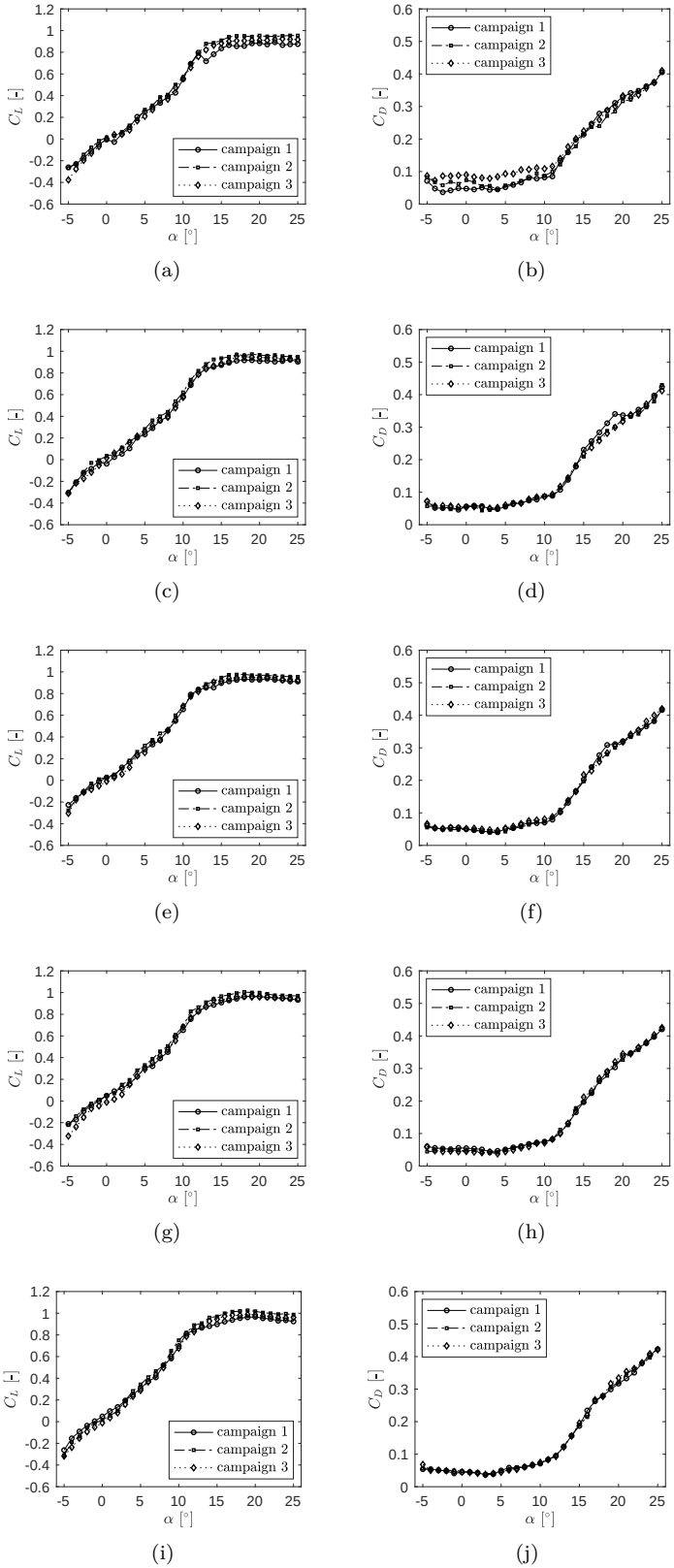



***Figure G.6:*** *Evolution of the lift (a)-(c)-(e)-(g)-(i) and drag (b)-(d)-(f)-(h)-(j) coefficients as a function of the angle of attack for* $Re_c = 15000$ *(a)-(b),* $Re_c = 20000$ *(c)-(d),* $Re_c = 25000$ *(e)-(f),* $Re_c = 30000$ *(g)-(h),* $Re_c = 35000$ *(i)-(j)*

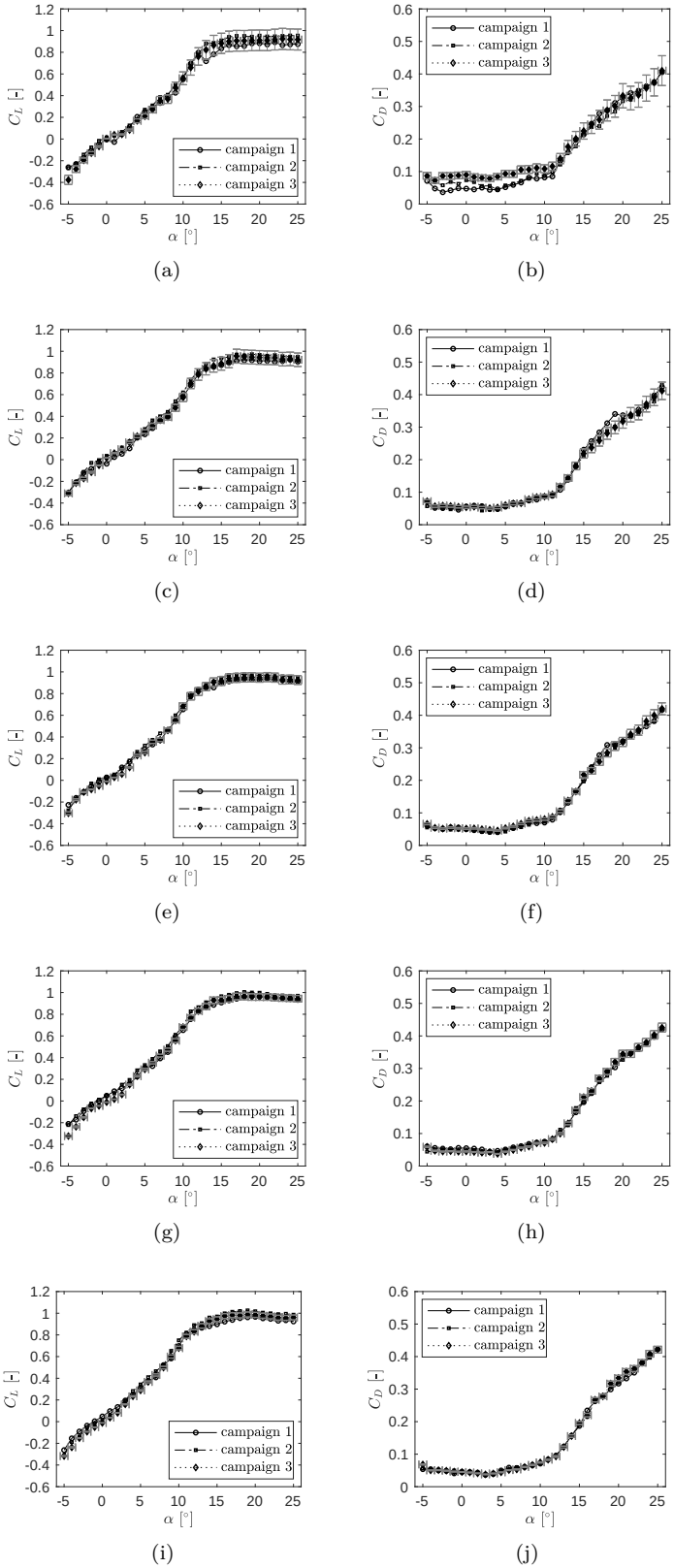



***Figure G.7:*** *Evolution of the lift (a)-(c)-(e)-(g)-(i) and drag (b)-(d)-(f)-(h)-(j) coefficients as a function of the angle of attack for* $Re_c = 15000$ *(a)-(b),* $Re_c = 20000$ *(c)-(d),* $Re_c = 25000$ *(e)-(f),* $Re_c = 30000$ *(g)-(h),* $Re_c = 35000$ *(i)-(j) with uncertainty bars for campaign 3*

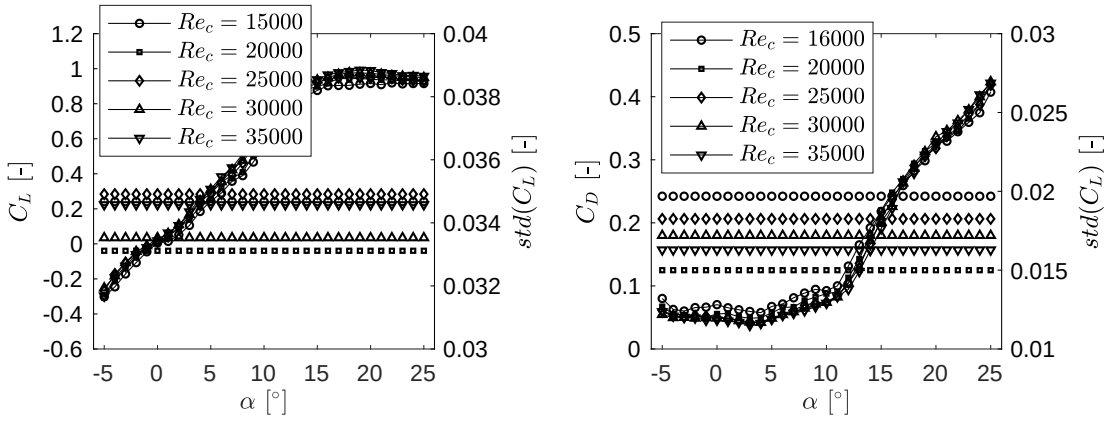



***Figure G.8:*** *Evolution of the lift (a) and drag (b) coefficients and their standard deviation as a function of the angle of attack for* $Re_c = 15000$ *to* $Re_c = 35000$ *by step of* $5000$.

APPENDIX H

# Wind farm power production

Figures H.1 shows the electrical and aerodynamic powers produced by the wind farm in configuration 1 subjected to ABL1 and ABL2 for different operations conditions: $R = 9\Omega$ for the three columns of wind turbines, $R = 3\Omega$ for the first column (WT1 - WT4 - WT7) of wind turbines and $R = 9\Omega$ for the two other columns, $R = 3\Omega$ for the first two columns of wind turbines and $R = 9\Omega$ for the last columns of wind turbines. The electrical power was obtained from the voltage and the current produced by the generator ($P^{elec} = UI$) while the aerodynamic power was obtained from the current using Eq. (5.4). With the view of future studies concerning wind farm optimization, the power production of the upstream turbines was throttled down to study the impact of power mitigation on the global wind farm power production. As it can be observed, the changes in operating conditions of the upstream turbines do not lead to a major increase in electrical power production for the downstream turbines and results therefore in a loss for the global power production $P^{elec}_{WF}$ of the wind farm ($P^{elec}_{WF} = (P^{elec}_{WF_1} + P^{elec}_{WF_2})/2$, where the indices denote the first and second set of data). Nevertheless, this first trial with this setup opens the way towards power optimization for wind farms in the VKI L-1B wind tunnel. Considering the aerodynamic power ($P^{aero}_{WF}$), the changes in the electrical resistances of the upstream turbines do not correspond to a "mitigation" process since they result in an increase in aerodynamic power for the upstream turbines. The power production of the wind farm thus increases. To study the impact of aerodynamic power mitigation of the first turbines, all turbines should have been loaded with $R = 3\Omega$, and then the loads of the upstream turbines should have been changed to $R = 9\Omega$.

Figure H.2 and H.3 show the electrical and aerodynamic powers produced by the wind farm in configuration 2 and configuration 3 subjected to ABL1 and ABL2 for different operating conditions. The conclusions for these two configurations are identical than for configuration 1. Furthermore, it is interesting to note that the increase in power production observed previously for the second wind turbine of the central row of the wind farm in configuration 3 subjected to ABL1 is also visible for the lateral rows (Fig. H.3(a)).

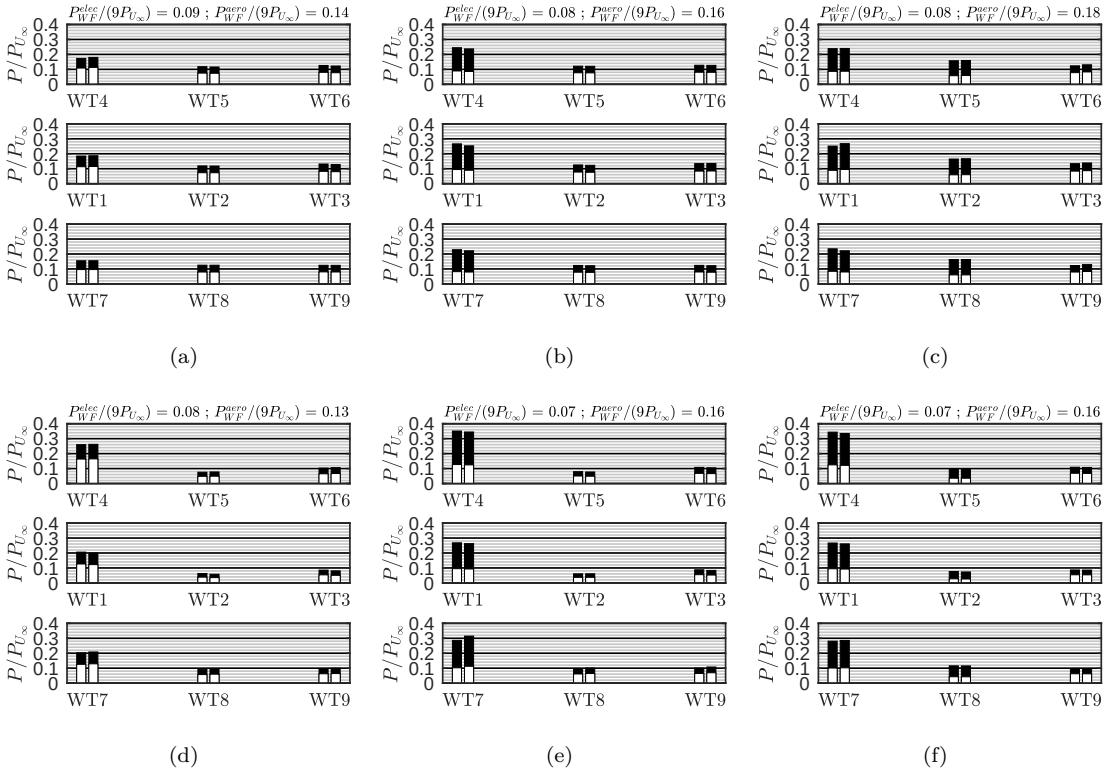



***Figure H.1:*** *Electrical (empty bar) and aerodynamic (entire bar) power produced by the wind farm in configuration 1 subjected to ABL1 (a)-(b)-(c) and ABL2 (d)-(e)-(f) for different operations conditions: $R = 9\Omega$ for the three columns of wind turbines (a)-(d), $R = 3\Omega$ for the first column (WT1 - WT4 - WT7) of wind turbines and $R = 9\Omega$ for the two other columns (b)-(e), $R = 3\Omega$ for the first two columns of wind turbines and $R = 9\Omega$ for the last columns of wind turbines (c)-(f); the second bar of each case corresponds to the second set of measurements*

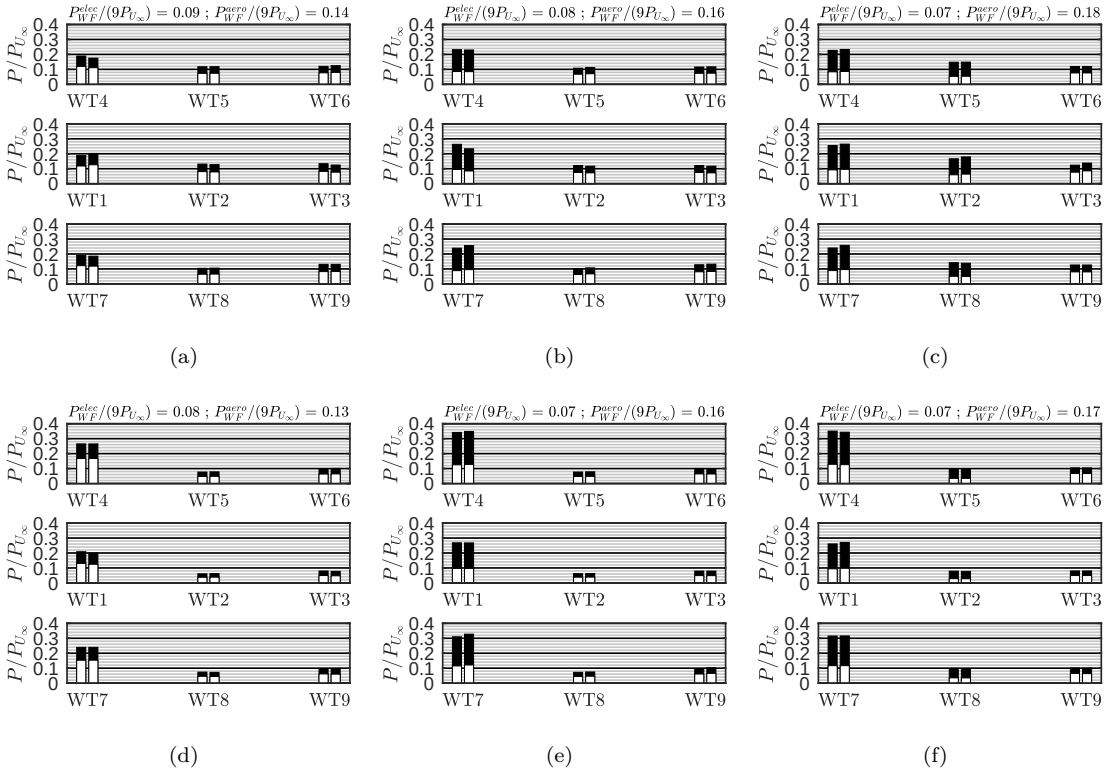



***Figure H.2:*** *Electrical (empty bar) and aerodynamic (entire bar) power produced by the wind farm in configuration 2 subjected to ABL1 (a)-(b)-(c) and ABL2 (d)-(e)-(f) for different operations conditions: $R = 9\Omega$ for the three columns of wind turbines (a)-(d), $R = 3\Omega$ for the first column (WT1 - WT4 - WT7) of wind turbines and $R = 9\Omega$ for the two other columns (b)-(e), $R = 3\Omega$ for the first two columns of wind turbines and $R = 9\Omega$ for the last columns of wind turbines (c)-(f); the second bar of each case corresponds to the second set of measurements*

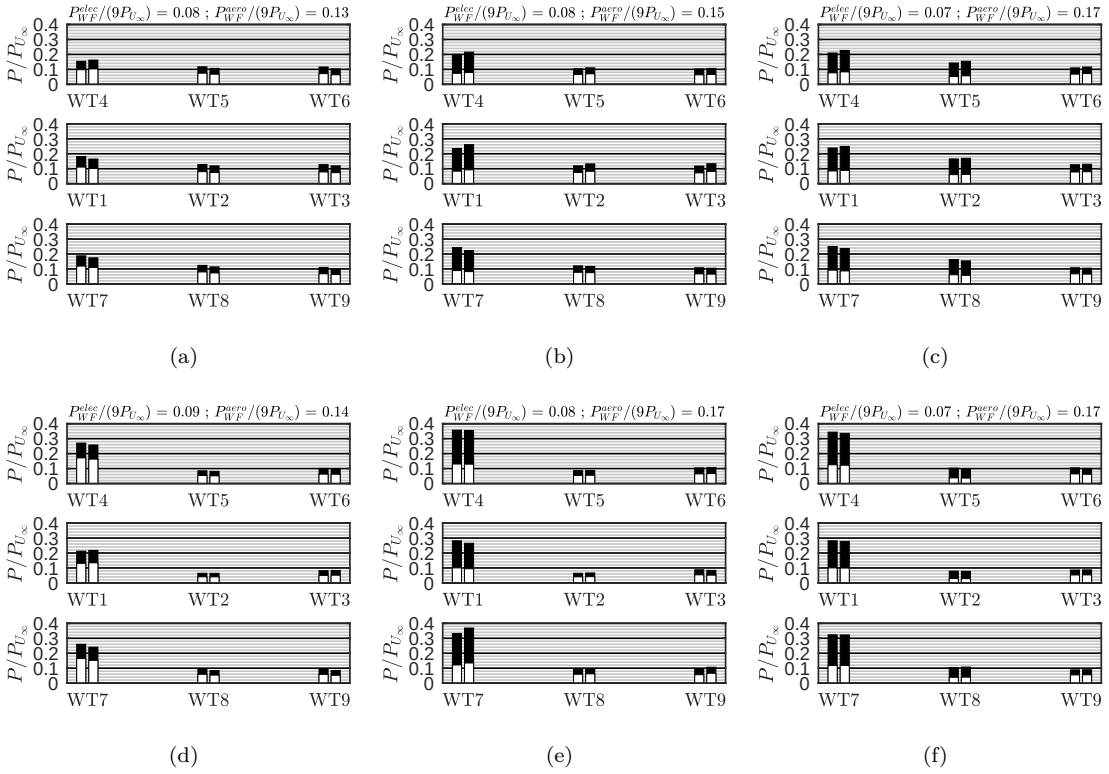



***Figure H.3:*** *Electrical (empty bar) and aerodynamic (entire bar) power produced by the wind farm in configuration 3 subjected to ABL1 (a)-(b)-(c) and ABL2 (d)-(e)-(f) for different operations conditions: $R = 9\Omega$ for the three columns of wind turbines (a)-(d), $R = 3\Omega$ for the first column (WT1 - WT4 - WT7) of wind turbines and $R = 9\Omega$ for the two other columns (b)-(e), $R = 3\Omega$ for the first two columns of wind turbines and $R = 9\Omega$ for the last columns of wind turbines (c)-(f); the second bar of each case corresponds to the second set of measurements*

Appendix I

# Probability distribution of the wake meandering amplitudes and wavelengths

# I.1 Isolated wind turbine

## I.1.1 Influence of Reynolds number

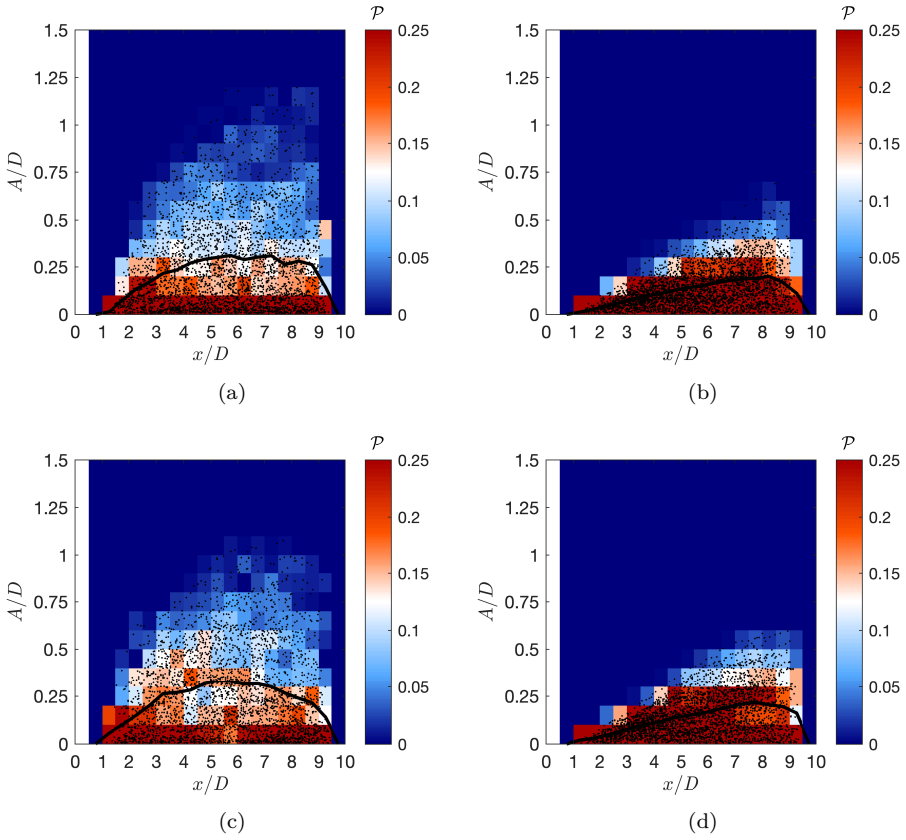



***Figure I.1:*** *Probability distribution of the wake meandering amplitude as a function of the streamwise position at* $Re \approx 8 \cdot 10^4$ *(a)-(b) and* $Re \approx 5 \cdot 10^4$ *(c)-(d) for ABL1 (a)-(c) and ABL2 (b)-(d)*

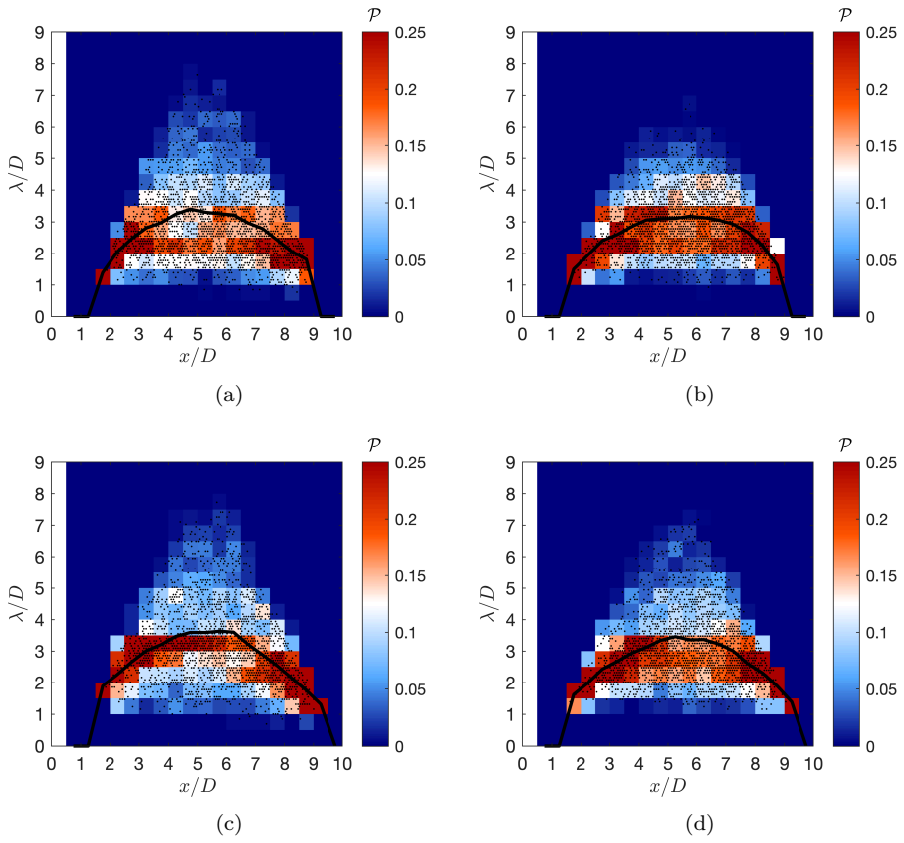



***Figure I.2:*** *Probability distribution of the wake meandering wavelength as a function of the streamwise position at* $Re \approx 8 \cdot 10^4$ *(a)-(b) and* $Re \approx 5 \cdot 10^4$ *(c)-(d) for ABL1 (a)-(c) and ABL2 (b)-(d)*

### I.1.2 Influence of wind turbine operating conditions

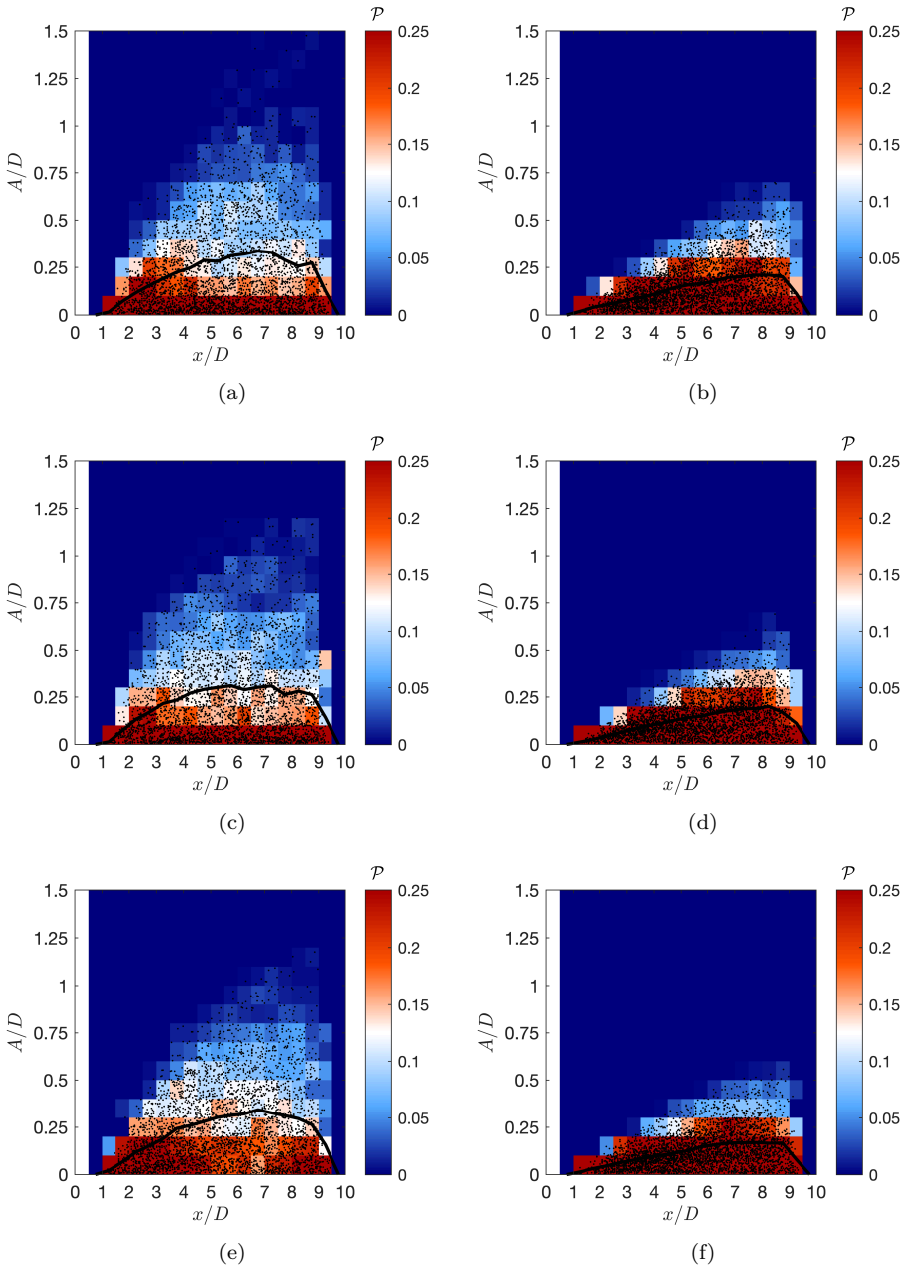



***Figure I.3:*** *Probability distribution of the wake centroid position as a function of space for ABL1 (a)-(c)-(e) and ABL2 (b)-(d)-(f) for different operating conditions: $R = 3\Omega$ (a)-(b), $R = 9\Omega$ (c)-(d), $R = 150\Omega$ (e)-(f)*

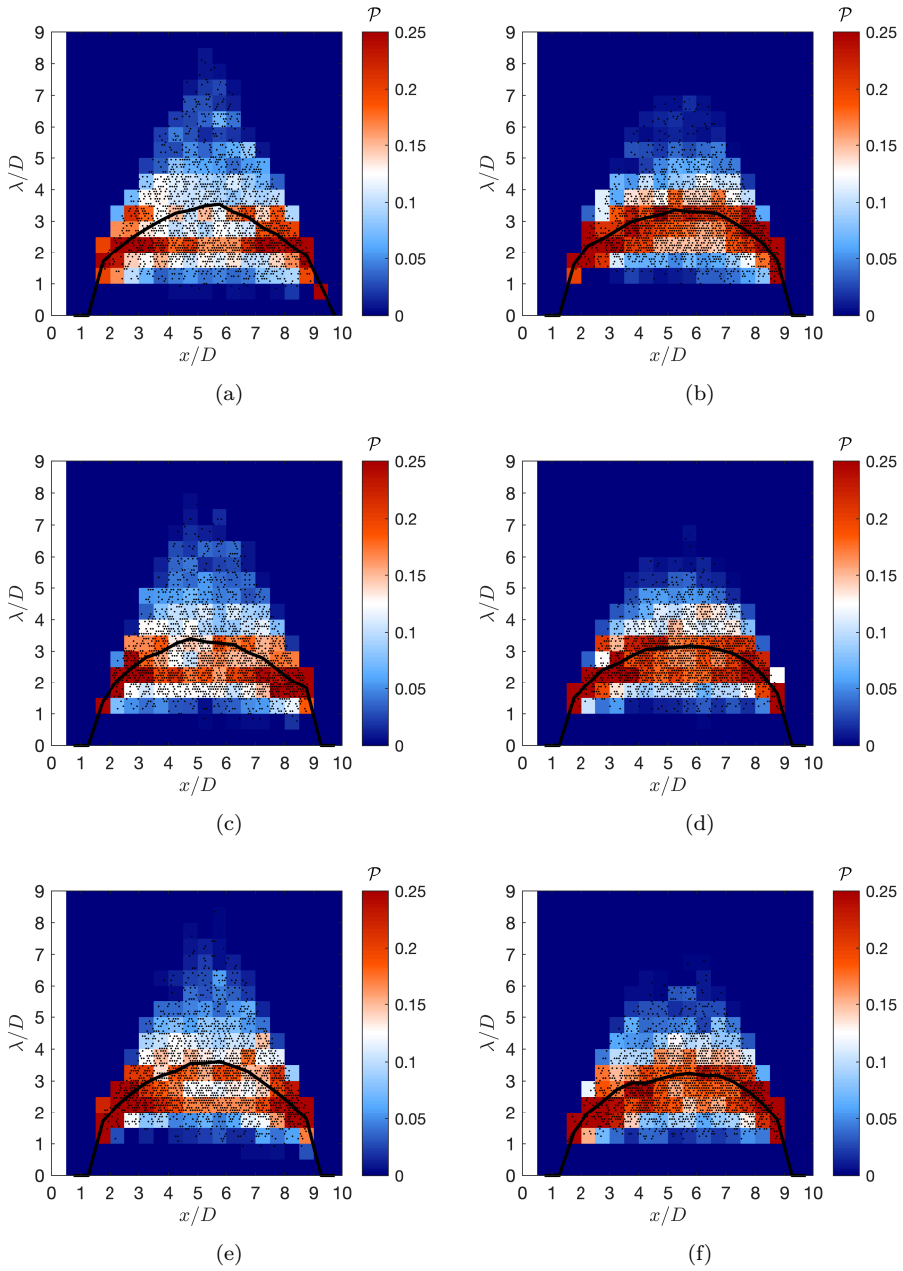



***Figure I.4:*** *Probability distribution of the wake centroid position as a function of space for ABL1 (a)-(c)-(e) and ABL2 (b)-(d)-(f) for different operating conditions:* $R = 3\Omega$ *(a)-(b),* $R = 9\Omega$ *(c)-(d),* $R = 150\Omega$ *(e)-(f)*

## I.2 Row of wind turbines

### I.2.1 Isolated wind turbine vs. first and second wind turbines

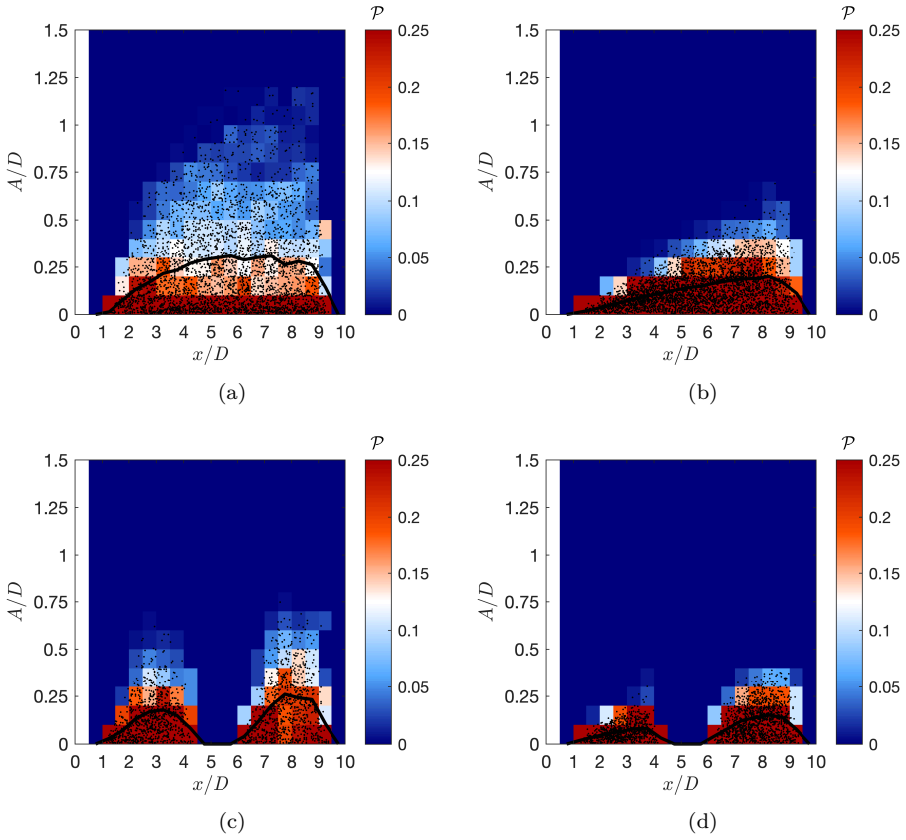



***Figure I.5:*** *Probability distribution of the wake meandering amplitude as a function of the streamwise position for the isolated wind turbine (a)-(b) and the third wind turbine (c)-(d) of the row for ABL1 (a)-(c) and ABL2 (b)-(d)*

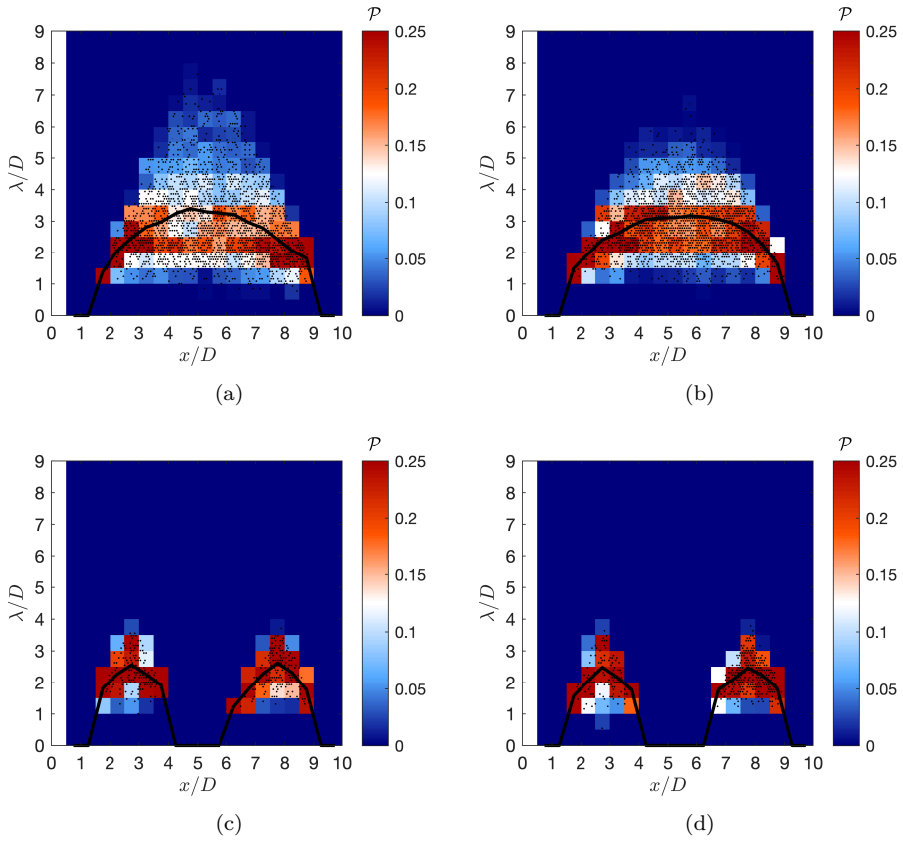



***Figure I.6:*** *Probability distribution of the wake meandering wavelength as a function of the streamwise position for the isolated wind turbine (a)-(b) and the third wind turbine (c)-(d) of the row for ABL1 (a)-(c) and ABL2 (b)-(d)*

### I.2.2 Isolated wind turbine vs. third wind turbine

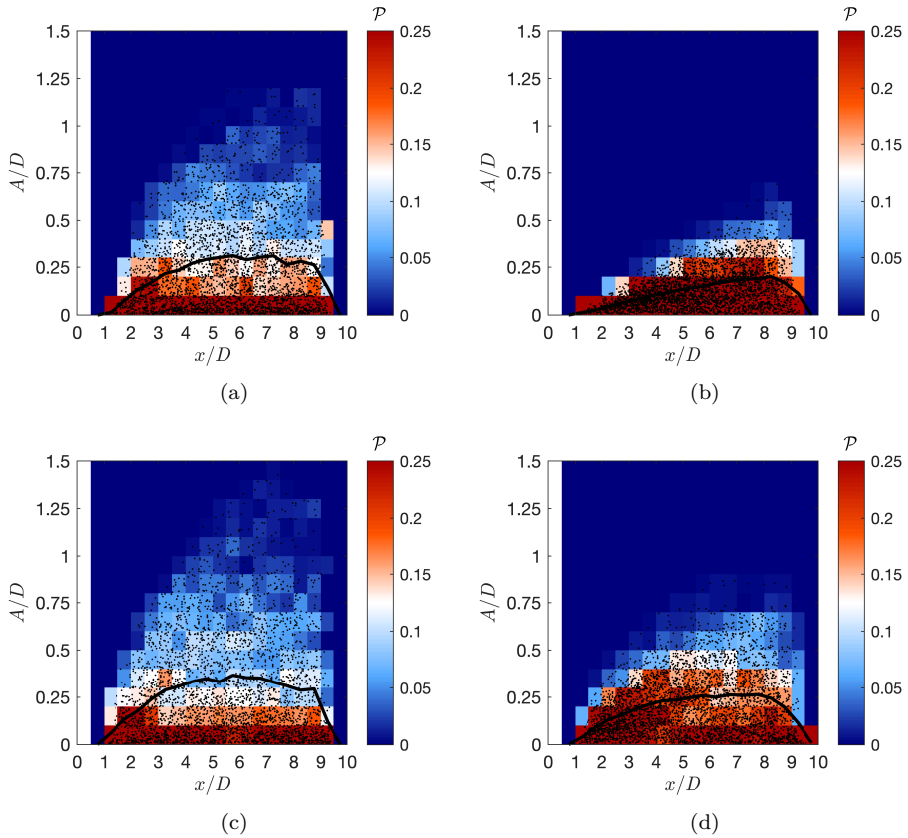



***Figure I.7:*** *Probability distribution of the wake meandering amplitude as a function of the streamwise position for the isolated wind turbine (a)-(b) and the third wind turbine (c)-(d) of the row for ABL1 (a)-(c) and ABL2 (b)-(d)*

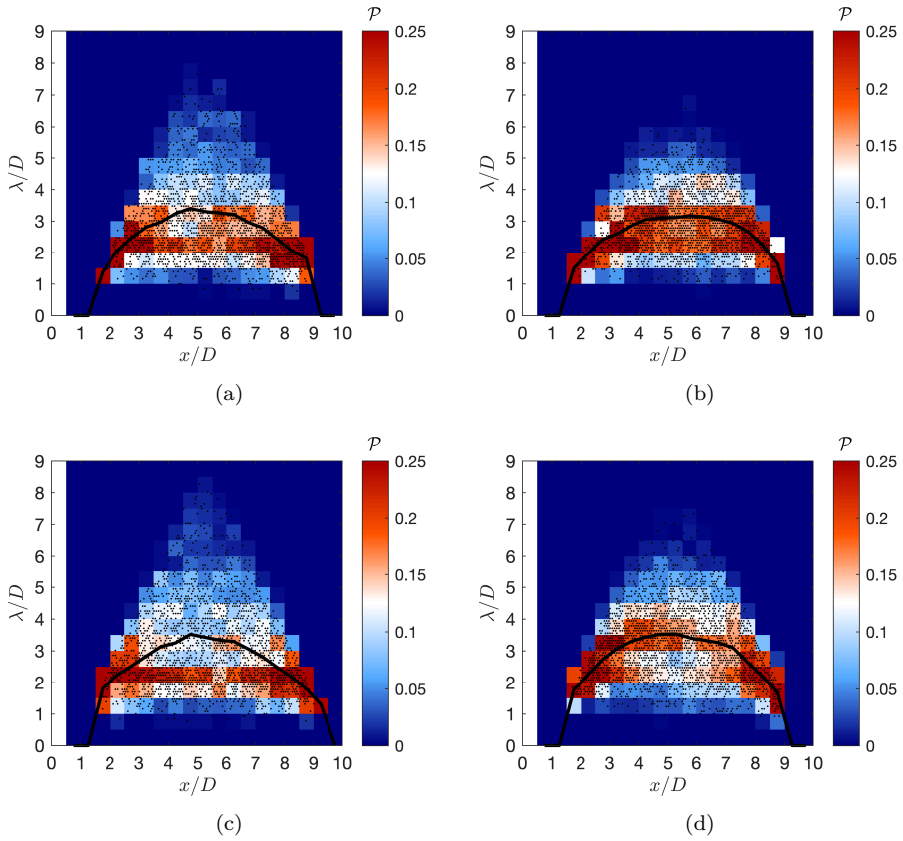



***Figure I.8:*** *Probability distribution of the wake meandering wavelength as a function of the streamwise position for the isolated wind turbine (a)-(b) and the third wind turbine (c)-(d) of the row for ABL1 (a)-(c) and ABL2 (b)-(d)*

## I.3 Wind farm

### I.3.1 Row vs. wind farm: first and second wind turbines

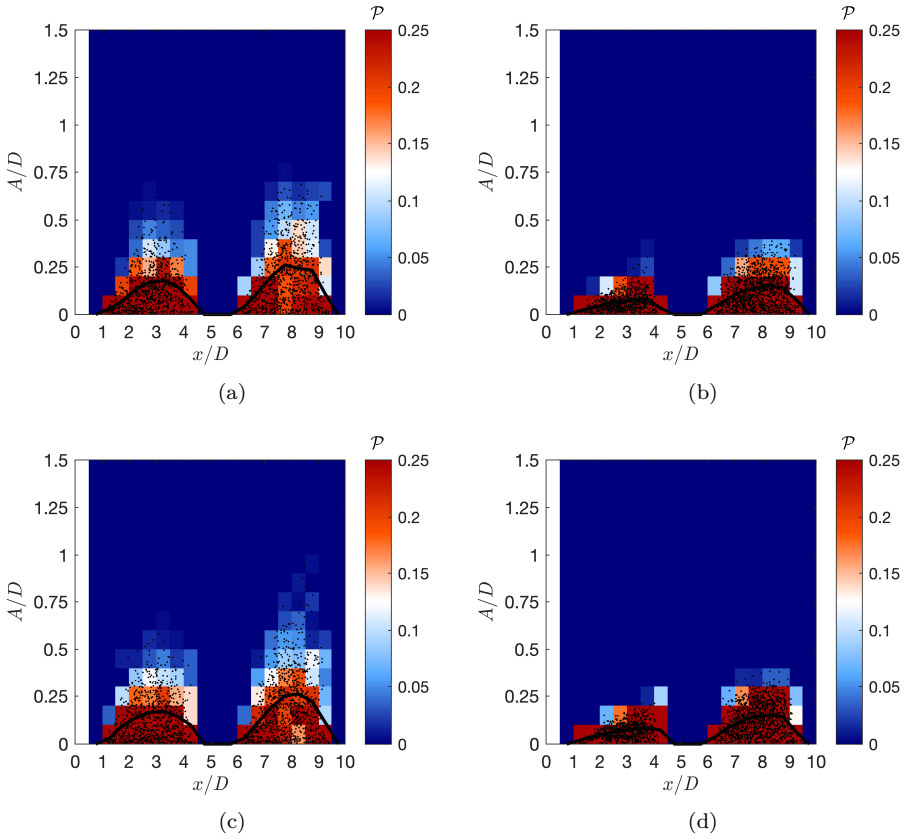



***Figure I.9:*** *Probability distribution of the wake meandering amplitude as a function of the streamwise position for the first and second wind turbines of the row (a)-(b) and for the second and third wind turbines of the central row of the wind farm (c)-(d) of the row for ABL1 (a)-(c) and ABL2 (b)-(d)*

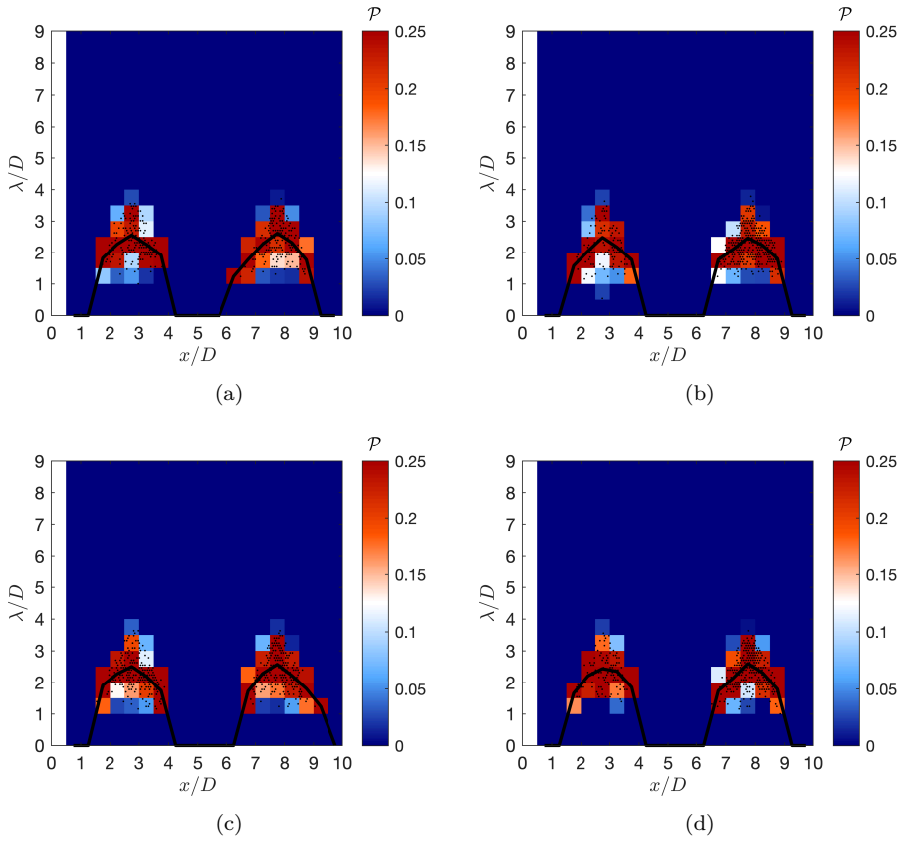



***Figure I.10:*** *Probability distribution of the wake meandering wavelength as a function of the streamwise position for the first and second wind turbines of the row (a)-(b) and for the first and second wind turbines of the central row of the wind farm (c)-(d) of the row for ABL1 (a)-(c) and ABL2 (b)-(d)*

### I.3.2 Row vs. wind farm: third wind turbine

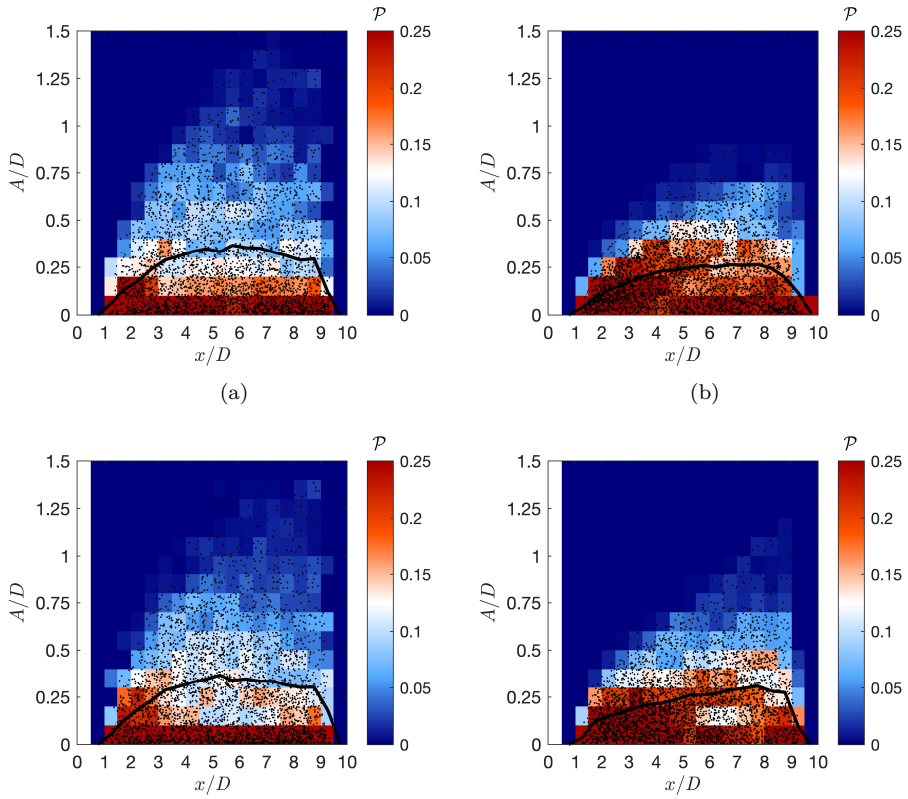



***Figure I.11:*** *Probability distribution of the wake meandering amplitude as a function of the streamwise position for the third wind turbine of the row (a)-(b) and of the central row of the wind farm (c)-(d) of the row for ABL1 (a)-(c) and ABL2 (b)-(d)*

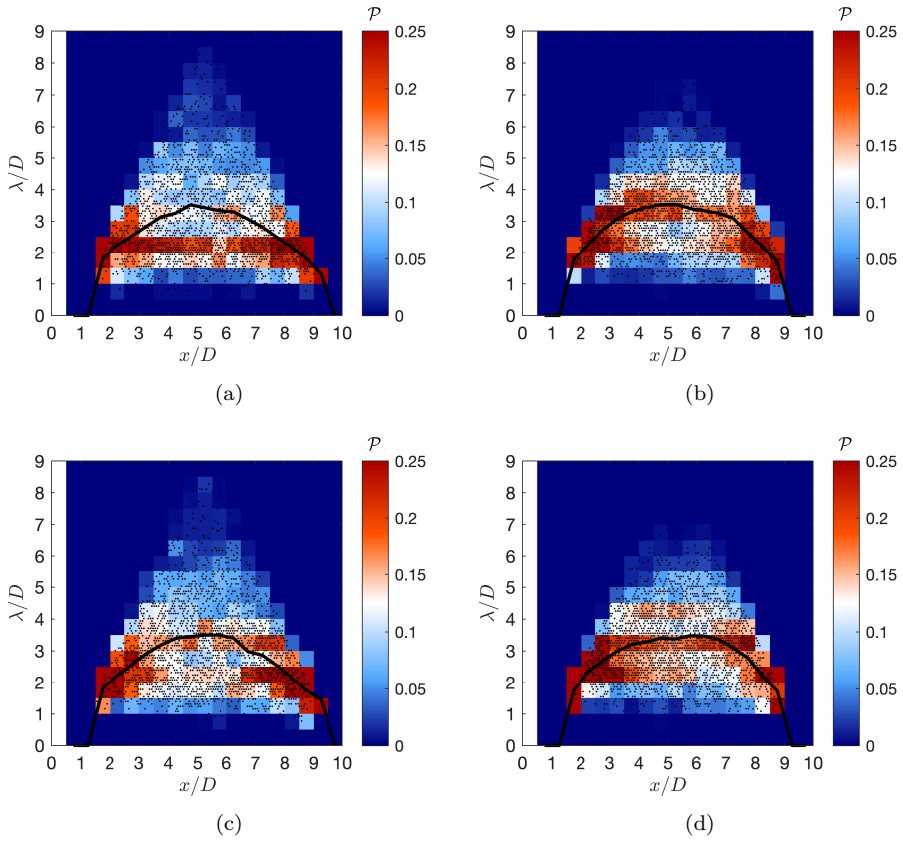



***Figure I.12:*** *Probability distribution of the wake meandering wavelength as a function of the streamwise position for the thrid wind turbine of the row (a)-(b) and of the central row of the wind farm (c)-(d) of the row for ABL1 (a)-(c) and ABL2 (b)-(d)*

### I.3.3 Porous disks

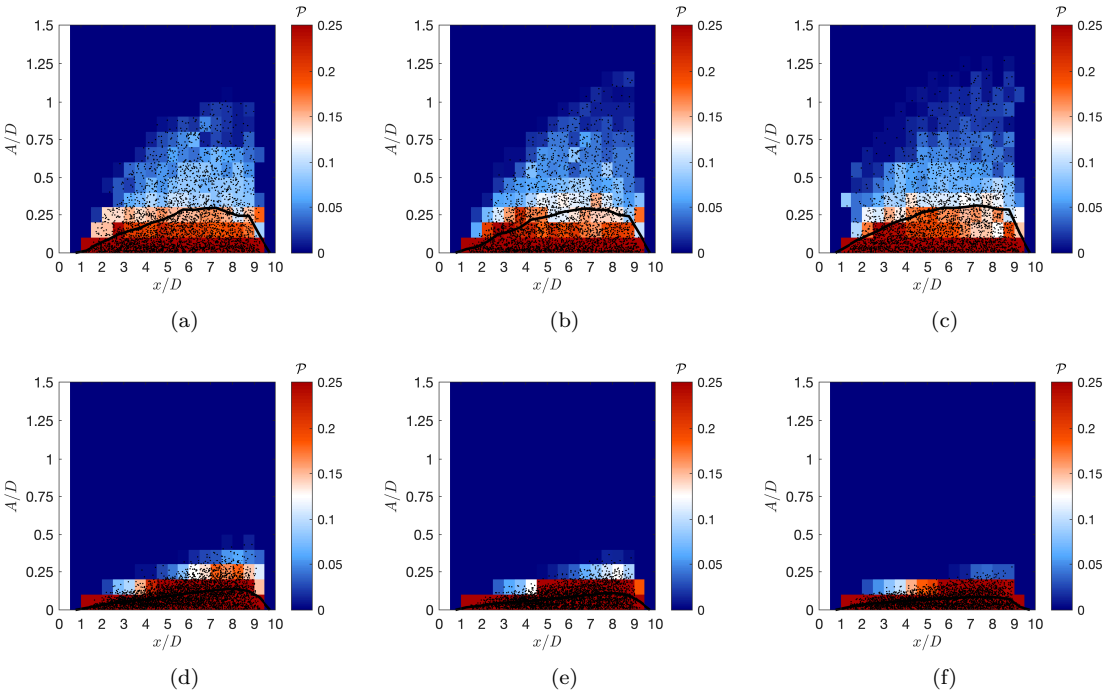



***Figure I.13:*** *Probability distribution of the wake meandering amplitude as a function of the streamwise position for ABL1 (a)-(b)-(c) and ABL2 (d)-(e)-(f) for different disk solidities: $\sigma = 56\%$ (a)-(d), $\sigma = 44\%$ (b)-(e), $\sigma = 36\%$ (c)-(f)*

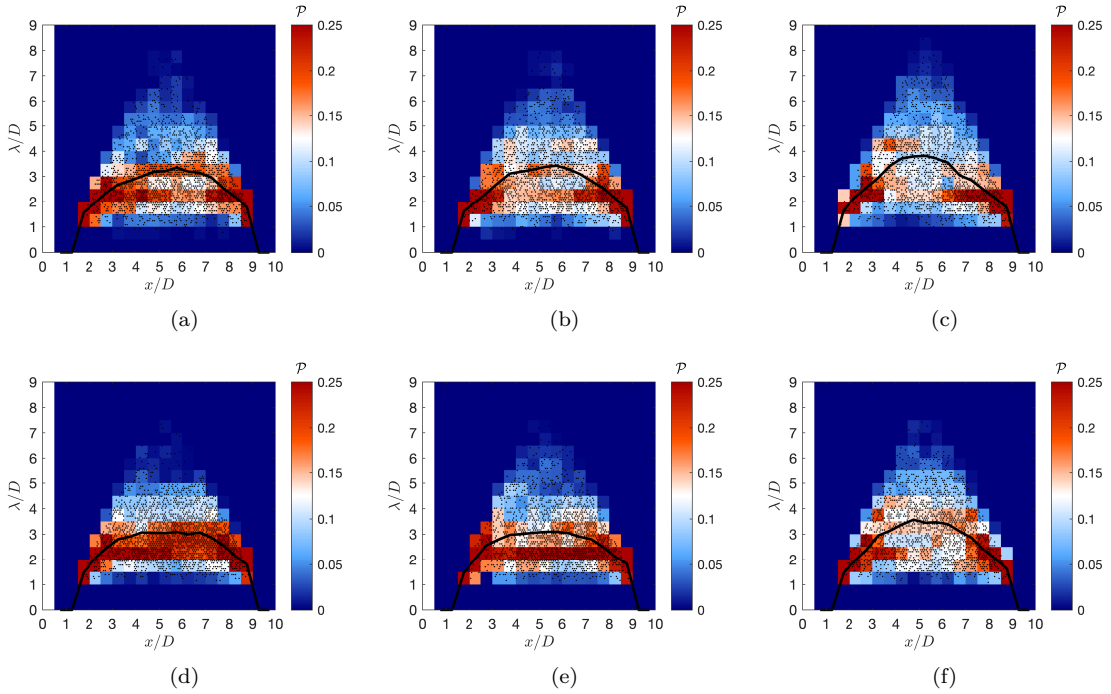



***Figure I.14:*** *Probability distribution of the wake meandering wavelength as a function of the streamwise position for ABL1 (a)-(b)-(c) and ABL2 (d)-(e)-(f) for different disk solidities: $\sigma = 56\%$ (a)-(d), $\sigma = 44\%$ (b)-(e), $\sigma = 36\%$ (c)-(f)*

Appendix J

# mPOD results for wind farm configuration

## J.1 Row vs. wind farm: first and second wind turbines

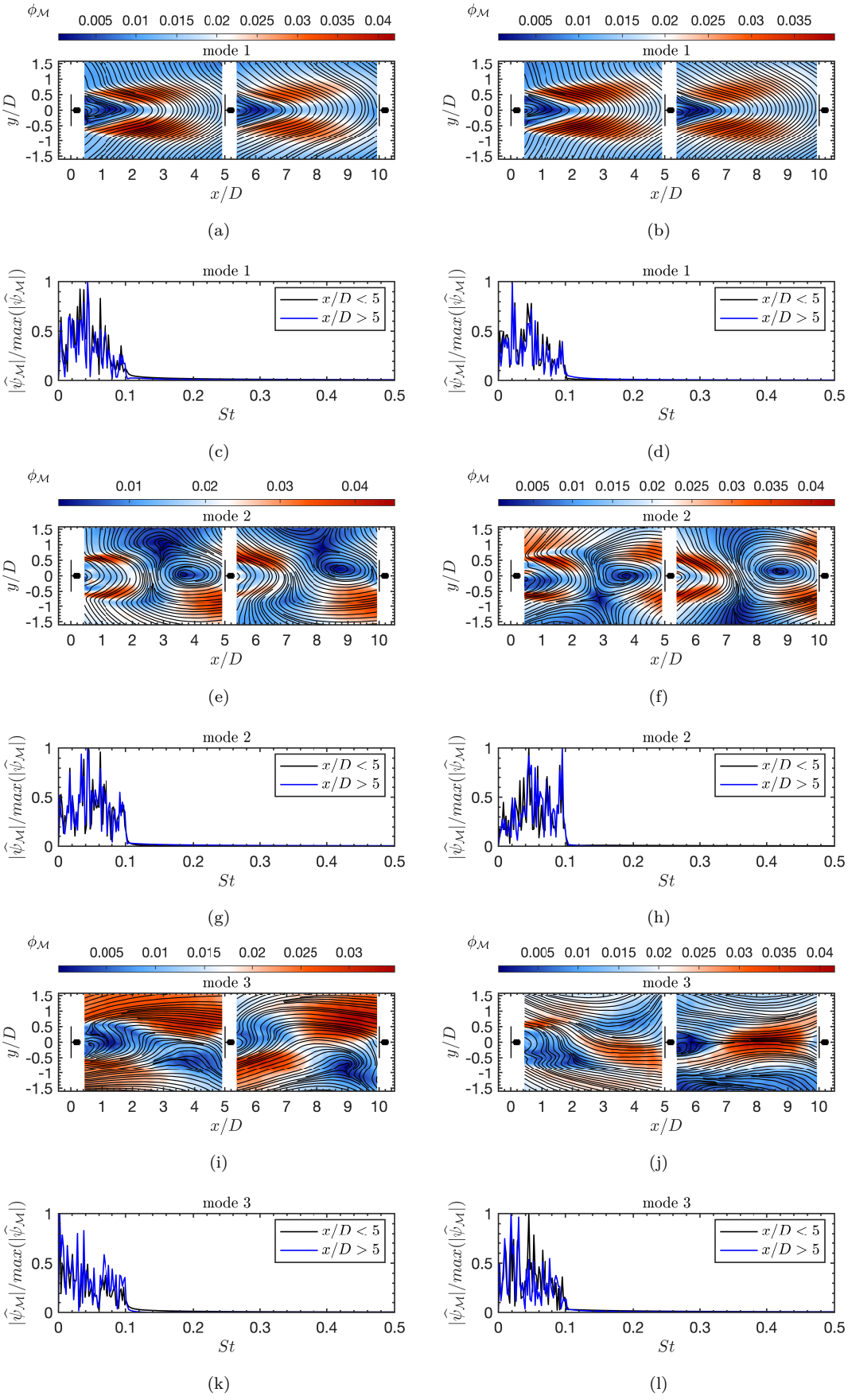



***Figure J.1:*** *Spatial structures and spectral content of temporal structures obtained from the mPOD analysis of the wake of the first and second wind turbines of the wind farm (left) and of the row of three wind turbines (right) subjected to ABL1*

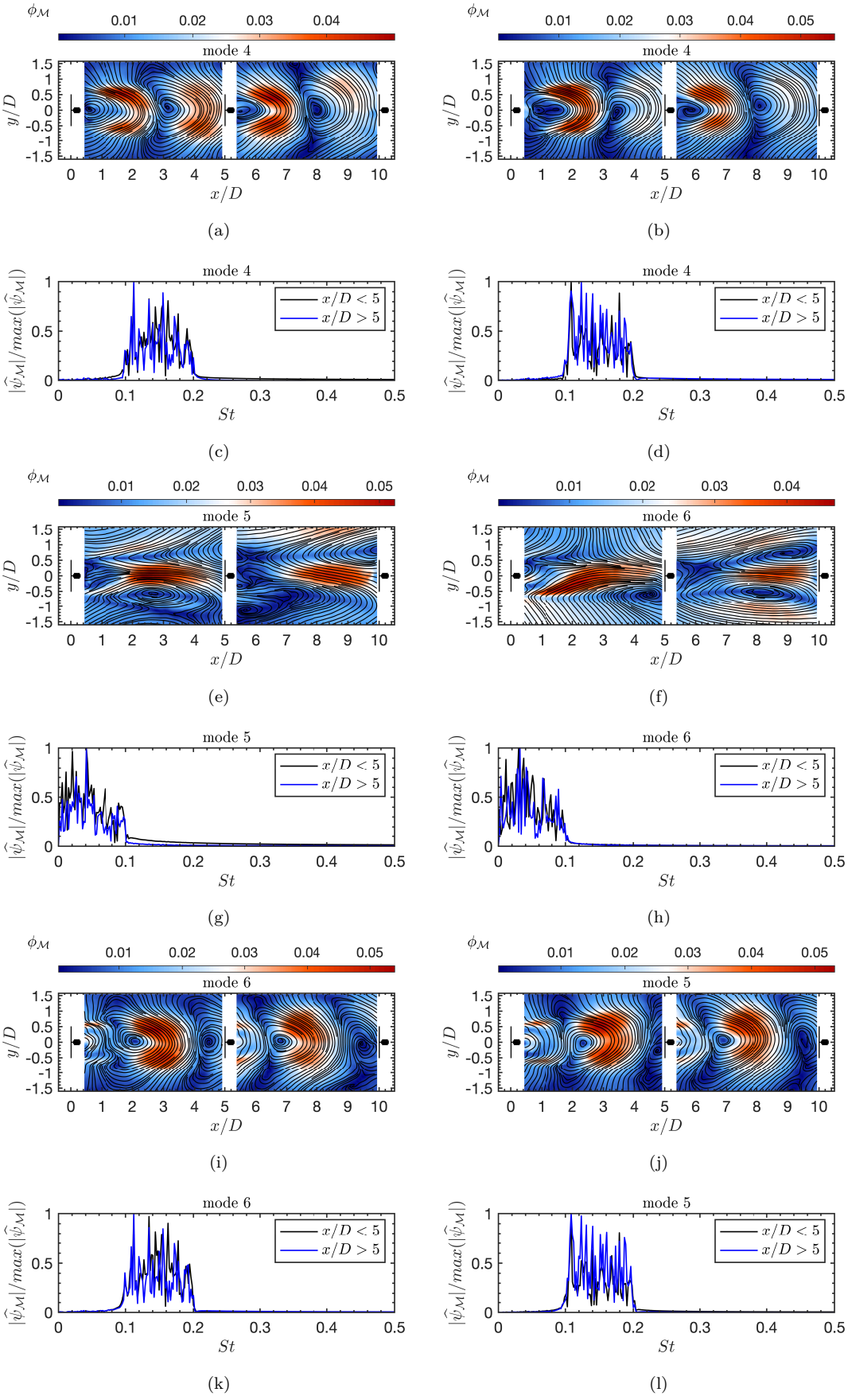



***Figure J.2:*** *Spatial structures and spectral content of temporal structures obtained from the mPOD analysis of the wake of the first and second wind turbines of the wind farm (left) and of the row of three wind turbines (right) subjected to ABL1 (continued)*

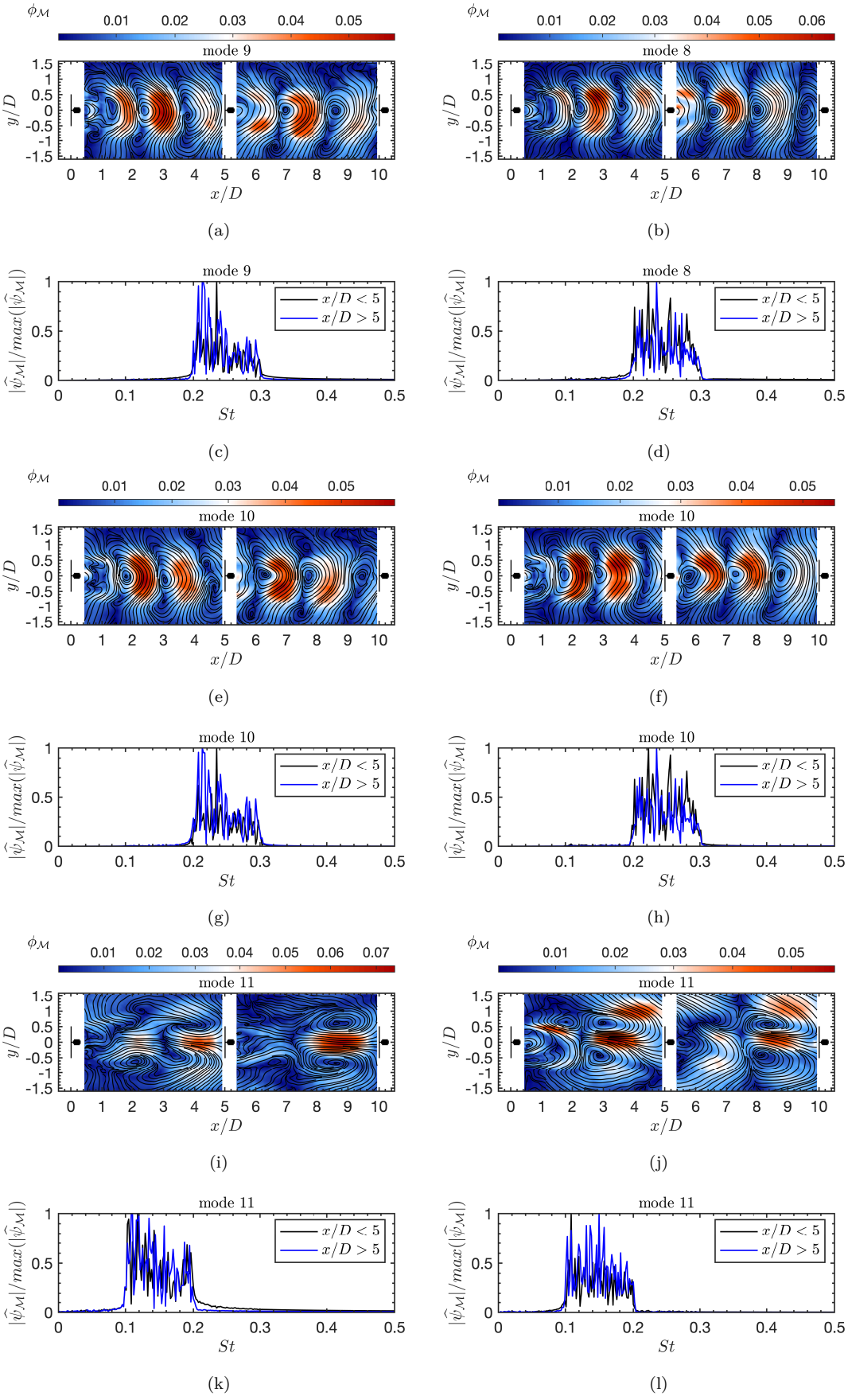



***Figure J.3:*** *Spatial structures and spectral content of temporal structures obtained from the mPOD analysis of the wake of the first and second wind turbines of the wind farm (left) and of the row of three wind turbines (right) subjected to ABL1 (continued)*

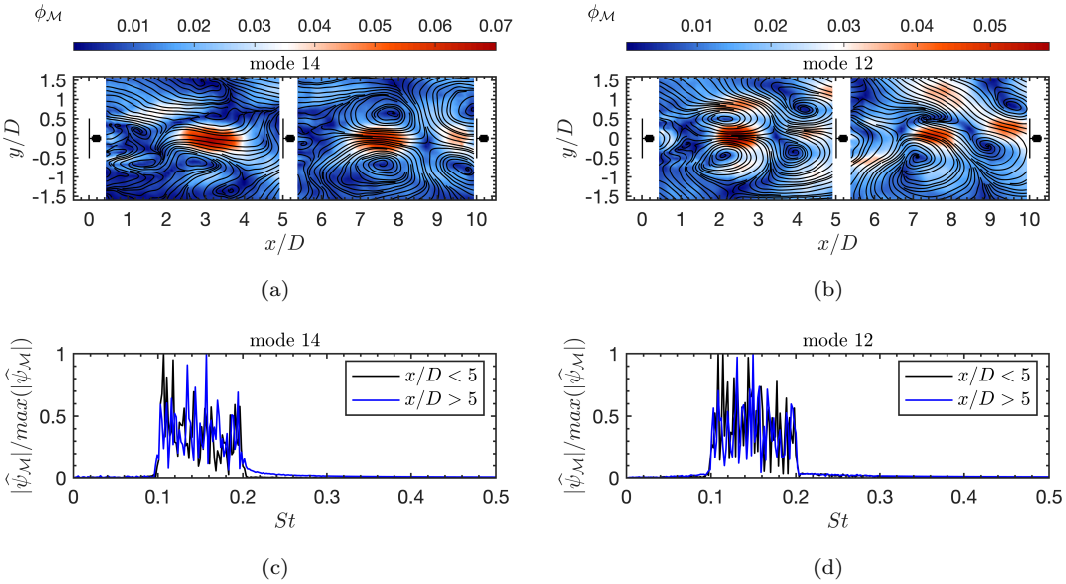



***Figure J.4:*** *Spatial structures and spectral content of temporal structures obtained from the mPOD analysis of the wake of the first and second wind turbines of the wind farm (left) and of the row of three wind turbines (right) subjected to ABL1 (continued)*

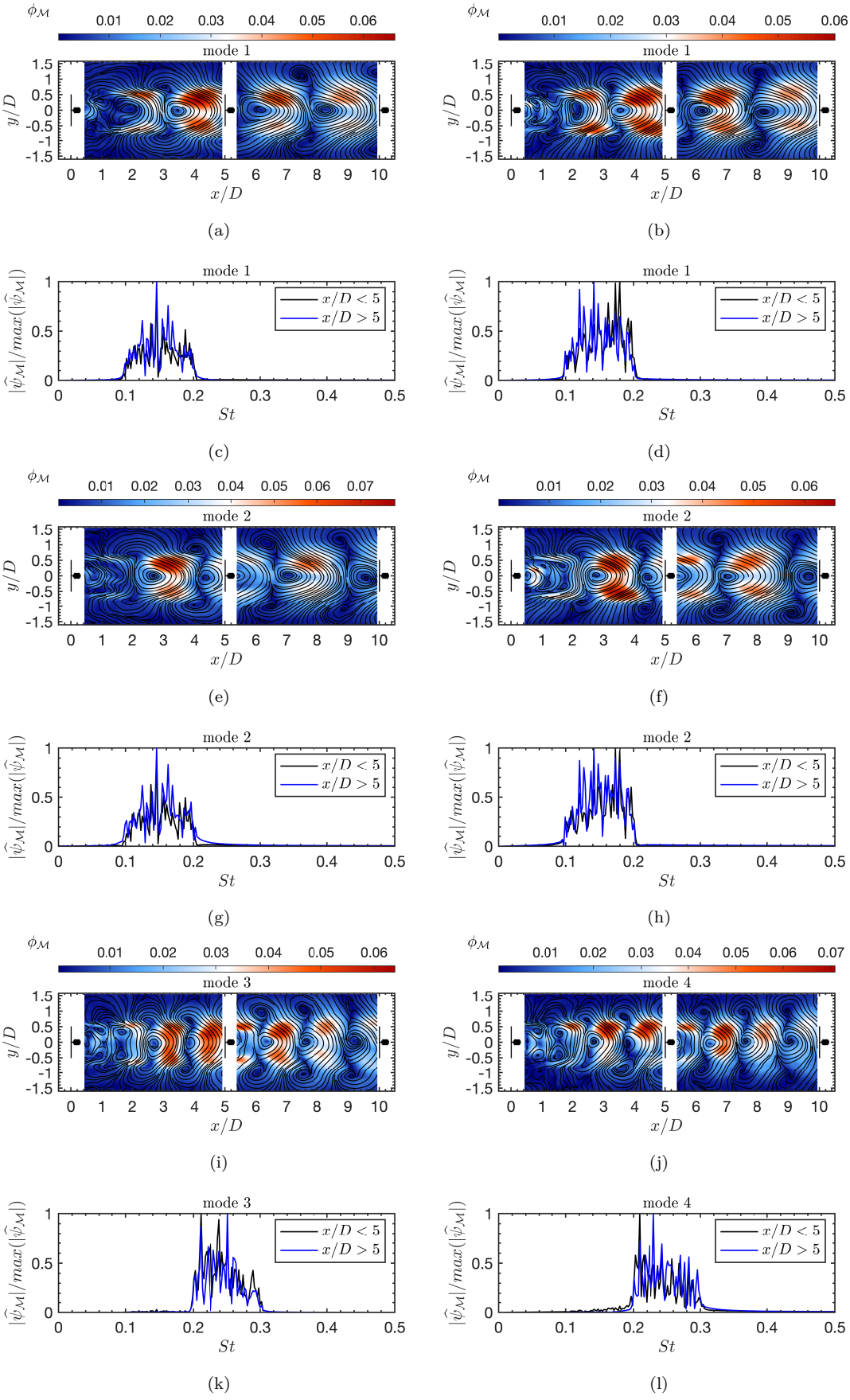



***Figure J.5:*** *Spatial structures and spectral content of temporal structures obtained from the mPOD analysis of the wake of the first and second wind turbines of the wind farm (left) and of the row of three wind turbines (right) subjected to ABL2*

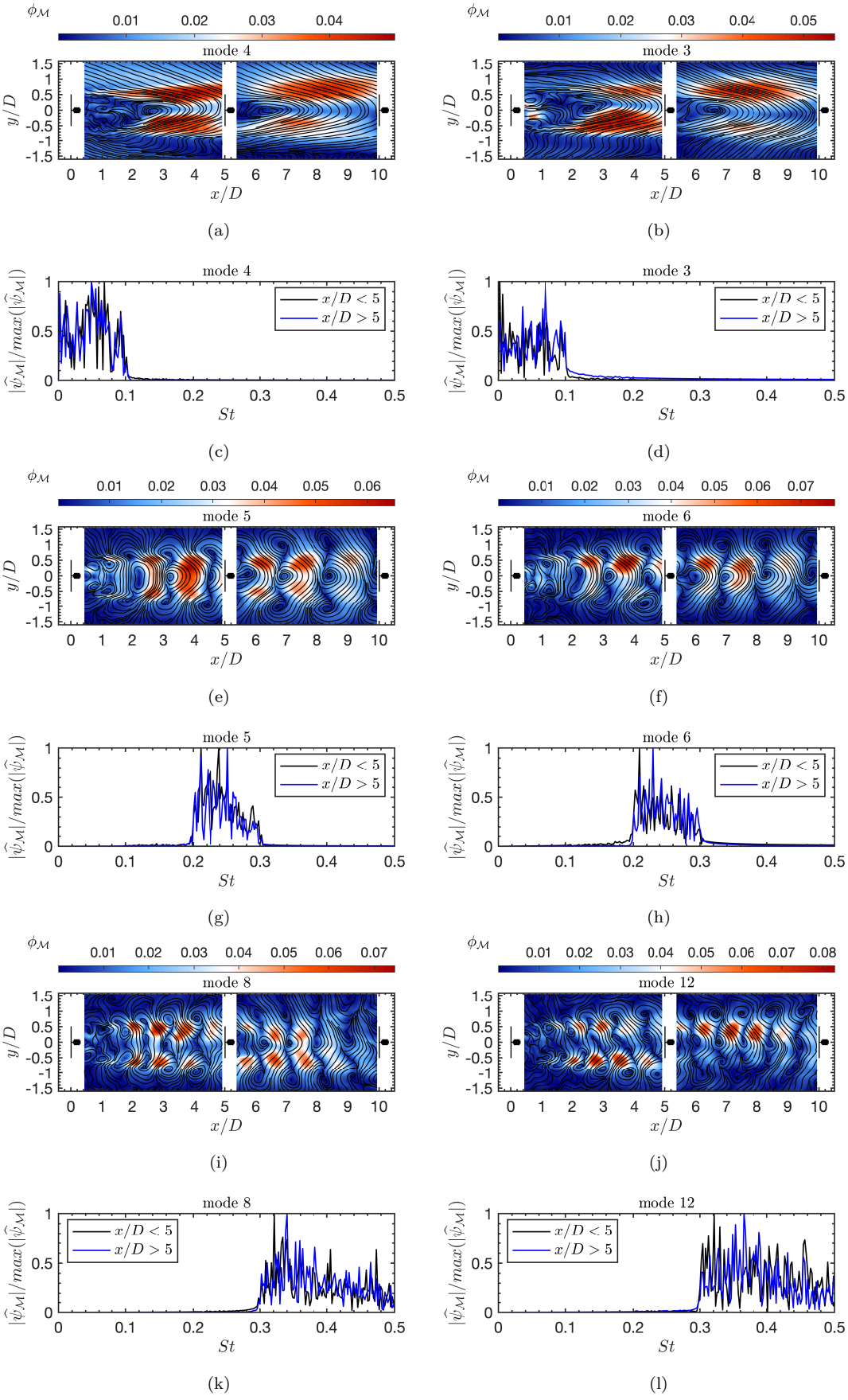



***Figure J.6:*** *Spatial structures and spectral content of temporal structures obtained from the mPOD analysis of the wake of the first and second wind turbines of the wind farm (left) and of the row of three wind turbines (right)subjected to ABL2 (continued)*

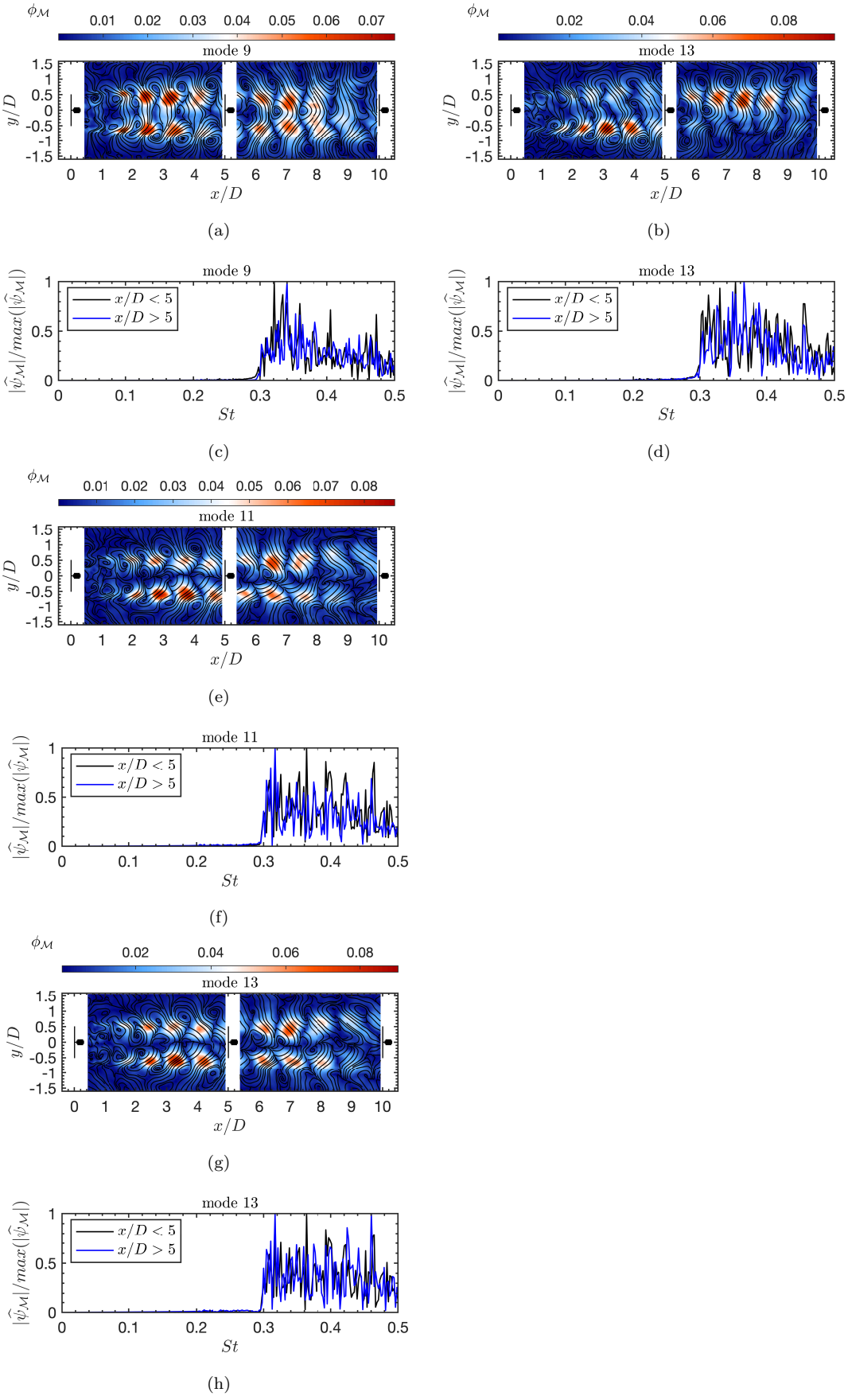
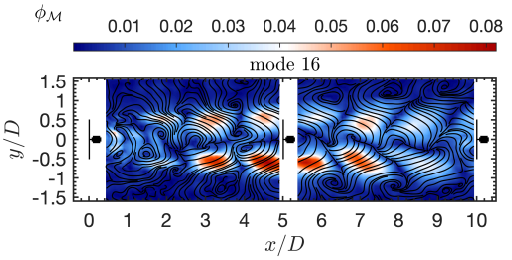
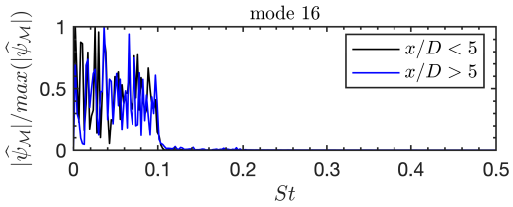



***Figure J.7:*** *Spatial structures and spectral content of temporal structures obtained from the mPOD analysis of the wake of the first and second wind turbines of the wind farm (left) and of the row of three wind turbines (right) subjected to ABL2 (continued)*




(a)




(c)

***Figure J.8:*** *Spatial structures and spectral content of temporal structures obtained from the mPOD analysis of the wake of the first and second wind turbines of the wind farm (left) and of the row of three wind turbines (right) subjected to ABL2 (continued)*

## J.2 Row vs. wind farm: third wind turbine

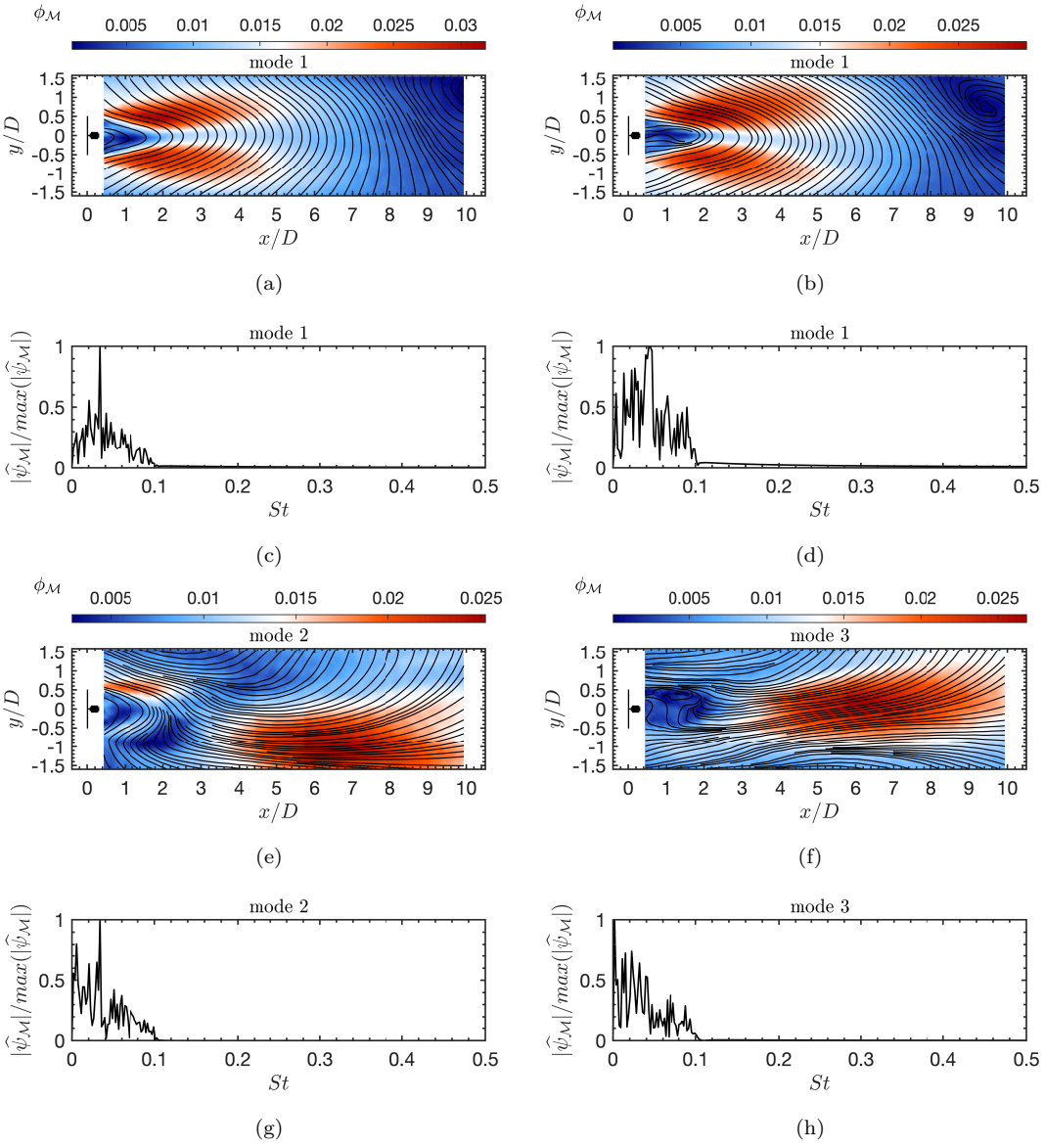



***Figure J.9:*** *Spatial structures and spectral content of temporal structures obtained from the mPOD analysis of the wake of the third wind turbine of the wind farm (left) and of the row of three wind turbines (right) subjected to ABL1*

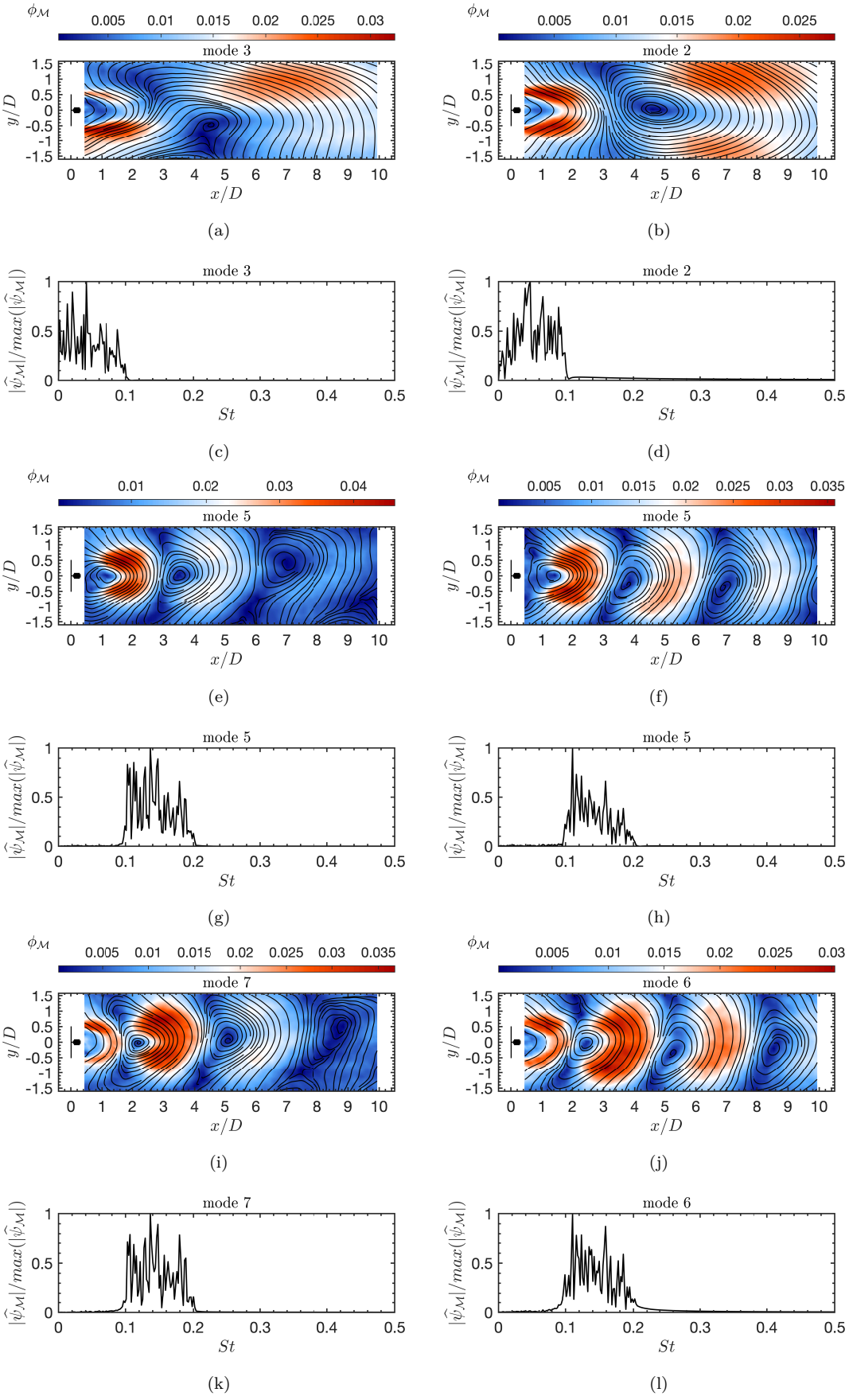



***Figure J.10:*** *Spatial structures and spectral content of temporal structures obtained from the mPOD analysis of the wake of the third wind turbine of the wind farm (left) and of the row of three wind turbines (right) subjected to ABL1 (continued)*

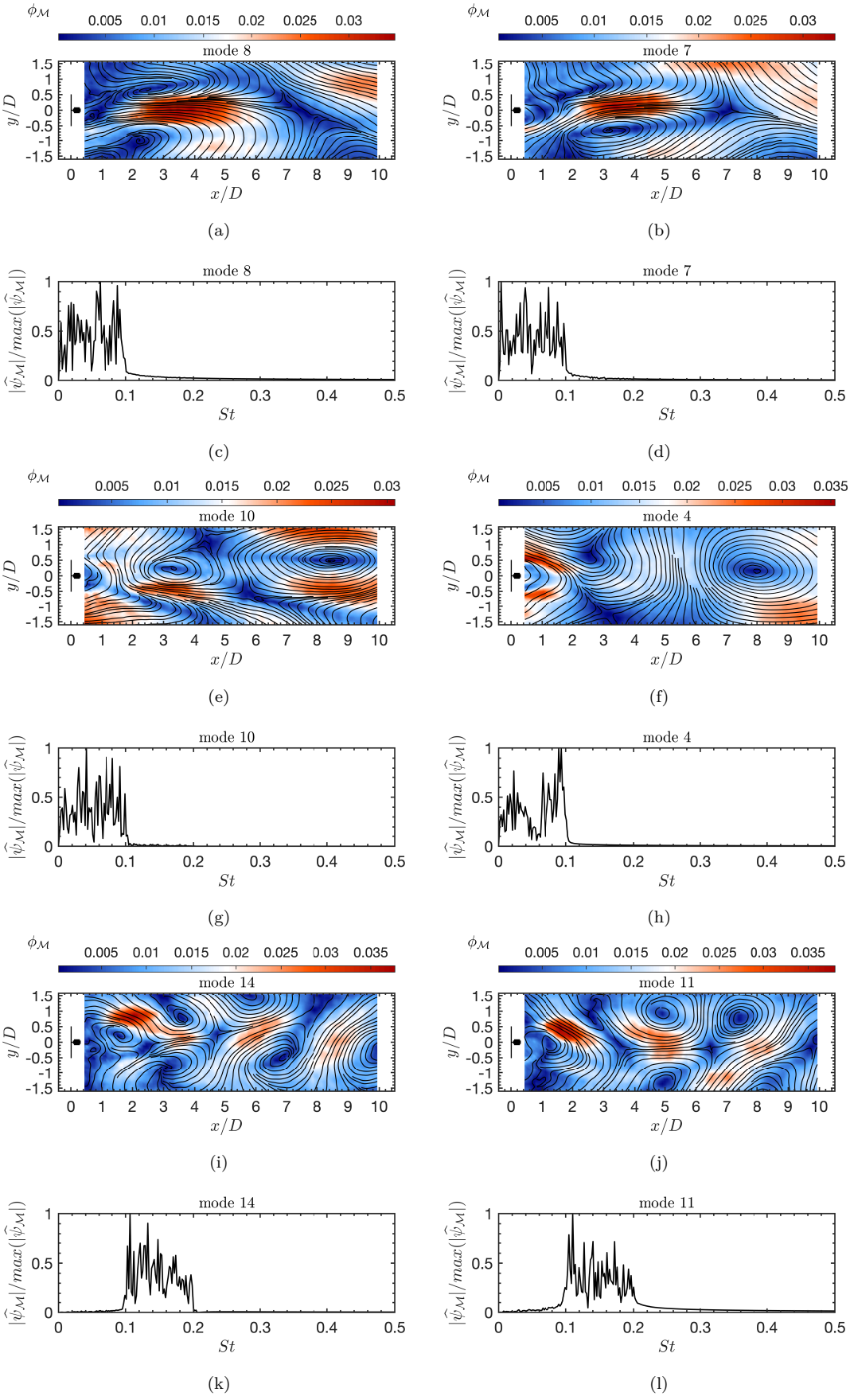



***Figure J.11:*** *Spatial structures and spectral content of temporal structures obtained from the mPOD analysis of the wake of the third wind turbine of the wind farm (left) and of the row of three wind turbines (right) subjected to ABL1 (continued)*

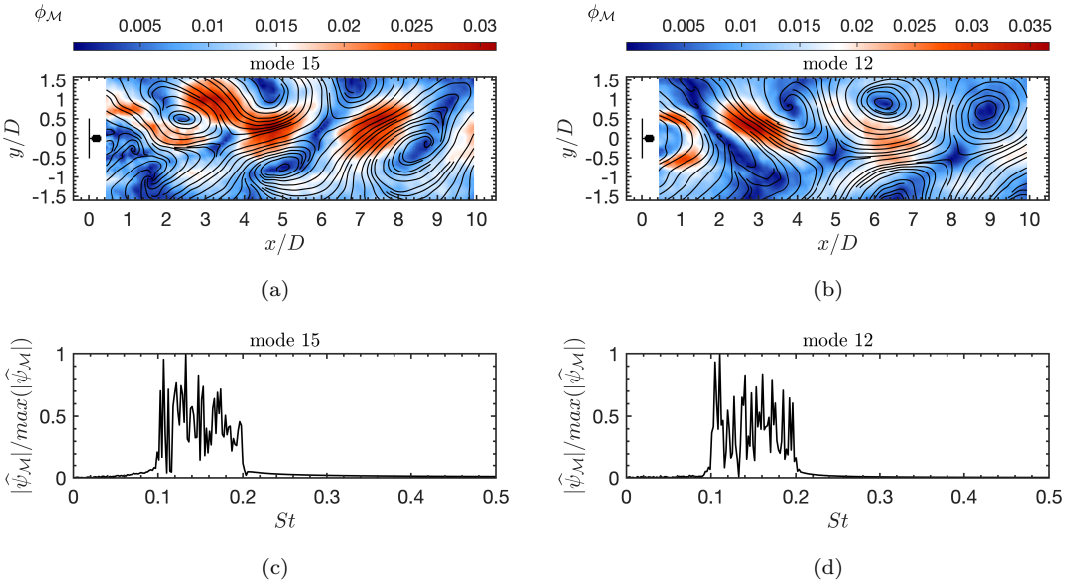



***Figure J.12:*** *Spatial structures and spectral content of temporal structures obtained from the mPOD analysis of the wake of the third wind turbine of the wind farm (left) and of the row of three wind turbines (right) subjected to ABL1 (continued)*

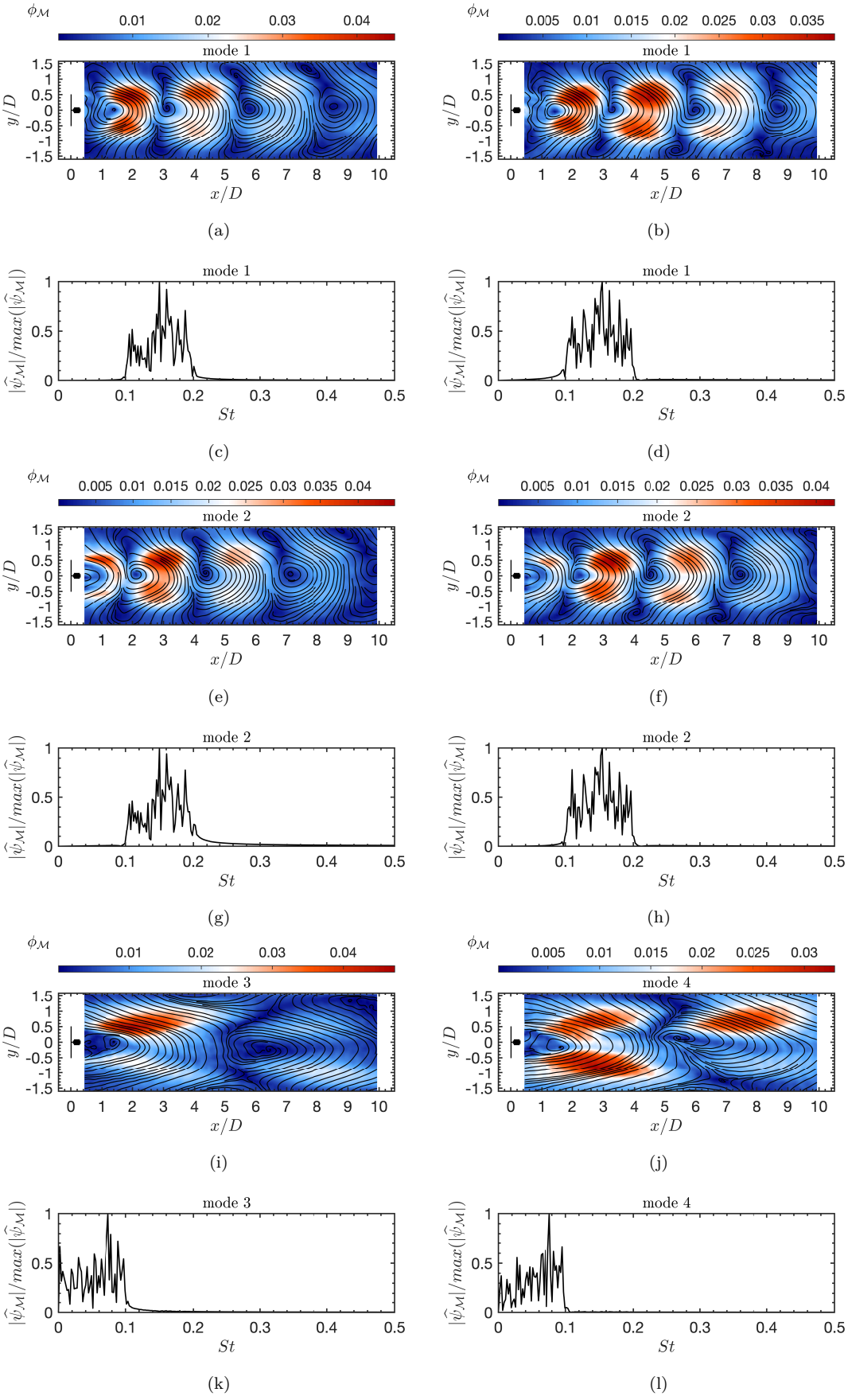



***Figure J.13:*** *Spatial structures and spectral content of temporal structures obtained from the mPOD analysis of the wake of the third wind turbine of the wind farm (left) and of the row of three wind turbines (right) subjected to ABL2*

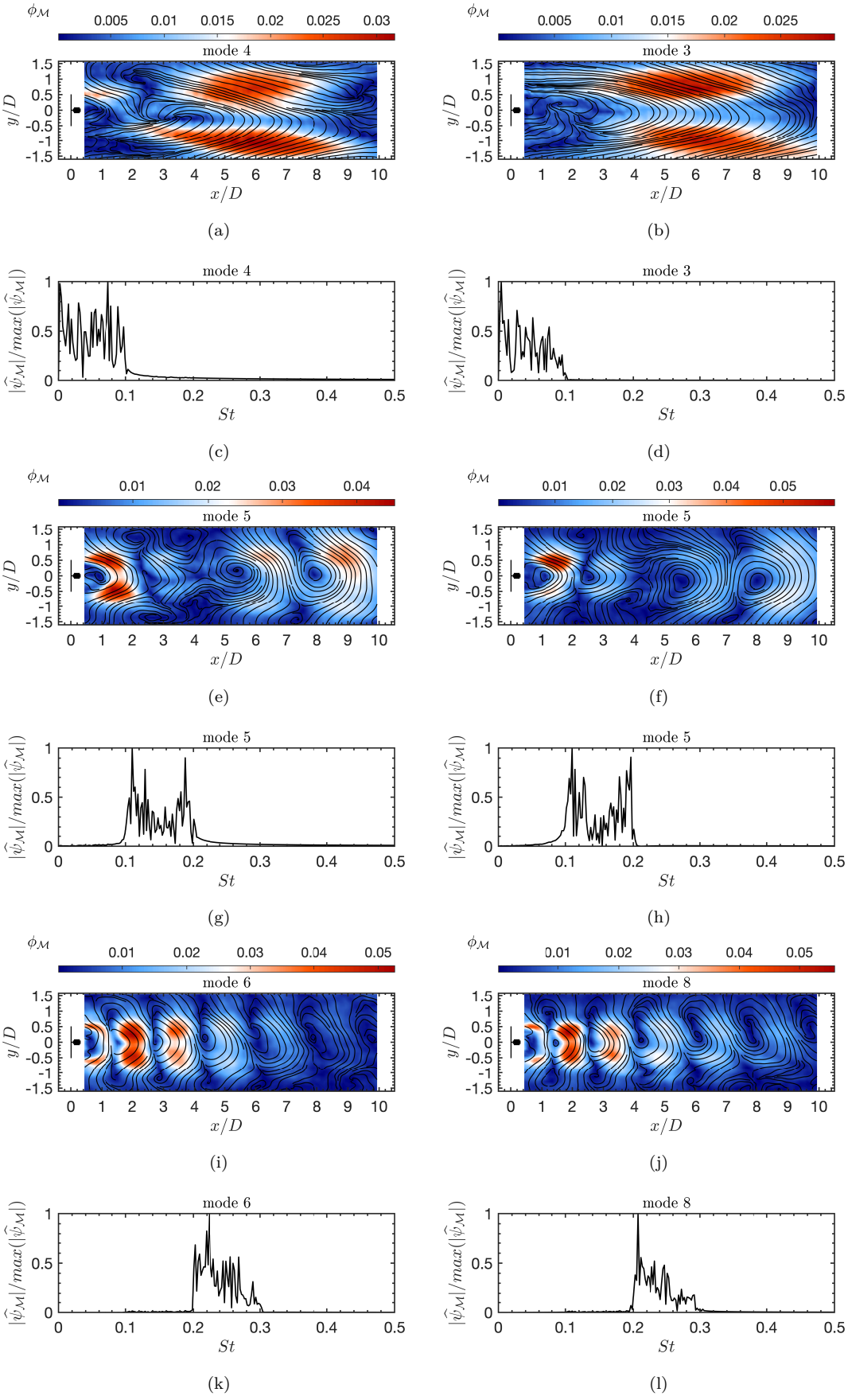



***Figure J.14:*** *Spatial structures and spectral content of temporal structures obtained from the mPOD analysis of the wake of the third wind turbine of the wind farm (left) and of the row of three wind turbines (right) subjected to ABL2 (continued)*

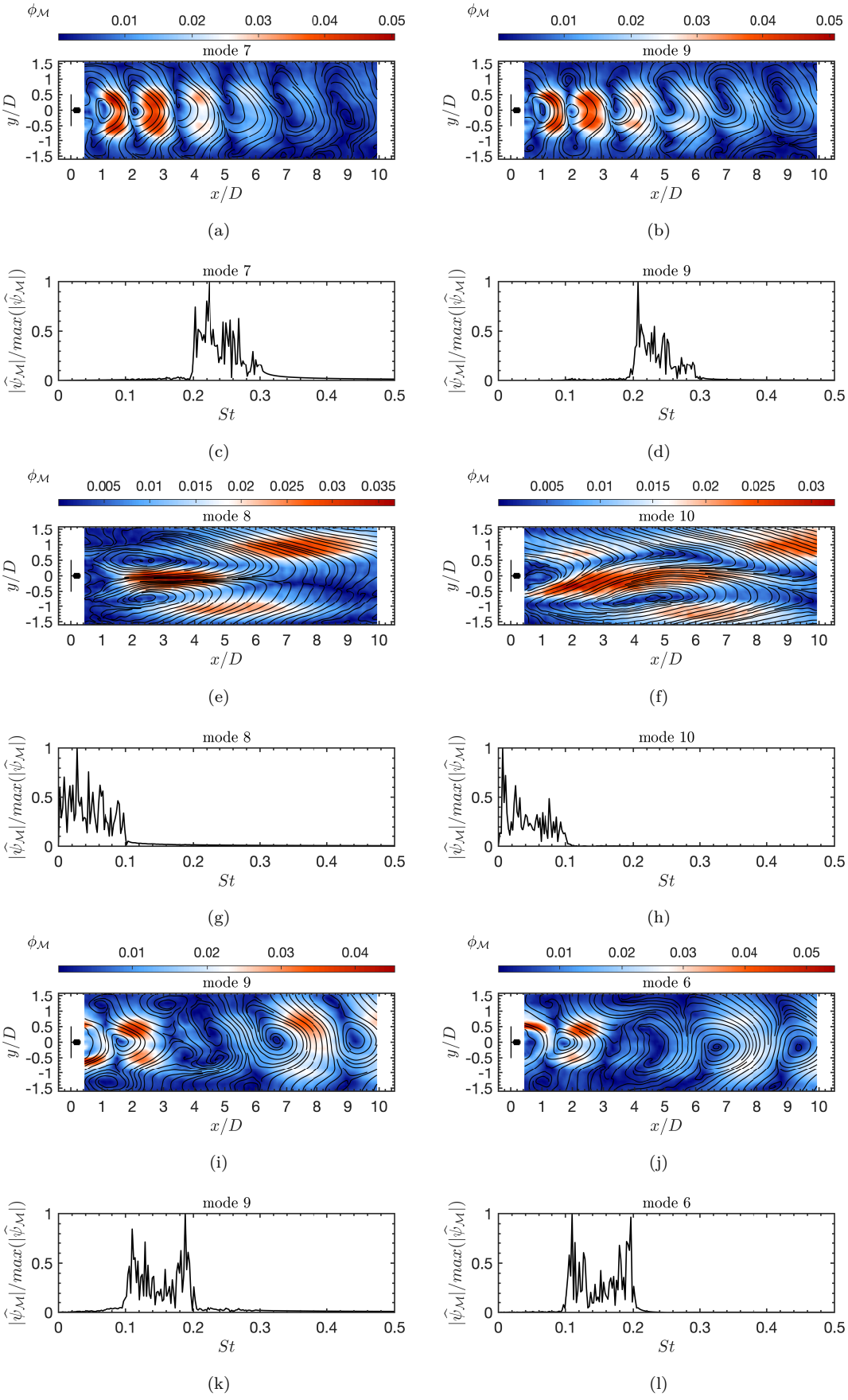



***Figure J.15:*** *Spatial structures and spectral content of temporal structures obtained from the mPOD analysis of the wake of the third wind turbine of the wind farm (left) and of the row of three wind turbines (right) subjected to ABL2 (continued)*

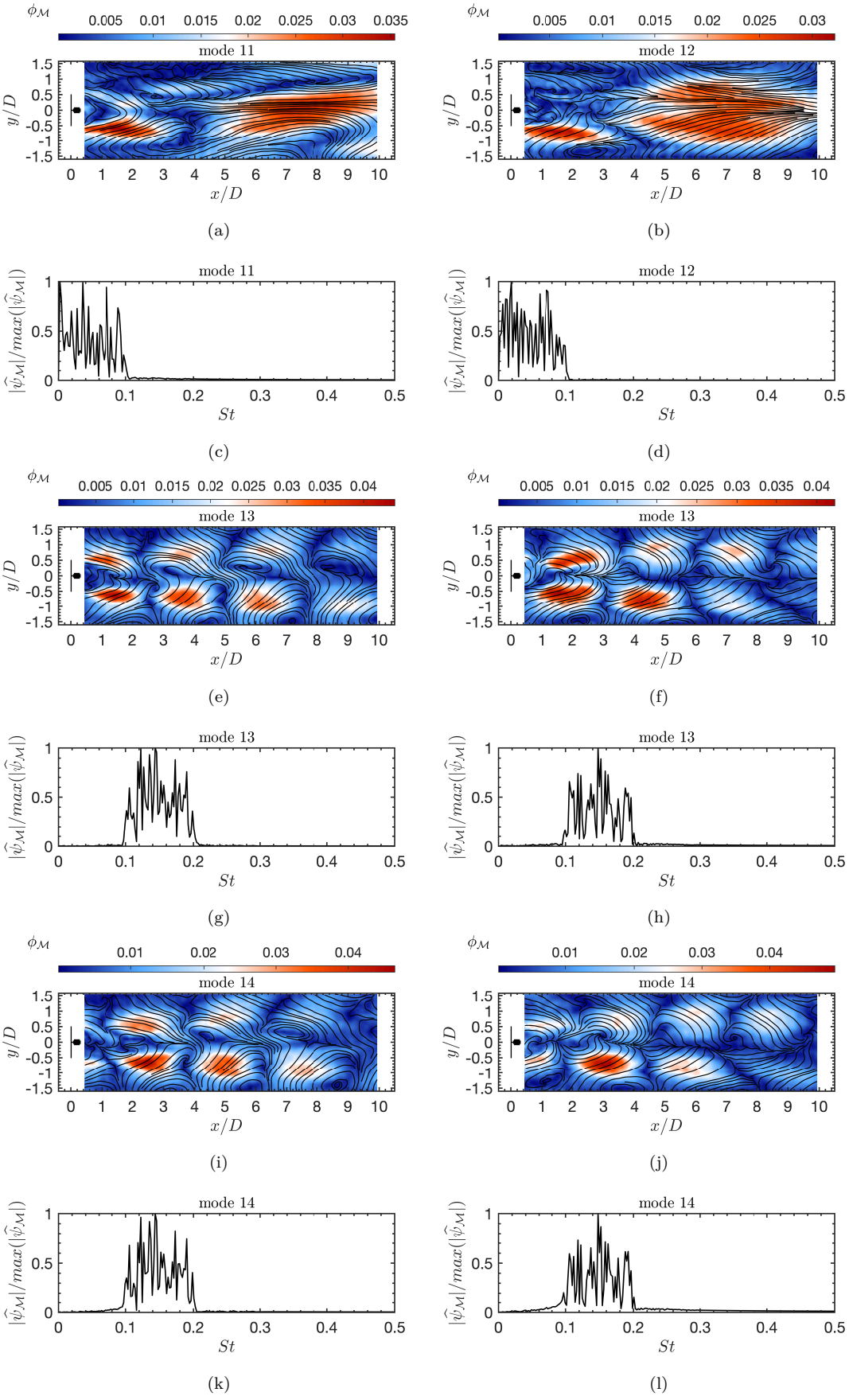



***Figure J.16:*** *Spatial structures and spectral content of temporal structures obtained from the mPOD analysis of the wake of the third wind turbine of the wind farm (left) and of the row of three wind turbines (right) subjected to ABL2 (continued)*